The influence of radiative feedback on star formation

observed by the James Clerk Maxwell Telescope Gould Belt Survey of nearby star-forming regions.

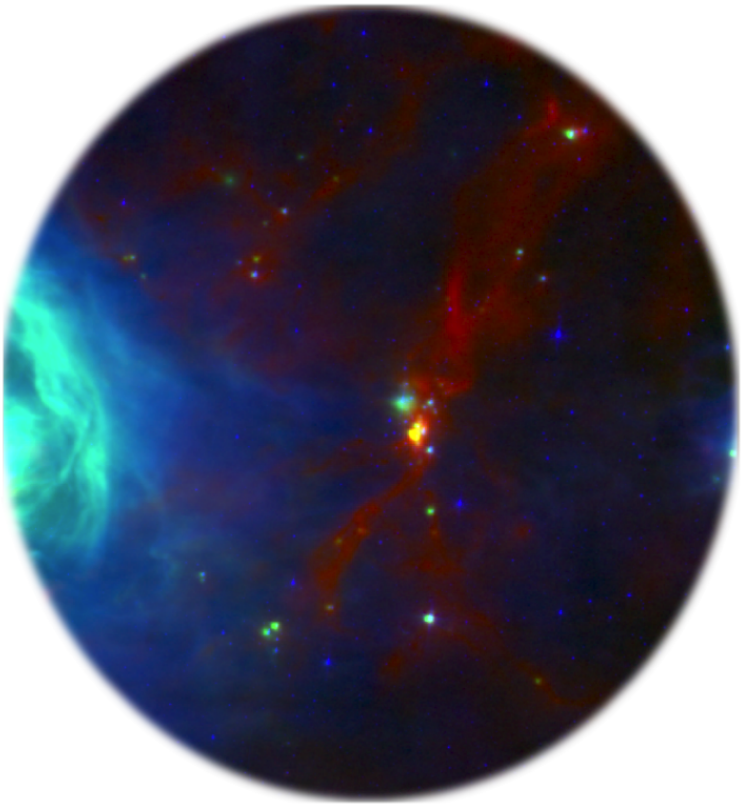

The Aquila W40 complex and Serpens South (SCUBA-2 850 μm, *Herschel* 70 μm, *Spitzer* 8 μm). Credit: CMT Gould Belt Survey/Herschel Gould Belt Survey/Spitzer Gould Belt Survey/Hatchell et al. in prep/Image created by R. Friesen.

Damian Jack Rumble

Submitted by Mr Damian Rumble to the University of Exeter as a thesis for the degree of Doctor of Philosophy in Physics, June, 2016.

I certify that all material in this thesis which is not my own work has been identified and that no material has previously been submitted and approved for the award of a degree by this or any other University.

Signed: .....

Mr D. J. Rumble

Date: .....

Abstract

The aim of this thesis is to investigate evidence of heating and radiative feedback in local Gould Belt star-forming regions. I discuss what impact, if any, radiative feedback is having on the star formation.

I primarily use Submillimeter Common-User Bolometer Array 2 (SCUBA-2) observations from the James Clerk Maxwell Telescope (JCMT) Gould Belt legacy Survey (GBS) of nearby star-forming regions. I analyse this data in conjunction with catalogues of candidate young stellar objects (YSOcs) from mid-infrared surveys with *Spitzer* IRAC and MIPS surveys.

I use the ratio of SCUBA-2 fluxes to calculate dust temperature, given a constant value of dust opacity spectral index, following the method of Reid & Wilson (2005). I employ a two-component beam (2CB) cross convolution to map the temperature of the Serpens MWC 297 region, achieving a resolution of 19.9″. I employ a convolution kernel to map the temperature of the majority of the JCMT GBS, including the Aquila W40 complex, achieving a resolution of 14.8″. I use the FELLWALKER clump finding algorithm to produce a global catalogue of 619 SCUBA-2 850 μm clumps across 26 distinct sub-regions of the JCMT GBS, calculating real temperatures where available.

I was the PI of a proposal to observe ^{12}CO 3-2 line emission, with the aim of decontaminating the SCUBA-2 850 μm band. I find ^{12}CO 3-2 line contamination has a significant impact, increasing the dust temperatures calculated per pixel, on average, by 3 K where contamination is less than 10%, and by 16 K where contamination is greater than 10% (in the Aquila W40 complex). I find evidence for 12 outflows in this region, associated with active star formation.

I also use archival VLA data to decontaminate both SCUBA-2 bands of free-free emission associated with massive star formation. Where compact free-free sources are sufficiently bright and optically thick, for example the B1.5Ve star MWC 297, their contribution can lead to prominent bright sources at the submillimeter wavelengths detected by SCUBA-2 and lower temperatures around Herbig stars.

I present published studies of the Serpens MWC 297 region and the Aquila W40 complex. In both cases I find evidence that the presence of young OB stars is raising the temperatures of nearby clumps. Examining clumps across the JCMT GBS, I find that those clumps isolated from OB stars have a mean temperature of 15±2 K, a value that is consistent with gas temperatures (Friesen et al., 2009) and Bonnor-Ebert sphere models (Kirk et al., 2006). I find no evidence of heating from embedded low-to-medium mass YSOs.

Clumps that lie within 3 pc of OB stars have a mean temperature of 21±4 K and O type stars heat clumps over the greatest range. By remodelling the heated clumps with a temperature of 15 K, I calculate that up to 10% of clumps in the JCMT GBS are no longer Jeans unstable, indicating that radiative feedback from OB stars is potentially suppressing fragmentation and allowing for the formation of more massive stars.

Contents

List of Figures

List of Tables

Declaration

This thesis contains work published as papers. Chapters 6 and 7 are primarily based on papers that have been published in the Monthly Notices of the Royal Astronomical Society (MNRAS). These are Volume 448, pp. 1551-1573, April 2015 (DOI: 10.1093/mnras/stu2695) and Volume TBC, pp. TBC-TBC, June 2016 (DOI:10.11570/16.0006). I am first author on these papers and my co-authors partake supervisory (JH, HK, TJ, DJ), data reduction (DN, DJ, HBF, JB, JH, TJ, DSB, JCM, JEP, CS, SWS, MJC, MF, CQ, ST) roles. These papers also form substantial parts of Chapter 2, 3, 4 and 5. Chapter 4 makes use of archival data, the source of which I explicitly state when they are introduced.

Acknowledgements

Over the four years that have gone into producing this thesis I have developed a number of professional and personal relationships that have aided my research and personal development. I seek to acknowledge some of those people here.

My supervisor, Dr. Jenny Hatchell, rightly deserves foremost credit for getting me to this stage. At times the PhD has been a real roller coaster of emotions; however, I am firmly of the belief that under Jenny's supervision I have developed immeasurably and in ways I did not foresee or even believe to be possible. The success that we have enjoyed over the last four years gives me the confidence to chart my own path in the years ahead.

In addition to Jenny, Dr. Chris Brunt, Prof. Alistair Hibbins, Dr. Ana Duarte-Cabral and Dr. Nina Meinzer (University of Exeter) have all played their part in supporting me throughout this process. Furthermore, collaborators have offered great insight and opportunity for me to expand my horizons and gain inspiration from their work, and I am very grateful for the time they have taken to support mine. I would like to acknowledge the roles of Dr. Emily Drabek-Maunder (Imperial), Dr. Kate Pattle (UCLAN), Dr. Helen Kirk (McMaster) and Dr. Tim Jenness (LSST) in this regard.

Out of the many people I have met along this journey the following are of note. Dr. Tom Haworth for his networking skills. Dr. Alex Pettit for his healthy cynicism and whit. Dr. Tom Goffrey for his insight into how unbelievably tedious numerical plasma physics is. Dr. Andrew McLeod for teaching me how to use a semi-colon. And Dr. Alex Pearce for his insight on how to manage expectations when writing papers.

Finally a shout out to my various non-physics house mates. Bas Verbruggen, Lewis Roland Elliot, Emily Birch, Charlie Shipperly, Katie Cassidy, Lilli Springer and Pizza Chow. Being able to come home each day and talk about something other than work really allowed me to keep my sanity and my feet rooted in the real world.

Damian J Rumble
Exeter, U.K.
30th June 2016

1 Introduction

"From Earth it appears as a warm, friendly ball. An integral part of everything living. But up close, it's a churning solar furnace that spouts solar flares with an atmosphere that's constantly changing, and explosive. Little wonder then that our star, the Sun, has been the focal point of scientific investigation for centuries"[1]. Humanity's understanding of what the Sun is and how it was formed has changed and developed considerably over millennia. But, for what is arguably the single most important astrophysical body to life on Earth, many scientific questions remain about the mechanisms that govern its formation, and by association, our own.

The science behind star formation has proceeded down connected, but ultimately different approaches. Authors such as Larson (1969), Shu (1977); Shu et al. (1987), Padoan & Nordlund (2002), Bate (2009) and many others have all led with a theory based approach, looking to simulate the stages of the star formation process by numerical means. Simulation has provided an incredible insight into the mechanisms and evolution of star formation in a way that the limitations on today's instrumentation mean they cannot. However, much of the theory is often idealised. Authors such as Myers & Benson (1983), Lada & Wilking (1984), Benson & Myers (1989) and Ward-Thompson et al. (1994) were some of the first to study the earliest phases of star formation. Adams et al. (1987), André et al. (1993), Evans et al. (2001), Shirley et al. (2002a), Young et al. (2003) and Robitaille et al. (2006) built on these preliminary studies to model observations of star formation.

Much of this thesis is centred around the observational discipline. As a member of the James Clerk Maxwell Telescope (JCMT) Gould Belt legacy Survey (GBS), I predominately use submillimeter Common-User Bolometer Array 2 (SCUBA-2) observations of nearby star-forming regions (Ward-Thompson et al., 2007). SCUBA-2 observes at 450 and 850 μm. Typically this frequency range encompasses thermal continuum emission from cold (approximately 10 - 20 K)

[1] 'Voyager', Solarstone (Pure recordings)

interstellar silicate and graphite dust that is found in great abundance in giant molecular clouds (GMCs). As some of the most massive structures in the Galaxy, GMCs have long been associated with sites of star formation. Recent infrared (IR) surveys, such as the Two Micron All Sky Survey (2MASS, Cutri et al. 2003) and the *Spitzer Space Telescope* legacy survey (Figure 1.1 upper left), have detected numerous pre-main sequence (PMS) stars in high extinction environments (Evans et al., 2003).

Radio telescopes like the JCMT, the Institute for Radio Astronomy in the Millimeter Range (IRAM) telescope and the *Herschel Space Telescope* (Figure 1.1 upper right) have been used to resolve the earliest stages of star formation on the scales of individual cores (Andre et al. 2000, André et al. 2010 and Salji 2014). Whilst starless, cores can be considered to be isothermal down to densities of $10^{-12}\,\mathrm{g\,cm^{-3}}$ (Larson 1969). However, Masunaga & Inutsuka (2000) use one-dimensional radiative transfer to show that the accretion luminosity from a protostar can heat gas by an order of magnitude out to hundreds of AU. Simulations, including those by Matzner & Levin (2005), Krumholz (2006b), Bate (2009), Offner et al. (2009) and Hennebelle & Chabrier (2011), have suggested that this radiative feedback, can have a significant impact on the stability of GMCs, potentially having an important role in fragmentation and the star formation process. At the same time methods have been developed by which the temperature of dust can be calculated from multiple submillimeter wavelength observations of star forming regions (Reid & Wilson, 2005), allowing regions of heating to be directly observed.

This thesis further develops observational techniques for extracting dust temperatures from SCUBA-2 data, with the aim of investigating whether there is observational evidence of radiative feedback from an existing generation of stars, influencing the formation of a subsequent generation, as has been suggested in simulations by Matzner & Levin (2005) and Krumholz (2006b), for example. I build on the work of Hatchell et al. (2013) who use the ratio of SCUBA-2 fluxes to calculate dust temperatures of the Perseus NGC 1333 region, and find evidence of raised dust temperatures associated with a population of young stellar objects (YSOs).

1.1 How do stars form?

Star formation describes how material left over from the formation of the universe, and previous generations of stars, transforms from a cold, dispersed and low density state, into a hot, high density and highly ordered state. It is a process that takes place between scale sizes of many parsecs to the size of individual stars, and is largely dictated by two classical forces, thermal motion and gravity. A typical low mass star will spend 10 Myrs as a YSO, equivalent to 0.1% of its overall lifetime.

1.1.1 Giant molecular clouds

On the largest scales, stars form from GMCs that are largely confined to the spiral arms of the Galaxy (Cohen & Kuhi 1979, Dame et al. 1987). These are some of largest structures in the Galaxy with masses ranging between 10^4 and $10^6\,\mathrm{M_\odot}$, and a scale size between 10 and 100 pc (Stark & Blitz 1978, Sanders & Mirabel 1985). These regions are exceptionally cold as they are not

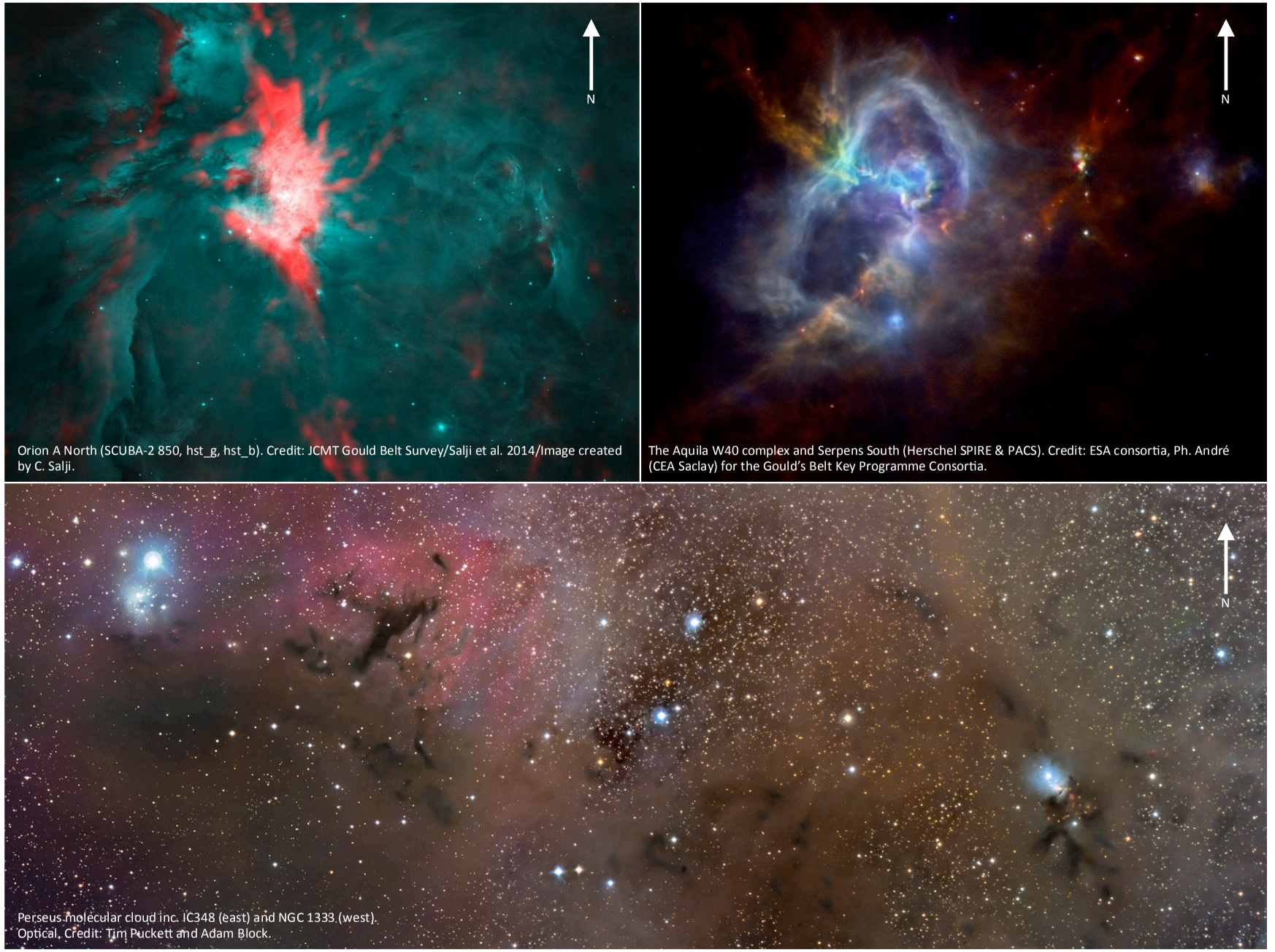

Figure 1.1: Examples of star forming regions in the Gould Belt. Upper left) the Orion A North massive filament mapped in *Spitzer* and SCUBA-2 bands. Upper right) the Aquila W40 complex mapped in *Herschel* SPIRE and PACS bands. The western star clusters trace the Serpens South filament. Lower) an optical image of the Perseus molecular cloud, detailing a number of bright, massive stars and darkened streaks of high extinction associated with dusty, star forming regions. Credit is given for each respective image.

visible at either optical or IR wavelengths, and instead have to be observed at longer wavelengths, corresponding to a temperature of approximately 10 K (Benson & Myers 1989, Stahler & Palla 2004).

GMCs are predominantly made up of molecular hydrogen which emits thermally at temperatures in excess of 6,000 K, and therefore H_2 cannot be used to directly observe the earliest stages of star formation. At sufficiently high densities GMCs can shield from cosmic rays and allow traces of more complex organic and inorganic molecules such as CO, OH and NH_3 to form. These species have been observed to enter excited states, as a result of collisions, that subsequently emit line emission as a function of density. As a result, molecular line emission is therefore used to observe high column density parts of the cloud. In addition to molecular gas, silicate and graphite dust accounts for approximately 1% of the mass of the GMC. This dust is primarily responsible for interstellar extinction of optical light (Figure 1.1). When these photons are scattered and absorbed they are subsequently re-emitted as a blackbody, giving rise to the thermal dust continuum that an be observed by infrared (IR) and submillimeter telescopes. At sufficiently high densities, the gas and dust are assumed to be well coupled. More detail on the nature of the dust is given in Section 2. An example of the spectral energy distribution (SED) of thermal dust continuum emission from a 10 K starless core is presented in Figure 1.2.

Larson (1981) observes that GMCs are rarely quiescent and instead have a structure that is turbulent and hierarchical in nature. Internally, turbulence has been observed in ^{13}CO 1-0 line emission by Brunt (2010) and NH_3 line emission by Levshakov et al. (2014). There is still a debate over what mechanism drives this with protostellar jets (Wang et al., 2010), winds and supernovae (Rey-Raposo et al., 2015) all candidates. Externally, GMCs are sufficiently large that they are believed to be influenced by the kinetic motion of the Galaxy. As a result of these various forces, GMCs have a complex, often fractal-like structure (Stutzki et al., 1998) where local over-dense sub-regions form pre-stellar cores where the conditions for cloud collapse and star formation become favourable (Padoan & Nordlund 2002, McKee & Tan 2003 and Hennebelle & Chabrier 2011).

1.1.2 Pre-stellar cores

The principles of pre-stellar core collapse are laid down in the virial theorem which describes how the 'outward' kinetic energy of a system, due to thermal motion, balances with the 'inward' potential energy of a system, due to gravitational attraction, when in hydrostatic equilibrium. If the potential energy of the system increases, or the kinetic energy drops, an uncontrolled collapse will occur on a free fall timescale as the system moves into an unstable state. Jeans (1902) derived a critical length scale, $\lambda_{\rm J}$, for density oscillations, in an otherwise homogenous medium, as,

$$\lambda_{\rm J} = \left(\frac{\pi c_s^2}{G\rho}\right)^{1/2}, \tag{1.1}$$

where ρ, c_s and G are density, sound speed and the gravitational constant. A cloud with a size greater than $\lambda_{\rm J}$ will contain sufficient mass that it cannot be supported by thermal pressure alone, and collapse will ensue. At this critical size, the critical mass of a spherical, isothermal cloud is

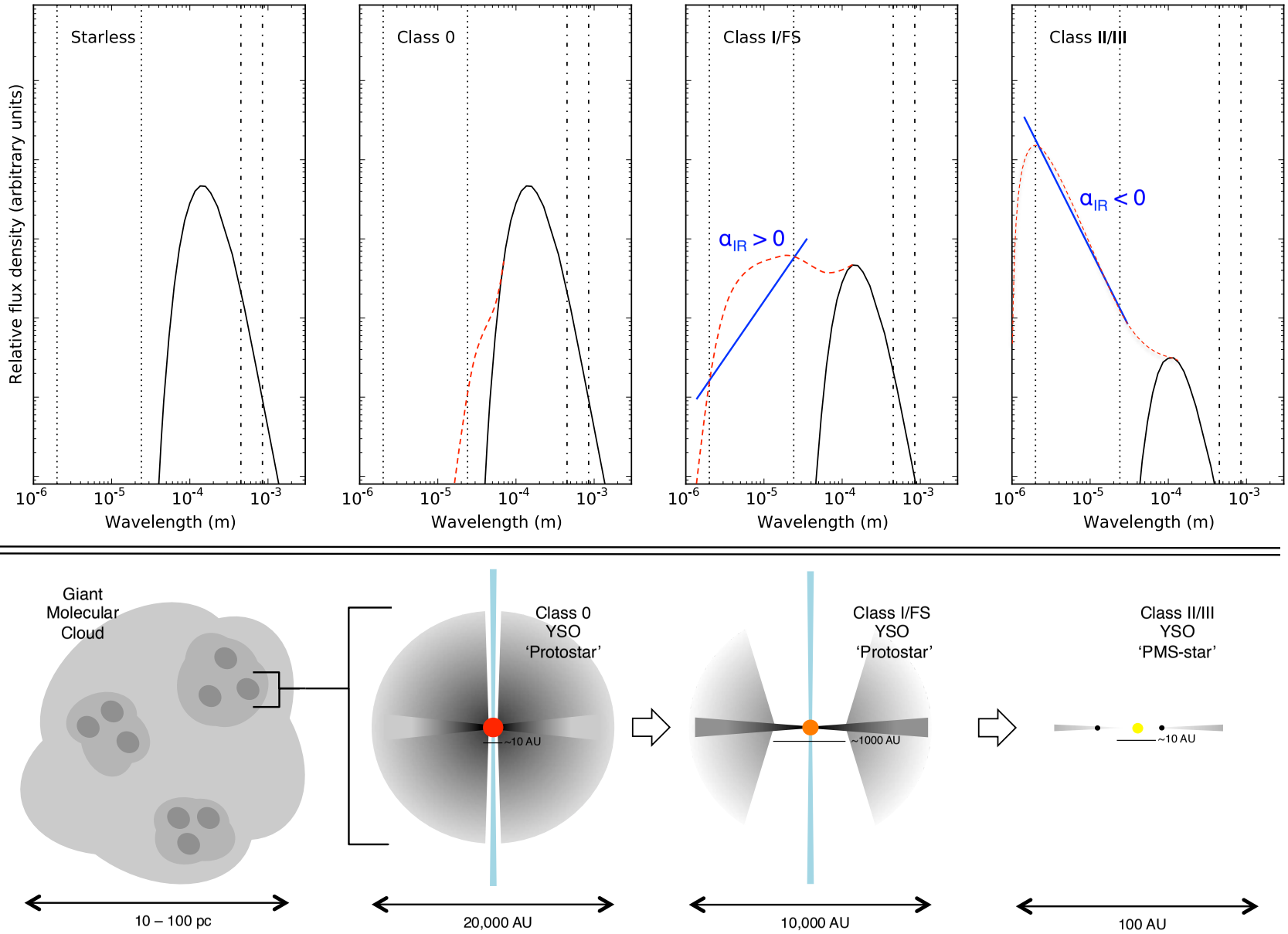

Figure 1.2: The stages of star formation, from a starless giant molecular cloud (left) through to a pre main sequence (PMS) star (right). Schematic YSO SEDs are plotted for the corresponding stage, from which the YSO classification is calculated (typically from the spectral index, α_{IR} between 2 and 24 μm, marked as the dotted lines). The cold dust is the black line and the warm dust is the red, dashed line. Note that observed SEDs for YSOs vary significantly depending on target inclination. SCUBA-2 bands are marked as dot-dashed lines.

given as

$$M_{\rm J} = \frac{4\pi}{3}\rho\left(\frac{\lambda_{\rm J}}{2}\right)^3 = \frac{\pi^2 c_s^2}{6G}\lambda_{\rm J}. \tag{1.2}$$

Featured in both Equations 1.1 and 1.2, c_s is a measure of the gas turbulence and kinetic energy and defined as a function of temperature, T, as

$$c_s^2 = \frac{k_B T}{\mu_{\rm H_2} m_{\rm p}}, \tag{1.3}$$

where k_B, $\mu_{\rm H_2}$ and $m_{\rm p}$ are the Boltzmann constant, mean molecular mass of 1 He to 5 $\rm H_2$ (2.8, Kauffmann et al. 2008) and the proton mass. Sadavoy et al. (2010) redefine the Jeans mass, given in Equation 1.2, in the context of a pre-stellar core as,

$$M_{\rm J} = 1.9\left(\frac{\bar{T}_{\rm g}}{10\,{\rm K}}\right)\left(\frac{R_{\rm c}}{0.07\,{\rm pc}}\right){\rm M}_\odot, \tag{1.4}$$

taking $R_{\rm c}$ as the core size, of order 0.07 pc, as equivalent to $\lambda_{\rm J}$, and $\bar{T}_{\rm g}$ as the average core temperature, of order 10 K, derived from the isothermal sound speed (Equation 1.3).

An alternative approach to the virial theorem was applied by Ebert (1955) and Bonnor (1956) who considered an isothermal gas sphere in a medium with a constant pressure, P_0, and determined a Bonnor-Ebert (BE) critical mass, $M_{\rm BE}$, of,

$$M_{\rm BE} = \frac{C_{\rm BE} c_s^4}{\sqrt{P_0 G^3}} \approx 2.4\frac{k_B T_d}{\mu m_p G} R_{\rm BE}, \tag{1.5}$$

where $\rm C_{BE}$ is a dimensionless constant of value approximately 1.18. Alternatively, Pattle et al., (submitted) model a BE critical mass a function of radius, $\rm R_{BE}$, and dust temperature.

In an idealised scenario modelled by Jeans and Bonnor, a perfectly spherical cloud will collapse across a single length-scale to a single point. In reality, GMCs are in-homogenous. Whilst the cloud may be stable on the largest scales, at smaller scales local density fluctuations due to turbulence may result in discrete parts of the cloud undergoing collapse, as $\lambda_{\rm J} \propto \rho^{-1/2}$. As a result cloud fragmentation can occur, as illustrated in Figure 1.2.

GMC with masses that exceed either the Jeans or BE critical mass can be considered unstable. However, both Jeans and Bonnor modelled highly idealised scenarios and as a result both $\rm M_J$ and $\rm M_{BE}$ should be considered lower limits as additional forces such as magnetism and turbulence could provide additional support against gravitational collapse (Crutcher 2001, 2005, Padoan & Nordlund 2002, Tassis & Mouschovias 2004, Sadavoy et al. 2010, Mairs et al. 2014). Pattle et al. (2015) find evidence of both pressure confined and gravitationally bound cores in Ophiuchus region, inferring that multiple mechanisms are likely contributing to the collapse of cores.

It remains unclear as to whether core cooling, mass accretion or turbulent pressure is the dominant force behind initiation of core collapse. Bertoldi (1989), Lefloch & Lazareff (1994), Thompson et al. (2004) and Urquhart et al. (2009) have suggested that shocks caused by the expansion of an H II region can trigger star formation in regions of massive star formation.

1.1.3 Young stellar objects (YSO)

In both the Jeans and BE models gas is assumed to be isothermal (Larson 1969 and Shu 1977). This is accurate up to densities of approximately $10^{-12}\,\mathrm{g\,cm^{-3}}$, above which dust becomes optically thick and thermal radiation cannot escape and instead starts to heat the cloud (Masunaga & Inutsuka 2000, Stamatellos et al. 2007). Collapse continues until densities reach $10^{-8}\,\mathrm{g\,cm^{-3}}$ when heating becomes sufficient for thermal support to be restored and the *first hydrostatic core* is formed (Masunaga et al., 1998; Saigo & Tomisaka, 2011; Bate et al., 2014).

Material from the less dense outer layers of the envelope will continue to fall on to the first core, causing it to contract and continue to increase in temperature until it reaches 2,000 K, at which point much of the thermal energy is utilised in the dissociation of molecular hydrogen. With the sudden loss in thermal support, a secondary stage of collapse begins and continues until all the molecular hydrogen is dissociated and a *second hydrostatic core* are formed containing the atomic hydrogen (and helium). At the formation of the second core, the heated material represents less than a 20th of the overall mass of the newly formed protostar and emission is dominated by dust in the cold envelope.

Prior to heating from the second core reaching a sufficient radius that the dust becomes optically thin as density decreases, IR emission cannot escape and it is not possible to observe the protostar. For all intents and purposes the proto-stellar cloud is indistinguishable from an especially dense, but starless core (Figure 1.2). When thermal photons are eventually able to escape the core, the newly formed protostar can be observed for the first time and the proto-stellar cloud is referred to as a Stage I YSO (as denoted on Figure 1.2). As sensitivity of IR telescopes has improved, it has become possible to conduct mid to far IR Galactic surveys of protostar populations and to study individual cores at wavelengths greater than 10 μm (Belloche et al., 2006; Pezzuto et al., 2012; Huang & Hirano, 2013).

Molecular clouds inevitably carry a small amount of angular momentum. As they undergo collapse this momentum is conserved causing the angular velocity of the cloud to increase as the radius decreases, leading to the formation of a disc (Terebey et al., 1984). The rotating cloud now funnels material towards the protostar parallel to axis of rotation, fuelling the disc which in turn accretes onto the surface of the protostar. As mass accretes onto the star, gravitational potential energy is released in the form of accretion luminosity. In the earliest stages of star formation accretion is at its most vigorous and accretion luminosity can outshine the protostellar core.

The release of potential energy that provides the accretion luminosity helps prevent the angular velocity of the star exceeding the escape velocity and the star disintegrating. Shklovskii (1967) was first to suggest that this transformation was behind observations of bipolar jets in accreting X-ray binaries, an analogous process to that observed around young stars. Winds from the protostar are believed to be funnelled perpendicular to the axis of rotation by magnetic fields and ejected over distances of order a parsec or larger (Shklovskii 1967, Arce et al. 2007, Bally et al. 2007).

Jets are a super heated plasma and emit Thermal Bremsstrahlung, or free-free emission (Reynolds, 1986). The mechanism behind this process is discussed in detail in Chapter 4. Upon ejection, the jet material has been observed to collide with the envelope and propel molecular gas

Table 1.1: YSO classification

Classification	$\alpha_{\rm IR}$	T$_{bol}$ (K)	$L_{\rm smm}/L_{\rm bol}$	Notes on stage
Class 0	-	$T_{\rm bol} < 70$	$\geq 3\%$	Stage 1
Class I	$0.3 \leq \alpha_{\rm IR}$	$70 \leq T_{\rm bol} \leq, 350$	$\leq 3\%$	Stage 1
Class 'FS'	$-0.3 \leq \alpha_{\rm IR} \leq 0.3$	-	-	Stage 1/2
Class II	$-1.3 \leq \alpha_{\rm IR} \leq -0.3$	$350 \leq T_{\rm bol} \leq, 650$	-	Stage 2
Class 'TD'	$-1.9 \leq \alpha_{\rm IR} \leq -1.3$	-	-	Stage 2/3
Class III	$\alpha_{\rm IR} \leq -1.9$	$650 \leq T_{\rm bol} \leq, 2800$	-	Stage 3

Note: FS stands for 'flat spectrum' and 'TD' for 'transition disc'. The IR spectral index, $\alpha_{\rm IR}$, bolometric temperature, T$_{bol}$, and luminosity ratio, $L_{\rm smm}/L_{\rm bol}$, methods are outlined in the text.

out of the core and into the ISM where it can be detected through line emission, for example ^{12}CO 3-2 (Snell & Edwards 1981, Ziener & Eislöffel 1999, McKee & Ostriker 2007). The mechanisms behind this are discussed in more detail in Chapter 3. Where the head of the jet has interacted with an especially dense part of the ISM, raised dust temperatures have been observed through IR emission from molecular hydrogen objects (MHOs), that are analogous to Herbig-Haro objects (Herbig 1974, Strom et al. 1974).

Accretion, winds and jets deplete the protostellar envelope over time, allowing more of photons from the photosphere to escape and be observed. At this point the photosphere is still relatively cool at 300 K and accretion luminosity still provides a significant proportion of overall luminosity, though overall accretion is less vigorous (Stahler & Palla, 2004). It should be noted that the form of this SED may vary significantly at this stage as dust is heavily depleted towards poles, but heavily populated in the accretion disc, providing less or more extinction depending on the inclination. In this way a YSO viewed edge on may appear as a highly embedded Stage 1 when viewed edge on, or a relatively cleared Stage 2 when viewed face on (Figure 1.2).

As the YSO continues to evolve it goes through a transition from protostellar to PMS when the brightness of the IR photosphere exceeds the submillimeter envelope (Figure 1.2). At this point they enter the Classical T-Tauri phase (low mass) or Herbig AeBe phase (intermediate mass) where by the envelope has dissipated and accretion has all but ceased, leaving a proto-planetary disc. Generally these are Stage 2 YSOs (as denoted on Figure 1.2). Irregular accretion on to these YSOs have been associated with observed variability and X-ray flaring. The proto-planetary disc dissipates over time leaving a debris disc (Figure 1.2) that are associated with Weak line T-Tauri PMS-stars, or Stage 3 YSOs. Finally, as the star stabilises and starts nuclear burning, the production of high energy UV photons photo-ionises and disperses the remaining gas that hasn't fallen onto any planets that may have formed.

1.1.4 YSO classification

It is not possible to directly observe a protostar being formed. Instead its SED is observed and used as a metric to classify the YSOs evolutionary status. There are various methods for classifying stars, often utilising different parts of the dust continuum. As the observed YSO SED reflects both the evolutionary stage of the object and its inclination, classification does not directly correspond to the YSO stage, as indicated in Table 1.1.

One method for classifying YSOs is the IR dust spectral index, $\alpha_{\rm IR}$. This is a direct measurement of the gradient of the SED slope over an range of IR wavelengths (typically 2 to 24 μm) and is expressed as,

$$\alpha_{\rm IR} = \frac{d\log(\lambda S_\lambda)}{d\log(\lambda)}. \tag{1.6}$$

As a classification tool for YSOs, $\alpha_{\rm IR}$ was developed by Lada & Wilking (1984) and Greene et al. (1994) and is summarised by Evans et al. (2009) who specify the boundaries, as demonstrated in Table 1.1.

IR dust spectral index is one the most commonly used methods for the classification of protostars and consequently is one of the most criticised. Uncertainties on $\alpha_{\rm IR}$ typically vary between 10 and 20 per cent. However, measurements have been shown to be highly susceptible to disc geometry and source inclination (Robitaille et al., 2007) whilst extinction is known to cause $\alpha_{\rm IR}$ to appear larger and IR contamination from background nebula can also lead to misclassification. Furthermore, the development of $\alpha_{\rm IR}$ predates the identification of the Class 0 protostar (Chandler et al., 1990; André et al., 1993; Eiroa et al., 1994; André & Motte, 2000) and therefore does not distinguish between Class 0 and Class I objects when $\alpha_{\rm IR}$ is measurable (absence of $\alpha_{\rm IR}$ is often taken to define a Class 0).

Bolometric temperature and luminosity are alternative classification methods utilise the full spectrum, including the submillimeter wavelengths where emission is believed to be dominant in protostars. The ratio of submillimeter luminosity ($L_{\rm smm}$, defined as ≥ 350 μm by Bontemps et al. 1996), to bolometric luminosity, $L_{\rm bol}$, is a method that has been used to classify YSOs by Myers et al. (1998) and Rygl et al. (2013). Both $L_{\rm bol}$ and $L_{\rm smm}$ are calculated using the flux density, S_ν, over their respective frequency, ν, ranges and source distance, d, as,

$$L_{\rm bol} = 4\pi d^2 \int_0^\infty S_\nu d\nu, \tag{1.7}$$

and,

$$L_{\rm smm} = 4\pi d^2 \int_0^{350\,\mu{\rm m}} S_\nu d\nu. \tag{1.8}$$

This method was developed by André et al. (1993) who originally set the Class 0/I boundary at 0.5%. Maury et al. (2011) and Rygl et al. (2013) revise this upwards to 3 % and most recently Sadavoy et al. (2014) use 1% outlining the lack of consensus on this issue. I follow the work of Rygl et al. (2013) and classify YSOcs in Chapter 6 with $L_{\rm smm}/L_{\rm bol} \geq 3\%$ as Class 0 protostars (Table 1.1).

Bolometric temperature, $T_{\rm bol}$, calculates a source temperature based on a flux weighted mean frequency of the SED. I follow the numerical integration method of Myers & Ladd (1993) and Enoch et al. (2009) who calculated the discrete integral of the SED of an object for a given number of recorded fluxes.

$$T_{\rm bol} = 1.25 \times 10^{-11} \bar{\nu}\,({\rm K\,Hz^{-1}}), \tag{1.9}$$

where $\bar{\nu}$ is the mean frequency of the whole spectrum,

$$\bar{\nu} = \frac{\int \nu S_\nu d\nu}{\int \nu d\nu}. \tag{1.10}$$

Chen et al. (1995) define the classification boundaries for $T_{\rm bol}$ and they are listed in Table 1.1. It is important to note that $T_{\rm bol}$ does not represent a physical temperature of the object.

As both $T_{\rm bol}$ and $L_{\rm smm}/L_{\rm bol}$ methods use a greater spectral range, they could be considered a more reliable method of classification than $\alpha_{\rm IR}$ which only covers 2 μm to 24 μm. Furthermore, both provide a quantifiable method for separating Class 0 and Class I IR sources. Throughout this thesis I refer to 'proto-stars' as Class 0/I/FS objects and 'PMS-stars' as Class II/TD/III objects.

Evans et al. (2009) classify protostars in the *Spitzer* c2d catalogue using $\alpha_{\rm IR}$. By using the known lifetime of a classical T-Tauri (Class II) YSO (2 Myr), Evans et al. (2009) calculate the lifetime of the Class 0, I and FS stages using counting statistics as 0.47, 0.10 and 0.44 Myr, respectively. Whitney et al. (2003) separately calculate the length of Class III stage as approximately 10 Myrs.

1.1.5 Stellar clusters

The star formation paradigm I have described outlines the formation of a single low-to-medium star in isolation. However, there is a substantial amount of evidence to suggest that this is the exception, and that the status quo favours clustered star formation. Lada & Lada (2003) describe how up to 90% of all stars formed in a GMC form as part of a cluster, with a given cluster often containing 100 or more members. Recent surveys of YSO populations by Evans et al. (2003), Winston et al. (2007) and Kuhn et al. (2010) have observed many of these clusters in association with star forming regions. Furthermore, photometric surveys have suggested that up to one third of all main sequence star systems are binaries, inferring that multiple stars can form from a single gravitationally bound envelope.

Observations of clusters have given rise to the concept of the initial mass function (IMF), a probability distribution for stellar masses that form in a cluster (Scalo 1986, Chabrier 2005). The IMF is thought to be invariant across stellar clusters, inferring the presence of massive (O, B or A Class) stars for a sufficiently massive GMC. The Salpeter mass function ($N \propto M^{-1.35}$) represents a rudimentary fit to the high mass end of the observed IMF that is often used a standard comparison of the mass distribution of a cluster (Salpeter, 1955). Various authors have sought to improve the models of the IMF with varying success (Kroupa 2001, Chabrier 2005). A handful of examples are presented in Figure 1.3.

Once a pre-stellar core has collapsed and formed its first core (or cores), the likelihood of its evolution being directly influenced by an interaction with another YSO is statically improbable. However, radiative heating from these objects may have an influence on the dust temperatures of isolated cores, in particular, in the cases where by a massive star is formed in parallel with its neighbours.

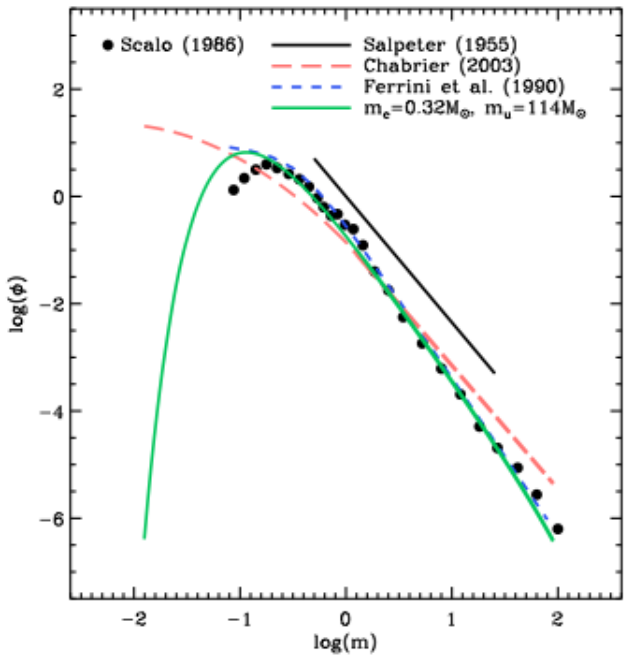

Figure 1.3: An example plot (taken from Mattsson 2010) of various IMF models fit to data observed by Scalo (1986) (black markers). m is clump mass (in units of $M_\odot$) whilst ϕ is probability distribution.

1.1.6 High mass star formation

Massive star (O, B or A Class) formation proceeds slightly differently to low mass stars. By definition these massive protostars have a free-fall timescale that is comparable to the Kelvin-Helmholtz timescale (Palla & Stahler 1993, Stahler & Palla 1993, Stahler et al. 2000). The PMS stage 2/3 massive Herbig AeBe star is defined by Herbig (1960), Hillenbrand et al. (1992) and Mannings (1994) as an intermediate mass (1.5 to 10 $M_\odot$) equivalent of Classical T-Tauri star, typically of spectral type A or B. Herbig AeBe stars are strongly associated with circumstellar gas (Natta et al., 2000, 2001; Fuente et al., 2003; Cesaroni et al., 2007), outflows and dust with a wide range of temperatures (Beuther & Shepherd, 2005).

Comparatively little is known about the formation of the most massive, O type stars. The IMF describes how O type stars are rare, with a total Galactic population accounting for 0.2% of all stars (Krumholz, 2015). Given the extreme masses of these objects (greater than 10 $M_\odot$) they only form in the highest density parts of the most massive GMCs (Salji et al. 2015, Peretto et al. 2016), and consequently their earliest stages are subject to exceptionally high levels of extinction, for example, $A_V \approx 500$ (Krumholz, 2015). As a result the study of massive star formation is confined to submillimeter and far IR wavelengths which are resolution limited, which complicates matters as massive stars are formed in highly populous clusters.

B4 type and earlier stars are sufficiently massive that they can start nuclear burning whilst still accreting. Hollenbach et al. (2000) summarises protostellar accretion disc dispersion mechanisms. Processes such as stellar wind stripping and photo-evaporation are significantly more potent around the most massive stars, acting to deplete discs far faster. This problem is known as

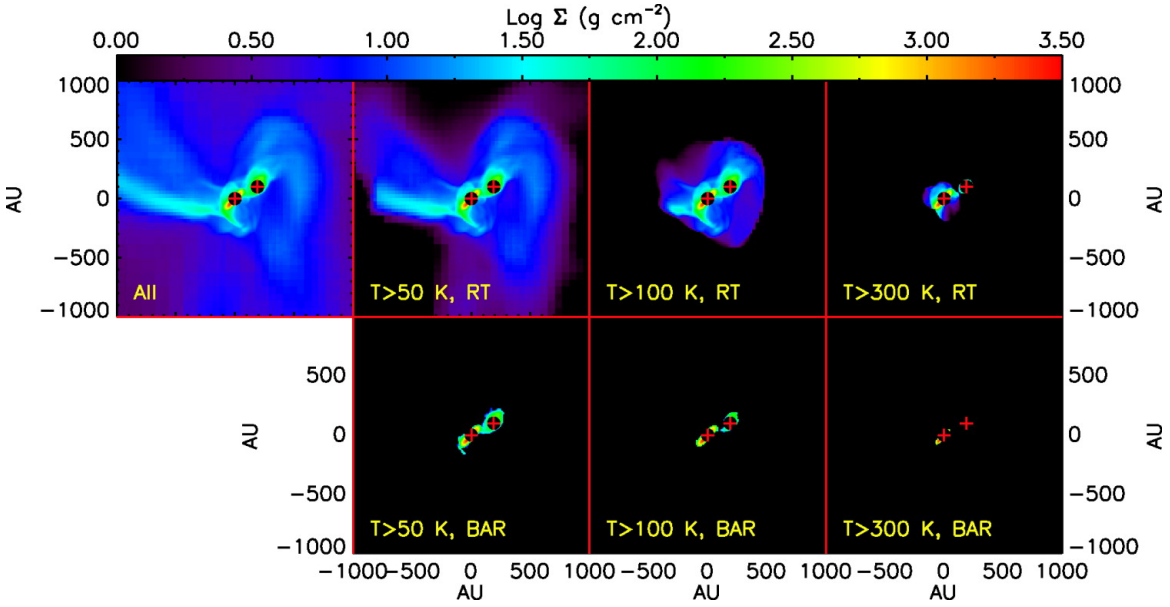

Figure 1.4: Column density in the gravito-radiation hydrodynamical simulation published by Krumholz et al. (2007). Left to right shows; all gas, gas with temperatures greater than 50 K, greater than 100 K and greater than 300 K. Temperature in the upper panels is based on 'real' radiative feedback from the stars whereas temperatures in the lower panels are calculated from barotropic equation of state. In both simulations, red crosses mark the location stars that have formed.

the Eddington limit (Larson & Starrfield, 1971). In addition to this the typical O star lifetime is 5 Myrs (Beuther & Shepherd, 2005) which is less than the lifetime of a low mass YSO inferring that many will enter the giant stage before reaching Class III phase (approximately 3 Mys), and supernova before ending the Class III stage. It therefore remains unclear how the most massive stars accrete mass given the barriers of low lifetime and high radiation pressure (Kahn 1974, Wolfire & Cassinelli 1987, Bonnell et al. 2004 and Krumholz 2006a).

Models by Jijina & Adams (1996), Stahler et al. (2000), Yorke & Sonnhalter (2002), McKee & Tan (2003) and Krumholz et al. (2005) argue that accretion onto massive stars has to happen extremely rapidly, over timescales of less that 10^5 yrs and at rates in excess of 10^{-4} $M_\odot$ yr^{-1}. This mechanism would require the formation of substantial bipolar jets as momentum is conserved. Commerçon et al. (2011) and Myers et al. (2013) suggest that magnetic fields could provide a mechanism for cloud support. Masunaga & Inutsuka (2000); Matzner & Levin (2005); Krumholz (2006b); Krumholz et al. (2007) also suggests that excessive radiative heating may play a key role in suppressing the fragmentation process (discussed in further detail in the following section). See Krumholz (2015) for a more detailed overview of the problems with contemporary models of massive star formation.

1.1.7 The impact of additional heating

Early models of GMCs describe a system in local thermal equilibrium (LTE) whereby a number of mechanisms regulate temperature, maintaining an equilibrium between energy coming in from the

ISRF, and radiation leaving via continuum or line emission. Dobbs et al. (2005), Bate & Bonnell (2005) and Whitehouse & Bate (2006) have published early attempts to produce three-dimensional simulations of collapsing GMCs. Many of these systems used primitive initial conditions and were isothermal. As discussed, an in-homogenous GMC will undergo fragmentation during collapse as the Jeans length is inversely proportional to density. Exceptionally large amounts of fragmentation is observed leading to an overpopulation of low mass stars and IMF that differs significantly from observations.

One proposed solution is that localised radiative feedback from stars that have either recently formed, or are in the process of forming, can provide additional heating to disc of envelope, causing the Jeans length to increase as $\lambda_{\rm J} \propto T^{1/2}$ and the Jeans mass will increase by $M_{\rm J} \propto T^{3/2}$, both acting to make the cloud more stable. Clouds that are more stable can accrete greater mass before collapse, potentially allowing for the formation of more massive stars. Krumholz (2006b) carried out a one-dimensional analytical analysis including radiative feedback from accreting protostars and found that heating substantially inhibited fragmentation. Krumholz et al. (2007) carried out three-dimensional simulations, and found that rapid accretion onto a single massive protostar raises gas temperatures and suppresses further fragmentation. Figure 1.4 demonstrates how radiative heating can raise temperatures over a range of 1000 AU or greater (consistent with the Shirley et al. 2002a and Young et al. 2003 models of protostellar heating), whereas as a primitive barotropic example is much more limited. Bate (2009, 2012) and Offner et al. (2009) extend this work and find the IMF produced from simulations including radiative feedback from protostars far better replicates the observed IMF and brown dwarf to star ratio.

Offner et al. (2009) find that the protostellar heating from low-to-intermediate mass stars is largely confined to a core; however, high temperatures allow for a larger Jeans length and subsequently greater mass. Furthermore, radiative feedback further stabilises the disc of the core during collapse, reducing further fragmentation and formation for fewer subsidiary stars. Simulations by Longmore et al. (2011) determine that gas temperatures around 100 K at the fragmentation point are required in order to replicate the existing stellar population of G8.68-0.37, a value that exceeds that which is provided by the observed stellar population. They postulate that the original cluster contained less mass, and has subsequently increased in density through global infall. Figure 1.5 describes how individual protostars heat their immediate environment, but also how the formation of dense clusters can lead to more wide spread heating, with central temperatures in excess of 50 K (Bate, 2012).

High resolution is key to investigating heating on the length scales described above. The resolution of the JCMT is 14.6″ at 850 μm. In the closest region in the GBS (Ophiuchus, 139 pc) this amounts to a length scale of 0.01 pc. Rygl et al. (2013) put the typical star forming core at a size of 0.05 pc, and as a result it may be possible to resolve individual envelopes and any temperature gradient across the core, allowing for the investigation of the high central temperatures calculated by Shirley et al. (2002a), Young et al. (2003) and Longmore et al. (2011). Where dense clusters of YSOs exist it will be of further interest to investigate whether the combined heating observed in Figure 1.5 is replicated in the observations, and whether this is altering the Jeans stability of any starless clumps in the close proximity.

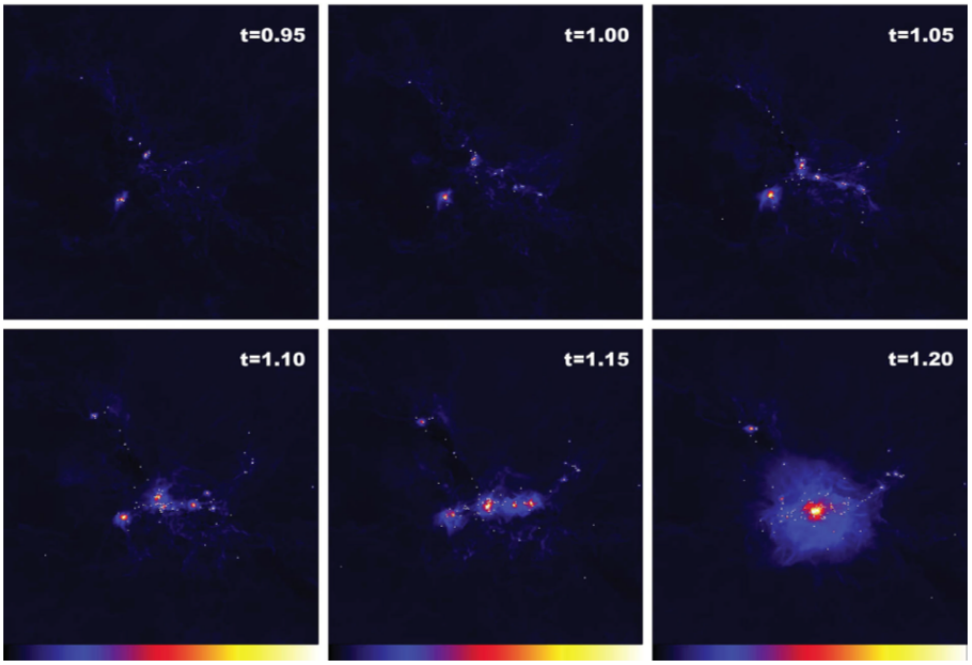

Figure 1.5: The global evolution of gas temperature in the radiation hydrodynamical calculation, that includes radiative feedback from protostars, published by Bate (2012). 't' represents the time step as multiple of the free-fall time. Panels show a logarithmic temperature scale between 9 and 50 K. White dots represent stars that have formed. Each panel has a width of 0.6 pc.

1.2 Heating and cooling in the interstellar medium

Models of star formation are largely derived from Jeans instability, a property that is fundamentally derived from the temperature of the gas and dust in the GMC. Understanding the nature of these components that are contained within GMCs, and the mechanisms that govern their heating and cooling is vitally important for understanding how they absorb light, and the resulting dust continuum emission.

1.2.1 Interstellar dust

When observing at optical or near IR wavelengths the GMCs are observed through their extinction of light from the background stars. Molecular gases are optically thin[2] and therefore this extinction is caused by scattering and absorption by interstellar dust grains. Much of our understanding of the nature of the dust comes from theoretical and lab modelling as pristine ISM dust grains are extremely rare in our solar system and are not found on Earth. By comparing the frequency dependance of interstellar extinction with that anticipated for range of complex structures, Mathis et al. (1977) deduced that the interstellar dust is likely composed of silicate and graphite grains. These metals are formed in highly evolved massive stars and supernovae and are themselves the products of previous generations of star formation. Further work by Draine & Lee (1984) and Ossenkopf (1993) have helped build up an understanding of interstellar dust as a coagulated, fluffy

[2] with the exception of specific absorption lines.

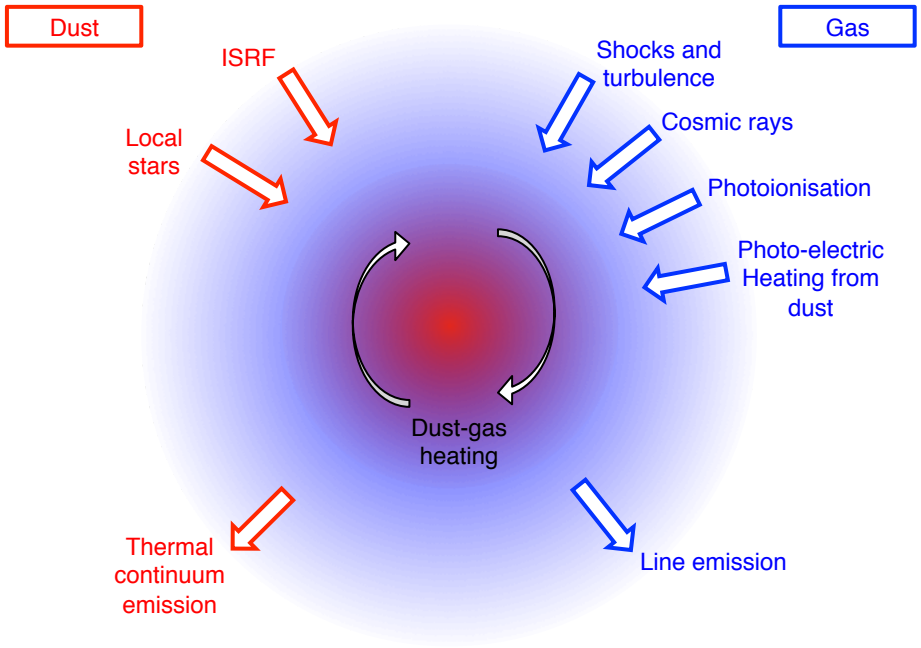

Figure 1.6: A schematic diagram demonstrating the various mechanisms that go into heating and cooling the dust (red) and gas (blue) components of the ISM. Note that both the gas and dust components heat each other when they are well coupled.

sub-micron sized structure with icy mantles where atomic gases have 'frozen out' onto the grain surface in the process of forming molecules. A typical dust grain size is 0.1 μm (Stahler & Palla, 2004) though Mathis et al. (1977) define a working range of 0.005 to 0.25 μm.

Dust is observed to be optically thick at optical wavelengths but optically thin at submillimeter wavelengths, inferring a frequency dependance on dust opacity, κ, of the form,

$$\kappa \propto \nu^{\beta}, \tag{1.11}$$

where β is the dust opacity spectral index (Erickson et al., 1981; Schwartz, 1982). A number of authors have sought to model the frequency dependance of dust opacity in dense molecular clouds, and today a consensus has been reached with the use of the popular OH5 model of Ossenkopf & Henning (1994) that predicts an opacity of 0.012 cm/g (with a gas + dust ratio of 161:1, based on the calculations of Draine & Lee 1984) at 850 μm. It is important to note that Ossenkopf & Henning (1994) quantify an uncertainty in opacity of an order of factor two across all frequencies.

A β value of two is anticipated for the large-scale ISM (Draine & Lee, 1984); however, a number of authors have observed evidence that β is not constant and instead changes with protostellar environment. Beckwith et al. (1990); Beckwith & Sargent (1991) and Chun-Yuan Chen et al. (2016) have all observed how β decreases towards protostellar cores and in accretion discs. Today's consensus is that the densest, coolest environments encourage dust grains to coagulate and form greater mantles of ice, thus increasing dust opacity in these star forming environments.

Ossenkopf (1993); Ossenkopf & Henning (1994) find that lower values of β are associated primarily with coagulation. However, as stars form they heat the dust, first causing the icy mantles to sublimate at temperatures greater than 100 K, and secondly the grains themselves to sublimate at temperatures greater than 1,000 K, inferring that dust is unlikely to survive in great quantities in the H II regions that form around OB stars.

1.2.2 ISM heating and cooling

As discussed, the ISM contains two components, gas and dust, often stated with a ratio of 161:1 (Draine & Lee, 1984). Both of those components are exposed to a variety of radiative mechanisms that can causing heating. Likewise, both cool through various emission processes. In GMCs these processes are considered to be in LTE. Under specific circumstances the heating and cooling of each component is not considered independent of the other and in these cases the gas and dust temperature is described as coupled. The mechanisms of heating and cooling for both gas and dust are shown in Figure 1.6.

The most dominant mechanism for heating gas is photo-electric heating, a process by which UV photons in the interstellar radiation field (ISRF) liberate electrons from the surface of the dust grains which subsequently heat the gas. Note that the mean far UV photon flux is referred to as the *Habing field* and has a value of $1.6{\times}10^{-3}$ erg cm^{-2} s^{-1} Sr^{-1} in one-dimension (Tielens, 2005). Collisions becoming increasingly likely at higher densities. UV photons may also directly excite and photoionize gas species, though the work function of this transition is much higher than the dust and a result it has has a negligible effect on temperature. Cosmic rays can also impart kinetic energy into the ISM to excite the gas. Cosmic rays can penetrate into the most dense environments that would otherwise be shielded from UV photons and as a result the heating provided by cosmic rays is also correlated with density. Bulk motion can further input kinetic energy into the gas; either on large-scales through turbulence, or smaller scales through shocks associated with molecular outflows or explosive expansion.

Gas cooling is primarily governed by line emission. Gas molecules can be excited into raised vibrational or rotational states through collisions with dust. The states subsequently de-excite through line emission. If temperature the gas exceeds the dust temperature, then the gas can be directly cooled through the transfer of kinetic energy to the dust.

Dust temperature is primarily dictated by heating from the ISRF, as

$$T_d = \frac{hc}{k_B}\left(\frac{U}{384\pi^2 ahc\zeta(5)}\right)^{1/5}, \tag{1.12}$$

where a is dust grain size, U is the energy density of the ISRF and $\zeta(5)$ is a constant equal to 1.037 (all other terms have their usual meanings). This expression is derived from equating absorption and emission energy of dust. In particular the emission energy is derived from Stefan-Boltzmann law and the Planck function (in the Rayleigh-Jeans limit) producing the factor of T_d^5 (Tielens, 2005). Tielens (2005) gives the energy density of the cosmic microwave background as $4{\times}10^{-13}$ erg cm^{-3} and energy density of stellar light as $7{\times}10^{-13}$ erg cm^{-3}, allowing Equation 1.12

to be re-written specifically for silicate and graphite grains as

$$T_{sil} = 13.6\left(\frac{1\mu m}{a}\right)^{0.06} \tag{1.13}$$

and

$$T_{grph} = 15.8\left(\frac{1\mu m}{a}\right)^{0.06}. \tag{1.14}$$

Whereas Equation 1.12 assumes the absorption efficiency is unity, this is not the case at UV and optical wavelengths. Tielens (2005) uses a reasonable approximation in Equations 1.13 and 1.14 that results in a shallower temperature dependance of 0.06. Heating due to various models of the ISRF have been discussed by Mathis et al. (1983) and Shirley et al. (2000a, 2002a) and are discussed in more detail in Chapter 8. Feedback also occurs via local mechanisms, from radiative heating by the stellar photosphere and accretion luminosity (Calvet & Gullbring, 1998) of stellar objects. In this former scenario, the Habing field is re-written as,

$$G_o = 2.1 \times 10^4 \left(\frac{\mathrm{L}_*}{10^4\, L_\odot}\right)\left(\frac{0.1\,\mathrm{pc}}{d}\right)^2, \tag{1.15}$$

where the field, G_o is a function of stellar luminosity, L_*, and distance, d. General dust temperature, T_d, is then calculated using,

$$T_d = 33.5\left(\frac{1\,\mu\mathrm{m}}{a}\right)^{1/5}\left(\frac{G_o}{10^4}\right)^{1/5}(\mathrm{K}). \tag{1.16}$$

Dust cooling is dominated by thermal continuum emission from the dust grains. However, the dust may also be cooled through collisions with the gas in an analogous process to the gas cooling. In this way, a well coupled ISM will maintain a degree of LTE. As discussed, much of the analysis of GMC temperature relies on the assumption that the gas and dust components are well coupled, that is to say, their temperatures can be considered similar as result of transfer of kinetic energy through collisions at sufficiently high density. Goldreich & Kwan (1974) first studied this process and found that LTE of gas temperature was maintained when the column density exceeds 10^4 cm^{-3}, a value that is updated to $10^{4.5}$ cm^{-3} (Goldsmith, 2001). Figure 1.7 (left) describes how this corresponds to an extinction of approximately three, above which temperatures are similar, though this scenario is specific to a photo-dissociative region (PDR, Tielens & Hollenbach 1985). Contemporary authors have produced observational evidence to support gas-dust coupling in dense cores, for example Rathborne et al. (2008) and Forbrich et al. (2014) observe cores in the Pipe nebula and find correlation between NH_3 gas temperatures and *Herschel* dust temperatures, as demonstrated in Figure 1.7 (right).

1.2.3 Radiative transfer for dust

Through scattering and absorption, dust reradiates shorter wavelength photons from background stars at longer wavelengths. When the dust is in LTE, this process is described by the source

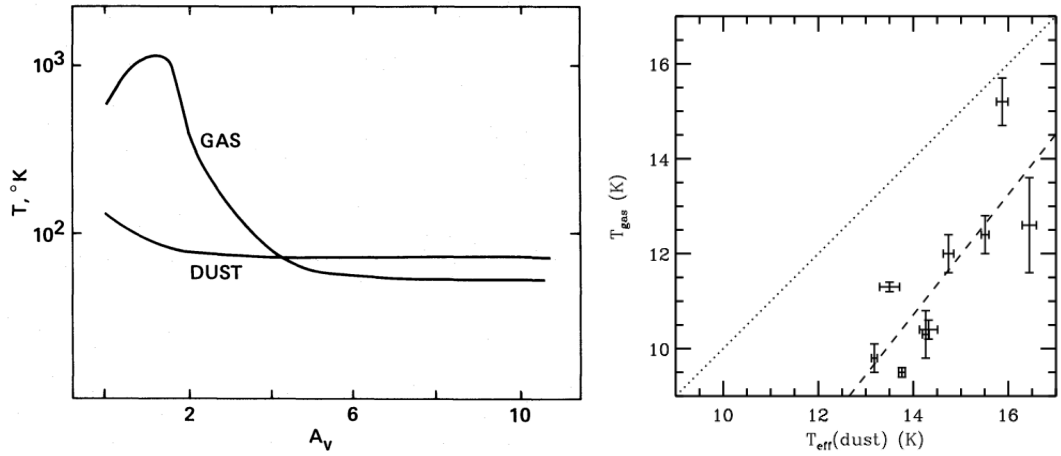

Figure 1.7: Left) gas and dust temperatures, calculated by Tielens & Hollenbach (1985) in their standard model of a photo-dissociative region, plotted as a function of visual extinction A_v into a cloud. Right) the correlation of T_{gas} (derived from NH_3 observations, published by Rathborne et al. 2008) and T_{eff} (derived from *Herschel* observations, Forbrich et al. 2014) for dense cores in the Pipe nebula that is consistent with coupled gas and dust temperature. The dashed line shows a linear fit to the data and the dotted line shows a parity line. Plot taken from Forbrich et al. (2014).

function, Σ_ν, in Kirchoff's law,

$$\Sigma_\nu = \frac{j_\nu}{\alpha_\nu}. \tag{1.17}$$

Dust absorptivity, α_ν, describes the fundamental ability of dust to absorb energy from incoming photons whilst *dust emissivity*, j_ν, describes the fundamental ability of dust to reradiate the absorbed energy. The source function is equivalent to the Planck function, B_ν, which describes emission from a 'black body' as a function of temperature, T_d, as

$$B_\nu(T_d) = \frac{2h\nu^3}{c^2}\frac{1}{(e^{-h\nu/k_B T_d} - 1)}, \tag{1.18}$$

where all the constants have their usual meaning.

The efficiency of a dust cloud to scatter and absorb high frequency photons from background stars, and therefore be heated by incident radiation, is dictated by its optical depth, τ, which can be expressed in terms of α_ν integrated across an arbitrary depth, s, as,

$$\tau = \int \alpha_\nu ds. \tag{1.19}$$

I now model a packet of photons of intensity (at a given frequency), I_ν, passing through the ISM, losing some fraction of its intensity due to absorption that is defined by Rybicki & Lightman (1979) as,

$$\delta I_\nu = -\alpha_\nu I_\nu \delta s. \tag{1.20}$$

Likewise, the packet of photons will gain some fraction of intensity due to emission from the

medium that is defined by Rybicki & Lightman (1979) as,

$$\delta I_\nu = j_\nu \delta s. \tag{1.21}$$

Summing these two terms gives an overall intensity gradient of

$$\frac{\delta I_\nu}{\delta s} = -\alpha_\nu I_\nu + j_\nu. \tag{1.22}$$

Dividing all terms by α_ν and using Equations 1.17 and 1.19, Equation 1.22 can be rewritten in terms of optical depth and the source function as a first order differential equation, with respect to τ,

$$\frac{\delta I_\nu}{\delta \tau} = -I_\nu + \Sigma_\nu. \tag{1.23}$$

Following Rybicki & Lightman (1979), this expression can be restructured by multiplying all terms by $e^{-\tau}$, and by using,

$$\frac{dI_\nu}{d\tau} e^{-\tau} + I_\nu e^{-\tau} = \frac{d}{d\tau}\left(I_\nu e^{-\tau}\right), \tag{1.24}$$

to rewrite Equation 1.21 in the integral form, between 0 and τ, as,

$$\int_0^\tau \frac{d}{d\tau}(I_\nu e^{-\tau'}) d\tau' = \int_0^\tau \Sigma_\nu e^{-\tau'} d\tau'. \tag{1.25}$$

By treating the source function as homogenous (and therefore invariant with τ) the integration can be simplified to give the equation of radiative transfer,

$$I_\nu - I_0 e^{-\tau} = \Sigma_\nu (1 - e^{-\tau}). \tag{1.26}$$

A simplified approach to intensity defines it as a power, per area, per solid angle, Ω. It is important to note that telescopes such as JCMT observe flux density, S_ν, the intensity integrated over solid angle,

$$S_\nu \simeq \int_\Omega I_\nu(\theta, \phi) d\Omega \simeq \int_A I_\nu \frac{(x, y)}{d^2} dA. \tag{1.27}$$

Solid angle is equivalent to a pixel area, A, over the square of the distance, d, to the source. By subtracting the background intensity, I_0, and employing Equation 1.27, the equation of radiative transfer (Equation 1.26) can be redefined as an expression of flux density as

$$S_\nu = \int_\Omega \Sigma_\nu (1 - e^{-\tau})\, d\Omega. \tag{1.28}$$

1.2.4 Properties of dust

Thermal continuum emission from dust is considered to be optically thin ($\tau \ll 1$) at submillimeter wavelengths. Therefore, by employing a series expansion, the Equation of radiative transfer (Equation 1.28) can be rewritten specifically for thermal dust emission as,

$$S_\nu = \int_\Omega B_\nu(T_d) \tau d\Omega, \tag{1.29}$$

where the source function Σ_ν has been replaced with the Planck function ($B_\nu(T_d)$, Equation 1.18) which describes the emission from a blackbody, and therefore the dust brightness.

By considering the expression for optical depth, Equation 1.19 can be rewritten as a function of the number density of hydrogen molecules, $N_{\mathrm{H_2}}$, and opacity (similar to the Hildebrand 1983 interpretation) as,

$$\tau = \kappa_\nu N_{\mathrm{H_2}} \mu_{\mathrm{H_2}} m_{\mathrm{p}}, \tag{1.30}$$

then Equation 1.29 can be rewritten as

$$S_\nu = \int_\Omega B_\nu(T_d) \kappa_\nu N_{\mathrm{H_2}} \mu_{\mathrm{H_2}} m_{\mathrm{p}} d\Omega. \tag{1.31}$$

This form is known as the opacity modified blackbody equation of radiative transfer. Examples of SEDs are given in Figure 1.2 and discussed in detail in Chapter 5.

The Planck function is a function of temperature and holds for all frequencies; however, when examining the black body at low frequencies, or high temperatures, the Planck function is simplified to the Rayleigh-Jeans approximation,

$$B_\nu(T_d) = \frac{2\nu^2 k_B T_d}{c^2}. \tag{1.32}$$

This approximation is applied at the Rayleigh-Jeans limit which is defined as $h\nu \ll k_B T_d$.

In the Rayleigh-Jeans limit this amounts to a flux density with a frequency power law dependance of $2+\beta$. The former term is taken from the Planck function in the Rayleigh-Jeans limit (Equation 1.32) and the latter term is taken from the opacity term (Equation 1.11). When in the Rayleigh-Jeans limit, flux is proportional to temperature and therefore temperature cannot be calculated from the spectral index. However, by assuming a full, opacity-modified Planck function, it is possible to show that the power law relation is derived from both β and the dust temperature, T_{d}. By taking the ratio of the full, opacity-modified Planck function at two separate wavelengths the 'Temperature equation' is derived by Reid & Wilson (2005) as,

$$\frac{S_{450}}{S_{850}} = \left(\frac{850}{450}\right)^{3+\beta} \left(\frac{\exp(hc/\lambda_{850} k_{\mathrm{b}} T_{\mathrm{d}}) - 1}{\exp(hc/\lambda_{450} k_{\mathrm{b}} T_{\mathrm{d}}) - 1}\right), \tag{1.33}$$

In Chapter 5 I go into more detail regarding the derivation and application of Equation 1.33 to calculate the dust temperature from the ratio of SCUBA-2 fluxes, given a constant β.

In addition to temperature, the opacity modified blackbody equation of radiative transfer (Equation 1.31) can also be used to calculate a number of other properties. For an observed flux over a given sky area and dust temperature, Equation 1.31 can be used to calculate the number density of hydrogen molecules, or column density. Submillimeter extinction, A_ν, can be calculated through the application of (Bohlin et al., 1978; Predehl & Schmitt, 1995),

$$0.9 \times 10^{21} \,\mathrm{molecules\,cm^{-2}\,mag^{-1}} \approx \frac{N_{\mathrm{H_2}}}{A_\nu}. \tag{1.34}$$

Furthermore, allowing that mass, M, is derived as the column density of molecular hydrogen

integrated over a given area, then Equation 1.31 can be re-arranged to give an expression for mass,

$$M = \frac{S_\nu d^2}{B_\nu(T_d)\kappa_\nu}. \tag{1.35}$$

These methods are often applied to calculating properties of star forming regions and are used, in context, in latter chapters.

1.3 Thesis outline

This thesis is composed of nine chapters. In this introductory chapter I have outlined the current consensus on the star formation paradigm, discussing how stars form from pre-stellar clouds and evolve as they progress towards the main sequence. I outline observational features during this evolution. I also discus how submillimeter observations are interpreted through the application of the equations of radiative transfer. In Chapter 2 I introduce the JCMT GBS and SCUBA-2, the primary instrument used in this thesis. I discuss the literature surrounding the Serpens-Aquila regions that are the primary target of my published research. I also introduce a number of ancillary surveys of YSOcs that are used to analyse the star formation in various regions.

In Chapters 2, 3, 4 and 5 I discuss the methodologies I develop throughout this thesis. I investigate a number of adaptations to the existing reductions of SCUBA-2 data to help mitigate some deficiencies in the ongoing development of the data reduction pipeline. I examine the evidence for contamination of SCUBA-2 bands, firstly with the ^{12}CO 3-2 line (850 μm only, Chapter 3), and secondly with free-free emission from any extended H II regions and ultra compact H II region (which affect both SCUBA-2 bands, Chapter 4). Both of these steps are in preparation for the calculation of SCUBA-2 dust temperature, using Equation 1.33, the methods for which I discuss in detail in Chapter 5. I pursue and compare two different methods for calculating the SCUBA-2 flux ratio. The first is a cross convolution of a two component model JCMT beam, based on the beam description produced by Dempsey et al. (2013). The second involves the implementation of a convolution kernel, produced by Pattle et al. (priv. comm.), and its adaptation, produced by Aniano et al. (2011). These methods are compared with each other and auxiliary methods for calculating dust temperature that exist the literature.

In Chapters 6, 7 and 8 I analyse the evidence for clump heating and any mechanisms providing that heating, firstly for individual regions - Serpens MWC 297 region (Chapter 6) and the Aquila W40 complex (Chapter 7) - before moving on to a statsitical analysis across the bulk of the JCMT GBS regions (Chapter 8). I produce catalogues of clumps based on the 850 μm data, for which real temperatures are calculated from the SCUBA-2 flux ratio temperature maps. Clump populations are compared to existing catalogues of YSOcs and I discuss the state of star formation and whether there is evidence that heating is directly influencing it.

In Chapter 9 I briefly discuss options for further work associated with this thesis before summarising my methods and conclusions.

2

The JCMT SCUBA-2 Gould Belt Survey of near-by star-forming regions

In this chapter I discuss the primary source of data used in this thesis, submillimeter observations from the ground based James Clerk Maxwell Telescope (JCMT) Gould Belt legacy Survey (GBS) of nearby star-forming regions (Ward-Thompson et al., 2007). I provide background to the telescope and techniques used to observe and reduce submillimeter Common-User Bolometer Array 2 (SCUBA-2) data. I discuss ancillary observations of the JCMT Gould Belt regions by the *Spitzer* Space Telescope and its associated YSO catalogues. I introduce the Serpens-Aquila region and summarise observations of 18 additional star-forming regions.

2.1 The JCMT Gould Belt Survey

The James Clerk Maxwell Telescope is a 15 m single dish telescope dedicated to submillimeter astronomy (EAO, 2016). It can operate between 400 and 1400 μm with a range of continuum and spectroscopic receivers. This frequency range is extremely sensitive to water vapour in the atmosphere and as a result the telescope is located at the summit of Mauna Kea, Big Island, Hawaii, where exceptionally dry conditions are favourable.

The Gould Belt refers to a ring of O-type stars and prominent HII regions (Lindblad, 1967), first discovered by Herschel (1847), and completed by Gould (1874), that the sun lies within. The Gould Belt is considered to be approximately 350 pc in radius and has an inclination of approximately $17.2 \pm 0.3\,^{\circ}$ (Clube 1967, Comerón 1992, de Zeeuw et al. 1999a, Pöppel 2001 and Grenier 2004). The majority of closest, star-forming regions are associated within the Belt, making it a prime target for the study of star formation. The names and locations of the star forming complexes, in Galactic coordinates, are presented in Figure 2.1.

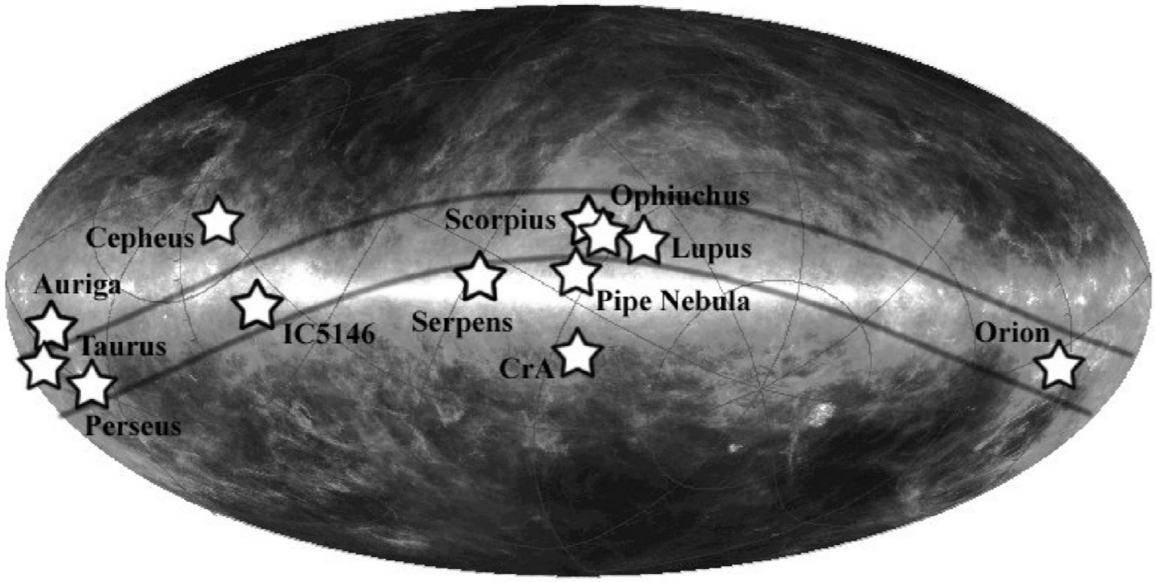

Figure 2.1: All-sky image of IRAS 100 μm data plotted in Galactic coordinates, showing the projection of the Gould Belt, and a number of star-forming complexes, onto the plane of the sky. Taken from Ward-Thompson et al. (2007).

The original science aims of the JCMT GBS were to: observe dense star-forming regions in the Gould Belt and to calculate the duration of protostellar lifetime, elucidate the nature of the evolution of protostellar collapse, discover the origin of the IMF and discern the connection between the protostars and the molecular cloud from which they form (Ward-Thompson et al., 2007). The survey underwent a rescope in 2011 following an update in instrument sensitivity (Hatchell, 2010). As a result the rescope focuses on scales comparable to the Jeans length, namely filaments, protostars and molecular outflows in areas of high (greater than 4 mag) extinction.

The JCMT GBS utilises the following instruments; the Submillimeter Common-User Bolometer Array 2 (SCUBA-2, Holland et al. 2013), the SCUBA-2 Polarimeter (POL-2, Bastien et al. 2005, commissioned early 2016) and the Heterodyne Array Receiver Programme for B-band (HARP, Buckle et al. 2009) that works in conjunction with Auto-Correlation Spectrometer and Imaging System (ACSIS; Hovey et al. 2000). HARP and ACSIS allow for observation of line emission from interstellar medium (ISM) molecular species between 325 and 375 GHz and can used for studying the kinematic structure of star forming regions. HARP will be discussed in full detail in the following chapter. POL-2 is designed to observe submillimeter polarisation and magnetic fields. As POL-2 has only recently been commissioned it does not feature further in this thesis. SCUBA-2 is the primary instrument of the JCMT, capable of observing submillimeter continuum emission at 450 and 850 μm. One of the primary aims of the JCMT GBS was to map all of the major low- and intermediate-mass star-forming regions within 0.5 kpc observable from the JCMT with SCUBA-2. This was completed in January 2015. SCUBA-2 will be discussed in depth in the following section. Much of the work presented in this thesis builds on analytical techniques developed for SCUBA (the predecessor to SCUBA-2) data (Johnstone et al., 2000; Kirk et al., 2006; Sadavoy et al., 2010) to analyse emission at 450 and 850 μm.

Table 2.1: SCUBA-2 signal components and models. Table adapted from Thomas & Currie (2014) and Chapin et al. (2013).

Model	Description
COM	Common-mode signal
GAI	Gain - the common-mode scaled to each bolometer
EXT	Extinction correction
FLT	Fourier transform filter
AST	Estimate of astronomical signal
RES	Residual noise estimate

2.2 SCUBA-2

SCUBA-2 can carry out continuum mapping of thermal dust emission at a resolution of 9.8″ and 14.6″ at 450 and 850 μm bands (Dempsey et al., 2013). By comparison the *Herschel* Space Telescope Photodetecting Array Camera and Spectrometer (PACS; Poglitsch et al. 2010) instrument observes in 250, 350, 500 μm but can only achieve a resolution of 18.2″, 25.0″and 36.4″, respectively (Aniano et al., 2011). SCUBA-2 also represents a significant advancement in mapping speed from its predecessor, SCUBA, being able to map a 30′ field to a sensitivity of 5 mJy/14″ beam in 2.6 hours (in Band 1 weather, Hatchell et al. 2011).

SCUBA-2 is a bolometer array composed of eight subarrays (four for each waveband) containing over 10,000 super-conducting Transition Edge Sensor (TES) bolometers. These detectors record a minute change in temperature when a submillimeter photon is incident upon them and a voltage is transmitted by a charge-coupled absorber and amplified by a Superconducting Quantum Interference Device (SQUID). In addition to water vapour in the atmosphere, the telescope itself is also a submillimeter emitter at room temperature and as a result SCUBA-2 is required to be cooled to approximately 100mK by liquid helium cryogen-free dilution refrigerator. The complete set up of SCUBA-2 is discussed in depth by Holland et al. (2006) and Robson & Holland (2007). SCUBA-2 has a field of view of 45′squared which allows larger regions to be observed quicker and to greater depth. Restricted to SCUBA, larger regions of star formation, for example Orion (Nutter & Ward-Thompson, 2007) and Perseus (Hatchell et al., 2007), were prioritised over lower mass regions, for example Serpens MWC 297.

The JCMT GBS extends the coverage of the local star-forming regions over those mapped by SCUBA, providing some of the most sensitive maps of star-forming regions where $A_V > 3$ with a target sensitivity of 3 mJy beam^{-1} at 850 μm and 12 mJy beam^{-1} at 450 μm, when observing in grade 1 ($\tau_{225\,GHz} \leq 0.05$) and 2 ($0.05 \leq \tau_{225\,GHz} \leq 0.08$) band weather (Hatchell et al., 2011). SCUBA-2 also offers much greater quality and quantity of 450 μm data, as a result of improved array technology and reduction techniques pioneered by Holland et al. (2006, 2013), Dempsey et al. (2013) and Chapin et al. (2013).

2.2.1 Data reduction

SCUBA-2 is composed of four, 30×42 bolometer arrays which return a voltage, per times series, from photons incident upon them (Holland et al., 2013). Over the length of the observation, the

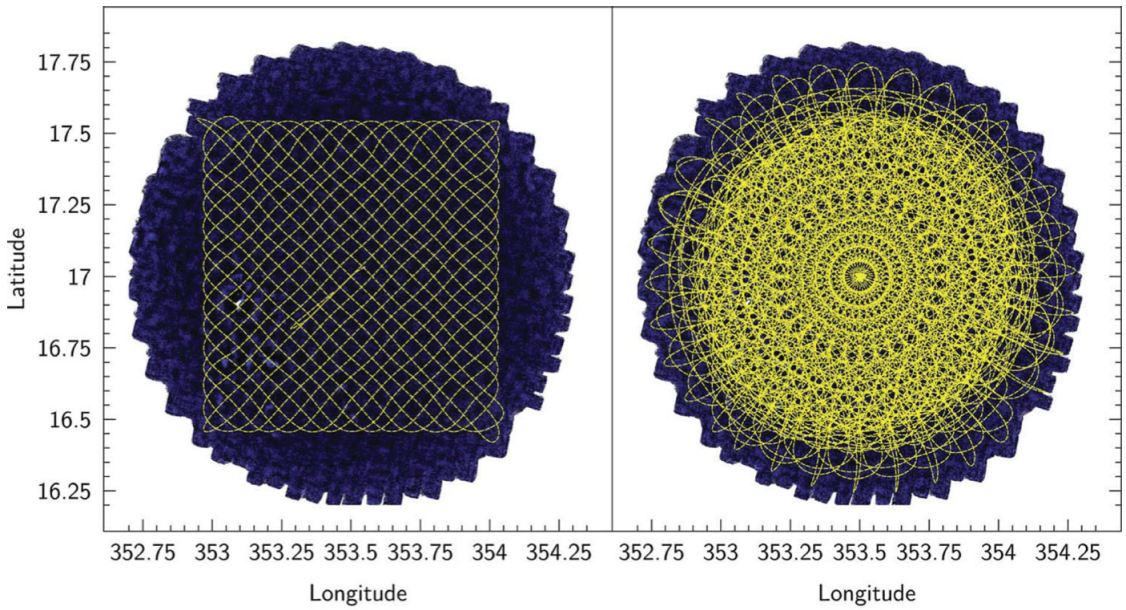

Figure 2.2: The JCMT SCUBA-2 tracking in the PONG mapping mode. The left panel shows a single scan pattern and the right panel shows multiple scans combined to provide maximum coverage of a 30′ diameter region (blue greyscale). Image adapted from Holland et al. (2013).

arrays will move across the source following a specific mapping mode so that each bolometer detects at a unique RA and Dec, per time. Signal is then averaged over common RA/Dec pixels to produce the raw data.

SCUBA-2 has two mapping modes. Constant velocity daisy (CVD) is a pseudo-circular pattern that is designed to keep the target on the array at all times and to maximise exposure. This mode is most useful for observing small, compact sources. The rotating PONG mode allows the array to track back and forth across a wide, circular area, iterating the observation angle slightly with each cycle. This mode is designed for mapping larger fields, typically 30′. Central regions of the PONG are mapped more frequently with this mode, leaving the edges with a comparatively worse signal-to-noise ratio (SNR) which can give rise to undesirable noise 'artefacts' in these regions. An example of the PONG scan mode tracking is given in Figure 2.2.

Typically a region will be scanned four to six times and the resulting maps mosaiced together to achieve a better SNR. Where the target region is larger than 30′, multiple PONGs are observed and mosaiced to produce the raw maps. Where the nosiey edges of the maps overlap, the increased sample size of the observations is sufficient to remove the additional artefacts.

Data reduction is carried out using a dynamic iterative map-maker (DIMM, `makemap` in the STARLINK SMURF package, Chapin et al. 2013, Jenness et al. 2013). In brief, this technique cleans the data before iteratively solving multiple signal components and finally regridding to produce the final map.

The first step in pre-processing is to calibrated the raw data with a flat field. This is the method by which any gain or current inherent to an individual bolometer can be mitigated. The time series is then resampled at a rate that matches the end pixel size. Likewise the raw data is masked so that malfunctioning or exceptionally noisy bolometers are removed. Additional

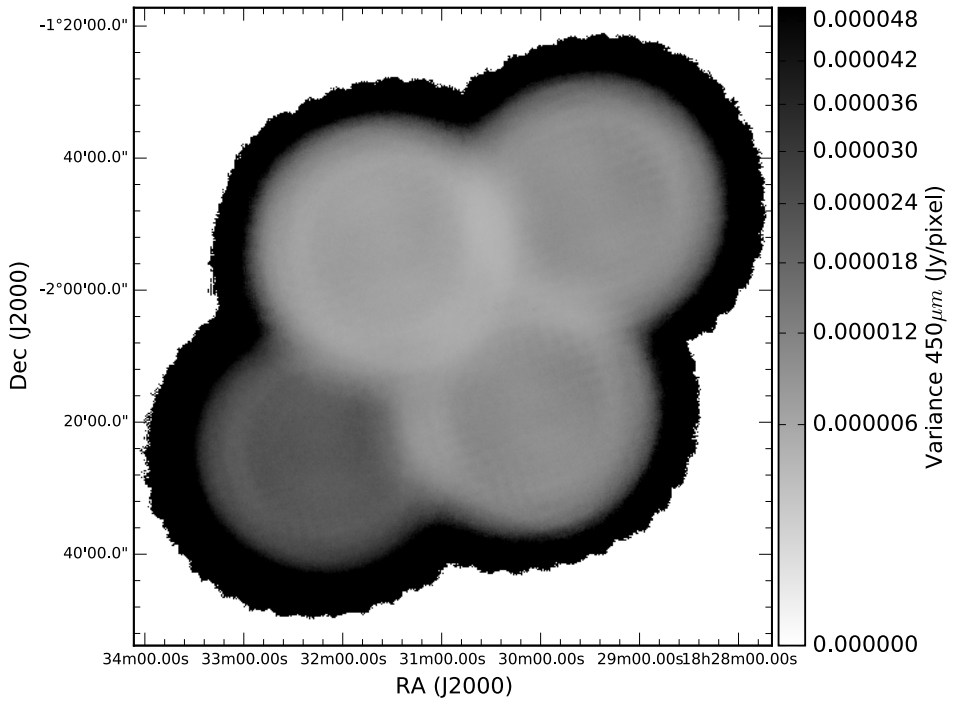

Figure 2.3: Variance array for the Aquila mosaic (at 450 μm).

preprocessing steps include spatial filtering and automatic subtraction of a polynomial baseline and any data spikes and dc steps. Finally, any resulting gaps in the time series are filled. I refer the reader to the SCUBA-2 data reduction cook book for further details (Thomas & Currie, 2014).

The iterative stage of the DIMM models various contaminating components of the target astronomical signal and progressively subtracts them in order of magnitude. Contributing component models are listed in Table 2.1 and examples of the time-series are presented in Figure 2.4, courtesy of Thomas & Currie (2014). The common mode signal (COM) and the gain (GAI) are the dominant contribution to noise in SCUBA-2 observations and are subtracted first. They represent the systematic fluctuations in gain common to all bolometers, such as sky signal. By taking the average signal across all bolometers the spurious outliers are removed. EXT is an extinction correction due to water vapour. FLT applies a Fourier transform to the data. The high and low-pass filters reduce the data in the frequency domain which corresponds to an angular spatial scale. At this point just the astronomical signal (AST) estimate and the residual noise (RES) model remain. DIMM estimates the AST model and subtracts it, checking to see if the remaining RES model matches the theoretical estimation of the noise. Where this is not case, the AST model is updated and reduction iterated until the RES model converges with noise field. The criteria for the convergence is dictated by a χ^2 test of the noise, and when AST map signal changes by less than a fraction of the estimated map rms noise. The DIMM and data reduction process is described in detail by Thomas & Currie (2014) and Chapin et al. (2013).

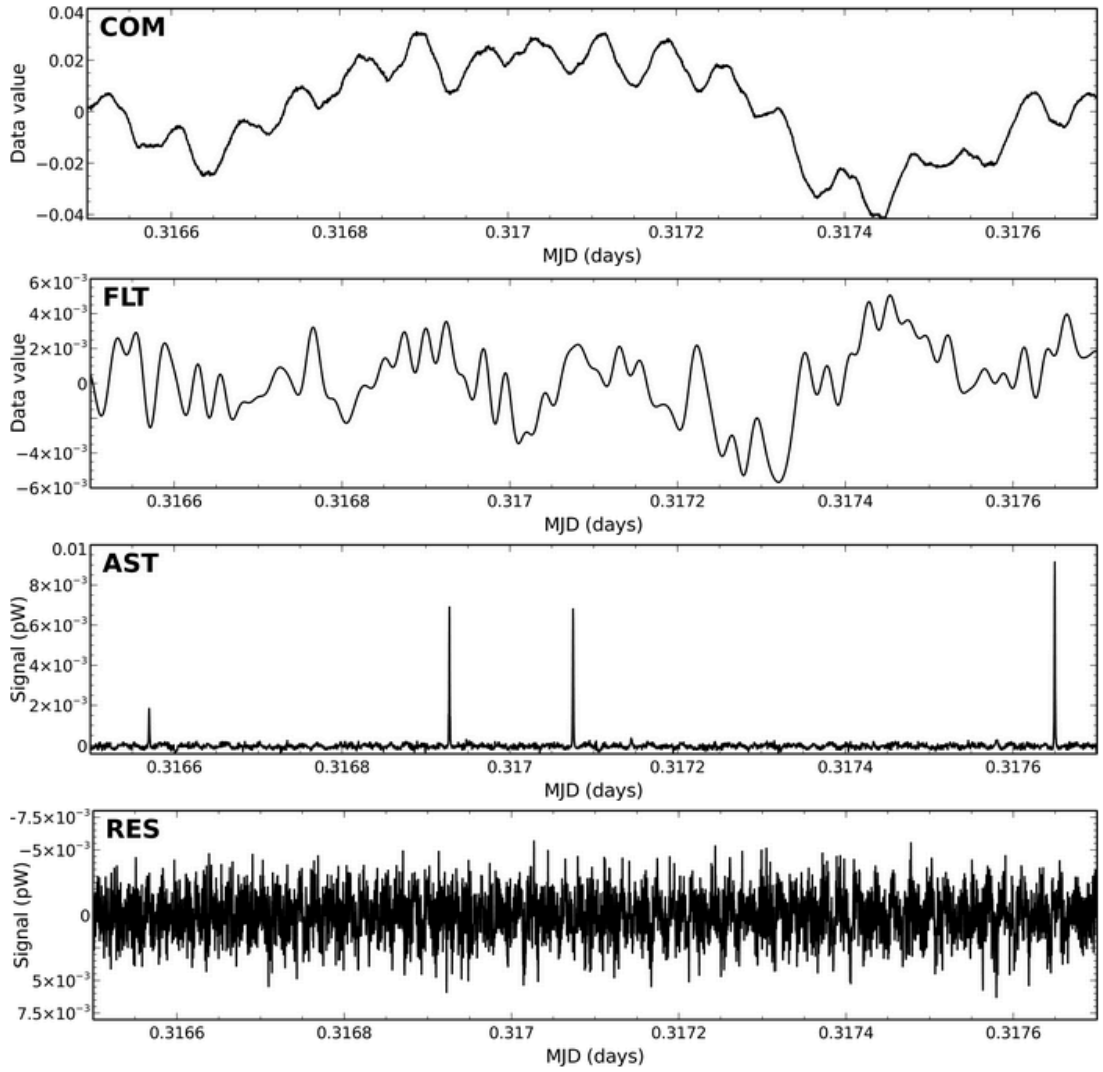

Figure 2.4: A sample of data reduction models, presenting signal power (pW) against time (days) for a single bolometer in an observation of CRL 2688. Upper presents the common model signal, COM. Upper middle presents the Fourier transform filter, FLT. Lower middle presents the astronomical signal complete with a source, AST. Lower plot presents the residual noise estimate, RES. Example models are taken from Thomas & Currie (2014).

Data reduction of the JCMT GBS

Throughout this thesis I make use of SCUBA-2 observations of the JCMT GBS regions that have been separately reduced by the SCUBA-2 data reduction team. Here I describe a number of adaptations are made to the SCUBA-2 data reduction pipeline that are specific to the reduction of the JCMT GBS regions and their science aims.

Whilst the SNR of the CVD scan mode is generally better, the greater coverage offered by the PONG mode is more suitable for observing extended filamentary structure that has been observed by the wider *Herschel* surveys. Whole regions often require many PONGs and are observed over a period of several days. Mosaicing PONGs observed in varying weather conditions can lead to discrepancies in the variance array, for example, Figure 2.3.

A spatial filter of 600″ is used in the JCMT GBS reduction pipeline, which means that flux recovery is robust for sources with a Gaussian FWHM less than 2.5′. Sources between 2.5′ and 7.5′ in size will be detected, but both the flux and the size are underestimates because the Fourier components with scales greater than 5′ are removed by the filtering process. Detection of sources larger than 7.5′ is dependent on the mask used for reduction.

The convergence criterion for the GBS is set at <0.1 % of AST model rms. The converged AST model is regridded onto a suitable pixel grid (typically 3″ pixels at 850 μm, 2″ pixels at 450 μm).

Further data reduction techniques for SCUBA-2 data have been developed by the GBS data reduction team and are used in Chapters 6 and 7. The SCUBA-2 data reduction pipeline is currently in its third iteration of parameters designed to observe bright, extended structure. Internal release 1 (IR1) and 2 (IR2) maps are widely used for analysis in this thesis.

The initial reductions from a set of parameters are coadded to form a mosaic from which a signal-to-noise mask is produced for each region. An updated mosaic is produced from a second reduction using this 'auto-mask' to mask the emission. Members of the JCMT GBS data reduction have developed more advanced masks that incorporate data from other telescopes to produce improved reductions. Figure 2.5 shows how the auto-mask reduction compares to those reductions based on masks adapted from solely SCUBA-2 data and SCUBA-2 combined with *Herschel* 500 μm observations. Detection of emission structure and calibration accuracy can be more robust within the masked regions, and are uncertain outside of the masked region. However, excessively large masks (like the SCUBA-2 + *Herschel* 500 μm mask shown in Figure 2.5 lower) risk including signal from regions with poor SNR into the reduction and can lead to excessive/unreliable flux in some regions (as is observed in the IR2 reductions of the Aquila W40 complex, see Section 5.2). In these examples a degree of smoothing allows for more large-scale structure to be included in the map and in extreme case, such as the SCUBA-2 and *Herschel* combined mask, drastically changes the amount of flux observed.

2.2.2 Calibration

SCUBA-2 data are initially calibrated in units of pW and are converted to Jy/pixel using Flux Conversion Factors (FCFs) derived by Dempsey et al. (2013) from the average values of JCMT calibrators. By correcting for the pixel area, it is possible to convert maps of units Jy/pixel to Jy/beam using

$$S_{\rm beam} = S_{\rm pixel}\left(\frac{\rm FCF_{peak}}{\rm FCF_{arcsec}}\right)\left(\frac{1}{\rm Pixel\ area}\right). \quad (2.1)$$

where $\rm FCF_{arcsec}$ = 2.34±0.08 and 4.71±0.5 Jy/pW/arcsec^2, at 850 μm and 450 μm respectively, and $\rm FCF_{peak}$ = 537±26 and 491±67 Jy/pW at 850 μm and 450 μm respectively. I note that IR1 maps produced by the GBS data reduction team are calibrated in units of Jy/beam whereas the later IR2 reductions are calibrated in units of Jy/pixel and Internal Release 3 (IR3) reductions are calibrated in units of mJy/arcsec^2.

When considering the ratio of SCUBA-2 fluxes (see Chapter 5 for details on how these are calculated), it is not the uncertainties at each wavelength but the uncertainties on the calibration

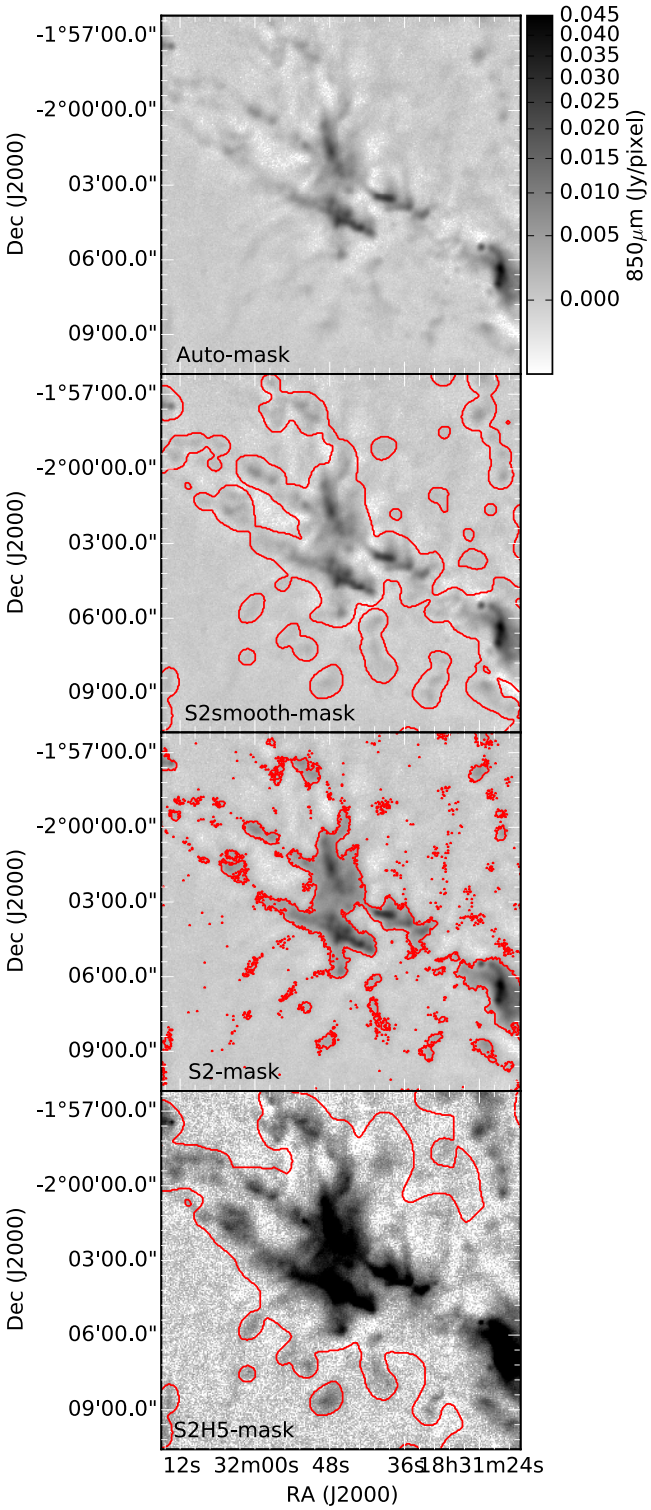

Figure 2.5: The SCUBA-2 850 μm observations of the W40-N region. Greyscale shows the reduced 850 μm data with red contours denoting the data reduction mask. Upper is 'auto-mask'. Upper-middle is SCUBA-2 smoothed mask. Lower-middle is the SCUBA-2 mask. Lower is the SCUBA-2 + *Herschel* 500 μm mask. All maps use the same greyscale.

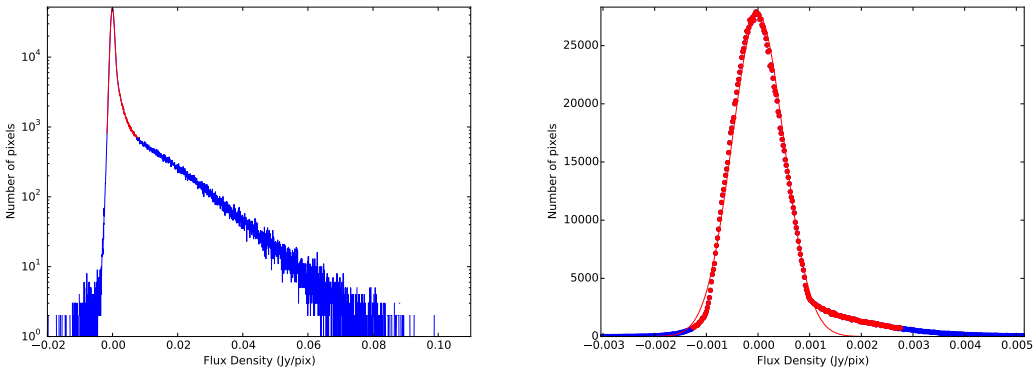

Figure 2.6: The distribution of flux densities, per pixel, for the Aquila region. Blue marks the entire set whereas red marks those pixels in the top 99.95 percentile of the distribution. The red line in the right hand figure shows a gaussian fit to the red data points from which the noise is calculated.

ratio that matter. Due to correlations between the 450 μm and 850 μm FCF measurements, the errors do not propagate simply. For a single scan, the calibration ratio is $FCF_{450}/FCF_{850} = 2.04\pm0.49$ (J. Dempsey, priv. comm.). The SCUBA-2 mosaics are made with at least four scans per region. Assuming these to be randomly drawn from the distribution of calibration ratios, the uncertainty on the ratio reduces to 2.04±0.25 or a calibration uncertainty of 10%.

2.2.3 Noise calculation

A consistent method is required for calculation of the noise level from which future SNR cuts will be based. Alongside signal, maps of uncertainty and variance are produced for each observed PONG. Hatchell et al. (2013) uses these uncertainty arrays as the basis of a $5\,\sigma$ cut to SCUBA-2 data. However, early data reduction methods omits significant residual atmospheric fluctuations on large spatial scales, and as a result the uncertainty on flux density, per pixel, is under estimated. I therefore calculate a single value for the uncertainty based on the standard deviation of the signal-masked flux density across the mosaic, following the method introduced by Salji (2014).

The typical distribution of flux density, per pixel, across a SCUBA-2 observation is shown in Figure 2.6. Astronomical signal found at high positive values is dominated by the statistical noise that has a mean value of 0. By clipping the distribution to include only the top 99.95% percentile it is possible to isolate just the noise and fit a gaussian (as in Figure 2.6 right), from which the FWHM, and subsequently the standard deviation, σ, or uncertainty can be calculated. A number of clipping sizes were sampled. Greater values often overestimated the fit whereas lower values underestimated. Often the lowest clipping sizes were unable to complete the fit.

The chosen clipping value represents an optimised solution that works for all maps in the JCMT GBS at both 450 and 850 μm. This fit was good in the majority of cases. Table 2.2 presents the 5σ noise level calculated at 450 and 850 μm for each of the sub-regions of Serpens-Aquila. Allowing for varying weather conditions and additional sky structure, all values are consistent to a satisfactory level. In a minority of cases a small, but systematic overestimate in the 450 μm

Table 2.2: Noise levels for the Serpens-Aquila regions

	5σ noise (mJy/pixel)	
Region	450 μm	850 μm
Serpens Main	21.8	3.1
Serpens East	35.5	2.5
Serpens West	18.0	2.7
Serpens MWC 297	43.5	3.0
Aquila	17.4	2.5

uncertainty is introduced. Manual assessment of individual regions could produce a better fit, but I opt for a method that can produce a consistent and robust form of measuring statistical noise across the majority of GBS regions that includes residual sky fluctuations.

When a region is comprised of multiple PONGs, the variance will vary systematically across the map due to varying weather conditions that the observations were observed in. As a result the cut level may be a slight over or under-estimate on some PONGS. In the example of the Aquila 450 μm variance array, presented in Figure 2.3, the variance can vary over a factor of three between 0.7 and 2.1×10^{-5}.

2.3 Clump finding

Star-forming regions are known to have a complex and often hierarchal structure when viewed across various length scales (Blitz & Shu, 1980). Nomenclature consistently tracks structures in ascending density, though the precise terminology is somewhat fluid in the literature. Throughout this thesis I consistently define the largest scales (greater than 5 pc, Murray 2011) as GMCs or 'star-forming complexes', descending to a collection of amorphous 'clouds' or 'filaments' (between 1 and 0.1 pc, Könyves et al. 2015) that may or may not be composed of spherical like 'cores' (0.05 pc, Rygl et al. 2013), that may or may not be forming one or more YSOs. It is worth noting that in most regions 'clouds' often appear fragmented in SCUBA-2 data due to the removal of large-scale structure by the data reduction process. Furthermore, in especially close star-forming complexes, individual Class II sources may have discs bright enough to be observed as isolated point sources.

Throughout this thesis I use clump finding algorithms to break down a star-forming complex into discrete regions for the purposes of measuring clump properties, as has been used by Johnstone et al. (2000), Hatchell et al. (2005), Kirk et al. (2006) and Hatchell et al. (2007), for example. A 'clump' does not have a well defined boundary within the ISM and is therefore defined separately, based not a set of consistent physical characteristics, but rather a consistent algorithm method and the flux density noise. Clump boundary is determined by the STARLINK CUPID package for the detection and analysis of objects (Berry et al., 2013). Figure 2.7 shows an example of how the FELLWALKER algorithm has defined multiple clumps within the Serpens Main cloud and ranked them by peak emission.

CUPID has a number of available methods for clump finding. Watson (2010) provides a comprehensive comparison of the methods and I summarise those most important methods below:

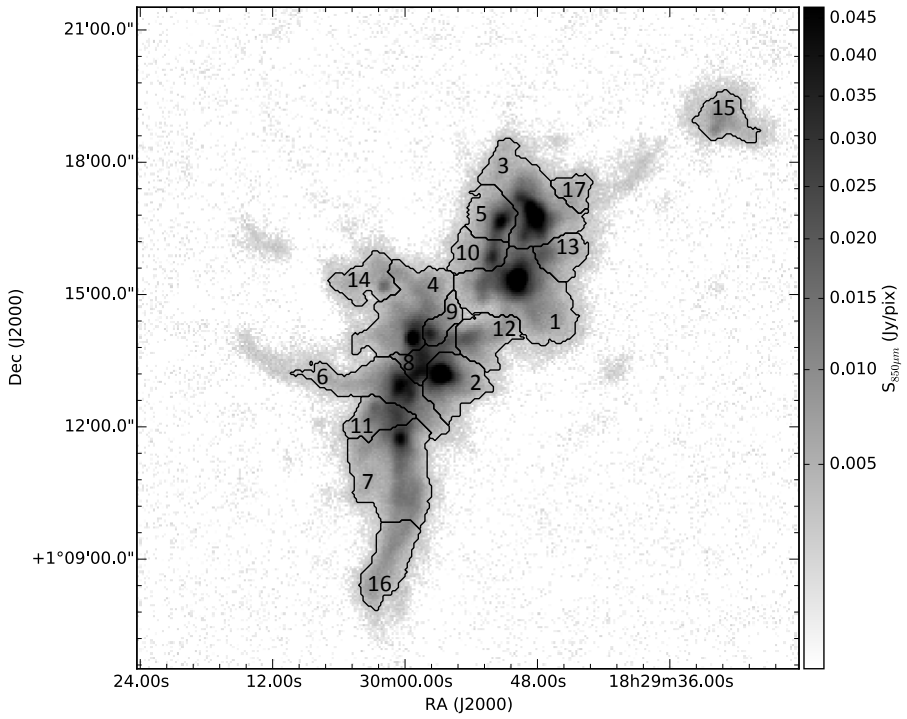

Figure 2.7: SCUBA-2 850 μm map of the Serpens Main cloud. Black contours shown how the FellWalker clump finding algorithm has segmented the cloud into discrete 'clumps' and indexed them according to their maximum brightness.

- FellWalker was developed by Berry et al. (2007) and Berry (2015). The algorithm considers a pixel in the data above the noise level parameter and then compares its value to the adjacent pixels. fellwalker then moves on to the adjacent pixel which provides the greatest positive gradient. This process continues until the peak is reached - when this happens all the pixels in the 'route' are assigned an index and the algorithm is repeated with a new pixel. All 'routes' that reach the same peak are assigned the same index and form the 'clump'. fellwalker has been used by Buckle et al. (2015), Kirk et al. (2015) and in Chapters 6, 7 and 8, for example. Figure 2.7 presents an example of fellwalker in use.

- ClumpFind was developed by Williams et al. (1994). The algorithm determines the peak emission in the data and draws contours at progressively lower levels, at each level determining how many unique peaks there are and defining them as a clump. This is a popular method that has previously been used by Reid & Wilson (2005), Enoch et al. (2006), Tanaka et al. (2013) and Shimajiri et al. (2015), for example.

- GaussClumps was developed by Stutzki & Guesten (1990); Stutzki (2014). This algorithm subtracts a gaussian profile from the brightest peak in the data and iterates this process many times until the integrated flux of the sum of gaussians equals the total flux of the original map. Unlike previous methods, clumps identified in GaussClumps may overlap with their neighbours. This algorithm has been used by Schneider et al. (1998), Curtis & Richer (2010) and Zhang et al. (2015), for example.

In addition to those clump finding algorithms provided in the STARLINK CUPID package, alternative methods exist. The CUTEx algorithm was developed by Molinari et al. (2011) and has been used by Veneziani et al. (2012) and Pattle et al. (2015). This method subtracts background and large-scale structure and then identifies compact sources in the resulting map. Alternatively dendogram analysis (Rosolowsky et al., 2008) can be used to reorganise a star-forming complex into 1-dimensional structure trees (Houlahan & Scalo, 1992). Dendograms have been used by Kauffmann et al. (2010a) and Kauffmann et al. (2010b) to examine the mass-size relation of clumps over several star-forming complexes, and by Duarte-Cabral et al. (in prep.) to examine the 3D structure of GMCs.

Both dendograms and CUTEx offer new and innovative ways to identify structure in complex star-forming regions. However, they do so at the expense of spatial information about the size of the clumps. The aim of this thesis is to address heating across star-forming regions. The requirement to calculate if a clump has a temperature gradient makes these methods unsuitable for answering these questions. Considering the CUPID methods, Watson (2010) concludes that the FELLWALKER algorithm has greater consistency over parameter space whilst providing discrete, spatial clumps to base future analysis on. For these reasons, I use the FELLWALKER algorithm in all work used in this thesis. However, it is important to note that FELLWALKER does not return clumps of a consistent size or shape, as demonstrated in Figure 2.7. Details of the parameters used in specific cases are given in Chapters 6, 7 and 8.

2.4 *Spitzer* YSOc catalogues

In order to address the central question of this thesis, 'does radiative feedback from stars influence star-formation?', I require prior knowledge of star formation in these regions. I identify a number of YSOc catalogues that cover the JCMT GBS regions. The most prominent of these is a product of the *Spitzer Space Telescope* legacy survey of star-forming regions.

Spitzer observations covers the mid IR parameter space well with $2''$ resolution photometry from the Infrared Array Camera (IRAC; Fazio et al. 2004) at 3.6, 4.5, 5.8 and 8.0 μm, and diffraction limited 24, 70 and 160 μm observations from the Multiband Imaging Photometer for *Spitzer* (MIPS; Rieke et al. 2004). Where available, auxiliary Two Micron All Sky Survey (2MASS; Skrutskie et al. 2006) J, H and K_s, SCUBA-2 450 and 850 μm, as well as *Herchel Space Telescope* PACS (70, 100 and 160 μm; Poglitsch et al. 2010) and Spectral and Photometric Imaging Receiver (SPIRE 250, 350, 500 μm; Griffin et al. 2010), can be used to build up a more complete spectral energy distribution (SED) for the YSOc. In addition to location, the YSO SED can act as a metric of classification (see Chapter 1).

The bulk of objects initially observed in a point source survey are field stars. These have an IRAC colour of approximately zero and are relatively easy to filter (Allen et al., 2004). Reddened cool, or giant stars are distinguished from YSOcs through identification of the infrared excess in 24 μm *Spitzer* observations (Allen et al. 2004, Gutermuth et al. 2004, Megeath et al. 2004, Evans et al. 2009 and Winston et al. 2010). This distinction comes through the application of the Flaherty et al. (2007) reddening law where by the [5.8] - [8.0] colour is relatively insensitive to Galactic

red field stars.

These methods are not effective at removing extragalactic sources which have comparable colour to YSOs (Stern et al., 2005). Harvey et al. (2007) summarise the selection criteria for identifying extragalactic candidates and Gutermuth et al. (2008) remove extragalactic sources by identifying those that are dominated by PAH features, or are exceptionally faint. However, this method will bias the sample to remove some of the faintest YSOs as well. IR bright nebulosity may further contaminate the YSO catalogue and Winston et al. (2010) develop a method whereby all sources with an excess in the [5.8] - [8.0] colour that do not show excess in 24 μm or [3.6] - [4.5] ≥ 0.1 are removed. Despite these innovations, a number of contaminating objects will remain in the final selection of YSOs. Gutermuth et al. (2009) calculate that this should account for less than 2 % of sources in the Serpens-Aquila region, for example.

The *Spitzer* "From Molecular Cores to Planet-forming Disks" (c2d) survey (Evans et al., 2003, 2009) mapped seven star forming systems (Serpens, Lupus I, II, IV, Ophiuchus, Perseus and Chamaeleon II) with *Spitzer*. Candidate YSOs required detections in IRAC bands and MIPS 24 μm. The observational setup, data reduction and source classification used the c2d pipeline as described in detail in the c2d delivery document (Evans et al., 2007). YSOcs are classified through the calculation of spectral index between 2 and 24 μm, as discussed in Chapter 1, Section 1.4.

The *Spitzer* legacy program "Gould's Belt: star formation in the solar neighbourhood" (SGBS, PID: 30574) is a mid-infrared survey of 11 star forming regions using *Spitzer* IRAC and MIPS bands aimed to complete the mapping of local star formation started by the c2d survey by targeting the regions IC5146, CrA, Scorpius (renamed Ophiuchus North), Lupus II/V/VI, Auriga, Cepheus Flare, Aquila (including MWC 297), Musca, and Chameleon to the same sensitivity and using the same reduction pipeline (Gutermuth et al., 2008; Harvey et al., 2008; Kirk et al., 2009; Peterson et al., 2011; Spezzi et al., 2011; Hatchell et al., 2012). The SGBS also provided MIPS 70 and 160 μm coverage, although the latter saturates in regions of exceptionally bright emission, for example.

A total of 140 YSO candidates presented in Winston et al. (2007) were compared to the c2d and SGBS surveys for the Serpens Main region. 92 sources are consistent between catalogs and have been identified by different methods making it likely they are indeed YSOcs as opposed to contaminants. Classification between protostars (Class 0/I) and PMS (Class II/III) stars is inconsistent in 14 cases. The disagreement between these various catalogues demonstrates the varying methods that are used to identify YSOs and highlights the need for a consistent catalogue across all regions of the JCMT GBS if meaningful analysis of protostellar populations is to be completed.

Dunham et al. (2015) combine the regions covered by SGBS and c2d catalogue to produce a consistent catalogue of almost 3,000 YSOcs for the majority of star forming regions in the JCMT GBS including dust spectral index, extinction, bolometeric temperature and luminosity. Global results across the survey indicate that YSOc populations are distributed among class as: Class 0/I 11 %, FS 7 %, II 42 % and III 40 %.

Dunham et al. (2015) does not cover Orion and Taurus. YSOc catalogues for this regions are compiled separately by Megeath et al. (2012) and Rebull et al. (2010). These catalogues are folded into the Dunham et al. (2015) catalogue, along with any new YSOcs identified in Chapter 6

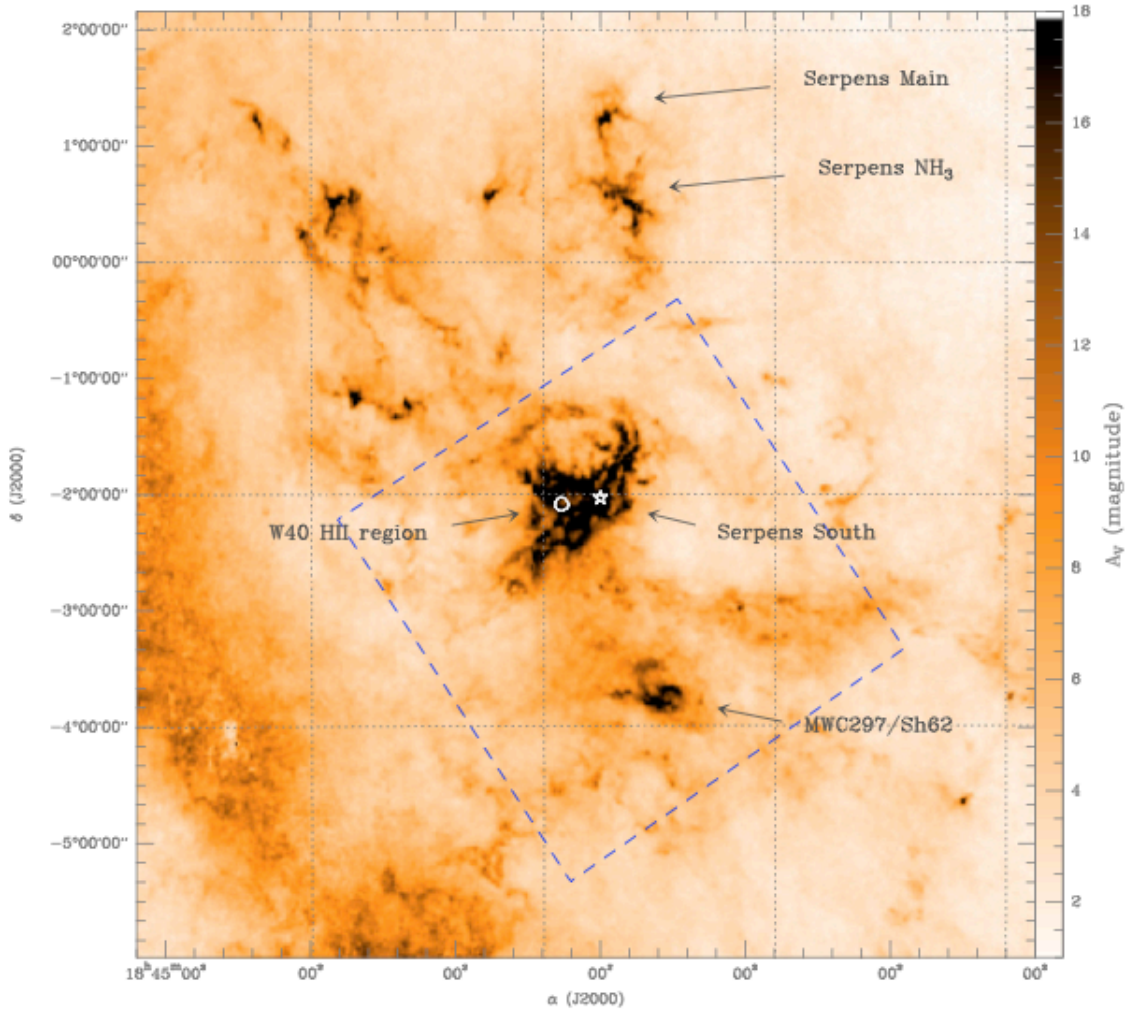

Figure 2.8: A visual extinction map of the whole Serpens/Aquila region derived from 2MASS data. Of particular interest are the Serpens Main and W40/Serpens South region. Note that whilst these two last regions appears as one continuous feature on this map, they are thought to be separate features (labelled respectively with the circle and star). The dashed rectangle indicates an area examined by Herschel. Plot taken from Bontemps et al. (2010).

and Mowat et al. (2016, in prep.), to produce the Dunham et al. (2015) c2d+GBS catalogue, which covers a total of 21 regions. In Chapters 6 and 7 I study Serpens MWC 297 and the Aquila W40 complex. Both of these regions feature only in the SGBS catalogue and therefore full use of the Dunham et al. (2015) catalogue is not required. Instead I assemble a bespoke catalogue for each region based on SGBS and additional catalogues. The details of these are discussed in Sections 2.5.1 and 2.5.2.

2.5 The Serpens-Aquila region

In this section, I introduce the properties of each sub-region of Serpens-Aquila. This region covers a rift of extinction at $l = 28°$, spanning approximately 5 °. I primarily focus on Serpens MWC 297 and the W40 complex, which are analysed in detail in Chapters 6 and 7, but I also discuss Serpens

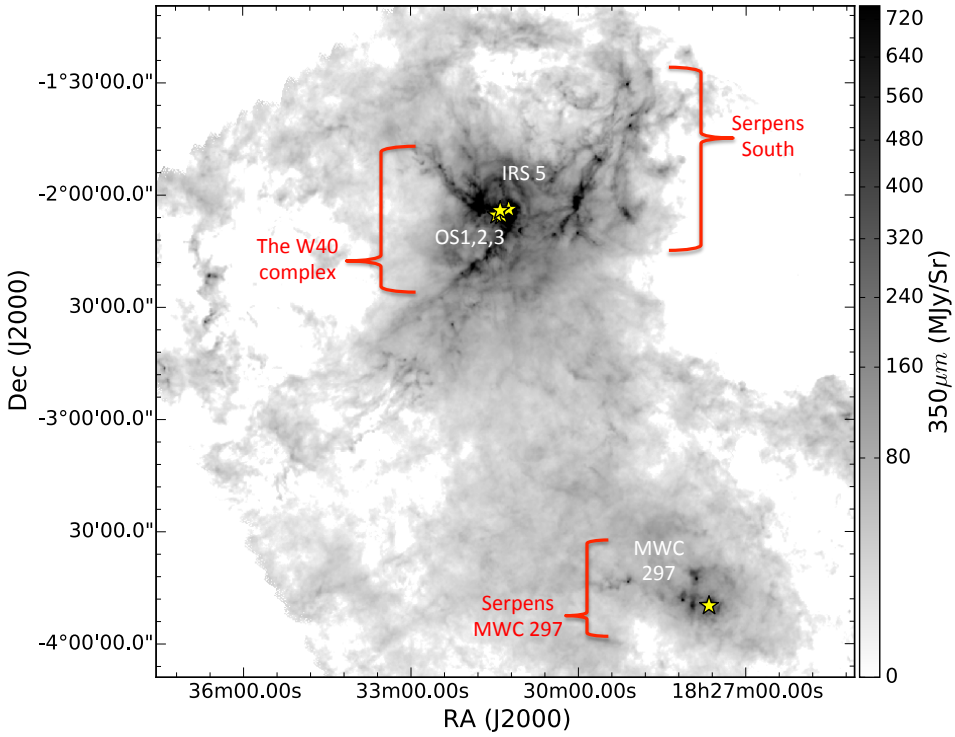

Figure 2.9: *Herschel* 350 μm map of the Aquila-Rift including the W40 complex, Serpens South and Serpens MWC 297. OB stars are marked with yellow crosses and labelled.

Main, NH_3, South, East and North. Straižys et al. (2003) put the distance to the 'extinction wall' of the Aquila rift at 225 ± 55 pc. Bontemps et al. (2010) present a visual extinction map of the whole region in Figure 2.8 where a number of over-dense sub-regions are labelled and have been observed as part of the JCMT GBS. Serpens Main, South and North are cold, younger star forming regions where YSOs are low mass. Serpens MWC 297, Serpens NH_3, Serpens East and the W40 complex are star forming regions where at least one high mass, OB star is present, and an associated nebulosity has been observed at IR wavelengths (Men'shchikov et al., 2010). I note that Serpens South and the W40 complex, and Serpens Main and NH_3 are observed simultaneously by SCUBA-2 as a result of their close proximity on the sky.

2.5.1 Serpens MWC 297

The star MWC 297 is an isolated, intermediate-mass zero-age main-sequence (ZAMS) star located to the south east of Serpens South in the Serpens MWC297 sub-region[1], as shown in Figures 2.8 and 2.9, at RA (J2000) = 18:27:40.6, Dec. (J2000) = -03:50:11.0. Drew et al. (1997) noted that MWC 297 has strong reddening due to foreground extinction (A_V = 8) and particularly strong Balmer line emission. The star has been much studied as an example of a classic Herbig AeBe star. Berrilli et al. (1992) and Di Francesco et al. (1994, 1998) find evidence of an extended disc/circumstellar envelope around the star MWC 297. Radio observations constrain disc size to <100 au and also find evidence for free-free emission at the poles that suggest the presence of

[1]This subsection is largely drawn from Rumble et al. (2015), *The JCMT Gould Belt Survey: evidence for radiative heating in Serpens MWC 297 and its influence on local star formation.*

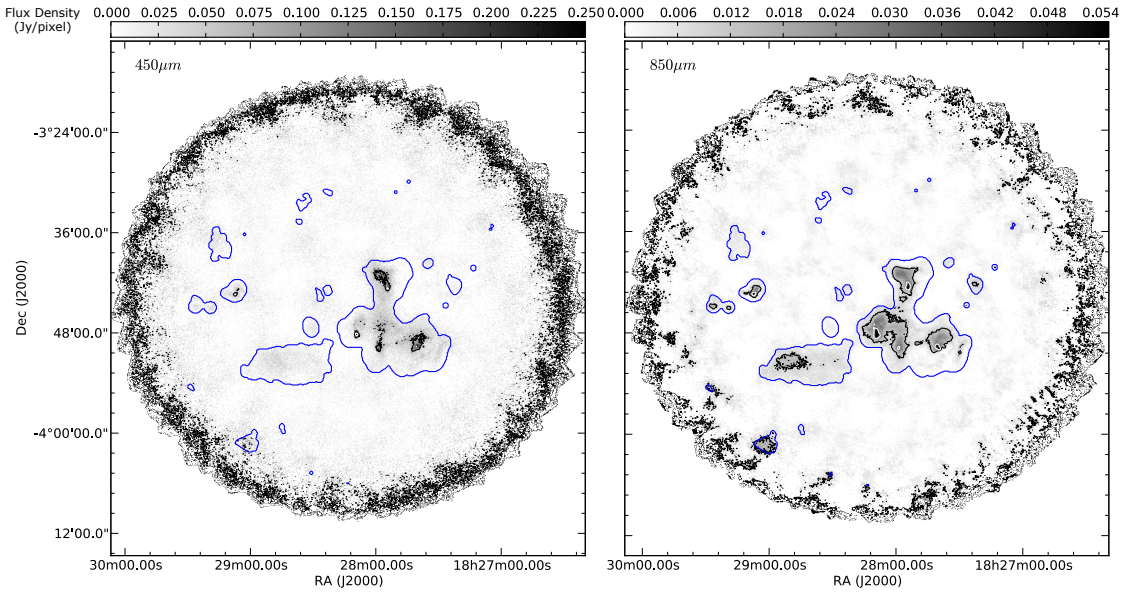

Figure 2.10: SCUBA-2 450 μm (*left*) and 850 μm (*right*) data. Contours show 5σ and 15σ levels in both cases: levels are at 0.082, 0.25 Jy/ 4″ pixel and 0.011, 0.033 Jy/ 6″ pixel at 450 μm and 850 μm respectively. The blue outer contour shows the data reduction mask for the region, based on *Herschel* 500 μm observations. Noise levels increase towards the edges of the map on account of the mapping method outlined in Section 2.1.

polar winds or jets (Skinner et al., 1993; Malbet et al., 2007; Manoj et al., 2007). MWC 297 is in a loose binary system with an A2 star, hereafter referred to as *OSCA*, which has been identified as a source of X-ray emission (Vink, O'Neill, Els & Drew, 2005; Damiani, Micela & Sciortino, 2006). There is evidence for an optical nebula, SH2-62, which is coincident with MWC 297 (Sharpless, 1959). Drew et al. (1997) compare the radial velocities of the star and the HII region (Fich et al., 1990) and find they are significantly different.

Distance

Preliminary estimates of the distance to the star MWC 297 were put at 450 pc by Canto et al. (1984) and 530 ± 70 pc by Bergner et al. (1988) using CO kinematics which are considered to unreliable at distances under 1 kpc. Drew et al. (1997) used a revised spectral class of B1.5Ve to calculate a closer distance of 250 ± 50 pc which is in line with the value of 225 ± 55 pc derived by Straižys et al. (2003) for the minimum distance to the extinction wall of the whole Serpens-Aquila rift of which the star MWC 297 is thought to be a part.

YSOc catalogues

Three YSOc catalogues are found for the Serpens MWC 297 region, each deploying a different method to identify and classify YSOcs. *Chandra* ACIS-I observations of X-ray flaring were carried out by Damiani et al. (2006) over an area of 16.9′ × 8.7′ centred on the star MWC 297 and

Table 2.3: A sample of *Spitzer* YSO candidates (YSOc) from the SGBS. The full table is available with DOI:10.11570/15.0002.

ID	SSTgbs	*Spitzer* IRAC				*Spitzer* MIPS		
		$S_{3.6}$ mJy	$S_{4.5}$ mJy	$S_{5.8}$ mJy	$S_{8.0}$ mJy	S_{24} mJy	S_{70} mJy	$\alpha_{\rm IR}$
YSOc2	J18271323-0340146	193.0 ± 10.4	220.0 ± 11.3	258.00 ± 13.40	354.00 ± 17.20	1170.0 ± 110.0	1610 ± 172	−0.17
YSOc11	J18272664-0344459	76.2 ± 3.7	87.4 ± 4.5	92.30 ± 4.33	116.00 ± 6.00	198.0 ± 18.4	312 ± 41	−0.49
YSOc15	J18273641-0349133	5.4 ± 0.3	3.5 ± 0.2	10.60 ± 1.77	38.60 ± 8.78	107.0 ± 28.4	...	0.03
YSOc16	J18273671-0350047	11.0 ± 0.6	16.7 ± 0.9	24.10 ± 2.55	29.00 ± 2.68	340.0 ± 84.2	...	0.75
YSOc17	J18273710-0349386	868.0 ± 43.7	985.0 ± 52.2	1100.00 ± 57.60	1230.00 ± 67.20	1780.0 ± 262.0	...	−0.43
YSOc21	J18273921-0348241	1.0 ± 0.3	1.3 ± 0.1	10.90 ± 1.48	38.70 ± 7.55	73.5 ± 15.2	...	1.51
YSOc38	J18275223-0344173	0.1 ± 0.0	0.0 ± 0.0	0.14 ± 0.05	0.38 ± 0.11	3.8 ± 1.2	454 ± 195	1.17
YSOc32	J18275019-0349140	44.2 ± 2.2	63.7 ± 3.1	84.40 ± 4.01	96.70 ± 4.79	427.0 ± 39.6	...	0.17
YSOc41	J18275472-0342386	153.0 ± 7.7	254.0 ± 12.7	370.00 ± 17.80	571.00 ± 27.20	2100.0 ± 202.0	3480 ± 446	0.56
YSOc47	J18280541-0346598	11.9 ± 0.6	37.0 ± 1.9	59.80 ± 2.80	70.10 ± 3.36	344.0 ± 32.1	3560 ± 386	0.96
YSOc73	J18290545-0342456	4.7 ± 0.2	14.2 ± 0.7	21.80 ± 1.04	25.00 ± 1.20	49.4 ± 4.6	662 ± 71	0.30

Table 2.4: YSO candidates in the MWC 297 region.

	YSO Classification		
	0/I	II	III
Damiani et al. (2006)	-	-	27
SGBS[a] - Gutermuth et al. (2008)	8	32	36
SYC - Gutermuth et al. (2009)	4	16	2
Connelley & Greene (2010)	1	-	-
Total[b]	10		72

a - Within a 20′ radius area centred at RA (J2000) = 18:28:13.8, Dec. (J2000) = -03:44:01.7.
b - The totals account for sources which feature in multiple catalogues.

as a consequence their sample is incomplete for the whole of the Serpens MWC 297 region (30′ diameter). They find that the star MWC 297 only accounts for 5.5 % of X-ray emission in the region. The rest is attributed to flaring low mass PMS-stars. As Damiani et al. (2006) do not make the distinction between YSOs and more evolved objects in their work it is not possible to use these data for the purposes of classification.

The Serpens MWC 297 region was observed twice by *Spitzer* in the mid-infrared and as a result two independent lists of YSOcs exist for this region; first, as part of the *Spitzer* Young Clusters Survey (SYC, Gutermuth et al. 2009), and second as part of the SGBS. In both surveys, mapping observations were taken with all the IRAC bands and at 24 μm with MIPS.

SYC targeted 36 young, nearby, star-forming clusters and had a 15′ × 15′ area centred on the star MWC 297. Observations, data reduction and source classification were carried out using ClusterGrinder as described in Gutermuth et al. (2009). SYC identifies 22 YSOcs using a colour-colour method, though the coverage is not comparable to the larger SGBS catalogue. SGBS identifies Class I and II YSOcs, detecting a total of 76 within a 20′ radius of the centre of the field (Table 2.3). Where the SGBS and SYC overlap I find notable differences between the catalogues. SGBS include five protostars whereas SYC include four. Of these samples, only three are consistent across catalogues. These are YSOc2, 47 and 11 presented in Table 2.3. Similarly SGBS identifies 22 PMS-stars whereas SYC identified 18. Across the sample 11 are consistent in both catalogues and are most likely to be real YSOs. Of the two *Spitzer* YSOc surveys, I use SGBS as the primary *Spitzer* catalogue because it covers all of the SCUBA-2 mapped area.

The c2d catalogue does not cover Serpens MWC 297 and therefore the combined Dunham et al. (2015) catalogue adds no further information to this region, and is consequently not used.

SCUBA-2 observations and data reduction

Serpens MWC 297 was observed with SCUBA-2 (Holland et al., 2013) on the 5th and 8th of July 2012 as part of the JCMT Gould Belt Survey (GBS, Ward-Thompson et al. 2007) MJLSG33 SCUBA-2 Serpens Campaign (Holland et al., 2013). One scan was taken on the 5th at 12:55 UT in good Band 2 with 225 GHz opacity $\tau_{225} = 0.04-0.06$. Five further scans taken on the 8th between 07:23 and 11:31 UT in poor Band 2, $\tau_{225} = 0.07 - 0.11$. Continuum observations at 850 μm and

Table 2.5: SCUBA-2 observations of Serpens MWC 297.

PONG	RA Dec (J2000)	# of Obs.	Weather band(s)	Observation dates	$\bar{\sigma}$ (Jy/pix)
MWC297	18:27:40.6, -03:50:11	6	2	5, 8 July 2012	3.0×10^{-4}

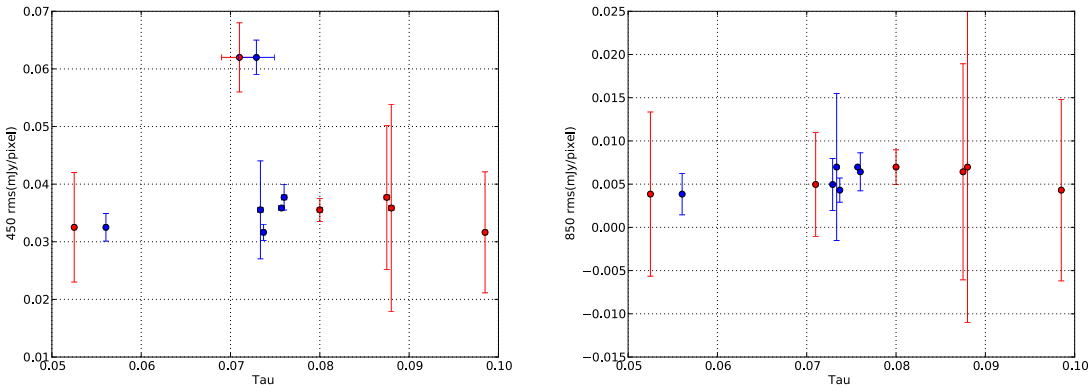

Figure 2.11: Plots of optical depth due to water vapour, τ, as a function of noise level of the data in the six component scans of Serpens MWC 297 at 450 μm *(left)* and 850 μm *(right)*. Tau is measured at two frequencies, 225GHz *(red)* and 186GHz *(blue)*.

450 μm were made using fully sampled 30′ diameter circular regions (PONG1800 mapping mode, Chapin et al. 2013) centered on RA (J2000) = 18:28:13.8, Dec. (J2000) = -03:44:1.7.

The data were reduced by the SCUBA-2 GBS data reduction team using the DIMM technique outlined in Section 2.2.1 and gridded to 4″ pixels at 450 μm and 6″ pixels at 850 μm. The final mosaic was produced using an 'auto-mask' combined with *Herschel* 500 μm emission at greater than 2 Jy beam^{-1} to include all potential emission regions. The reduced map is calibrated in units of Jy/pix using Equation 2.1 and is presented alongside the mask in Figure 2.13. Typical noise levels are 16.5 and 2.2 mJy/pixel at 450 μm and 850 μm respectively. This corresponds to a 5σ level of 43.5 mJy/4″ pixel and 3.0 mJy/6″ pixel at 450 μm and 850 μm, respectively (Table 2.2).

Selection

Science ready data products from SCUBA-2 invariably include all of the scans observed (between four and six depending on the weather conditions) in order to achieve the best SNR. However, I examined the individual scan maps and find significant deviation in the SNR and quality of the observation. Examining the Serpens MWC 297 region, presented in Table 2.6, I found scan 34 had a significantly large number artefacts that are attributed to many bolometer failures in one 850 μm case. Furthermore, in scan 14 the optical depth due to water vapour, τ_{225} and τ_{186}, was found to be significantly outside the mean value at 450 μm, as demonstrated in Figure 2.11, justifying possible deselection from the mosaic.

I masked the variance maps of the Serpens MWC 297 region with the data reduction mask to eliminate the high variance edges of the PONG. I compared the variance of each pixel in one scan

Table 2.6: Fraction of artefact pixels in Serpens MWC 297 region, masked

	Fraction of artefacts				
Scan	450 μm	Selection	850 μm	Selection	Comments
14	0.123	X	0.169	X	Poor weather
20	0.097	X	0.499	X	Excessive artefacts
23	0.028	Y	0.051	Y	
26	0.075	Y	0.061	Y	
34	0.028	Y	0.062	X	Bolometer failure.
48	0.044	Y	0.054	Y	
Mean	0.061		0.149		

to the mean of the remaining five. Where this pixel value was greater than three standard deviations from the mean it was flagged as an artefact. Typical fractions of artefacts due to statistical noise within the data reduction masks of MWC 297 region were between 3 % and 6 % for 450 μm and 850 μm, respectiely. Scans 14 and 20 were flagged with artefact fractions of 12.3 % and 9.7 % at 450 μm and 16.9 % and 49.9 % at 850 μm.

Of the six scans observed, only 23, 26 and 48 pass these tests and were selected for the updated mosaic at each wavelength for SNR testing. The omission of half of the components has a non-negligible affect on the background noise level of the maps, causing it to increase by 24 % at 450 μm and 20 % at 850 μm in the updated map. On this basis, the SCUBA-2 analysis of the Serpens MWC 297 region (Chapter 6) uses all the available scans in order to achieve the best possible SNR across the whole map. However, in a minority of areas there is evidence that artefacts in individual scans may contribute to the overall flux.

2.5.2 Aquila W40 Complex

The Aquila W40 complex[2] (presented in Figure 2.9) is located in the eastern half of the Serpens-Aquila region at RA (J2000) = 18:31:26, Dec. (J2000) = -02:05:30. The Aquila W40 complex is a site of high-mass star formation associated with a cold molecular cloud (Dobashi et al., 2005) and includes a blistered H II region (Westerhout, 1958) powered by an OB association (Zeilik & Lada, 1978; Smith et al., 1985). The OB association is comprised of OS1a (O9.5), OS2b (B4) and O3a (B3) and an associated stellar cluster of pre-main-sequence (PMS) stars that are detected in the X-ray by Kuhn et al. (2010). OS1aS is the primary ionising source of the H II region that was detected in the radio via free-free emission (Vallee & MacLeod, 1991). The OB association drives the formation of the larger nebulosity Sh2-64 (Sharpless, 1959). The Aquila W40 complex is detected in the mid and far-IR by the *Herschel* Space Telescope (André et al., 2010; Men'shchikov et al., 2010; Könyves et al., 2010; Bontemps et al., 2010; Könyves et al., 2015) with three significant filaments (W40-N, W40-S and the Dust Arc). Rodney & Reipurth (2008) presents a further review of the Aquila W40 complex.

[2]This subsection is largely drawn from Rumble et al. (2016), *The JCMT Gould Belt Survey: Evidence for radiative heating and contamination in the W40 complex.*

Table 2.7: The composite YSO catalogue for the Aquila W40 complex, produced from the combined SGBS (Dunham et al. 2015), the Mallick et al. (2013) *Spitzer* catalogue, the Maury et al. (2011) MAMBO catalogue, the Kuhn etal. (2010) X-ray catalogue, and the Rodríguez etal. (2010) catalogue of radio YSOs. The full catalogue is associated with DOI: 10.11570/16.0006.

Name[a]	YSO class	α^b (2-24 μm)	$T_{bol}{}^b$ (K)
2MASS18303312-0207055	II	-0.78	1400
2MASS18303314-0220581	II	-1.93	1700
2MASS18303324-0211258	II	-0.48	950
2MASS18303509-0208564	II	-0.86	1200
2MASS18303590-0206492	II	-1.45	1700

a - 2MASS or CXO name where available. RA and Dec coordinates (J2000) where not.
b - T_{bol} and α values as published by Dunham et al. (2015).

Distance

The neighbouring Serpens South filament is thought to be part of the Aquila Rift, sharing the distance of 225 ± 55 pc (Straižys et al., 2003) with the nearby Serpens MWC 297 region (Drew et al., 1997; Sandell et al., 2011). Despite the close proximity of the Aquila W40 complex to these regions, its distance is a contentious issue. Kuhn et al. (2010) calculate a distance of 600 pc via fits to the X-ray luminosity function. Bontemps et al. (2010) and Maury et al. (2011), however, argue that the assumptions in these calculations are unreliable and conclude a physical association with Serpens South. Shuping et al. (2012) construct SEDs from IR data of bright objects in the Aquila W40 complex and estimate a distance between 455 pc and 536 pc and I use this mean distance of 500 ± 50 pc, following Radhakrishnan et al. (1972), Shuping et al. (2012), and Mallick et al. (2013). The Aquila W40 complex is therefore assumed to be spatially separated from the Serpens South region (Straižys et al., 2003; Gutermuth et al., 2008).

YSOc catalogues

The Aquila W40 complex has a known high mass star population including one late O type, three B type and two Herbig AeBe stars (Smith et al., 1985; Shuping et al., 2012) as well as a young stellar cluster of approximately 420 stars, derived from the intrinsic X-ray luminosity function (Kuhn et al., 2010, 2015). The SGBS provides specific locations and properties of the YSOs. This catalogue is incomplete due to saturation of *Spitzer* at the heart of the OB association and may also be contaminated by the IR bright clouds in the nebulosity. Additional catalogues are required to verify and complete the YSO population.

I create a new, conservative YSO catalogue of SGBS objects matched with Mallick et al. (2013)'s *Spitzer* catalogue, Maury et al. (2011)'s MAMBO catalogue of submillimeter objects, and Kuhn et al. (2010)'s x-ray catalogue. The SGBS objects are matched with the Mallick et al. (2013) sources, except where the SGBS is saturated around the H II region. In those cases, I turn to the Kuhn et al. (2010) catalogue of K-band excess objects as a proxy list of Class II and III objects. By matching the Kuhn et al. (2010) and Mallick et al. (2013) sources, IR bright clouds which may have been misidentified as sources can be exorcised. These two sub-catalogues are subsequently

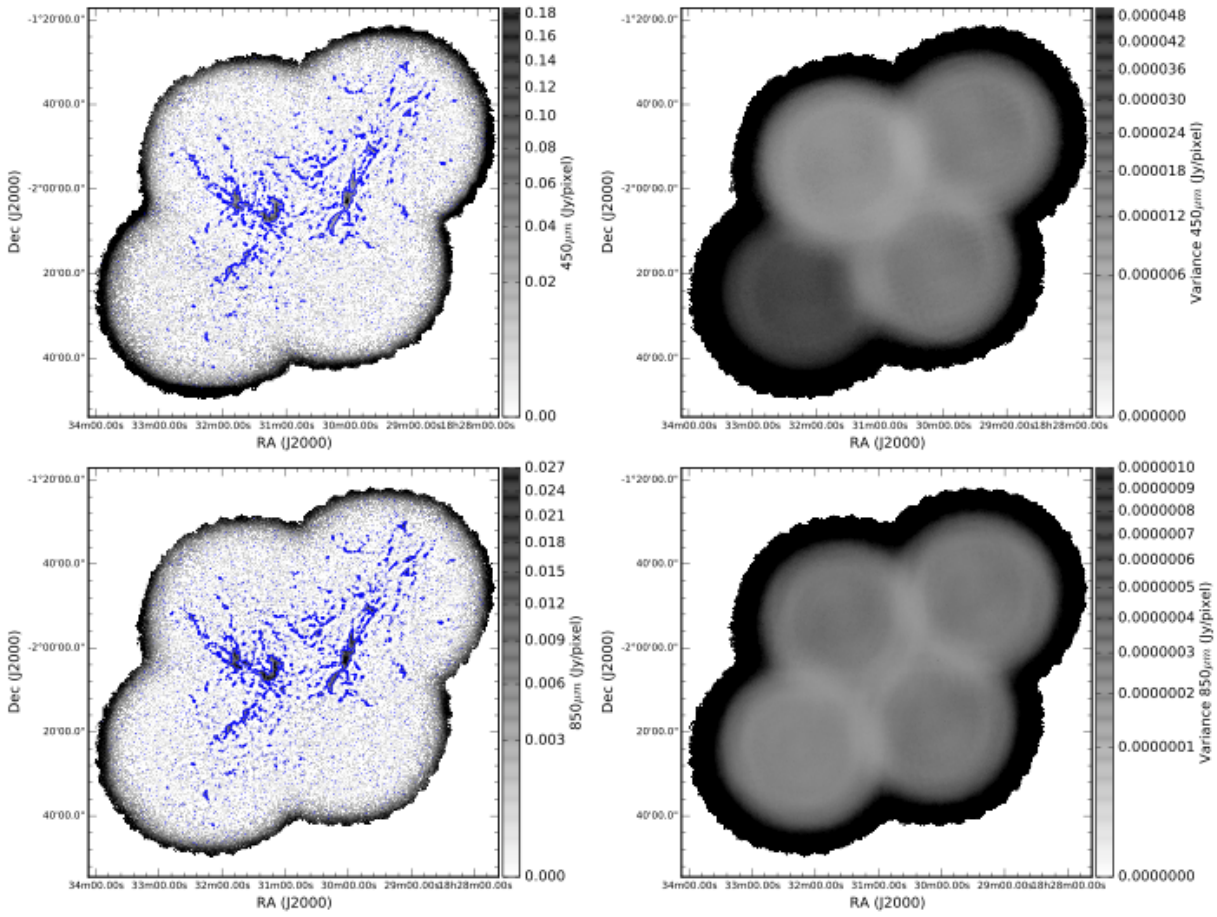

Figure 2.12: SCUBA-2 IR2 reductions of the Aquila region (east the Aquila W40 complex, west Serpens South) featuring data and variance maps at 450 and 850 μm. Contours show the outline of the SCUBA-2 external mask used in the reduction process.

merged, with any duplicates removed.

In addition to direct observations of IR YSOs, Rodríguez et al. (2010) and Ortiz-León et al. (2015) resolve compact radio sources (at 0.26″ resolution) that are consistent with 2MASS sources and, by monitoring time-variability, are able to classify eight variable YSOs and seven non-variable UCH II candidate regions associated with a high mass PMS-star. Likewise, Maury et al. (2011) catalogue 77 millimetre objects and find evidence for eight Class 0 protostars. These samples are added separately to my merged catalogue and are not examined for IR contamination. I include a classification where it is reported by an author, otherwise Class is determined by IR dust spectral index. In lieu of a comprehensive YSO catalogue covering the whole of the Aquila W40 complex, my composite catalogue, presented in Table 2.7, will allow a conservative analysis to be made of the global YSO distribution.

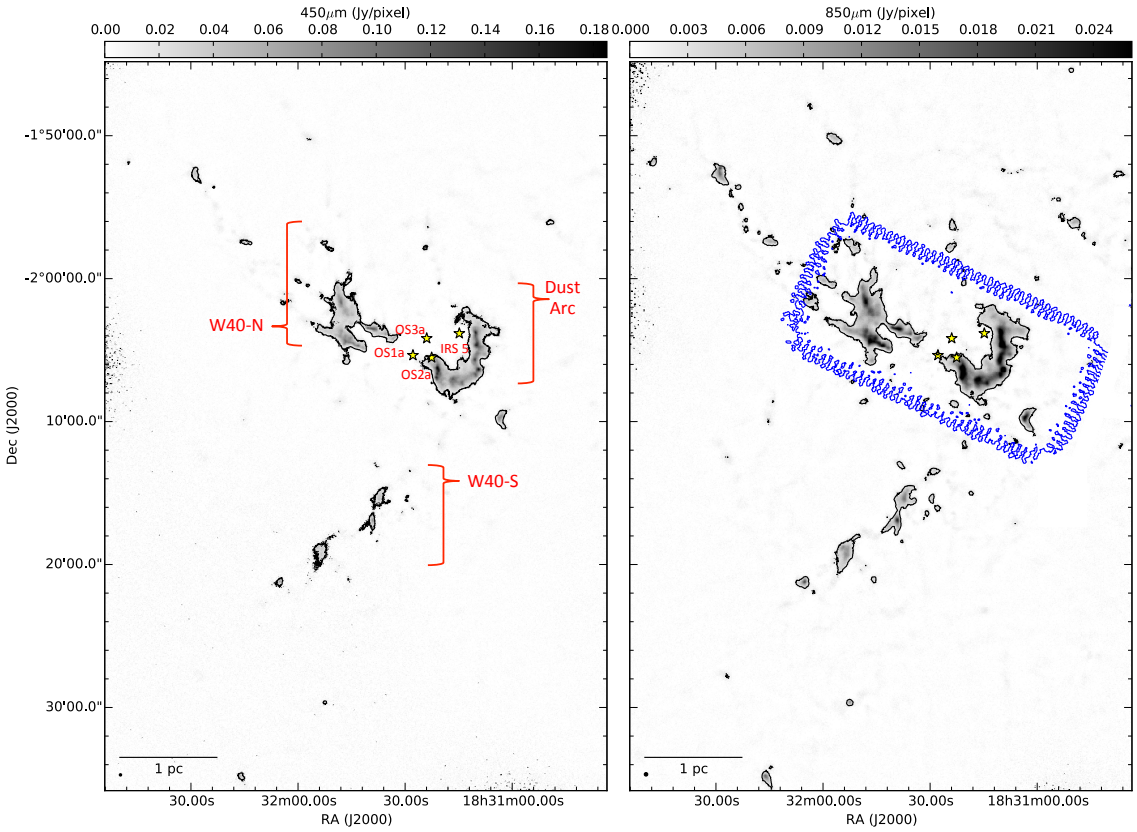

Figure 2.13: SCUBA-2 450 μm (*left*) and 850 μm (*right*) data. The SCUBA-2 850 μm data have had contaminating CO emission covering an 6′43″ ×17′54″ area removed (region outlined in blue, see Chapter 3 for more details). The resulting maps have been further filtered to remove structure above 4′ in size (see Section 2.2.3). The contours show 5 σ levels in both cases: levels are at 17.3 mJy/ 2″ pixels and 2.5 mJy/ 3″ pixels at 450 μm and 850 μm respectively.

Observations and data reduction

Aquila was observed with SCUBA-2 (Holland et al., 2013) between the 21st of April and 5th of July 2012 as part of the JCMT GBS MJLSG33 SCUBA-2 Serpens Campaign. Four separate fully sampled 30′ diameter circular continuum observations (PONG mapping mode, Kackley et al. 2010) were taken simultaneously at 450 and 850 μm, and subsequently combined into mosaics. The 450 and 850 μm maps for the entire Aquila W40 / Serpens South area covered by SCUBA-2 are shown in Figure 2.12 along with the data reduction masks and variance maps. The spatially-filtered 450 and 850 μm mosaics for the W40 region are shown in Figure 2.13; the 850 μm emission also has CO contamination removed (see Chapter 3). The dates, central positions and weather conditions of the observations are listed in Table 2.8.

The IR2 data were reduced by the SCUBA-2 GBS data reduction team as part of the GBS Legacy Release 1 (LR1, Mairs et al. 2015) using the DIMM technique outlined in the previous section and gridded to 2″ pixels at 450 μm and 3″ pixels at 850 μm. The initial reductions of each individual scan were coadded to form a mosaic from which a signal-to-noise ratio (SNR) mask was produced for each region. Masks were selected to include regions of emission in the automask reductions with SNRs higher than 3 with no additional smoothing. The final mosaic

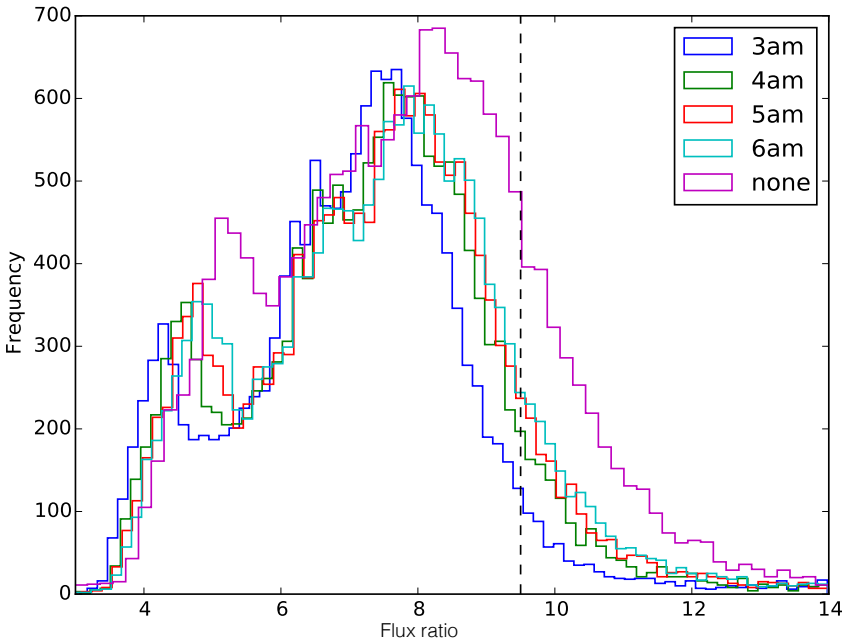

Figure 2.14: Histograms of flux ratio for the Aquila CO subtracted SCUBA-2 reductions with varying spatial filters applied. Filter sizes, in arcminutes, are labelled on the plot. The flux ratios calculated with no filter are also included for comparison. Histograms are examined for total volume below 9.5, a value above which ratios correspond to unphysical dust temperatures.

Table 2.8: SCUBA-2 observations of Aquila

PONG	RA Dec (J2000)	# of Obs.	Weather band(s)	Observation dates	$\bar{\sigma}$ (Jy/pix)
NE	18:31:34.6 -01:54:05.30	4	1	21, 23 April, 3 May 2012	4.7×10^{-4}
NW	18:29:30.6 -01:47:30.30	4	1, 2	3, 4, 5 May 2012	4.5×10^{-4}
SE	18:32:13.8 -02:24:12.30	6	1, 2, 3	8 May, 10, 11 June, 5 July 2012	4.0×10^{-4}
SW	18:30:09.8 -02:17:37.30	4	1	7, 8, 18 May 2012	4.6×10^{-4}

was produced from a second reduction using this mask to define areas of emission. Detection of emission structure and calibration accuracy are robust within the masked regions and are uncertain outside of the masked region (Mairs et al., 2015).

The data were initially calibrated in units of pW and are converted to Jy/pixel using FCFs derived by Dempsey et al. (2013). The calibration uncertainties on the standard FCFs are 3% at 850 μm and 11% at 450 μm. Typical noise levels are 3.5 mJy per 2″ pixel at 450 μm or 0.50 mJy per 3″ pixel at 850 μm.

Filtering

The SCUBA-2 reduction process is an ongoing process and as a result not all internally released reductions are of a science ready standard. This was true of the IR2 reductions of Aquila W40 complex where I found that the SCUBA-2 data reduction process was removing less large scale structure at 450 μm, relative to 850 μm. As a result, a significant number of pixels had 450 μm to 850 μm flux ratio values that would lead to highly uncertain temperatures (defined as ratios higher

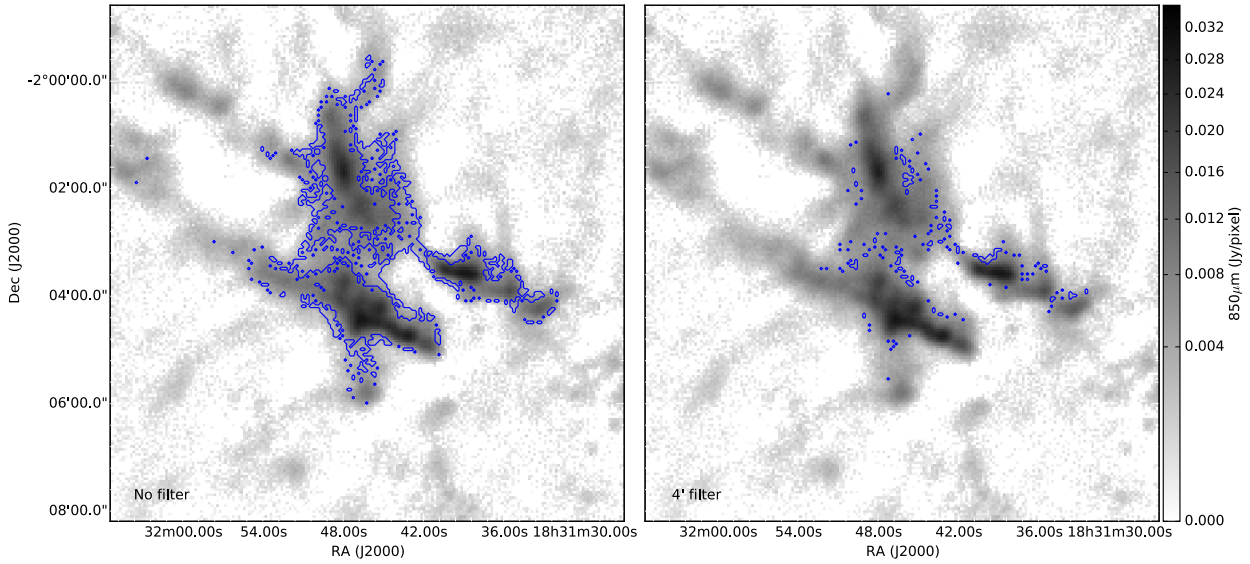

Figure 2.15: SCUBA-2 850 μm observations of the W40-N cloud in the Aquila region. The greyscale compares the unfiltered (left) and 4′ filtered (right) fluxes. Blue contours show where the ratio of 450 μm to 850 μm exceeds 9.5, corresponding to highly uncertain dust temperatures and symptomatic of where the data reduction process and choice of mask has removed insufficient large-scale structure.

Table 2.9: Pixel populations of 450 μm to 850 μm flux ratio maps of the W40-N cloud (Aquila region) from various filter sizes. See Chapter 5 for details of how flux ratio is calculated.

	No filter	3′	4′	5′	6′
Total ratio pixels	3960	3333	3673	3773	3844
Total 'bad' pixels[a]	1142	54	210	331	444
Percentage 'bad' pixels[a]	28.8%	1.6%	5.7%	8.8%	11.6%
Total 'good' pixels[a]	2818	3279	3463	3442	3400

a - A flux ratio of 9.5 is defined as a threshold, above which the ratio will correspond to highly uncertain dust temperatures, thus indicating the presence of additional large-scale that has been left in during the original data reduction.

than 9.5, corresponding to temperatures greater than 50 K). Flux ratio and temperature are related through the 'Temperature equation' (Equation 1.33). Details of how the flux ratio is calculated are given in Chapter 5.

Spatial filters were applied to the data using the CUPID tool `findback` (Berry et al. 2007, Berry et al. 2013) to reduce excess large-scale structure in the SCUBA-2 reductions. This tool works by twice filtering pixels (firstly to a minimum and secondly a maximum value) with respect to those pixels within a pre-defined spatial scale or 'box' parameter which is referred to as the filter size. Using this method a lower envelope of the data is estimated.

The results of tests of various filter sizes are presented in Figure 2.14 and Table 2.9, alongside the unfiltered data, as the distribution of flux ratios for a control area of the Aquila W40 complex (W40-N). Tests include; the total number of unreliable, or 'bad', flux ratio pixels (ratios higher than 9.5) as a percentage of the total population, and the total number of reliable, or 'good', flux ratio pixels (lower than 9.5). Larger filters were found to maximise the number of pixels in

the data whilst including excessive 'bad' flux ratios. I set a criterion for the ideal filter that was a compromise between the highest absolute number of pixels retained (post filtering and $5\,\sigma$ cut), in a sample area of the map and the lowest percentage of 'bad' pixels (ratios higher than 9.5). A scale size of $4'$ is the optimum solution with 5.7% of pixels returning unphysical ratios (down from 28.8% in the unfiltered data).

Figure 2.15 shows the unfiltered and filtered data at 850 μm and the impact the filter has on the coverage of 'bad' pixels in the resulting flux ratio map. I find that the filtered and unfiltered IR2 850 μm maps have a KS-test p-value of 44%, further indicating the significant impact of the filtering on the fluxes. These results were fed back into the SCUBA-2 data reduction pipeline by the GBS data reduction team with the aim of producing improved IR3 reductions of this region. I compare the IR3 850 μm reductions of the Aquila W40 complex with my filtered IR2 850 μm map and find a KS-statistic of 0.11. This low value indicates how these techniques are robust when compared to the GBS data reduction pipeline.

Filtered SCUBA-2 maps of the Aquila W40 complex undergo ^{12}CO 3-2 and free-free contamination subtraction in Chapter 3 and 4 before the data the region is analysed in depth in Chapter 7.

2.5.3 Serpens South

The Serpens South cloud (presented in Figure 2.9), is located in the western half of the Serpens-Aquila region at RA (J2000) = 18:30:04, Dec. (J2000) = -02:03:07. It is an extended, filamentary cloud (Men'shchikov et al., 2010) with an unbroken length of $16'$ that is among the brightest submillimeter object in the Serpens-Aquila regions, peaking at over 350σ (at 850 μm). Maury et al. (2011) estimate the mass and column density of the primary star forming core as $610\,M_\odot$ and $3.1 \times 10^{22}\mathrm{cm}^{-2}$ over the projected area of $1\,\mathrm{pc}^{-2}$, respectively. The star formation efficiency (SFE) is estimated as approximately 7% and the star formation rate (SFR) is approximately $23 M_\odot$ $\mathrm{Myr}^{-1}\mathrm{pc}^{-2}$ which is significantly higher than the typical values for GMCs (Evans et al., 2009). Figure 2.13 also demonstrates the extent and complexity of Serpens South with many extraneous sub-cores possibly containing embedded protostars.

Könyves et al. (2010, 2015) do not observe an IR nebulosity associated with the main filament of Serpens South in the same way that is observed for the Aquila W40 complex indicating a lack of evolved OB stars. However, *Herschel* 70 μm emission shows isolated heated dust symptomatic of a faint nebulosity/H II region, MSX6C G028.5532+03.9958, associated with the IR point source IRAS 18265-0205 (RA (J2000) = 18:29:11.9, Dec. (J2000) = -02:03:50), inferring that massive star formation has occurred away from the present day filament (Figure 2.16). Levshakov et al. (2014) study this object and is unable to verify whether IRAS 18265-0205 is physically connected to Serpens South. However, Könyves et al. (2015) study the extended filamentary structure of the Aquila which suggests that it could be.

Serpens South is complicated by the presence of the nearby Aquila W40 complex (separation of approximately $20'$) and extended sections of each region may overlap. As outlined in the previous section, I argue that the Aquila W40 complex is sufficiently more distant from Serpens South that the two objects are not spatially connected, and that their alignment is mere chance.

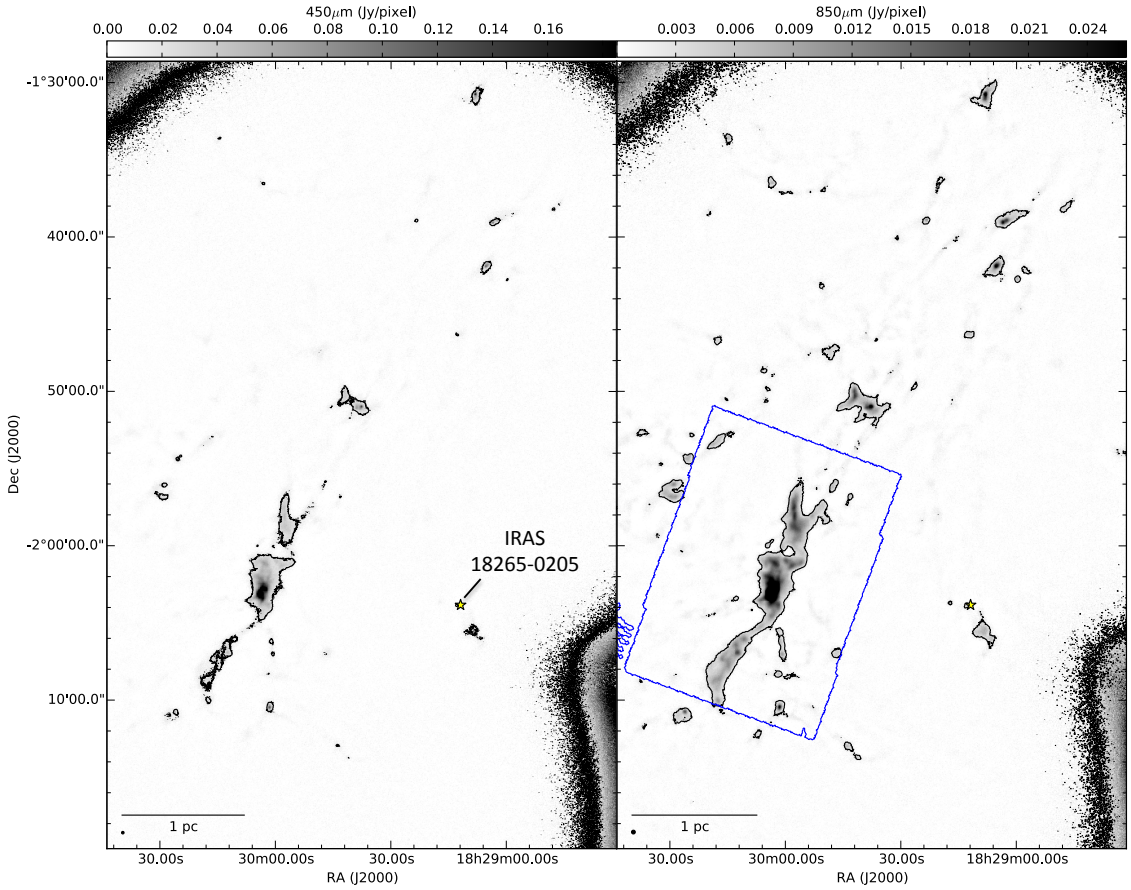

Figure 2.16: SCUBA-2 450 μm (*left*) and 850 μm (*right*) observations of Serpens South, part of the Aquila observation. The SCUBA-2 850 μm data have had contaminating CO emission removed (region outlined in blue, see Chapter 3 for more details). The resulting maps have been further filtered to remove structure above 4′ in size (see Section 2.2.3). The contours show 5 σ levels in both cases: levels are at 17.3 mJy/ 2″ pixels and 2.5 mJy/ 3″ pixels at 450 μm and 850 μm respectively.

Table 2.10: SCUBA-2 observations of Serpens Main and NH_3.

PONG	RA Dec (J2000)	# of Obs.	Weather band(s)	Observation dates	$\bar{\sigma}$ (Jy/pix)
Main1	18:31:34.6 -01:54:05.30	4	1	18, 19 May 2012	1.6×10^{-4}
NH3	18:29:07.0 +00:30:29.5	6	2, 1, 2	8 Jul., 18 Aug., 3 Sep. 2012	1.0×10^{-4}

Alternatively, Bontemps et al. (2010) argue that large uncertainties in previous measurements of distance do not allow for a reliable estimate and therefore they favour that Serpens South is physically connected to the Aquila W40 complex and the Aquila rift. Comparing CO observations show that the velocity range observed by the SubMillimeter Array (SMA) in Serpens South by Ho et al. (2004) of 6-11 km s^{-1} are comparable to the closer Serpens Main cloud (8 km s^{-1}, White et al. 1995), and not the velocities observed in the Aquila W40 complex (2-6 km s^{-1}) by Zeilik & Lada (1978), Vallée & MacLeod (1992) and Zhu et al. (2006). On this basis Serpens South is considered part of the Aquila-Rift along with Serpens MWC 297 and therefore has a distance of 250±50pc. CO observations of the Seprens South region are presented in Chapter 3.

As Serpens South is observed on the same mosaic as the Aquila W40 complex, details of its reduction and calibration have already been presented in the previous section.

2.5.4 Serpens Main

The Serpens Main cloud, presented in Figure 2.17, is located in the north of the Serpens-Aquila region at RA (J2000) = 18:29:59.9, Dec. (J2000) = +01:14:18.9. The Serpens (Main) cloud has been well studied and as a result my investigations into this sub-region have been cursory.

The Serpens Main molecular cloud was first identified as a region of active star formation by Strom et al. (1974). Since then it has been extensively mapped for molecular line emission (Dame & Thaddeus, 1985; Dame et al., 1987, 2001; Davis et al., 1999), extinction (Cambrésy, 1999; Dobashi et al., 2005), IR (Eiroa & Casali, 1992; Harvey et al., 2006), submillimeter (Casali et al., 1993; Davis et al., 1999) and radio (Eiroa et al., 2005) continuum wavelengths, to name but a few. Eiroa et al. (2008) present a comprehensive review of the region where they summarise the evidence for a core temperature between 25-30 K (Williams, 2000), $C^{18}O$ 1-0 mass of 250-300 $M_\odot$ (McMullin et al., 2000), in-falling (Williams, 2000) and outflow-like (Davis et al., 1999) line profiles confirming the presence of active star formation.

Serpens Main was observed with SCUBA-2 (Holland et al., 2013) between the 18th May and 3rd September 2012 as part of the JCMT GBS MJLSG33 SCUBA-2 Serpens Campaign. Two separate PONGs for Serpens Main and Serpens NH_3 were observed simultaneously at 450 and 850 μm, and subsequently combined into mosaics. The 450 and 850 μm maps for the Serpens Main area are shown in Figure 2.17; the 850 μm emission also has had CO contamination removed for a 23′ squared area centred on Serpens Main (see Chapter 3, Kirk, priv. comm.). The dates, central positions and weather conditions of the observations are listed in Table 2.10. The data were reduced and calibrated as part of the GBS Legacy Release 1 following the procedures outlined for Aquila. Typical noise levels are 2.6 mJy/pix or 0.4 mJy/pix per 2″or 3″ pixels at 450 μm and 850 μm, respectively.

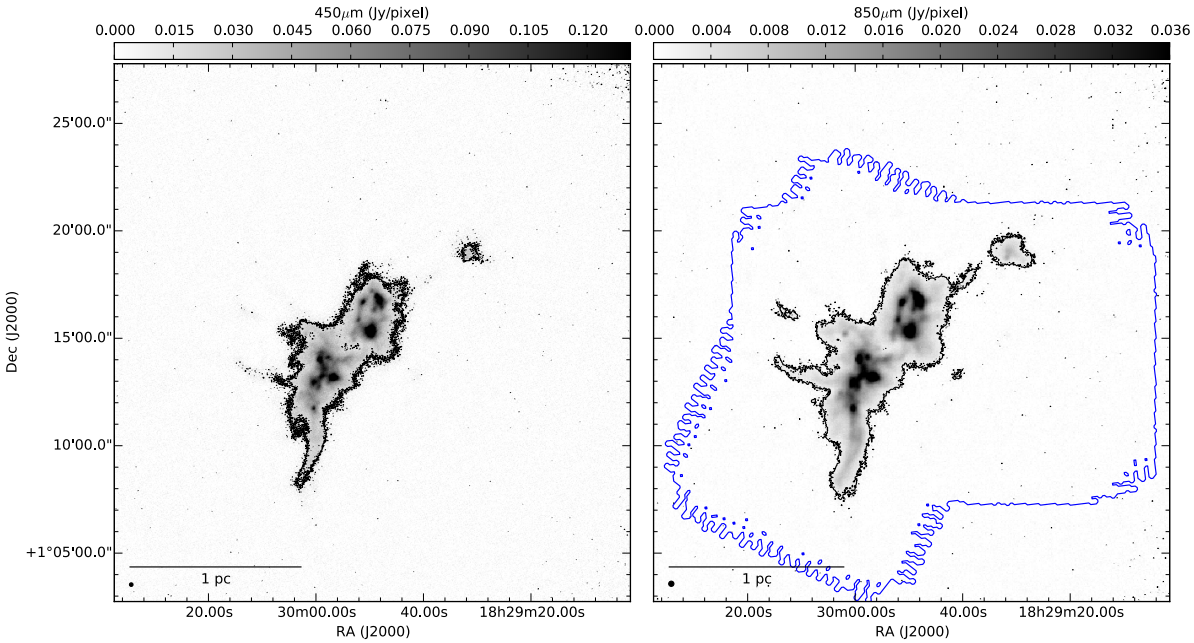

Figure 2.17: SCUBA-2 450 μm (*left*) and 850 μm (*right*) observations of the Serpens Main cloud core. The SCUBA-2 850 μm data have had contaminating CO emission removed (region outlined in blue, see Chapter 3 for more details). The contours show 5 σ levels in both cases: levels are at 0.0173 Jy/ 2″ pixels and 0.0025 Jy/ 3″ pixels at 450 μm and 850 μm respectively.

850 μm maps (Figure 2.17) of Serpens Main show peaks in flux and column density into separate northwestern (NW) and southeastern (SE) clouds. Both structures are of similar size, distance and are in close proximity, being separated by 200″ (Casali et al., 1993).

In addition to the c2d YSOcs (Evans et al., 2003, 2009) (plotted in Figure 2.18) and SGBS *Spitzer* YSOc surveys, x-ray surveys can also be used to indirectly detect YSOs through accretion flaring associated with late evolution PMS-stars. Preibisch (2003) used *XMM-Newton* data to identify one Class I and two Class FS YSOs in the Serpens Main cloud. This study was then followed by Winston et al. (2007) who used *Spitzer* and *Chandra* observations to identify 183 YSOcs in Serpens Main. Similarly radio observations can detect free-free emission from ultra compact H II regions and protostellar jets around high mass protostars. Eiroa et al. (2005) looked at 3.5 cm radio emission from Serpens Main using the very large array (VLA). 16 of the 22 sources detected were classified as YSOcs, with the radio emission most likely resulting from thermal jets.

Many studies have been conducted into the exact distance of Serpens Main. Initial studies by Racine (1968), Zhang et al. (1988) and put the distance at between 700 pc and 200 pc. The Straižys et al. (2003) observation of the Aquila rift only represents the distance to the front side of the cloud and it should be considered a lower limit. Straižys et al. (2003) claim Serpens Main is located within the cloud which they estimate has a depth of 80 pc. Dzib et al. (2010, 2011) present trigonometric parallax measurements of the Herbig stars EC 95a and b, which they consider to be part of Serpens Main, through association with the star cluster SVS 4 (Eiroa & Casali, 1992), and they calculate a distance of 429±2 pc. This method is by far the most robust to date leading to the conclusion that Serpens Main is not part of the Aquila rift. As discussed in the previous section,

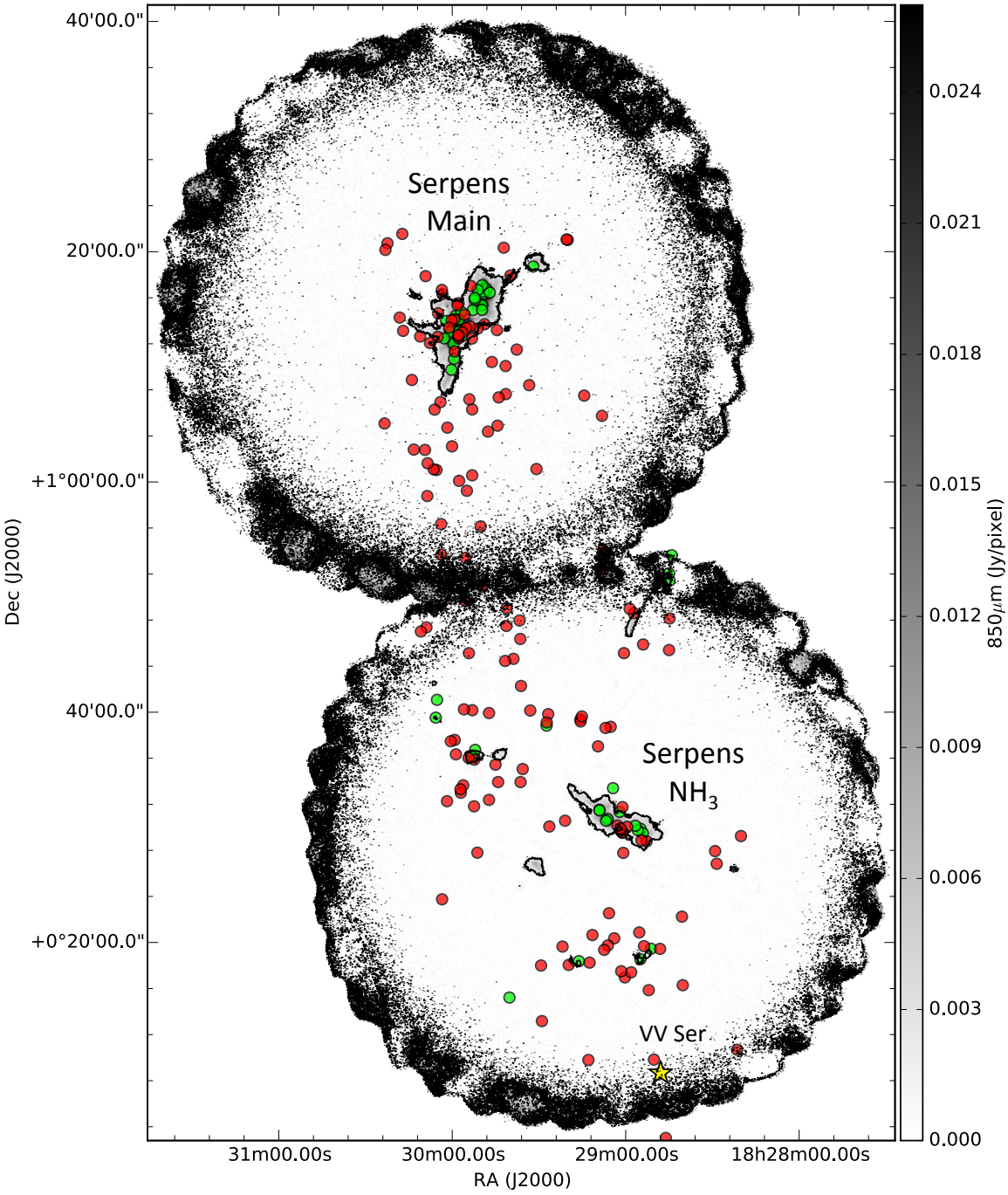

Figure 2.18: SCUBA-2 850 μm observations of the Serpens cloud cores. The contours show 5 σ levels. The c2d YSOcs (Evans et al., 2003, 2009) are marked: Class 0/I in green and Class II/III in red. The star marks the location of the A0 UX Variable Orion star VV Ser.

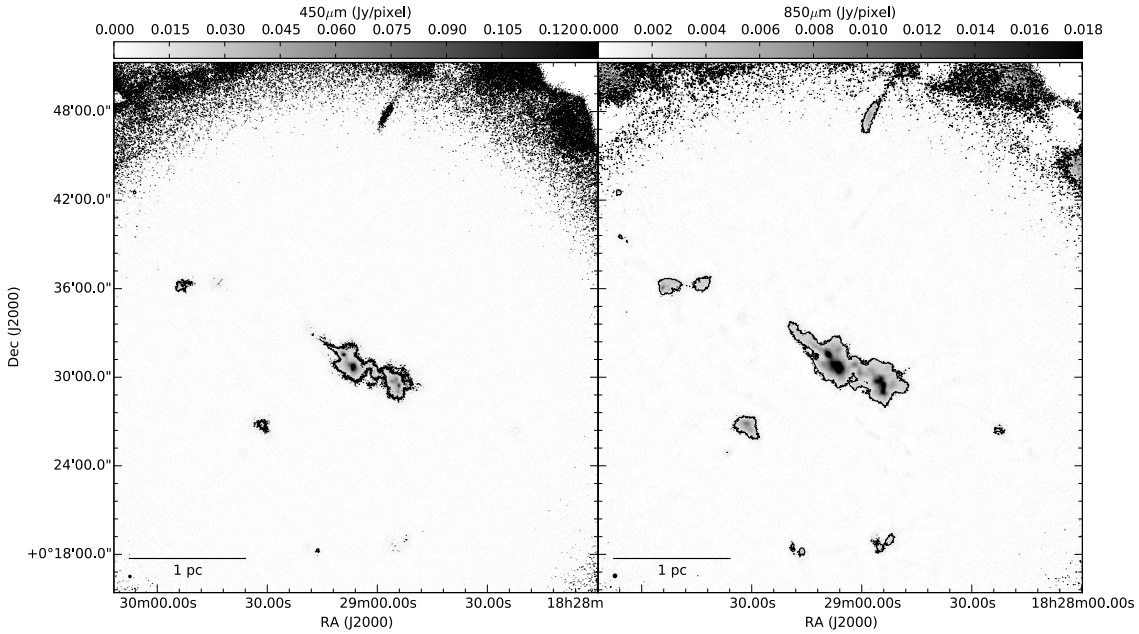

Figure 2.19: SCUBA-2 450 μm (*left*) and 850 μm (*right*) observations of the Serpens NH_3 cloud core. No ^{12}CO 3-2 observations of these region are known by which an assessment of level of SCUBA-2 850 μm band contamination can be made. The contours show 5 σ levels in both cases: levels are at 17.3 mJy/ 2″ pixels and 2.5 mJy/ 3″ pixels at 450 μm and 850 μm respectively.

cloud velocities in Serpens Main are similar to Serpens South, whose current distance is based on the same lower limit presented by Straižys et al. (2003). I therefore cannot rule out the possibility that Serpens South also resides at a distance similar to Serpens Main.

2.5.5 Serpens NH_3 and VV Ser

The Serpens NH_3 cloud, presented in Figure 2.19, is located to the south of the Serpens Main cloud at RA (J2000) = 18:29:07.0, Dec. (J2000) = +00:30:29.5. The Serpens NH_3 cloud is a low mass region with no high mass stars and as a result my investigations into this sub-region have been cursory.

Serpens NH_3 was first observed by Cohen & Kuhi (1979) who identified 4 optical T-Tauri stars (Serpens G3, 4, 5, 6). The morphology of NH_3 is similar to Serpens Main as it has two separate clouds of dense star formation with connected filaments with a NE-SW orientation. Djupvik et al. (2006) use 1.3 mm observations from IRAM to quantitatively show that emission is, in general, less intense in NH_3 than in Main. The surrounding region was then mapped by Clark (1991) who also identified two additional sources with strong ammonia 1,1 emission lines (for which the cluster is named). Additional Herbig-Haro objects (Ziener & Eislöffel, 1999) and H_2O masers (Persi et al., 1994) were found providing further evidence of ongoing star formation. Djupvik et al. (2006) present a comprehensive review of the region.

The distance of 225±55 pc has widely been adopted for the distance to Serpens NH_3 in line with the findings of Straižys et al. (2003). Results from the c2d YSO survey (Evans et al., 2003; Harvey et al., 2006; Harvey & Dunham, 2009) have a found number of YSOcs ranging from Class

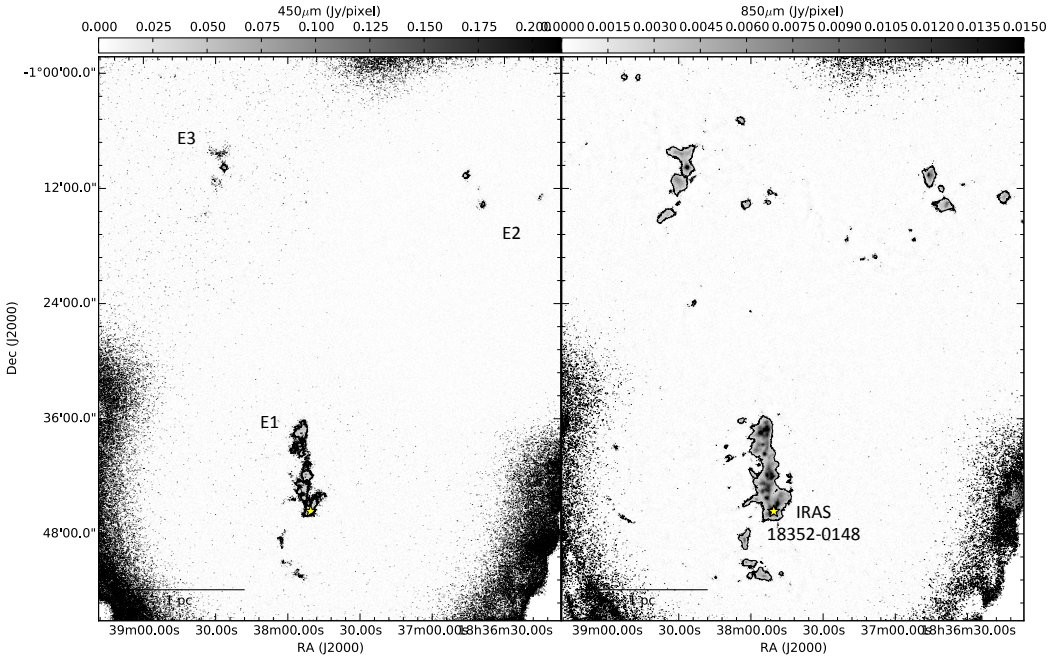

Figure 2.20: SCUBA-2 450 μm (*left*) and 850 μm (*right*) observations of the Serpens East cloud core. No ^{12}CO 3-2 observations of these region are known by which an assessment of level of SCUBA-2 850 μm band contamination can be made. The contours show 5 σ levels in both cases: levels are at 21.3 mJy/ 2″ pixels and 1.5 mJy/ 3″ pixels at 450 μm and 850 μm respectively.

0 to III, including a filament of more evolved PMS-stars that are not observed in SCUBA-2 bands stretching between Serpens NH_3 and Main, as presented in Figure 2.18, providing evidence that the two clouds are evolved parts of the same structure. This would therefore place Serpens NH_3 at a similar distance as Serpens Main (429±2 pc, Dzib et al. 2011).

VV Serpens is a young, A0 (Mora et al., 2001) UX Variable Orion Star (whereby the star is inclined such that its disc is appears edge on to the observer) located at RA (J2000) = 18:28:47.9, Dec. (J2000) = +00:08:39.8, roughly 20′ to the south of Serpens NH_3 in Figure 2.18. VV Ser is driving an extended, low density nebulosity spanning 94,000 Au (Chavarria-K. et al. 1988 Pontoppidan et al. 2007) that has no detectable optical or IR counter parts and therefore is not considered to be heating any of the material in Serpens NH_3.

2.5.6 Serpens East

Serpens East is the most prominent of several smaller eastern regions located approximately at RA (J2000) = 18:37:49.0, Dec. (J2000) = -01:42:3.9. It contains a bright submillimeter filament to the south an a number isolated clumps in the north west and east of the region, as shown in Figure 2.20.

Serpens East was observed with SCUBA-2 (Holland et al., 2013) between the 3rd September 2012 and 28th July 2013 as part of the JCMT GBS MJLSG33 SCUBA-2 Serpens Campaign. Three separate PONGs were observed simultaneously at 450 and 850 μm, and subsequently combined into mosaics. The 450 and 850 μm maps for the Serpens East area covered by SCUBA-2 are shown in Figure 2.20. No CO observations exist of this region from which to asses the magnitude

Table 2.11: SCUBA-2 observations of Serpens East.

PONG	RA Dec (J2000)	# of Obs.	Weather band(s)	Observation dates	$\bar{\sigma}$ (Jy/pix)
E1	18:37:49.0 -01:42:30.9	6	2	3, 8 Sep. 2012, 2 Jul. 2013	1.2×10^{-4}
E2	18:36:22.6 -01:17:39.8	6	2	14, 18, 19 Jul. 2013	0.4×10^{-4}
E3	18:38:29.8 -01:10:09.9	6	2	19, 27, 28 Jul. 2013	0.5×10^{-4}

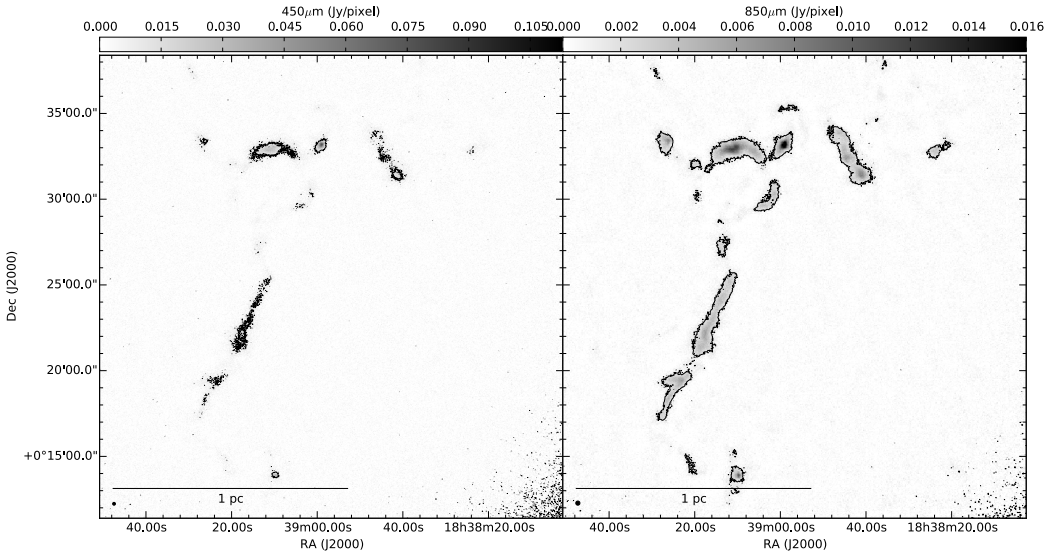

Figure 2.21: SCUBA-2 450 μm (*left*) and 850 μm (*right*) observations of the Serpens North cloud core. No ^{12}CO 3-2 observations of these region are known by which an assessment of level of SCUBA-2 850 μm band contamination can be made. The contours show 5 σ levels in both cases: levels are at 21.3 Jy/ 2″ pixels and 1.5 Jy/ 3″ pixels at 450 μm and 850 μm respectively.

of CO contamination. The dates, central positions and weather conditions of the observations are listed in Table 2.11. The data were reduced and calibrated as part of the GBS Legacy Release 1 following the procedure outlined for Aquila. Typical noise levels are 4.3 mJy/pix or 0.3 mJy/pix per 2″or 3″ pixels at 450 μm and 850 μm, respectively.

Serpens East is covered very sparsely in the literature with no known YSO catalogs in the region. Szymczak et al. (2000) survey IRAS 6.7GHz methanol maser emission and similarly Wu et al. (2006) and Lu et al. (2014) studied a selection of sources with strong ammonia lines, including IRAS 18352-0148, marked in Figure 2.20, which is embedded in East. This source is also a strong H_2O maser (Wang et al., 2007) and has an associated H II region MSX6C G029.8129+02.2195 (Urquhart et al., 2011), both are which synonymous with high mass star formation and the potential for heating through radiative transfer. No distance measurements to this cloud core are known and therefore I adopt a lower limit distance of 225±55 pc in line with the Aquila rift (Straižys et al., 2003).

2.5.7 Serpens North

Serpens North is a low mass region located at approximately RA (J2000) = 18:39:05.7, Dec. (J2000) = +00:27:23.6. The morphology of this region is a faint filament with a small number

Table 2.12: SCUBA-2 observations of Serpens North.

PONG	RA Dec (J2000)	# of Obs.	Weather band(s)	Observation dates	$\bar{\sigma}$ (Jy/pix)
N	18:39:05.7 +00:27:23.6	6	2, 1 1, 1	29 Sep. 2013, 26 Feb. 1, 5 Mar. 2014	0.7×10^{-4}

of bright cores. No high mass stars are associated with this region.

Serpens North was observed with SCUBA-2 (Holland et al., 2013) between the 29th September 2013 and 5th March 2014 as part of the JCMT GBS MJLSG33 SCUBA-2 Serpens Campaign. A single PONG was observed at 450 μm and 850 μm. The 450 and 850 μm maps for the Serpens North area covered by SCUBA-2 are shown in Figure 2.21. No CO observations exist of this region from which to asses the magnitude of CO contamination. The dates, central positions and weather conditions of the observations are listed in Table 2.12. The data were reduced and calibrated as part of the GBS Legacy Release 1 following the procedures outlined for Aquila. Typical noise levels are 2.2 mJy/pix or 0.3 mJy/pix per 2″or 3″ pixels at 450 μm and 850 μm, respectively.

As is the case with Serpens East, Serpens North has not been widely studied in the literature. No distance measurements to this cloud core are known and therefore I adopt a lower limit distance of 225±55 pc in line with the Aquila rift (Straižys et al., 2003). However, the Dunham et al. (2015) c2d+GBS YSOc catalogue does cover this region, providing details of star formation. No high mass stars have been observed in this region.

2.6 Other GBS regions

So far I have focused on the Serpens-Aquila regions. The majority of the work in this thesis aims to develop methods for analysing dust temperature relative to YSO/high mass star populations in the JCMT GBS, firstly in Serpens Aquila, before subsequently expanding this work to rest of the survey. This includes the regions listed in Tables 2.13 and 2.14.

As discussed, the Dunham et al. (2015) c2d+GBS catalogue is used throughout these regions to study the distribution of YSOs, where coverage extends there. Responsibility for other research in each region is distributed amongst the members of the JCMT GBS. I address the reader to the publications listed in Tables 2.13 and 2.14, where completed or in progress, for a detailed description of the regions and the reduction/contamination procedure for the SCUBA-2, and associated observations. Specific regions are introduced and discussed, in the context of dust temperature and heating from OB stars and stellar populations, in Chapter 8. Tables 2.13 and 2.14 summarise the location of each region, its distance, SCUBA-2 sensitivity and whether it contains OB star/s. As outlined in Section 2.2.6, a minority of noise estimates are slight over- or underestimates, depending on how good the gaussian fit is to the distribution of the flux density, clipped to the largest 99.95% of bins. Where this is the case the specific region is noted in Tables 2.13 and 2.14.

Table 2.13: A summary of SCUBA-2 observations of the JCMT GBS regions *part 1*.

Region (SCUBA-2[a])	Sub-region	RA (J2000)	Dec (J2000)	Distance (pc)	5σ noise [b] (Jy/pix) 450 μm	850 μm	CO[c] 850 μm	OB[d] stars	JCMT GBS reference
Auriga Central	Central North	04:10:50.6	+38:09:20.3	450±23[1]	0.0221	0.0028	-	-	Broekhoven-Fiene et al. (2016)
Auriga Main	LkHa-101	04:30:16.5	+35:17:47.9	450±23[1]	0.0115	0.0029	-	Yes[2]	Broekhoven-Fiene et al. (2016)
	Central East	04:18:00.0	+35:20:00.0				-	-	
	Central West	04:16:00.0	+35:10:00.0				-	-	
	North West	04:03:00.0	+35:30:00.0				-	-	
Cepheus L1228	Cepheus L1228	20:57:43.8	+77:38:16.9	200±20[3]	0.0207^o	0.0032	-	-	Pattle et al. (2016)
Cepheus L1251	Cepheus L1251	22:37:33.5	+75:14:50.0	300±10[3]	0.0283	0.0031	-	-	Pattle et al. (2016)
Cepheus South	Cepheus L1172/74	21:01:37.8	+68:14:18.3	288±25[3]	0.0427^o	0.0041	Yes	Yes[4]	Pattle et al. (2016)
	Cepheus L1152/55/57	20:44:30.0	+67:54:00.0					-	Pattle et al. (2016)
Corona Australis	CRa-A	19:01:35.3	-36:55:59.6	130±25[5]	0.0411	0.0030	-	Yes[6]	Bresneham et al. (in prep.)
Cygnus	IC 5146	21:53:42.9	+47:15:21.2	950±80[7]	0.0302	0.0026	Yes[7]	Yes[7]	Ward-Thompson et al. (2015)
Lupus	Lupus I	15:42:45.5	-34:04:33.3	140±20[8]	0.0653^o	0.0032	-	-	Mowat et al. (2016)
Ophiuchus	L1688	16:27:00.0	-24:30:00.0	139±6[9]	0.0355	0.0043^o	Yes	Yes[10]	Drabek et al. (2012)
	L1689	16:32:00.0	-24:50:00.0				-	Yes[10]	Pattle et al. (2015)
Ophiuchus North	North 2	16:47:40.2	-12:05:03.0	139±6[9]	0.0382	0.0032^o	-	-	-
	North 3	16:50:53.8	-15:21:49.0	139±6[9]	0.0482	0.0035^o	-	-	-
	North 6	16:21:09.7	-20:07:04.4	139±6[9]	0.0422	0.0031^o	-	-	-
Orion A	Orion A	05:35:14.4	-05:22:24.5	450[11]	0.011^u	0.0015^u	Yes	Yes	Salji et al. (2015)
Orion B	B2023	05:41:17.5	+02:18:39.0	415[12]	0.0205	0.0024	Yes	Yes	Kirk et al. (2015)
	B2068	05:47:33.8	+00:44:57.1	415	0.0241	0.0025	?	Yes	Kirk et al. (2015)
Persues IC348	B5	03:48:00.0	+32:50:00.0	250±50[13]	0.0247^o	0.0029^o	-	-	Chun-Yuan Chen et al. (2016)
	IC 348	03:44:23.8	+32:02:00.1				Yes	Yes[5]	Sadavoy et al. (2013)

a - Title of the JCMT GBS region observed by SCUBA-2. Where the mosaic is comprised of a number of subregions they are listed separately. Distance and noise are assumed constant across the mosaic, in line with the first listing, unless they are listed separately.
b - 5σ noise represents the lower limit on sensitivity in each region at each of the SCUBA-2 bands. The values are calculated following the method outlined in section 2.2.6. Where noise is tagged with *o* the value is an overestimate, with *u* the value is an underestimate.
c - Denotes whether these regions have had ^{12}CO 3-2 contamination of the 850 μm band removed. A negative result here does not necessarily state that no CO observations exists in this region.
d - Denotes whether the region contains an OB star as part of the star-forming complex. Details of the specific stars will be discussed in detail in Chapters 6, 7 and 8.
References: 1 Lada et al. (2009), 2 Herbig et al. (2004), 3 Kirk et al. (2009), 4 Witt & Cottrell (1980), 5 de Zeeuw et al. (1999b), 6 Neuhäuser & Forbrich (2008), 7 Harvey et al. (2008), 8 Franco (2002), 9 Mamajek (2008), 10 Houk & Smith-Moore (1988), 11 Salji et al. (2015), 12 Kirk et al. (2015), 13 Herbst (2008).

Table 2.14: A summary of SCUBA-2 observations of the JCMT GBS regions *part 2*.

Region (SCUBA-2[a])	Sub-region	RA (J2000)	Dec (J2000)	Distance (pc)	5σ noise [b] (Jy/pix) 450 μm	850 μm	CO[c] 850 μm	OB[d] stars	Ref
Perseus West	B1	03:33:12.2	+31:07:15.0	250±50[14]	0.0230[o]	0.0033	Yes	-	Chen et al. (2016)
	L1455	03:28:00.0	+30:12:00.0				-	-	Chen et al. (2016)
	L1448	03:44:23.8	+30:44:00.0				-	-	Chen et al. (2016)
	NGC 1333	03:29:00.0	+31:16:00.0	235±18[15]			-	Yes[16]	Hatchell et al. (2013)
Pipe	PipeE1	17:30:00.0	-25:00:00.0	145±16[17]	0.0176	0.0026	-	-	Duarte-Cabral et al. (in prep)
	B59								
Serpens	Serpens Main	18:29:59.9	+01:14:18.9	429±2[18]	0.0218	0.0030	Yes	-	Duarte-Cabral et al. (2010)
	Serpens NH_3	18:29:07.0	+00:30:29.5				-	-	Djupvik et al. (2006)
Serpens E	Serpens E	18:37:49.0	-01:42:03.9	225±55[19]	0.0355	0.0025	-	-	
Serpens N	Serpens N	18:39:05.7	00:27:23.6	225±55[19]	0.0180	0.0027	-	-	
Serpens MWC 297	MWC 297	18:28:14.2	-03:44:04.3	250±50[20]	0.0850	0.0111		Yes[20]	Rumble et al. (2015)
Serpens-Aquila	Sepens South	18:30:04.0	-02:03:07.0	225±55[19]	0.0174	0.0025	Yes	Yes[21]	Gutermuth et al. (2008)
	Aquila W40	18:31:26.0	-02:05:30.0	500±50[22]			Yes	Yes[23]	Rumble et al. (2016)
Taurus L1495	L1495	04:18:40.3	+28:20:57.0	140[24]	0.0304[o]	0.0028	Yes	Yes[25]	Ward-Thompson et al. (2015)
	L1592								
Taurus TMC	TMC	04:41:06.3	+26:08:28.3	140[24]	0.0347[o]	0.0026	-	-	
Taurus South	Taurus South	04:29:38.6	+24:34:54.9	140[24]	0.0281[o]	0.0028	-	-	

Annotation is consistent with Table 2.13.

References: 14 Bally et al. (2008), 15 Hirota et al. (2007),16 Straižys et al. (2002), 17 Alves & Franco (2007), 18 Dzib et al. (2011), 19 Straižys et al. (2003), 20 Drew et al. (1997), 21 Levshakov et al. (2014), 22 Mallick et al. (2013), 23 Smith et al. (1985), 24 Ward-Thompson et al. (2015), 25 Skiff (2014).

2.7 Summary and conclusions

In this chapter I have presented the aims and motivations of the JCMT GBS of nearby star-forming regions. I have discussed SCUBA-2, the primary instrument of this survey, and what insight it can provide into understanding of the star formation process. I look at detail at the operation of SCUBA-2 and how submillimeter continuum emission from cold dust in star forming regions is observed, reduced and calibrated. Furthermore, I have developed techniques for cleaning, selecting and filtering the data in order to achieve more reliable flux densities, and ultimately calculate more reliable dust temperatures. To further analyse SCUBA-2 maps I refine a method for consistently calculating the uncertainty on the flux across all regions in SCUBA-2 450 and 850 μm bands. I assess the various options available for deconstructing hierarchal structure in star forming regions and chose to use the STARLINK CUPID package with the FELLWALKER method as it offers the highest consistency over parameter space. I present the SCUBA-2 reduced data for the JCMT GBS Serpens-Aquila regions and summarise the results from the rest of the survey. I summarise *Spitzer* IR YSOc surveys and describe how these resources have been combined to allow full coverage of the JCMT GBS regions.

1. I develop scan selection as part of the SCUBA-2 data reduction process. I find evidence that 50% of the scans going into the Serpens MWC 297 mosaic at both 450 and 850 μm contain a significant number of artefacts with the worst case having 49.9% unreliable pixels within the data reduction mask area. The cost of omitting unreliable scans is to increase the mean uncertainty across all pixels in the PONG by between 20 and 24 %. It is therefore justified to use all available scans in the reduction process, with the caveat that local artefacts may render some pixels more unreliable.

2. I develop large scale structure filtering as a post-data reduction process for maps where the SCUBA-2 reduction pipeline has removed less structure at 450 μm, relative to 850 μm, as is in the case of the JCMT GBS IR2 reductions of the Aquila (Serpens-South/W40) region. Through examination of the SCUBA-2 450 μm/850 μm dust ratio (constructed using the methods outlined in Chapter 5) an optimal filter size of 4′(for both bands) is applied, reducing the fraction of 'bad' (greater than 9.5) flux ratio pixels from 28.8% to 5.7%.

3. I refine a consistent method for calculating a single value of noise at both 450 and 850 μm across a multi-PONG SCUBA-2 mosaic, first developed by Salji (2014). This method involves clipping the top 99.95% of the distribution of flux density pixel bins such that a minority of pixels bins containing significant astronomical signal are masked, leaving only a normal distribution of noise pixels. A gaussian is fitted to the noise and the uncertainty is calculated from the FWHM of the distribution for the 23 regions in the JCMT GBS.

4. The focus of the bulk of the work of this thesis is on the Serpens-Aquila region and its seven subregions. I discuss evidence that these regions are spatially separated over a distance of at most 250 pc and identify high mass stars forming in Aquila W40 complex, Serpens South, Serpens East, Serpens MWC 297 and Serpens NH_3 which may be heating their local environment.

5. I compile *Spitzer* multi-wavelengths surveys completed by previous authors to produce a single YSOc catalogue from which the star formation in the majority of the regions in the JCMT GBS can be assessed. Where these surveys lack IR coverage due to saturation, I outline methods for completing the coverage calling on x-ray, submillimeter and radio observations.

In the following chapters I will discuss the methods I have developed to analyse SCUBA-2 data. Looking at the contamination of ^{12}CO 3-2 line emission to the SCUBA-2 850 μm band in Chapter 3, and the contribution of thermal Bremsstrahlung, or free-free, continuum emission to both SCUBA-2 bands in Chapter 4. Following these further post-processing steps I will then present my methods for calculating the dust temperatures from SCUBA-2 flux ratios in Chapter 6.

3

CO observations of star-forming regions

In this Chapter I examine how observations of CO line emission with the Heterodyne Array Receiver Programme for B-band (HARP) instrument as part of the JCMT GBS can provide information about the position-position-velocity morphology and motion of star-forming regions. In addition to observing gas coupled to dust in the cloud, it also allows for observation of transient features, such as molecular outflows, signifying the presence of active star-formation. I was the principle investigator (PI) on a proposal to observe ^{12}CO 3-2 line emission in the Serpens-Aquila region and conducted a full subtraction of CO contamination of SCUBA-2 850 μm bands, in addition to analysing the data for the evidence for outflows and shocks.

3.1 Introduction to CO contamination and outflows

CO is known to be found in conjunction with dust and molecular hydrogen gas in giant molecular clouds (GMCs), either in its ground or excited states. It has a relative abundance to H_2 of 8×10^{-5} making it more abundant, and therefore requiring lower sensitivities to detect, than any other molecular species (Stahler & Palla, 2004). ^{12}CO 3-2 is one of the commonly observed transition and is used to trace medium column density ($10^{4-5}\,\mathrm{cm}^{-3}$) regions of molecular gas where line emission is optically thin.

^{12}CO is the most common isotopologue, followed successively by ^{13}CO, C^{18}O, etc. At low column densities the emission is optically thin and the entire cloud is observed. The majority of CO species become optically thick at sufficiently high column densities and as a result only the foreground part of the cloud is observed. Given the declining abundance, rarer species, such as C^{18}O, are more effective tracers of high density gas but requires greater sensitivities to detect. Conversely ^{12}CO is more prevalent in star forming regions but quickly becomes optically thick,

and as a result only emission from the near side of the cloud is observed. Whilst the majority of the cloud is turbulent, the velocity fluctuations remain relatively small, for example less than $3\,\mathrm{km\,s^{-1}}$, and with a normal distribution such that the line profile is gaussian-like, as described in Figure 3.1 (upper left). When emission is optically thick, a gaussian-like profile will be absorbed at its peak (Figure 3.1 upper right). Figure 3.1 demonstrates how ^{12}CO observations of a turbulent cloud change given the opacity of the line emission, and how this compares to the same cloud observed with an optically thin tracer.

For all of the examples discussed in Figure 3.1 it is worth noting that the 3 dimensional structure of star-forming regions will often result in multiple features being observed simultaneously. Real line profiles are complex and require careful analysis with additional information about the distribution of YSOs and dust, for example Davis et al. (1999). Analysis is further limited by the optically thick nature of ^{12}CO line which impacts upon understanding of the large scale 3-dimensional structure of a star forming complex. However, the increased abundance makes ^{12}CO ideal for observing low density features, such as outflows and heated shells, providing their velocity is shifted sufficiently away from the systemic cloud velocity where emission will likely be optically thick.

The intensity of line emission is usually given as the Rayleigh-Jeans brightness temperature, corrected antenna temperature, T_A*. This describes the power emission (per area, per frequency bin, per solid angle) of a source and is an empirical measurement of emission intensity and is related to the physical source temperature of the black body (and the background temperature) by,

$$T_A* = \frac{I_\nu(\tau)c^2}{2k_B\nu^2}, \tag{3.1}$$

where

$$I_\nu(\tau) = [B_\nu(T_s) - B_\nu(T_{bg})](1 - e^{-\tau(\nu)}). \tag{3.2}$$

I_ν is the observed line intensity for an optical depth, τ, and is defined by the emission from the source, at temperature T_s, minus the emission from the cosmic microwave background,T_{bg} = 2.73 K. The 1–0, 2–1 and 3–2 transitions are most commonly studied. ^{12}CO 3-2 line emission is known to contribute to 850 μm fluxes as it lies within the 850 μm filter passband making it a known contaminant of SCUBA-2 dust emission (Gordon, 1995).

Using the Doppler shift of molecular lines along the line of sight, observations of CO (and all molecular line species) allow for both spatial and kinetic analysis of astrophysical structures, whereas continuum observations of dust by SCUBA-2 allow only spatial analysis. Regions where the gas velocities are similar to that of the systemic cloud material are assumed to have a similar spatial location. In these cases, relative differences in velocities can allow for discussion of the kinetic motions and turbulence of the clouds on large scales, and the presence of molecular outflows and shock fronts on small scales. Where the cloud velocity differs significantly from that of the systemic cloud material, it can be considered spatially separated from the main star forming complex, as either foreground or background clouds (Shimoikura et al., 2015). Where multiple velocity components are observed with an optically thin tracer, for example C^{18}O, simultaneously (Schneider et al. 2010, Duarte-Cabral et al. 2011) have suggested cloud-on-cloud collision or con-

vergence of flows as a possible explanation.

CO is rarely observed inside H II regions. Whilst CO provides a degree of self-shielding against UV photons, sufficient exposure will photo-dissociate the molecule, for example Manoj et al. 2007). Where CO emission is observed in conjunction with an H II region, gas will likely be in the foreground/background of the ionised bubble. In the photo-dissociative region (PDR) UV photons are likely to heat and excite line emission in greater quantities leading to observations of molecular shells around an H II region (Heyer & Terebey, 1998; Bieging & Peters, 2011; Shimoikura et al., 2015).

3.1.1 CO as a tracer of outflows

Accretion of molecular gas on to the surface of protostars is known to drive bipolar jet activity. The bulk motion of the jet has been observed to sweep up the surrounding ISM and propel them to greater velocities than the systemic cloud velocity (McKee & Ostriker, 2007). This outflow ISM has been associated with molecular-line emission where mechanical shocks produced by the jet can excite electrons to higher energy levels (Davis et al., 1999). Hα lines are most prominent in these outflows, but species such as CO are also observed. Line emission from outflows tends to be relatively faint compared to that of the systemic CO gas. However, the kinetic motion of the jets shifts much of this emission in velocity space allowing these faint features to be observed when emission at the systemic velocity is optically thick.

The bipolar nature of the jet means that often relatively blue- and red-shifted lobes of outflow emission can often be seen in close proximity, for example Figure 3.1 (lower left) and Figure 6 in Graves et al. (2010). This has proven an excellent marker for hidden Class 0 protostars (Lee et al., 2013). However, there are numerous cases where the complex, 3 dimensional structure of star forming regions can make analysis of individual molecular outflows very challenging. For instance, White et al. (1995), Davis et al. (1999) and Graves et al. (2010) studied molecular outflows in Serpens Main, observing a complex network of overlapping red- and blue-shifted lobes interspaced with dense cores and cavities observed in submillimeter continuum with SCUBA, and a number of HH objects visible at IR wavelengths. Outflow activity is thought to be ubiquitous with Class 0/I sources, however not all may be detectable. Studies by Hatchell et al. (2007) have found that 73% of submillimeter sources in Perseus have outflows, and that outflow detection largely matches the detection of Class 0/I protostars by Spitzer (Graves et al. (2010) cannot assign individual outflows to protostars in Serpens Main as a result of the complexity of the region).

Gas perturbed by a protostellar jet can reach greater velocities and as a result the red- or blue-shifted side of the cloud can be appear as extended 'line-wings', as demonstrated in 3.1 (lower left). Line-wings are often observed in isolated lobes where they are often asymmetrical. When the outflows lie along the line-of-sight a double peaked P Cygni profile can be observed with warm, red-shifted material for the interior of the cloud observed simultaneously with cold, blue-shifted material from the exterior of the cloud. I note that P Cygni profiles are synonymous with deeply embedded objects and therefore are rarely observed in the more abundant species, such as ^{12}CO 3-2, because they deplete out onto grains at low critical densities and are less effective at tracing high density regions.

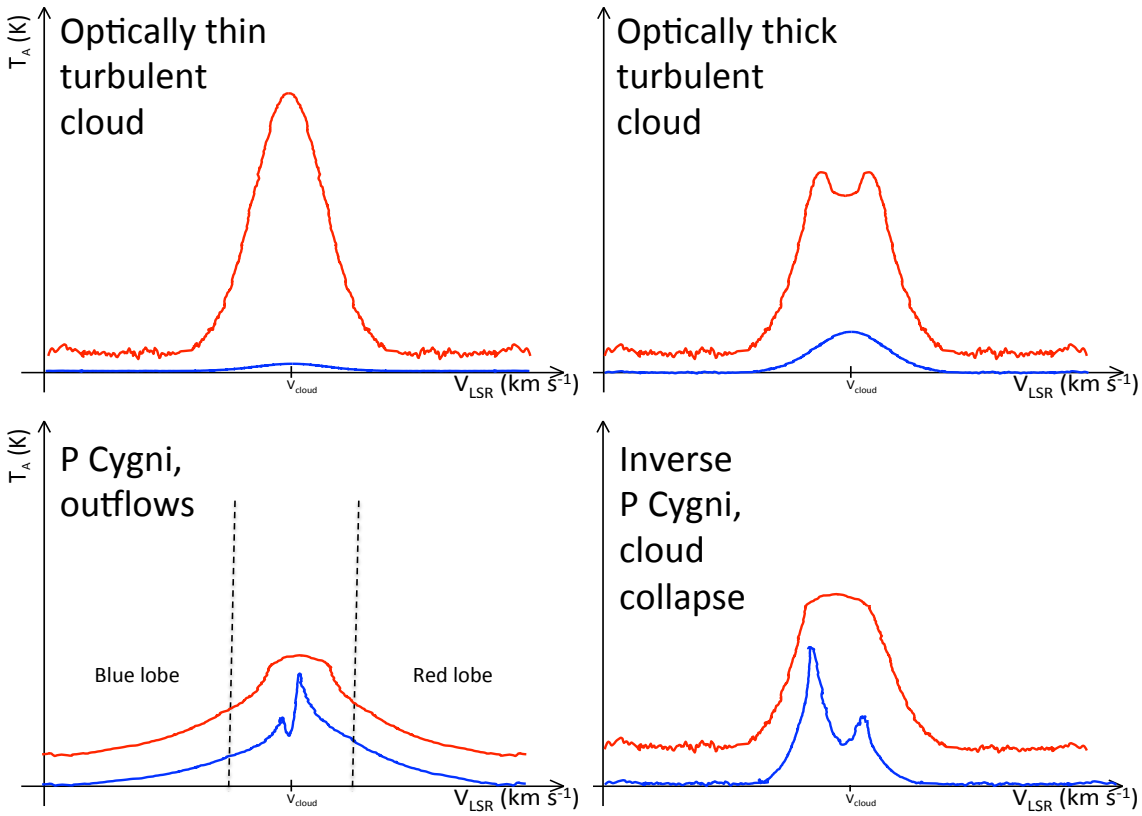

Figure 3.1: Examples of schematic ^{12}CO 3–2 (red) line profiles of astrophysical phenomena. A fainter, but optically thin tracer, for example C^{18}O, is also shown (blue) for the same features. Upper left shows typical observation of an optically thin, low density, stable but turbulent cloud. Upper right shows a high density stable cloud, where ^{12}CO 3–2 is optically thick towards the center and emission is absorbed. The lower panels show typical P Cygni profiles that are associated with star formation. In these cases C^{18}O is tracing dense envelope that is being heated by a protostar, causing material nearer the core to be brighter than that at the edge of the core. When motion is dominated by outflows from a protostar (lower left) then the red lobe is brighter. In addition, protostars with outflows propel material to higher velocities and have extended 'line-wings' as marked. Lower left shows an outflow perpendicular to the plane of the sky such that both red and blue lobes can be observed simultaneously. It is also common for the jet alignment to lead to only a single outflow lobe being observed, and the line having a characteristic asymmetric profile. When the envelope motion is dominated by free-free fall onto the protostar (lower right) the blue lobe is brighter, also referred to an inverse P Cygni profile. Note how ^{12}CO 3–2 can only provide information about the lower density outflows because the line emission becomes optically thick towards the higher density protostellar core.

The criterion for an outflow is defined by Hatchell et al. (2007) as where the intensity of the line-wing is greater than 3 times the standard deviation on the noise, σ, at $\pm 3 \mathrm{km\,s^{-1}}$ from the systemic cloud velocity. Note that this method is specific for the Perseus cloud and is therefore to be treated as a guide for further GBS regions. In general this condition should be based on a fit to an optically thin tracer of the systemic cloud profile. Once a candidate outflow has been detected in the line spectra, it is possible to produce an integrated intensity map of the region by restricting the velocity space to the line-wing. The limits on this tend to be somewhat arbitrary between approximately the half line peak intensity and sufficiently off of the line so that only noise is detected. Where this method is used it is therefore important to use a consistent set of limits. Integrated maps of blue- and red-line-wings can then be mapped in position-position space, for example, Davis et al. (1999) and Shimoikura et al. (2015).

Studying the kinematics of outflows, through molecular line emission, can allow for the properties of outflows to be characterised. For example, outflow mass flux rate (momentum, Bontemps et al. 1996), kinetic energy (White et al., 2015), lifetime and length (Davis et al., 1999) and excitation temperature (Graves et al., 2010) can all provide new insight into a young protostar that might otherwise be shrouded in its natal cloud. For example, Graves et al. (2010) analyse the global outflow energy of outflows in Serpens and find it contributes 70% of the total turbulent kinetic energy in the region.

3.1.2 CO contamination related to dust temperature.

SCUBA and SCUBA-2 850 μm have been routinely examined for ^{12}CO 3–2 contamination. Davis et al. (2000), Hatchell & Dunham (2009), Drabek et al. (2012), Pattle et al. (2015), Buckle et al. (2015) and others find evidence for CO contamination ranging between less than 10 % to up to 90 %. Given that ^{12}CO 3–2 contamination affects the 850 μm band, but not the 450 μm band, an assessment of this line emission is vital for an accurate assessment of dust temperature, with unaccounted CO emission producing artificially lower SCUBA-2 450 μm/850 μm flux ratios, and therefore cooler temperatures (Equation 1.33).

The methods for producing temperature maps from SCUBA-2 data are discussed in Chapter 5. The change in dust temperatures calculated when CO contamination is removed (for the W40 complex) are quoted in Section 3.5 whilst full details of these findings are discussed in detail in latter chapters.

3.2 HARP observations and reduction

The submillimeter line emission of CO, and other species, can be observed with the Heterodyne Array Receiver Programme for B-band (HARP) instrument that is mounted at the JCMT. This instrument is composed of 16 heterodyne receivers in a 4×4 array and is sensitive over a range of 325-375 GHz. This range is equivalent to the 850 μm band on SCUBA-2 and therefore its angular resolution is 14.6″. The output of the heterodyne receivers is the corrected antenna temperature (T_A*) Equation 3.2. Buckle et al. (2009) provide a detailed description of the set up of HARP.

HARP maps used in this work were primarily observed using the 'Scan' mapping mode. This involves the instrument scanning rows across a rectangular region and is often carried out in conjunction with a 'basket-weaving' pattern (two independent maps scanned perpendicular to each other and mosaiced together). Additional mapping modes include 'Jiggle' and 'Stare'. All scanning modes are used in conjunction with an 'off position', a control region where there is not thought to be any significant emission. Poorly, or automatically identified 'off positions' can lead to an incorrect background subtraction (Equation 3.2) of the observed region.

Post-observation, the antenna temperature requires a correction for telescope or instrumental inefficiencies as the observed temperatures are an underestimate of the true value. Primarily the main beam efficiency ($\eta_{\rm MB}$) measures how the complex beam shape of the JCMT differs from that of a simple gaussian profile. $\eta_{\rm MB}$ can be empirically measured by observing a point source of known intensity, for example Uranus. Previous authors have studied this correction and the results are stored in the JCMT efficiency archive[1]. When observing sources that are significantly larger than the beam size the forward spillover and scattering efficiency, $\eta_{\rm fss}$, starts to dominate over $\eta_{\rm MB}$. For these reasons using $\eta_{\rm css}$ is preferable when observing molecular clouds. However, use of $\eta_{\rm MB}$ is a standard across the scientific community therefore the main beam efficiency is favoured so that results are comparable. As a result I deal only with $\eta_{\rm MB}$ in the reduction of observations of the W40 complex (Section 5).

3.3 Methods for removing ^{12}CO 3–2 contamination of the SCUBA-2 850 μm band

I will summarise the existing methodology for removing contamination here, based on the previous work of Drabek et al. (2012) and Hatchell et al. (2013). An integrated intensity map of the ^{12}CO 3–2 observations has the large-scale structure (greater than 5′) removed by converting to Fourier space and filtering in the time domain (see FLT mode, Chapter 2, Section 2). In practise, this large-scale structure removal is processed by running the CO observations through the SCUBA-2 reduction pipeline. Alternatively, the CUPID `findback` technique, as described in Chapter 2, can be also be used to mimic the SCUBA-2 data reduction process. The main beam efficiency correction, $\eta_{\rm MB}$, is then applied to correct the antenna temperature. A further CO-conversion factor is required to translate pixels values from a temperature, $T_{\rm MB}$, into a flux, S_{ν_0}. In the case of the ^{12}CO 3–2 line this is given as,

$$\frac{S_{\nu_0}}{\rm Jy/pixel} = a \times 10^{-3} \frac{\rm FCF_{arcsec}}{\rm FCF_{peak}} \frac{2k_B\nu_0^3}{c^3} \frac{g_{\nu_0,\rm line}}{\int g_{\nu,\rm cont} d\nu} \Omega \int T_{\rm MB} d\nu, \tag{3.3}$$

where a is the pixel area, Ω is the telescope beam, FCF is the flux conversion factors (see Chapter 2), $g_{\nu_0,\rm line}$ is the transmission profile of the submillimeter filter at the line frequency, ν_0, and $g_{\nu,\rm cont}$ is the transmission profile of the SCUBA-2 filter (Drabek et al., 2012). All other parameters have their usual meaning. The free parameter in the CO-conversion factor is the SCUBA-2 filter profile, which is dictated by the weather grade in which the SCUBA-2 observations were observed.

[1] https://www.eaobservatory.org/jcmt/instrumentation/heterodyne/calibration/ - 28/01/2016

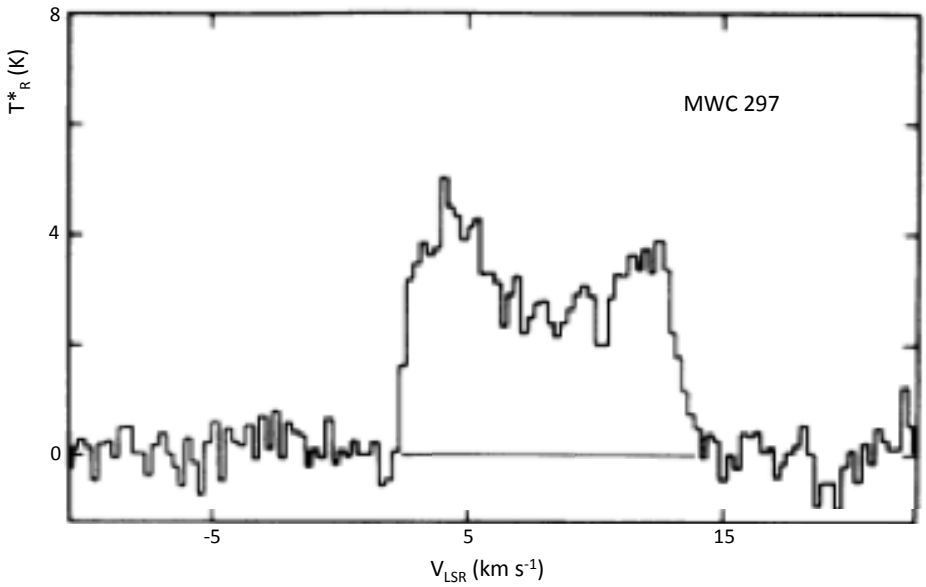

Figure 3.2: Spectra of ^{12}CO 1–0 line emission for MWC 297 observed with 11m radio telescope at NRAO (adapted from Figure 1, Canto et al. 1984). The source antenna temperature, T_R*, is defined by Kutner & Ulich (1981). Velocity resolution is 0.26 km s^{-1}.

Drabek et al. (2012) calculate these factors for each weather grade at JCMT for a 13.8″ effective beam, and Sadavoy et al. (2013) update these for a 14.2″ effective beam. Full details of these calculations are described in Drabek et al. (2012). This method has been used successfully by Drabek et al. (2012), Pattle et al. (2015), Buckle et al. (2015) and in Chapter 7 to remove contaminating ^{12}CO 3–2 line emission from SCUBA-2 850 μm data.

Provided then the pixel grid of the updated CO data matches that of the SCUBA-2 850 μm data, the CO contamination can be removed via subtraction. In reality, this method has been streamlined to be included within the SCUBA-2 data reduction pipeline in order to produce consistent results.

The CO contamination and outflow studies in this chapter are related entirely to the Serpens-Aquila region of the JCMT GBS, in particular Serpens MWC 297 and the W40 complex. ^{12}CO 3–2 contamination of the SCUBA-2 850 μm band has been observed in other GBS regions. Where decontaminated maps have been made internally available within the GBS they have used similar methods as presented here. Those regions and authors have been identified in Chapter 2, Tables 2.13 and 2.14.

3.4 CO in Serpens MWC 297

Limited CO line emission data exist for the Serpens MWC 297 region. Canto et al. (1984) observe ^{12}CO 1–0 and ^{13}CO 1–0 lines with the 66″ resolution 11m radio telescope at NRAO as part of a wider survey of Herbig stars. Manoj et al. (2007) observe the same lines at a significantly higher resolution with the Submillimeter Array (SMA) and find no evidence of CO emission within 80 AU of MWC 297 and conclude this near-star-depletion is caused by photoionisation due to an ultra-

compact H II (UCHII) region that as has been detected by Drew et al. (1997) and Malbet et al. (2007). These observations have been focused the star MWC 297 at the expense at less luminous regions of star formation in Serpens MWC 297.

A very rough estimate of the ^{12}CO contaminating flux, $S_{CO,850\mu m}$, towards the star MWC 297 can be made based on the published spectra of Canto et al. (1984), presented in Figure 3.2, by

$$S_{CO,850\mu m}(\mathrm{Jy/pix}) = T_{peak}(\mathrm{K}) \times \Delta\nu(\mathrm{km\,s^{-1}}) \times \mathrm{C(Jy/K\,km\,s^{-1}/pixel)} \quad (3.4)$$

where T_{peak} is the peak line intensity at the centre of the line, $\Delta\nu$ is the line width and C is the CO conversion factor outlined in Equation 3.3. The ^{12}CO lines are broad ($\sim$ 12 km s^{-1}) but do not show line wings characteristic of outflows. Making the simplest assumption that the ^{12}CO is optically thick and fills the beam in both the J = 1–0 and J = 3–2 lines, the integrated intensity of the latter, $\sim$ 36 K km s^{-1}, corresponding to a ^{12}CO 3–2 contamination of 1.14 mJy/pixel/K km s^{-1} (13 % of peak flux) at the position of the star MWC 297 using the conversion in Drabek et al. (2012) updated for the beam parameters in Dempsey et al. (2013).

Drabek et al. (2012) noted that regions where ^{12}CO 3–2 emission accounts for less than 20% of total peak emission are not consistent with major contamination. However, given the conclusions regarding the impact of low levels of CO contamination on calculated dust temperatures, 13% CO contamination would justify HARP observations of the ^{12}CO 3–2 line in this region with the aim to fully decontaminate the SCUBA-2 850 μm data. As no HARP data of coverage comparable to the SCUBA-2 observations of Serpens MWC 297 exists, the analysis of the region conducted in Chapter 6 is completed without CO decontamination.

3.5 CO in the W40 complex

Very Large Array (VLA) 3.6 cm observations by Rodríguez et al. (2010), presented in Figure 3.3 covering a 5′×5′ area of the W40 complex in the Aquila region (outlined in Chapter 2) appear to provide evidence for knots of radio emission associated with OB stars and potentially star forming cores, sites where CO contamination could feature. In addition, many YSOcs have been detected in the *Spitzer* GBS YSOc catalogue (Gutermuth priv. comm. and Dunham et al. 2015) and Maury et al. (2011) has found evidence for Class 0/I protostars which are though to be synonymous with outflow activity.

A number of CO observations exist for the W40 complex. A first wave of ^{12}CO 1-0 observations by Zeilik & Lada (1978) found extended emission (beam size 3′) with a bulk velocity of approximately 4.5 km s^{-1} across the Aquila region. Zhu et al. (2006) studied the ^{13}CO 2–1, ^{12}CO 1–0 and 3–2 line emission from the Dust Arc and observed profiles symptomatic of outflows as well as calculating a mass of between 188 to 319 $M_\odot$ that is consistent with massive star formation. Both of these observations confirm the presence of significant quantities of CO, but lack the resolution for detailed analysis of star-formation.

More recently, archival JCMT HARP ^{12}CO 3–2 observations by van der Wiel et al. (2014) of a 2′×2′ region, shown in Figure 3.3 relative to W40 complex, confirm the presence of red- and blue-shifted clouds presented as spectra in Figure 3.4 and as a map in Figure 3.5. Line-

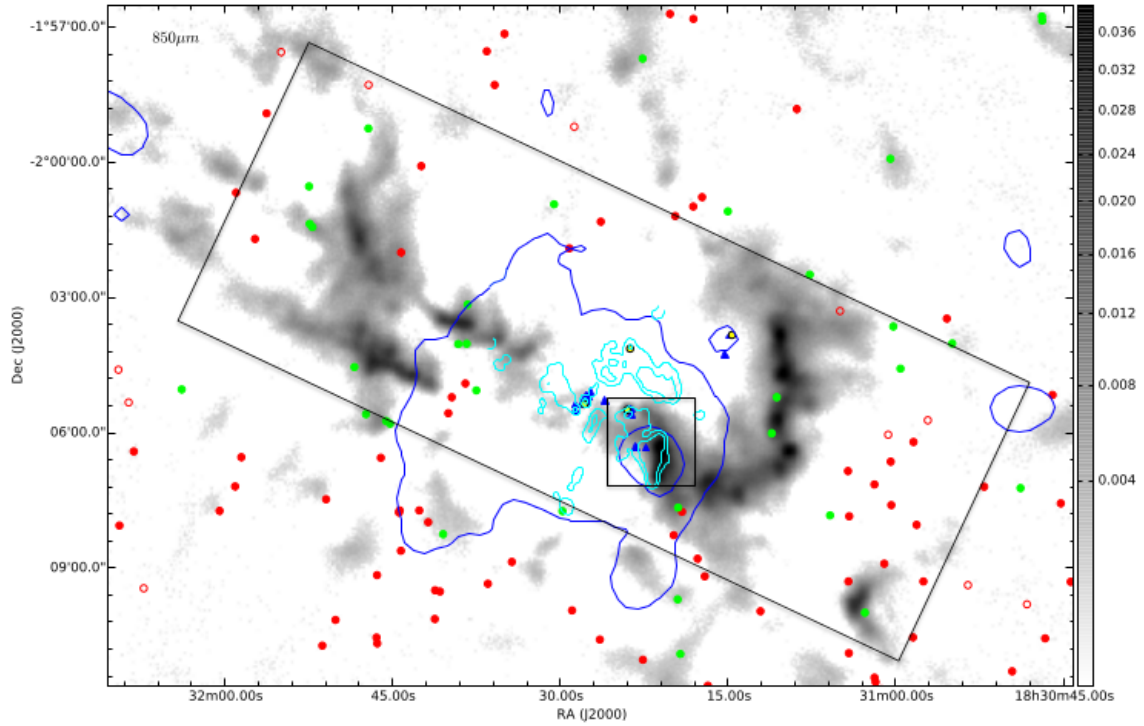

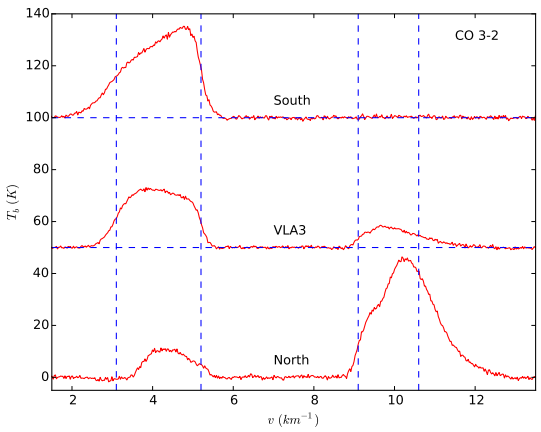

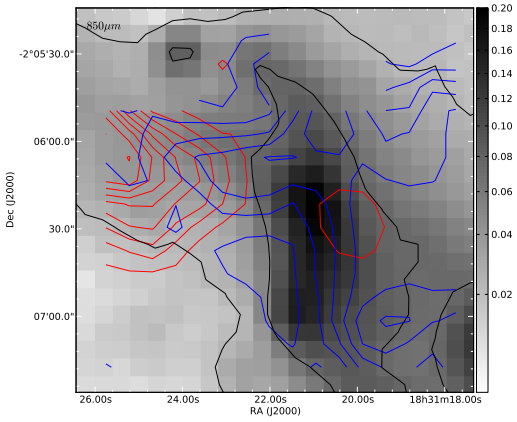

Figure 3.3: **Top:** SCUBA-2 850 μm emission from W40 displaying the Van der Wiel et al. (2012) ^{12}CO 3-2 region (small rectangle) and area covered by the ^{12}CO 3–2 observations presented in this thesis (large rectangle). YSOcs from the *Spitzer* GBS are markers in green (Class O/I), red filled (Class II) and red hollow (Class III). Cyan contours show 10″resolution archival AUI/NRAO 3.6 cm emission at 0.001 and 0.005 Jy along with the Rodriguez et al (2010) compact radio sources marked as blue triangles. Blue contours of 0.01 and 0.1 Jy per 45″ beam for 21 cm emission (Felli et al. 1972) show the extent of the HII region in W40.

Figure 3.4: **Bottom Left:** ^{12}CO 3-2 line widths for the compact object VLA 3 and redhsifted and blushifted emission (Van der Wiel et al. 2012).

Figure 3.5: **Bottom Right:** SCUBA-2 850 μm data of VLA 3 overlaid with ^{12}CO 3-2 contours. The area of this existing ^{12}CO 3-2 map is shows as the smaller box in the top figure. The redshifted peak is at 4.78 kms^{-1} and the blue shifted peak is at 10.21 kms^{-1}.

wings observed are typical of molecular outflows (Lee et al., 2013). However, full interpretation is limited due to ^{12}CO 3-2 line emission becoming optically thick and the limited coverage of the observation. Shimoikura et al. (2015) published ^{12}CO 3–2 and HCO^+ 4–3 line observations of the W40 complex with the Atacama Submillimeter Telescope Experiment (ASTE) with a greater coverage that includes W40-N and the Dust Arc at a resolution of 22″.

3.5.1 Observations and data reduction

I was principle investigator (PI) of the M15AI31 "Active star-formation in the W40 complex" proposal to observe ^{12}CO 3–2 line emission in the W40 complex, including the whole of the Dust Arc and W40-N, as presented in Figures 3.3 and 3.6. This coverage is comparable to Shimoikura et al. (2015) but has an improved resolution of 14.6″. This proposal was accepted prior to the data of Shimoikura et al. (2015) being published.

^{12}CO 3–2 (345.7960 GHz) in Aquila was observed with HARP on the 4th of July 2015. The efficiency, $\eta_{\rm MB}$, taken from the JCMT efficiency archive is 0.61at 345 GHz. Two sets of four basket-weaving scan maps were observed over an 6′43″×17′54″ area (position angle = 65°) at 345.796 GHz to observe the ^{12}CO 3–2 line, making a total integration time of 128 minutes, given a sample time of 0.4 s. A sensitivity of 0.3 K was achieved on 1 km s^{-1} velocity channels in Grade 4 weather (τ_{225} = 0.16). Observations have a 0.488 GHz (0.423 km s^{-1}) spectral resolution and are gridded to an appropriate pixel size (Buckle et al., 2012). Maps were referenced against an off-source position at RA(J2000) = 18:33:29.0, Dec.(J2000) = -02:03:45.4, which had been selected as being free of any significant CO emission in the Dame et al. (2001) CO Galactic Plane Survey. The proposed region contains 17 Class 0/I protostars. Such CO observations allow further constraints on whether these objects are actively accreting from their envelopes, and aid classification.

Prior to data reduction, the HARP receptors were calibrated using a known source such as the Moon (see Curtis et al. 2010 for full details). Typical raw data from HARP consists of four sets of two time series. Previous observers have noted systematic and random failures of certain pixels during the observations and therefore it is necessary to mask any bad pixels in the raw data before reduction. Reduction uses the `makecube` command in the Starlink SMURF package to assemble the time series into a position-position-velocity cube (Jenness et al., 2015). The frequency range is further constrained such that it excludes the uncertain edges of the band filter. The third axis is then calibrated in units of km s^{-1}. The map is regridded onto a pixel scale comparable to the SCUBA-2 850 μm band. These processes are automated within the established JCMT GBS 'narrow' line data reduction pipeline for HARP data.

Reduced HARP observations are delivered in the form of a 'position-position-velocity (PPV) cube' with individual position-position maps per velocity bin (for a given velocity resolution) between the range 345.8996 and 345.6775 GHz (+100 to -90 km s^{-1} from the kinematic local standard of rest, LSR). Neighbouring velocity bins can be binned together to increase the SNR on each pixel at the expense of velocity axis resolution. Integrated intensity maps can be created for a specific velocity range by summing bins across said range. As the total velocity range of HARP falls within the SCUBA-2, 850 μm band (325-375 GHz), all bins have the potential to contribute to the flux observed by SCUBA-2, and it is therefore necessary to produce an

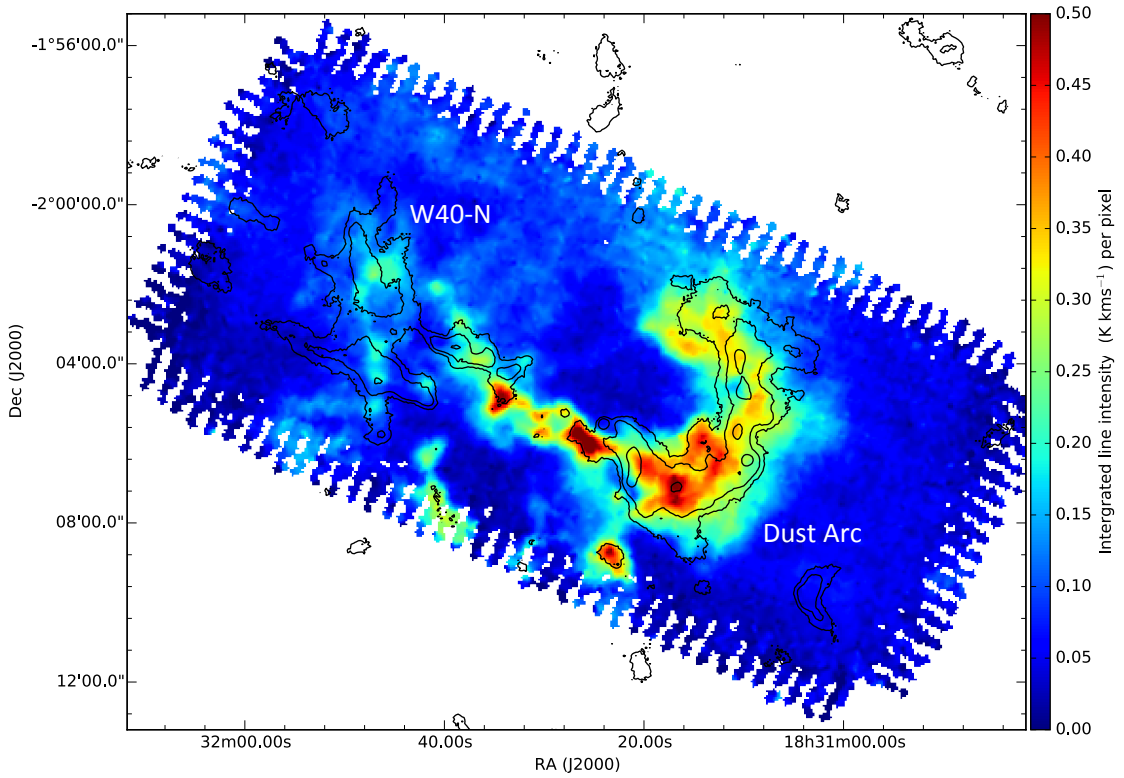

Figure 3.6: ^{12}CO 3–2 integrated intensity map over the entire range (from -90 to +100 km s^{-1}) of the central region of the W40 complex. Contours show SCUBA-2 850 μm emission at the 5 σ, 15 σ and 50 σ levels.

integrated intensity map across all velocity bins to assess the total contribution of ^{12}CO 3–2 to the dust emission.

In order to remove the ^{12}CO 3–2 (345.7960 GHz) contamination from SCUBA-2 850 μm, an integrated intensity map, corrected for main beam efficiency, was produced by collapsing the cube along the entire velocity range and subsequently passed through the SCUBA-2 data reduction pipeline to consistently remove the large-scale structure as per the method described in Chapter 2. Figure 3.6 presents the final ^{12}CO 3–2 integrated intensity map for the W40 complex.

3.5.2 Contamination results

Evidence of red- and blue-shifted clouds were found in archival HARP ^{12}CO 3-2 data (JCMT GBS M12AC21 HARP programme). These were observed over a 2′×2′ region covering the brightest submillimeter emission in the Aquila W40 complex. The respective peak intensities were 45.3 K at 6.4 km s^{-1}, and 35.7 K at 12.0 km s^{-1} with measured line widths of Δv = 3.9 and 4.8 km s^{-1}. Following the method of Drabek et al. (2012), the fraction of CO contamination was estimated at 23% and 43% making it essential for a full CO subtraction from SCUBA-2 850 μm data to be carried out before accurate dust fluxes can be measured (Figure 3.5).

The integrated intensity of ^{12}CO 3–2 line emission was converted to a flux, following the methods outlined in the previous section, before being subtracted from the original SCUBA-2 850 μm maps using a joint data reduction process. A 4′ filter was applied following the method

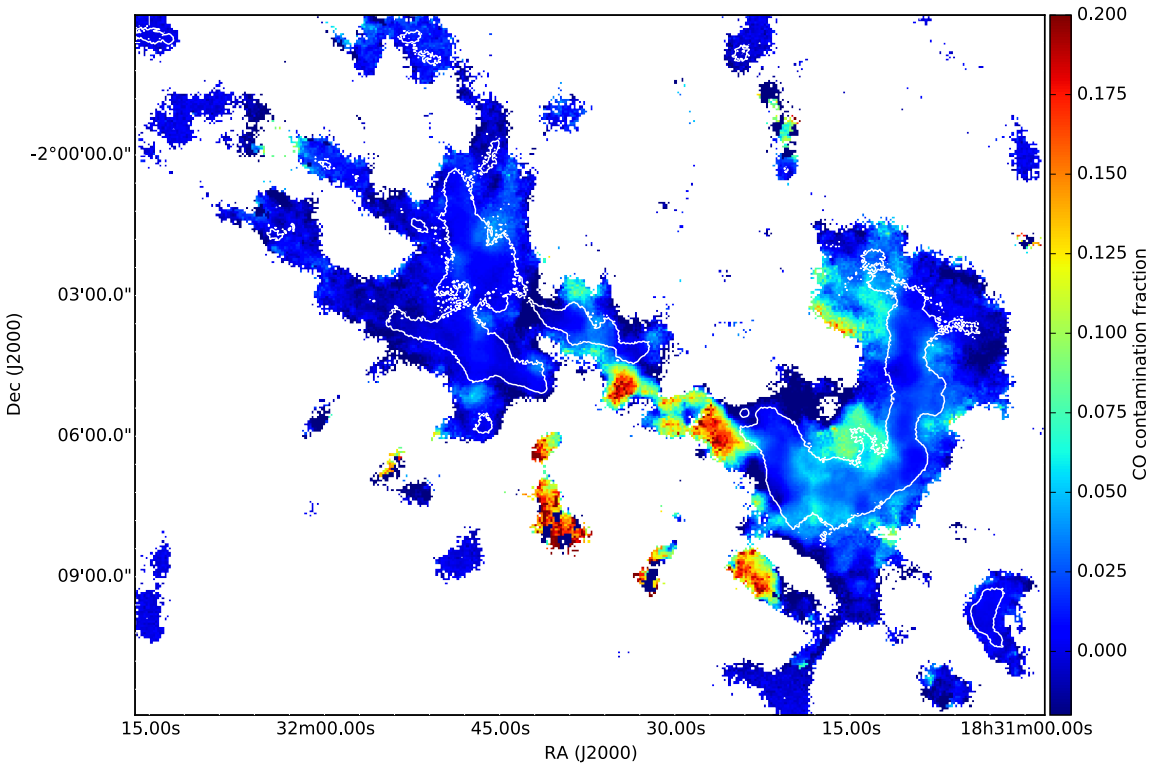

Figure 3.7: The fraction of SCUBA-2 850 μm that can be attributed to ^{12}CO 3–2 345 GHz line emission. The SCUBA-2 data are masked at 3σ and the 5σ level is shown in white.

outlined in Chapter 2. The fraction of SCUBA-2 emission that can be accounted for by ^{12}CO 3–2 line emission is presented in Figure 3.7. Contamination in W40-N is minimal with levels up to 5%. The Dust Arc has significant contamination at a level of 10%, reaching up to 20% in a minority of locations.

Figure 3.8 shows the distribution of SCUBA-2 450 μm to 850 μm flux ratio pixels (see Equation 1.33 and the method given in Chapter 5) with and without CO contamination contributing to the 850 μm intensities. These results show how even a small degree of CO contamination can have a significant effect on measuring temperatures in the cloud, e.g, the modal flux ratio increases from 6.8 to 7.8 when CO is subtracted. Furthermore, the FWHM of the distribution increases from 1.9 to 2.8. Subtracting CO from my maps increases the mean and standard deviation of temperature in regions where ^{12}CO 3–2 is detected, in comparison with temperatures derived from uncorrected maps. Dust temperatures are, on average, reduced by 3.3 K per pixel where contamination is less than 10%, and reduced by 16.4 K where contamination is greater than 10% per pixel. Full details of these results are discussed in Chapter 5.

The distributions of flux ratios across the map, with and without the CO contamination, are compared and found to have a KS-statistic of 0.253, corresponding to 1.3% probability that the two samples are drawn from the same parent sample. CO contamination in the W40 complex is therefore having a significant impact on the distribution of flux ratios and temperatures.

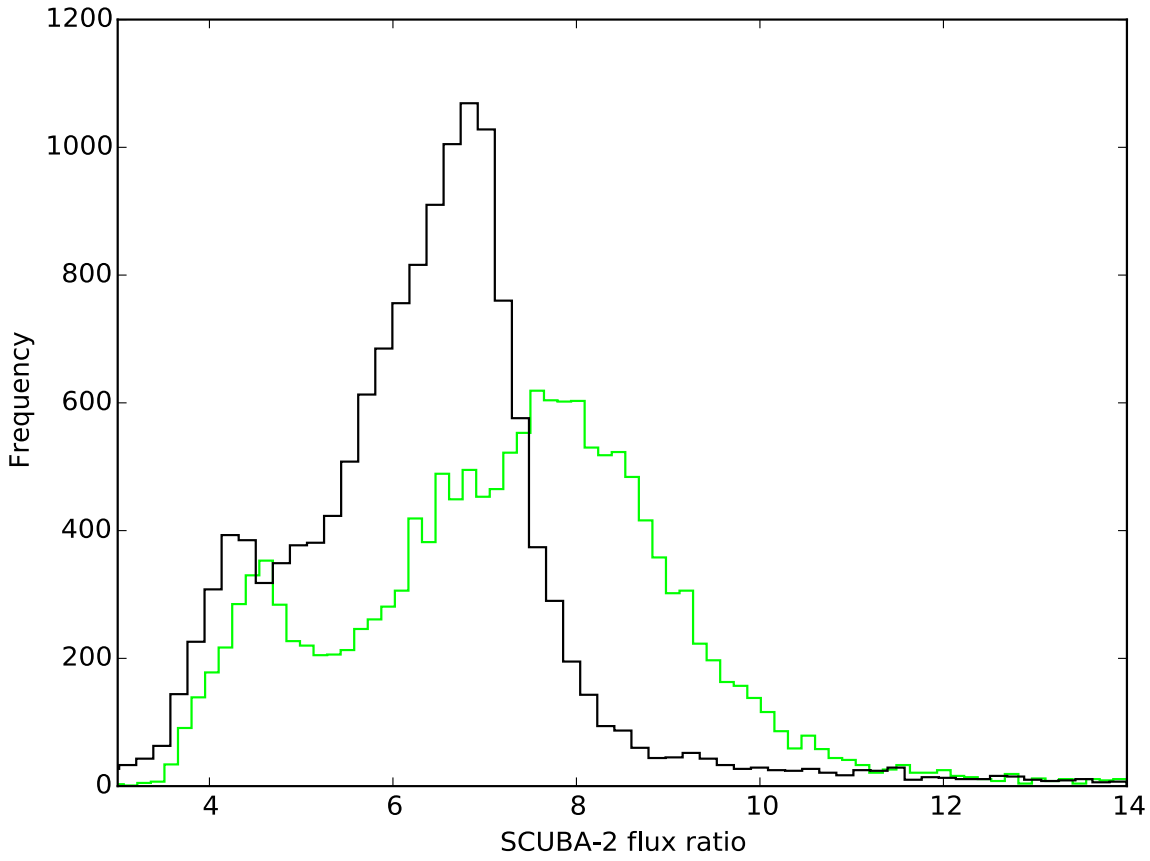

Figure 3.8: The distribution of 450 μm/850 μm flux ratio for the original (blue - S2-4′) and CO subtracted (green - S2-CO-4′) Aquila reductions with additional 4′ spatial filtering. KS-statistics reveal a 1.3% chance that the two data sets are drawn from the same distribution.

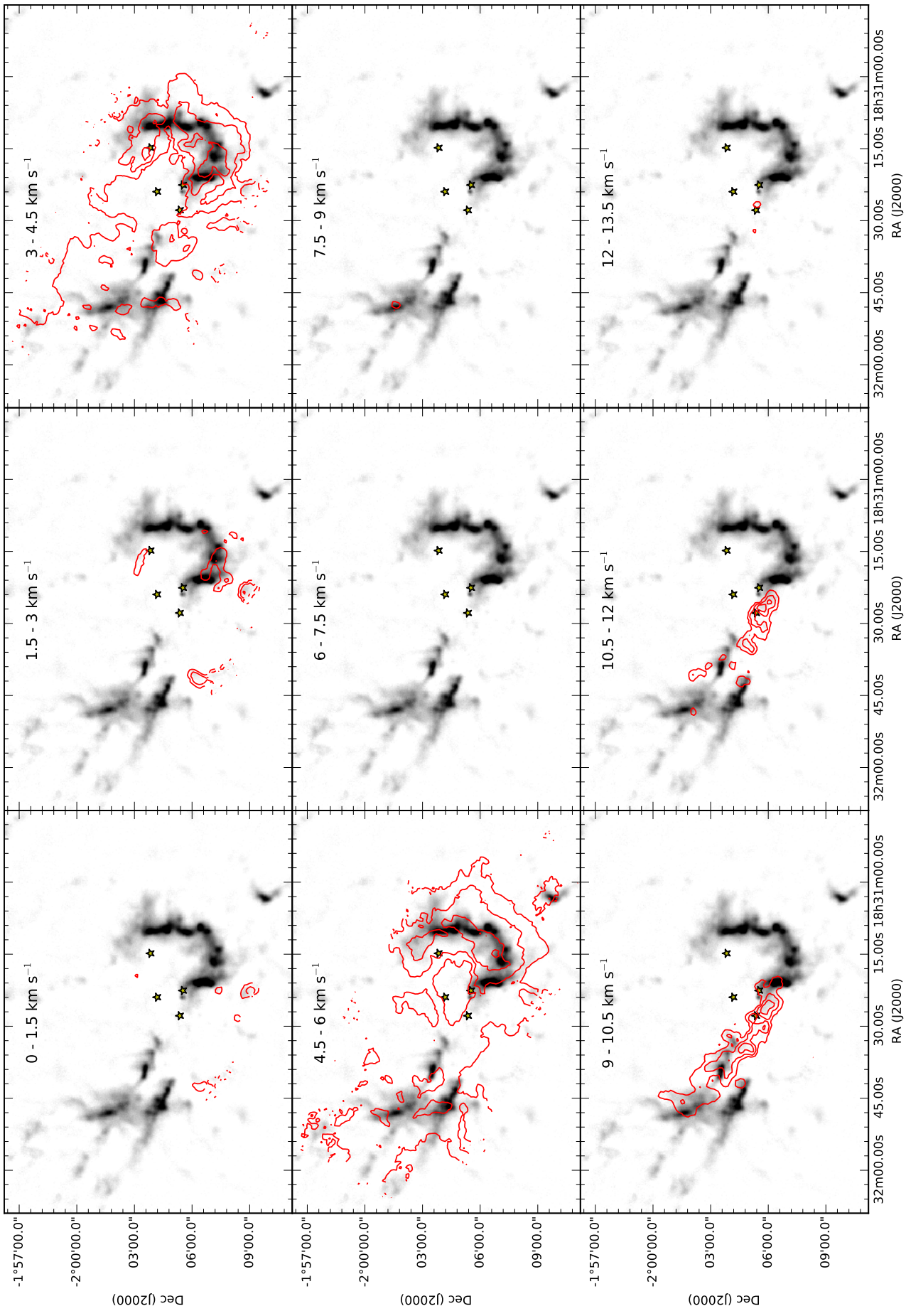

Figure 3.9: SCUBA-2 850 μm continuum emission (grey) scale of the W40 complex Dust Arc and the W40-N clouds. Red contours show ^{12}CO 3-2 line emission in successive velocity bins. Levels represent 5, 15, 30, 50 and 70 K km s^{-1}.

3.5.3 Cloud morphology

The velocity structure of ^{12}CO 3-2 line observations of the W40 complex from 0 to 13.5 km s^{-1} is presented in Figure 3.9. Two distinct components are visible in the velocity space and are presented in Figure 3.10. A blueshifted component is observed at approximately 5 km s^{-1} (consistent with Zeilik & Lada 1978 and Shimoikura et al. 2015) with peak integrated intensity of 88 K km s^{-1} that is coincident with the SCUBA-2 emission in the Dust Arc and, to a lesser extent, W40-N. A redshifted component is observed at approximately 10 km s^{-1} with an peak integrated flux of 86 K km s^{-1} and traces a filament of emission between W40-N and the Dust Arc, passing through the location of the OB association in the W40 complex.

Since CO is photo-dissociated in H II regions, the redshifted 10 km s^{-1} filament is either sufficiently massive that CO can self-shield from the UV photons in side the H II region, or it is located in the foreground or background of the H II region. SCUBA-2 does not detect a significant dust filament coincident with the redshifted ^{12}CO 3-2 line emission, therefore I discount the former premise. The presence of bright rimmed clouds (BRCs) observed in Herschel 70 μm data that are consistent with peaks of redshifted ^{12}CO 3-2 emission, confirming that the CO gas is part of the nebulosity. This structure is consistent with the findings of Shimoikura et al. (2015) who suggested the redshifted filament is a shell of heated CO gas swept up in the expanding shockwave around the H II region.

ASTE observations by Shimoikura et al. (2015) provide evidence of a third velocity of approximately 7 km s^{-1} observed in HCO$^+$ 4–3 at the submilimetre peak of the cloud (their Figure 2). HCO$^+$ 4–3 remains optically thin at higher column densities where ^{12}CO 3-2 may become optically thick. Shimoikura et al. (2015) argue that the sharp partition between 5 and 10 km s^{-1}, as seen in the insert of Figure 3.10, may be due to a dense cloud at 7 km s^{-1} in which ^{12}CO 3-2 is absorbed but HCO$^+$ 4–3 is observed because it remains optically thin. The partition in cloud velocities, illustrated in Figure 3.10, is consistent with some of the brightest SCUBA-2 850 μm emission, and highest column densities assuming typical ISM temperatures, supporting the argument that ^{12}CO 3-2 is optically thick in these regions.

I find less evidence to support the claim of Shimoikura et al. (2015) that the systemic gas in the W40 complex has a velocity of 7 km s^{-1} as I detect no ^{12}CO 3-2 emission at that velocity in the relatively low density filaments that are significantly outside of the H II shell. It is unlikely that this component extends to the off position as it was throughly examined in Dame et al. (2001) CO Galactic Plane Survey and found to be clear. One explanation is that the ^{12}CO 3-2 is optically thick across the whole of the W40 complex at 7 km s^{-1}, though it is difficult to explain the complete absence of significant emission at this velocity this way. The velocity structure of the cloud will be discussed at depth, and in conjunction with the dust temperatures, in Chapter 7.

In addition to the 5, 7 and 10 km s^{-1} clouds discussed above, a small number of isolated, bright clouds are observed to the south of the map that have a approximate cloud velocity of 3 km s^{-1}. As the upper panel of Figure 3.11 shows, these clouds are associated with faint, isolated dust clouds in SCUBA-2 emission after the 850 μm contamination has been removed, suggesting that there is additional, if sparse, filamentary structure along the line of sight. SCUBA-2/HARP observations support the conclusions of Shimoikura et al. (2015) that the 3 km s^{-1} clouds are not

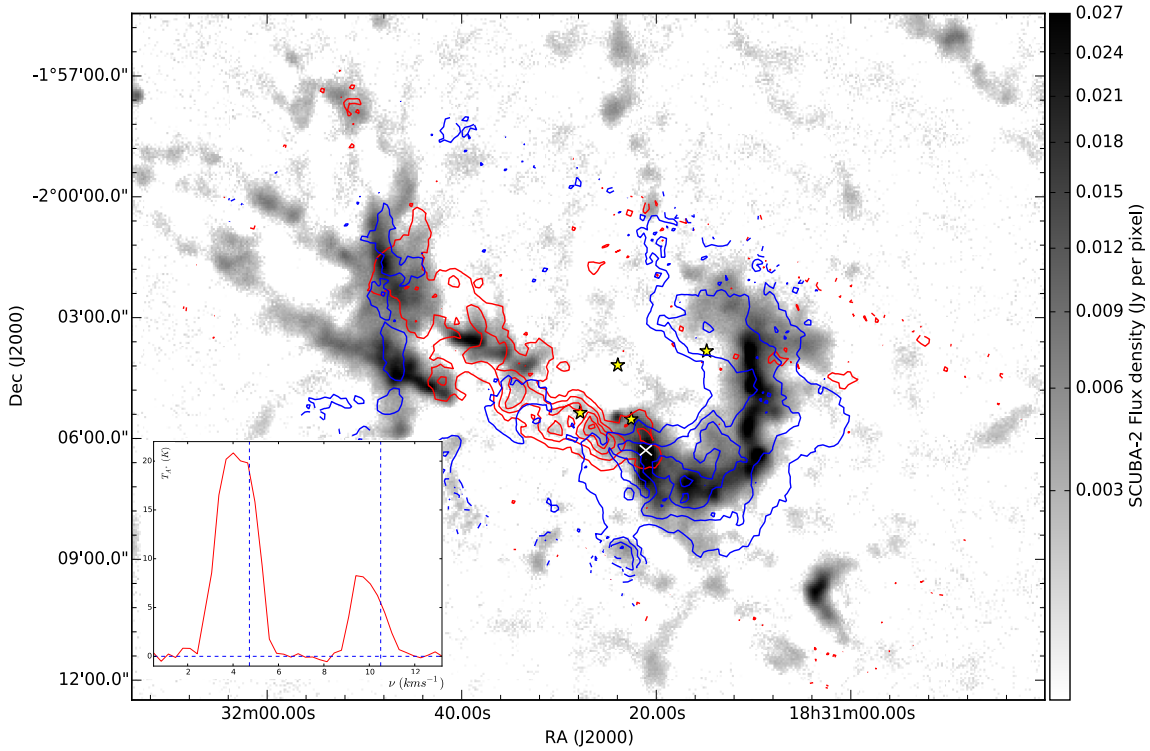

Figure 3.10: SCUBA-2 850 μm continuum map of the W40 complex with ^{12}CO 3-2 integrated intensity contours of red (10 km s^{-1}) and blueshifted (5 km s^{-1}) emission that trace out the location of two separate clouds within the region. Blue contours are at 20, 40, 60, 80 K km s^{-1} and red are the same levels with an additional contour at 5 K km s^{-1}. The greyscale SCUBA-2 850 μm shown here has not had CO emission subtracted. Yellow stars mark the location of the OB stars in the W40 complex. The insert shows the line emission spectra at the position of peak SCUBA-2 luminosity, marked with a white cross. Two CO clouds are visible at 5 and 10 km s^{-1} with a significant vacancy at 7 km s^{-1} where Shimoikura et al. (2015) find HCO 4–3 emission, indicating that my ^{12}CO 3-2 absence is due to exceptionally high density of gas making emission optically thick.

spatially associated with main W40 complex.

3.5.4 Cloud distance

As discussed in Chapter 2, there is some debate as to the distance of the W40 complex. I use the distance of 500±50 pc favoured by Radhakrishnan et al. (1972), Shuping et al. (2012) and Mallick et al. (2013), putting the region outside of the Aquila Rift. Authors such as Bontemps et al. (2010) and Maury et al. (2011) have argued that the complex is an extension of the Serpens South filament, and is thus at the closer distance of 255±55 pc. Alternatively, the Serpens Main cloud is forming to the north at the intermediary distance of 429±2 pc (Dzib et al., 2011) and could be associated with either region, or not at all. Gutermuth et al. (2008) find that Serpens South, Main and NH_3 all have similar systemic velocities of 6-8 km s^{-1}, suggesting they are all at a similar distance. However, I plot the mean spectra, across a +25 to -10 km s^{-1} range, in Figure 3.12 and find that systemic velocities in Serpens South are more comparable to the W40 complex than Serpens Main. By further examining the relative motion of the systemic gas in these regions can help determine whether any of these objects are forming from the same large-scale structures within the local region of the Galaxy, and hence advise on the distances of single/multiple components of the clouds.

Integrated intensity maps for the 3, 5, 7 and 10 km s^{-1} clouds are produced for the W40 complex from my HARP ^{12}CO 3-2 data, and for Serpens Main (Graves et al., 2010) and Serpens South (Brenda Matthews, priv. comm.) from archival HARP ^{12}CO 3-2 data. Each map is integrated over a velocity range ±0.5 km s^{-1} of the systemic cloud velocity and is presented in Figure 3.13. Figure 3.12 demonstrates the location and relative brightness of material in each region.

In the W40 complex the 3 km s^{-1} cloud represents some faint outflows and a small number of brighter, isolated clouds. Similar faint emission is detected at this velocity in Serpens Main and South but brighter components are not, suggesting that these isolated clouds are unique to the W40 complex. All three regions are bright at 5 km s^{-1}, though W40 is significantly brighter than the other regions, as a result of heating by the OB association. W40 and Serpens South have no emission detected at 7 km s^{-1}. As this region has very high densities of dust and gas, and ^{12}CO 3-2 emission is optically thick here (Gutermuth et al., 2008). However, bright ^{12}CO 3-2 line emission is detected at 7 km s^{-1} in Serpens Main (Davis et al., 1999). I note that there are artefacts across the Serpens Main mosaic around 7 km s^{-1} that are a result of large-scale emission from optically thick ^{12}CO 3-2 across the region. Again the W40 complex is brightest at 10 km s^{-1}, whereas Serpens Main has a large amount of extended faint emission that is likely associated with outflows (Figure 3.12). Figure 3.13 appears to show no emission at 10±0.5 km s^{-1} in Serpens South, however Figure 3.12 shows a rising profile with a systemic velocity of 12 km s^{-1}. The mean spectra for Serpens South and Main extends significantly to higher velocities suggesting that there are outflows forming from a cloud at 10-12 kms^{-1}. These line-wings are not observed in W40 complex suggesting that star-formation is limited to the lower velocity 5 km s^{-1} cloud.

All three regions studied here show similar velocity structures, with systemic material present between 5 and 7 km s^{-1} and evidence of shocks at 3 and 10 km s^{-1}. Additional research is required to determined the origin of the 12 km s^{-1} emission in Serpens South and the bright

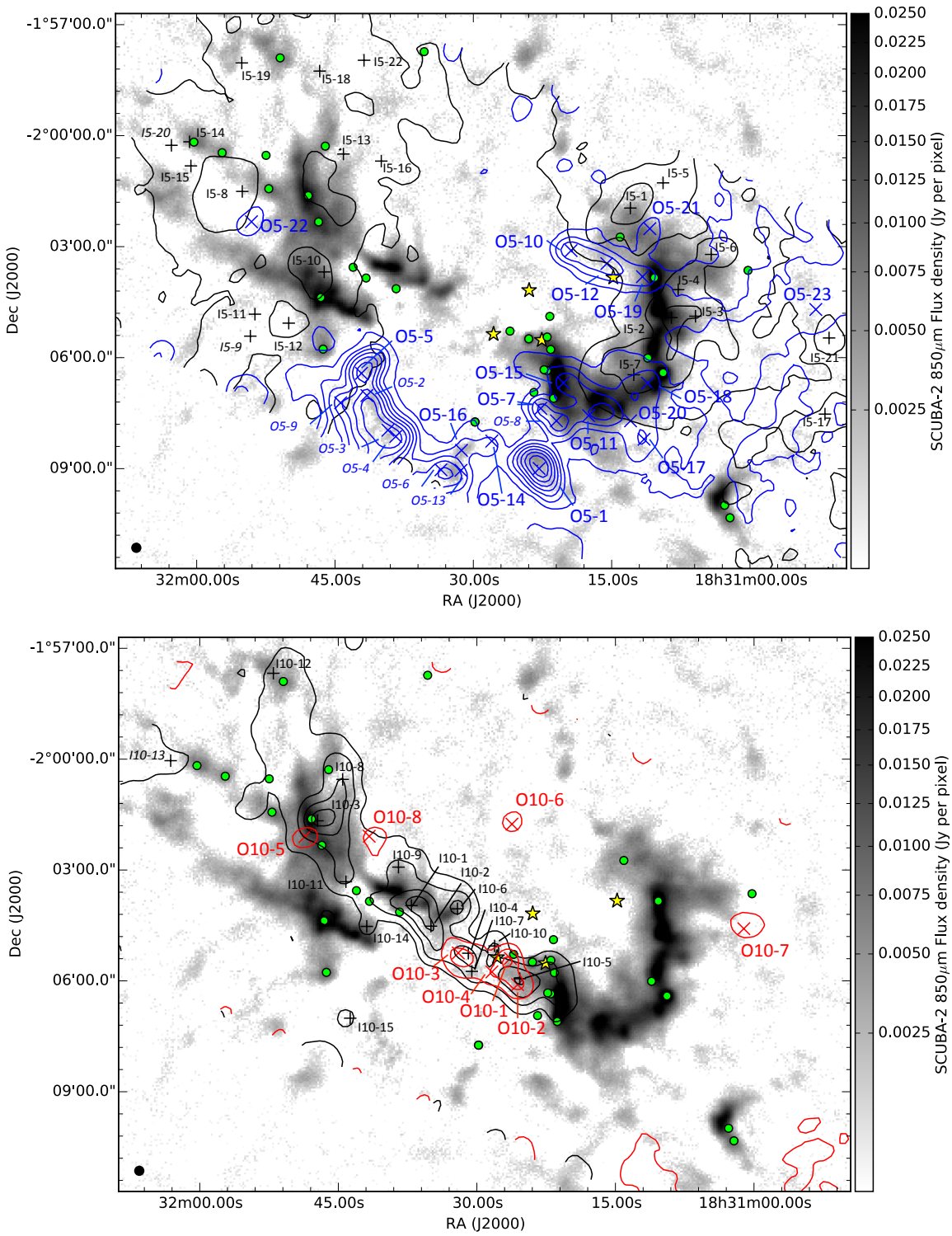

Figure 3.11: SCUBA-2 850 μm flux density map (greyscale). ^{12}CO 3-2 integrated line emission in the outer component of the 5 km s^{-1} cloud (upper plot, blue contour), and outer component of the 10 km s^{-1} cloud (lower plot, red contour). The absorbed inner components of the 5 and 10 km s^{-1} clouds are marked as black contours in their respective plots. All contours have levels of 1, 3, 6, 10, 15, 21, 28 and 37 K km s^{-1}. See text for the velocity ranges of each component. Line-wing sources are identified as crosses and plus-signs with respective colours. Yellow stars and green circles indicate the location of the OB stars and protostars (from the composite YSOc catalogue).

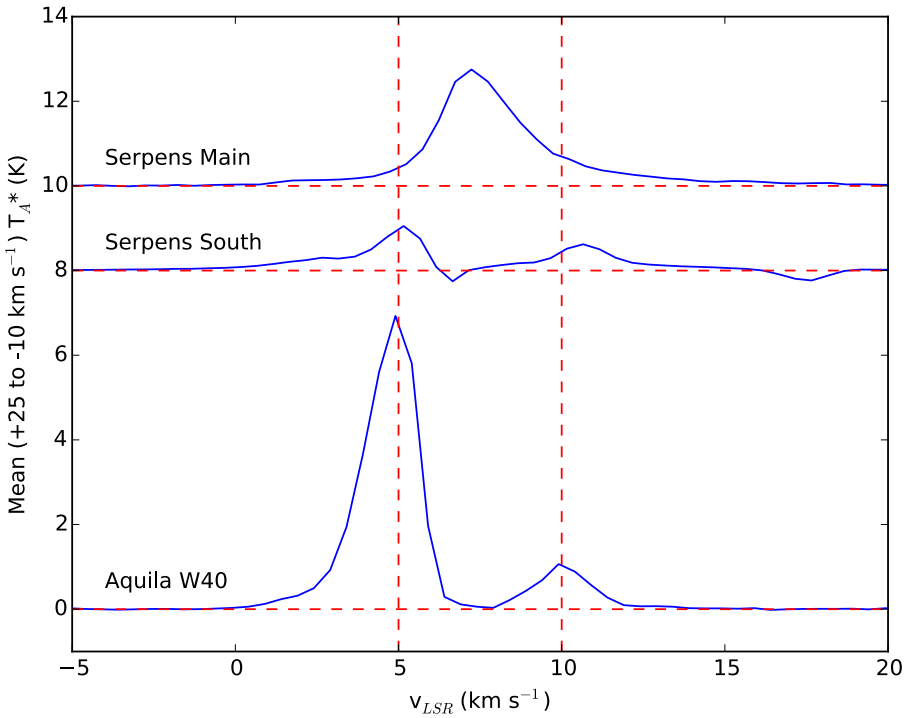

Figure 3.12: The mean spectra across each of the Serpens-Aquila regions mapped in Figure 3.13. Every available 0.5 km s^{-1} velocity bin in each cube is included in the mean, however the resulting intensity is normalised for a +25 to -10 km s^{-1} range. Vertical dashed lines mark the cloud components identified in Figure 3.10.

3 km s^{-1} emission in the W40 complex. These findings suggest that all the regions are formed from the same large-scale structures within the local region of the Galaxy, and are therefore inconclusive when it comes to answering the debate over the distance of the W40 complex, relative to Serpens South and Serpens Main.

3.5.5 Outflow analysis

The complex velocity structure of emission in the W40 complex makes direct analysis of individual outflows very difficult. Instead I use the method of identifying local peaks in ^{12}CO 3-2 intensity maps, integrated over the velocity ranges red- and blue-ward of the 5 km s^{-1} and 10 km s^{-1} clouds, respectively, as used by Shimoikura et al. (2015). Peaks can be used to identify molecular outflows from protostars where the line profile shows a line-wing similar to those observed by Graves et al. (2010) in Serpens Main. This method is also sensitive to the systemic motion of shocked gas around the shell of the H II region, local variations in bulk gas velocity and foreground clouds at different velocities. Figure 3.14 shows how the 'outer' velocity components (-3.2≤v$_{LSR}$≤2.8 km s^{-1} and 11.7≤v$_{LSR}$≤14.5 km s^{-1}) and 'inner' components of each cloud (5.7≤v$_{LSR}$≤8.4 km s^{-1} and 8.5≤v$_{LSR}$ ≤9.2 km s^{-1}) are sampled for outflows from the 0.5 km s^{-1} resolution ^{12}CO 3-2 PPV cube. The resulting blue- and red-shifted line-wing objects for each cloud are mapped in Figure 3.11.

Typical outflows, like those presented in Graves et al. (2010) and Lee et al. (2013), have

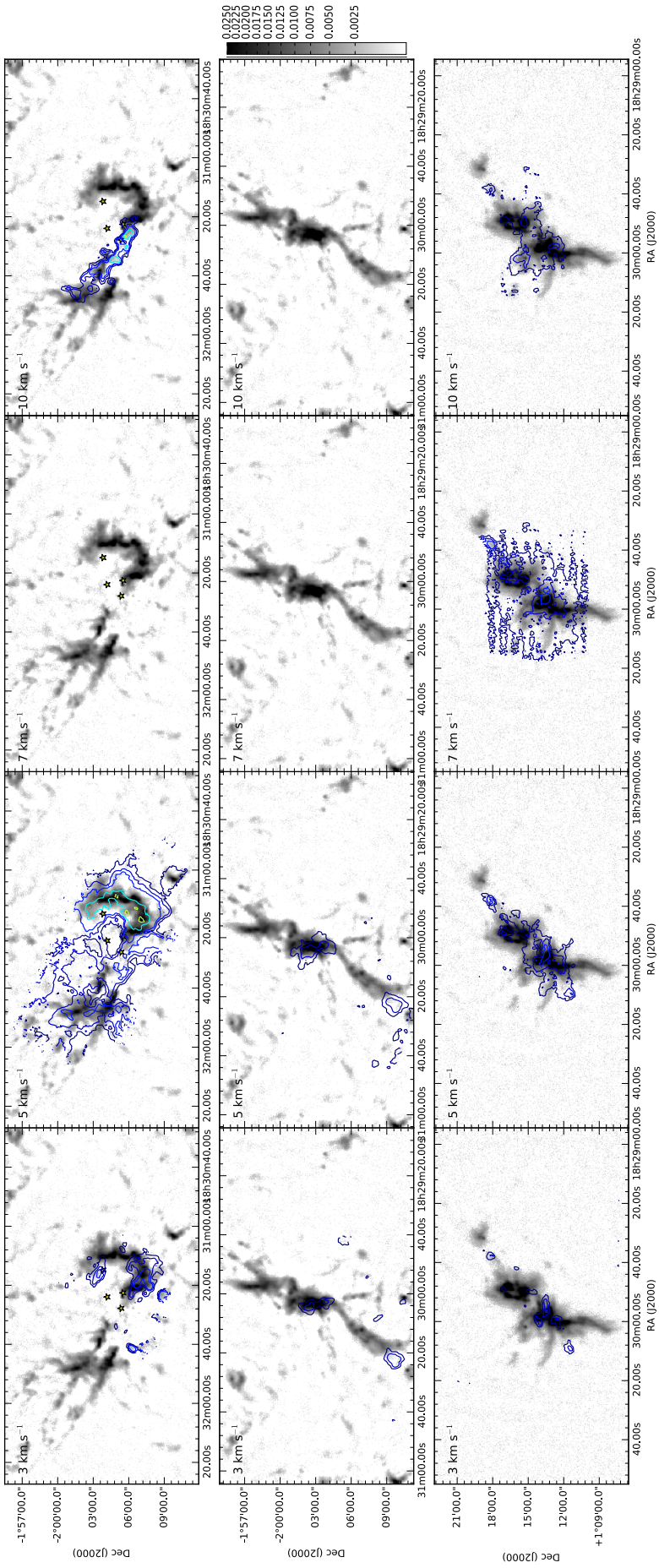

Figure 3.13: Major ^{12}CO 3-2 clouds observed at 3, 5, 7 and 10 km s^{-1} in the W40 complex (upper), Serpens South (middle) and (Serpens Main), as shown in SCUBA-2 850 μm greyscale. ^{12}CO 3-2 levels are 3, 6, 10, 20 and 30 K km s^{-1}. ^{12}CO 3-2 maps represent the integrated intensity (antenna temperature) of $\pm$0.5 km s^{-1} from the natural cloud velocity given on each panel.

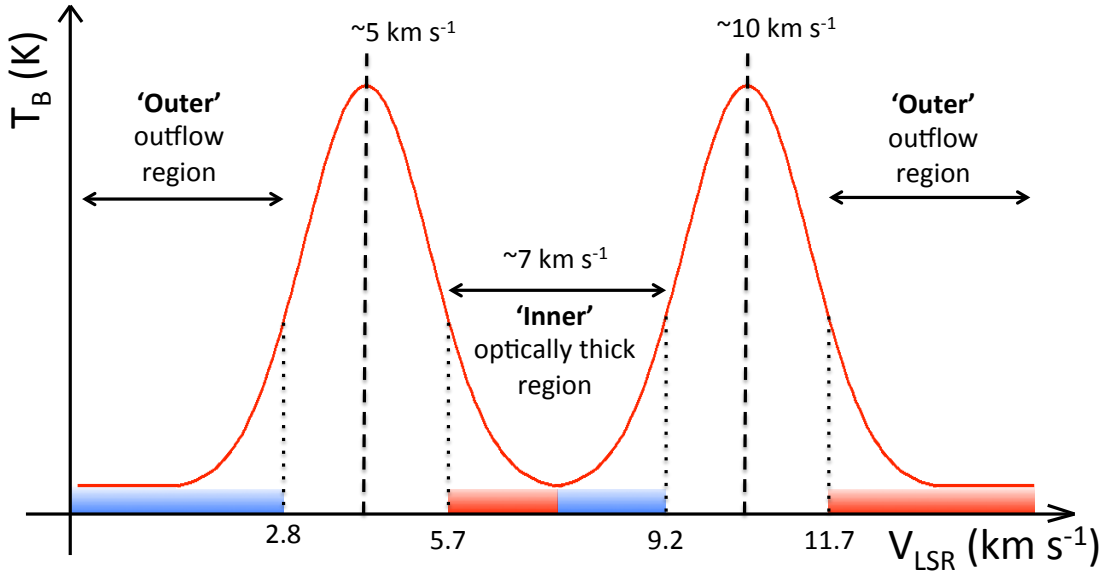

Figure 3.14: An adaptation of Shimoikura et al. (2015)'s Figure 5. A schematic description of the velocity cloud structure observed in the W40 complex. ^{12}CO 3-2 line profiles peaks at ~5 and 10 km s^{-1} denoting two distinct clouds. Shimoikura et al. (2015) detect a third cloud structure at ~7 km s^{-1} in ASTE HCO$^+$ 4–3 observations that is not detected in ^{12}CO 3-2 due to high density gas causing the line to become optically thick. By constraining the velocity space to the outer and inner regions of the observed clouds it is possible to map the location and size of various 'line-wing' objects and asses them as potential outflows (as shown in Figures 3.11.)

two bright lobes of emission shifted red- and blue-ward from the bulk cloud velocity. Whilst this is true for the 'outer' line-wing objects shown in Figure 3.11, 'inner' components of the two clouds are significantly more faint and diffuse. Shimoikura et al. (2015) outline how ^{12}CO 3-2 emission becomes optically thick due to dense material at 7 km s^{-1} which heavily absorbs any outflows in this region of the spectrum. As a result of this absorbtion, it is considered very unlikely that outflows will be detected in the inner components, and that any physical understanding gained from these spectra will be extremely limited. Bright emission in the spectrum at 5 and 10 km s^{-1} and absorbtion at 7 km s^{-1} are illustrated in a schematic spectrum shown in Figure 3.14. This example compares favourably to the ^{12}CO 3-2 spectrum observed at the peak of the SCUBA-2 emission (Figure 3.10 insert).

The FELLWALKER algorithm is used to detect position-position clumps in ^{12}CO 3-2 intensity maps, integrated over the velocity range of each 'outer' and 'inner' line-wing component. The FELLWALKER parameters are consistent with those outlined for SCUBA-2 850 μm clumps in Chapter 7, with the exception of the Noise parameter which is set to 3σ to ensure that the most faint of the line-wing objects are detected. A total of nine clumps that were fragmented by the edges of the map were rejected as unreliable. A total of 37 line-wing objects are detected in the 5 km s^{-1} cloud, 17 on the optically thin outer component and 20 on the optically thick inner component. Likewise, a total of 22 line-wing objects are detected in the 10 km s^{-1} cloud, eight on the optically thin outer component and 14 on the optically thick inner component. These objects are recorded in Tables 3.1 and 3.2. The outer line-wing objects detected in the HARP ^{12}CO 3-2 observations

are twice as many detected by Shimoikura et al. (2015) using ASTE, primarily as a result of the higher resolution of the JCMT.

The line spectra for the peak of each line-wing object as marked on Figure 3.11, in position-position space, are listed in Tables 3.1 and 3.2 are subsequently plotted in Figures 3.15 and 3.16. The noise level is set from the standard deviation on the spectra, per bin, averaged across the whole spectrum. Using the Hatchell et al. (2007) criteria, described in Section 3.1.1, I detect six confirmed outflow lobes (where the line-wing intensity is $\geq 3\,\sigma$ at $\pm 3\,\mathrm{km\,s^{-1}}$ from the bulk cloud) and six candidate outflows (where the line-wing approximately equal to $3\,\sigma$ at $\pm 3\,\mathrm{km\,s^{-1}}$ from the systemic cloud velocity (set as either 5 or $10\,\mathrm{km\,s^{-1}}$).

Of the total 12 outflows, 2/3 are found in the $5\,\mathrm{km\,s^{-1}}$ cloud that is coupled with the Dust Arc and W40-N filaments where stars are known to be forming. Whilst those found in the $10\,\mathrm{km\,s^{-1}}$ cloud have line-wings consistent with a molecular outflow, they are significantly more symmetric than the $5\,\mathrm{km\,s^{-1}}$ outflows. As Figure 3.11 shows, all the candidate $10\,\mathrm{km\,s^{-1}}$ outflows are found in a shell of shocked, heated gas that surounds the H II region and therefore it is likely that these spectra portray this motion, as opposed to that of a protostellar outflow. 11 'outer' objects are displaced cloud components with no line asymmetries or wing-like features. Four are noise artefacts or have very low SNRs. The 'inner' regions are also studied for outflows, but as expected, none come close to fulfilling the Hatchell et al. (2007) criterion for a molecular outflow due to self-absorption at high densities.

Of the six confirmed outflows detections, four have nearby protostars identified in the W40 composite YSO catalogue, presented in Chapter 2. Figure 3.11 suggest that line-wing objects O5-10, 12 and 19 are all parts of one outflow from the $0.8\,\mathrm{M_\odot}$ Class 0 protostar W40-MM5 (Maury et al., 2011), in the western Dust Arc. Outflow O5-18 lies in close proximity to W40-MM3 whereas O5-17 lies close to the starless section of the Dust Arc. The upper panel of Figure 3.11 shows how the ^{12}CO 3-2 emission is widespread and morphologically diverse near these outflows making full interpretation difficult. However, the presence of O5-17 could suggest the presence of an embedded, young protostar in the Dust Arc that is not included in this YSO catalogue. O5-21 is a faint detection that may be associated with the protostar W40-MM9 in the northern Dust Arc. Outflow O5-22 is found in the W40-N cloud, however association with any of the protostars there is inconclusive as it is exceptionally faint. Due to the complexity of the region and lack of reliable observations from the 'inner' wings of the cloud, it would be premature to infer that the completeness of the Class 0/I protostellar population of the composite YSOc catalogue (as outlined in Chapter 2, Section 5.2) is near 100%. All of the outflow candidates observed by Shimoikura et al. (2015) are included in this catalogue of line-wing objects.

A number of Class 0/I protostars outflows cannot be easily be attached to any of the observed line-wing objects. Firstly I discuss a cluster of protostars surrounding OS2a. These protostars are aligned with the H II region and therefore one possible explanation is that UV radiation from OS1aS has dissociated a significant amount of the CO in the vicinity of these stars. Given that the H II region represents a lower density region in space, it seems unlikely that CO emission here is absorbed. More likely is that IR contamination from the nebulosity that led to the misclassification of these object, and that these are in fact PMS-stars where outflow activity has

declined.

There are 13 Class 0/I protostars in the W40-N cloud without a confident association with a line-wing object. This region is outside of the main nebulosity of the W40 OB association so misclassification is less likely.

The highest velocity line-wing offset measured in the survey is source O5-10. This clump is associated with the MM5 protostellar outflow. A manual assessment of this feature puts the maximum line-wing offset at 7.5 km s^{-1} at a position of RA(J2000) = 18:31:19.84 Dec(J2000) = -02:03:09.49, as presented in Figure 3.17. The O5-10/12/19 outflow subtends 3″, giving the object a length of 0.43 pc. Line-wings found in Serpens Main by Graves et al. (2010) are detected out to -30 km s^{-1} and +37 km s^{-1} from a systemic cloud of similar velocities to the W40 complex. There is evidence that significantly powerful protostellar outflows can contribute additional localised heating of dust through shocks (Buckle et al., 2015), however the outflows in the W40 complex are relatively weak and any radiative heating is likely negligible, relative to the levels of the radiative feedback from the protostar itself (to be discussed further in Chapter 7).

3.6 Conclusions

I have investigated CO observations of the Serpens MWC 297 and W40 complexes, part of the JCMT GBS Serpens-Aquila region. I have discussed methods and results for decontaminating SCUBA-2 850 μm observations, and the impact of ^{12}CO 3–2 line emission on dust temperatures, as well as the velocity structures of clouds and evidence for molecular outflows from young stars. My conclusions about the regions, methods and star-formation as a whole, are summarised below.

1. ^{12}CO 3–2 contamination of the Serpens MWC 297 region is estimated at 13% of peak flux of the Herbig B1.5ve star MWC 297 using the published ^{12}CO 1–0 line spectra of Canto et al. (1984).

2. I was the PI of a HARP proposal to observe ^{12}CO 3–2 line emission in the W40 complex that are observed and reduced in the summer of 2015. I found evidence for significant levels of ^{12}CO 3–2 line emission contaminating the 850 μm band range between 3 and 10% in the majority of the filaments. In a minority of areas contamination reaches up to 20%. Removing the ^{12}CO 3–2 contamination significantly increases the dust temperatures calculated per pixel, on average, by 3.3 K where contamination is less than 10%, and by 16.4 K where contamination is greater than 10%. Given the contamination estimate produced for Serpens MWC 297, it would be advisable to observe this region in ^{12}CO 3–2 with HARP with the aim of decontaminating the SCUBA-2 850 μm band.

3. Two distinct clouds of ^{12}CO 3–2 emission are observed in the W40 complex with systemic velocities of a 5 km s^{-1} and a 10 km s^{-1}. A region of absorbtion in the cloud spectra around 7 km s^{-1} is consistent with ASTE observations of the HCO$^+$ 4–3 line by Shimoikura et al. (2015) which trace higher density material where ^{12}CO 3–2 line emission is optically thick. The 5 km s^{-1} cloud is largely coupled with the Dust Arc and W40-N, as observed by SCUBA-2. The 10 km s^{-1} cloud traces a filament that passes directly through the centre of

Table 3.1: Line-wing objects detected in 10 km s^{-1} ^{12}CO 3-2 emission cloud in the W40 complex.

Outflow ID[a]	Coords (J2000)	$T^*_{A,peak}$ (K)	v_{peak} (km s^{-1})	v^b_{wing} (km s^{-1})	YSO[c] (c)	Outflow?[d] (c)	Comments[e]
O10-1	18:31:26.38 -02:05:23.5	16.7	12	-	Y	-	'R1'
O10-2	18:31:25.59 -02:06:06.2	9.0	10	13.4	(c)	(c)	
O10-3	18:31:32.01 -02:05:14.7	7.6	10	-	-	-	'R2'
O10-4	18:31:28.38 -02:05:45.5	9.6	10.5	13.4	(c)	(c)	
O10-5	18:31:48.60 -02:02:05.6	17.8	-	-	Y	-	Bad detection, 'R4'
O10-6	18:31:26.20 -02:01:45.5	11.1	-	-	-	-	Bad detection
O10-7	18:31:01.10 -02:04:35.3	4.1	-	-	-	-	Bad detection
O10-8	18:31:41.65 -02:02:05.2	3.4	11	-	-	-	'R3'
I10-1	18:31:37.08 -02:03:57.8	18.2	10	-	Y	-	
I10-2	18:31:34.97 -02:04:31.2	18.4	10	-	-	-	
I10-3	18:31:47.25 -02:01:40.1	14.7	10	-	Y	-	
I10-4	18:31:30.93 -02:05:15.2	14.7	10	13.4	-	(c)	Redshifted line
I10-5	18:31:25.36 -02:05:56.5	13.3	10	12.9	(c)	(c)	Redshifted line
I10-6	18:31:32.10 -02:04:03.1	12.2	10	-	-	-	
I10-7	18:31:30.55 -02:05:44.6	11.3	10	-	-	-	
I10-8	18:31:44.53 -02:00:32.9	9.7	10	-	(c)	-	
I10-9	18:31:38.49 -02:02:55.3	6.3	10	-	-	-	
I10-10	18:31:28.08 -02:05:03.3	6.9	11	-	Y	-	
I10-11	18:31:44.18 -02:03:19.0	5.6	-	-	(c)	-	Bad detection
I10-12	18:31:52.03 -01:57:40.5	3.9	-	-	Y	-	Bad detection
I10-14	18:31:41.92 -02:04:31.6	10.2	11	-	-	-	
I10-15	18:31:43.71 -02:07:00.6	6.0	-	-	-	-	Bad detection

a - Line-wing object index as defined by the FELLWALKER algorithm. 'O' indicates object is on the 'outer' limb of the cloud whereas 'I' indicates the 'inner' limb of the cloud. See text for details of the velocity ranges associated with these objects.

b - Wing length, the maximum extent of the line-wing where the intensity is greater than 3σ.

c - Indicates whether a protostar (as marked in Figure 3.11) is located with the line-wing object. Less than 5 JCMT beam widths is marked as a candidate (c) and less than 2 beam widths is marked as confirmed (Y).

d - Line-wing assignment follows as non-outflow, confirmed outflow (Y) and candidate outflow (c).

e - Including Shimoikura et al. (2015) designation.

Table 3.2: Line-wing objects detected in 5 km s^{-1} ^{12}CO 3-2 emission cloud in the W40 complex. (Table headings same as Table 3.1.)

Outflow ID[a]	Coords (J2000)	T*$_{A,peak}$ (K)	v$_{peak}$ (km s^{-1})	v$^{b}_{wing}$ (km s^{-1})	YSO[c] (c)	Outflow?[d] (c)	Comments[e]
O5-1	18:31:22.87 -02:08:59.8	50.4	3	-	-	-	
O5-5	18:31:42.13 -02:06:25.4	37.7	3	-	-	-	
O5-7	18:31:22.69 -02:07:22.2	31.8	4	-	Y	-	'B8'
O5-8	18:31:20.99 -02:07:42.5	25.2	4	-	(c)	-	
O5-10	18:31:19.40 -02:03:06.4	22.3	5	-1.6	(c)	Y	'B3'
O5-11	18:31:17.50 -02:07:34.1	17.1	5	1.9	-	(c)	'B6'
O5-12	18:31:15.53 -02:03:27.5	13.2	5	-	(c)	-	
O5-14	18:31:28.00 -02:08:15.4	16.6	5	-	(c)	-	
O5-15	18:31:20.22 -02:06:40.9	12.7	5	1.9	Y	(c)	
O5-16	18:31:31.28 -02:08:30.3	12.7	5	-	(c)	-	'B7'
O5-17	18:31:11.49 -02:08:12.4	10.4	5	0.9	-	Y	'B5'
O5-18	18:31:11.10 -02:06:41.4	10.0	5	1.4	Y	Y	'B4'
O5-19	18:31:11.66 -02:03:48.6	10.8	5	-0.1	Y	Y	'B2'
O5-20	18:31:12.95 -02:07:42.5	10.3	5	-	-	-	
O5-21	18:31:10.87 -02:02:30.8	9.7	5	1.4	(c)	Y	
O5-22	18:31:54.06 -02:02:19.7	6.4	5	1.4	-	Y	'B1'
O5-23	18:30:52.86 -02:04:41.9	4.2	-	-	-	-	Bad detection, 'B9'
I5-1	18:31:12.98 -02:01:57.4	11.3	5	-	-	-	
I5-2	18:31:08.52 -02:04:55.0	10.2	5	-	-	-	
I5-3	18:31:05.91 -02:04:52.8	8.4	5	-	-	-	
I5-4	18:31:07.79 -02:04:09.8	7.6	5	-	(c)	-	
I5-5	18:31:09.43 -02:01:16.6	7.5	5	-	-	-	
I5-6	18:31:04.21 -02:03:12.6	6.2	5	-	-	-	
I5-7	18:31:12.60 -02:06:27.8	6.0	5	-	(c)	-	
I5-8	18:31:55.05 -02:01:30.4	5.9	5	-	-	-	
I5-10	18:31:46.17 -02:03:41.0	5.4	5	-	-	-	
I5-11	18:31:53.68 -02:04:49.5	6.0	5	-	-	-	
I5-12	18:31:50.02 -02:05:04.1	5.1	5	-	-	-	
I5-13	18:31:44.09 -02:00:29.8	4.6	5	-	-	-	
I5-14	18:32:00.77 -02:00:09.9	4.7	5	-	(c)	-	
I5-15	18:32:00.62 -02:00:49.1	4.7	5	-	-	-	
I5-16	18:31:39.98 -02:00:41.3	4.3	5	-	-	-	
I5-17	18:30:51.87 -02:07:31.6	4.1	-	-	-	-	Bad detection
I5-18	18:31:46.66 -01:58:15.3	3.7	5	-	-	-	
I5-19	18:31:55.11 -01:58:02.1	3.5	-	-	-	-	Bad detection
I5-21	18:30:51.43 -02:05:28.1	3.9	-	-	-	-	Bad detection
I5-22	18:31:41.85 -01:57:57.7	3.0	5	-	-	-	

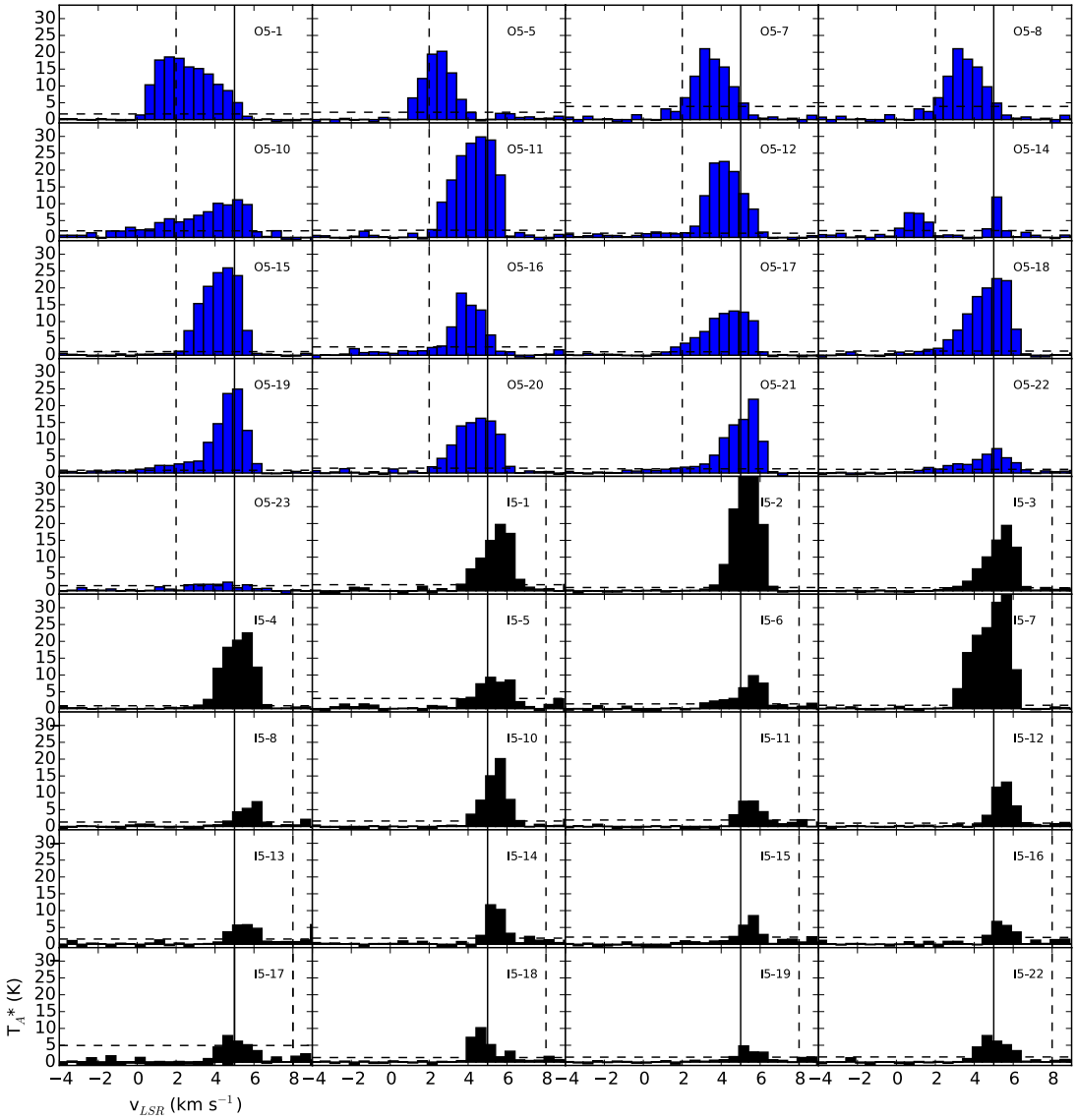

Figure 3.15: Spectra of ^{12}CO 3-2 for line-wing objects observed for the 'outer' and 'inner' limbs of the 5 km s^{-1} cloud in the W40 complex. See Figure 3.14 and text for details of this selection. Note that the black, inner regions are heavily absorbed by high density material. Horizontal dashed lines represent the $3\,\sigma$ detection level, calculated as the mean noise across all velocity bins. Vertical dashed lines represent the ± 3 km s^{-1} marker from the local cloud velocity (5 km s^{-1} solid line). Velocity resolution is 0.5 km s^{-1}.

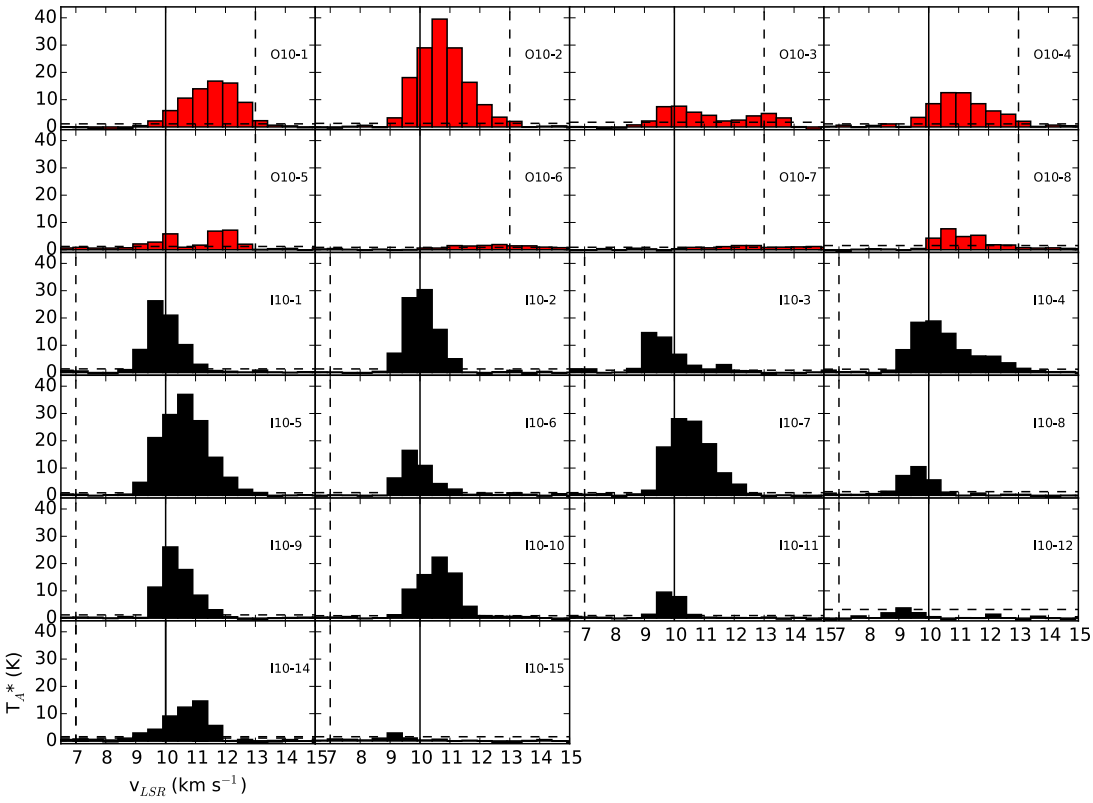

Figure 3.16: Spectra of ^{12}CO 3-2 for line-wing objects observed for the 'outer' and 'inner' limbs of the 10 km s^{-1} cloud in the W40 complex. See Figure 3.14 and text for details of this selection. Note that the black, inner regions are heavily absorbed by high density material. Horizontal dashed lines represent the 3 σ detection level, calculated as the mean noise across all velocity bins. Vertical dashed lines represent the $\pm$3 km s^{-1} marker from the local cloud velocity (10 km s^{-1} solid line). Velocity resolution is 0.5 km s^{-1}.

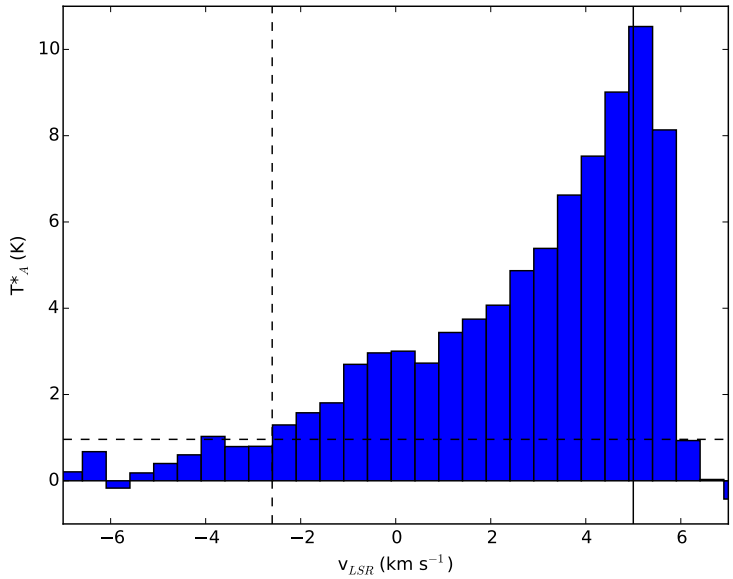

Figure 3.17: ^{12}CO 3-2 line profile of the MM5 (Maury et al., 2011) protostellar outflow, found in the western Dust Arc and associated with the 5 km s^{-1} CO cloud. Horizontal dashed lines represent the 3 σ detection level, calculated as the mean noise across all velocity bins. Vertical dashed lines represent the maximum extent of the line-wing. Velocity resolution is 0.5 km s^{-1}.

the OB association and is not coincident with any SCUBA-2 emission, and instead traces a shell of heated CO gas that has been swept up by the expanding H II region and is observed as a foreground/background object. The W40 complex has an extremely complex velocity structure with up to three velocity components observed at the same position, indicating multiple cloud structures along the line of sight, likely dispersed around the shell of the H II region.

4. The two velocity clouds observed in HARP ^{12}CO 3–2 line emission are sampled for outflows. Each cloud is separated into an 'outer' component where ^{12}CO 3–2 is optically thin, and an 'inner' component where ^{12}CO 3–2 is optically thick. The FELLWALKER algorithm identifies a total of 25 line-wing objects in the 'outer' components of the two clouds, almost double the number detected by Shimoikura et al. (2015) as a result of the higher resolution of the JCMT beam.

5. Spectra of the line-wing objects were observed and examined for outflows that fit the Hatchell et al. (2007) criterion. 12 outflows (six confirmed and six candidates) are identified. Eight were associated with the 5 km s^{-1} cloud and four in association with the 10 km s^{-1} cloud, though there is a strong argument to explain these later objects as shocked gas in a shell around the H II region in the W40 complex, as opposed to protostellar outflows. The 0.8 M$_\odot$ Class 0 protostar MM5 in the western Dust Arc, as identified by Maury et al. (2011), is confirmed as the most prominent outflow source with a maximum line-wing offset of 7.5 km s^{-1}. This is a relatively weak outflow compared to those in Serpens-Main. Of the six confirmed outflows detected, five can be associated with nearby protostars.

4

Free-Free contamination of SCUBA-2 bands

In this chapter I examine the arguments for a thermal Bremsstrahlung, or free-free, contribution to the observed SCUBA-2 bands, addressing questions regarding the free-free spectral index and location of the turnover from optically thick to optically thin. I examine the various sources of free-free emission in the JCMT GBS Serpens MWC 297 region and Aquila W40 complex, and assess the magnitude of the contribution from small- and large-scale phenomenon.

4.1 Introduction to thermal Bremsstrahlung emission

Thermal Bremsstrahlung, or free-free emission, is a thermal process by which photons are produced from the acceleration of an electron in a plasma (Larmor, 1897) in local thermal equilibrium (LTE). I discuss this process in the context of star formation in this chapter. For a full derivation of free-free emission please see Rybicki & Lightman (1979).

As a thermal process, the spectral energy distribution (SED) of the free-free flux density is governed by the equation of radiative transfer,

$$S_\nu = \int_\Omega B_\nu(T_d)(1 - e^{-\tau})\, d\Omega, \tag{4.1}$$

which has been discussed at length in Chapter 1 (Equation 1.28). In order to evaluate how the spectrum changes across the continuum, it is necessary to consider how the opacity of free-free emission changes as a function of wavelength by the considering Kirchoff's law (Equation 1.17) that relates the free-free absorption coefficient, κ_ν, to the free-free emission coefficient, ϵ_ν and defines a source function that is equivalent to a black body in the Rayleigh-Jeans limit (Equation 1.32).

The free-free emission coefficient, ϵ_ν, is derived by considering an encounter between an

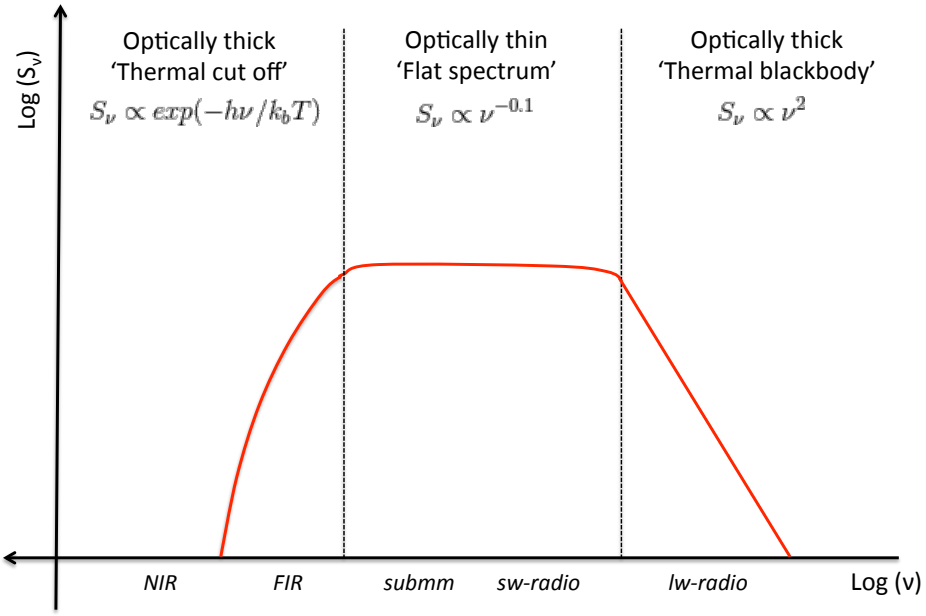

Figure 4.1: A schematic SED typical of free-free emission.

electron and a single ion, per unit time, at a velocity range v to $v + dv$ and with impact parameter (the perpendicular distance between the unperturbed path of the electron, and the ion) b to $b + db$. The distribution of electron velocities, v, is described by a non-relativistic Maxwellian distribution,

$$f(v) = \frac{4v^2}{\sqrt{\pi}} \left(\frac{m_e}{2k_B T_e} \right)^{3/2} \exp\left(-\frac{m_e v^2}{2k_B T_e} \right), \tag{4.2}$$

where m_e the mass of the electron, T_e is the temperature of the free-free plasma (typically 10,000 K Dyson 1997) and all other constants have their usual meaning. This process is then scaled up to a number of encounters, $N(v, b)$, per unit time, per unit volume (that contains N_e electrons and N_i ions). With each encounter, a photon is emitted by free-free process. Condon & Ransom (2016) give the average power output, W_ν, per unit frequency, of the photon as,

$$W_\nu \approx \frac{\pi^2}{2} \frac{Z^2 e^6}{c^3 m_e^2} \left(\frac{1}{b^2 \nu^2} \right). \tag{4.3}$$

Note that Z is the atomic number (equal to one for hydrogen) and all other constants have their usual meaning. The free-free emission coefficient, ϵ_ν, is the product of the number of encounters and the average power output, per unit frequency, of the photon, integrated over a range of velocities and impact parameters. Condon & Ransom (2016) define this as,

$$\epsilon_\nu = \frac{\pi^2 Z^2 e^6 N_e N_i}{4c^3 m_e^2} \left(\frac{2m_e}{\pi k_B T_e} \right)^{1/2} \ln\left(\frac{b_{\max}}{b_{\min}} \right). \text{ (C.G.S)} \tag{4.4}$$

where $b_{\min}$ and $b_{\max}$ are the minimum and maximum impact parameters. Condon & Ransom (2016) describe how $b_{\min}$ is derived from the net momentum impulse of an encounter and is a function of electron velocity. $b_{\max}$ is derived from the maximum distance that an encounter can

occur with sufficient power to generate a photon at a certain frequency, and as a result $b_{\max}$ is a function of both electron velocity and frequency. Dallacasa (2016) describes the ratio of maximum and minimum impact parameters ($\ln(b_{\max}/b_{\min})$ in Equation 4.4) as the Gaunt factor. Condon & Ransom (2016) go further and derives a free-free gaunt factor of,

$$\langle g_{\rm ff} \rangle \approx \ln\left[4.955 \times 10^{-2}\left(\frac{\nu}{\rm GHz}\right)^{-1}\right] + 1.5\ln\left(\frac{T_e}{\rm K}\right), \tag{4.5}$$

which is weakly inversely proportional to frequency due to $b_{\max}$ (Oster, 1961; Altenhoff et al., 1970).

The free-free emission coefficient can now be used in conjunction with Kirchoff's law to calculate the absorption coefficient, κ_ν, as,

$$\kappa_\nu = \frac{\pi^3}{\sqrt{48}T^{3/2}}\frac{g_{\rm ff}}{\nu^2}\left[\frac{Z^2e^6}{c}N_eN_i\frac{1}{\sqrt{2\pi\,(m_ek_B)^3}}\right]. \tag{4.6}$$

The opacity, κ_ν, of free-free emission can be approximated to,

$$\kappa_\nu \propto \frac{N_e^2}{\nu^{2.1}T^{3/2}}. \tag{4.7}$$

Writing the absorption coefficient in terms of optical depth, τ_ν, Equation 4.7 demonstrates that at low frequencies free-free emission will become optically thick ($\tau_\nu \gg 1$) and at very high frequencies free-free emission will become optically thin ($\tau_\nu \ll 1$).

Considering the equation of radiative transfer, when free-free emission is optically thick, the optical depth term in Equation 4.1 tends to unity and frequency dependancy of the flux is dictated by the Planck function in the Rayleigh-Jeans limit, and therefore the SED resembles a black body ($S_\nu \propto \nu^2$, Oster 1961). When emission is optically thin, the optical depth term simplifies to τ_ν and therefore the frequency dependance of the free-free opacity ($\kappa_\nu \propto \nu^{-2.1}$, Altenhoff et al. 1970) is included, and as a result the SED is approximately flat ($S_\nu \propto \nu^{-0.1}$, Mezger & Henderson 1967; Wright & Barlow 1975). When $\tau_\nu = 1$ free-free emission will undergo a 'turnover' from the optically thick to the optically thin regime.

At very high frequencies another break in the spectrum occurs when the Rayleigh-Jeans limit no longer holds and the free-free flux density becomes dominated by the full Planck function (Equation 1.18) and subsequently undergoes an exponential drop off ($S_\nu \propto e^{-h\nu/k_BT}$). For an electron temperature, $T_e = 10^4$ K, the exponential decay break can be estimated at occurring short ward of 1 μm. The three phases of the free-free SED are presented in Figure 4.1.

4.2 H II observations

In star-formation, free-free emission is typically observed from H II regions formed by photoionisation of molecular hydrogen by UV photons from B4V stars or earlier (Mezger & Henderson, 1967; Kuiper et al., 1976). H II regions are large scale, low density structures with radii greater than 0.3 pc and N_e less than 10^4 cm^{-3}. The plasma bubble of the H II region expands adiabatically

into the neutral interstellar medium (ISM). Disruption in high density regions take considerably longer than lower density regions, and as a result 'Champagne' flows (Wood & Churchwell, 1989; Dale et al., 2012) are observed where the molecular cloud has been ruptured by an internal ionising source and photons are exiting through a narrow opening.

OB stars can produce a UV, or Lyman photon flux, N_{Ly}, required to maintain the ionisation of an H II region. This flux is dependant on the luminosity, L_ν, and electron temperature, as a function of frequency, through,

$$\left(\frac{N_{Ly}}{\mathrm{s}^{-1}}\right) \approx 6.3 \times 10^{52} \left(\frac{T_e}{10^4 \mathrm{K}}\right)^{-0.45} \left(\frac{\nu}{\mathrm{GHz}}\right)^{0.1} \left(\frac{L_\nu}{10^{20}\,\mathrm{W\,Hz^{-1}}}\right), \tag{4.8}$$

as given by Condon & Ransom (2016). The stellar N^*_{Ly} for OB stars capable of producing H II regions is typically greater than $10^{46}\,\mathrm{s}^{-1}$. By considering N^*_{Ly} at specific frequencies, Kurtz et al. (1994) calculate the flux density that would be observed if viewing an H II region at a distance, d, using

$$S_\nu(\mathrm{Jy}) = 1.32 \times 10^{-49} \xi N^*_{Ly} a(\nu, T) \left(\frac{\nu}{\mathrm{GHz}}\right)^{-0.1} \left(\frac{T_e}{\mathrm{K}}\right)^{0.5} \left(\frac{d}{\mathrm{kpc}}\right)^{-2}, \tag{4.9}$$

where a(ν, T) is a constant equal to 0.98 (Mezger & Henderson, 1967) and ξ is the fraction of UV photons not absorbed by the dust, set at 10%. Free-free emission from large scale, diffuse H II regions is predicted to be optically thin at radio and submillimeter frequencies where the power law becomes approximately flat with an α_{ff} = -0.1 (Oster, 1961; Mezger & Henderson, 1967; Wright & Barlow, 1975).

In addition to large scale H II structures, free-free emission is also detected with a power-law frequency dependance from stellar wind sources at scale sizes comparable to the JCMT beam (Panagia & Felli, 1975). Early type OB stars are sufficiently massive (greater than $8M_\odot$) that their Kelvin-Helmholtz contraction timescale is shorter than their free-fall and accretion timescale (Palla & Stahler 1993, Stahler & Palla 1993, Stahler et al. 2000). These stars reach the main sequence and start producing ionising radiation whilst still embedded within their protostellar envelope (Wright & Barlow, 1975). These compact regions of highly ionised winds have been detected by Wood & Churchwell (1989), Kurtz et al. 1994, Drew et al. (1997), Molinari et al. (1998), Malbet et al. (2007) et al. These regions can be considered either compact (≤0.5 pc), ultra compact (≤ 0.1 pc) or hyper compact (≤ 0.03 pc) H II regions (Wright & Barlow, 1975; Harvey et al., 1979). I follow Wood & Churchwell (1989)'s description of an UCH II sources as a region with electron density greater than $10^4\,\mathrm{cm}^{-3}$ within a diameter of less than 0.1 pc. These UCH II regions are the precursors of evolved H II regions (Kurtz 2005) and have a lifetime estimated at $4{\times}10^5$ years, approximately 10% the lifetime of a typical O star.

Whereas H II regions are diffuse, homogenous fields of emission, UCH II regions have an electron density inversely proportional to radius. Assuming spherical winds of constant velocity Panagia & Felli (1975) and Wright & Barlow (1975) derive the spectral index of the free-free emission as α_{ff} = 0.6. Large surveys of UCH II candidate regions are consistent with this result (Harvey et al., 1979; Wood & Churchwell, 1989; Kurtz et al., 1994; Molinari et al., 1998; Walsh et al., 1998; Kurtz, 2005). As UCH II regions are heavily embedded they often cannot be detected

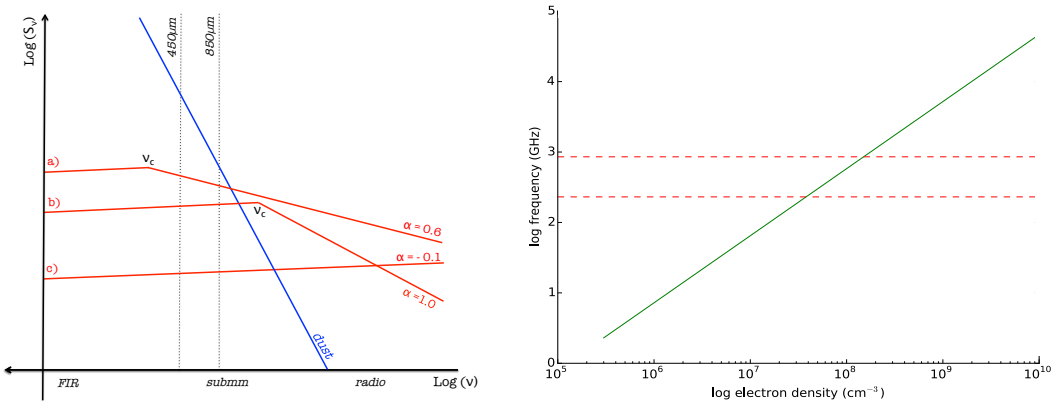

Figure 4.2: Left) A schematic of the SED shape for three hypothetical scenarios of 4.2 free-free emission. Case a) an UCH II with $\alpha_{\rm ff}$ = 0.6 has a turnover that occurs short ward of the submillimeter regime, and as a result has a majority contribution to the 850 μm band and a significant contribution to the 450 μm band. Case b) a YSO emits free-free emission, $\alpha_{\rm ff}$ = 1.0, from a collimated jet. However the spectrum turns over to the optically thin regime long ward of submillimeter wavelengths, and consequently free-free emission contributes roughly equally to both SCUBA-2 bands. Case c) a H II region has free-free emission from diffuse gas of $\alpha_{\rm ff}$ = -0.1 that outshines that from compact objects at long wavelengths. However, the flat spectrum means that at submillimeter wavelengths the emission is all but negligible. Right) Free-free turnover as a function of launching electron density (as described by Olnon 1975 in Equation 4.10). Dashed lines indicate the submillimeter regime (1.3 mm to 350 μm).

optically and are instead observed through free-free processes or the indirect heating of dust.

A minority of radio bright young OB stars are observed with $\alpha_{\rm ff} \geq 0.6$, for example MWC 349 (Olnon, 1975), MWC 297 (Skinner et al., 1993; Sandell et al., 2011) and AB Aur (Rodríguez et al., 2014). Reynolds (1986) provide a comprehensive examination of models for stellar winds and find that, where the outflow is highly collimated and accelerating (as is the case in bi-polar jets) the spectral index becomes increasingly opaque moving towards $\alpha_{\rm ff} \simeq 1.0$. As discussed in Chapter 3, jets are thought to be synonymous with the early stages of massive star-formation and are often bright in Hα, indicating the presence of ionised hydrogen, and therefore free-free emission.

4.3 Free-free contribution to SCUBA-2

As discussed in Section 1, the free-free continuum is often optically thin through out radio, submillimeter and IR wavelengths. Where the free-free emission is significantly bright, it may be detected by SCUBA-2 in both 450 and 850 μm bands, and therefore contribute to observations of dust. Here I present methods for calculating and subtracting the free-free contribution from SCUBA-2 data[1].

Radio observations are required to isolate the dust continuum flux from free-free processes. Throughout this chapter I study radio data to determine the brightness of the free-free emission at those wavelengths. Where multiple wavelength observations exist it is possible to construct a

[1]The details of which are included in Chapters 6 and 7

SED from which the free-free spectral index of the source can be determined. As discussed in the previous section, the nature of the free-free source dictates $\alpha_{\rm ff}$, with values between -0.1 and 1 having been observed. As well as radio brightness, the value $\alpha_{\rm ff}$ has a significant impact on how bright the free-free source will be in the SCUBA-2 bands. SED (c) in Figure 4.2 (left) demonstrates how a free-free source may be bright at radio wavelengths, but due to the steep nature of the dust SED, may have a negligible contribution at SCUBA-2 bands if $\alpha_{\rm ff}$ is low.

On this basis, I anticipate that the contribution from large-scale H II regions, typically with a flat spectral index, is low, relative to the dust observed by SCUBA-2. However, due to the flat nature of this SED, the relative contribution of free-free at 850 μm will be significantly greater than that at 450 μm. As a result, the SCUBA-2 450 μm/850 μm flux ratio, and dust temperature, could be adversely effected by sufficiently bright large scale free-free emission from an H II region (see Chapter 5 for details).

When considering the free-free contribution to SCUBA-2 bands for emission from UCH II sources the picture is more complex. MWC 349 (Olnon, 1975; Harvey et al., 1979; Tafoya et al., 2004; Rodríguez et al., 2007) and MWC 297 (Habing & Israel, 1979; Churchwell, 1993; Drew et al., 1997; Skinner et al., 1993) are early B-class Herbig stars where empirical observations have suggested that the free-free emission is sufficiently bright that it dominates over the dust emission at submillimeter wavelengths and produces a distinct point-like source in SCUBA-2 data consistent with a compact object. Determining exactly how much free-free contributes to the total flux is a non-trivial process. Over the course of this chapter I look at how very-high resolution (sub arc second) observations are preferred to resolve emission from binary partners or transient features, such as jets, and to avoid detecting extraneous large-scale free-free emission from the diffuse H II region. I develop methods for estimating the free-free spectral index, where there are insufficient observations to produce an SED, and the location of the free-free turnover between a partially optically thick ($\alpha_{\rm ff}$ = 0.6) to an optically thin ($\alpha_{\rm ff}$ = -0.1) SED.

4.3.1 Free-free spectral index

Where a sufficient range of photometry exists a free-free SED can be constructed from which the free-free spectral index can be calculated using linear regression. Alonso-Albi et al. (2009) present photometry of the Herbig AeBe stars MWC 137, R Mon, MWC 1080, MWC 297, LKHα 215 and Z CMa between 1.3 mm and 3.6 cm and calculates the residual dust once the free-free component has been extracted. Sandell et al. (2011) note that at wavelengths shorter than 2.7 mm there is potential for a thermal dust component to be observed alongside the free-free flux, and as a result these fluxes should not be included in the calculation of $\alpha_{\rm ff}$.

Where limited to a small number of high resolution observations calculation of $\alpha_{\rm ff}$ will be more unreliable. Where observations are limited to a single wavelength, it is not possible to directly calculate $\alpha_{\rm ff}$ at all. In order to get around this problem, I assess the protostellar properties of a radio source to determine whether or not it can be classified as a diffuse H II region ($\alpha_{\rm ff}$ = -0.1), UCH II region with a spherical wind ($\alpha_{\rm ff}$ = 0.6) or collimated jet ($\alpha_{\rm ff}$ = 1.0). Elongation of a radio point source, like those presented in Skinner et al. (1993) and Sandell et al. (2009), may indicate the presence of a jet. Knots of radio emission that are not associated with IR point sources

can be evidence of HH objects formed by a jet from a nearby protostar (Rodríguez et al., 2010) and likewise if the protostar has been observed to have a substantial disc then it has the potential to be fuelling a jet (AMI Consortium, 2012; Rodríguez et al., 2014).

In the event that there is insufficient information to argue the case for a UCH II region with a collimated jet, it is possible to use SCUBA-2 observations to place limits on $\alpha_{\rm ff}$. In this method, the free-free source is modelled as a point source and the SCUBA-2 flux at 850 μm for a beam sized aperture is measured. The starting assumption is that 100% of emission detected in the SCUBA-2 band is produced by a UCH II region. It is then possible to measure the theoretical maximum free-free spectral index as a linear regression fit between the SCUBA-2 850 μm datum and the radio frequency datum. This initial assumption will be an overestimate so this test can be revised by plotting a spectral index of $\alpha_{\rm ff} \sim$ -0.1, 0.6 or 1.0 from the single radio point and calculating the percentage contribution of free-free to the total observed SCUBA-2 flux. If any particular model returns an unphysical percentage contribution it can be discarded.

4.3.2 Free-free turnover

Where the free-free emission mechanism is an UCH II region with a spherical ionised stellar wind, emission can be thought of as *partially optically thick* with lower frequencies probing greater depths of emission within the wind before becoming fully optically thin at shorter wavelengths where only the diffuse H II region is being observed[2].

The exact location of this free-free turnover, ν_c, has been much debated in the literature. If the turnover occurs short-ward of submillimeter wavelengths, then it is possible that the free-free emission may contribute in part to SCUBA-2 observations of dust emission. Turnover can be inferred from a complete SED. Rodríguez et al. (2014) find evidence that the free-free emission in AB Aur has an $\alpha_{\rm ff} = 1.1$ at cm wavelengths, before becoming optically thin by 1.3 mm, leading to the conclusion that $\nu_c \sim 70$ GHz (4.3 mm).

An incomplete SED and submillimeter degeneracy (observing both dust and free-free emission) makes it difficult to determine if the steeper spectral index holds into the submillimeter regime, or if it prematurely turns-over to a shallower index. In these scenarios an indirect method is required to determine if the free-free emission of an UCH II region is optically opaque in the SCUBA-2 bands.

Olnon (1975) defines ν_c as a function of UCH II electron density, $N_e(r) = N_{e,0}$ where $r \leq R$, or $N_e(r) = N_{e,0}(r/R)^{-2}$ where $r \geq R$, as

$$\log_{10}\left(\frac{\nu_c}{\rm GHz}\right) = -0.516 + \frac{1}{2.1}\log_{10}\left(\frac{8}{3}\left(\frac{R}{\rm AU}\right)\left(\frac{N_{e,0}}{\rm s^{-1}}\right)^2\left(\frac{T_e}{\rm K}\right)^{-1.35}\right), \tag{4.10}$$

where R is the launching radius of the wind (typically 10 AU) and T_e is the electron temperature (typically 10^4 K). Using this method, Olnon (1975) calculates a $\nu_c \sim 575$ GHz (520 μm) for MWC 349 using Equation 4.10, given that R ~ 11 AU and $N_{e,0} \sim 9{\times}10^8$ cm^{-3} (Greenstein, 1973). Harvey et al. (1979) go further and argue that free-free emission may be opaque up to 100 μm.

[2]The tests for estimating $\alpha_{\rm ff}$ outlined in the previous section assume that the free-free SED remains partially optically thick up until SCUBA-2 wavelengths.

Where the SED is incomplete, I look to make a general statement about what systems will produce free-free emission that is opaque at submillimeter wavelengths using Equation 4.10, and hence may subsequently be contributing to SCUBA-2 emission. Figure 4.2 (right) shows how ν_c is related to $N_{e,0}$. A minimum value of $N_{e,0} \sim 2{\times}10^8\,\mathrm{cm}^{-3}$ is required for a turnover that occurs at wavelengths greater than the submillimeter regime (1.3 mm to 350 μm). However, the electron density of an UCH II region cannot easily be determined from observations. I therefore assume that $N_{e,0}$ is proportional to stellar mass, and by association varies with spectral class, as the more massive stars are known to produce more vigorous winds and greater mass loss. By using Equation 4.10 it is possible to relate turnover frequency as proportional to electron density and therefore proportional to spectral class (Olnon, 1975).

Harvey et al. (1979), Kurtz et al. (1994) and Sandell et al. (2011) present multi-wavelength radio surveys of Herbig systems. A number of A and late B class stars have faint free-free UCH II detections that appear to become optically thin long-ward of the submilimetre regime, and therefore have negligible flux relative to the dust. The early B systems of MWC 349, MWC 279 and LkHα 101 are observed to have strong free-free wind or jet emission which fits a power law right up to the submillimeter regime where the free-free flux provides a substantial, if not the majority of emission at these wavelengths. Sandell et al. (2011)'s results indicate that the free-free contribution is significant for early B stars in their sample, but not for late B and A class stars. MWC 297 is the lowest mass star in their sample for which free-free contributes at SCUBA-2 wavelengths and I therefore mark it as a lower limit of stellar class for which free-free emission may contribute in both SCUBA-2 bands. MWC 297 has a luminosity of $3 \times 10^3\,\mathrm{L}_\odot$ (Drew et al., 1997) which corresponds to a class B1.5Ve star. Given the nature of these assumptions, I are limited to assigning an upper estimate of spectral class B1.5Ve, above which the free-free turnover can occur in the submilimeter regime.

4.4 The free-free contribution in Serpens MWC 297

In this section I discuss an investigation into free-free emission from the Herbig B star MWC 297 contributing to SCUBA-2 450 and 850 μm emission in the Serpens MWC 297 region[3]. I start by considering VLA radio observations of MWC 297, calculating a free-free spectral index directly from the radio SED and subtracting this emission by modelling the object as a point source. I refer the reader to Chapter 2 for a detailed description of the star.

Skinner et al. (1993) studied 3.6 cm and 6.0 cm radio emission from stellar winds around MWC 297. Combining these wavelengths with those compiled by Alonso-Albi et al. (2009) from Skinner et al. (1993), Mannings (1994) and Manoj et al. (2007) (amongst others), Skinner et al. (1993) plot the free-free SED of MWC 297 and find a free-free spectral index equal to 0.6238, consistent with an UCH II region with a spherical wind. Sandell et al. (2011) extended the study down to 3 mm and revised α_{ff} to 1.03±0.02 which is consistent with an UCH II region with a collimated jet. A point source detection at SCUBA-2 450 and 850 μm bands confirms that the free-free power law extends into the submillimeter spectrum. The photometry for SCUBA-2 is

[3]The majority of this work is published in Rumble et al. (2015)

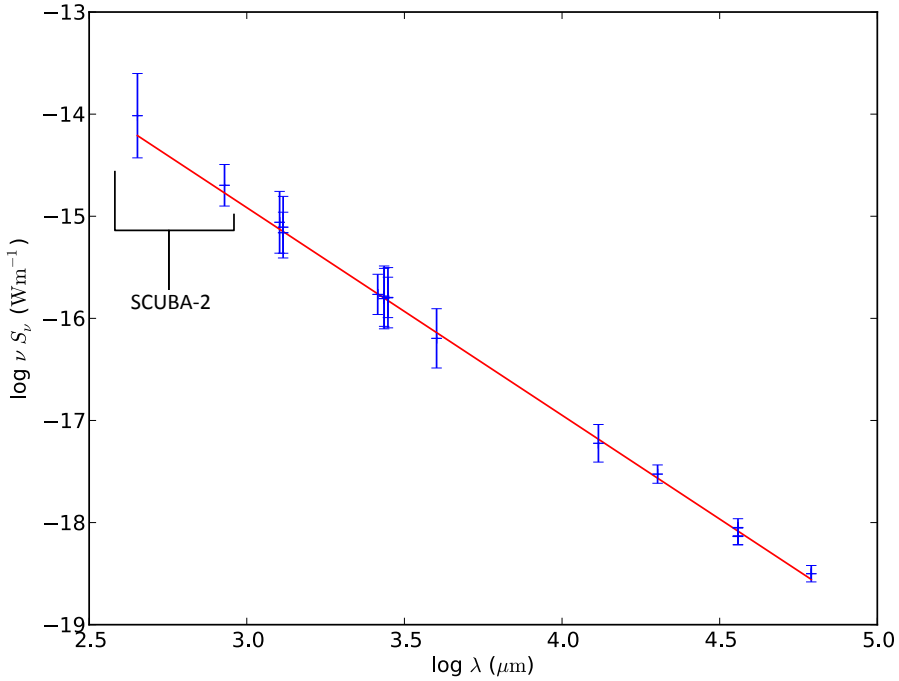

Figure 4.3: The Spectral Energy Distribution of MWC 297 from submillimeter to radio wavelengths. SCUBA-2 fluxes (found using aperture photometry as described in Section 5.2.) are presented alongside those collated by Sandell et al. (2011) who fit a power law $\alpha = 1.03 \pm 0.02$, consistent with free-free emission from an UCH II region and polar jets or outflows.

plotted alongside the Alonso-Albi et al. (2009) data points in Figure 4.3.

Figure 4.4 displays 6 cm radio emission from the VLA CnD configuration in conjunction with SCUBA-2 850 μm data (Skinner 1993, Sandell priv. comm). Both sets of data show peaks in emission which are coincident with a point source at the location of the star MWC 297 in 1 mm and 3 mm data presented by Alonso-Albi et al. (2009). The peak of the SCUBA-2 850 μm emission in Figure 4.4 is 86 mJy/pixel, consistent with the SCUBA 850 μm value of 82 mJy/pixel (Alonso-Albi et al., 2009).

The VLA data also show extended emission to the north and south of MWC 297. Drew et al. (1997) identify these as evidence for an edge on disc but 6 cm observations (Skinner 1993, Sandell priv. comm, Figure 4.4) show how fragmented emission extends up to 2′ beyond the compact object which can only be explained by jet emission. The intensity of emission is significantly weaker than that of the UCH II region point source. I note that the elongated beam shape of the VLA CnD observations (21.1″× 5.2″, PA= −61°.3) accounts for much the E/W elongation of the emission leaving the jet as the N/S elongation. Jets are typically associated with less evolved objects where luminosity is dominated by accretion processes. However, MWC 297 is considered to be a Class III / ZAMS star where the majority of the disc has fallen onto the star or been dissipated by winds. X-ray flares are thought to be a signature of episodic accretion and Damiani et al. (2006) detect a number of X-rays flares from the Serpens MWC 297 region but find that only 5.5 % of total flaring is directly associated with MWC 297, suggesting that accretion onto it is minimal. The majority of X-ray emission is associated with additional YSOs and the companion

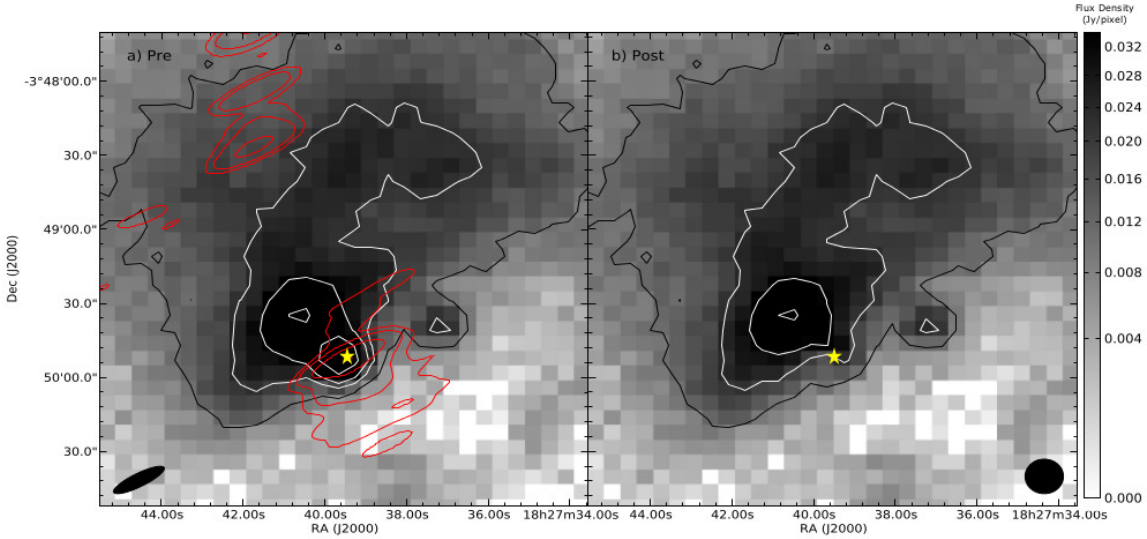

Figure 4.4: IR1 SCUBA-2 850 μm data before *left* and after *right* removal of free-free contamination from an UCH II region and polar jets/winds (represented by the point source contours in the *left* plot). SCUBA-2 contours are at 5, 10, 15 and 25 σ. 6 cm VLA contours (red) from Sandell (private comm.) at 2, 5, 20, 72, 83 mJy/beam are overlaid on the left hand panel. The location of MWC 297 is marked with a star. Beam sizes are shown at the bottom of the image (VLA CnD config. *left* and JCMT *right*.)

of MWC 297, *OSCA*, an A2V star identified by Habart et al. (2003) and Vink et al. (2005) at a separation of 850 AU.

In addition to this, Manoj et al. (2007) describe this UCH II emission as coming from within 80 AU of MWC 297. This is much smaller than the JCMT beam and therefore I model the dominant free-free emission from MWC 297 as a point source. By taking the revised power law least square fit to Skinner et al. (1993) and Sandell et al. (2011)'s results at radio and millimetre wavelengths of $\alpha_{\rm ff}$ = 1.03, and an associated intercept, log(k) = 0.047±0.037, I are able to calculate the free-free flux, as a power-law function of frequency (see Figure 4.3), due to a point-like UCH II region. By extrapolating this to SCUBA-2 wavelengths I calculate integrated free-free fluxes of 934±128 mJy at 450 μm and 471±62 mJy at 850 μm.

Single pixels with these values were then implanted into blank SCUBA-2 450 and 850 μm PONGs and the map convolved with the JCMT beam to produce SCUBA-2 free-free emission maps. These are subtracted off of the original SCUBA-2 maps to leave SCUBA-2 dust maps. The calculated fluxes for the free-free and dust contributions to the MWC 297 flux, alongside the original SCUBA-2 detections, are presented in Table 4.1.

Figure 4.3 and Figure 4.4 show that free-free emission due to an UCH II region and polar winds/jets is responsible for the majority of flux from the star MWC 297. The original SCUBA-2 peak fluxes are 188±16 mJy pixel^{-1} and 86±22 mJy pixel^{-1}, at 450 μm and 850 μm, respectively. The free-free contribution corresponds to approximately 73±5% and 82±4% of the 450 μm and 850 μm peak flux, respectively, leaving residual dust peak fluxes of 51 ± 10 mJy pixel^{-1} and 15 ± 3 mJy pixel^{-1} flux at 450 μm and 850 μm respectively. The dust residuals are the flux above

Table 4.1: Summary of the peak free-free contribution to SCUBA-2 wavelengths from MWC 297. The uncertainty on flux density at 450 μm is 16.5 mJy/pixel and 850 μm is 2.2 mJy/pixel.

	VLA (mJy)	SCUBA-2 (mJy)								
Object	$S_{3.6\,cm}$	$S_{450\,\mu m}$	S_{ff}	S_d	%	$S_{850\,\mu m}$	S_{ff}	S_d	% xs	α_{ff}
MWC 297	9.9	188.6	137.7	51.0	73±5	86.0	70.9	15.0	82±4	1.03

S_{ff} is flux contribution from free-free process whereas S_d is the flux from thermal dust emission. These two components are observed simultaneously by SCUBA-2 at 450 and 850 μm.

the free-free power law fit of α_{ff} = 1.03±0.02 in Figure 4.3. Free-free subtraction increases the residual dust spectral index by 35%. Given my estimate of 13% CO contamination (see Chapter 3 Section 4), dust emission could potentially account for as little as 5% of peak emission at 850 μm.

The typical noise levels on SCUBA-2 observations are 16.5 mJy pixel^{-1} and 2.2 mJy pixel^{-1} at 450 μm and 850 μm respectively. As a result, the residual dust observed at 450 μm represents approximately a 3σ detection, and at 850 μm represents approximately a 7σ detection. The uncertain nature of the dust detected at 450 μm means it is not possible to calculate reliable temperatures of the residual circumstellar envelope/disc around the star (See Chapter 5 for full details). The assumption of point-like free-free emission may add further uncertainty to the residual flux and therefore I cannot say whether any dust emission contributes to SCUBA-2 observations at the position of MWC 297.

Based on these observations I suggest the following arrangement whereby we are observing both the B star, MWC 297, and the companion A star, *OSCA*. MWC 297 has evolved further to the extent that it is producing the UCHII region observed. I find it unlikely that such a system could still be accreting matter on a large scale, or that the magnetic fields required to produce collimated jets could survive the UCHII region, and therefore I associate the jet emission observed by Skinner et al. (1993) to *OSCA*, an object that may be less evolved and more likely to still be in the accreting phase. Further evidence for active accretion onto *OSCA* has been provided by Damiani et al. (2006) who found substantial X-ray flaring from the object. A more massive disc structure would likely exist around the lower mass, and therefore less evolved, *OSCA* than MWC 297 and therefore this is likely the source of any residual SCUBA-2 flux and *Spitzer* MIPS flux observed in the combined SED. The separation at 850 AU is too small to resolve the two objects with the JCMT beam.

See Chapter 6 for further discussion on how this works impacts our understanding of the star MWC 297.

4.5 The free-free contribution in the W40 complex

In this section I discuss an investigation into multiple sources of free-free emission in the W40 complex, some of which may be contributing to SCUBA-2 450 and 850 μm emission in the Serpens-Aquila region[4]. I address questions regarding the free-free source mechanism, brightness, spectral index and location of the SED turnover and I examine the various sources of free-

[4]The majority of this work is published in Rumble et al. (2016).

Table 4.2: Summary of bright radio objects in the W40 complex and evidence for variability, jet emission and free-free opacity at SCUBA-2 wavelengths, from which a value of $\alpha_{\rm ff}$ can be estimated (if not previously calculated).

Source	2MASS ID	VLA ID[a]	Type [b]	Time [a] variable?	Jet[a]?	SCUBA-2 source?	Optically thick?	Spectral index $\alpha_{\rm ff}$	Distance[b] (pc)
OS 1a (North)	J18312782-0205228	15	Herbig AeBe	N	N	Y	Y	-0.3±0.2[c]	536^{+42}_{-95}
OS 1a (South)	J18312782-0205228	-	O9.5	-	N	Y	-	-	536^{+42}_{-95}
OS 1b	J18312866-0205297	18	Class II	N	Y	N	N	-0.8±0.5[c]	-
OS 1c	J18312601-0205169	8	Class II	Y	N	N	N	-0.6±0.2[c]	-
OS1d	J18312766-0205097	13	Class II	Y	N	Y	N	0.1±0.2[c]	-
OS 2a	J18312397-0205295	7	Herbig AeBe	Y	Y	Y	Y	1.0	-
OS 2b	J18312257-0205315	-	B4	Y	Y	N	N	-0.1	455^{+71}_{-59}
OS 3	J18312395-0204107	-	B3*(binary)	-	-	N	-	-	454^{+87}_{-48}
IRS 5	J18311482-0203497	1	B1	-	-	N	N	0.3±0.2[c]	469^{+217}_{-129}
-	J18312232-0206196	3	Class II	N	Y	N	N	1.1±0.2[c]	-
-	-	14	-	N	N	N	N	0.0±0.1[c]	-

[a] Radio source ID and characterisation based on the findings of Rodríguez et al. (2010).

[b] Spectral classifications and distances calculated from Spectral Energy Distributions in Shuping et al. (2012).

[c] Free-free spectral index calculated by Ortiz-León et al. (2015).

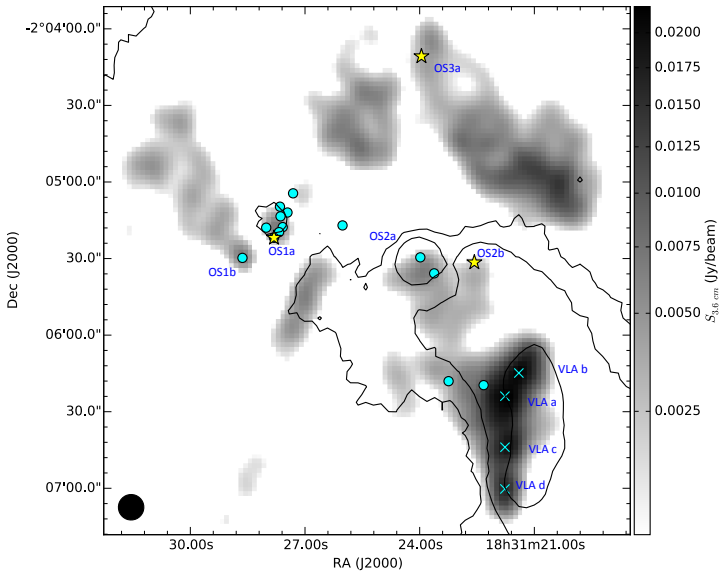

Figure 4.5: Archival AUI/NRAO 3.6 cm map of the W40 complex OB association (NRAO/VLA Archive Survey, (c) 2005-2007, 10″ resolution greyscale). SCUBA-2 850 μm contours of dust emission at 5 σ, 15 σ and 50 σ overlaid. Yellow markers indicate the locations of the OB stars while cyan circles indicate the location of compact radio sources identified by Rodriguez et al 2010. Cyan crosses mark the four peaks identified separately in the AUI/NRAO 3.6 cm map.

free emission in the W40 complex and assess their impact on the dust spectral index observed by SCUBA-2.

Shuping et al. (2012) conduct a NIR study of the brightest objects in the W40 complex, identifying a list of one late O star, three B stars and two Herbig AeBe stars. These objects are listed in Table 4.2 and build on early IR studies by Smith et al. (1985). The O9.5 star OS1aS is the primary ionising source of the H II region that was detected in the radio via free-free emission (Vallee & MacLeod, 1991). The OB association drives the formation of the larger nebulosity Sh2-64 (Sharpless, 1959). Rodríguez et al. (2010) resolve 15 compact radio sources (at 0.26″ resolution) which are consistent with 2MASS sources and, by monitoring time-variability, are able to classify eight variable YSOs with episodic accretion processes (that could potentially be fuelling a jet) and seven non-variable UCH II candidate regions, as shown in Figure 4.5. Ortiz-León et al. (2015) confirm variability in these objects by carrying out follow up observations. Rodríguez et al. (2010) also identify irregular radio sources without IR counterparts and these are interpreted as shock fronts from thermal jets that were likely formed by local Herbig AeBe stars.

Free-free emission in the W40 complex comes from a large-scale H II region as well as several small-scale UCH II regions within the star cluster (Rodríguez et al., 2010; Shuping et al., 2012). Pirogov et al. (2013) suggest a secondary H II region, being powered by the B star IRS 5. Building on the methods outlined in Section 4.3, I model small- and large-scale free-free emission (separately), based on an assumed free-free spectral index that I cannot directly measure, and calculate its contribution to the SCUBA-2 maps.

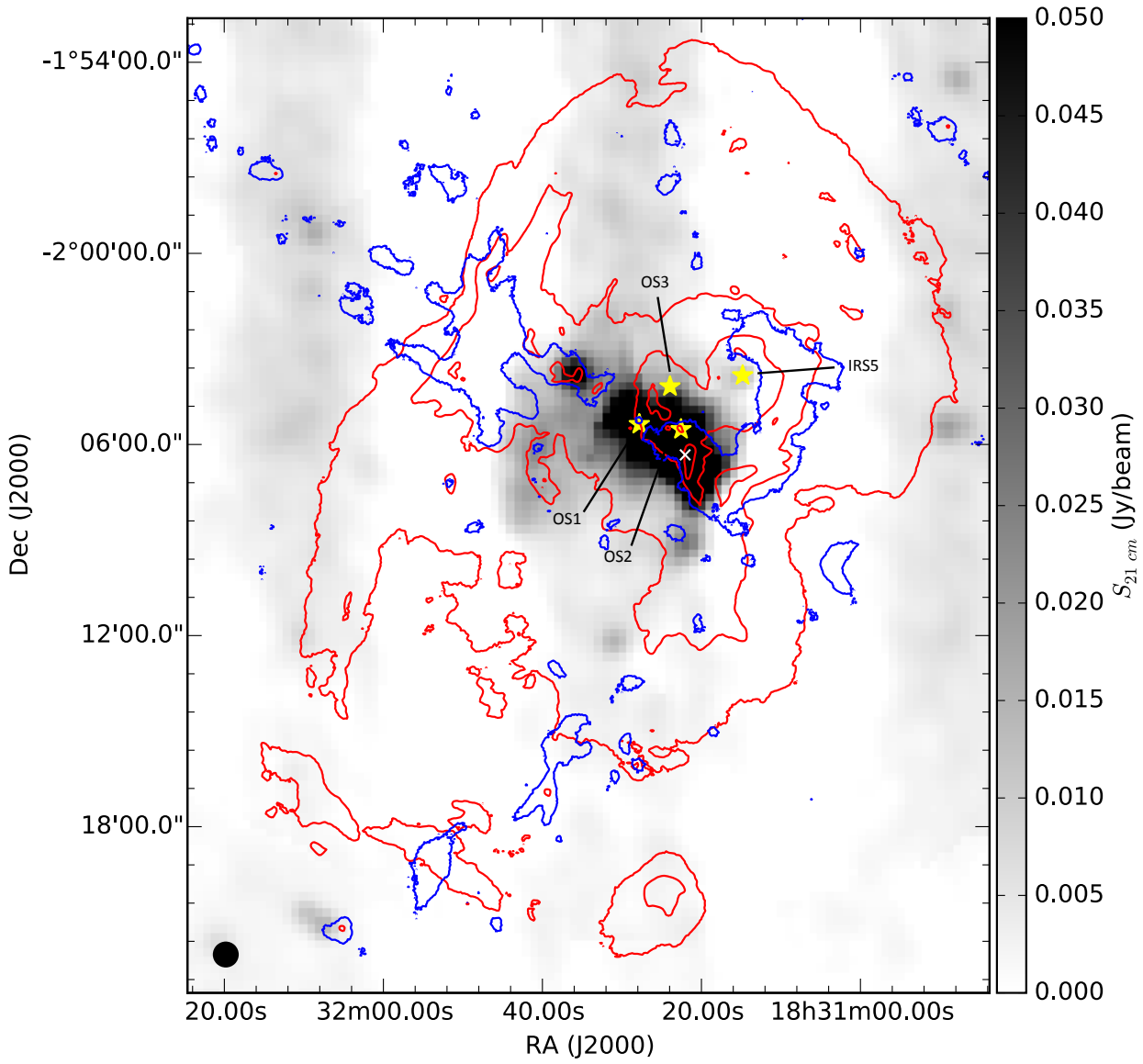

Figure 4.6: Archival 21 cm NRAO VLA Sky Survey (Condon & Kaplan, 1998a) continuum map of the W40 complex H II region (45″ resolution greyscale). Red: *Herschel* 70 μm contours of the nebulosity Sh2-64 at 300, 1200, 4800, 12000 MJy/Sr. Blue: SCUBA-2 850 μm contours of the dust cloud at the 5 σ level. Yellow stars indicate the locations of the OB stars, with the O9.5 star OS1 being the primary ionising object of the region. The white cross indicates the peak of the VLA 21 cm continuum emission.

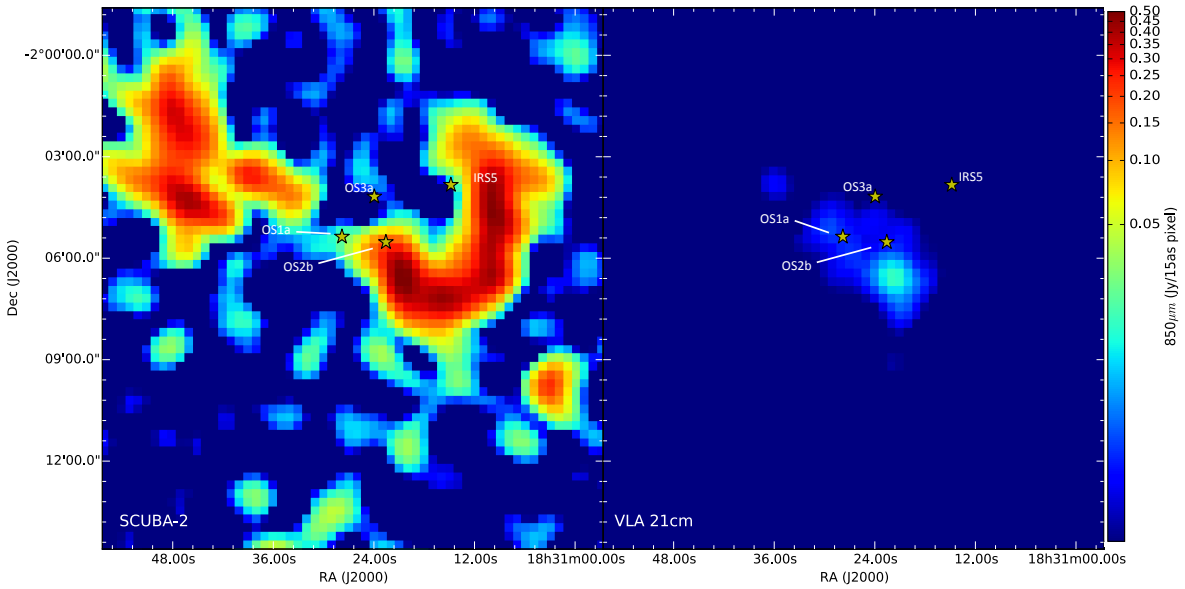

Figure 4.7: The free-free contribution from large-scale H II gas, modelled using archival VLA 21 cm observations (Condon & Kaplan, 1998a) assuming $\alpha_{\rm ff}$ = -0.1 (right), compared to SCUBA-2 dust emission at 850 μm (left). Maps have common 15″ pixels and 45″ resolution. Markers indicate the locations of the OB stars.

4.5.1 Large-scale free-free contribution

Figure 4.6 shows archival VLA 21 cm continuum data of the H II region ($\alpha_{\rm ff}$ = -0.1) associated with Sh2-64 (Condon & Kaplan, 1998a) but not associated with the IRS 5. Vallee & MacLeod (1991) initially measured the size the H II region as 6′ by 3′ with a 1.7′ diameter incomplete shell. Figure 4.5 presents free-free emission from small-scale features in the 10″ resolution archival AUI/NRAO VLA Archive Survey, (c) 2005-2007 3.6 cm continuum data.

For large-scale H II emission, I extrapolate the archival VLA 21 cm data presented in Figure 4.6 up to SCUBA-2 wavelengths of 450 and 850 μm, assuming a flat spectral index of $\alpha_{\rm ff}$ = -0.1. The FINDBACK tool (see Chapter 2) is used to remove structures larger than 5′ (mimicking the SCUBA-2 data reduction process). Using a simple gaussian, I convolve the SCUBA-2 850 μm data up to the 45″ resolution of the VLA data so the fluxes are comparable. Likewise I re-grid the data on to a common pixel size of 15″. The large-scale VLA 3.6 cm free-free contribution can then be subtracted from the SCUBA-2 data. The two maps are compared in Figure 4.7.

Given that free-free emission from the large-scale H II region is essentially flat in spectrum, it is not surprising that the contribution is very limited. Peak 21 cm flux density is 29.8 mJy which corresponds to 16.3 and 17.4 mJy at 450 and 850 μm, per 15″ pixel. The contribution of this peak flux to the SCUBA-2 observations is 5% at 850 μm and 0.5% at 450 μm. Whilst these contributions may be small, they are separated by an order of magnitude. When considering the ratio of SCUBA-2 450 μm flux to 850 μm flux the impact of the large scale free-free emission is non-negligible. I calculate that the dust spectral index at the peak of free-free emission increases by 2% from 3.46 to 3.53 when the contribution is removed.

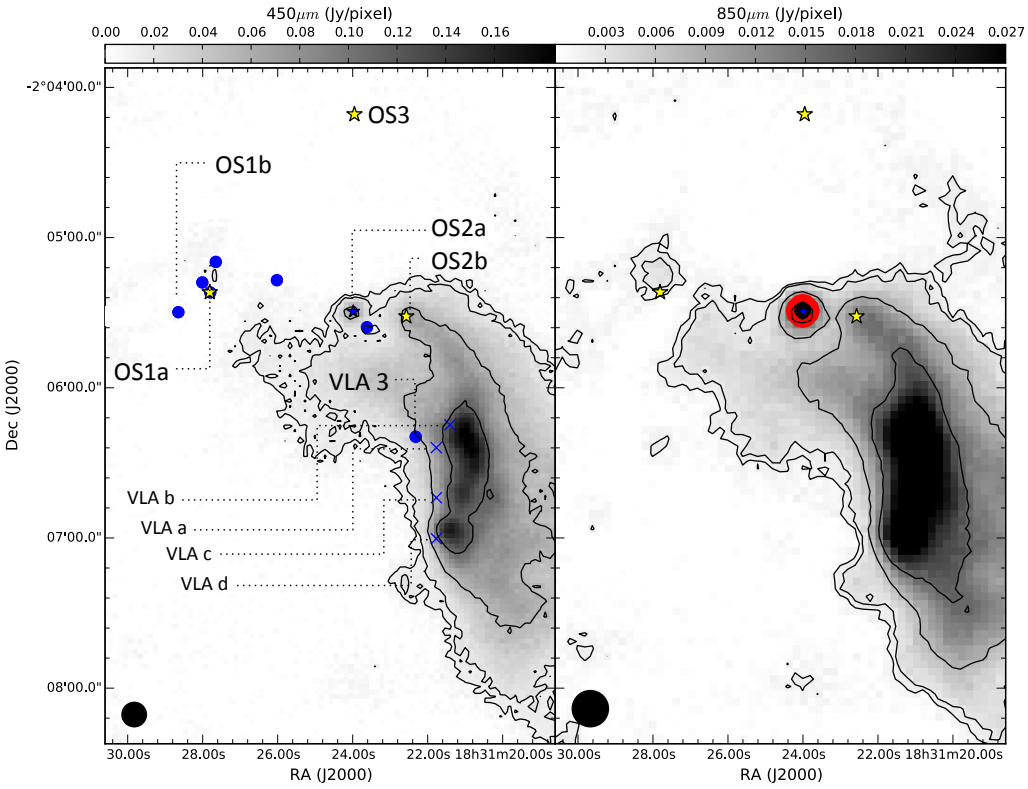

Figure 4.8: The free-free contribution of the compact radio source OS2a (marked as a blue star) at 450 μm (left) and 850 μm (right), modelled as point sources with fluxes extrapolated from the Rodriguez et al. (2010) 3.6 cm fluxes and assuming an $\alpha_{\rm ff}$ = 1.0. Yellow stars indicate the locations of the OB stars, blue filled circles the location of all the Rodriguez et al. (2010) and Ortiz-León et al. (2015) compact radio source matches. Blue crosses mark the location of four peaks identified separately in the AUI/NRAO 3.6 cm map (450 μm only). Black contours trace SCUBA-2 data at 3σ, 5 σ, 15 σ and 30σ. Red and black filled contours trace the optically thick free-free contribution at 3σ and 5 σ (see Table 4.2).

4.5.2 Small-scale free-free contribution

Archival AUI/NRAO 3.6 cm data is used to examine small-scale free-free sources. The coverage of this region, presented in Figure 4.5, is limited to approximately 5′×5′and the resolution of 9.97″ is comparable to SCUBA-2 bands. As a result the AUI/NRAO 3.6 cm map is not able to resolve individual sources, but can pick up extended radio emission associated with jets. Rodríguez et al. (2010) supplement these data with high-resolution photometry at the same wavelength but with a reduced coverage of 4′. Ortiz-León et al. (2015) calculate the free-free spectral index for the 14 YSOs, marked in Figure 4.8, that are detected in both their 4 cm observations and the Rodríguez et al. (2010) 3.6 cm observations. Many of YSOs in the Ortiz-León et al. (2015) observations have less than -0.1 $\alpha_{\rm ff}$, indicating non-thermal gyrosynchrotron emission from low mass Class III objects, and do not have a corresponding point source in either SCUBA-2 band (Figure 4.8). As a result, these objects are not considered further for contamination.

Where the free-free spectral index can be calculated, I model each object as a point source and extrapolate the Rodríguez et al. (2010) 3.6 cm fluxes up to 450 and 850 μm based on $\alpha_{\rm ff}$, and

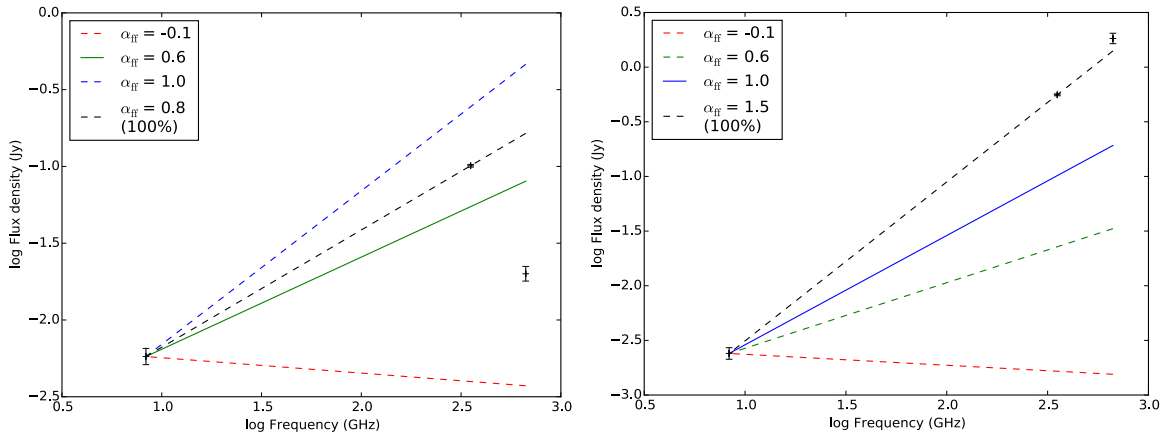

Figure 4.9: Modelling free-free emission in OS1a (left) and OS2a (right) from the Rodriguez et al. (2010) 3.6 cm data for a given α_{ff} = -0.1 (red), 0.6 (green), 1.0 (blue), and the theoretical maximum α_{ff} where 100% of SCUBA-2 emission comes from free-free processes (black). The filled line represents the most likely free-free spectral index.

then convolve by the JCMT beam using its primary and secondary components for comparison with the SCUBA-2 data. Where no additional observations of alternative wavelengths at comparable resolution are available, an indirect method is used to infer α_{ff} from the high resolution Rodríguez et al. (2010) data. This also requires examining the evidence for sufficient electron density, N_e, for any free-free emission to remain optically thick up to the submillimeter regime. I also use the variability and HH objects detected by Rodríguez et al. (2010) to indirectly infer whether or not a YSO has an UCH II region and/or jet. Where a Rodríguez et al. (2010) source, marked in Figure 4.8, lacks a corresponding point-like source in SCUBA-2 emission, it is likely that the free-free SED turns over too early, or that the free-free emission is not bright enough to have a significant impact on the total SCUBA-2 flux density.

The OS1 cluster, OS2a, b and VLA-3 (J18312232-0206196) are all consistent with SCUBA-2 emission, as shown in Figure 4.8, and are considered for free-free contamination. These objects are summarised in Table 4.2.

OS1

OS1 is a dense stellar cluster that includes the primary ionising object, OS1a(South), that is driving the H II region, and four cluster objects (OS1a(North), VLA-12, VLA-14, VLA-16). VLA-14 is the brightest radio source in the OS1 cluster at 5.78 mJy at 3.6 cm (Table 4.2). The cluster is a faint detection at 850 μm and is not detected at 450 μm. Figure 4.9 left presents a theoretical maximum free-free spectral index of 0.8, suggesting that none of the cluster members have a bright collimated outflow. In the scenario where the OS1a cluster objects have a spherical wind with α_{ff} = 0.6, the UCH II region accounts for an integrated free-free flux of 64 mJy at 850 μm, a 62% contribution to the total SCUBA-2 flux. The residual dust in OS1 has an integrated flux of 38 mJy. All four sources are assumed to be partially optically thick in the submillimeter regime. As OS1 is not detected by SCUBA-2 at 450 μm it is not possible to calculate a spectral index for this cluster. I note that the calculated free-free emission at 450 μm exceeds the sensitivity of SCUBA-2, but is

Table 4.3: Summary of integrated free-free flux contributions to SCUBA-2 wavelengths from bright objects in the Aquila W40 complex.

	VLA[a] (Jy)		SCUBA-2 (Jy)							
Object	$S_{3.6\,cm}$	$S_{450\,\mu m}$	S_{ff}	S_d	%	$S_{850\,\mu m}$	S_{ff}	S_d	%	α_{ff}[d]
OS1[b]	0.00578	≤0.02	0.11[c]	≤0.02	-	0.101	0.064	0.038	62	0.6
OS2a	0.00240	1.83	0.16	1.67	9	0.558	0.069	0.489	12	1.0

S_{ff} is flux contribution from free-free process whereas S_d is the flux from thermal dust emission. These two components are observed simultaneously by SCUBA-2 at 450 and 850 μm.
[a] VLA 3.6 cm compact object fluxes (Rodríguez et al., 2010).
[b] OS1 covers a cluster for stellar objects where OS1a(North), VLA-12, VLA-14, VLA-16 are all radio emitters. The flux of the most prominent source, VLA-14, is included in this table but in reality the SCUBA-2 free-free flux of OS1 is a combination of all 4 of these objects.
[c] Non-detection in SCUBA-2 450 μm is interpreted as optically thin free-free emission at this wavelength.
[d] The value of α_{ff} presented in this table is an upper limit, based on indirect observations. Empirical values α_{ff} for OS1 have been published by Ortiz-León et al. (2015). A high degree of variability has prevented an accurate of α_{ff} for OS2a. The uncertainty on flux density at 450 μm is 0.03 Jy/pixel and 850 μm is 0.0025 Jy/pixel.

not detected, suggesting that the free-free spectrum has turned over to optically thin prior to this frequency.

Using 4 cm observations, in conjunction with the Rodríguez et al. (2010) 3.6 cm data, Ortiz-León et al. (2015) calculate an α_{ff} of -0.3±0.2 for OS1a(North) which is consistent with an optically thin H II region. VLA-14 has the most positive spectral index of α_{ff} = 0.0±0.1. This corresponds to a peak 850 μm flux of 0.17 mJy, a value that falls well below the 1σ noise level of that SCUBA-2 band. I therefore conclude that there is no evidence that free-free emission from the OS1a cluster is contributing to the faint 850 μm emission detected by SCUBA-2.

VLA 3

Rodríguez et al. (2010) and Ortiz-León et al. (2015) calculate that VLA-3 has the most positive spectral index with α_{ff} of 1.1±0.2. This index is consistent with a collimated jet source. Zhu et al. (2006) and Shimoikura et al. (2015) studied the ^{13}CO 2–1, ^{12}CO 1–0 and 3–2 line emission in this region and observed profiles symptomatic of outflows. However, I observe that the ^{12}CO 3–2 line in this region is highly extincted due to emission becoming optically thick at high densities, making reliable analysis of these features impractical. Figure 4.8 shows that VLA-3 is heavily embedded within the Dust Arc; however, it is not associated with a strong point source in either SCUBA-2 bands in the same way that OS2a is. From this I conclude that free-free emission from YSO VLA-3 has turned over to optically thin at wavelengths longer than the submillimeter regime and does not provide a significant contribution to the SCUBA-2 bands.

OS2a

OS2a is a Herbig AeBe star that is detected as a strong point source by SCUBA-2 at both 450 μm and 850 μm (Figure 4.8). Rodríguez et al. (2010) detect OS2a at 3.6 cm, finding it to be variable and having evidence for jets through outflow knots. The object is not detected in ^{12}CO 3-2 (Figure 3.6) suggesting the presence of an UCH II region that has depleted the molecule through photo-dissociation. By contrast Ortiz-León et al. (2015) detect emission at the location of OS2a, but do not report it as its SNR falls below their detection criteria (Ortiz-Leon. priv. comm.). Such behaviour is consistent with a variable object, and therefore it is not possible calculate a reliable $\alpha_{\rm ff}$.

As a result I can model various free-free spectral indices, using the test outlined in Section 4.3.1, and consider their contributions to the overall SCUBA-2 flux detected using the Rodríguez et al. (2010) high resolution detection at 3.6 cm. Two results are returned from Figure 4.9 right; an $\alpha_{\rm ff}$ = 0.6 represents a 5% contribution to peak flux (1.86 mJy) and an $\alpha_{\rm ff}$ = 1.0 represents a 22% contribution to peak flux (8.18 mJy), at 850 μm. This test confirms that both scenarios are viable and in both cases free-free emission will be dominated by dust emission. Rodríguez et al. (2010) find time variability and evidence for jets in OS2a. As a result, I assign OS2a an $\alpha_{\rm ff}$ = 1.0, in line with a collimated outflow UCH II region.

In order to make an estimate of the upper limit of the free-free contribution of OS2a, I model OS2a as a point source and extrapolate the Rodríguez et al. (2010) 3.6 cm flux up to 450 and 850 μm based on an $\alpha_{\rm ff}$ of 1.0. I make the optimistic assumption that OS2a is optically thick at SCUBA-2 wavelengths on the basis of the bright point source at that location that is observed at 450 and 850 μm (Figure 4.8). The fluxes are subsequently convolved by the JCMT beam using its primary and secondary components for comparison with the SCUBA-2 data and presented in Table 4.3. The integrated free-free flux over the JCMT beam area is 160 mJy at 450 μm and 69 mJy at 850 μm, corresponding to a free-free contribution to the SCUBA-2 bands for OS2a of 9% at 450 μm and 12% at 850 μm. I remind the reader that these are considered upper limits. Having accounted for possible CO and free-free contamination, the residual flux detected from OS2a is 1.67 and 0.489 Jy at 450 and 850 μm respectively. I find that this gives OS2a a dust spectral index of α = 1.6±0.1, representing an increase of 3%.

I note that, in spite of the subtraction of free-free emission, OS2a has an exceptionally low dust spectral index. Lower values of α have previously been explained by very low β associated with grain growth (Manoj et al., 2007). Given a β=1.0, typical for circumstellar discs, an α = 1.6 would require a temperature of less than 2 K. Alternatively, an exceptionally low β approaching 0.0 would still require a temperature of less than 7 K. In both scenarios, dust temperatures this low have never been observed. Therefore the results calculated for OS2a should be considered with a high degree of scepticism.

A similar case of a very low dust spectral index was observed in Serpens MWC 297 in the previous section. In both cases, a Herbig star is contributing free-free emission from a collimated outflow, with $\alpha_{\rm ff}$ = 1, to the dust flux and was found to be distorting α. Free-free emission from the B1.5ve ZAMS star MWC 297 contributes 9.9 mJy at 3.6 cm, corresponding to a free-free luminosity of 7.4×10^{10} W. This is as bright as OS2a where the free-free integrated flux is 2.4 mJy

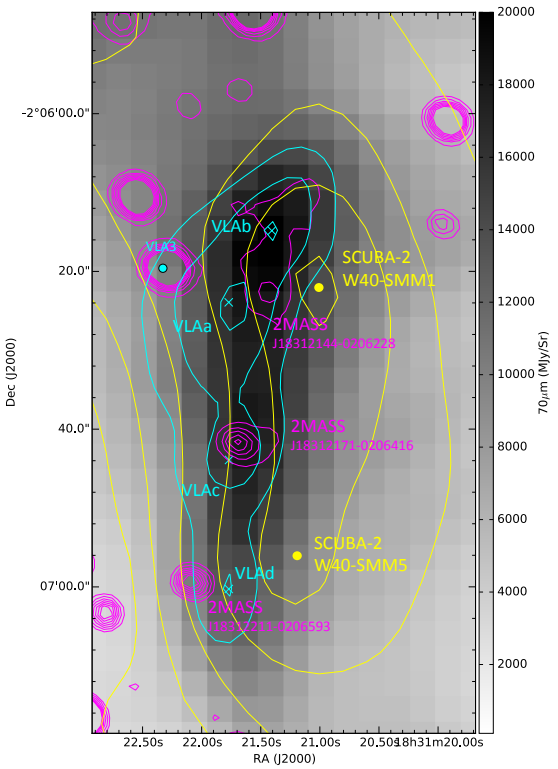

Figure 4.10: Archival *Herschel* 70 μm data for W40-SMM1 and 5. Magenta contours (560, 570, 580, 590, 600, 610, 620 mag.) show several 2MASS point sources embedded within the eastern Dust Arc which is shown in the yellow SCUBA-2 850 μm 5, 10, 20, 40, 60, 80σ contours with circle markers at the peaks of the W40-SMM1 and 5 clumps (see Section 6). Cyan crosses show the four peaks in Archival AUI/NRAO 3.6 cm map (contours at 0.01, 0.016 and 0.021 Jy/beam). The Rodriguez et al. 2010 YSO 'VLA3' is also shown.

and free-free luminosity is 7.2×10^{10} W. Considering the total flux observed by SCUBA-2 for the objects, I find that OS2a has an 850 μm luminosity of 1.67×10^{13} W (flux of 558 mJy), over 151 times brighter than MWC 297 which has 6.43×10^{11} W (15 mJy). Given this assumption, I would conclude that OS2a is significantly less evolved than MWC 297, with more of its mass residing in a cold circumstellar disc and producing a far weaker outflow. However, with more material present in the disc for fewer UV photons to ionise, the result is a similar radio luminosity for each star.

OS2b

No radio or submillimeter point source has been observed at the location of OS2b, as shown in Figure 4.8. I therefore assume that any free-free radio emission must be faint and optically thin at SCUBA-2 wavelengths. This is consistent with its classification as a weak UV-photon-emitting B4 star (Shuping et al., 2012).

4.5.3 Additional free-free sources

Observations by Rodríguez et al. (2010) did not cover the four brightest peaks in the AUI/NRAO 3.6 cm data that lie to the southwest, referred to here as VLAa, b, c, and d (Figure 4.5 and 4.10).

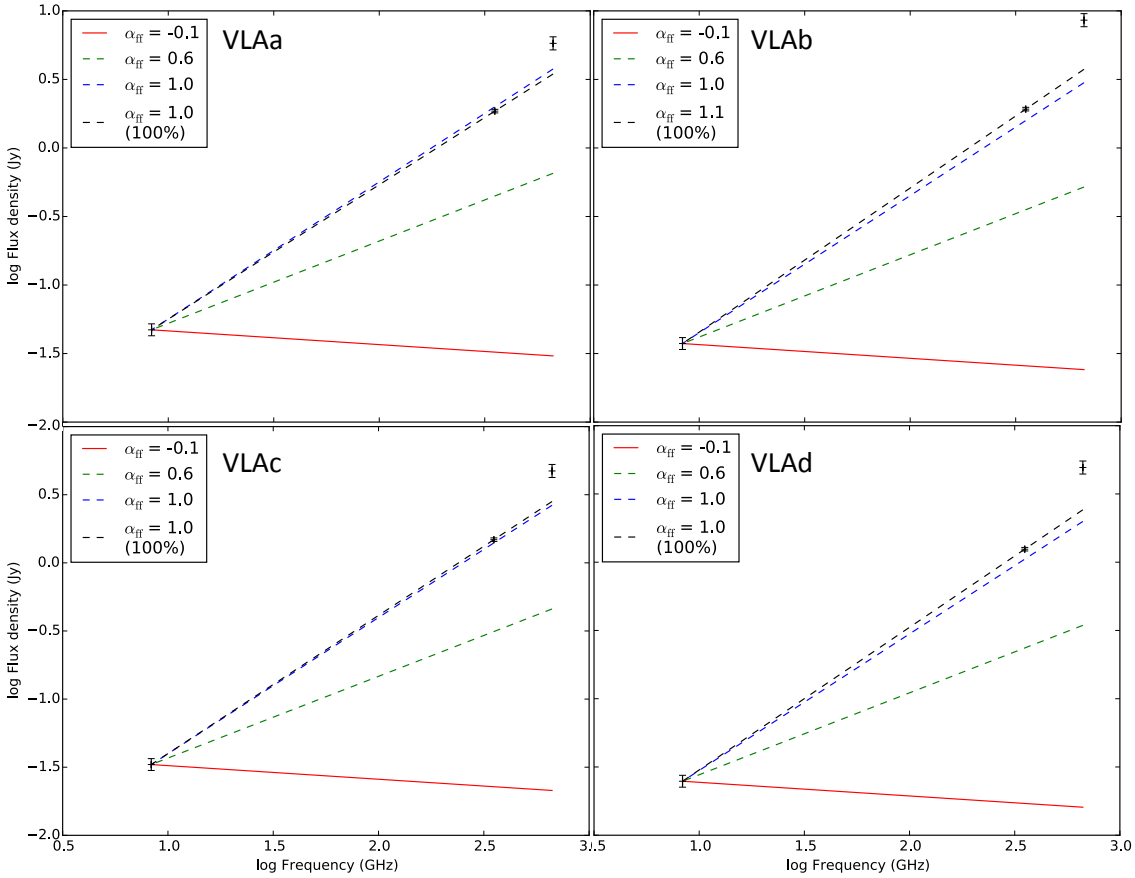

Figure 4.11: Modelling free-free emission in VLAa, b, c and d from the Archival AUI/NRAO 3.6 cm data for a given α_{ff} = -0.1 (red), 0.6 (green), 1.0 (blue), and the theoretical maximum α_{ff} where 100% of SCUBA-2 emission comes from free-free processes (black). The filled fill represents the most likely free-free spectral index.

These objects are orders of magnitude brighter than the Rodríguez et al. (2010) sources and appear in

Testing values of $\alpha_{\rm ff}$ in Figure 4.11 rules out each source as a collimated jet but is inconclusive regarding a spherical wind UCH II region. I do not observe significant SCUBA-2 peaks at the positions of these objects and therefore conclude that any free-free emission observed here at 3.6 cm is optically thin at SCUBA-2 wavelengths and therefore regardless of their nature, they produce no significant free-free contributions. I therefore take no further action with regard to the small-scale free-free contribution.

Alternatively, I could be observing free-free emission from the shock/ionisation front from where the OS1a H II region is interacting with the eastern Dust Arc, as proposed by Vallee & MacLeod (1991). Using Equation 4.9, I calculate that a Lyman photon flux of $4.0{\times}10^{46}$ s^{-1} is required to produce the a total flux density of 0.167 Jy that I observe across all four unidentified VLA sources at 3.6 cm, given an electron temperature of 10,000 K and a distance of 0.5 kpc. I compare this value to the fraction of photon flux produced by OS1a which is incident upon the cloud. The 09.5V star has a photon flux of $7.94{\times}10^{47}$ s^{-1}. I assume a minimum distance between OS1a and the filament of 3′, and that the filament area exposed is an ellipse of 1.5′×0.5′, consistent with Vallee & MacLeod (1991). This geometry represents the most optimistic estimate with the aim of calculating an upper limit. I calculate that the proposed ionisation front across the eastern Dust Arc would be exposed to, at most, 2.1% of Lyman photons produced by OS1a at this distance. This percentage corresponds to a Lyman photon flux of $1.67{\times}10^{46}$ s^{-1}, which is comparable to the flux observed at 3.6 cm, given the approximate nature of this calculation.

Given the speculation about the nature of the VLA sources a, b, c and d I cannot reliably estimate a value of $\alpha_{\rm ff}$ for the individual objects. However, the combined flux from the four objects correspond to the 21 cm peak in the NRAO VLA Sky Survey (Condon & Kaplan, 1998a) continuum map presented in Figure 4.6. By scaling the resolution of AUI/NRAO 3.6 cm data, presented in Figure 4.5, down to the 45″ of the 21 cm continuum data it is possible to directly compare the free-free emission from the eastern Dust arc and estimate a free-free spectral index using,

$$\alpha_{\rm ff} = \frac{\log(S_{21}) - \log(S_{3.6})}{\log(\nu_{21}) - \log(\nu_{3.6})}. \tag{4.11}$$

The peak flux at 21 cm is 29.8 mJy pixel^{-1} and at 3.6 cm it is 12.0 mJy pixel^{-1} resulting in a value of $\alpha_{\rm ff}$ = -0.5. This is likely a lower limit as the AUI/NRAO 3.6 cm data is thought to have had large-scale structures subtracted from it during the reduction process.

I therefore conclude that this free-free spectral index is consistent with an H II region where $\alpha_{\rm ff}$ = -0.1 and that diffuse large-scale free-free emission is dominant in the eastern Dust Arc. These findings favour an H II bubble interacting with a filament, as opposed to deeply embedded UCH II regions, though this does not rule out on-going formation of massive stars in this filament.

4.6 Conclusions

In this chapter I have examined the impact of free-free contamination on SCUBA-2 observations of the star-forming regions Serpens MWC 297 and the Aquila W40 complex. I develop techniques that are used to subtract free-free emission from the submillimeter observations, measure the residual dust flux and estimate the contamination fraction. Where insufficient radio observations exist to directly calculate $\alpha_{\rm ff}$, I assess the physical characteristics of individual sources to make a judgement on whether they are large-scale H II regions ($\alpha_{\rm ff}$ = -0.1), small-scale spherical wind UCH II regions ($\alpha_{\rm ff}$ = 0.6) or collimated jet UCH II region ($\alpha_{\rm ff}$ = 1.0).

My results are summarised as:

1. The spectral index of free-free emission from stellar winds or outflows has a steeper value at low frequencies before turning over to become flat at high frequencies. The location of the turnover on the spectrum is dictated by the electron density at the base of the outflow, which is dictated by the stellar mass and class. I define the stellar class B1.5Ve as a lower limit at which the free-free emission from this star will contaminate the dust in the SCUBA-2 bands.

2. Free-free emission from the B star MWC 297 was found to contribute approximately 73±5 % and 82±4 % of the 450 and 850 μm integrated flux respectively. Residual integrated dust fluxes are 51±10 mJy and 15±3 mJy flux at 450 μm and 850 μm respectively. Subtracting the free-free emission increases the dust spectral index by 35%. Dust at 850 μm represents a 3σ detection and at 450 μm dust represents a 7σ detection.

3. A number of radio bright stars are observed in the Aquila W40 complex. OS1b, c, OS3a and IRS 5 have flat free-free spectral indices and are not detected by SCUBA-2, confirming that any free-free emission from these objects is too faint to be detected at submillimeter wavelengths. Ortiz-León et al. (2015) observe the VLA-3 radio source to have a jet-like free-free spectral index of $\alpha_{\rm ff}$ = 1.1±0.2. Whilst this source is deeply embedded in the Dust Arc filament, it is not associated with a SCUBA-2 point source suggesting that the free-free emission from the YSO has turned over prior to the submillimeter regime on account of its low mass. The OS1 cluster (VLA-12,14,15 and 16) are detected at 850 μm. Ortiz-León et al. (2015) calculate a flat spectral index for this cluster, consistent with an evolved H II region, confirming that any free-free emission from these objects is not significant in SCUBA-2 bands.

4. Free-free emission from the Herbig AeBe star OS2a (in the Aquila W40 complex) observed in AUI/NRAO 3.6 cm data, and by Rodríguez et al. (2010) at the same wavelength, was found to contribute approximately 9% and 12% of the 450 and 850 μm integrated flux respectively, given an assumed collimated jet UCH II with an $\alpha_{\rm ff}$ = 1.0 based on a variable compact radio source consistent with episodic accretion and radio shock fronts that are observed in the vicinity. A significant residual dust flux of 1.67 and 0.489 Jy at 450 and 850 μm respectively is associated with this object giving an unusually low dust spectral in-

dex 1.6±0.1 (an increase of 2% follow the subtraction of the free-free contribution) which is not possible to explain without invoking exceptionally cold dust temperatures.

5. Free-free emission observed in 21 cm VLA data from the large, diffuse H II region in the Aquila W40 complex was found to contribute to approximately 0.5% and 5% of the 450 and 850 μm peak flux respectively, given a typically flat spectrum ($\alpha_{\rm ff}$ = -0.1). Subtracting the free-free emission increases the spectral dust index by at most 2%.

6. I conclude that there are sufficient UV photons being produced by OS1aS to ionise part of the tip of the eastern Dust arc filament, making it the brightest source of free-free emission in the W40 region. I estimate its free-free spectral index to be essentially flat, signifying an evolved H II region.

Where free-free emission is sufficiently bright and optically thick, its contribution can lead to the observation of prominent point sources in the SCUBA-2 data and significantly lower dust spectral indices, and therefore temperatures around Herbig stars. Where the free-free emission is less prominent, in faint UCH II regions and from large-scale H II regions, it can still have a limited, if non-negligible impact on the dust spectral index. In the following chapter I will look at what quantifiable effects the free-free emission has when examining the dust temperature.

5

Temperature mapping

5.1 Introduction to dust temperature

In this chapter I outline how dust temperature is calculated from SCUBA-2 observations of star forming regions in the Gould Belt with the aim to study the temperature morphology at a resolution comparable to a Jeans length (equivalent to the core diameter, of the order 0.05 pc, Rygl et al. 2013). Using SCUBA-2 data allows for studying temperature at the earliest stages of protostellar evolution and assessing the impact of heating on ongoing star-formation.

Understanding the impact of heating, via radiative feedback, is of vital importance for the wider inquiry into what mechanisms govern the behaviour of molecular clouds (Jeans, 1902). Feedback occurs, via internal mechanisms, from radiative heating by the stellar photosphere and accretion luminosity (Calvet & Gullbring, 1998) of YSOs. Molecular outflows and shocks (Davis et al., 1999) may also radiatively heat a cloud to a lesser extent. External sources of heating include photons produced by stars, which can drive strong stellar winds (Canto et al., 1984; Ziener & Eislöffel, 1999; Malbet et al., 2007) and H II regions (Koenig et al., 2008; Deharveng et al., 2012), as well as the interstellar radiation field (ISRF; Mathis, Mezger & Panagia, 1983; Shirley, Evans, Rawlings & Gregersen, 2000a; Shirley, Evans & Rawlings, 2002a). Simulations, including those by Krumholz (2006b); Krumholz et al. (2007) and Bate (2009), have suggested that internal radiative feedback can suppress cloud fragmentation, leading to higher mass star-formation (as discussed in Chapter 1, Section 1.7.

In order to investigate the evidence for radiative feedback and dust heating in the JCMT GBS regions, I calculate the ratio of SCUBA-2 450 μm and 850 μm flux. Then by fitting a full, opacity-modified Planck function to the flux ratio dust temperature can be calculated (Reid & Wilson, 2005). The flux ratio method does not compromise on the high resolution of the JCMT

Table 5.1: JCMT beam properties. JCMT beam FWHM (θ) and relative amplitudes from Dempsey et al. (2013) Table 1. α and β represent the beam amplitude. $V_{\rm MB}$ and $V_{\rm SB}$ represent beam volume. Pixel sizes are those chosen by the JCMT SGBS data reduction team for the Internal Release (IR) 1 reduction.

	450 μm	850 μm
$\theta_{\rm MB}$	7.9″	13.0″
$\theta_{\rm SB}$	25.0″	48.0″
α	0.94	0.98
β	0.06	0.02
$V_{\rm MB}$	0.6	0.75
$V_{\rm SB}$	0.4	0.25
Pixel size	4″	6″

(14.6″) but does introduce an inherent degeneracy between temperature and the dust opacity index, β (Shetty et al., 2015).

The method by which temperature maps are made can be split into two distinct parts: creating maps of flux ratio from input 450 μm and 850 μm data, and building temperature maps based on those ratio maps. Both parts are developed by Hatchell et al. (2013). I focus on the development of the Hatchell et al. (2013) (from now on referred to as the H13) method. I Chapter 6 I introduce a more realistic Gaussian beam convolution that incorporates both the primary and secondary component of the JCMT beams. In Chapter 7 I incorporate a convolution kernel developed by Aniano et al. (2011) and Pattle et al. (2015) to achieve a dust temperature map with a resolution comparable to the JCMT effective beam area at 850 μm.

5.1.1 Submillimeter flux ratio

In this thesis, I develop a method which takes the ratio of SCUBA-2 450 μm and 850 μm fluxes and fits them to an opacity modified black-body model from which dust temperature ($T_{\rm d}$) or the dust opacity index, β, can be constrained.

The spectral index, α, of the SCUBA-2 fluxes, S_ν, is given as a power law of frequency ratio,

$$\frac{S_{450}}{S_{850}} = \left(\frac{\nu_{850}}{\nu_{450}}\right)^{\alpha}, \tag{5.1}$$

where ν_{450} and ν_{850} are the frequencies of the SCUBA-2 bands (666 and 353 GHz). Given the equation of radiative transfer, when the continuum emission is optically thin,

$$S_\nu = \int_\Omega B_\nu(T_d)\tau_\nu \, d\Omega, \tag{5.2}$$

the ratio of SCUBA-2 fluxes can be given in the form of,

$$\frac{S_{450}}{S_{850}} = \frac{B_{\nu_{450}}(T_d)}{B_{\nu_{850}}(T_d)} \frac{\kappa_{\nu_{450}}}{\kappa_{\nu_{850}}}, \tag{5.3}$$

where $B(T_d, \nu)$ is the Planck function and κ_ν is the dust opacity which is approximated to the form of a power-law with spectral index β,

$$\kappa_\nu = \kappa_{\nu_0} \left(\frac{\nu_0}{\nu}\right)^{-\beta}, \tag{5.4}$$

for a given $\kappa_{\nu_{850\,\mu\mathrm{m}}} = 0.012\,\mathrm{cm}^2/\mathrm{g}$ at $\nu_0 = \nu_{850}$. In the Rayleigh-Jeans limit, Equation 5.4 shows how α can be approximated to $2 + \beta$. However, by observing cool bodies at shorter wavelengths (i.e. the SCUBA-2 450 μm band) off of the Rayleigh-Jeans tail, it is possible to calculate a dust temperature, assuming a single value for β and an opacity modified black-body model of emission. Under these circumstances, Equation 5.1 can be expanded into the 'temperature equation' (Reid & Wilson, 2005),

$$\frac{S_{450}}{S_{850}} = \left(\frac{850}{450}\right)^{3+\beta} \left(\frac{\exp(hc/\lambda_{850}k_\mathrm{b}T_\mathrm{d}) - 1}{\exp(hc/\lambda_{450}k_\mathrm{b}T_\mathrm{d}) - 1}\right). \tag{5.5}$$

Note that λ_{450} and λ_{850} are the wavelengths of the SCUBA-2 bands. Removing the requirement for an assumed β requires data at additional wavelengths, for example 250 μm and 350 μm as observed by *Herschel*, and is discussed further in Section 6.3.

Similar methods have been applied by Wood, Myers & Daugherty (1994), Arce & Goodman (1999) and Font, Mitchell & Sandell (2001) and used by Kraemer et al. (2003) at 12.5 and 20.6 μm and by Schnee et al. (2005) at 60 and 100 μm. Use of the shorter SCUBA and SCUBA-2 450 μm band allows for dust temperatures up to 50 K to be reliably calculated for an opacity modified black-body model fit to a flux ratio. However, first analysis of SCUBA data was limited by the quality and quantity of the 450 μm data. Mitchell et al. (2001) only observe sufficient data to calculate temperatures in 54% of 850 μm clumps detected. Calculated temperatures become increasingly unreliable at higher values as the shorter wavelength approaches the Rayleigh-Jeans tail where temperature information is lost. On this basis Mitchell et al. (2001) give a lower limit of 30 K for all temperatures above this value. A more rigorous analysis of SCUBA data was completed by Reid & Wilson (2005) who were better able to constrain errors on the temperature maps from sky opacity and the error beam components.

The lower noise levels and wider coverage at 450 μm from SCUBA-2 offer improved quality and quantity to the extent that temperature maps can be constructed, as demonstrated by the H13 method in NGC 1333 and Buckle et al. (2015) in NGC 2264. This thesis looks to utilise these methods to further investigate radiative feedback, specifically in Serpens MWC 297 (Chapter 6) and the Aquila W40 complex (Chapter 7), and more widely in the rest of the JCMT GBS (Chapter 8).

5.1.2 Dust opacity

To derive the dust temperature from the 450 μm and 850 μm flux ratio, the dust spectral index, β, is assumed to be a constant across a region; however, observations and theory provide evidence that this is not the case.

Smaller values of β are found to be consistent with grain growth which only occurs sufficiently close to compact structures (Ossenkopf & Henning, 1994). Similarly, temperature is

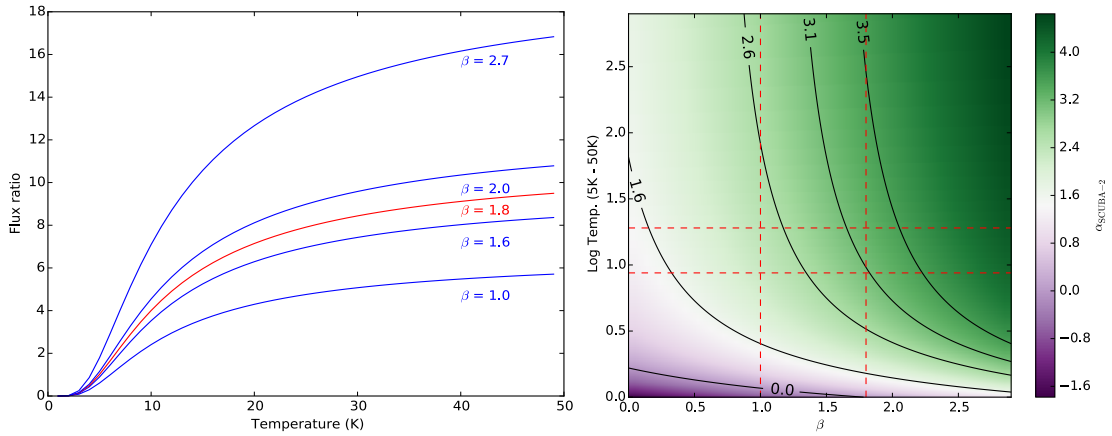

Figure 5.1: Right) flux ratio as a function of temperature as described by Equation 5.5 for a range of β values reported by Sadavoy et al., (2013) and Chun-Yuan Chen et al. (2016). Left) SCUBA-2 spectral index as a function of β, across a similar range, and temperature. The temperature range in both plots is of that commonly observed in protostellar cores.

known to influence the process by which dust grains coagulate and form icy mantles and therefore the value of β. Observations by Beckwith et al. (1990), Ubach et al. (2012), Sadavoy et al. (2013), Buckle et al. (2015) have shown a β value of 1.0 is typical for protoplanetary discs. Larger values of β are associated with extended, filamentary regions and β values of up to 2.7 have been found by fitting *Herschel* 160 μm to 500 μm data with SCUBA-2 data (Sadavoy et al. 2013, Chen et al, 2016).

The wide range of β values observed lead to the conclusion that environmental factors in the ISM, such as the gravitational collapse of dense clouds or heating by radiative sources, can lead to the evolution of dust grains and the value of β (Hildebrand 1983, Ossenkopf & Henning 1994 and Draine & Lee 1984). Chun-Yuan Chen et al. (2016) outline three categories of β (based on the work by Testi et al. 2014). Pristine β values of 1.5 to 2.0 are typical of pre-stellar ISM before transitioning to values of 2.0 to 3.0 on the path to an evolved state associated with discs where β drops to1.5 or less.

Figure 5.1 (left) describes how small changes in β can lead to a large range of flux ratios, especially at higher temperatures. For ratios of 3, 7 and 9, a β of 1.6 would return temperatures of 8.9, 25.4 and 85 K whereas a β of 2.0 would return temperatures of 7.6, 15.7 and 25 K. Given a reasonable value of β (as outlined), higher ratios indicate heating above that available from the interstellar radiation field (ISRF).

Stutz et al. (2010) use the dominance of extended structure over compact structure in CB244 region to argue for a uniform, higher value of β. Likewise Hatchell et al. (2013) assumed a constant $\beta = 1.8$, arguing that variation in temperature dominates to that of β in NGC1333. On this basis I follow Ossenkopf (1993) and Hatchell et al. (2005) and adopt a uniform β of 1.8 over a wavelength range of 30 μm–1.3 mm. This value is consistent with *Planck* observations (Juvela et al., 2015) and that used in other GBS papers (Salji et al. 2015, and Pattle et al. 2015). I note that in this regime an apparent fall in temperature towards the centre of a core might be symptomatic of lower β values, typically found in accretion discs, and therefore these temperatures may be underestimates.

Following Hatchell et al. (2005) and the popular OH5 model (Ossenkopf & Henning, 1994) of opacities in dense ISM, for a specific gas-to-dust ratio of 161 over a wavelength range of 30 μm–1.3 mm, I assume a dust opacity of 0.012 cm^2/g at 850 μm There is a high degree of uncertainty in the value of κ_{850}. Studies comparable to Ossenkopf & Henning (1994) suggest values of 0.01 (Johnstone et al., 2000), 0.019 (Eiroa et al., 2008) and 0.02 $\mathrm{cm}^2\mathrm{g}^{-1}$ (Kirk et al., 2006). Henning & Sablotny (1995) report that κ_{850} can vary by up to a factor of two.

5.2 Hatchell (2013) method

Hatchell et al. (2013) use the Reid & Wilson (2005) 'temperature equation', in the form of Equation 5.5, for SCUBA-2 data in Perseus NGC 1333 where they observe a range of temperatures in association with cold dusty filaments and heating from OB stars. Much of this thesis extends this work with the aim of creating more accurate and realistic temperature maps. I will therefore review the existing methodology before discussing my own developments.

The H13 method is run in two parts. Firstly a map of the SCUBA-2 flux ratio is calculated and followed by production of a dust temperature map. Pre-processing of the 450 and 850 μm flux maps involves (in the following order):

1. Calibrating the maps in units of Jy/pixel (from Jy/beam, Equation 2.1).
2. Removing unphysical negative flux.
3. Single-beam cross-convolution of each wavelength map with the alternate wavelength beam to achieve a common resolution.
4. Alignment of the 450 μm map on the grid of the 850 μm data to achieve a common grid size.
5. Clipping of low SNR pixels based on the SCUBA-2 error arrays.
6. Division of modified SCUBA-2 maps to produce a map of flux ratio.

There are a number of free parameters that go into this process alongside the SCUBA-2 data. Cross-convolution is based on the model of the JCMT beam as a simple 2-dimensional Gaussian with a FWHM of 9.8″ at 450 μm and 14.6 at 850 μm (Hatchell et al., 2013). Typically a SNR of five is used alongside calibration factors of 491 Jy/beam/pW at 450 μm and 537 Jy/beam/pW at 850 μm (Dempsey et al., 2012).

Equation 5.5 provides no analytical solutions to temperature and therefore this value is inferred from a look up table. In a separate routine, each pixel in the flux ratio map is replaced with its paired temperature value. The look-up table is limited to a range of between 5 and 1000 K, with a resolution of 0.01 K, as shown in Figure 5.2. As discussed in the previous section, the flux ratio method requires use of a constant β and this term is entered as a free parameter at this stage of the routine.

The temperature map is then returned to the ratio map routine where it undergoes a final round of clipping. The upper and lower limits of temperature uncertainty are calculated in parallel

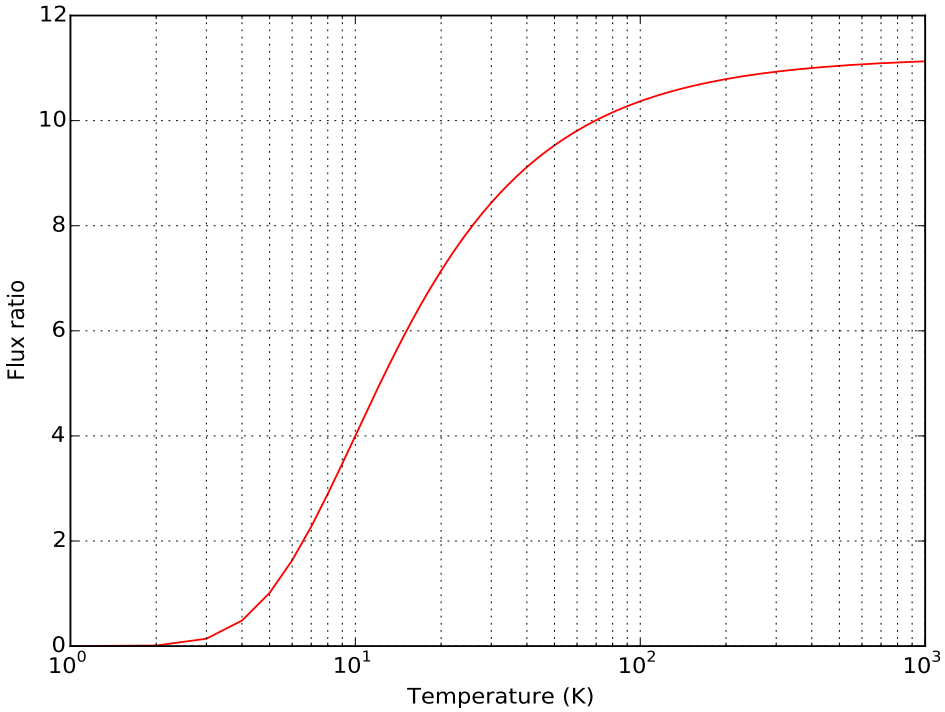

Figure 5.2: Flux ratio as a function of temperature as described by Equation 5.5, given a constant β of 1.8. The temperature range matches that used by the H13 method and my subsequent versions of the method.

from the arrays and these form the basis for an arbitrary cut of pixels with standard deviation greater than 5.5 K and any stray pixels that have exceptionally high values (greater than 999.98 K).

The H13 method is somewhat rudimentary and there are a number of caveats that inhibit a comprehensive interpretation of the resulting dust temperature maps. Chief among these is the beam shape. Hatchell et al. (2013) model the beam as a single Gaussian whereas Dempsey et al. (2013) and Reid & Wilson (2005) use a two-component beam comprised of a primary and secondary Gaussian (as presented in Table 5.1). Work by Pattle et al. (2015) show that whilst a two component model is more realistic than a single Gaussian, the real JCMT beam is in fact more complex than this.

Further issues with the H13 method include the unresolved presence of high value pixels around the edges of the maps, observed temperature gradients, application of the SNR cut and its level and the assumption of constant β across the whole region. Furthermore, the cross-convolution method used by Hatchell et al. (2013) achieves a resolution lower than the theoretical minimum of 14.6 (i.e. the effective beam size at 850 μm). I address some of these issues tin the rest of this chapter.

5.3 Two-Component Beam method

The primary aim of the 'Two-Component Beam method', from here on referred to as the '2CB method' is to introduce the JCMT secondary beam from Dempsey et al. (2013) into the cross-

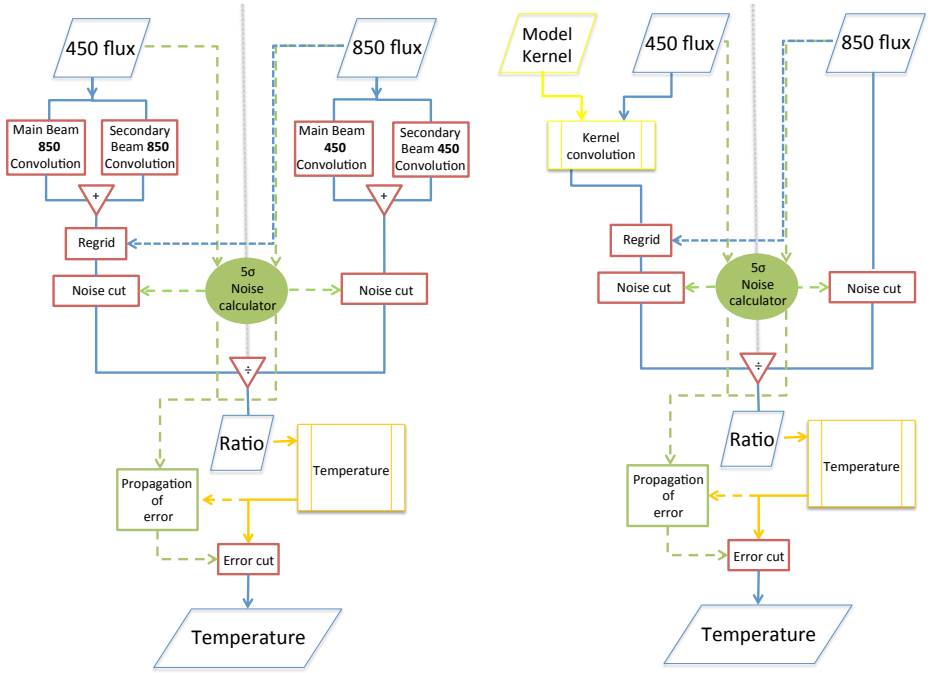

Figure 5.3: A flow chart providing a simplified description of the ratio mapping process for the 2CB method (left, discussed in Section 3) and Kernel-convolution method (right, discussed in Section 4).

convolution model[1] following Reid & Wilson (2005). I also assess the existing structure of the H13 method, as listed above.

Following the implementation of my adaptations, the 2CB method is summarised in the following steps:

1. Two-Component Beam cross-convolution of each wavelength map with the alternate wavelength beam to achieve a common resolution of 19.9″.

2. Alignment of the 450 μm convolved map onto the grid of the 850 μm convolved map to achieve a common pixel size.

3. Masking of both maps with a 5σ signal to noise cut.

4. Division of the modified SCUBA-2 maps to produce a map of flux ratio.

The steps are presented in the left hand flowchart in Figure 5.3.

5.3.1 Two-component beam cross-convolution

The JCMT beam is modelled as the sum of two, 2-dimensional normalised Gaussians, $G(x, y)$, of the form,

$$G(x,y) = \int \int_{-\infty}^{\infty} \frac{1}{2\pi\sigma^2} \exp\left(-\frac{(x^2+y^2)}{2\sigma^2}\right) dxdy = 1, \tag{5.6}$$

[1]The results of this method are discussed in detail in Chapter 6.

with a beam width of σ derived from the beam FWHM, $\theta = 2\sqrt{2\ln 2}\sigma$. The primary (or main) beam contains the bulk of the signal and is described by, $G_{\rm MB}$. The secondary beam is much wider and lower in amplitude, $G_{\rm SB}$. The relative amplitudes are dictated by the α and β values calculated by Dempsey et al. (2013) and presented in Table 5.1. Together they make up the 2-component beam of the telescope,

$$G(x,y) = \alpha G(x,y)_{\rm MB} + \beta G(x,y)_{\rm SB}, \tag{5.7}$$

where α and β are the relative amplitudes of each component, listed in Table 5.1 alongside the FWHM, θ, of the primary (MB) and secondary (SB) beams. I introduce a secondary beam component into the H13 method, which previously assumed that the secondary component was negligible. This adds complexity to the convolution process as it requires convolution of the data with a normalised Gaussian of the form of both the JCMT beam's primary and secondary components for the alternative wavelength.

By following the form of Equation 5.7, the JCMT beam at 450 μm can be modelled by the MB and SB components as,

$$f_{450} = A\,\left[\alpha_{450}\, f_{MB_{450}} + \beta_{450}\, f_{SB_{450}}\right]. \tag{5.8}$$

Likewise the JCMT beam at 850 μm is

$$h_{850} = B\,\left[\alpha_{850}\, h_{MB_{850}} + \beta_{850}\, h_{SB_{850}}\right]. \tag{5.9}$$

A and B are residual normalisation factors,

$$A = 1/2\pi\left(\alpha_{450}\sigma^2_{MB_{450}} + \beta_{450}\sigma^2_{SB_{450}}\right), \tag{5.10}$$

and

$$B = 1/2\pi\left(\alpha_{850}\sigma^2_{MB_{850}} + \beta_{850}\sigma^2_{SB_{850}}\right). \tag{5.11}$$

Note that the main and secondary beam α, β and σ parameters at 450 and 850 μm are given in Table 5.1.

In order to carry out the two-component beam cross-convolution, the SCUBA-2 850 μm map, h'_{850}, has to be convolved separately with both the main beam and secondary beam components of the corresponding 450 μm model, f_{450}. Likewise for the SCUBA-2 450 μm map, f'_{450}, with the 850 μm model, h_{850}. This convolution is carried out using the Gaussian smoothing kernel GAUSMOOTH (Currie & Berry, 2015). GAUSMOOTH takes input parameters of FWHM per pixel and convolves by a normalised 2-dimensional Gaussian, of the form of Equation 5.6, in order to conserve flux. The normalisation is undesirable and it is therefore necessary to include an additional factor of the form $2\pi\sigma^2$ associated with each model to acquire the four model convolved components,

$$f_{MB_{450}} = 2\pi\sigma^2_{MB_{450}} \cdot \left(h'_{850} * \tilde{f}_{MB_{450}}\right), \tag{5.12}$$

$$f_{SB_{450}} = 2\pi\sigma^2_{SB_{450}} \cdot \left(h'_{850} * \tilde{f}_{SB_{450}}\right), \tag{5.13}$$

$$h_{MB_{850}} = 2\pi\sigma^2_{MB_{850}} \cdot \left(f'_{450} * \tilde{h}_{MB_{850}}\right), \tag{5.14}$$

$$h_{SB_{850}} = 2\pi\sigma^2_{SB_{850}} \cdot \left(f'_{450} * \tilde{h}_{SB_{850}}\right). \tag{5.15}$$

Note that $\tilde{f}$ and $\tilde{h}$ represented the normalised Gaussian models. Each convolved component is then factored back into the full model from Equations 5.8 and 5.9. Incorporating the existing normalisation factors (Equations 5.10 and 5.11) and relative amplitudes that are associated with the model, gives a single expression for each map with two unique normalisation factors,

$$f'_{450} * h_{850} = B\left(2\pi\alpha_{850}\sigma^2_{MB_{850}}\left[f'_{450} * \tilde{h}_{MB_{850}}\right] + 2\pi\beta_{850}\sigma^2_{SB_{850}}\left[f'_{450} * \tilde{h}_{SB_{850}}\right]\right), \tag{5.16}$$

and

$$h'_{850} * f_{450} = A\left(2\pi\alpha_{450}\sigma^2_{MB_{450}}\left[h'_{850} * \tilde{f}_{MB_{450}}\right] + 2\pi\beta_{450}\sigma^2_{SB_{450}}\left[h'_{850} * \tilde{f}_{SB_{450}}\right]\right) \tag{5.17}$$

where $f'_{450}*\tilde{h}_{MB_{850}}$ and $f'_{450}*\tilde{h}_{SB_{850}}$ represents the convolution of the 450 μm data by the normalised 850 μm main beam and secondary beam models, respectively, calculated using the GAUSMOOTH routine (and vice versa for reverse convolution). Expanding out the various normalisation factors in Equations 5.16 and 5.17 gives

$$\begin{aligned} f'_{450} * h_{850} &= \frac{\alpha_{850}\sigma^2_{\mathrm{MB}_{850}}}{\alpha_{850}\sigma^2_{\mathrm{MB}_{850}} + \beta_{850}\sigma^2_{\mathrm{SB}_{850}}} \cdot \left(f'_{450} * \tilde{h}_{MB_{850}}\right) \\ &+ \frac{\beta_{850}\sigma^2_{\mathrm{SB}_{850}}}{\alpha_{850}\sigma^2_{\mathrm{MB}_{850}} + \beta_{850}\sigma^2_{\mathrm{SB}_{850}}} \cdot \left(f'_{450} * \tilde{h}_{SB_{850}}\right), \end{aligned} \tag{5.18}$$

and

$$\begin{aligned} h'_{850} * f_{450} &= \frac{\alpha_{450}\sigma^2_{\mathrm{MB}_{450}}}{\alpha_{450}\sigma^2_{\mathrm{MB}_{450}} + \beta_{450}\sigma^2_{\mathrm{SB}_{450}}} \cdot \left(h'_{850} * \tilde{f}_{MB_{450}}\right) \\ &+ \frac{\beta_{450}\sigma^2_{\mathrm{SB}_{450}}}{\alpha_{450}\sigma^2_{\mathrm{MB}_{450}} + \beta_{450}\sigma^2_{\mathrm{SB}_{450}}} \cdot \left(h'_{850} * \tilde{f}_{SB_{450}}\right), \end{aligned} \tag{5.19}$$

I generate 2-dimensional models of each beam using Equations 5.18 and 5.19 and test that these shapes are consistent with the analytical model described in Equations 5.8 and 5.9. Figure 5.4 demonstrates that the analytical model 450 and 850 μm beams are a good fit to the synthetic beams produced by this routine. I go further and examine the FWHM of the synthetic beams and calculate an effective beam size of 9.84″ and 14.54″ at 450 and 850 μm respectively using,

$$S_{\mathrm{int}} = 2\pi S_{\mathrm{peak}}\sigma^2_{\mathrm{eff}}. \tag{5.20}$$

Note that S_{int} is the integrated flux, S_{peak} is the peak flux and σ_{eff} is the effective standard deviation from which the effective beam size is calculated. These differ from the Dempsey et al. (2013) values (9.8″ and 14.6″) by less than 1% and less than 0.1% at 450 and 850 μm, respectively.

By feeding synthetic 450 and 850 μm 2-dimensional beams profile into the full ratio routine

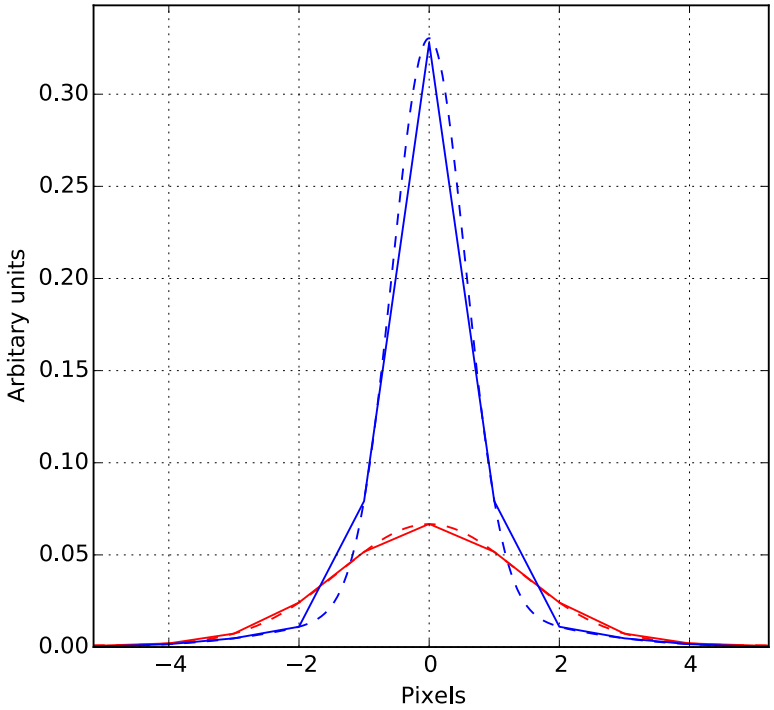

Figure 5.4: The beam shape for the analytical model (dashed line) of the SCUBA-2 450 μm (blue) and 850 μm (red) fit well with model produced by my routine (solid line) that is described in Equation 5.16. Note that the discrepancy in fit is a result of pixel grid size.

I produce a synthetic model of the cross-convolved beams from which I calculate an effective resolution of 19.9″. Additional tests on the ratio method confirm that the 2CB method could successfully calculate the expected ratio for flat maps of a given flux and that the total flux in the real observation is conserved at each stage.

5.3.2 Alignment and collapsing

Following the two-component beam cross-convolution of the SCUBA-2 maps to achieve a common resolution, the convolved SCUBA-2 maps require a common pixel size and dimension before a flux ratio can be produced. Maps of both wavelengths initially have their velocity space (see Chapter 3), or 3-dimension components (if they exist) collapse to unity. The 450 μm fluxes are then regridded onto the 850 μm pixel grid based on the world co-ordinate system (WCS) coordinates of the reference map whilst conserving the total flux. The internal release 1 (IR1) SCUBA-2 maps used in the initial run of the 2CB method had pixel sizes of 4″ at 450 μm and 6″ at 850 μm. Alternatively, IR2 maps use pixel sizes of 2″ at 450 μm and 3″ at 850 μm. Further details on the SCUBA-2 data reduction process in given in Chapter 2.

I investigate three methods for sampling pixels when regridding. The H13 method uses a 'sincsinc' method which samples pixels based on a sinc(πx)sinc(kπx) kernel, where x is the pixel offset from the input pixel position. In some regions the SCUBA-2 data reduction process may leave large areas of negative flux in the final mosaics. The 'sincsinc' method risks incorporating this spurious data into the regridding process and therefore I investigate an alternative method.

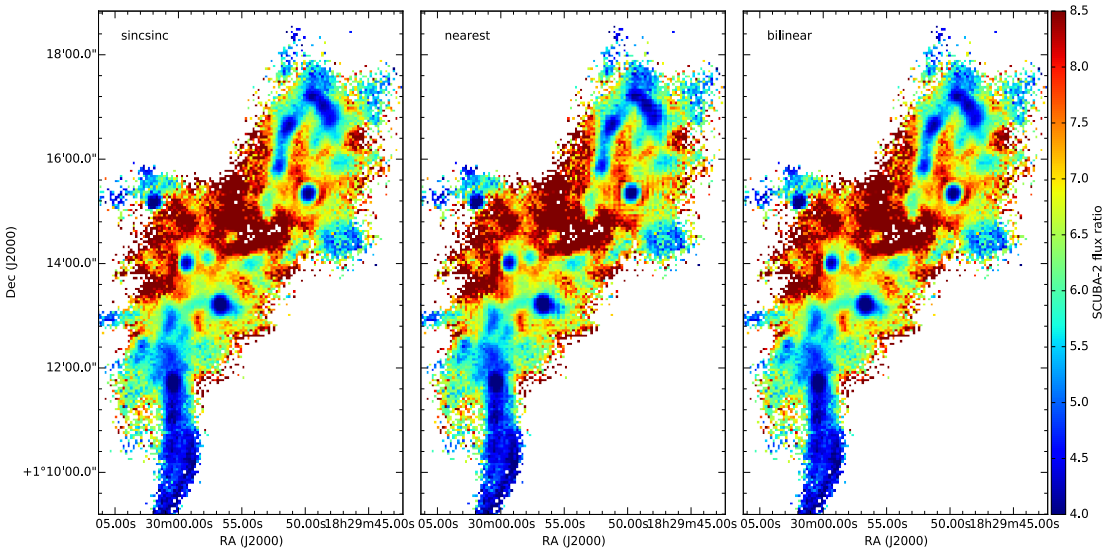

Figure 5.5: The SCUBA-2 flux ratio values in the Serpens Main region calculated by the 2CB method with regridding by 'sincsinc' (left), 'nearest' (middle) and 'bilinear' (right) method. Note how the ratio maps produced with the 'nearest' method contain cross-hatching artefacts around in the inner region of the map that are undesirable. Figure 5.6 further demonstrates the discrepancies between the methods. SCUBA-2 maps for the Serpens Main region are used in this test.

Currie & Berry (2015) outline how the 'sincsinc' method is an intermediary in visual effect between the 'nearest' and 'bilinear' methods, both of which sample a much smaller area. Plots of flux ratios calculated with each method are presented in Figure 5.5 for the Serpens Main region.

Flux ratio maps of the Serpens MWC 297 region used in Chapter 6 were aligned with the 'nearest' sampling method, assigning output pixels based the nearest sampled input pixel. However, I discovered that this method produced gridding artefacts (presented in Figure 5.5) when examining the more substantial Aquila region (presented in Chapter 7), amongst others, and the decision was made to move to a 'bilinear' sampling method that samples from the four nearest input pixels. Figure 5.6 shows how the two methods compare and how the 'nearest' method has a much greater spread around parity. I take the ratio of the two samples and calculate the standard deviation (about a mean value of one) as a measure of spread. 'sincsinc'/'nearest' has a spread of 0.042. By contrast 'sincsinc' is a much tighter fit to the 'bilinear' method and has a narrower spread of 0.007, confirming the impact the 'nearest' method has on introducing the gridding artefacts, presented in Figure 5.5, into the data.

5.3.3 The SNR cut

Water vapour in the atmosphere is primarily responsible for the uncertainty on the flux which makes observing fainter, large-scale structure particularly unreliable. As a result the JCMT GBS was commissioned to primarily investigate small-scale structure comparable to that of the Jeans length. Unreliable large-scale structure is filtered from observations during the SCUBA-2 data

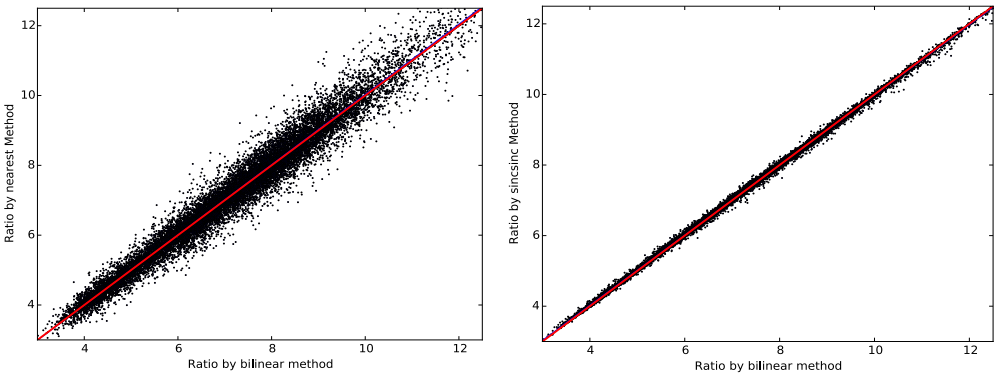

Figure 5.6: The SCUBA-2 flux ratio values of pixels calculated using various methods of pixel alignment sampling. The red line shows the expected parity line whereas the blue line shows a linear regression fit to the data. The left panel shows 'nearest' method compared to 'bilinear' method. The right panel shows 'sincsinc' method compared to 'bilinear' method.

reduction process. A further SNR cut (of the order 5σ) is included to mask those remaining fluxes below this uncertainty level. The SNR cut is applied independently to the 450 and 850 μm maps after the convolution and alignment. The SNR is therefore based on an uncertainty that has been propagated through these steps before it can be applied to the maps. The details of these calculations are given in the following section.

The H13 method uses an automatic clipping routine that uses the SCUBA-2 error array produced in parallel with the SCUBA-2 data. As outlined in Chapter 2, Section 2.6, the SCUBA-2 error arrays may not include additional large-scale structure along the line of sight and are an under-estimate. I upgrade the H13 method to use a noise value calculated from the standard deviation of SCUBA-2 flux density maps (with the astronomical signal masked out) adapting the method used by Salji (2014, 2015). See Chapter 2 for a full description of this method. Figure 5.7 left demonstrates the differences between the SNR clipping method used by Hatchell et al. (2013) and my method as outlined here.

Applying a 5σ cut to mask uncertain regions of large scale structure after the beam convolution can lead to spuriously high values around the edges of our maps where fluxes from pixels below the threshold are contributing to those above, producing false positives. These 'edge effects' are mitigated by clipping but I advise that where the highest temperature pixels meet the map edges these data be regarded with a degree of scepticism.

5.3.4 Propagation of error

In order to calculate a SNR cut, the root-mean-square (rms) noise level, Δ, on the input 450 and 850 μm maps has to be propagated through the various steps in the 2CB method that have been outlined above and in Figure 5.3.

Propagation of map uncertainty through the 2CB beam model of the form of Equations 5.18 and 5.19 follows as the uncertainty of each beam component (with the same value) added in

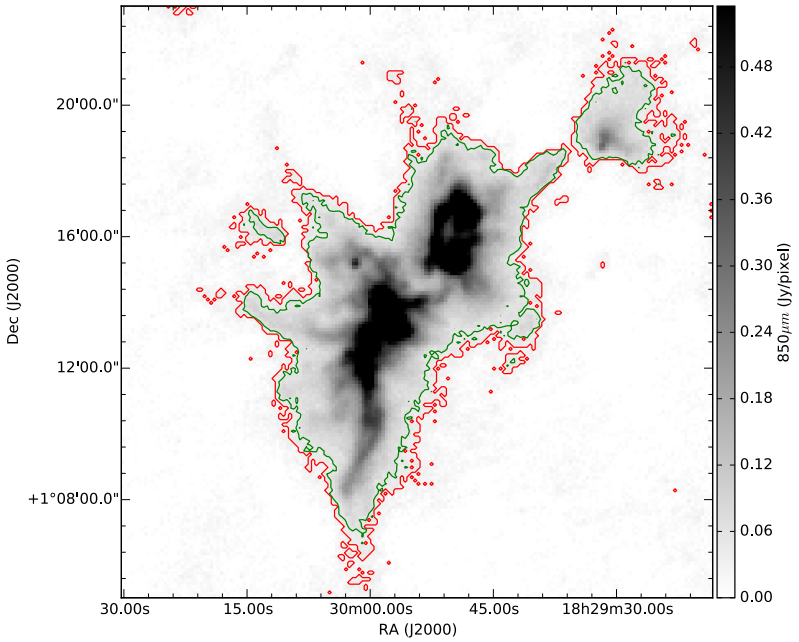

Figure 5.7: The SCUBA-2 850 μm flux density map of Serpens Main. Red contours represent a 5σ cut based on the uncertainty array produced by SCUBA-2. Green contours present a 5σ cut based a single value of uncertainty calculated from the standard deviation of the flux density cropped to remove the astronomical signal (as outlined in Chapter 2, Section 2.6).

quadrature with the relative amplitudes of each beam in the form of,

$$\Delta G^2 = \alpha^2 \Delta G^2_{\rm MB} + \beta^2 \Delta G^2_{\rm SB}. \tag{5.21}$$

The alignment of the 450 μm map adds an additional factor of the ratio of the pixel sizes to the corresponding uncertainty. The uncertainty in flux ratio is then calculated from the sum of fractional errors at each SCUBA-2 band.

To verify these methods I run tests on the propagation of uncertainty using a Monte-Carlo method. The uncertainty calculated for each band forms the basis for the FWHM of a Gaussian distribution from which values are drawn through a random number generator. These synthetic noise maps are run though the 2CB method and the resulting Gaussian distribution is reproduced, from which the propagated uncertainty can be measured. This method was tested with artificial data with the results being consistent with the analytical method outlined above. When tested with several sets of real SCUBA-2 data from the Serpens-Aquila region I found that uncertainty always decreases by a common factor between the input data and the convolved, aligned maps. These are 2.66 at 450 μm and 2.75 at 850 μm. I note that an alternative method could involve directly calculating the rms noise on the convolved, aligned maps prior to the ratio calculations; however, this would involve significant recalibration of the noise calculation method from Chapter 2.

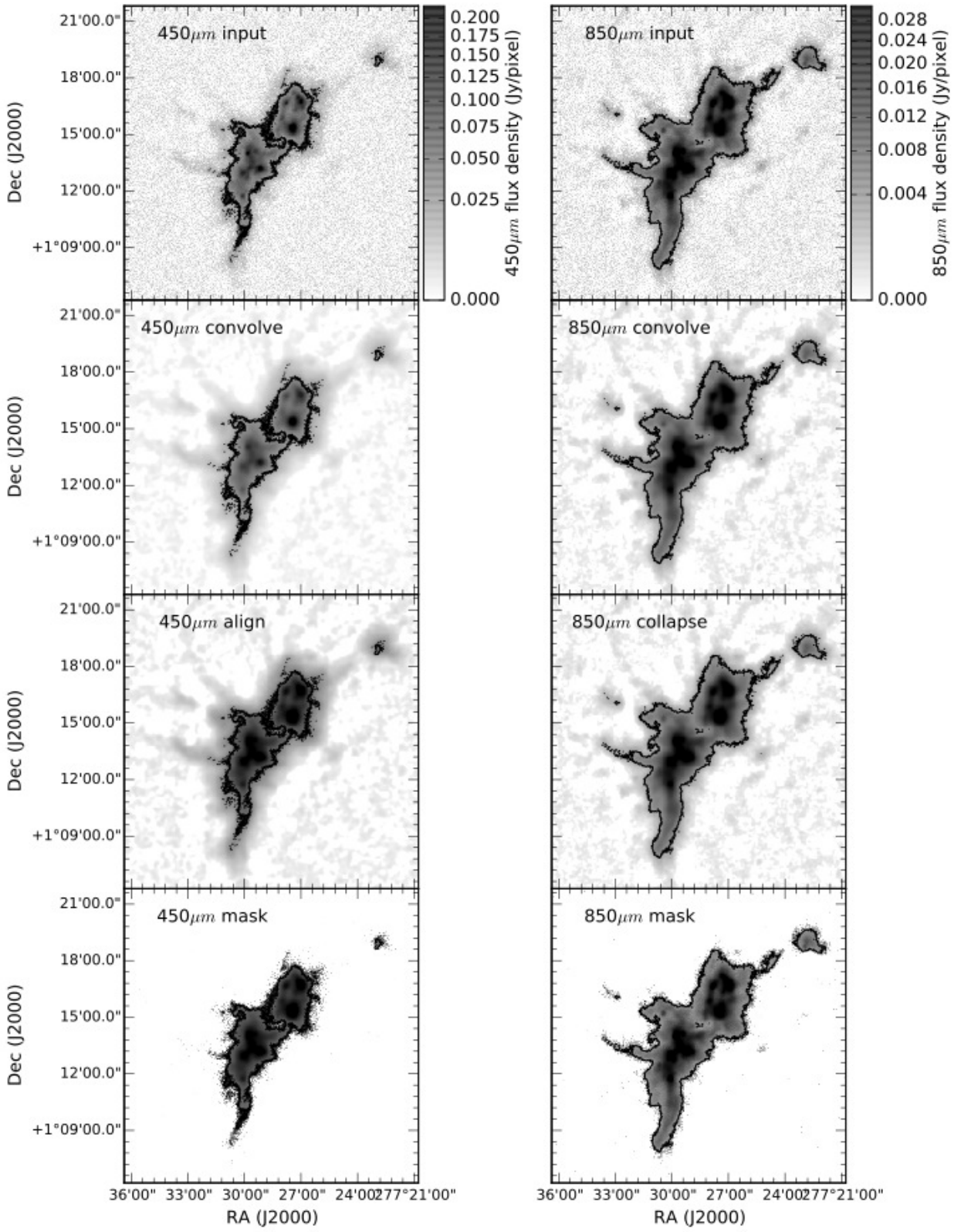

Figure 5.8: Maps of the Serpens Main region at various stages of the 2CB method. Input (top) 450 μm data (left) and 850 μm data (right) is prepared through the convolution (upper middle), alignment/collapse (lower middle) and 5σ masking (bottom) stages before a SUCBA-2 flux ratio map, like those presented in Figure 5.6, can be produced.

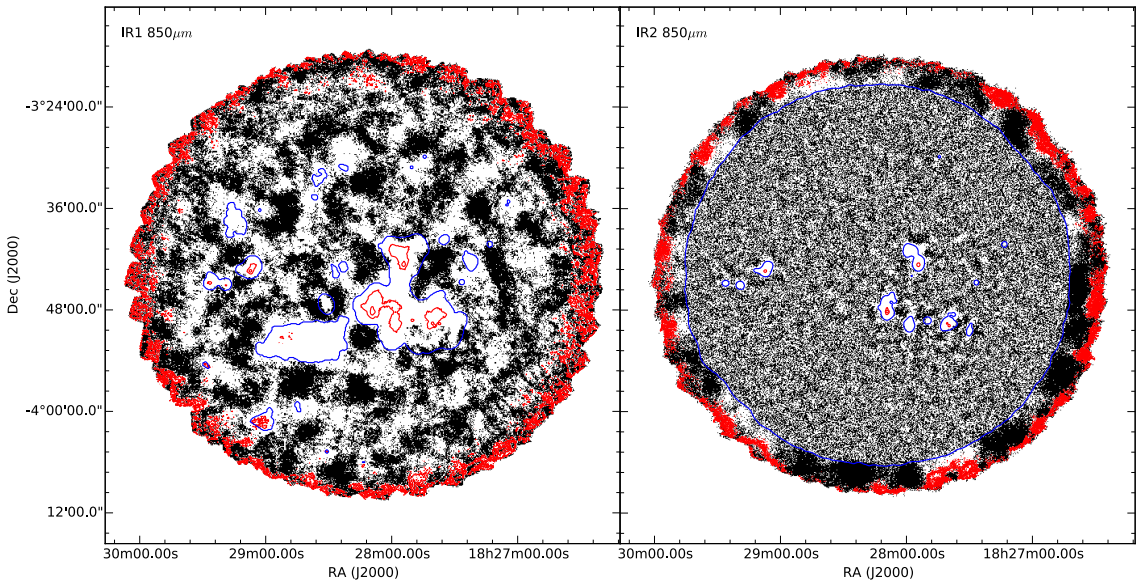

Figure 5.9: SCUBA-2 850 μm observations of the Serpens MWC297 region. The left plot shows the IR1 reduction whereas the right plot shows the internal release 2 (IR2) reduction. Red contours show the 5 and 15σ noise levels of each reduction. The blue contours show the data reduction mask used, a SCUBA-2 and *Hershcel* joint mask in the case of IR1 and solely SCUBA-2 mask in the case of IR2. Black pixels indicate the location of spurious negative data.

5.3.5 Negative pixel reductions

I tested the impact of setting unphysical negative pixels to zero on the flux during the convolution. This was originally included in the H13 method to mitigate negative bowling in early reductions. The Ophiucus North 6 region is used as a test region as it is comprised of a single PONG and has no significant astronomical signal. One version of the region had the negatives set to zero and the other acted as a control. Both were convolved down to a resolution of 20″, comparable to that of the H13 method, and it was found that the mean flux of the noise across the map (excluding the PONG edges) increased by 20% from 0.0314 mJy/pix to 0.0378 mJy/pix as a result of the removal of negative values. In areas where signal is below the SNR threshold this change is unlikely to be significant, but along the border of significant signal additional flux may be added during the convolution, distorting the final ratio. On this basis I can remove this routine from the H13 method. It is worth noting that latter SCUBA-2 reductions have largely removed the excessive areas of negative pixels, as shown in Figure 5.9, further rendering this adaptation obsolete.

5.3.6 Calculating temperature

Given a constant value of β and a ratio of SCUBA-2 fluxes, Equation 5.5 is used to calculate the dust temperature. However, there is no analytical solution for temperature from Equation 5.5 and so temperature values are inferred from a lookup table of given flux ratios. I use the same method used by the H13 method to calculate temperature for the 2CB method. Unlike the value of temperature, T, the uncertainty in temperature can be solved analytically given an uncertainty in

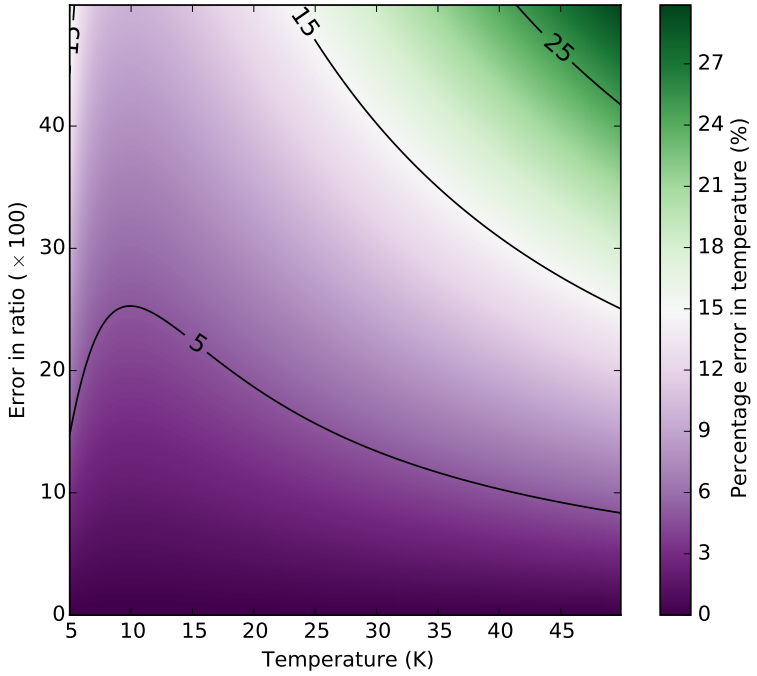

Figure 5.10: The percentage error in temperature plotted as a function of temperature and the error in SCUBA-2 flux ratio.

flux ratio, S_R. Starting with Equation 5.5 and through application of the propagation of uncertainty equation, it is possible to reach an expression for ΔS_R as a function of ΔT,

$$\Delta S_R^2 = \Delta T^2 \left(\frac{\delta}{\delta T} S_R(T) \right)^2 , \tag{5.22}$$

which, through application of the quotient rule, gives,

$$\Delta T = \Delta S_R T^2 \left(\frac{450}{850} \right)^{3+\beta} \left[\frac{\exp\left(\frac{32}{T}\right) + \exp\left(\frac{-32}{T}\right) - 2}{17\exp\left(\frac{-15}{T}\right) + 32\exp\left(\frac{17}{T}\right) - 17\exp\left(\frac{17}{T}\right) - 32} \right]. \tag{5.23}$$

Note that the numerical factors of 15, 17 and 32 arise from the exact result of 450/850 in Equation 5.5. In the 2CB method I replace the arbitrary cut based on the error arrays in the H13 method with a cut of pixels of an uncertainty in temperature of greater than 5%. Figure 5.10 describes how this cut reflects over temperatures ranging from 5 - 50 K and flux ratio error ranging from 0 to 0.5.

5.3.7 Comparison

A comparison between ratios and temperatures calculated using the single beam and two component beam methods is shown in Figure 5.11. The methods are tightly correlated at lower ratios/temperatures whereas there is significant scatter about parity at high values. This scatter likely reflects the uncertainty on the ratio that increases with its value. The scatter is much exaggerated in the temperature plot as a result of the exponential function in Equation 5.5.

A majority of pixels across Serpens Main, East and Aquila regions below a flux ratio of five,

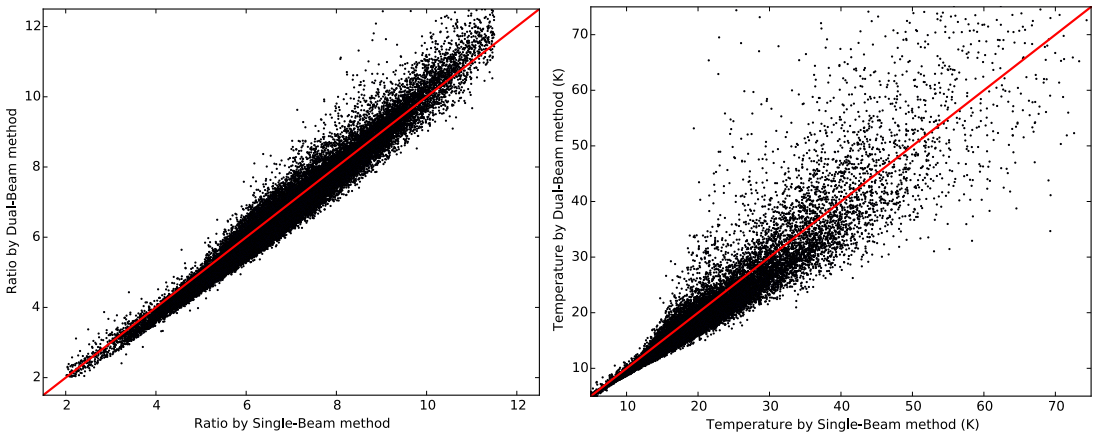

Figure 5.11: The SCUBA-2 flux ratio (left) and temperature (right) pixels values calculated using a single component model of the JCMT beam compared to those calculated using the dual component method. The red line shows a parity line. This plots includes the Serpens Main, Serpens East and Aquila mosaics.

as calculated by the 2CB method, are overestimated by a single-beam (Figure 5.11 left). Figure 5.11 (right) supports this trend, illustrating that a majority of pixels (77%) have lower temperatures when the 2CB method is used, confirming that using a single-beam model in the cross-convolution systematically biases calculated temperatures to be warmer. The inclusion of the secondary beam was found to decrease temperatures by between 5% and 9% in the Serpens MWC 297 region with the coldest regions experiencing the largest drop in temperature and warmest the least.

The root of this effect comes from the difference in relative volume between the main and secondary beam components calculated by Dempsey et al. (2013) and presented in Table 5.1. During the cross-convolution, the peak flux of a single pixel is distributed around its neighbours following the beam models presented in Equations 5.8 and 5.9. At 850 μm 25% of the beam volume is contained in the secondary beam. However, this volume is 40% at 450 μm and as a result the relative amplitude of the main beam at 450 μm is less than at 850 μm.

Nominally, the flux dispersed from an initial pixel to the adjacent pixels by the convolution with a Gaussian should be recouped by the initial pixel from its neighbours through the same process. However, Figure 5.12 describes how when there is a gradient in value between the initial pixel and its neighbours, the flux recouped by the high value pixel will be less than the flux lost. Figure 5.12 shows how, as a result of the relative volume of the secondary beam, that varies between SCUBA-2 bands, the value of the initial high value pixel, post-convolution with a 450 μm beam, is relatively lower than the same pixel convolved with a 850 μm beam. This bias is responsible for lower ratios and temperatures in the 2CB method, and the systematic trend for the brighter regions to experience a greater drop in temperature.

5.4 Kernel method

In this section I outline how the dust temperature is calculated from the ratio of SCUBA-2 fluxes at a common resolution obtained using a convolution kernel, following the methods used by Salji

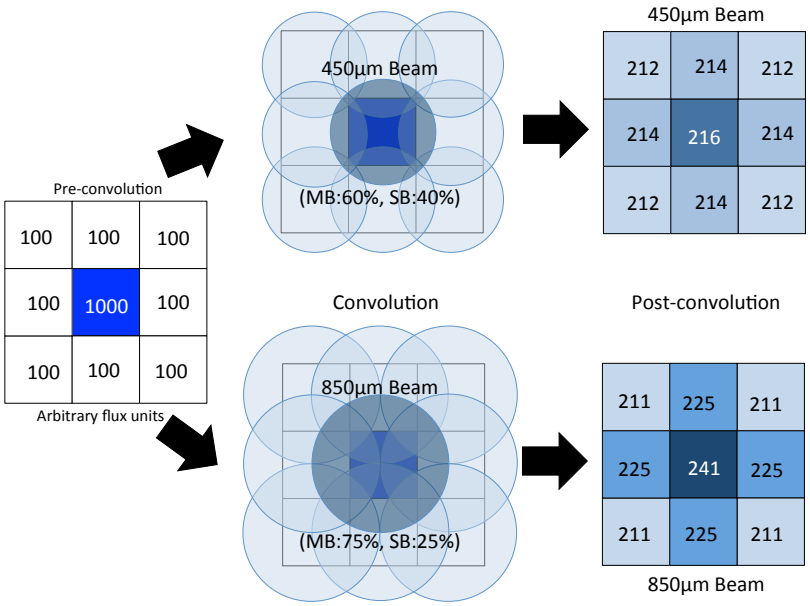

Figure 5.12: A hypothetical schematic describing how the differing shape of the JCMT beam at 450 and 850 μm results in relatively less flux conserved, per pixel, at the brightest points in the convolved SCUBA-2 maps. An example grid of nine pixels (of arbitrary flux units) contains eight faint pixels of value 100 surrounding a bright source of value 1000. This grid is convolved separately by the 450 μm and the 850 μm two-component beam. During the convolution the flux of each pixel is dispersed according to the relative volume fractions calculated by Dempsey et al. (2013) and presented in Table 5.1. The remaining flux is then summed with that from its neighbours. The numbers presented here represent the accurate conservation of arbitrary flux during this process, demonstrating how the flux conserved on the original point source changes due to the beam shape for either SCUBA-2 band. This schematic represents a much simplified version of reality that can explain how using a 2CB method can lead to bright sources appearing relatively cooler than when only a single beam is used. In this example the 450 μm/850 μm ratio of the central pixel decreases by 10%.

et al. (2015). Using the 2CB method from the previous section, I was able to produce maps of dust temperature, with a compromised resolution of 19.9″. In theory, a convolution kernel offers a method by which the 450 μm beam can be convolved to the same shape as the 850 μm beam allowing a theoretical maximum resolution of 14.6″ to be achieved without the need to process the 850 μm map.

5.4.1 Convolution kernel

The JCMT has a complex beam shape at each of the SCUBA-2 bands and producing a kernel to convolve between the two is a non-trivial task. There are two methods to go about this. A Beam-Kernel, presented in Figure 5.13, can be produced from archival beam map observations. This better represents the complex structure of the JCMT beam profile; however, it does not accurately reproduce the JCMT effective FWHM. Alternatively the Model-Kernel, presented in Figure 5.13, is produced from analytical model-beam map PSFs by Pattle (priv. comm.), based on the 2CB model of Dempsey et al. (2013). These models are based on observations of calibrators that simplify the JCMT beam shape into a primary and secondary component (as described in Section 5.3). With updated beam maps from JCMT currently under development I choose to proceed with the Model-Kernel. Note that Figure 5.13 describes how the 2CB Model-Kernel reproduces an effective FWHM of 14.9″ (based on a simple Gaussian fit to the beam) which is comparable to the 14.6″ calculated from the analytical beam models in the previous section. The discrepancy in value reflects how the prototype 2CB model-kernel I use differs from the true JCMT beam shape.

The following explanation of the convolution kernel method follows that given by Aniano et al. (2011) and Pattle et al. (2015). A convolution kernel, $K\,(A \Rightarrow B)$, maps a point spread function A (PSF) onto a PSF B using

$$\mathrm{PSF_B} = K(A \Rightarrow B) * \mathrm{PSF_A}. \tag{5.24}$$

The kernel itself can therefore be defined by Aniano et al. (2011) using the convolution theorem as

$$K(A \Rightarrow B) = \mathrm{FT}^{-1}\left(\frac{\mathrm{FT(PSF_B)}}{\mathrm{FT(PSF_A)}}\right) \tag{5.25}$$

where FT is the fourier transform operator. Division of the higher resolution PSF_A acts to amplify the noise in the system and therefore high spatial frequency, k, filtering is required. This acts in two parts, firstly through the high-pass filter $\phi(k)$,

$$\phi(k) = \begin{cases} 1 & \text{for } k \leq k_\alpha \\ \exp\left[1.82 \times \frac{k-k_\alpha}{k_\alpha - k_\beta}\right]^4 & \text{for } k_\alpha \leq k \leq k_\beta \\ 0 & \text{for } k_\beta \leq k \end{cases}, \tag{5.26}$$

acting on both PSFs between the regimes of $k_\alpha = 0.9k_\beta$ and $k_\beta = 8\pi/\mathrm{FWHM}_{PB}$. Hereafter, $\mathrm{FT}_\phi = \phi(k) \times$FT and FWHM_{PB} is the primary beam effective size of each respective PSF. A secondary low-pass filter, $f_A(k)$, acts to further filter the highest frequencies between the regimes of $k_{L,A} =$

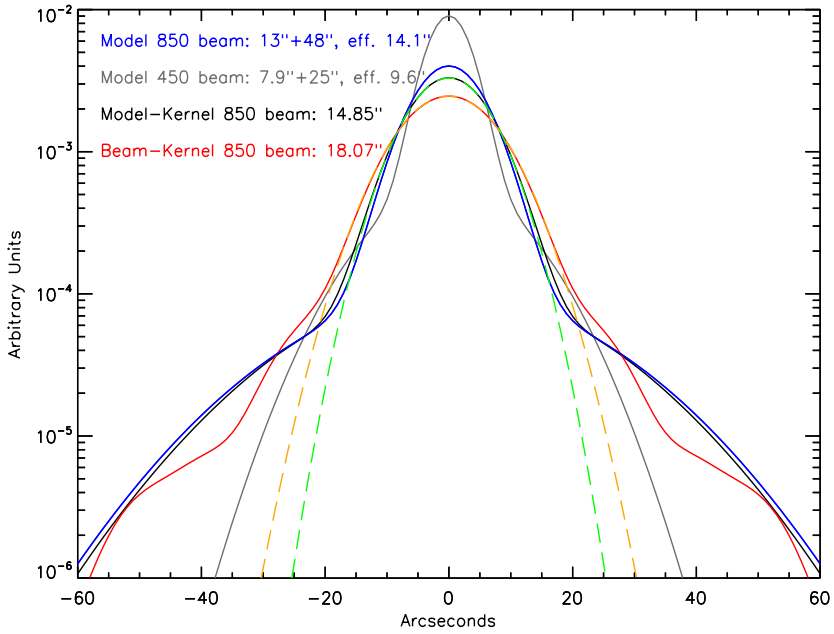

Figure 5.13: Models of 450 and 850 μm used in the 2CB method from Section 5.2 compared to the 850 μm analytical Model-Kernel and observed Beam-Kernel. Green and orange dashed lines show respective Gaussian fits to these kernels from which the effective beam size is calculated. Plot taken from Pattle (priv. comm.).

$0.7k_{H,A}$ and $k_{H,A}$ and takes the form of

$$f_A(k) = \begin{cases} 1 & \text{for } k \leq k_{L,A} \\ \frac{1}{2}\left[1 + \cos\left(\pi \times \frac{k-k_{L,A}}{k_{H,A}-k_{L,A}}\right)\right] & \text{for } k_{L,A} \leq k \leq k_{H,A} \\ 0 & \text{for } k_{H,A} \leq k \end{cases} \tag{5.27}$$

$k_{H,A}$ is the high frequency cut and is defined as $k_{H,A} = \kappa_A \times 2\pi/\mathrm{FWHM_A}$ (FWHM_A is effective beam size of $\mathrm{PSF_A}$, κ_A is an instrument specific constant, typically of order 1.08-1.4, Aniano et al. 2011). Accounting for the high-pass, ϕ(k), and low-pass, $f_A(k)$, filters the convolution kernel given in equation 5.25 can be rewritten as

$$K(A \Rightarrow B) = \mathrm{FT}^{-1}\left(\frac{\mathrm{FT}_\phi(\mathrm{PSF_B})}{\mathrm{FT}_\phi(\mathrm{PSF_A})} \times f_A\right). \tag{5.28}$$

5.4.2 Application of the convolution kernel

I apply the kernel convolution algorithm from Aniano et al. (2011), using the Pattle et al. (2015) adaptation, to SCUBA-2 images. I summarise the implementation here. Full details of the method are summarised in those authors' papers. The flowchart in Figure 5.3 (right) describes the convolution kernel method and compares those steps to the 2CB method.

Prior to running the convolution process presented in Equation 5.24, both the SCUBA-2 450 μm map and bespoke kernel have to undergo a degree of manipulation to make them com-

patible. Firstly bad pixels are temporarily replaced with values interpolated from the existing data using a simple Gaussian. The map and kernel are then aligned and regridded onto the same pixel scale before a PSF routine centres the kernel on the map (Aniano et al., 2011). The two images are entered into a convolution routine that converts each image to Fourier space and finds their product, before returning the inverse Fourier transform as the newly convolved map.

There are two practical routes to go about implementing the Aniano et al. (2011) routine into my existing method. The most thorough method involves directly reproducing the Kernel pre-processing within the 2CB method in place of the two-component cross-convolution. However, I had access to the throughly tested and publicly available script developed by Aniano et al. (2011) which I opted to implement this wholesale into my existing method. This saved a significant amount in time and preserved the published documentation and support network for the kernel in the event of problems.

A small number of minor adaptations were required to allow the various routines to run smoothly together. One such example is that the Aniano et al. (2011) routine was configured to read the pixel scale from the header of the input map. However, the header format of the SCUBA-2 data was incompatible and therefore a kernel pixel size of 4″ was manually hard-coded into the Kernel-convolution method. Testing with constant flux maps confirmed that flux is conserved and that a correct ratio is calculated with this value.

Testing the effective beam size of the kernel-convolved 450 μm map required producing two-component beam models at 450 and 850 μm using the 2CB method described above. The 450 μm beam model was then run through the Kernel-convolution method before being compared to the 850 μm beam. A measured FWHM of 14.9″ was recorded for the Kernel-convolved beam by examining the beam size at half peak magnitude. This value is consistent with the Model-Kernel value produced by Pattle (priv. comm.) and presented in Figure 5.13.

It is important to note here that these effective beam sizes were produced from beam models projected on to empty SCUBA-2 maps with pixel sizes of 2″ at 450 μm. Running the convolution kernel on larger grid sizes was found to run into alignment problems when the kernel was re-centred, as illustrated in Figure 5.14. This subroutine requires finding the position of the image maximum, i.e. the centre of the PSF, and aligning the kernel to it. On a 2″ grid this routine can effectively identify a single maximum pixel but on a 4″ grid it cannot and instead returns the combined peak of four adjacent pixels. The Kernel-convolution method was tested with the IR1 reductions of the Serpens MWC 297 region (Figure 5.14) which demonstrated how a 4″ pixel grid results in a systematic shift of 2×2 pixels. This problem with the centre PSF routine is systemic to the Aniano et al. (2011) method and cannot be removed without rewriting that routine. Practically this means the current implementation of the Kernel-convolution method is not compatible with pixel sizes of 4″ or larger.

5.4.3 Flux ratio and dust temperature maps

As with the 2CB method, post-convolution the maps are prepared to ensure a common pixel grid and masking at a 5σ level. The Kernel-convolution method results in a SCUBA-2 flux ratio map with a resolution of 14.9″. This process is not an exact replica of the 850 μm map resolution

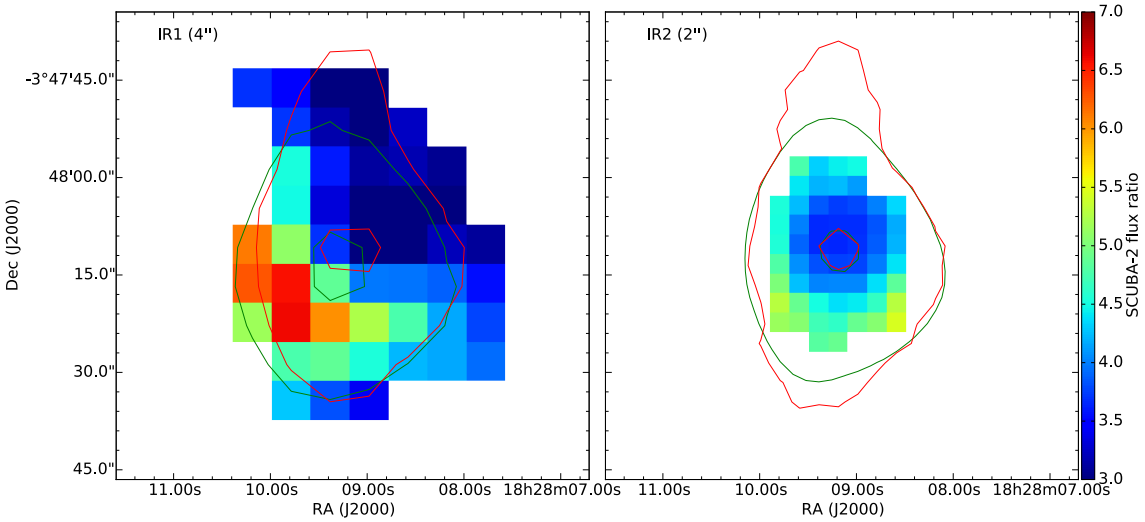

Figure 5.14: SCUBA-2 flux ratio maps of SMM1 in Serpens MWC 297 region IR1 (left) and IR2 (right) reductions produced using the Kernel-convolution method. Contours show the convolved 450 μm (green) map compared to the unaltered 850 μm (red) map. Levels highlight how the centre-psf routine in the Aniano et al. (2011) method is causing a misalignment with a grid size of 4″ that is not present with the smaller grid size of 2″.

as I am only using a model beam kernel, as opposed to a kernel derived from observed beam maps that would more accurately resemble the JCMT beam. How the input maps are altered by each stage of the process is demonstrated in Figure 5.15. For the bulk of this process the 850 μm input map remains unchanged whilst the 450 μm map undergoes the convolution stage, via the Model-Kernel.

Flux ratio maps are converted to temperature maps following the same method outlined in the previous section. Supplementary to these plots I also produce maps of SCUBA-2 spectral index, following Equation 5.1, to allow for a more detailed examination of the relationship between α and β. See Chapter 7 for more discussion on this topic.

5.4.4 Propagation of error

In the 2CB method I calculated the noise propagated through the flux ratio algorithm analytically; however, this treatment of uncertainty is not trivial when the convolution kernel is included in the method and therefore I calculate uncertainty through a Monte-Carlo process, as described in Section 3.4. As the 850 μm map does not undergo any convolution or alignment, its uncertainty remains unchanged. The 450 μm uncertainty decreases by a factor of 1.84 through the kernel and alignment process (given SCUBA-2 IR2 reduction grid sizes of 2″ and 3″ at 450 μm and 850 μm, respectively).

As in Section 3.5, Equation 5.23 is used to propagate the uncertainty in the ratio map into an uncertainty on the temperature. I find that the ratio uncertainties produced by the kernel method of Aniano et al. (2011) are systematically higher than those produced by the 2CB method used in Chapter 6 by a factor of approximately two. Increasing resolution inevitably increases

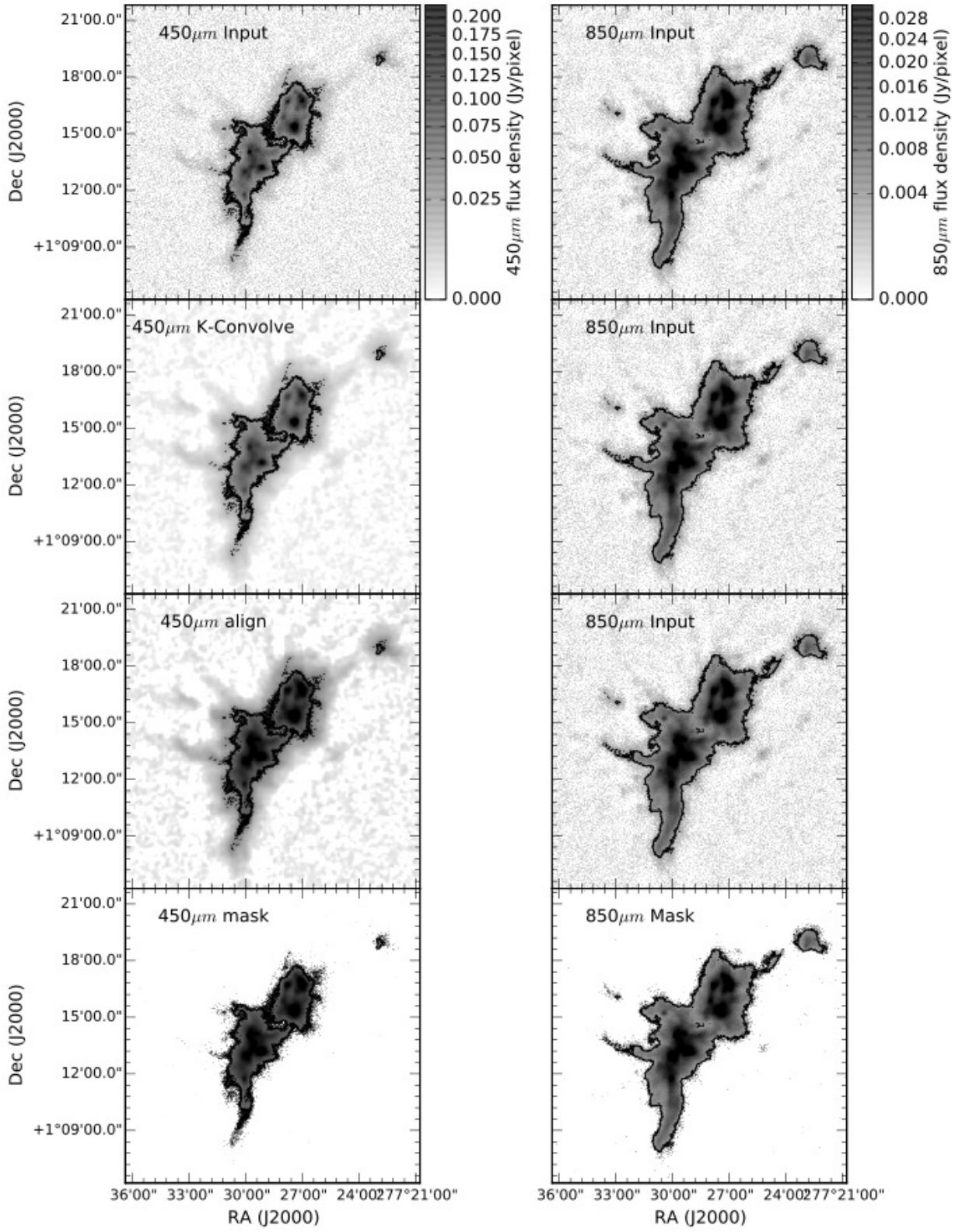

Figure 5.15: Maps of the Serpens Main region at various stages of the Kernel-convolution method. Input (top) 450 μm data (left) and 850 μm data (right) is prepared through the convolution (upper middle), alignment (lower middle) and 5σ masking (bottom) stages before a SCUBA-2 flux ratio map, like those presented in Figure 5.6, can be produced.

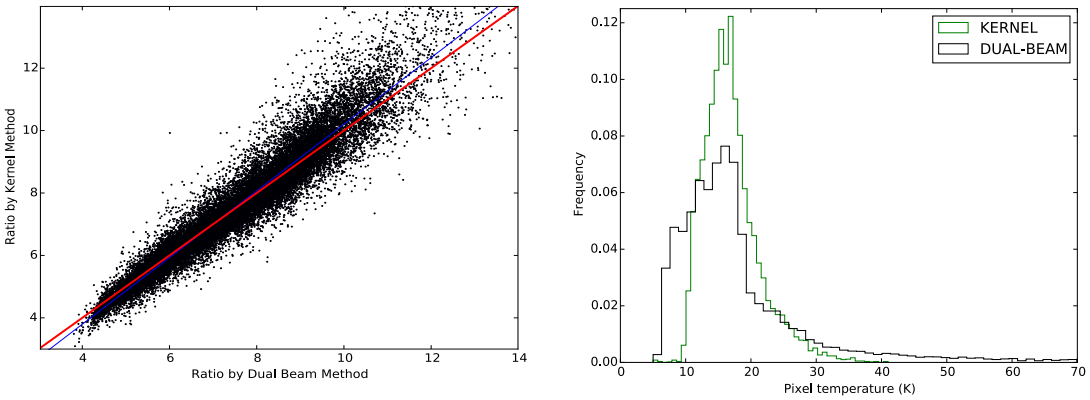

Figure 5.16: Left) a comparison of the pixel flux ratio values (from Aquila, Serpens Main and East regions) from the 2CB and kernel convolution methods. The blue line shows a linear regression fit to the distribution with a Pearson-correlation coefficient of 96% to parity (red line). Right) the normalised distribution of pixel temperatures in Serpens Main using the 2CB and Kernel-convolution methods (as labelled)

uncertainty as the beam area samples fewer data points. The ratio of beam areas between the Kernel-convolution method and the 2CB method is 1.9, consistent with the observations. Furthermore, because the 850 μm map no longer under goes a degree of smoothing, individual noise spikes from this map may also be preserved.

Whereas the 2CB method uses a temperature cut based on 5%, the Kernel-convolution method cuts temperature pixels where the fractional error is greater than 34%. This less stringent criterion is effective at removing uncertain edge pixels (a known problem with the 2CB cross-convolution method).

5.5 Comparing ratio methods

Throughout this chapter I have discussed how I have developed the H13 method, used by Hatchell et al. (2013) to calculate dust temperatures from the ratio of SCUBA-2 fluxes, into two separate methods designed to improve the accuracy of the temperatures calculated. The 2CB method uses a four-component cross-convolution to achieve a common 450 μm/850 μm resolution of 19.9″ before applying a 5% cut to the temperature results. The Kernel-convolution method uses a model-beam convolution kernel developed by Pattle (priv. comm.) and, following the implementation of Aniano et al. (2011), is able to achieve an improved resolution of 14.9″; however, this method compromises on the uncertainty, due to lower sampling area across a beam, and as a result applies a less stringent cut criteria of approximately 34% to the results.

Figure 5.16 (left) shows that, despite the increase in uncertainty, the absolute values of the dust flux ratios calculated by the two methods are found to be comparable with a Pearson-correlation coefficient of 96%. The mean pixel temperature in each method are 17.0 K and 17.7 K (across the Aquila, Serpens Main and East regions using the Kernel-convolution and 2CB methods respectively). However, the range of pixel temperatures in the 2CB method, as illustrated in Figure

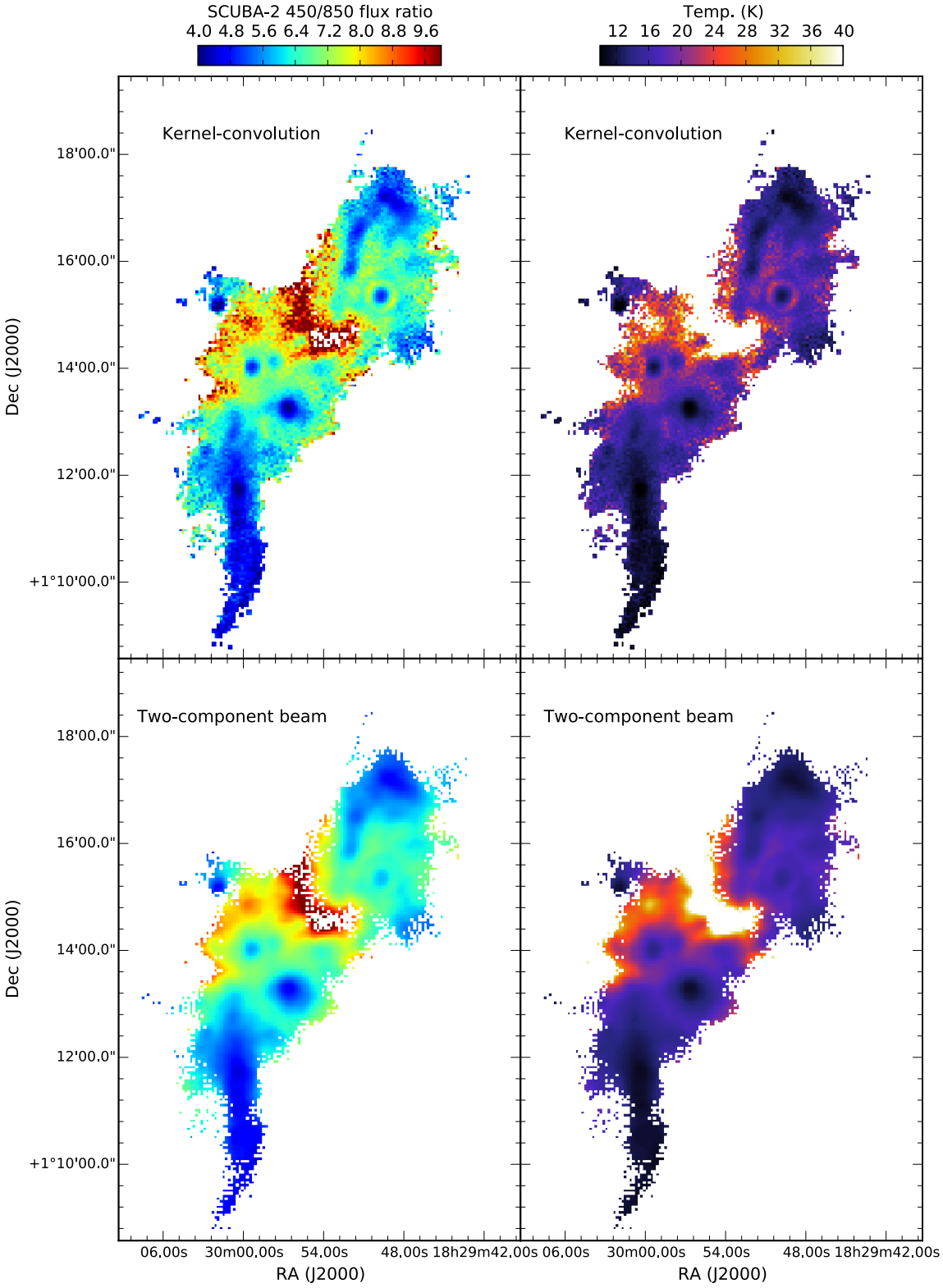

Figure 5.17: Comparison of the flux ratio and dust temperature maps of Serpens Main using the Kernel-convolution method (top) and 2CB method (bottom).

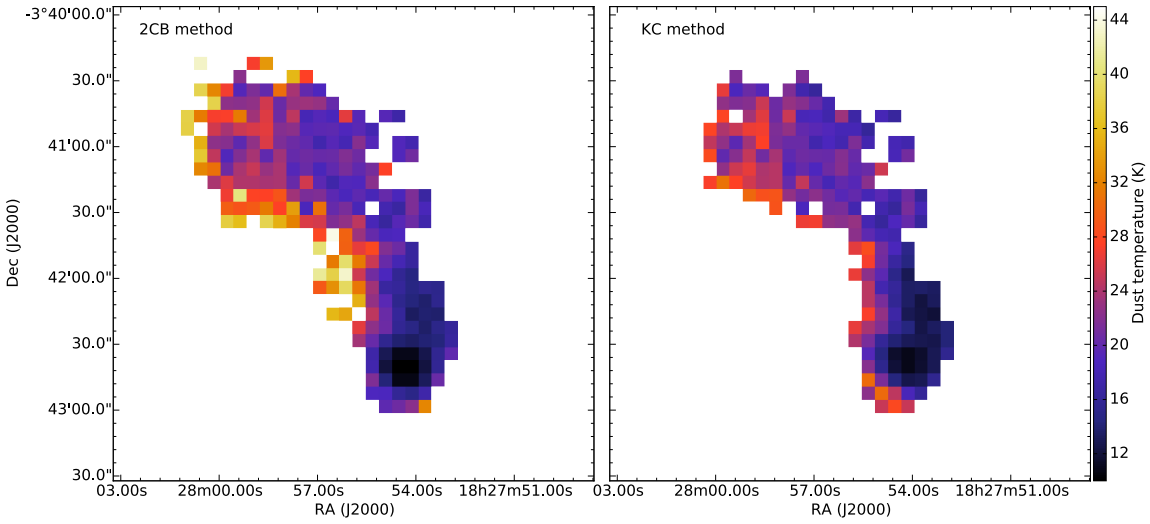

Figure 5.18: SCUBA-2 temperature maps of a cloud in the Serpens MWC 297 region demonstrating high temperature 'edge effect' artefacts that are present in the 2CB method (left), and how these have been reduced in the Kernel-convolution method (right).

5.16 (right), covers five to 60 K, far greater than those in the Kernel-convolution method which cover nine to 35 K. This greater spread in temperatures is reflected in the linear regression fit in Figure 5.16 (left) and confirms that the lower resolution 2CB method systematically under- and over-estimates at lower and higher flux ratios, and therefore temperatures, respectively.

The Serpens Main region is mapped in both flux ratio and dust temperature in Figure 5.17 for both the Kernel-convolution and 2CB methods. Note how in both cases the flux ratio map has greater coverage, with many of the excessively high value pixels being cut by the during the production of the temperature map. The varying area in the temperature map reflects the varying cut criteria described in the previous sections. The cross-convolution and lower resolution of the 2CB method is immediately obvious with these maps appearing considerably more smooth than the Kernel-convolution method results which retain a degree of pixelisation that is present in the original, and unaltered data.

Both methods show similar areas of heating in the Serpens Main region that may be attributed to the presence of molecular outflows (Davis et al., 1999) or protostellar heating. Despite a greater than 5% error cut in temperature the 2CB method, regions of excessive heating along a number of the edges are present. These are candidates for the 'edge-effects' eluded to in Section 5.3.2. Figure 5.16 (right) demonstrates how pixels with suspiciously high temperatures (greater than 40 K) are retained in the 2CB method, but are cut by the Kernel-convolution method. The visual effect of this larger cut is illustrated in Figure 5.18 for the Serpens MWC 297 region.

I also note a bright source that manifests itself as a cold core in the northern cloud of Serpens Main (Figure 5.17, 18:29:49.8 +01:15:20.4) appears to be surrounded by a ring of warmer material that is present in both the 2CB and Kernel-convolution method. I believe this to be an artefact of the convolution process and not real. One possible solution could be that this is caused by a mismatch in beam size between 450 and 850 μm, though the systematic presence of this

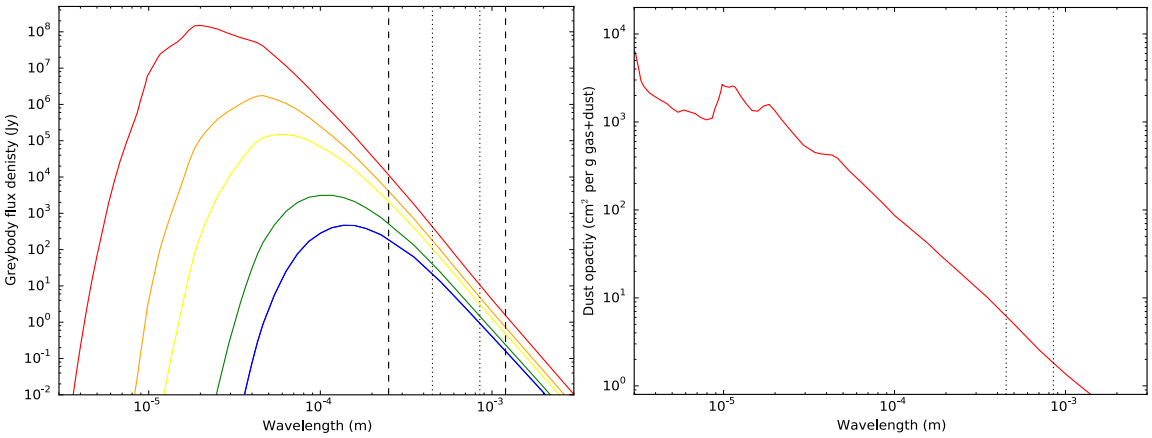

Figure 5.19: Opacity modified, blackbodies plotted for a range of temperatures (descending red to blue, 100, 50, 35, 20 and 15 K) demonstrating the extent of the Rayleigh-Jeans tail at longer wavelengths. The location of SCUBA-2 450 and 850 μm bands are plotted in dots whereas the *Herschel* 250 μm and MAMBO 1.2 mm bands are marked in dashes. The OH5 model of dust opacity, used to calculate SEDs in the left figure, and presented as a function of wavelength in the right figure, resembles a power law at long wavelengths but this breaks down at shorter wavelengths and is responsible for the irregularities observed in those regions (Ossenkopf & Henning 1994, Pollack et al. 1994).

artefact in both methods suggests a deeper issue. At the present time I do not have a solution to this problem; however, these ring artefacts are only associated with the brightest sources in JCMT GBS and to date less than five examples of this feature have been noted and therefore I conclude it will not have a significant impact on the majority of temperature results.

5.6 Comparing temperature methods

5.6.1 Alternative flux ratio

A significant draw back of the three SCUBA-2 ratio methods outlined has been in the 5σ cut to the final temperature maps, often limiting information to only the brightest parts of the star forming complex. The high noise level on the 450 μm maps due to extra susceptibility to water vapour in the atmosphere leads to a lower SNR, making this band the limiting factor in temperature coverage. One potential alternative is to explore using an alternative submillimeter wavelength with better SNR, in place of 450 μm.

One alternative is the Institute for Radio Astronomy in the Millimeter Range (IRAM) 1.2 mm observations with MAx-Planck Millimeter BOlometer array (MAMBO). IRAM is a ground based telescope with a dish diameter of 30 m that can achieve a 13″ effective beam width, comparable to the JCMT (Bertoldi et al., 2000). Maury et al. (2011) carry out observations of the Aquila region that have the potential to be utilised in conjunction with SCUBA-2 850 μm for the purposes of producing maps of dust temperature.

A significant drawback of using longer wavelengths like MAMBO comes from the reliability of Equation 5.5 as both 1.2 mm and 850 μm will lie increasingly on the Rayleigh-Jeans tail at

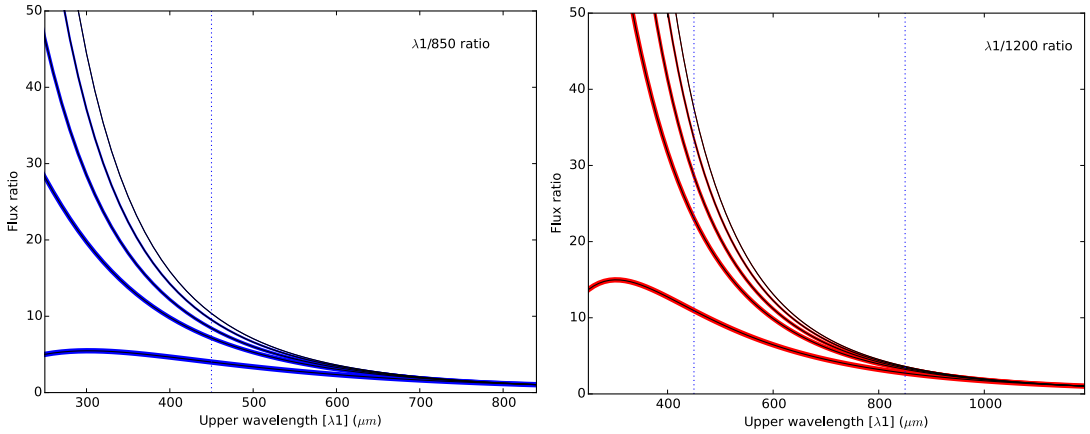

Figure 5.20: Flux ratio calculated using Equation 5.5 for a temperatures 10 (thickest), 20, 30, 50 and 100 K (thinnest). The left plot (blue) shows the ratio for a range of wavelengths, $\lambda 1$, paired with 850 μm. The right plot (red) shows the ratio for a range of wavelengths, $\lambda 1$, paired with 1200 μm. The SCUBA-2 bands are marked as dotted lines.

high to medium temperatures, as show in Figure 5.19. No temperature information is contained in the gradient of the Rayleigh-Jeans tail and therefore the ratio method cannot be used to measure temperature when both wavelengths lie on it. The convergence of flux ratio is shown in Figure 5.20 for a range of temperatures, confirming that 850 μm/1.2 mm ratio would not be sensitive to temperatures above 20K, whereas the SCUBA-2 450 μm/850 μm ratio is sensitive up to 50 K. It is interesting to note that the 450 μm/1.2mm ratio is able to discriminate temperatures up to 100 K and could therefore be used to investigate heating in areas where the 450 μm/850 μm ratio is unreliable.

There is potential for incorporating MAMBO data into the flux ratio methods I have discussed with the aim of studying low temperature (less that 20 K) star formation, with the benefit that the improved SNR at 1.2 mm would allow for extended coverage into regions where the SCUBA-2 450 μm observations are not significant. Robustly accounting for variations in data reduction, large-scale structure reconstruction and the calibration uncertainties for the two telescopes are non-trivial tasks that go beyond the scope of this thesis.

The risk of measuring temperature in the Rayleigh-Jeans tail becomes less of a problem when shorter wavelengths are used as the numerator of the flux ratio, allowing for larger dust temperatures to be calculated (Figure 5.20). However, at shorter wavelengths extinction and noise due to water vapour becomes increasingly more of a problem. As a result, instruments that observe at wavelengths shorter than 450 μm are almost exclusively limited to orbital observatories and as a result have significantly worse resolution than the JCMT.

5.6.2 Multiple cloud components

By sampling only two wavelengths and fitting a single temperature opacity modified blackbody, the flux ratio method makes the assumption that only a single cloud component is being observed along the line-of-sight at any one time. In complex regions this assumptions this may not be

accurate, making the inability to discern multiple cloud components with varying temperature along the l.o.s a potential limitation of this method.

I design a series of tests to determine what influence a hypothetical 'hot' cloud of a given temperature and mass would have on the observed temperature of a typical 'cold' clump of ISM, dust temperature 15 K. I construct a model opacity modified black body SED of the two cloud components using,

$$S_\nu = \frac{B_\nu(T_d) M \kappa_\nu}{d^2}, \tag{5.29}$$

where M is mass and d is the distance to the source. Opacity is modelled as power law at submillimeter wavelengths, as described by Equation 5.4 and illustrated in Figure 5.19 (right). Mass is related to the column density, N_{H_2}, of the ISM integrated over an area, A. I set the mass of the hot cloud as a fraction of the target cold cloud mass and compare the two model SEDs, as shown in Figure 5.21 (left). I calculate the flux of the combined SEDs at the SCUBA-2 bands and calculate how the ratio of the SCUBA-2 fluxes changes with the cold/hot cloud mass fraction (15 K, Figure 5.21 right). The greater the mass fraction and the higher the temperature of the hot cloud component, the greater the observed temperature for both bodies increases. Given a typical clump of temperature 15±2 K, an increase in flux ratio of 8% is required to observe a significant (±2 K), systematic increase in temperature due to an additional cloud. I find that a 3% mass fraction of a 50 K hot cloud is sufficient to produce this change (Figure 5.21 right).

In general, warm cloud components with temperatures less than 30 K require a mass fraction of greater than 10% to achieve a significant increase in the observed temperature. Alternatively, hot clouds with temperatures greater than 100 K require a mass fraction less than 1% to achieve this. Given the exceptional heating required to reach these higher temperatures, this latter scenario need only be considered when OB stars lie in close proximity to the target. The SCUBA-2 flux ratio method is therefore considered a reliable measure of a cooler target cloud, presuming that the target dominates in mass (95% or greater) over any warmer (35 K or less) components.

5.6.3 SED fitting

The SCUBA-2 flux ratio method (Equation 5.5) discussed in this chapter is just one method of extracting dust temperature from a thermal continuum. A popular alternative is spectral energy distribution (SED) fitting which can incorporate many wavelengths including those shorter or longer than the SCUBA-2 bands. This method has been widely used to derive both dust temperatures and β from *Herschel* (Griffin et al., 2010) SPIRE and PACS bands (Shetty et al. 2009, Bontemps et al. 2010 and Gordon et al. 2010).

The full SED fitting of submillimeter wavelengths has been widely used by Bontemps et al. (2010), Könyves et al. (2010) and Könyves et al. (2015) to process *Herschel* data to construct low-resolution temperature maps for the Aquila and Polaris regions through fitting an opacity-modified blackbody to dust continuum fluxes. *Herschel* data offer five bands of FIR and submillimeter observations and low noise levels; however, it lacks the high resolution of the JCMT which can study structure on a scale of 9.8″ (450 μm) and 14.6″ (850 μm; Dempsey et al., 2013) as opposed to 25.0″ and larger for 350 μm or greater submillimeter wavelengths.

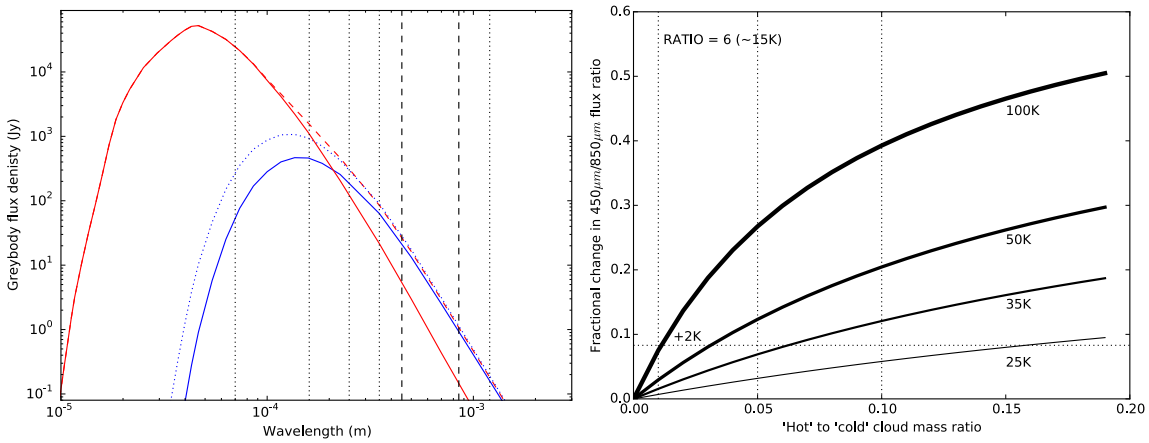

Figure 5.21: Left) model opacity-modified blackbody SEDs for a cold (blue, 15 K) cloud and a hot (red, 50 K) cloud at 3% of the mass of the cold cloud. The red dashed SED represents the two cloud components combined and the blue dotted SED represents how the combined SED resembles a single 17 K cloud at SCUBA-2 450 and 850 μm bands (dashed vertical lines). The *Herschel* 70, 160, 250 and 350 μm bands, and the MAMBO 1.2 mm band are also marked (dotted vertical lines). Note how the 50 K component dominates the fluxes at 70 and 160 microns. Right) the fraction of flux ratio increase when the flux from a 15 K cloud is combined with that from a 25 (thinest), 35, 50 and 100 K (thickest) cloud of a given mass fraction of the former. Dotted vertical lines mark 1, 5 and 10% mass fraction for reference, and dotted horizontal line marks an 8% increase in flux ratio, equivalent to a temperature increase of 2 K.

SCUBA-2 bands have been incorporated along side *Herschel* bands to improve completeness at longer wavelengths by Sadavoy et al. (2013) and Chun-Yuan Chen et al. (2016). The SCUBA-2 data reduction process explicitly filters out large-scale structure that may trace lower density, warmer material so that dense cores and filaments can be targeted. This large-scale structure is retained in *Herschel* observations. Sadavoy et al. (2013) outlines additional spatial filtering and corrections to be made to *Herschel* images so that they can be combined with SCUBA-2 images.

SED fitting can be limited by the completeness of the spectrum, the emission model and local fluctuations of β (Bontemps et al., 2010; Könyves et al., 2010). Incorporating additional wavelengths requires all the data to take the lowest common resolution. Using all available *Herschel* bands requires a common resolution of 36.3″ associated with the 500 μm band. At this resolution, analysis is limited to a general overview of temperatures in the region. The 14.6″ resolution achieved using the SCUBA-2 450/850 μm flux ratio method (as outlined in Section 5.4) allows temperatures to be studied down to the length scale of a protostellar core under the assumption of constant β. By omitting the low resolution *Herschel* 350 and 500 μm bands it might be possible to produce temperature maps that preserve a resolution comparable to the JCMT. The loss of completeness of the spectrum could be in part mitigated for by the inclusion of the longer wavelength MAMBO observations.

By using a more complete spectral range, SED fitting can discern multiple temperature cloud components in a way that the ratio method cannot. Should a target contain both hot (~50 K

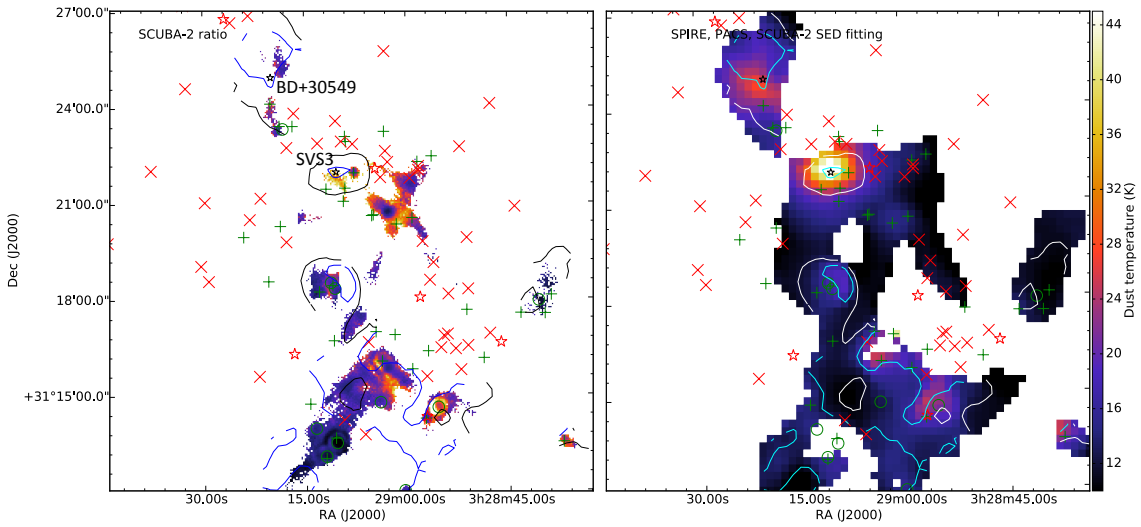

Figure 5.22: Dust temperature maps of the Perseus NGC 1333 region. Left) shows the map produced using the SCUBA-2 Kernel-convolution flux ratio method. Right) shows the map produced by Chun-Yuan Chen et al. (2016) using SED fitting of *Herschel* 160, 250, 350 and 500 μm and SCUBA-2 850 μm bands. Markers show YSOcs from the Dunham et al. (2015) c2d+GBS catalogue (green circles = Class 0, green plus = Class I, red cross = Class II, red star = Class III and black star = evolved OB stars). Contours show the Chun-Yuan Chen et al. (2016) β map produced in parallel with the dust temperature (blue/cyan = 1.6, black/white = 2.0).

or greater) and cold (~15 K) cloud components, emission from the hot dust can dominate emission at shorter wavelengths (70 and 160 μm) at even a small fraction of the mass of the cold component, as illustrated in Figure 5.21 (left). As a result it is common place to omit wavelengths less than 100 μm from SED fits to pre/protostellar objects. Furthermore, as was discussed Chapter 2, Section 4, in regions with OB stars, for example Aquila, emission in the shortest wavelengths are often saturated as a direct result of emission from high temperature dust, rendering flux extraction impossible.

Fitting only the wavelengths longwards of the SED peak will preferentially sample the colder cloud components that dominate in mass (Shetty et al., 2009). The SCUBA-2 450/850 μm flux ratio is well positioned on the SED to measure the temperature of these colder components for the purposes of calculating their Jeans masses. The flux ratio method also provides an independent comparison to the temperatures derived from the SED fitting method. In Chapter 7 I directly compare the dust temperatures calculated by the Kernel-convolution method to those calculated using SED fitting carried out by Maury et al. (2011) and Könyves et al. (2015).

5.6.4 Fluctuations in β

A fundamental limitation of the flux ratio method is the degeneracy between dust temperature and dust opacity spectral index, β. As discussed in Section 5.1.1, I set β to a constant value of 1.8, consistent with observations of the extended ISM (Stutz et al., 2010; Juvela et al., 2015). The JCMT GBS observes star formation covering the pre-stellar to Class II stages. β is considered to

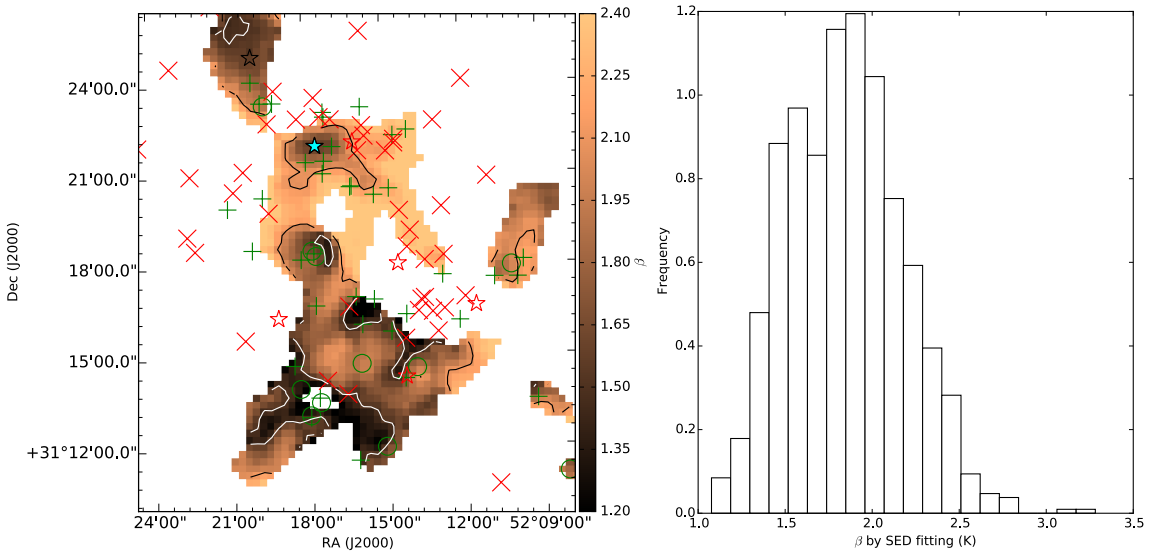

Figure 5.23: Left) the Chun-Yuan Chen et al. (2016) β map for the Perseus NGC 1333 region. YSOcs are marked following the notation in Figure 5.22. White and black contours represent a level of $\beta = 1.5$ and 2.1, respectively. Right) a histogram of Chun-Yuan Chen et al. (2016) β values (across the whole of Perseus West).

evolve in parallel with the stellar environment and as a result the use of a single constant value may result in inaccurate temperatures being calculated in specific environments.

Sadavoy et al. (2013) describe how SED fitting to *Herschel* data and the longer wavelengths of SCUBA-2 can be used to calculate both dust temperature and β. Chun-Yuan Chen et al. (2016) use *Herschel* 160, 250, 350 and 500 μm and SCUBA-2 850 μm bands to produce maps of temperature and β in the Perseus NGC 1333 region (36.3″ resolution) and these are presented in Figures 5.22 and 5.23. I compare these temperature maps to those calculated from SCUBA-2 450 and 850 μm (14.9″ resolution) using a constant β of 1.8. The low SNR of the 450 μm curtails coverage of the more extended regions when using the ratio method but temperatures for most Class 0 sources are calculated for both methods (Figure 5.22).

There is agreement between my results and Chun-Yuan Chen et al. (2016)'s regarding evidence of heating associated with the primary B stars SVS 3 and BD +30 549. However, Chun-Yuan Chen et al. (2016) observe a drop in β to values around 1.5 at these locations. Referring to Figure 5.1 (right), I observe that the SCUBA-2 flux ratio of approximately 9 calculated for SVS 3 corresponds to a temperature of 37 K with $\beta = 1.8$ and a temperature of 260 K at $\beta = 1.5$. This latter temperature is sufficiently high that both SCUBA-2 bands would lie on the Rayleigh-Jeans tail, and therefore it cannot be considered reliable. I note that the uncertainties on flux ratio could also allow for lower temperatures, given lower values of β, whilst a lower β could be symptomatic of grain growth in an accretion disc/dense envelope. However, SVS 3 is sufficiently evolved that it is believed that the envelope will have been largely stripped and any surviving disc would be very low mass. Instead, this result is, at least in part, symptomatic of an anti-correlation between β and temperature observed by Agladze et al. (1996) and presented in Figure 5.24 (right) that is systematic of the SED fitting method.

Chun-Yuan Chen et al. (2016) suggest that outflows from protostars may be expelling low β material from more dense environments, leading to variations in β in the extended filaments of the region. This mechanism may have consequences for the temperatures calculated using constant β that are in close vicinity of an outflow.

To compare how variable β influenced temperatures across the whole of NGC 1333 I convolved the SCUBA-2 temperature map, presented in Figure 5.22 (left), down a resolution of 36.3″ and regridded to 14″ pixel size used by Chun-Yuan Chen et al. (2016) in Figure 5.22 (right) before plotting the two distributions against each other in Figure 5.24 (left). The two methods show a loose correlation, though the majority of pixels are warmer when calculated by the SCUBA-2 flux ratio method (in some cases the difference is over 20 K). Only 13% of SED fitted temperatures exceed the SCUBA-2 flux ratio temperatures that would be indicative of an underestimate of β. However, the majority of the β values calculated by Chun-Yuan Chen et al. (2016) across Perseus West (mean value β of 1.9±0.3, shown in Figure 5.23 right) are consistent with the constant value of 1.8 used throughout this thesis.

I note that the coverage of SCUBA-2 flux ratio data is less than the SED fitting method as Chun-Yuan Chen et al. (2016) does not include the low SNR 450 μm band. Figure 5.24 (right) demonstrates those pixels which are common to both methods and highlights that there is a selection bias, with 73% of high β pixels (greater than 2.1) feature in both methods, but only 49% of low β pixels (less than 1.5). Allowing for the anti-correlation between β and temperature, the discrepancy in coverage can explain why the majority of pixels are warmer when calculated by the SCUBA-2 flux ratio method.

In addition to this effect, the higher resolution of the SCUBA-2 ratio method allows for the resolution of small-scale heated structure that would otherwise have been smoothed with cooler fluxes in the lower resolution SED fitting method. This acts to further increase the scatter observed between the two methods.

5.6.5 Temperatures from line emission

The temperature of star-forming regions have been observed and calculated using line emission from the molecular clouds: for example, Ladd, Myers & Goodman (1994) and Curtis et al. (2010) examine the CO excitation temperature and Huttemeister et al. (1993) looked at a multilevel study of ammonia lines. These methods assess the temperature of interstellar gas as opposed to dust. As discussed in Chapter 1, GMC stability can be modelled as a Bonnor–Ebert sphere (Ebert, 1955; Bonnor, 1956; Johnstone et al., 2000) of ideal gas and therefore molecular gas excitation temperature can allow for direct calculation of these properties. Alternatively dust temperatures are calculated and used to infer the temperature of the gas, assuming that the two are well coupled (accurate for densities greater than $10^{4.5}$ cm^{-3}, Goldreich & Kwan 1974 and Goldsmith 2001).

5.7 Summary and conclusions

In this chapter I have introduced the ‘temperature equation’, a method developed by Reid & Wilson (2005) by which the temperature of thermal dust emission at submillimeter wavelengths can be

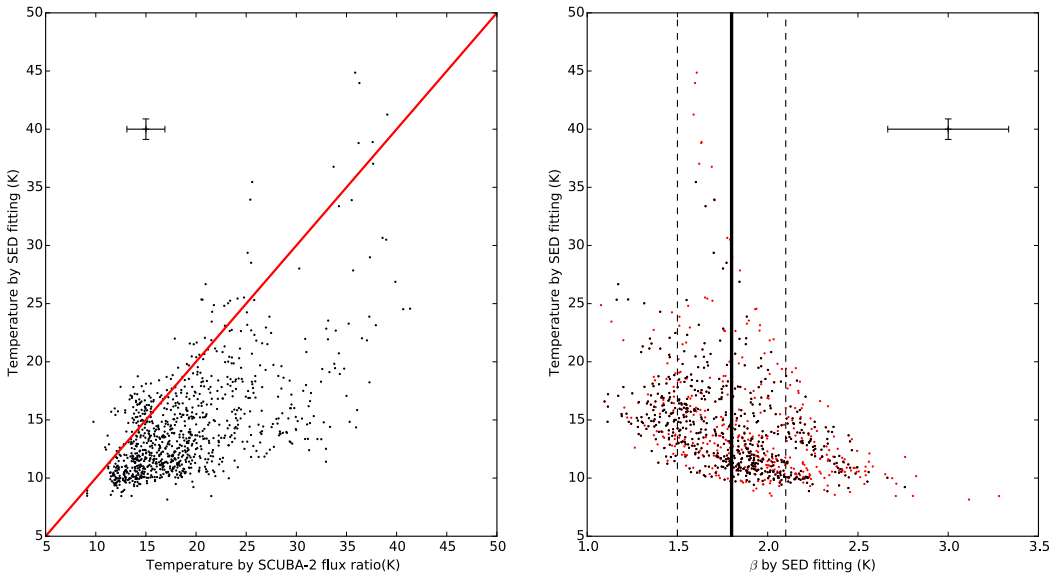

Figure 5.24: Left) a comparison between Perseus NGC 1333 temperatures calculated using the SCUBA-2 flux ratio method and *Herschel* + SCUBA-2 full SED fitting published by Chun-Yuan Chen et al. (2016). Both maps have a resolution of 36.3″ and pixel size of 14″. A parity line is marked in red. The mean error on each result is also presented. Right) Chun-Yuan Chen et al. (2016) β values plotted against temperature values. The SCUBA-2 β value of 1.8 is marked with a solid line, and its upper and lower bounds are marked as a dashed line. Black markers represent all pixels in the full SED maps, whereas red represents only those that are present in both maps.

determined from the ratio of fluxes at two frequencies, when fitted to an opacity modified full blackbody. This method contains a degeneracy between the dust temperature and the dust opacity spectral index, β. I set β as a constant equal to 1.8, a number that reflects the nature of the dust grains found in extended/filamentary structure that is the primary target of the JCMT GBS with SCUBA-2.

This method was used by Hatchell et al. (2013), in conjunction with SCUBA-2 data, to observe evidence of protostellar heating in Perseus NGC 1333. This method took a simplified approach by modelling the JCMT beam as a single Gaussian before cross-convolving the 450 and 850 μm maps to achieve like resolution. Dempsey et al. (2013) provide evidence for a two component model of the JCMT beam and I have developed the method used by Hatchell et al. (2013) to include this, albeit along two different paths. I find that by not including the secondary beam in the convolution process, Hatchell et al. (2013) systematically overestimate the dust temperatures by between 5 and 9%. This affect is most prominent in the coldest regions and can be explained by the difference in the relative volume that the secondary beam fills at 450 μm, compared to 850 μm. The convolution methods I develop are as follows:

- The two-component beam method: I employ a two-component cross-convolution that uses both JCMT main beam and secondary beam models to achieve a common resolution of 19.9″.

- The Kernel-convolution method: I employ a Model-Kernel developed by Pattle (priv. comm.)

that is based on the 2CB model of Dempsey et al. (2013) and implemented using the method of Aniano et al. (2011). The Kernel-convolution method convolves only the 450 μm map and can achieve an improved resolution of 14.9″, albeit at a cost of propagating uncertainties that are twice as large as the 2CB method.

Both methods produce consistent flux ratios with a Pearson-correlation of 96%.

I look critically at the SCUBA-2 flux ratio methods outlined here with respect to existing and alternative methods for calculating the temperature of pre- and proto-stellar objects. Using longer wavelengths, for example MAMBO 1.2 mm, instead of the SCUBA-2 450 μm band, allows for greater coverage but places an upper limit on temperature of 20 K. Using SCUBA-2 data in conjunction with *Herschel* observations to carry out full SED fitting can be used to distinguish between temperature and β (though it cannot yet completely remove the degeneracy). However, SED fitting has the tendency to over emphasize higher temperature cloud components if the shortest wavelengths are included. Use of the *Herschel* 350 and 500 μm can further compromise on resolution. Whilst these alternatives have specific strengths, the SCUBA-2 flux ratio method remains reliable for studying the temperature of cool star forming regions on the scale of the Jeans length.

Throughout this chapter I demonstrate these methods using SCUBA-2 450 and 850 μm observations of the Serpens Main region. Chapter 6 uses the 2CB method to produce dust temperature maps for the Serpens MWC 297 region. Chapter 7 uses the Kernel-convolution method to produce dust temperature maps for the Aquila W40 complex. Further examples of temperature maps of JCMT GBS regions are produced and discussed in Chapter 8.

6

Radiative heating in the Serpens MWC 297 region

This chapter is drawn from Rumble et al. (2015), *"The JCMT Gould Belt Survey: evidence for radiative heating in Serpens MWC 297 and its influence on local star formation"*, which focuses on SCUBA-2 observations of the Serpens MWC 297 region, a region of low mass star formation associated with the B star MWC 297. I adopt a distance of $d = 250 \pm 50$ pc, following Sandell et al. (2011), for the following analysis. The background to the Serpens MWC 297 region is presented in Chapter 2, Section 2.5.1, along with the data and details of its reduction. Both the sets of 450 and 850 μm data were de-contaminated for free-free emission based on a 6 cm VLA point source associated with the B1.5Ve star MWC 297 (Skinner 1993, Sandell priv. comm). Full details of the free-free analysis are given in Chapter 4. ^{12}CO 3-2 line emission was assessed based on the published line spectra of Canto et al. (1984) and 850 μm decontamination was deemed unnecessary. Full details of the CO analysis are given in Chapter 3.

In this Chapter I identify clumps, using the FELLWALKER clump finding algorithm, in the 850 μm data and calculate masses from dust temperature maps produced using the two component beam (2CB) method, described in Chapter 5. I present temperature maps of the region and I examine external catalogues of YSO candidates (SGBS) for the region and produce my own SCUBA-2 catalogue of star-forming cores. I discuss the findings in the context of radiative feedback and global star formation within the region and ask if there is any evidence that radiative feedback from previous generations of stars is influencing present day and future star formation.

6.1 Temperature maps of Serpens MWC 297

The 450 μm and 850 μm SCUBA-2 data for the MWC 297 region are presented in Figure 6.1 alongside a map of temperature of submillimeter dust in that region, produced using the 2CB

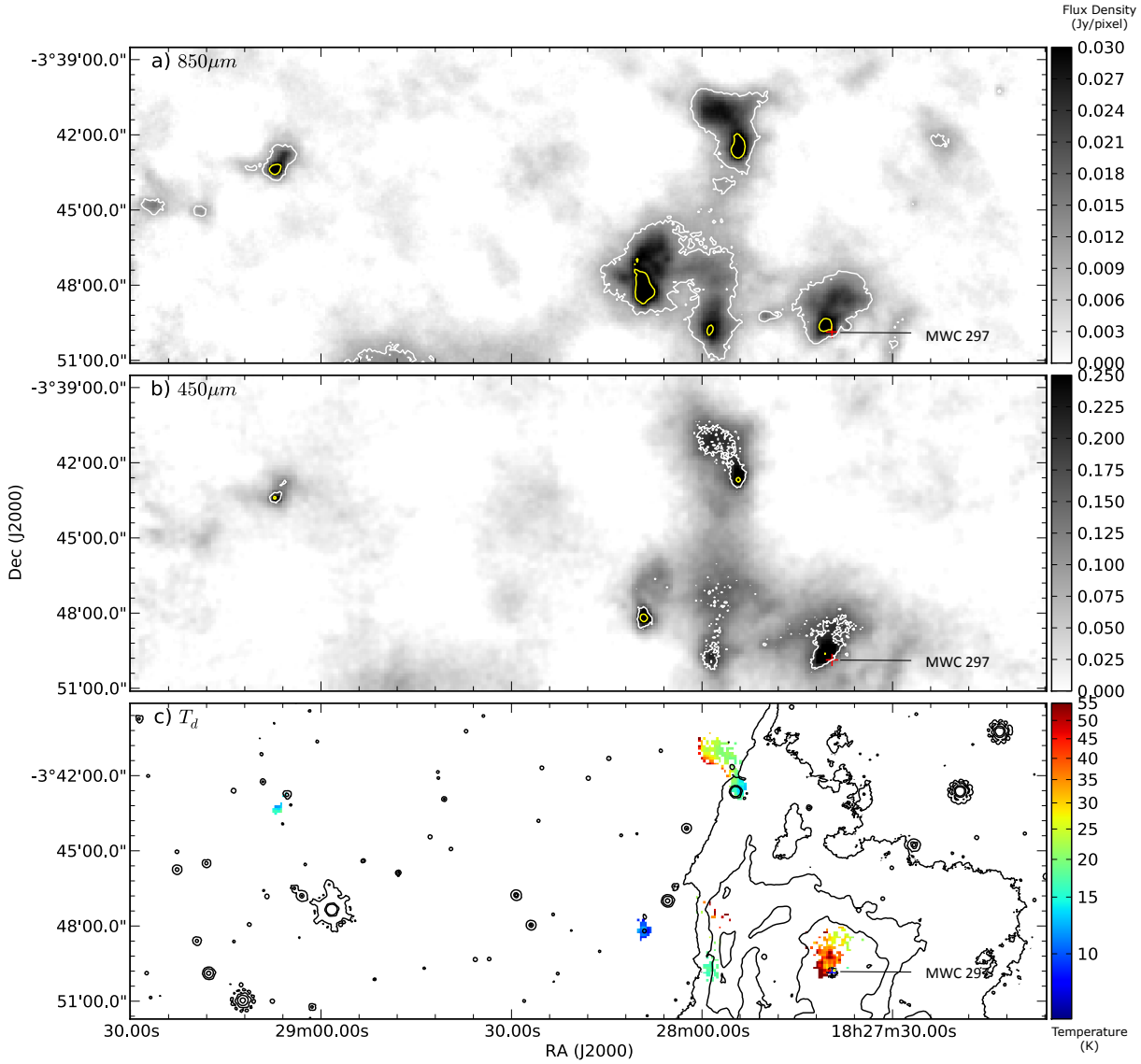

Figure 6.1: Top to bottom: a) SCUBA-2 convolved 850 μm flux map of Serpens MWC 297. Contours from the original 850 μm data are at 0.011 and 0.033 Jy/pixel (corresponding to 5 and 15 σ). b) SCUBA-2 convolved and aligned 450 μm flux map of Serpens MWC 297 in Jy/pixel. Contours from the original 450 μm data are at 0.082 and 0.25 Jy/pixel (corresponding to 5 and 15 σ). The crosses in a) and b) mark the location of the ZAMS B1.5Ve star MWC 297 and its binary partner *OSCA* (A2v). c) Dust temperature map of Serpens MWC 297 for β = 1.8. Contours of *Spitzer* 24 μm emission at 32, 40 and 70 MJy per Sr are overlaid.

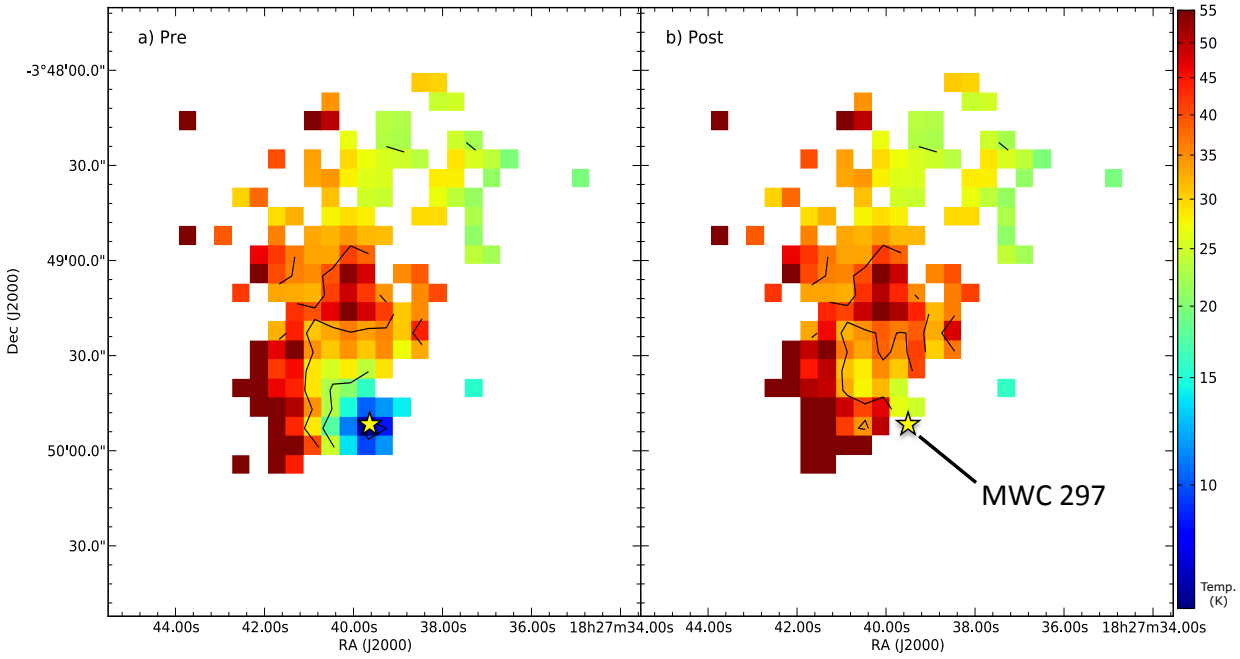

Figure 6.2: Temperature maps of MWC 297 from the ratio of 450 μm and 850 μm emission pre (*left*) and post (*right*) free-free contamination subtraction. Contours are at 11, 25 and 38 K. The location of MWC 297 is marked with a star.

method (Chapter 5). These maps show a large diversity in temperature across five isolated regions of significant flux (shown in Figure 6.1c). Cloud mean temperatures range from 10.1±0.9 K and 15±2 K for regions which are relatively cold and isotropic, to 25±17 K for warmer regions with a large diversity of temperatures. Figure 6.2 shows one cloud that has a temperature of 41±19 K which is hot to the extent that this would suggest an active heat source. The range in temperatures suggests that the regions within the Serpens MWC 297 vary in physical conditions.

Men'shchikov et al. (2010) infer temperature variation from contrasting strengths of 350 μm flux bands to the shorter 70 μm and 160 μm bands of *Herschel*. They quote a temperature range for dense, starless filaments of 7.5 to 15 K across the whole Aquila rift. However, I do not observe a typical filamentary structure in the Serpens MWC 297 region (Figure 2.10). Könyves et al. (2010) and Bontemps et al. (2010) used single-temperature modified black-body fitting of SEDs of *Herschel* SPIRE and PACS data points in Aquila and Polaris. Their study includes Serpens MWC 297 and they find temperatures for the region ranging between 24 and 26 K. Though *Herschel* 500 μm data is at a lower resolution than the JCMT effective beam, the general temperatures of the region seem consistent with my findings.

Hatchell et al. (2013) calculate dust temperatures from the ratio of SCUBA-2 450 μm and 850 μm flux, using only the primary JCMT beam, in Perseus NGC1333. They report typical dust temperatures ranging from 12 to 16 K. They also argue for a heated region pushing temperatures up as high as 35 to 40 K near the location of the B star SVS3. When the moderating effects of the secondary beam are taken into account, these results are largely consistent with my findings (Serpens MWC 297 also contains a B star).

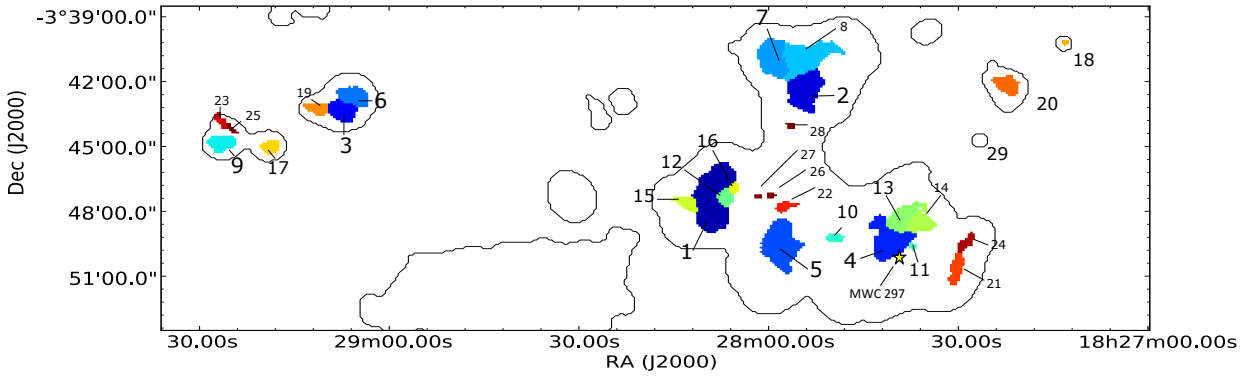

Figure 6.3: Clumps identified in 850 μm data with the STARLINK clump-finding algorithm FELLWALKER index numbered in order (highest to lowest following the colour scale) of integrated flux. The data reduction mask is overlaid as a black contour.

Figure 6.1c shows *Spitzer* MIPS 24 μm flux for the Serpens MWC 297 region. These data show hot compact sources associated with individual stellar cores. It also shows the morphology of an extended IR nebulosity, associated with SH2-62, that is centred on MWC 297. As well as the dust within the immediate vicinity of the star MWC 297 showing high temperatures, I observe 24 μm emission that is coincident with heating in the SCUBA-2 temperature maps. As 24 μm emission provides independent evidence of heating, where I observe high temperature pixels that are not coincident with 24 μm emission (for example in the northernmost cloud) I conclude that these are the result of data reduction artefacts as opposed to warm gas and dust.

In addition to providing evidence for direct heating by MWC 297, the 24 μm data also provide strong evidence that the B star is physically connected to the clouds observed by SCUBA-2 and they are located at a common distance.

In Chapter 4 I discussed the evidence for free-free emission from an UCH II around the B1.5ve star MWC 297 contributing to the 450 and 850 μm flux observed by SCUBA-2. Figure 4.4 shows how a bright point source in 6 cm VLA observations (Sandell, priv. comm.) is associated with MWC 297. Skinner et al. (1993), Alonso-Albi et al. (2009) and Sandell et al. (2011) calculate that the free-free emission has a spectral index of $\alpha_{\rm ff} = 1.03 \pm 0.02$ and I calculate that this is a majority contribution to both SCUBA-2 bands. Figure 4.4 presents the 850 μm map before and after free-free subtraction and Figure 6.2 presents the impact of free-free emission on temperature maps of the region.

The impact of this contamination on the temperature maps is remarkable. An $\alpha_{\rm ff} = 1.03 \pm 0.02$ produces relatively greater flux at 850 μm than 450 μm. As the free-free emission is the dominant flux mechanism, the resulting ratio 450 μm to 850 μm emission appears artificially lower, resulting in lower temperatures. This is consistent with the cold spot seen in Figure 6.2a at the location of the UCHII region, with a temperature of approximately 11 K. I conclude that free-free emission may contaminate temperature maps derived from submillimeter wavelengths where cold spots are coincident with OB stars.

Table 6.1: FELLWALKER parameter settings.

Parameter	Setting
MinPix	4 pixels
MaxJump	1 pixel
MinDip	1σ
MinHeight	3σ
Noise	3σ
FWHMbeam	$0''$

6.2 The SCUBA-2 clump catalogue

In this section I use the clump-finding algorithm FELLWALKER use to identify clumps in the SCUBA-2 data presented in Figure 2.10. I calculate clump masses and compare these to their Jeans masses to determine whether or not the objects are unstable to gravitational collapse.

6.2.1 Fellwalker parameters

I tune the FELLWALKER algorithm to produce a set of objects consistent with a by-eye decomposition using the parameters given in Table 6.1. *MinPix* is the minimum number of pixels per valid clump. Setting this parameter too low will allow the algorithm to include noise artefacts around the map edges, where as too high may omit low luminosity point sources. *MinHeight* is the minimum height of clump peak to register as a valid clump. This is set as equal to the *Noise* level, or detection threshold, to further ensure that the detection of low luminosity point sources. *MinDip* is the minimum flux between two peaks and is used to define the difference between two adjacent clumps, with lower values more effectively breaking up large, continuous clouds. *MaxJump* (distance between clump peaks) was found to be largely insensitive clump detection. Flux weighting of beam sizes was not used, again as it omitted low luminosity point sources. Therefore the FWHM of instrument parameter (*FWHMBeam*) was set to 0.

Throughout this process I used a constant noise level, $\sigma = 0.011$ Jy/beam, calculated via the method described by Salji (2014) and described in Chapter 2. Watson (2010) discusses the FELLWALKER parameters in depth and concludes *MinDip* and *MaxPix* are the most influential in returning the maximum breakup of clouds into clumps, a subset of which will later be used to compile a list of protostellar cores. The 3σ level allows for the detection of the smallest clumps that may be missed at the 5σ level on account of insufficient pixels for detection as outlined above. This method also included a number of spurious clumps associated with high variance pixels at the maps edges. In order to avoid these I first masked the SCUBA-2 data with the data reduction mask shown in Figure 2.10.

Using these parameters, 28 submillimeter clumps were detected in 850 μm data and are presented in Figure 6.3. Two sources (SMM 23 and 25) were immediately discarded as they were not consistent with a 5σ detection. A further two clumps were split into two separate objects by the algorithm when there was no discernible peak in the submillimeter data. In these cases (SMM 7 & 8 and SMM 13 & 14) the objects were recombined into single objects. I note that this is a side effect of having a low *MinDip* parameter to maximise the detection of smaller clumps. In

total a sample of 23 clumps are presented in Table 6.2. I note that there is a known bias that underestimates the size of a clump as its peak flux approaches the cutoff level and therefore biases against the detection of cold, faint objects (examples might be SMM 26 and 27). Modelling clump profiles could be used to better estimate the full extent of these objects. However, as these present a minority of cases I take no further action on this issue (Rosolowsky & Leroy, 2006).

The FELLWALKER algorithm is insensitive to low mass, isolated objects where detections were limited to less than five pixels above the noise level. I find that one potential source (S2-YSOc 29,) was missed on account of it only exhibiting a single significant pixel above the 5σ noise level. Here object flux was measured with aperture photometry (see Section 3.2). Due to the higher noise level of the 450 μm data many objects detected at 850 μm were not present at 450 μm. Therefore I apply the 850 μm clump boundaries to the 450 μm data when calculating integrated intensity at that wavelength to ensure consistent flux extraction at both wavelengths for each object.

6.2.2 Clump mass and temperature

SCUBA-2 observations of the Serpens MWC 297 region were used to calculate the masses of the FELLWALKER clumps using Equation 1.35, reformatted for a clump containing N pixels, i, with flux, $S_{850,i}$, and temperature, $T_{d,i}$, at a distance d,

$$\begin{aligned} M &= 0.39 \sum_i^N S_{850,i} \left[\exp\left(\tfrac{17\mathrm{K}}{T_{d,i}}\right) - 1\right] \\ &\times \left(\tfrac{d}{250\mathrm{pc}}\right)^2 \left(\tfrac{\kappa_{850}}{0.012\mathrm{cm^2 g^{-1}}}\right)^{-1} M_\odot. \end{aligned} \tag{6.1}$$

I use a dust opacity of $\kappa_{850} = 0.012\,\mathrm{cm^2\,g^{-1}}$ following Hatchell et al. (2005). Henning & Sablotny (1995) finds that the value of κ_{850} can vary by up to a factor of two depending on the assumed dust nature and the dust-to-gas ratio. For example, Johnstone et al. (2000) use 0.01 and Kirk et al. (2006) use $0.02\,\mathrm{cm^2\,g^{-1}}$. Not all the clumps shown in Figure 6.3 have temperature data due to the noise constraints of the temperature mapping process and the requirement that the region is also detected at 450 μm. For those that do not, a constant clump temperature of 15 K, consistent with those derived for cores in Perseus using Bonnor-Ebert models (Kirk et al. 2006) and the value calculated from kinetic gas temperatures in Ophiuchus by Friesen et al. (2009).

Some clumps have only partial temperature data. In these cases the remaining pixels are filled with a value equal to the mean of the existing data. In some cases (SMM 6 and 11 for example), temperature data is limited to a few pixels whereas the total clump area is an order of magnitude larger. As it is unlikely that such a small sample of data will accurately represent the whole clump, results for objects such as these should be treated with a larger degree of uncertainty. Work by Evans et al. (2001), Shirley et al. (2002b), Shirley et al. (2003) and Young et al. (2003) use a one-dimensional radiative transfer model of core temperature profile, taking into account internal heating by the star and external heating by the ISM, and find temperatures of 10 K at the edge of the maximum core radius that rise to an excess of 50K in the interior (see Chapter 8 for further analysis of internal heating). My results potentially show limited signs of external heating,

though artefacts in the data prevent further analysis. Edge effects have a negligible influence on clump mass as high temperatures reduce the contribution in Equation 5. Clump masses are listed in Table 6.2.

The total mass of clumps in the Serpens MWC 297 region is 40±3 $M_\odot$. Individual clump masses range over 2 orders of magnitude from 0.05 to 19 $M_\odot$ with 29 % of objects having a mass of 1 $M_\odot$ or higher. Figure 6.3 shows how FELLWALKER divides the areas of star formation into five large-scale star-forming clouds and a small number of isolated objects. Of these clouds, SMM 1, 12, 15 & 16 is the most massive at 21±2 $M_\odot$, containing 53 % of all the mass detected by FELLWALKER, followed by SMM 2, 7 & 8 at 6.6±0.3 $M_\odot$ (17 %), SMM 4, 10, 11, 13, 14, 21 & 24 at 3.3±0.1 $M_\odot$ (9 %), SMM 3, 6 & 19 at 3.1±0.1 $M_\odot$ (8 %) and SMM 5, 22, 26 & 27 at 3.1±0.3 $M_\odot$ (8 %).

Shirley et al. (2000b) calculate masses from SCUBA data from a sample of known YSOs in Taurus, Ophiuchus, Aquila and Perseus regions and find the mean mass of 1.8±0.9 $M_\odot$, given constant temperature of 20 K, which is consistent with my value of 1.7±2.5 $M_\odot$ and with their viral mass calculations. Johnstone et al. (2000) comment that incompleteness in SCUBA clumps in Ophiucus becomes a problem at masses less than 0.4$M_\odot$. Of the sample detected with SCUBA-2, 39 % of the sample have a mass of 0.4 $M_\odot$ or lower. The lowest mass clump in the SCUBA-2 sample is 0.05±0.02 $M_\odot$ representing a significant improvement in mass sensitivity.

6.2.3 Jeans mass

Jeans mass, as a function of Jeans length, R_J, and mean dust temperature, $\bar{T}$ is calculated using Equation 1.4. R_J is taken as the effective radius of the clump, as determined by clump area (in pixels) from FELLWALKER and assuming spherical structure (Table 6.2). This measure of R_J is typically twice the flux weighted clump radius and better represents the complete extent of the clump. I note that effective radius is a lower limit on clump size. Whereas mass was calculated on a pixel-by-pixel basis, this is not possible for M_J as the characteristic length scale of the Jeans instability covers the entire object. The mean dust temperature, $\bar{T}$, across the clump is calculated directly from the temperature maps and is assumed to be constant in line with an isothermal cloud and well coupled to the gas temperature. In lieu of observational evidence, additional forces such as magnetism and turbulence are neglected. I note that Sadavoy et al. (2010) and Mairs et al. (2014) describe how these mechanisms could provide additional support against gravitational collapse.

Furthermore, all of the clumps in Serpens MWC 297 are less than 0.15 pc in size, the scale-size, calculated by Arzoumanian et al. (2011) who extrapolate Larsons size-linewidth relationship to the point where the velocity dispersion equals the sound speed. I therefore take the Serpens MWC 297 region to be sub-sonic and thermal pressure to dominate over turbulent pressure.

Temperatures and Jeans masses of clumps are also shown in Table 6.2. The masses of clumps calculated with the temperature data in the previous section deviate from the equivalent masses calculated with a uniform mean clump temperature (set at 15 K) by 12 % on average per clump which is sufficiently similar to allow this analysis. In Chapter 8 I extend this analysis to specifically heated clumps across the JCMT GBS.

This method is based on the work by Sadavoy et al. (2010) who performed a similar analysis

Table 6.2: Properties of submillimeter clumps in MWC 297.

ID[a]	Object name[b]	S^{c}_{450} (Jy)	S^{c}_{850} (Jy)	M^{d}_{850} ($M_\odot$)	T^{e}_{d} (K)	Area[a] (pixels)	M^{f}_{J} ($M_\odot$)	M_{850}/M_J	SGBS YSOc ID[g]
SMM1	JCMTLSG J1828090-0349497	45.7	11.5	19±2	10.1±0.5	358	2.1±0.1	9.12±1.05	-
SMM2	JCMTLSG J1827542-0343197	33.2	5.0	3.5±0.2	17.9±0.9	205	2.9±0.1	1.21±0.1	YSOc41
SMM3	JCMTLSG J1829071-0344378	11.2	1.9	1.6±0.1	14.6±0.7	94	1.58±0.08	1.03±0.1	-
SMM4	JCMTLSG J1827405-0350257	43.9	4.7	0.91±0.05	46±2	213	7.4±0.4	0.12±0.01	-
SMM5	JCMTLSG J1827590-0350137	36.8	5.4	3.3±0.3	18.2±0.9	265	3.3±0.2	0.99±0.09	-
SMM6	JCMTLSG J1829055-0343138	7.7	1.3	1.2±0.1	14.2±0.7	94	1.53±0.08	0.77±0.08	YSOc73
SMM7*	JCMTLSG J1827586-0342557	59.4	7.7	3.1±0.2	25±2	419	8.2±0.3	0.37±0.03	-
SMM9	JCMTLSG J1829260-0345139	3.1	0.8	0.67±0.06	15.0 -	73	1.43±0.07	0.47±0.05	-
SMM10	JCMTLSG J1827501-0350437	3.5	0.4	0.29±0.03	15.0 -	26	0.85±0.04	0.35±0.04	YSOc32
SMM11	JCMTLSG J1827373-0350197	1.1	0.2	0.1±0.02	17.6±0.9	9	0.59±0.03	0.17±0.03	YSOc17
SMM12	JCMTLSG J1828074-0348437	4.1	1.0	0.86±0.07	15.0 -	42	1.08±0.05	0.79±0.08	-
SMM13*	JCMTLSG J1827393-0349257	30.9	3.8	1.25±0.06	28±2	199	6.3±0.2	0.20±0.01	-
SMM15	JCMTLSG J1828126-0348197	1.8	1.0	0.8±0.07	15.0 -	50	1.18±0.06	0.68±0.07	-
SMM16	JCMTLSG J1828058-0347017	2.2	0.4	0.33±0.03	15.0 -	18	0.71±0.04	0.47±0.05	YSOc47
SMM17	JCMTLSG J1829187-0346559	2.7	0.4	0.34±0.03	15.0 -	42	1.08±0.05	0.32±0.03	-
SMM18	JCMTLSG J1827133-0341438	0.2	0.1	0.05±0.02	15.0 -	7	0.44±0.02	0.12±0.04	YSOc2
SMM19	JCMTLSG J1829107-0344378	2.5	0.4	0.33±0.03	15.0 -	47	1.14±0.06	0.29±0.03	-
SMM20	JCMTLSG J1827225-0343378	1.4	0.7	0.61±0.05	15.0 -	73	1.43±0.07	0.43±0.04	-
SMM21	JCMTLSG J1827297-0351378	5.1	0.6	0.46±0.04	15.0 -	65	1.35±0.07	0.34±0.04	-
SMM22	JCMTLSG J1827582-0348137	4.7	0.5	0.1±0.01	42±2	31	2.6±0.1	0.04±0.0	-
SMM24	JCMTLSG J1827285-0350378	3.5	0.4	0.29±0.03	15.0 -	37	1.02±0.05	0.29±0.03	-
SMM26	JCMTLSG J1827594-0348437	1.5	0.2	0.15±0.02	15.0 -	10	0.53±0.03	0.28±0.04	-
SMM29	JCMTLSG J1828022-0348377	0.6	0.1	0.09±0.02	15.0 -	6	0.41±0.02	0.23±0.05	-

a) Clumps as identified by the FELLWALKER algorithm.
b) Position of the highest value pixel in each clump (at 850 μm).
c) Integrated fluxes of the clumps as determined by FELLWALKER. The uncertainty at 450 μm is 0.3 Jy and at 850 μm is 0.02 Jy. There is an additional systematic error in calibration of 10.6 % and 3.4 % at 450 μm and 850 μm.
d) As calculated with Equation 6.1. Errors are calculated from error in total flux, described in c., and error in mean temperature of 5 %. These results do not include the systematic error in distance (20 %) and opacity (100 %).
e) Mean temperature as calculated from the temperature maps (Figure 6.1). Where no temperature data is available an arbitrary value of 15K - is assigned that is consistent with the literature.
f) As calculated with Equation 6.1. These results have a systematic error uncertainty due to distance of 20 %.
g) Where a FELLWALKER source is coincident with a SGBS YSOc, that object is listed here. A complete list is presented in Table 2.3 .
Objects indicated with * have been merged with an adjacent object which was incorrectly identified as a separate clump by FELLWALKER.

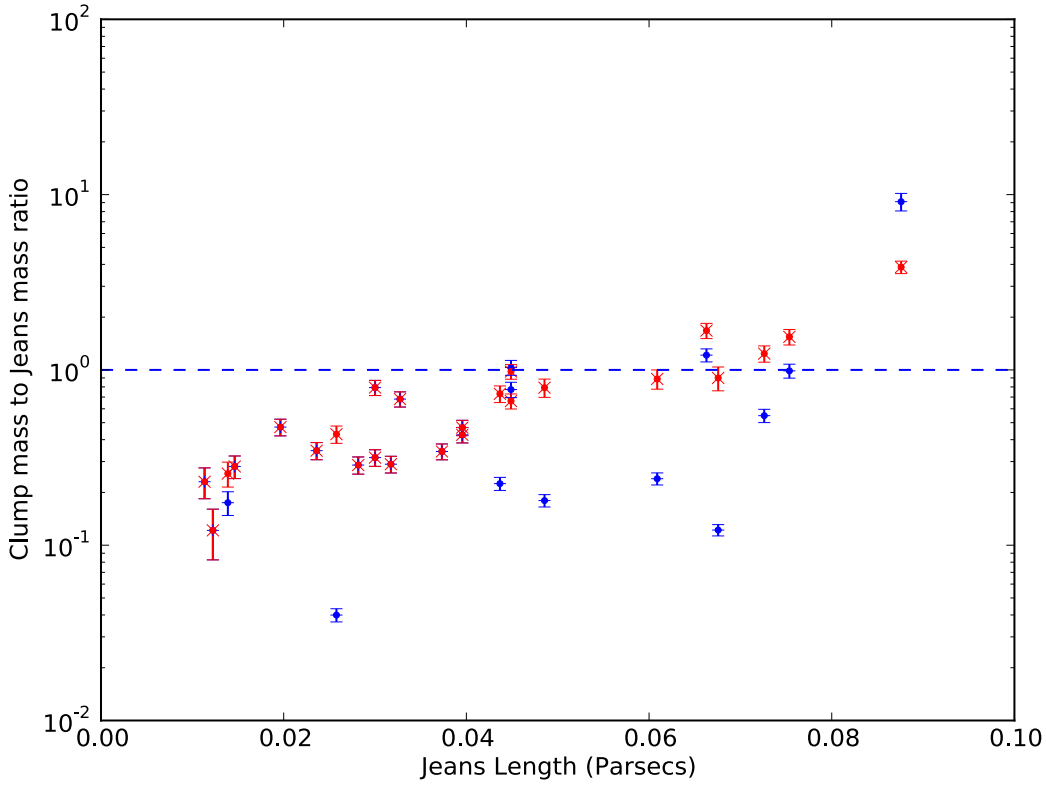

Figure 6.4: Jeans stability plotted against Jeans length. All clumps with $M_{850}/M_J > 1$, as shown by the dashed line, are expected to be undergoing collapse. Blue circles represent calculations made with real temperature data whereas red crosses indicate those made with an assumed temperature of 15 K. Systematic error in the measurement of distance to MWC 297 accounts for 20 % uncertainty on Jeans length.

for starless cores in the Gould belt. They used the assumption of a typical cold (10K) molecular cloud core size of 0.07 pc (Di Francesco et al., 2007). Rosolowsky et al. (2008) determined a range of temperatures of 9 K to 26 K in Perseus (a similar region to Serpens-Aquila) from ammonia observations. This paper goes a step further and is able to use mean temperatures specific to each clump to calculate the Jeans mass.

Under the assumption that only internal pressure can balance self-gravity, M_J sets an upper limit on the mass of a sphere of gas for a given radius. If the observed mass, M_{850}, is greater than the calculated M_J, or alternatively $M_{850}/M_J > 1$, that would suggest that the clump is unstable to gravitational collapse and hence active star formation is likely (Mairs et al., 2014). An object that has $M_{850}/M_J \ll 1$ is currently stable and will not collapse (alternatively it has already collapsed and the majority of the mass is now contained within the protostar). Given the uncertainties present in theory and observations, the stability of objects where $2 \geq M_{850}/M_J \geq 1$ is ambiguous. Figure 6.4 plots M_{850}/M_J against the Jeans length scale for the clumps identified in Serpens MWC 297 and reveals that at least three out of a total 22 clumps detected by FELLWALKER are Jeans unstable and may already contain protostars. Evidence for these are addressed in Section 3. For comparison, M_{850}/M_J is plotted for the same list of objects, assuming a single clump temperature of 15 K (the red crosses in Figure 6.4). I observe that in a majority of cases using a real temperature has caused the ratio to decrease and I therefore conclude that previous authors who have used a constant temperature of 15 K have underestimated the stability of their clumps.

Di Francesco et al. (2007) address the issue of gravitational binding as a key indicator of when a clump can be considered a pre-stellar core, but concludes that any distinction will contain systematic uncertainties in mass, distance, temperature and magnetic fields. My method removes the assumption of constant temperature across a sample of clumps and offers improved accuracy of masses. However, the remaining uncertainty in mass is between a factor 2 to 3 and this limits full interpretation of these findings. I extend this analysis of stability in Chapters 7 and 8 by looking specifically at starless clumps.

6.3 The SCUBA-2 YSO catalogue

In this section I cross-reference my list of SCUBA-2 clumps, as identified by FELLWALKER, with the SGBS YSOc catalogue discussed in Chapter 2 and produce my own SCUBA-2, confirmed YSOc catalogue for the Serpens MWC 297 region (Table 2.3). I calculate the relative distribution of protostars to PMS stars in the region as a measure of the dynamical evolution of YSOcs within a star-forming cluster. I produce spectral energy distributions (SEDs) of the YSOcs where supplementary data exist. With the addition of new SCUBA-2 data at 450 μm and 850 μm I update the classification of the YSOcs in the Serpens MWC 297 region.

6.3.1 YSO distribution

Kaas et al. (2004), Winston et al. (2007) and Harvey et al. (2007) discuss how evolutionary class (determined by IR spectral index) and spatial distribution in a star-forming region are correlated, finding that Class 0/I and FS sources are concentrated towards the central filaments of the Serpens

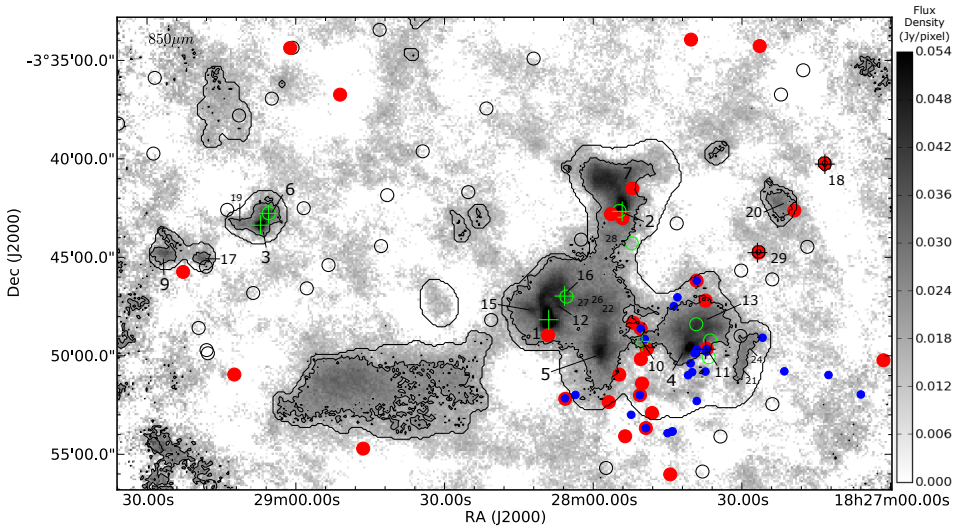

Figure 6.5: 850 μm greyscale map of Serpens MWC 297. Outer contours mark the data reduction mask (Figure 1) and inner contours the 3σ detection level (0.0079 Jy/pixel). Circular markers indicate the location of YSOcs as catalogued by SGBS and crosses indicate the location of SCUBA-2 confirmed YSOs (Table 6.4). YSOcs are coded by evolutionary classification based on their spectral indices ($\alpha_{\rm IR}$) in the *Spitzer* case and by bolometric temperature, $T_{\rm bol}$, in the SCUBA-2 case (Table 6.4). *Spitzer* YSOcs are indicated by hollow black circles (Class III), solid red circles (Class II) and green hollow circles (Class 0/I). SCUBA-2 confirmed YSOs are indicated by black crosses (Class II) and green crosses (Class 0/I). Small, solid blue circles mark the location of Damiani et al. (2006) X-ray sources, typically associated with Class II/III objects.

Table 6.3: Ratios of protostars (Class 0, I, FS) to PMS stars (Class II, TD, III) in the SGBS and SCUBA-2 catalogue.

	Protostars	PMS-stars	Ratio
Control region	0	49	0.0
Herschel 2Jy beam^{-1} mask	10	23	0.43
SCUBA-2 3σ mask	8	10	0.80

Main region whereas Class II, TD and III sources are much more widely distributed. I incorporate SCUBA-2 data into this method, allowing for direct comparison of the evolutionary class spatial distribution with H_2 column density.

Figures 6.5 presents the positions and evolutionary classification of the SGBS YSOcs on the 850 μm flux map (Figure 2.10). In Figure 6.5 I show whether or not the Spitzer YSOcs are consistent with the Damiani et al. (2006) X-ray sources. Kaas et al. (2004), Winston et al. (2007) and Harvey et al. (2007) discuss how evolutionary class (determined by IR spectral index) and spatial distribution in a star-forming region are correlated, finding that Class 0/I and FS sources are concentrated towards the central filaments of Serpens Main region whereas Class II, TD and III sources are much more widely distributed. I incorporate SCUBA-2 data into this method, allowing for direct comparison of evolutionary class spatial distribution with H_2 column density.

My method takes the ratio of the number of protostars (Class 0/I) to PMS (Class II/III) stars. Ratios are calculated for the region within the data reduction mask (a large scale region defined as where *Herschel* 500 μm emission is greater than 2 Jy/beam; see Figure 2.10), and the emission 'cloud' defined as above the 3σ detection in SCUBA-2 850 μm, consistent with the levels set for FELLWALKER clump analysis in Section 4.1. In addition the ratio was calculated for the space outside of the data reduction mask up to the boundaries of the SCUBA-2 data in Figure 6.5 as a control region. Table 6.3 shows the results for these corresponding areas for the YSOcs catalogues listed in Table 2.[4] and plotted in Figure 6.5.

Preliminary work by Kaas et al. (2004) suggested that Class I to Class II ratios were 10 times greater within cloud regions of Serpens Main than outside them. Harvey et al. (2007) conducted a similar analysis and found ratios of 0.37 for the whole region and 1.4 and 3.0 for the cloud regions. Whereas these ratios are not as large (0.8), they do follow the same trend of greater numbers of protostars in regions of higher column density, supporting the conclusion that protostars form in regions of high column density and then migrate away from these regions as they evolve into PMS-stars.

6.3.2 SCUBA-2 YSOcs

In this section I determine which members of the SCUBA-2 clump catalogue (Table 6.2) are starless and which host YSOs, as FELLWALKER is parameterised to identify both. The FELLWALKER algorithm is ideal for identifying larger scale, often irregular and extended clumps, but not effective for extracting the flux of individual YSOs, which are smaller. I extract a revised catalogue of YSOcs (Table 6.4) based on the position of the clumps listed in Table 6.2 and calculate the flux

using aperture photometry with a fixed 40″ diameter aperture.

Six clumps are found to contain SGBS YSOcs (Table 2.3) by cross-referencing the SCUBA-2 clumps in Table 6.2 (Figure 6.7) with IR sources (Table 2.3). Two further SCUBA-2 clumps (SMM 1 and 3) are found with extremely faint (less than 3σ) 24 μm emission when he data is assessed by eye. These clumps are found to be centrally condensed and have $M_{850}/M_J > 1$ signifying they are gravitationally unstable and may be early protostellar (Class 0) YSOcs.

The following YSOcs-hosting clumps detected (SMM 1, 2, 3, 6, 10, 11, 16 and 18) are listed in Table 6.4 as SCUBA-2 YSO candidates (S2-YSOc). The remaining clumps listed in Table 6.2 do not contain YSOcs and are considered starless. SMM 4 and 7 are notable as they have relatively high masses (greater than 1 $M_\odot$) but are not currently forming stars. SMM 5 has $M_{850}/M_J = 1$ but there is no evidence for a 24 μm source there. It could be argued that this is a prestellar object on the cusp of becoming protostellar.

In addition to all those submillimeter objects identified by FELLWALKER, I also include one additional YSOc, S2-YSOc 29, as listed in Table 6.4 and YSOc11 in Table 2.3 . This object fulfils the criterion of coincidence with a strong IR source in the *Spitzer* 24 μm MIPS data and a corresponding Class III identification in the SGBS YSOcs catalogue. S2-YSOc 29 registers a 5σ detection with one pixel and resembles S2-YSOc 10 and 18 which are also believed to be an isolated, Class III PMS-stars with the remnants of an envelope/cold accretion disc contributing to their observed submillimeter flux.

Apertures were placed over the peak positions of the FELLWALKER clumps (Table 6.2) in addition to the *Spitzer* YSOcs positions and the integrated SCUBA-2 flux calculated with the intention to measure the flux from any dense, protostellar core associated with the SCUBA-2 clump peak and/or Spitzer YSOc. I follow Di Francesco et al. (2007),Sadavoy et al. (2010) and Rygl et al. (2013)'s definition of a core as a gravitationally bound, dense object, of diameter less than 0.05 pc and set apertures at this size (40″at 250 pc). Some larger scale emission is likely to be observed. However, through careful selection of aperture size I can assume that emission from the core dominates at this length scale.

Figures 6.5 and 6.6 show the locations of the SCUBA-2 YSOcs as well as those catalogued in the SGBS catalog. Figure 6.7 shows the relationship between the submillimeter peaks and the *Spitzer* YSOc position, with the SCUBA-2 fluxes for *Spitzer* YSOcs presented in Table 6.5. The mass of the SCUBA-2 YSOcs are calculated with Equation 6.1, using a constant, mean temperature derived from the temperature maps, and the results presented in Table 6.4.

A small number of *Spitzer* YSOcs inside the *Herschel* 500 μm data reduction mask are consistent with SCUBA-2 YSOcs with identical peak positions, for example in S2-YSOc 18 (Figure 6.7). In some cases, positions appear offset, for example S2-YSOc 2. This anomaly can be explained by virtue of the deeply embedded nature of the source and that *Spitzer* might be observing IR emission from an outflow cavity rather than the YSO itself.

YSOcs classified as 0/I by *Spitzer* should also have evidence of a SCUBA-2 peak at the same position. Those *Spitzer* detected protostars (YSOc16 and 38; Table 2.3) that lie outside of the 5σ detection limit at 850 μm and have no obvious peak in emission are unlikely to be YSOcs and are discarded as incorrectly classified objects.

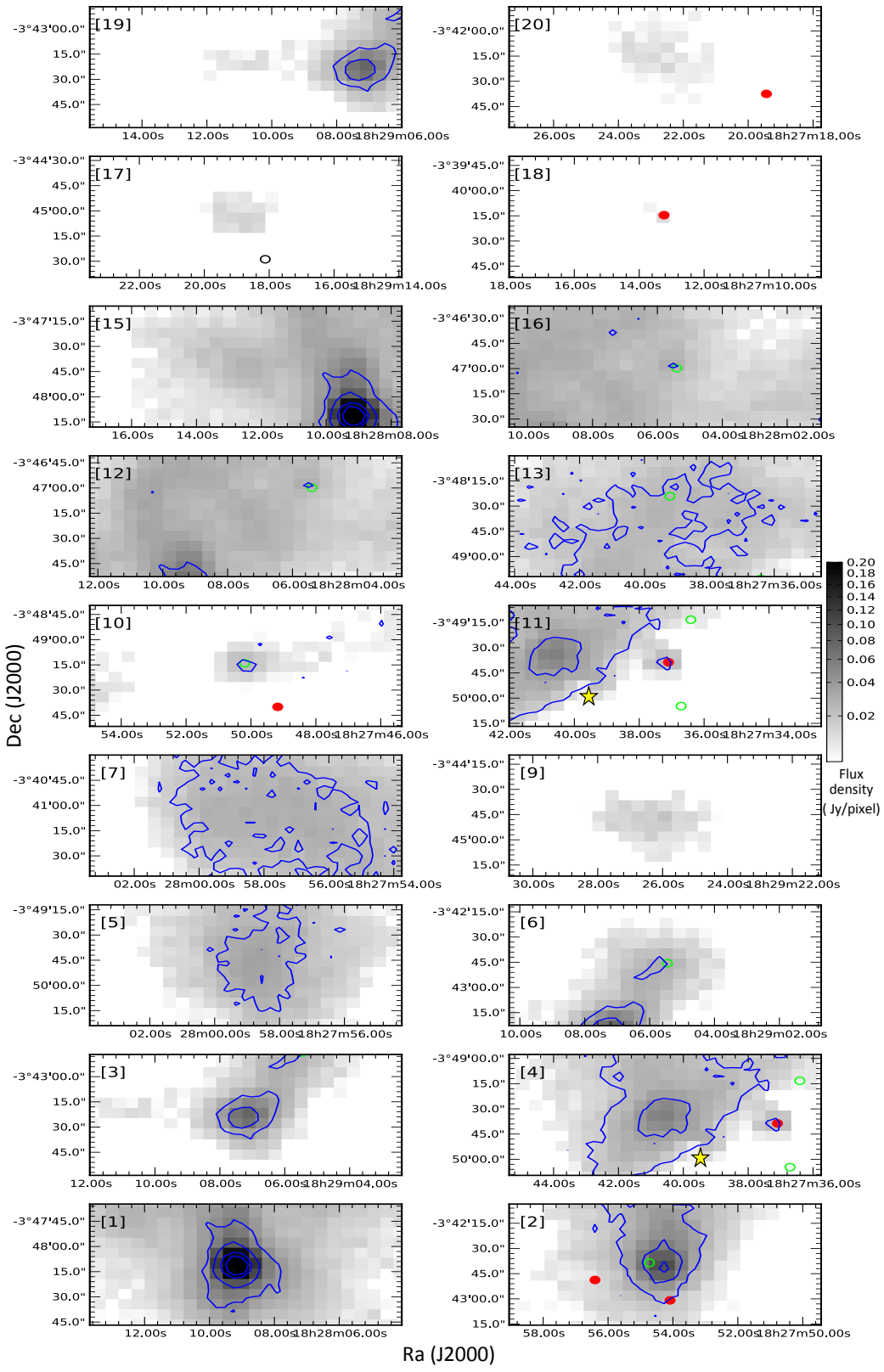

Figure 6.6: Comparison of SCUBA-2 fluxes from FELLWALKER clumps at 450 μm (contours), 850 μm (greyscale) and the SGBS YSOcs (markers). Numbers in square brackets correspond to the objects in Table 6.2. Maps show contours of 450 μm submillimeter flux at 5, 10, 20 and 30 σ (σ = 0.016 Jy/pixel). *Spitzer* YSOcs are indicated by hollow black circles (Class III), solid red circles (Class II) and green hollow circles (Class 0/I). The star indicates the location of the star MWC 297.

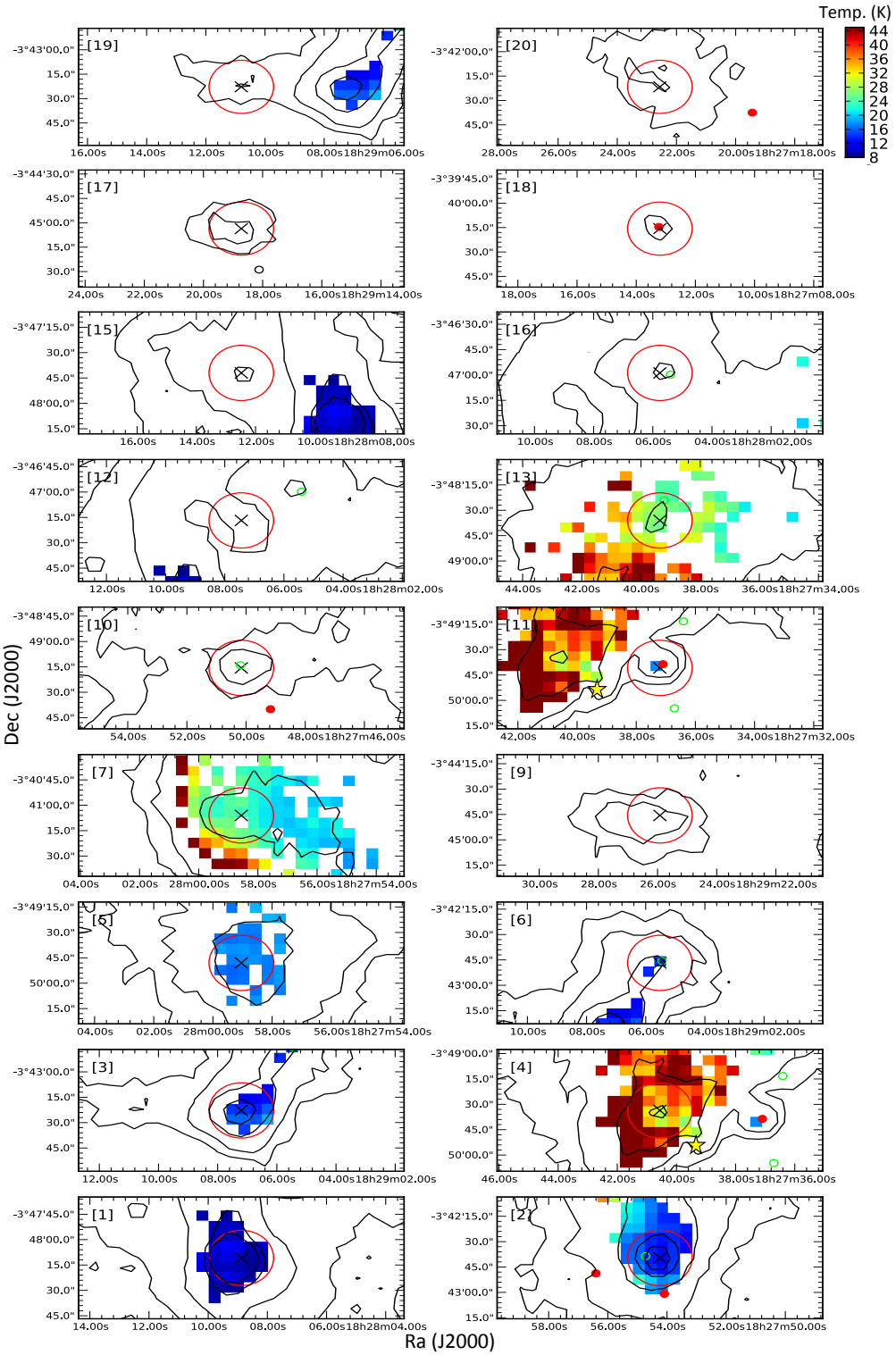

Figure 6.7: Submillimeter clumps in Serpens MWC 297 as identified by the FELLWALKER clump-finding algorithm. Numbers in square brackets correspond to the objects in Table 6.2. Maps show contours of 850 μm submillimeter flux at 5, 10, 20 and 30 σ (σ = 0.0022 Jy/pixel) up to the position of peak flux (black cross). The aperture from which SED flux density was calculated is plotted as the scale size of a protostellar core (0.05 pc). Temperature is shown where it is statistically significant and is used to calculate the masses shown in Table 6.4. *Spitzer* YSOcs are indicated by hollow black circles (Class III), solid red circles (Class II) and green hollow circles (Class 0/I). The star indicates the location of the star MWC 297.

For a minority of cases flux greater than 5σ is detected, but there is no significant peak in emission, for example YSOc15 and 21. Examining these specific cases, both are classified as protostars and are deeply embedded within S2-YSOc13. Figure 6.1c shows how this region is near the centre of the reflection nebulae SH2-62 and therefore I interpret YSOc15 and 21 as IR emission from dust heated by the star MWC 297 and not real YSOcs. Many of the remaining *Spitzer* YSOcs detect low level, extended SCUBA-2 flux with no significant peak. No significant flux is detected for objects outside the mask.

6.3.3 Spectral energy distributions

SEDs are powerful tools for determining the properties of a star and I use these as an aid to classification through measurement of the spectral index across their IR wavebands, bolometric temperature and luminosity ratio (Evans et al., 2009).

SEDs are constructed from archival Two Micron All Sky Survey (2MASS) fluxes, *Spitzer* fluxes, and from SCUBA-2 fluxes. For the SCUBA-2 fluxes I conducted aperture photometry (as described in Section 5.2) at both 450 μm and 850 μm centred on the FELLWALKER clump peaks from Table 6.2. None of the SCUBA-2 sources overlapped sufficiently to make blended emission a problem.

Our primary sources are IRAC and MIPS data from the SGBS. Six out of nine objects are identified in the SGBS YSOc catalogue. I access the full SGBS source catalogue, which includes sources not classified as YSOcs, and find fluxes of each of the remaining three objects. S2-YSOc 1 and 3 are low luminosity objects that cannot be reliably classified as a YSOc by *Spitzer* and are therefore labelled 'Red' and 'Flat' following a description of their SEDs. Both objects have IRAC and MIPS fluxes that are many orders of magnitude less than their peers. S2-YSOc 16 has been classed as a F5V star. Following the work of Alonso-Albi et al. (2009) I bring together fluxes and present the SEDs in Figure 6.8 with specific cases of individual YSOs discussed in depth the following sections.

Many of the following methods directly use the SEDs constructed in this section to classify YSOs by examining how the flux of the object varies with wavelength.

6.3.4 YSO classification

Spectral index, $\alpha_{\rm IR}$, is a direct measurement of the gradient of the SED slope over an range of IR wavelengths (typically 2 to 24 μm). Gutermuth et al. (2008) calculated $\alpha_{\rm IR}$ from the fluxes in the SGBS catalogue and I display these results in Tables 2.3 and 6.4 for SGBS. The sample contains four Class 0/I, two FS and three Class II sources. Saturation of *Spitzer* bands prevent measurement of $\alpha_{\rm IR}$ for MWC 297.

I calculate bolometric temperature, $T_{\rm bol}$, and luminosity, $L_{\rm bol}$, as alternative methods of classification of YSOs using the methods outlined in Chapter 1, Section 1.4. By adding SCUBA-2 data to that from the SGBS source catalogue, I extend the SEDs (Figure 6.8) for the YSOcs into the submillimeter spectrum and allow for a more complete integral from which I calculate $T_{\rm bol}$, the temperature of a black body with the same mean frequency of the observed SED, via Equation

Table 6.4: Properties of YSO candidates in MWC 297.

ID[a]	S^{b}_{450} (Jy)	S^{b}_{850} (Jy)	M^{c}_{850} ($M_\odot$)	T^{d}_{d} (K)	T^{e}_{bol} (K)	α^{f}_{IR}	L^{e}_{bol} ($L_\odot$)	L_{smm}/L^{e}_{bol} (%)	SGBS class[g]	Class
S2-YSOc1	14.4	3.09	5.1±0.5	10.3±0.5	30±3	1.65± 0.08	1.1±0.1	5.0±0.5	'Red'	0
S2-YSOc2	11.1	1.56	1.3±0.1	15.6±0.8	290±30	0.56±0.05	2.1±0.2	1.9±0.2	'YSOc red'	I
S2-YSOc3	7.0	1.09	0.95±0.08	14.8±0.7	8±1	1.4±0.7	0.8±0.1	3.0±0.3	'Flat'	0
S2-YSOc6	4.1	0.68	0.62±0.06	14.2±0.7	100±10	0.30±0.05	0.28±0.03	5.2±0.5	'YSOc'	0/I
S2-YSOc10	4.5	0.37	0.31±0.03	15.0 -	190±20	0.17±0.05	0.820.08	1.8±0.2	'YSOc star+dust'	I
S2-YSOc11	3.9	0.35	0.22±0.02	17.60.9	780±60	-0.43±0.06	3.3±0.2	0.3±0.0	'YSOc'	II
S2-YSOc16	3.7	0.73	0.60±0.05	15.0 -	120±10	0.9±0.3	0.73±0.07	1.9±0.2	'star F5V'	I
S2-YSOc18	0.1	0.11	0.09±0.02	15.0 -	820±50	-0.17±0.05	1.32±0.08	0.1±0.0	'YSOc star+dust'	II
S2-YSOc29	4.0	0.36	0.30±0.03	15.0 -	860±50	-0.49±0.05	0.34±0.02	0.1±0.0	'YSOc star+dust'	II
MWC	-	1.05	-	-	6606	-	4224	0.10.0	'2mass'	III

a) SCUBA-2 YSOcs (S2-YSOc) as identified by cross-referencing the SCUBA-2 clumps in Table 6.2 (Figure 6.7) with IR sources (Table 2.3).
b) Integrated fluxes of the YSOcs determined by fixed 40″ diameter aperture photometry. The uncertainty at 450 μm is 0.0165 Jy/pixel and at 850 μm is 0.0022 Jy/pixel. There is an additional systematic error in calibration of 10.6 % and 3.4 % at 450 μm and 850 μm.
c) Mass as calculated with equation 6.1. Errors are calculated from error in total flux, described in b., and error in mean temperature of 5 %. These results do not include the systematic error in distance (20 %) and opacity (factor of two).
d) Mean temperature as calculated from the temperature maps (Figure 6.1). Where no temperature data is available an arbitrary value of 15K - is assigned that is consistent with the literature.
e) YSOcs are classified using the T_{bol}, L_{bol} and L_{smm}/L_{bol} methods which are described in Section 5.4.
f) Values for spectral index are taken from the SGBS catalogue.
g) SGBS notation is described in Evans et al. (2009).

Table 6.5: SCUBA-2 40″ aperture fluxes for the *Spitzer* YSOc listed in Table 2.3. The full Table is associated with DOI:10.11570/15.0002.

YSO-ID	S_{450} Jy	S_{850} Jy	S2-YSOc ID
YSOc1	$< 0.72^b$	$< 0.065^b$	-
YSOc2	< 0.72	0.115 ± 0.013	S2-YSOc18
YSOc3	$< 0.72^b$	$< 0.065^b$	-
YSOc4	$< 0.72^b$	$< 0.065^b$	-
YSOc5	$< 0.72^b$	$< 0.065^b$	-
YSOc6	$< 0.72^b$	$< 0.065^b$	-
YSOc7	$< 0.72^b$	$< 0.065^b$	-
YSOc8	$< 0.72^b$	$< 0.065^b$	-
YSOc9	$< 0.72^b$	$< 0.065^b$	-
YSOc10	$< 0.72^b$	$< 0.065^b$	-
YSOc11	< 0.72	0.154 ± 0.013	S2-YSOc29
YSOc12	$< 0.72^b$	$< 0.065^b$	-
YSOc13	1.73 ± 0.14^a	0.184 ± 0.013^a	-
YSOc14	$< 0.72^b$	$< 0.065^b$	-
YSOc15	3.30 ± 0.14^a	0.408 ± 0.013^a	-
YSOc16	2.08 ± 0.14^a	0.071 ± 0.013^a	-
YSOc17	3.11 ± 0.14	0.362 ± 0.013	S2-YSOc11
YSOc18	2.10 ± 0.14^a	0.263 ± 0.013^a	-
YSOc19	$< 0.72^b$	$< 0.065^b$	-
YSOc20	1.11 ± 0.14^a	0.112 ± 0.013^a	-
...	...	...	...

(a) Extended low level emission in aperture. No significant peak at YSOc position ($> 3\sigma$).
(b) Outside data reduction mask. No significant flux detected in initial data reduction stage ($< 5\sigma$).

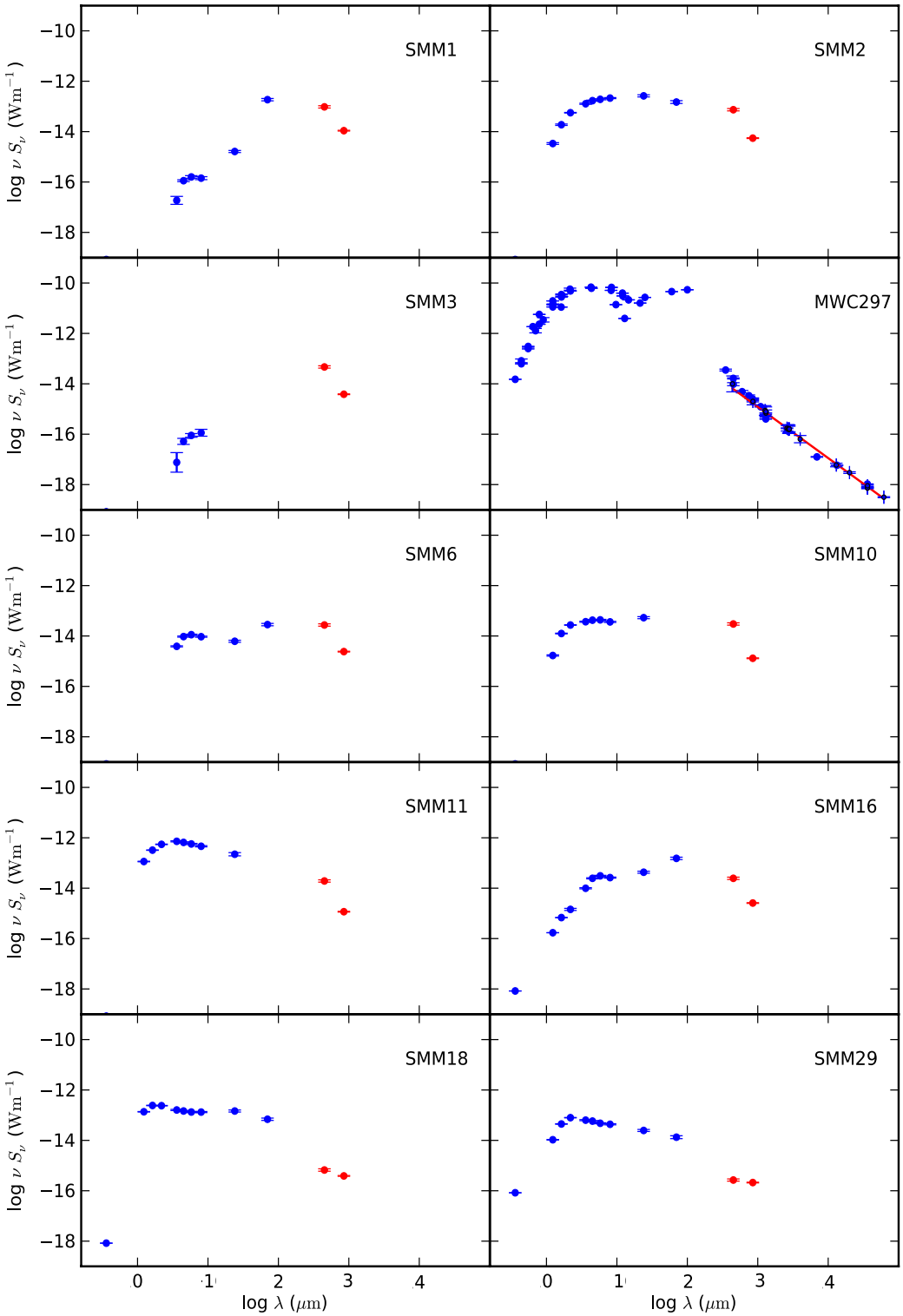

Figure 6.8: Spectral Energy Distributions for YSOcs associated with FELLWALKER clumps (Table 6.4). Blue points represent archive data sourced from *Spitzer* and 2MASS. Red points show new data provided by SCUBA-2 at 450 μm and 850 μm (note that the star MWC 297 was not identified by FELLWALKER after free-free contamination was accounted for). The straight line overlaid on the MWC 297 plot describes free-free emission from an UCHII region and polar jet/wind with a spectral index α=1.03.

1.9. T_{bol} measurements for my sources are listed in Table 6.4.

Similarly I calculate the ratio of submillimeter luminosity (L_{smm}), defined as L ≥ 350 μm by Bontemps et al. (1996), to L_{bol} in the method described by Myers et al. (1998) and Rygl et al. (2013), to classify YSOs. The classification schemes for each method is outlined in Table 1.1. The results for L_{smm}/L_{bol} are listed in Table 6.4. The sample contains two Class 0 sources, four Class I and three Class II by T_{bol} and three Class 0 to six Class I, II & III sources by L_{smm}/L_{bol}.

Uncertainties on L_{bol}, L_{smm}/L_{bol} and T_{bol} were calculated using a Monte Carlo method. A normal distribution of fluxes, with the mean on the measured flux at each wavelength for each YSO with a standard deviation equal to the original error on the measurements was produced. From each set of fluxes the classifications were calculated and the standard deviation on results listed in Table 6.4. The size of the uncertainties are consistent with Dunham et al. (2008). Dunham et al. (2008) and Enoch et al. (2009) both study the error on L_{bol} and T_{bol} and conclude incompleteness of the spectrum is a major source of systematic error in results of order approximately 31 % and 21 % (respectively) when compared to a complete spectrum. Enoch et al. (2009) find that the omission of the 70 μm flux is particularly critical when interpreting classification, leading to an overestimate of L_{bol} by 28 % and underestimate of T_{bol} by 18 %.

Figure 6.9 shows a direct comparison between the α_{IR}, L_{smm}/L_{bol} and T_{bol} methods of classifying YSOs. As outlined in Chapter 1, each specialises in classification at different stages of evolution with T_{bol} arguably being the most effective for classifying protostars. Young et al. (2005) studied the merits of T_{bol} and L_{smm}/L_{bol} and concluded that the latter is the more robust method for classifying Class 0 objects when compared to models of core collapse. However, it is also more sensitive to incompleteness of the submillimeter spectrum. With only two fluxes at wavelengths greater than 350 μm for the majority of the YSOs in the Serpens MWC 297 region, I must consider the results from L_{smm}/L_{bol} to be incomplete and therefore less reliable than T_{bol}.

Out of the three objects classified as Class 0 by both L_{smm}/L_{bol} and T_{bol} methods, only S2-YSOc 1 is consistent in both regimes. This object has a significantly positive value of α_{IR} and so I classify this object as Class 0. The other two objects, S2-YSOc 3 and S2-YSOc 6, are forming in close proximity to each other but relatively isolated from the rest of the cloud. With a minimum separation of approximately 10,000 AU it seems likely that these objects formed together and therefore they are likely to be a similar class. S2-YSOc 3 has no noticeable IR flux at 24 μm. However, the S2-YSOc 3 SED (Figure 6.8) shows *Spitzer* data consistent with emission from a heated region and so I conclude that the emission at 24 μm is sufficiently weak that it does not surpass the noise level and therefore does not appear in Figure 6.1c. Such low luminosity emission would be typical of Class 0 and therefore I label it as such. S2-YSOc 6 has a weak, if non-negligible, detection at 24 μm data. Therefore, I label it as Class 0/I. S2-YSOc 2 and 10 consistently fall into the Class I bracket by all three methods.

S2-YSOc 11, 18 and 29 all represent highly evolved and largely isolated cores that are consistently classified as Class II/III objects and have 24 μm detections in Figure 6.1c. Finally I discuss S2-YSOc16, an object labelled Class I by T_{bol} and by α_{IR} and with a strong peak in the 24 μm data. Figure 6.7 shows how this object appears deep within an extended dust cloud. This scenario fits the definition of a Class I and the low mass of the object (0.60 $M_{\odot}$) when compared

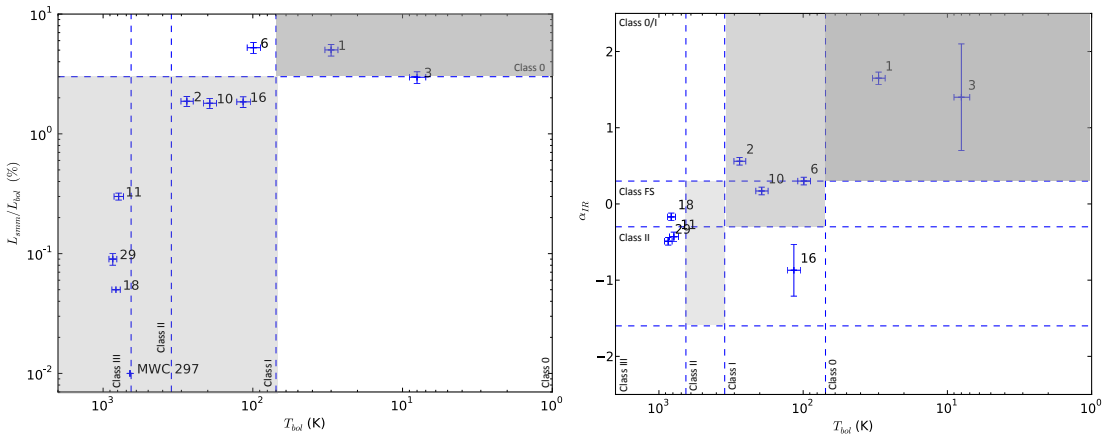

Figure 6.9: Bolometric temperature plotted against L_{smm}/L_{bol} (*left*) and α_{IR} (*right*) for the 10 YSOcs listed in Table 6.4. Dashed lines indicate the boundaries of classification of objects (greyed boxes indicating regions of class space where methods agree).

to the mass available in the neighbouring clumps (approximately 21 $M_{\odot}$) suggests that this object is early in its accretion life cycle.

6.4 Discussion

6.4.1 The state of star formation in Serpens MWC 297

Star formation is active and ongoing over a wide range of physical stages, from prestellar objects to Class III PMS-stars. I have detected 22 clumps in SCUBA-2 850 μm data using the clump-finding algorithm FELLWALKER (Table 6.2), from which I classify eight as YSOcs through consistency with 24 μm data and the SGBS YSOc catalogue. I include an additional *Spitzer*-detected YSOc (YSOc11) which was missed by FELLWALKER to provide us with a sample size of nine (Table 6.4), in addition to the 10 $M_{\odot}$ zero age main sequence (ZAMS) star MWC 297. Seven (YSOc2, 11, 17, 32, 41, 47, 73) of these are found in the SGBS YSOc catalogues and two in the general SGBS source catalogue. Three Class 0, three Class I and three Class II sources are classified with SCUBA-2 data.

72 Class II/III and 10 Class 0/I sources are listed in the SGBS catalogue for the region. I do not expect to detect a high proportion of the Class II objects or any Class III objects with SCUBA-2. Figure 6.5 shows how few of these objects lie within the 3σ detection level. I do expect to detect all Class 0 and most Class I objects with SCUBA-2 and therefore four (YSOc 15, 16, 21, 38) out of 10 Class 0/I sources listed in the SGBS catalogue that are not associated with SCUBA-2 peaks should be considered with scepticism. The remaining 16 objects identified by FELLWALKER are considered to be prestellar objects and diffuse clouds. From the SCUBA-2 and *Spitzer* YSOc catalogue every stage in star formation is represented up to stars on the main sequence. Given the assumed lifetime of each class, star formation has been active in this region for at least 3 Myr.

Star formation is observed at various stages in five large-scale clouds in the region which

are composed of a number of fragmented clumps (Figure 6.3), the most evolved of which contain star forming cores. S2-YSOc 1 represents the most massive core I detect at 5.1±0.5 $M_\odot$ and is the most prominent object in a larger cloud of mass 21±2 $M_\odot$ (see Figure 6.7). S2-YSOc 1 is the coolest YSO I have observed with mean temperature of 10.3±0.5 K and there is no evidence of heating in this region. If all the mass detected in S2-YSOc 1 accretes onto the core, allowing for a star formation efficiency of 30 % (Evans et al., 2009), this object may go on to form an intermediate mass star similar to MWC 297.

A second cloud appears somewhat less fragmented with only two objects as opposed to four but also less massive with a peak core mass of 1.3±0.3 $M_\odot$ and total cloud mass of 3.5 $M_\odot$ (Figure 6.7 - S2-YSOc 2). Likewise a 30 % star formation efficiency would limit the final mass to around 1 $M_\odot$. S2-YSOc 3 and 6 (Figures 6.7) form a potentially loosely bound proto-binary composed of a Class 0 and Class I object with separation of 10,000 AU and masses 0.95±0.08 and 0.62±0.06 $M_\odot$.

In addition to these deeply embedded, less evolved objects, a number of more evolved, isolated objects were observed. S2-YSOc 10, 18 and 29 are detached from the larger clouds and are much less luminous than the younger objects (Figure 6.7). At these stages, PMS-stars are dominated by discs rather than envelopes and I calculate masses of 0.31±0.03 $M_\odot$, 0.09±0.02 $M_\odot$ and 0.30±0.03 $M_\odot$ for these objects. Note that these calculations were made based on an opacity with a spectral index of $\beta = 1.8$. As discussed in Chapter 5, lower values of β have been associated with more evolved objects where discs have been observed, and as a result these masses represent an upper limit. The protostar to PMS ratios suggest that these objects may have been formed in a dense region and later been ejected or that the associated molecular cloud was larger in the past. Typical core migration speeds of 1 pc per Myr are consistent with the size of the observed region (30′ diameter) and birth of these objects in one of the large clouds, most likely that associated with the star MWC 297 as it is the most evolved. S2-YSOc 11 and 16 are likely transition cores between Class I and II stages (Figure 6.7).

The remaining objects are not considered to be star-forming. The most massive of these are SMM 5 and 7 at 3.3±0.3 and 3.1±0.2 $M_\odot$ (see Figure 6.7). I calculate free-fall timescales of 2.1 and 1.8 Myrs for these objects. These are significantly larger than the typical protostellar (Class 0/I/FS) timescale of 1 Myr (Evans et al. 2009) are therefore unlikely to form stars without cooling further. The mean temperature of starless clumps is over twice that of star-forming cores (32±4 K to 15±2 K). The observed core temperature is consistent with the assumption made in Section 2.2 and used by Kirk et al. (2006). The remaining objects all have masses less than 1 $M_\odot$ and are too diffuse to produce reliable temperature data. If these objects go onto to form stars, they are unlikely to form anything more massive than a brown dwarf.

A global analysis of the region reveals that, of a total cloud mass of 40 $M_\odot$, only 12.5 $M_\odot$ is not currently associated with ongoing star formation. Assuming a mean YSO mass of 0.5 $M_\odot$ based of IMF observations (Chabrier, 2005; Evans et al., 2009), and given a mass of MWC 297 of 10 $M_\odot$ (Drew et al., 1997), I conclude that the total stellar (Class II or higher) mass of the region is 46 $M_\odot$. To date, approximately 85 % of the original cloud mass has gone into forming stars. From this I conclude that once this current generation of stars are formed, there is unlikely to be any

further massive star formation without further mass accreting from the diffuse ISM and as a result I envisage a large distribution of low mass objects with the massive MWC 297 system dominating the region.

6.4.2 What does SCUBA-2 tell us about the star MWC 297?

The B1.5Ve star MWC 297 is a well known object. I comment on its relevant features and refer the reader to Sandell et al. (2011) for a comprehensive review the star's properties.

MWC 297 is considered to be physically associated with the YSOcs within a 1′ radius identified in SGBS and the additional YSO catalogues identified in Table 2.4 and displayed in Figure 6.5. MWC 297, objects 2MASS J18273854-0350108 (undetected in SCUBA-2) and 2MASS J18273670-0350047 (detected as S2-YSOc 11 in SCUBA-2) were found to have a mean group velocity of 0.01″per year (Röser et al., 2008; Zacharias & Zacharias, 2012; Zacharias et al., 2013) providing evidence they were formed from same cloud. Further evidence in 24 μm data shown in Figure 6.1c shows how emission from warm dust heated by MWC 297, associated with SH2-62, is consistent with the location of dust clouds in the SCUBA-2 data. The angular distance between MWC 297 and the nearest clump (SMM 4) detected in SCUBA-2 amounts to a minimum physical separation of 5,000 AU, approximately half the size of my definition of a core (0.05 pc, Rygl et al. 2013).

Previous observations have interpreted a submillimeter source consistent with the location of MWC 297 as an accretion disc or circumstellar envelope (Di Francesco et al., 1994; Drew et al., 1997; Di Francesco et al., 1998). I believe that these observations can now be explained as free-free emission, as outlined in Chapter 4. Manoj et al. (2007) constrain the disc radius with radio observations to 80 AU and calculate a disc mass of M = 0.07 $M_\odot$. These results are supported by Alonso-Albi et al. (2009) who conclude that this 'exceptionally low' disc mass is partly due to photoionisation by an UCHII region. Manoj et al. (2007) calculate a disc mass of 0.07 $M_\odot$.

Our results do not rule out the presence of a disc or residual envelope following subtraction of the free-free emission, but they do confirm that any residual disc is low mass, though with a high degree of uncertainty as the submillimeter flux observed at the position of MWC 297 likely contains a component from the clump SMM 4 which overlaps this location. Taking the Manoj et al. (2007) disc mass of 0.07 $M_\odot$ and using equation 6.1, with the residual dust flux at 850 μm of 15 mJy/pixel, I calculate this would correspond to a disc temperature of approximately 7 K. It therefore appears more likely that any flux observed by SCUBA-2 material at the location of MWC 297 comes from cold material along the line of sight, rather than a warm disc which typically have temperatures closer to 50 K.

Temperature information about MWC 297 is also limited by the low and uncertain flux of the residual emission. I note that throughout this paper I have assumed a constant value of $\beta = 1.8$. I have argued this a fair assumption for the ISM and extended envelope but this does not hold for protostellar discs where the value of β is known to be closer to 1.0 (Beckwith et al., 1990; Buckle et al., 2015), leading to higher dust temperatures, but lower masses (see Figure 5.1).

6.4.3 Is there evidence for radiative feedback in Serpens MWC 297?

The star MWC 297 is directly associated with the star-forming clumps identified in the SCUBA-2 data and the B star is directly heating those objects, none more so than SMM 4 where the result suggests that MWC 297 is directly influencing its evolution. A mean temperature of 46±2 K for SMM 4 was calculated, almost a factor of three times higher than the typical clump temperature of 15 K. The standard deviation of pixel temperature in this clump is high at 11 K. The clump is warmest around the exterior with temperatures peaking above 55 K (potentially contributed to by edge effects) but it appears to have a cooler centre of 29 K (Figure 6.7). This is warmer than the mean temperature (18 K) of all the other clumps (discounting SMM 22 on account of its small size) detected by FELLWALKER. Heating of this object is not internal and the ISRF is not sufficient to produce such high temperatures. Only MWC 297 can provide sufficient external heating as it is displaced just 0.03 pc (6,000 au) from the SMM4. Theoretical dust heating due to OB stars is investigated in chapter 8.

SMM 4 has a dust mass of 0.91±0.05 $M_{\odot}$ but is the fourth most luminous clump in the region with a well defined, centrally condensed core. Raised temperatures mean that the object is gravitationally stable with a M_{850}/M_J ratio of 0.12. From these results I conclude that, in the past, SMM 4 may have begun to collapse on a similar timescale to MWC 297; however upon the B star producing sufficient radiation, MWC 297 has directly heated the larger part of the neighbouring clump to the extent that gravitational collapse is no longer possible, in effect suppressing, or even halting, the star formation process. Whether or not the low mass of SMM 4 or the power of MWC 297 is the limiting factor in this process remains unknown.

The majority of the other clumps detected show little or no external heating and no objects show evidence of internal heating. Table 6.2 outlines a range of mean clump dust temperatures, between 10 and 46 K, across the region. This is wider than the range of 12 to 20 K assumed by Motte et al. (1998) for Ophiuchus. Examining the mean temperatures of the Class 0 objects I find values of 12.6±0.9 K, below the assumed 15 K used by Kirk et al. (2006) but within the range of Motte et al. (1998). Of the six Class 0/I objects, two (S2-YSOc 2 and 10) lie within the nebulosity whereas the remainder lie in regions with little significant emission from large scale heated dust as shown in Figure 6.7. None of the YSOcs show significant heating. However, use of a constant β may not hold towards the centre of a protostar and the use of $\beta = 1.8$ appropriate for large structures maybe be systematically underestimating temperatures in these regions.

Starless object SMM 7 shows heating (Figure 6.7) along its eastern edge which is not consistent with the 24 μm emission. I suspect these are the 'edge effect' artefact produced in the map making process and this consequently increases temperature to 25±2 K. Conversely SMM 5 shows evidence of heated gas along its western edge in 24 μm emission (Figure 6.1c) but is relatively cool and homogenous in Figure 6.7 with a mean temperature of 18.2±0.9 K. Prohibitively high noise in the 450 μm data prevents wider examination of this feature.

6.5 Conclusions

I observed the Serpens MWC 297 region with SCUBA-2 at 450 μm and 850 μm as part of the JCMT Gould Belt Survey of nearby star-forming regions. The observations cover a 30′ diameter circular region centred on RA(J2000) = 18:28:13.8, Dec. (J2000) = -03:44:01.7 including the B1.5Ve Herbig Be star MWC 297 and a collection of local dense clouds. I use the clump-finding algorithm FELLWALKER to identity submillimeter clumps in the data and compare the catalogue to YSOc catalogues produced by the *Spitzer* Gould Belt Survey (SGBS), and to *Spitzer* 24 μm data of the region. The latter shows heating of surrounding clouds associated with the star MWC 297 and the optical nebula SH2-62, providing evidence that the two are physically located in space.

In Chapters 3 and 4 I accounted for sources of submillimeter contamination, finding an insignificant CO contamination estimated at 13 % but a significant amount from free-free emission as the result of an ultra-compact HII region and polar winds/jets associated with the star MWC 297. I use the two-component beam SCUBA-2 flux ratio method to build maps of dust temperature for Serpens MWC 297 with the aim of investigating evidence for radiative heating in the region. To do this I employed a method whereby each dataset is convolved with both the primary and secondary beam components of the JCMT beam at the other wavelength to achieve like resolution of 19.9″ before calculating the flux ratio and consequently temperature.

Our key results are:

1. I detect 22 clumps in SCUBA-2 850 μm observations of the Serpens MWC 297 region. By cross referencing this list with *Spitzer* YSOcs and a comparison of mass to Jeans mass as a test of gravitational stability, I identify nine YSOcs

2. I calculated masses based on calculated temperatures (as opposed to an assumed value) across the whole region. Clump masses range between 0.02-19 M⊙ and core masses range between 0.09-5.1 $M_{\odot}$. Starless clumps are consistently warmer than star forming cores with mean temperatures of 32±4 K compared to 15±2 K.

3. I classify the YSOs using T_{bol} and L_{smm}/L_{bol} as two Class 0, one Class 0/I, three Class I and three Class II sources. 30 % of Class 0/I objects and 8 % of Class II objects catalogued in SGBS were also detected by SCUBA-2. No Class III objects were detected by SCUBA-2. SCUBA-2 detected two potential Class 0 and one Class I/II YSOcs that were not included in the SGBS YSOc catalogue.

4. The residual dust emission for MWC 297 was insufficiently bright to be distinguishable from a larger clump (SMM 4) projected behind it on the sky. Any residual disc in the MWC 297 system is therefore very low mass.

5. I conclude that radiative heating from one generation of stars is directly influencing the formation of another, but I note that the effect is not large across the region. My findings suggest that clump SMM 4 had begun collapsing before radiative heating from MWC 297 raised the temperatures to 46±2 K, to the extent that gravitational collapse is now suppressed or even halted.

The Serpens MWC 297 region represents a low mass star-forming region with a limited number of YSOcs. I believe that in the future, this region will become dominated by the HII region associated with the star MWC 297. The expansion and shock front of this region will likely play an important role in the subsequent evolution of the cores and clumps I have detected. In subsequent chapters I look at expanding these methods to produce temperature maps for larger regions within Serpens-Aquila and other GBS regions, with a particular eye to possible free-free contamination where OB stars are observed to be forming.

7

Radiative heating in the Aquila W40 Complex

This chapter is drawn from Rumble et al. (2016), *The JCMT Gould Belt Survey: Evidence for radiative heating and contamination in the W40 complex*, which focuses on SCUBA-2 observations of the W40 complex in the Aquila region, a region associated with high extinction (Dobashi et al., 2005) and massive star formation that is driving a blistered H II region (Westerhout, 1958) powered by an OB association, the details of which are listed in Table 7.1 (Zeilik & Lada, 1978; Smith et al., 1985). I adopt a distance of 500 ± 50 pc, following Radhakrishnan et al. (1972) and Mallick et al. (2013), for the following analysis. The full characteristics of this region are presented in Chapter 2, Section 5.2, along with the data and details of its reduction.

In this Chapter I identify clumps in the 850 μm data, using the FELLWALKER clump finding algorithm, and calculate masses and peak column densities from dust temperature maps produced using the Kernel-convolution method, described in Chapter 5. By giving constraints on core size I also produce a separate catalogue of dense cores and compare this to the composite YSOc catalogue produced from the SGBS list merged with the catalogues published by Kuhn et al. (2010), Rodríguez et al. (2010), Maury et al. (2011) and Mallick et al. (2013) (described in Chapter 2, Section 5.2) to examine the star formation. I discuss the evidence for radiative heating and its sources, and whether this radiative feedback is influencing the ongoing formation of stars in the region.

7.1 Temperature maps of the W40 complex

The results of the common resolution convolution kernel maps in the form of temperature and SCUBA-2 spectral index α are presented in Figures 7.1 and 7.2 (left) respectively. The range of dust temperatures (9 to 63 K) in the W40 complex is presented in Figure 7.2 (right) and is

Table 7.1: Summary of bright radio objects in the W40 complex and evidence for variability, jet emission and free-free opacity at SCUBA-2 wavelengths, from which a value of $\alpha_{\rm ff}$ can be estimated (if not previously calculated).

Source	2MASS ID	VLA ID[a]	Type [b]	Time [a] variable?	Jet[a]?	SCUBA-2 source?	Optically thick?	Spectral index $\alpha_{\rm ff}$	Distance[b] (pc)
OS 1a (North)	J18312782-0205228	15	Herbig AeBe	N	N	Y	Y	-0.3±0.2[c]	536^{+42}_{-95}
OS 1a (South)	J18312782-0205228	-	O9.5	-	N	Y	-	-	536^{+42}_{-95}
OS 1b	J18312866-0205297	18	Class II	N	Y	N	N	-0.8±0.5[c]	-
OS 1c	J18312601-0205169	8	Class II	Y	N	N	N	-0.6±0.2[c]	-
OS1d	J18312766-0205097	13	Class II	Y	N	Y	N	0.1±0.2[c]	-
OS 2a	J18312397-0205295	7	Herbig AeBe	Y	Y	Y	Y	1.0	-
OS 2b	J18312257-0205315	-	B4	Y	Y	N	N	-0.1	455^{+71}_{-59}
OS 3	J18312395-0204107	-	B3*(binary)	-	-	N	-	-	454^{+87}_{-48}
IRS 5	J18311482-0203497	1	B1	-	-	N	N	0.3±0.2[c]	469^{+217}_{-129}
-	J18312232-0206196	3	Class II	N	Y	N	N	1.1±0.2[c]	-
-	-	14	-	N	N	N	N	0.0±0.1[c]	-

[a] Radio source ID and characterisation based on the findings of Rodríguez et al. (2010).

[b] Protostellar and main sequence star classifications and distances calculated from Spectral Energy Distributions in Shuping et al. (2012).

[c] Free-free spectral index calculated by Ortiz-León et al. (2015).

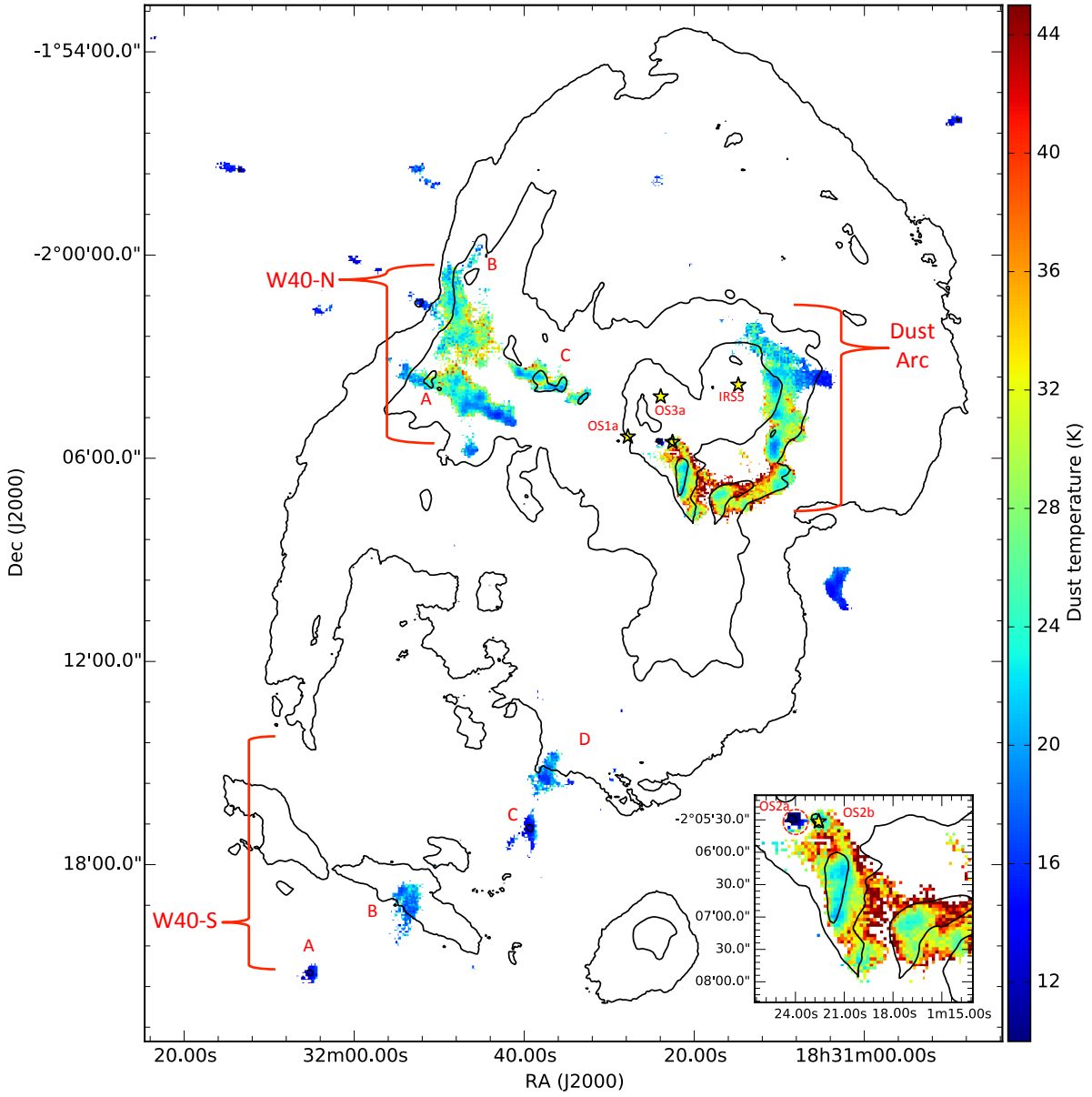

Figure 7.1: Temperature map of the W40 complex with *Herschel* 70 μm contours at 300, 1200, 4800 and 12000 MJy/Sr. Note that the 850 μm flux has been decontaminated for CO in all areas except W40-S. Temperatures are given at positions where the 850 μm flux is at least five times the noise level and the fractional error on the temperature is less than 0.34. The insert shows a zoom in on the Eastern Dust Arc and the high mass stars OS2a/b.

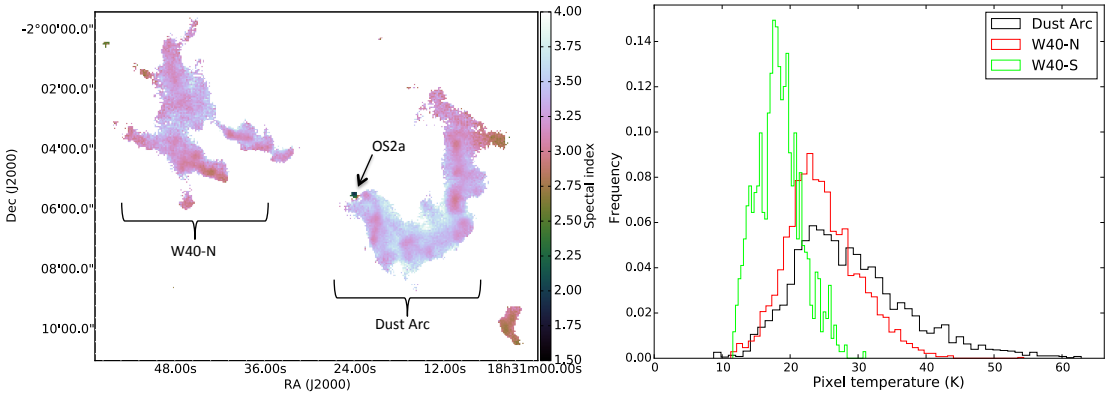

Figure 7.2: left) SCUBA-2 spectral index α of W40-N and the Dust Arc. The spectral index for W40-S is not shown but is similar in value to W40-N. Right) the normalised distribution of pixel temperatures across the W40 complex clouds: Dust Arc (black, warmest), W40-N (red) and W40-S (green, coolest).

comparable to those calculated from SCUBA-2 data in NGC1333 by Hatchell et al. (2013) and in Serpens MWC 297 in Chapter 6. I break the complex into major star-forming clouds. The Dust Arc, W40-N, and W40-S have mean temperatures of 29, 25 and 18 K, respectively. Figure 7.2 (right) presents the distributions of temperatures in these clouds.

The Dust Arc shows a large range of temperatures along its length with some of the coolest temperatures (16±2 K) found in the west and warmest (in excess of 50 K) are found in the east. The temperature morphology of the Dust Arc includes a number of cooler spots (approx. 20 K) associated with brightest SCUBA-2 cores and much high temperatures around the core exterior, though these regions have much higher uncertainties (between 20 to 30%). The northern side of the Dust Arc has a slight over-density of warmer pixels compare to the souther side. The temperatures associated with OS2a are the lowest (9 K) in the whole region in spite of allowing for free-free and CO emission.

W40-N is a little studied object as it is not in close proximity to the OB association and star cluster. W40-NA, B and C have a remarkably consistent temperatures with standard deviation of 4 K (compared to 8 K in the Dust Arc). It is significantly cooler than the Dust Arc with a mean temperature of 21±4 K compared to 26±4 K.

W40-S is a filament composed of four major clouds. The bulk of the filament is on the periphery of the H II region/nebulosity SH-64. There is a sharp contrast between the temperatures of the four clouds with B and D the warmer bodies both 20±3 K. A and C are significantly cooler with temperatures of 14±1 and 16±2 K. In addition to W40-S there are a number of smaller clouds of similar temperatures that are not associated with the three identified regions of the W40 complex.

The dust temperatures in the Aquila region have also been mapped by Könyves et al. (2015) through SED fitting to *Herschel* SPIRE and PACS bands. Figure 7.3 demonstrates cooler temperatures associated with large-scale structures and the Serpens South filament, as well a heated region that includes the 70 μm W40 complex nebulosity, SH2-64, mapped in Figure 7.1. A smaller heated nebulosity, SH2-62, is also observed to the south that is associated with the B star MWC

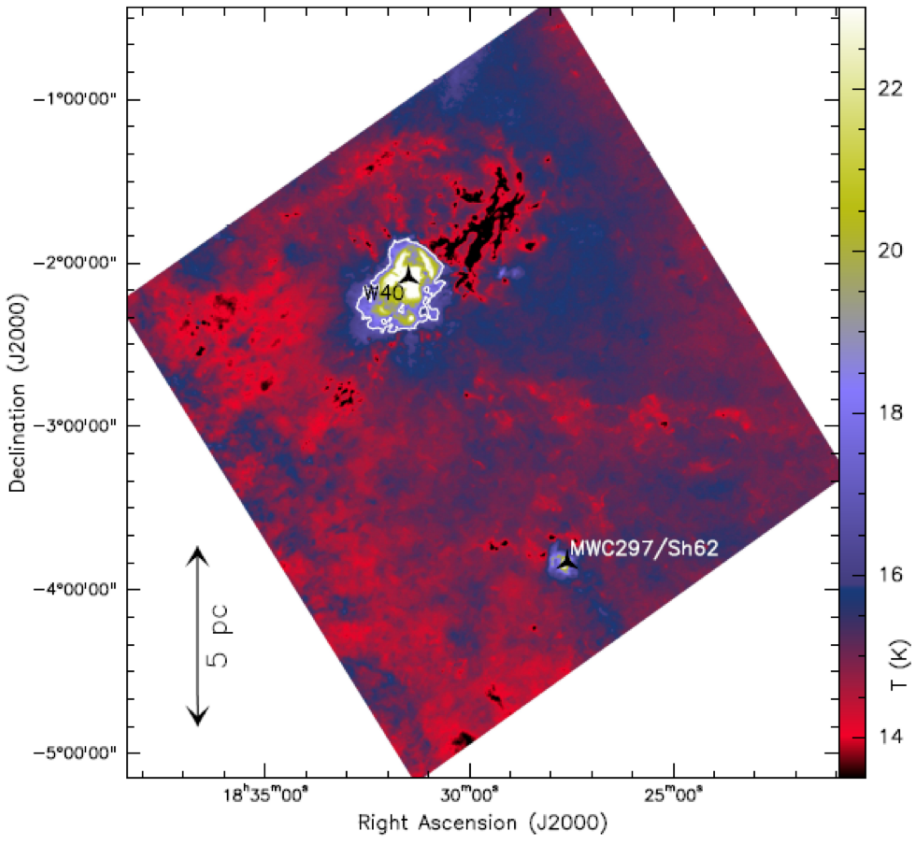

Figure 7.3: *Herschel* dust temperature map of the Aquila rift. White contours denotes 17 K. Map resolution is 36.3″. Figure reproduced from Könyves et al. (2015).

297 and 24 μm emission that was discussed in Chapter 6. Temperatures in the W40 complex peak in excess of 25 K, comparable to those calculated from the SCUBA-2 flux ratios and presented in Figure 7.1. Full comparison is limited due to the lower resolution of the Könyves et al. (2015) map (36.3″).

A map of the SCUBA-2 flux spectral index (Figure 7.2 left) is a more objective summary of the submillimeter SED. I find that α values are fairly constant across the filaments of the W40 complex with a mean $\alpha = 3.1 \pm 0.2$, as expected for the ISM with $\beta = 1.8$ and temperature approximately 20 K. However, the value of α associated with OS2a (marked in Figure 7.1) is notably lower with a minimum value of $\alpha = 1.6 \pm 0.1$.

A low α has previously been explained by very low β, associated with grain growth (Manoj et al., 2007), or low temperatures. Chapter 6 demonstrated that lower spectral indices can also be caused by free-free emission contributing to SCUBA-2 detections, but in this case the free-free emission does not have a significant impact on α. SCUBA-2 dust temperatures towards OS2a are some of the lowest in the whole region with values less than 9 K (see Figure 7.1 insert). Given a β=1.0, typical for circumstellar discs, $\alpha = 1.6$ would require an unphysical temperature of less than 2 K. Alternatively, an exceptionally low β approaching zero would still require an excessively low temperature of less than 7 K, comparable to the SCUBA-2 dust temperature of 9 K (see Figure 7.1 insert) observed at β=1.8. It is therefore unlikely that β alone can explain these results.

OS2a was detected by the VLA in Rodríguez et al. (2010) in the autumn 2004 and noted as a variable radio source. Subsequent observations by Ortiz-León et al. (2015) in summer 2011 failed to make a significant detection of OS2a, confirming the object as highly variable. The transient nature of OS2a could offer an alternative explanation for the exceptionally low dust spectral index observed by SCUBA-2 in the summer 2012. I note that Maury et al. (2011) calculate a dust temperature of 40±8 K for OS2a from the 2 μm - 1.2 mm SED which incorporates observations from 2007 and 2009. Further work is required to fully address the nature of this source.

SCUBA-2 observations of the W40 complex were used to calculate masses and column density using Equation 1.35 and 1.30, following the methods described in Chapter 6 and assumptions given in Section 1. A map of column density is presented in Figure 7.4 (left). Previous authors, for example Johnstone et al. (2000) and Sadavoy et al. (2010) have often used an assumed constant temperature these calculations.

7.2 The SCUBA-2 clump catalogue

In this section the Starlink `fellwalker` algorithm (Berry, 2015) is used to extract a catalogue of irregular clumps from the SCUBA-2 850 μm, CO subtracted, 4′ filtered, free-free subtracted data. Each clump then forms the basis of a mask from which the clumps' fluxes, temperatures, column densities and YSO densities are determined. Masses, Jeans masses, Jeans stability and projected distance between each clump and OS1aS (from here on in referred to as OS1a), the primary ionising star in the OB association, are subsequently calculated.

Details of how FELLWALKER is applied to SCUBA-2 data is given in Chapter 6. The parameter MinDip is set to 3σ so that FELLWALKER is tuned to break up large-scale continuous clouds with multiple bright cores into discrete clumps. The Noise and MinHeight parameters are set to $5\,\sigma$ and MaxJump is set to one pixel ensuring that all extracted clumps are significant detections but allowing for fragmentation peaks. By setting MinPix to four pixels, a large number of single-pixel objects that were likely noise artefacts were removed from the catalogue. Beam deconvolution of clump sizes was set to false. However, the flux weighted beam sizes were calculated using a FWHMbeam parameter of 1 pixel, or 3″. This was found to be equivalent to the FWHM given high SNR. At low SNR (less than 10) FELLWALKER will significantly underestimate the size of the clump, as demonstrated in Figure 7.5. A reduced beam size was used to ensure that point-like sources, such as isolated protostellar envelopes or discs, were not omitted by the algorithm.

The original observations also include objects that are part of Serpens South which is located near to the W40 complex on the sky. There is no physically defined point in the SCUBA-2 data that describes where the W40 complex ends and Serpens South begins and so I define an arbitrary cut off along the meridian RA(J2000) = 18:30:40 with all objects eastward belonging to the W40 complex and westward to Serpens South. Whilst this approach may risk associating some clumps with the wrong region, I estimate this will affect less than 5% of members overall.

I identify 82 clumps in the W40 complex and their fluxes at 850 μm, as well as 70 μm, 450 μm and 21 cm from *Herschel*, SCUBA-2 and Archival VLA maps, respectively, are presented in odd Tables 7.3 through to 7.11. Clump positions in the W40 complex are presented in Figure

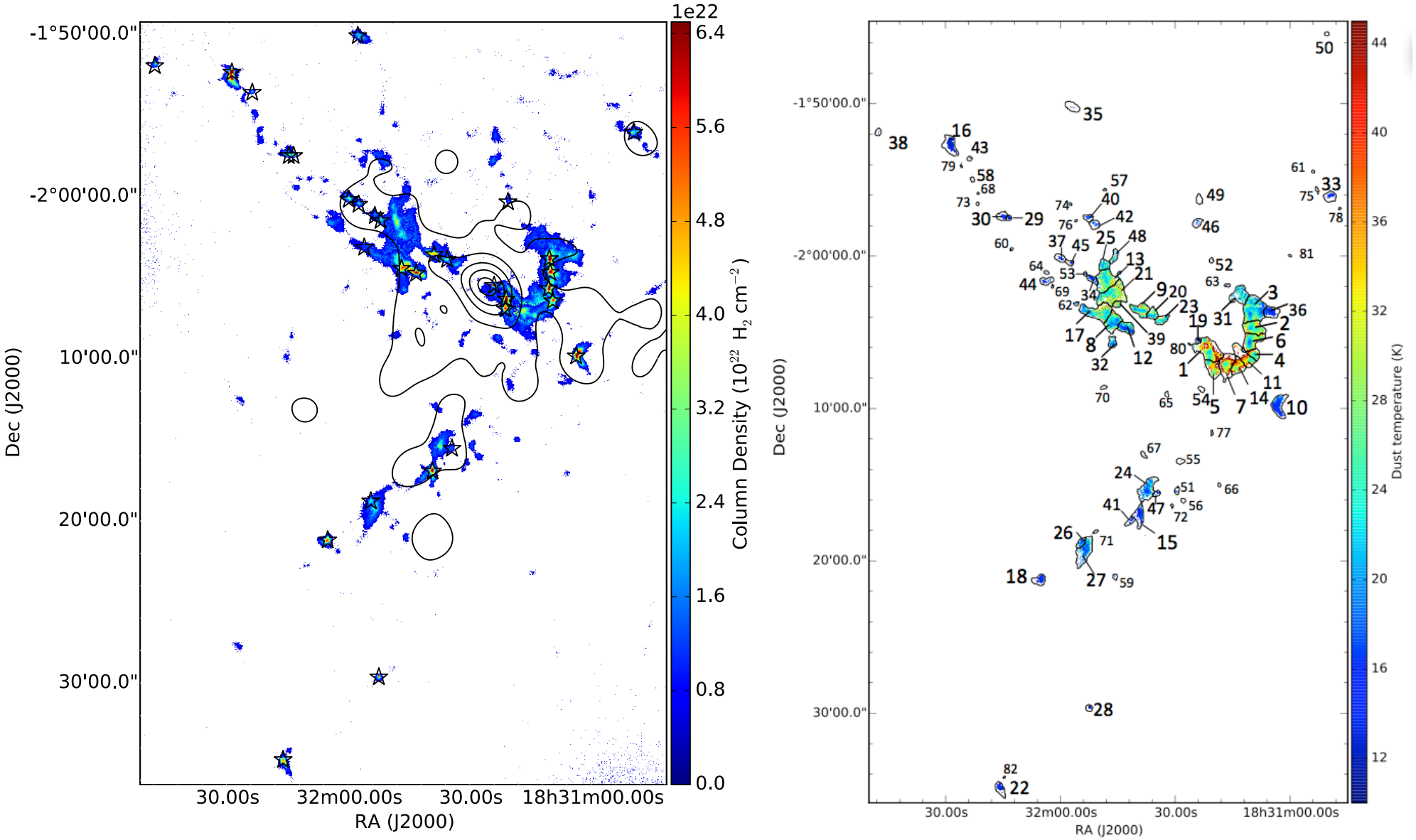

Figure 7.4: Left) SCUBA-2 column density map of the W40 complex. Column density is shown for areas where emission is detected at or above S/N = 3 at 850 μm. Column density is calculated using temperatures as presented in Figure 7.1 where available and a constant value of 15 K where a derived temperature is not. Contours describe YSO surface density with levels at 20, 60, 110, 160 and 210 YSOcs pc^2. Stars mark the location of each dense core identified in Table 7.2. Right) temperature map of the W40 complex with clumps identified in the SCUBA-2 CO subtracted, 4′ filtered, and free-free subtracted 850 μm data using the STARLINK clump-finding algorithm FELLWALKER plotted as contours. Clumps are indexed in order of highest to lowest flux density, matching the order presented in Tables 7.3 and 7.4.

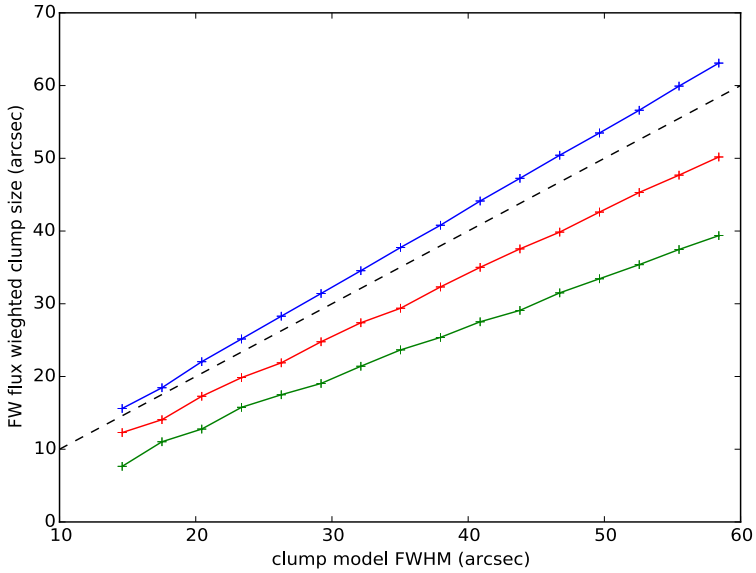

Figure 7.5: A range of clumps, modelled as Gaussians with a FWHM between one and four times that of the JCMT effective beam (at 850 μm), are fed into the FELLWALKER algorithm and their resulting, flux weighted clumps sizes compared when the clumps are extracted at a SNR level of 20σ (blue), 10σ (red) and 5σ (green). A parity line is shown for comparison (dashed line).

7.4 (right). The outer boundary of the clumps approximately corresponds to the 5 σ contour in Figure 2.13.

7.2.1 Clump temperatures

The unweighted mean value of temperature across all of the pixels in a clump in the W40 complex is calculated and presented in even Tables 7.4 through to 7.12. There are no temperature data for 21 clumps as they are not detected at 450 μm above the 5 σ noise level (0.0035 Jy per pixel). For these cases I assign a temperature of 15±2 K, consistent with Chapter 6. Where temperature data only partially cover the 850 μm clump, I assume the vacant pixels have a temperature equal to the mean of the occupied pixels.

Partial coverage tends to occur towards the edges of clumps as a result of lower signal-to-noise at 450 μm, relative to 850 μm. Setting missing pixels to the clump average could introduce a temperature bias if clump edges are systematically warmer (or colder) than the clump centres. This was tested by replacing vacant pixels with the average of the top 20% of pixels values in each clump, rather than the average of all the pixels, given the assumption that the edges of the clumps were warmer than their centres. I find the mean clump temperature increases by at most 2.2K (averaged over all clumps). From observation, only a few clumps have systematically warmer edges, whereas the majority of clumps have warm pixels randomly distributed within them. I therefore treat this value as an upper limit on any bias.

Where a clump carries only a small number of temperature pixels, the recorded clump temperature is unlikely to be representative of the whole clump. I find that 20 % of clumps are missing more than 75 % of the total potential temperature pixels with the most prominent of this

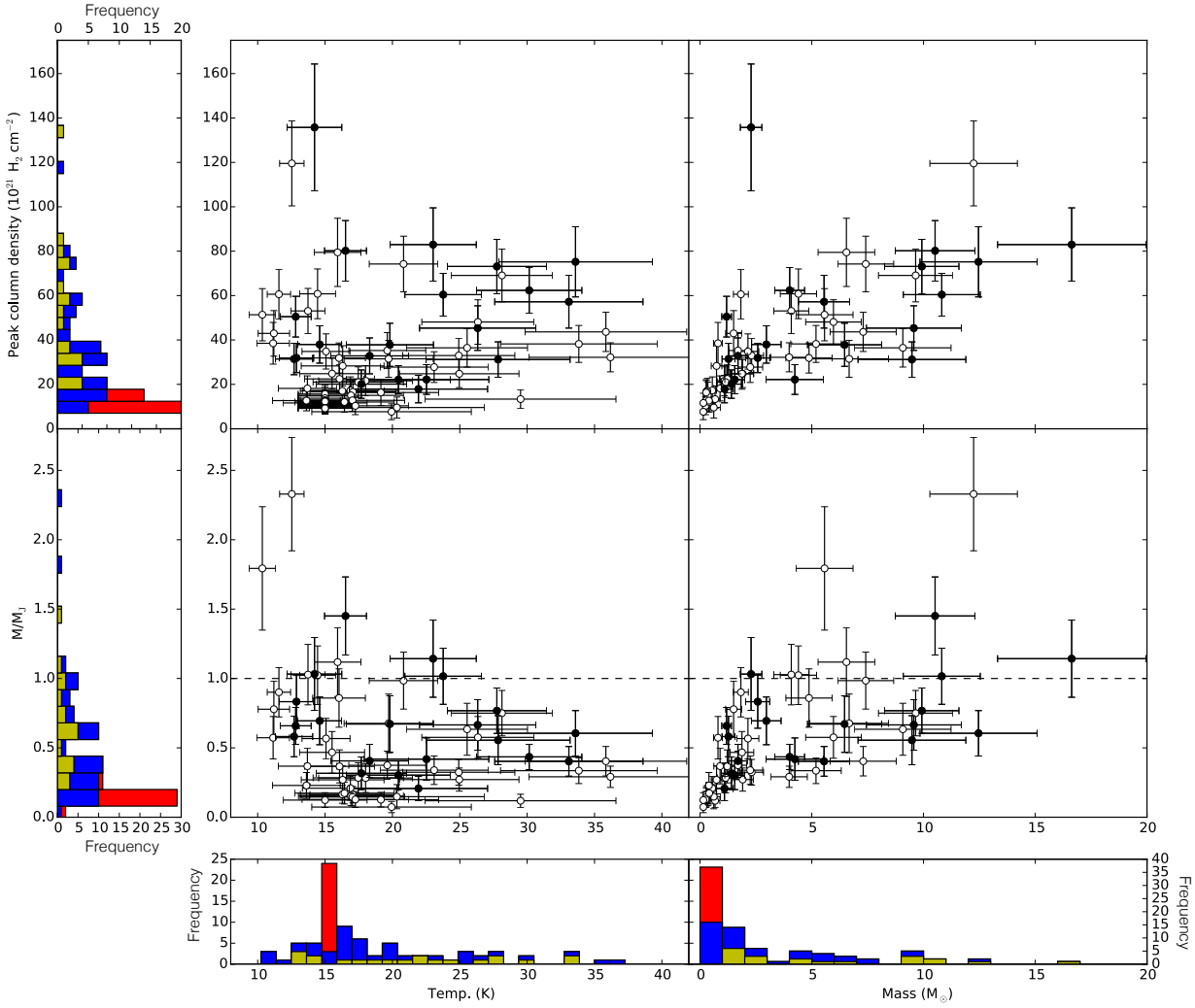

Figure 7.6: Properties of clumps within the W40 complex. Histograms show the distribution of mass, temperature, M/M_J and peak column density. The total height of each bar represents the total number of clumps in each bin whereas each colour represents a specific subset: blue for clumps that have measured temperature, yellow for clumps with measured temperatures that contain at least one YSO, and red for clumps with no temperature data, for which the value 15±2 K is assumed. Scatter plots show any existing correlation between clump properties: top left shows column density as a function of temperature, top right shows column density as a function of mass, bottom left shows Jeans stability, M_{850}/M_J, as a function of temperature and bottom right shows Jeans stability as a function of mass. Filled markers indicate protostellar clumps and hollow markers indicate starless clumps.

set being W40-SMM 35. The following discussion concerns only clumps with complete or partial temperature data.

Figure 7.6 (lower left) shows the distribution of derived temperatures. The W40 complex has a mean clump temperature of 20±3 K with a mean percentage error across all clumps of 16% due to calibration uncertainty. The mean temperature of the peripheral clumps (i.e. those not attributed to W40-N, W40-S or the Dust Arc) is 15±2 K, equal to that found from dust temperatures in Serpens MWC 297 region (Chapter 6), gas temperatures in Ophiuchus (Friesen et al., 2009), and the assumptions used by Kirk et al. (2006). These findings are consistent with those of Foster et al. (2009) who found that isolated clumps in Perseus were systematically cooler than the those in clusters.

I compare the clump temperatures produced by the SCUBA-2 flux ratio method to those calculated by Maury et al. (2011) and Könyves et al. (2015) using SED fitting between 2 μm and 1.2 mm, for sources extracted using the *getsources* algorithm. The mean temperature of the 19 sources common to all three catalogues is 19.8±2.8 K. This is comparable to the Maury et al. (2011) value of 18.5±0.4 K, but higher than the Könyves et al. (2015) value of 14.1±1.3 K. Whilst all three methods calculate similar minimum source temperatures (10-12 K), the SCUBA-2 flux ratio method calculates the highest maximum source temperatures (33.6 K, compared to 27.0 K and 20.6 K in Maury et al. 2011 and Könyves et al. 2015, respectively). This is because the warmest dust lies in the low column density edges of filaments (see Figure 10) where it is likely to be omitted by the *getsources*, a multi-scale, multi-wavelength source extraction algorithm (Men'shchikov et al., 2010) parameterised to extract dense cores and YSOs and as a result heated dust is likely omitted by a *getsources* algorithm.

Figure 7.7 (upper left) shows clump temperature as a function of projected distance from OS1a. In Figure 7.7 (lower left) I place clumps into distance bins of 0.5 pc. The clumps at distances greater than 1.2 pc (marked) have near-constant temperatures (on average 16±3 K), again consistent with those of isolated clumps (Friesen et al. 2009, Kirk et al. 2006 and Chapter 6). There is no evidence in Figure 7.7 (lower left) that the presence of an internal protostar will significant;y increase the clump temperature.

At distances of less than 1.2 pc there is a strong negative correlation between temperature and projected distance to OS1a. The lower panel in Figure 7.7 (left) shows how clump temperature does not increase significantly given the presence of a protostar with all protostellar clumps having the same mean temperature (as a function of distance) as the starless clumps, within the calculated uncertainties. This suggests that internal heating from a protostar is not significant enough to raise the temperatures of clumps in the W40 complex. However, use of a constant $\beta = 1.8$, consistent with the ISM, may mask heating in protostars where low values of β have been observed (Chun-Yuan Chen et al., 2016).

VLA 21 cm continuum data trace free-free emission from the super-heated H II region. Figures 4.6 and 4.7 show the extent of the H II region and where it coincides with several of the SCUBA-2 clumps in the Dust Arc and W40-N. The size of the H II region corresponds to a 0.17 pc radius, but Figure 7.7 shows temperatures increasing inversely with radius from OS1a out to 1.2 pc (8.25′). Figure 7.7 shows none of the clumps within the H II region has a temperature of less than

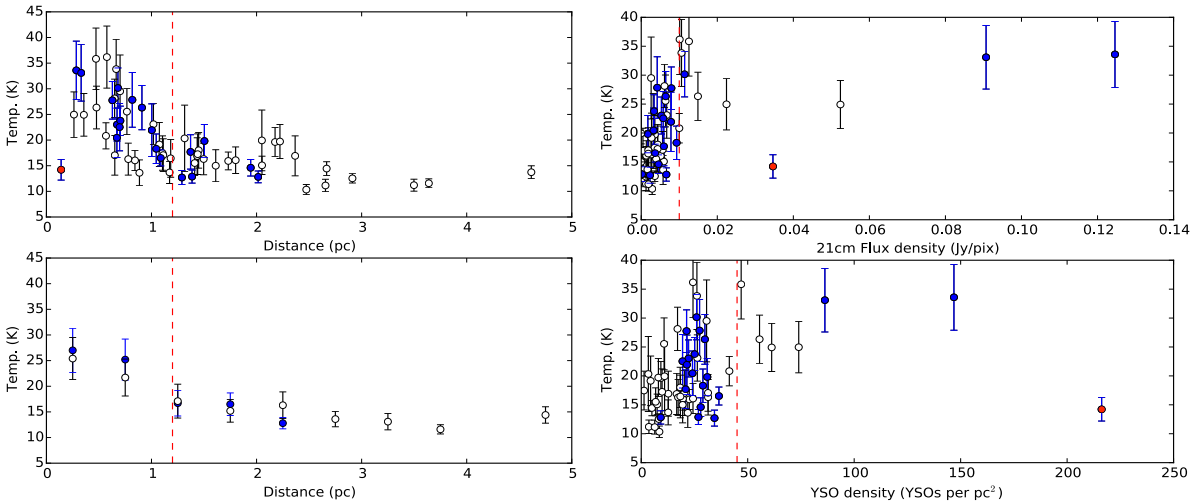

Figure 7.7: Upper left) clump temperature as a function of projected distance, in pc, to OS1a, the most luminous star in the W40 complex. The upper plot shows all clumps individually plotted. Upper right) Clump temperature as a function of mean VLA 21 cm flux detected in the area of each clump. Lower left) the mean temperature (and uncertainty) of clumps in 0.5 pc bins. Lower right) clump temperature as a function of YSO surface density. In all plots, filled markers represent protostellar clumps whereas hollow markers represent starless clumps. W40-SMM 19 is considered anomalous and its data are flagged as a red point. Red lines mark the partition between clump temperature regimes. Red lines mark the partition between clump temperature regimes.

21 K (ignoring W40-SMM 19) and the mean clump temperature of 29 K is almost twice the temperature of an isolated clump. My conclusions support the Matzner (2002) model where radiative feedback from the OB association (including ionising and non-ionising photons) is the dominant external mechanism for heating clumps.

7.2.2 Clump column density and mass

Temperature measurements are incorporated alongside the SCUBA-2 850 μm fluxes to calculate clumps masses and peak clump column densities, using Equations 6.1 and 1.26, and these results are also presented in Table 7.4.

Figure 7.6 (lower right histogram) shows the distribution of clump masses in the W40 complex. The total mass of all clumps in the W40 complex is 239±9 $M_\odot$. 50% of all clumps have a mass of 1.2 $M_\odot$ or less whereas the 12 most massive clumps contain more mass than all the others combined. Five clumps have masses greater than 10 $M_\odot$ with W40-SMM3 the most massive clump at 17±3 $M_\odot$. The Dust Arc, W40-N and W40-S have collective masses of 87±6, 73±5 and 31±3 $M_\odot$ respectively confirming the Dust Arc as the most massive structure in the W40 complex. W40-SMM 10 and 16 are two clouds that, with masses of 11±2 and 12±2 $M_\odot$, are amongst the most massive in the complex; however, they are isolated clouds well outside of Sh2-64. Like W40-SMM 22, 33 and 35, these peripheral clouds all have relatively low temperatures often less than 15 K

The distribution of peak column densities in the W40 complex as a function of temperature

are presented in Figure 7.6 (upper left). I find the median peak clump column density is $22{\times}10^{21}$ H_2 cm^{-2}, larger than the $7{\times}10^{21}$ H_2 cm^{-2} reported by Könyves et al. (2015) using *Herschel* data. This is due to a selection bias due to the atmospheric subtraction in SCUBA-2 reduction that omits lower column density clumps from the sample (Ward-Thompson et al., 2015).

I find a minimum peak column density of $1.7{\times}10^{22}$ H_2 cm^{-2} for clumps containing a protostar. Above this value there is no significant correlation between peak column density and temperature or protostellar occupancy. The upper right panel of Figure 7.6 shows how peak column density is tightly correlated with mass in the clumps. Above 3 $M_\odot$, the correlation is looser with several examples of clumps of similar column density having masses varying between 3 and 12 $M_\odot$.

The peak column density of *Herschel* sources, detected by Könyves et al. (2015), are compared to 69 matching (within 15″, one JCMT beam width at 850 μm) SCUBA-2 clumps as this value is independent of clump size. Figure 7.8 (left) shows that the two sets are loosely correlated. The mean peak column density of the SCUBA-2 clumps ($3.2{\pm}0.7{\times}10^{22}$ H_2 cm^{-2}) is comparable to that of the *Herschel* sources ($2.6{\times}10^{22}$ H_2 cm^{-2}). It is notable that the majority of objects have a lower peak column density recorded by *Herschel* than by SCUBA-2. This can be explained by the SED fitting method used by Könyves et al. (2015) which can be biased towards higher temperature clouds, and has a lower resolution of 36.6″ (consistent with the *Herschel* 500 μm beam size).

I calculate a lower limit on the average volume density along the line of sight for clumps from the ratio of peak column density and clump depth (assumed equal to the flux weighted clump diameter as calculated by FELLWALKER, which is equivalent to the clump FWHM).

From the sample of clumps, Table 7.2 lists 31 'dense cores' with a volume density greater than 10^5 cm^{-3}, along with any protostars within these clump and their respective Jeans stabilities (see section 6.3). At densities greater than $10^{4.5}$ cm^{-3} I can be confident the dust and gas temperatures are well coupled (Goldreich & Kwan 1974 and Goldsmith 2001). Dense cores account for approximately 63% of the mass observed by SCUBA-2 at 850 μm. The Dust Arc has nine dense cores, W40-N has nine, W40-S has four, and there are 11 isolated dense cores. In total, 42% of the dense cores contain at least one protostar, confirming that a significant proportion of clumps in the W40 complex are likely to be undergoing star formation.

Clouds in the W40 complex have a mean peak extinction of 34±7 mag, calculated from column densities assuming $N_{H_2} = 0.94 \times 10^{21} A_\nu$ mag (Bohlin et al., 1978). This extinction exceed the optical extinctions in Aquila given by Vallee (1987) and the Dobashi et al. (2005) Dark Cloud Atlas as expected. *Spitzer* GBS extinction maps of Aquila are higher resolution and can probe to significantly higher extinctions than optical methods and these are consistent with the SCUBA-2 peak extinctions where A_ν is typically around 30.

7.2.3 Clump stability

Jeans mass is calculated using Equation 1.4 following the methods outlined in Chapter 6. I note that the dust and gas may be poorly coupled for clumps not included in the dense cores list ($n >$ 10^5 H_2 cm^{-3}; see Table 7.2); if gas temperatures drop below the dust temperature (Tielens & Hollenbach, 1985), their Jeans stability may be overestimated.

Additional forces such as magnetism and turbulence could provide additional support against

Table 7.2: Dense cores in the W40 complex.

Clump ID (W40-SMM)	Region[a]	Diameter[b] (pc)	Density[c] (cm^{-3})	Proto-stars	M/M_J
1	E-DA	0.20	1.2×10^5	4	0.6±0.2
2	W-DA	0.14	1.5×10^5	-	0.8±0.2
3	W-DA	0.21	1.2×10^5	1	1.1±0.3
4	W-DA	0.10	2.1×10^5	1	0.4±0.1
5	E-DA	0.16	1.2×10^5	1	0.4±0.1
6	W-DA	0.17	1.4×10^5	1	0.8±0.2
8	W40-N	0.14	1.4×10^5	1	1.0±0.2
9	W40-N	0.13	1.2×10^5	-	0.6±0.2
10	ISO	0.16	1.7×10^5	2	1.5±0.3
12	W40-N	0.13	1.8×10^5	-	1.0±0.2
15	W40-S	0.13	2.0×10^5	-	1.1±0.2
16	ISO	0.15	2.6×10^5	-	2.3±0.4
18	W40-S	0.09	2.1×10^5	-	1.0±0.2
20	W40-N	0.10	1.1×10^5	-	0.3±0.1
22	ISO	0.1	1.7×10^5	n/a[d]	1.0±0.2
26	W40-S	0.08	1.5×10^5	-	0.4±0.1
28	ISO	0.05	3.9×10^5	n/a[d]	0.9±0.2
29	ISO	0.04	3.3×10^5	1	0.7±0.1
30	ISO	0.08	1.3×10^5	-	0.6±0.1
33	ISO	0.10	1.2×10^5	2	0.7±0.2
34	W40-N	0.09	1.2×10^5	1	0.4±0.1
35	ISO	0.11	1.5×10^5	-	1.8±0.4
37	ISO	0.09	1.2×10^5	1	0.8±0.2
38	ISO	0.06	2.4×10^5	-	0.8±0.2
43	ISO	0.04	2.5×10^5	-	0.6±0.2
45	ISO	0.07	1.5×10^5	1	0.6±0.1
47	W40-S	0.06	1.5×10^5	-	0.3±0.1
52	ISO	0.04	1.1×10^5	-	0.2±0.1
53	W40-N	0.03	1.1×10^5	-	0.2±0.1
62	W40-N	0.04	1.1×10^5	-	0.1±0.1

[a] Region key: eastern Dust Arc (E-DA), western Dust Arc (W-DA), W40-N, W40-S and isolated clumps (ISO).
[b] Flux weighted effective diameter as calculated by the clump-finding algorithm FELLWALKER (values were not deconvolved with respect to the JCMT beam).
[c] The average volume density of a dense core along the line of sight. Each observation is a lower limit as effective size of the cloud is typically larger than a core. A dense core is defined where the density limit is greater than 10^5 cm^{-3}, a value five times greater than the typical density of a star forming filament (2×10^4 cm^{-3}, André et al. 2014) and where the gas and dust temperatures are well coupled (Goldsmith, 2001).
[d] Clumps beyond the coverage of the composite YSO catalogue.

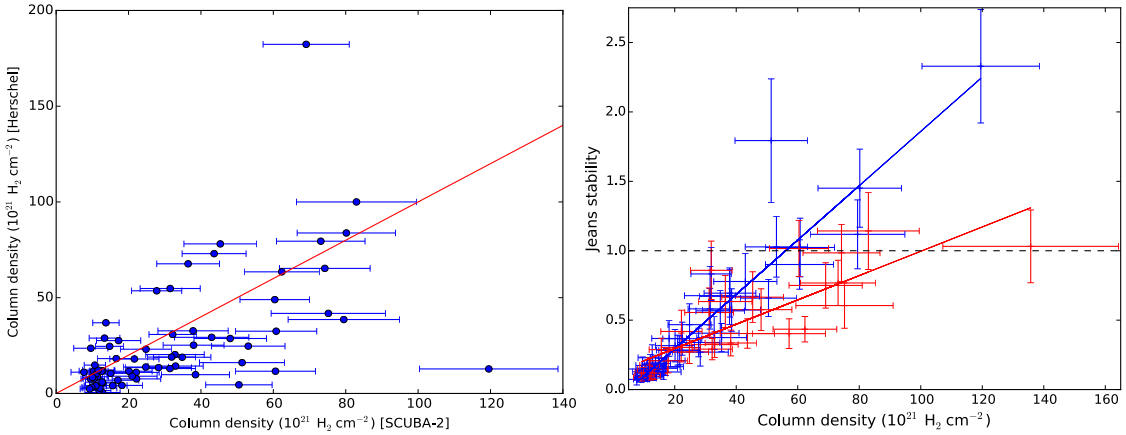

Figure 7.8: Left) the peak column density of SCUBA-2 clumps compared to *Herschel* sources, as published by Könyves et al. (2015). A parity line is marked in red. Clump pairs are matched within a separation of 15″. Right) Jeans stability, M_{850}/M_J, as a function of peak column density. Exterior peripheral clumps (defined as having a mean *Herschel* 70 μm flux of less than 1000 MJy/Sr) are marked in blue, interior clumps within the nebulosity Sh2-64 are marked in red. The unweighted linear regression fit to each population is marked as a line of the same colour.

gravitational collapse (as explained in, Sadavoy et al. 2010 and Mairs et al. 2014). Due to the high optical depth of the ^{12}CO 3-2 line data, it is not possible to use these data to calculate the turbulent support. Arzoumanian et al. (2011) calculate a sonic scale of 0.05–0.15 pc below which the sound speed is comparable to the velocity dispersion and turbulent pressure dominates over thermal pressure. This scale range includes 83% of all the clumps in the W40 complex so my working assumption (in the absence of direct measurements) is that the majority of the W40 complex is subsonic or transonic. This is supported by observations of starless cores in Ophiuchus, which is similarly located on the edge of an OB association; these cores are transonic or mildly supersonic (Pattle et al., 2015). Providing the W40 complex is similar, then clumps could be stable against gravitational collapse to a few times the Jeans mass. Magnetic support is poorly characterised and also left out of the stability analysis.

Jeans stability (M_{850}/M_J) values for each clump are presented in Table 7.4, Table 7.2 and Figure 7.6 (lower left). Out of 82 clumps in the W40 complex, I find that 10 are unstable with $M_{850}/M_J \geq 1$. Given the likely variety in clump morphologies, only those with $M_{850}/M_J \geq 2$ can be considered truly unstable (Bertoldi & McKee, 1992); the stability threshold is raised further if turbulent support is significant.

As with column density, I find M_{850}/M_J is tightly correlated with mass below 3 $M_\odot$ and more loosely correlated above 3 $M_\odot$. I can also determine that M_{850}/M_J is loosely negatively correlated with temperature; see bottom left panel of Figure 7.6. Below 24 K there is a mixture of stable and unstable clumps but above this temperature all clumps are stable.

W40-SMM 14 is an example of a clump with high M_{850}/M_J (0.3) and high temperature (36 K). Measuring the clump radius as 0.05 pc and flux as 3.96 Jy, I can estimate mass and Jeans mass using Equations 1.35 and 1.4 that if this clump had a typical temperature of 15 K, it would have a mean M_{850}/M_J of 6.5. Whilst this number is only an estimate, it is over 20 times the mea-

sured value and therefore I have confidence that the raised temperature of this clump is reducing M_{850}/M_J and potentially suppressing collapse. The two most unstable clumps are W40-SMM 16 (2.3±0.4) and 35 (1.8±0.4) which are cold, isolated clumps on the periphery of the W40 complex. W40-SMM 16 contains a protostar whereas 35 is currently starless.

The eastern Dust Arc is positioned on the edge of the H II region. Raised temperatures mean that clumps here have a mean Jeans mass of 17 $M_\odot$ for clumps in the eastern Dust Arc, compared to 12 $M_\odot$ in the western Dust Arc, and 5 $M_\odot$ for the average clump in the W40 complex. Likewise the median M_{850}/M_J is 0.4 compared to 0.8 in the western Dust Arc which is considered outside of the H II region and consequently has lower temperatures. Note that both filaments have similar mean clump masses of these regions (7 and 8 M⊙, respectively). Given its common CO gas velocity (Figure 3.10) the Dust Arc, as a whole, is likely a continuous filament, and therefore I might expect its clumps to evolve at a similar rate due to similar initial conditions along the length of the filament. Significant differences in stabilities along the length of the filament as a result of heating by the OB association, however, hint that star formation may take place there at different rates.

I further examine the impact of radiative heating by the OB association on the global sample of clumps in the W40 complex by comparing the stabilities of the population inside the nebulosity to those on the outside. The limit of the nebulosity is defined as where the mean 70 μm flux from *Herschel* is less than 1000 MJy/Sr. The M_{850}/M_J of interior and exterior populations, as a function of peak column density, is plotted in Figure 7.8 (right). A degree of correlation is expected as both M_{850}/M_J and column density are derived from the SCUBA-2 data. Two correlations are observed, with a clear divergence between the two clump populations. A clump found within the nebulosity is more likely to be stable than one with the same peak column density on the outside.

Figure 7.8 (right) provides direct evidence that radiative heating from the OB association is directly influencing the Jeans stability of clumps and star formation within Sh2-64 (the red population). I note that whilst this divergence is prominent amongst clumps with high column densities, the two populations have similar distributions below $55{\times}10^{21}$ H_2 cm^{-2} (within the uncertainties).

7.2.4 YSO distribution

In this section I consider the YSO distribution based on the composite YSO catalogue produced from the SGBS list merged with the catalogues published by Kuhn et al. (2010), Rodríguez et al. (2010), Maury et al. (2011) and Mallick et al. (2013) (see Section 2.3 for full details). The locations of YSOs in the composite catalogue are plotted in Figure 7.9 (left). Several protostars are coincident with local peaks in the SCUBA-2 emission as expected. Several protostars are found in the body of the filament, far from a significant peak in the SCUBA-2 emission. These objects are considered to be either very low-mass or potentially mis-identified (due to IR contamination from the OB association). Those protostars found outside of SCUBA-2 850 μm emission are considered misidentified false detections or discs (Heiderman & Evans, 2015). The YSO distribution was mapped by convolving the YSO positions with a 2′ FWHM Gaussian to produce surface density maps with units of YSOs pc^{-2}.

The more evolved PMS- and less evolved proto-stellar clusters are presented in Figure 7.9

(left). The more evolved PMS-stars are distributed in a roughly spherical cluster situated in the dust cavity between W40-N and the Dust Arc with the peak YSO density coincident with the most massive star, OS1aS, in the complex. By contrast protostar distribution is more fragmented, with dense regions roughly coincident with the dust filaments as observed by SCUBA-2 with the peak YSO density located near the peak 850 μm emission. The Western Dust Arc and W40-S have comparatively low density of YSOs compared to the Eastern Dust Arc and W40-N, suggesting that star formation in these parts of the W40 complex is less advanced. This difference between the peak PMS-star density (195 YSOs pc^{-1}) and peak protostar density (59 YSOs pc^{-1}) show how in the past a significant burst of star formation has occurred and that the protostellar population is part of a 2nd generation of star formation in the W40 complex.

The whole YSOc cluster is visible in Figure 7.4 (left) and has a FWHM size of approximately $3.5' \times 2.5'$. The Dust Arc has its eastern end located towards the centre of the star cluster where the density peaks at 232 YSOs pc^{-2}. However, this value quickly drops off to 20 YSOs pc^{-2} at its western edge near W40-SMM 31. Overall the Dust Arc has an average YSO surface density of 61 YSOs pc^{-2} which is significantly more than either W40-N (26 YSOs pc^{-2}) or W40-S (17 YSOs pc^{-2}).

An increase in clump temperatures is also observed when the YSO surface density is greater than 45 YSO pc^{-2} (Figure 7.7 lower, marked). The YSO surface density map does not distinguish between embedded protostars and free-floating PMS-stars and therefore the YSO densities will be over-estimates of the densities of objects embedded within clumps. Given these uncertainties, I conclude that the radiative feedback from OS1a is dominating over any potential heating by the embedded YSO within this region.

The absolute number of protostars located within each clump was recorded. A total of 21/82 clumps have at least one Class 0/I protostar. Figure 7.6 shows how the distribution of clumps with protostars, compared to those without, is shifted to greater values in mass (5.5±1.3 from 2.0±0.6 $M_\odot$), column density (49±11 from $26\pm7\times10^{21}$ H_2 cm^{-2}), temperature (21±3 from 18±3 K) and M_{850}/M_J (0.6±0.2 from 0.4±0.1). These results are consistent with those of Foster et al. (2009) who observed that protostellar clumps appear warmer, more massive and more dense than starless clumps in Perseus.

For all cases in Figure 7.6, a threshold is observed, below which protostars are not found in clumps. These results argue that more massive, dense clumps are more likely to be unstable and contain a Class 0/I object. They also suggest that these clumps may be warmer, though the significant overlap in the temperature range renders this result inconclusive.

The SGBS can detect a significant number of free-floating Class II objects that formed in the first generation of stars and have subsequently dispersed (Figure 7.9 left). However, only one of these PMS-stars is detected as a low mass (less than 1 $M_\odot$) disc by SCUBA-2. This implies that these PMS-stars are sufficiently distant that their discs are too faint to be detected by the JCMT. By contrast, a number of PMS-disc sources are detected in the Serpens MWC 297 region which is believed to be part of the closer Aquila rift (250 pc).

7.3 What is the evidence for radiative heating in the W40 complex?

In this discussion section I examine the evidence for radiative feedback from internal and external sources influencing clump temperature and assessing whether there is evidence that radiative feedback is influencing the star formation process. The W40 complex is home to a number of prominent sources of radiative feedback. Photons from OS1a and its companion B stars are ionising molecular hydrogen gas that is subsequently detected as free-free emission at radio wavelengths as seen in Figure 4.6. Lower energy photons have produced the nebulosity SH2-64 which is detected by *Herschel* at 70 μm where dust is being heated. *Chandra* observations by Kuhn et al. (2010) have revealed a significant PMS-star cluster alongside the OB association. Submillimeter observations by Maury et al. (2011) have found populations of protostars embedded deep within the molecular clouds which are confirmed with SCUBA-2 data, supported by up to 12 molecular outflows identified in ^{12}CO 3–2 observations (Figure 3.11).

The most prominent heating in the W40 complex occurs along the eastern Dust Arc, a very complex region of star formation running from W40-SMM 19 to 14, and is the direct result of external heating from the nearby OS1a. The O9.5v star is primarily responsible for a mean clump temperature of 35±6 K in this filament. By comparison, a number of isolated clumps, with or without protostars, found well outside of the nebulosity have a mean temperature of 15 K, consistent with those assumed for cores in Perseus using Bonnor-Ebert models (Kirk et al. 2006) and those calculated from kinetic gas temperatures in Ophiuchus by Friesen et al. (2009). Bright free-free emission observed in the eastern Dust Arc, as shown in Figures 4.6 and 4.11, is considered evidence of an interaction between the eastern Dust Arc and the H II region. Figure 7.10 shows a possible configuration for this interaction.

The western Dust Arc leads from W40-SMM 31 southeast towards W40-SMM 11, and includes the B1 star IRS 5 which appears to be producing a secondary nebulosity visible in *Herschel* 70 μm data (Figure 7.9 right) that is consistent with Hα emission (Mallick et al. 2013). A population of Class 0/I protostars is observed in the western Dust Arc by Maury et al. (2011), some of which coincide with dense cores W40-SMM 2, 3, 4, and 6. This filament lies well outside of the main stellar cluster associated with OS1a and has a YSO density of 22 YSO pc^{-2} which is comparable to W40-N. I observe a mean clump temperature of 26±3 K for the western Dust Arc. Though this is warmer than the average clump in the W40 complex, it is notably cooler that the eastern Dust Arc (35±6 K).

Shimoikura et al. (2015) argue that the western Dust Arc is a shell of material forming around the H II region of OS1a. However, my temperature maps lead us to believe that the Dust Arc is located significantly outside of the H II region as heating and free-free emission is not observed along its length to the extent of that observed in the eastern Dust Arc. Figure 7.10 presents a schematic layout of the W40 complex in RA/Dec/Line-of-sight space (by assimilating 3D information from the CO maps presented by us and Shimoikura et al. 2015, and the distance measurements of Shuping et al. 2012).

Evidence from the Serpens MWC 297 region suggests that radiative heating from a primary generation of high-mass stars can raise clump temperature, and potentially suppress any subsequent star formation in the neighbouring clumps. In Section 6.3 I have shown how heating

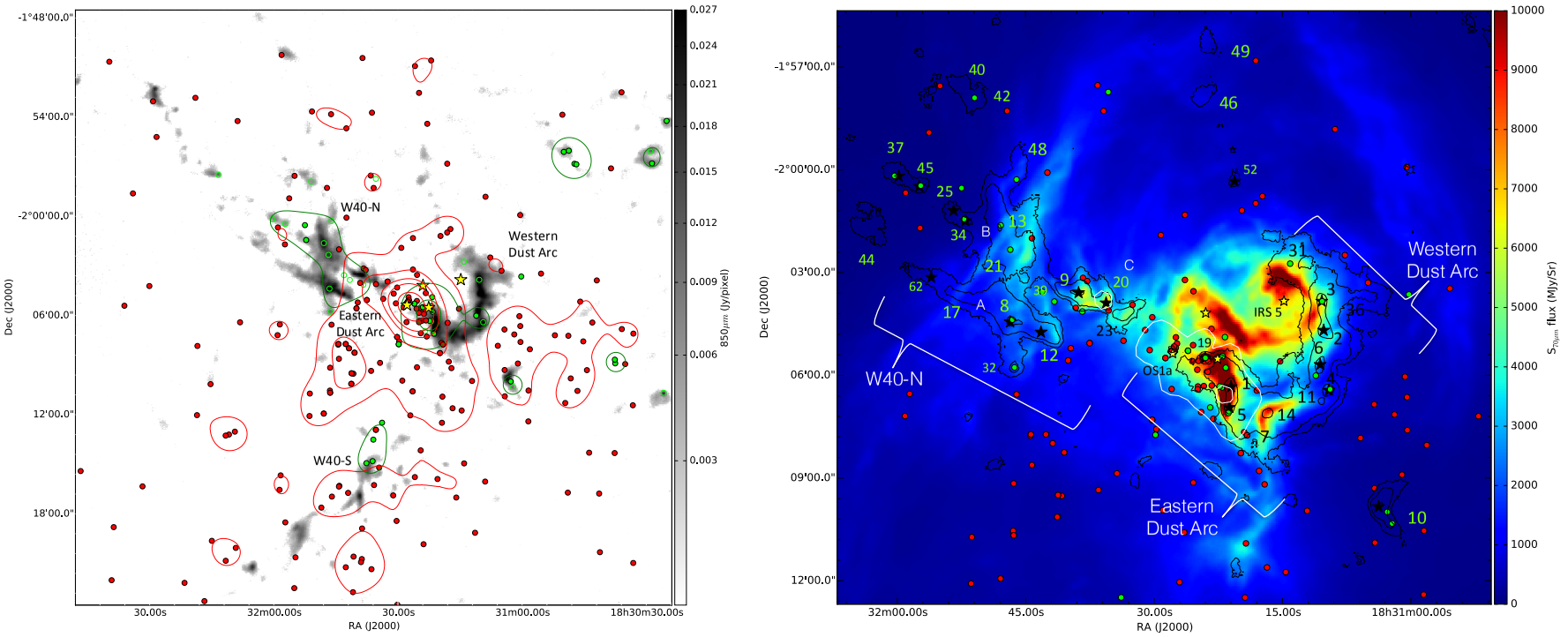

Figure 7.9: Left) SCUBA-2 850 μm continuum data of the W40 complex. Markers indicate the location of Class 0 (geeen, hollow), Class I/FS (green, filled), Class II/TD (red, filled) and Class III (red, hollow) YSOcs, given in the composite YSO catalogue. Contours show the YSO distributions for protostar and PMS-star (15, 45, 75, 100, 150 YSOs per pc^{-2} in the same colour scheme). Right) Archival *Herschel* 70 μm flux density map of the W40 complex (colour scale). Morphological features of W40-N and the Dust Arc are labelled alongside major clumps detected in SCUBA-2 850 μm emission (see Figure 7.4 (right) for accurate clump positions). Black contours show SCUBA-2 850 μm at the 5 σ, 15 σ and 50 σ level. White contours show archival VLA 21 cm emission at 5 σ and 25 σ (Condon & Kaplan, 1998b). The four OB stars OS1a, 2a, 3a and IRS 5 are marked as yellow stars. YSOs from the composite catalogue are displayed. Protostars (Class 0/I) are marked as green and PMS-stars (Class II/III) are marked as red. Dense cores identified in Table 7.2 are marked as black stars in their associated clump.

from OS1a in the eastern Dust Arc is making these clumps, in particular W40-SMM 14, more stable to gravitational collapse (due to the increase of thermal support) than those in the western Dust Arc. By increasing the Jeans mass, the heating has the potential to skew the initial mass function to larger masses. However, as none of the clumps in the eastern Dust Arc have sufficient mass to exceed their enlarged Jeans mass, fragmentation under gravitational collapse is less likely to occur and the star formation rate may be suppressed. Given the continued radiative feedback from OS1a/expansion of the H II region, it seems unlikely that clumps in the eastern Dust Arc will cool sufficiently to allow self-gravity to overwhelm thermal support and fragmentation to occur. I therefore conclude that it is likely that the eastern Dust Arc is less active in star formation than the western Dust Arc.

In addition to the OB stars, there is an association of low-mass PMS-stars, observed by Kuhn et al. (2010), that also produces photons that may further externally heat the ISM. However, it is not possible to draw conclusions about the general significance of this mechanism given the dominance of the OB star heating in this region.

Addressing internal sources of radiative feedback, and their influence on the ISM, requires an assessment of embedded star formation occurring within the clumps. Considering clumps containing protostars (21±3 K) compared to those without protostars (18±3 K), there is no significant difference between the mean temperatures of the two populations (within the uncertainties). Figure 7.7 (left) shows how this trend is independent of distance from OS1a, though I note that some of the temperatures calculated for distances less than 1.2 pc are likely influenced by OS1a. Yellow bars in Figure 7.6 show how the temperature distribution of protostars has no obvious trend compared to M_{850}/M_J.

I consider the specific case of OS2b. The B4 star appears embedded in the tip of W40-SMM1 (see Figures 4.8 and 7.9 right), where a peak in SCUBA-2 emission at 450 and 850 μm is detected, suggesting that a Class 0/I YSO is observed. OS2b has a mean temperature of 31±1 K (for a beam-sized aperture centred on the object, Figure 7.1 insert). This value is over twice that of a typical star-forming core but is consistent with the average temperature of W40-SMM1 (34±6 K). Given the proximity of this clump to the OB association, internal heating could be masked by external heating from OS1a. A better test of whether or not this object is providing significant internal heating is to measure the temperature of the dust at the core centre (defined as the peak of local SCUBA-2 emission). Its value is 21±2 K (Figure 7.1, insert). This value is comparable to the mean temperature of the dense cores in the Dust Arc (21 K, W40-SMM1, 2, 3, 4, 5, 6). No significant variation in temperature is noted amongst this sample irregardless of whether or not they contain a protostar. These findings suggest there is no evidence that embedded stars, up to B4 in spectral type, significantly heat their immediate clump environment (given the resolution of JCMT and a constant β). This finding supports the conclusions of Foster et al. (2009) that mid-B or latter type stars have a relatively weak impact on their environment. However, these results may be consistent if the local value of β is reduced as a result of grain growth.

Sufficiently powerful protostellar outflows have been observed to contribute localised heating of dust through shocks (Buckle et al., 2015). In the absence of massive stars, outflows observed by Davis et al. (1999) are thought to be a likely candidate for heating observed in Serpens Main

(Figure 5.17). They may also contribute to variation in the value of β in extended regions (Chun-Yuan Chen et al., 2016). I discuss the evidence for 12 outflows in the W40 complex in Chapter 3, Figure 3.11. The highest velocity line-wings recorded are 7.5 km s^{-1} (outflow O5-10, clump W40-SMM2). This outflow is relatively weak when compared to those in Serpens Main (approximately 30 km s^{-1}, Graves et al. 2010). I conclude that radiative feedback from the outflows in the W40 complex is unlikely to be significant.

7.4 What is the state of star formation in the W40 complex?

There are at least two generations of star formation in the W40 complex. The first generation of star formation includes the OB association and the associated PMS- and stellar-cluster. The second generation is currently forming in the filaments and cores that are observed by SCUBA-2.

By accounting for the mass of the OB stars (Table 7.1, Shuping et al.2012) and the population of 36 solar-like PMS-stars within the cluster (defined as within the half YSO density radius), I estimate that the total mass required to form the first generation of stars was 76 $M_\odot$. Allowing for a regional star formation efficiency (SFE) of 40% (Könyves et al., 2015) implies that a total of 190 $M_\odot$ of material has already been used in the star formation process with 240 $M_\odot$ remaining (as observed by SCUBA-2). I conclude that there is sufficient mass remaining in the W40 complex to form more OB stars.

My list of dense cores (Table 7.2) represents the most likely sites of future star formation, with 39% of the sample currently containing a protostar. Many of these cores have bright-rimmed clouds (BRCs) observed at *Herschel* 70 μm, indicative of exposure to heating from the OB association (Figure 7.9 right). BRCs are found along the length of W40-N and the Dust Arc tracing back to OS1aS. BRCs in the western Dust Arc trace back towards IRS 5, indicating that this star and filament complex lie outside of the main nebulosity (Figure 7.10). No BRCs are found in W40-S indicating that it too is located outside of the Sh2-64.

Many dense cores are associated with BRCs. I find that the peak 70 μm flux is correlated with clump temperature, as illustrated in Figure 7.11, inferring a degree of coupling between low and high column density dust. The Jeans masses of these objects will be higher, making gravitational collapse and fragmentation more difficult, and the formation of fewer, more massive stars more likely. The most massive clump in the W40 complex is W40-SMM 3 at 17±3 $M_\odot$ which has the potential to form a late B-type star. Examining the distribution of protostars in the Dust Arc in Figure 7.9 (right), in the east a number of low-mass protostars are observed to be only loosely associated with SCUBA-2 peaks. Outflows appear relatively weak (Figure 3.11) suggesting that these are more evolved Class I objects. In the west the protostars are typically associated with bright SCUBA-2 peaks and prominent outflows, suggesting that these are less evolved Class 0 objects. These findings fit with those of Maury et al. (2011), Mallick et al. (2013) and Pirogov et al. (2013) who conclude that the eastern Dust Arc is more evolved than the western Dust Arc.

^{12}CO 3–2 observations, presented in Figure 3.6, describe how the Dust Arc has a consistent, systemic velocity along its length, confirming that is one body. However, as discussed, evidence from BRCs, SCUBA-2 dust heating and YSO cluster populations imply that the eastern limb lies

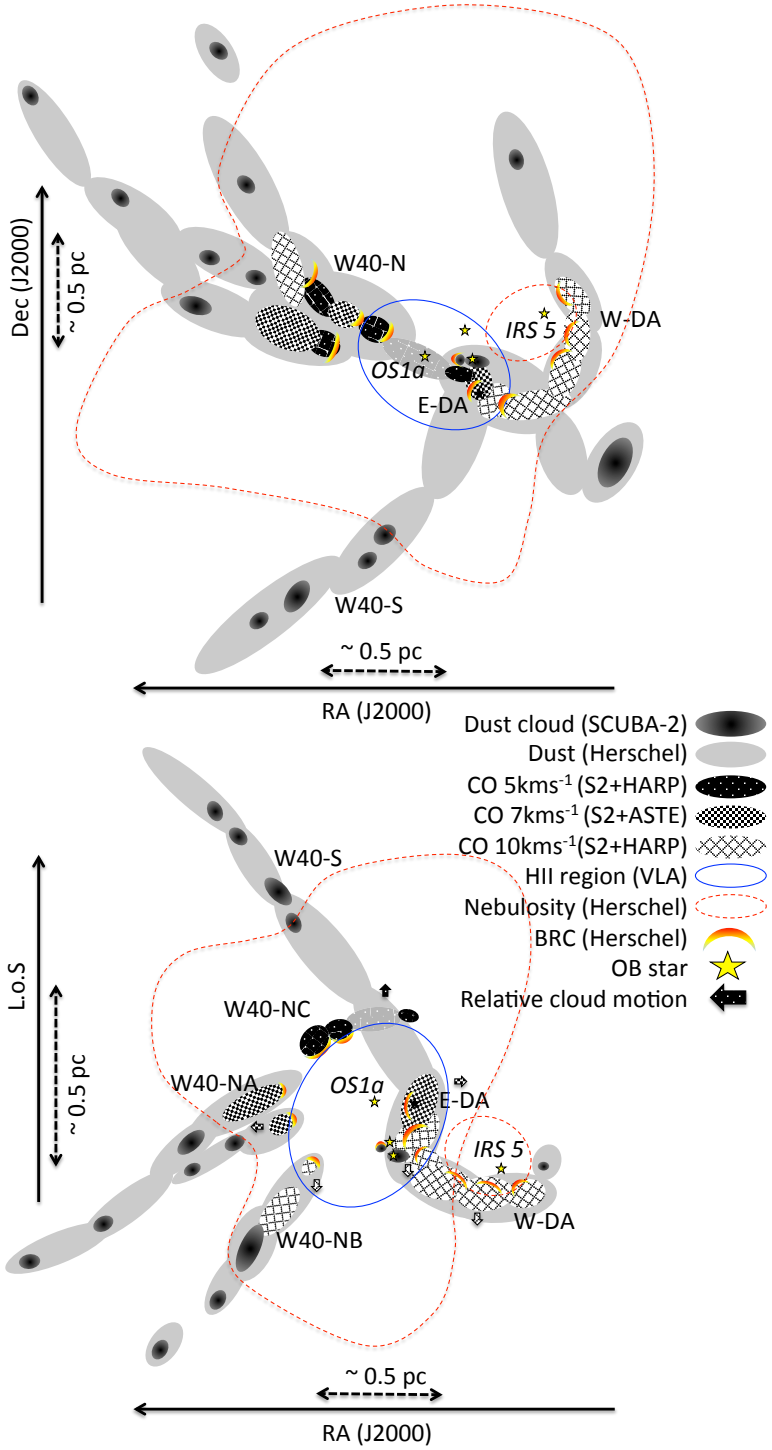

Figure 7.10: A schematic diagram of the location of clouds and features within the W40 complex. The upper figure represents the RA/Dec view of the *Herschel*/SCUBA-2 data presented in Figures 2.7 and 2.12 with cloud velocities observed by HARP and ASTE (Shimoikura et. al. 2015). Other features are explained in the key. The lower sketch shows the same region, this time viewed in line-of-sight vs RA space. The 5 km s^{-1} blue-shifted clouds are considered to be on the far side of the expanding H II bubble and at a further distance. Likewise the 10 km s^{-1} red-shifted clouds are considered to be on the near side and at a closer distance. The 7 km s^{-1} clouds observed by ASTE are taken to be moving perpendicular and at an intermediate distance. Where clouds have no velocity information, distance is inferred through attachment to clouds with a known distance.The location of the massive stars is given by Shuping et. al. (2012).

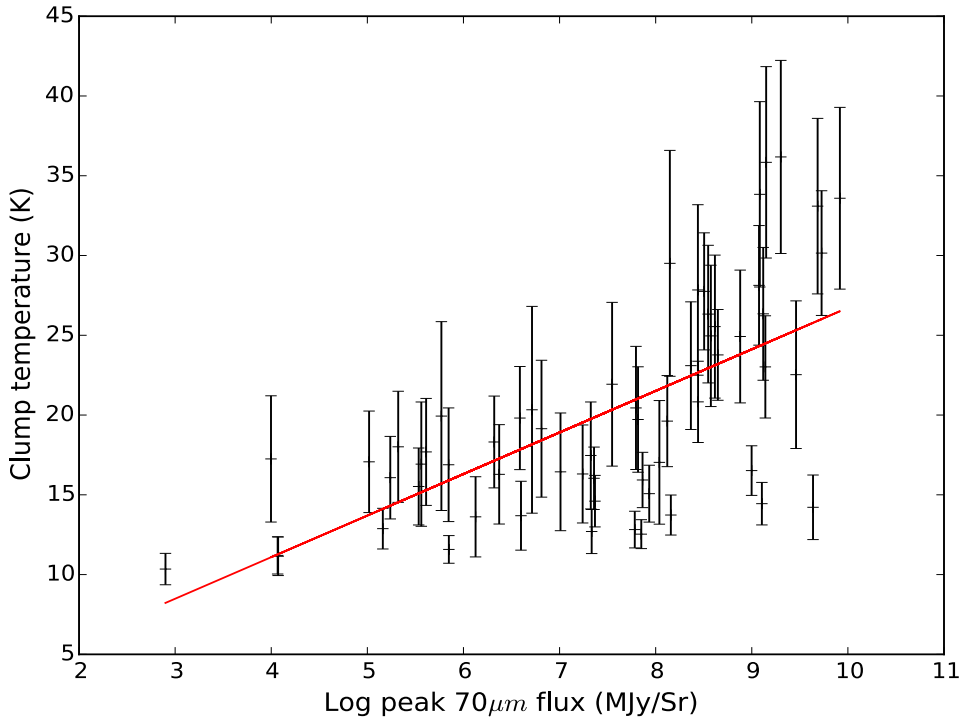

Figure 7.11: Clump temperature as a function of peak clump *Herschel* 70 μm flux. The red line shows a linear regression fit to the distribution. Only clumps with real temperature data are included.

within the nebulosity, in part in contact with the H II region, and the western limb lies outside the nebulosity. Clumps in the eastern Dust Arc would need to cool significantly before collapse and further star formation can occur. Clumps in the western Dust Arc are cooler and more massive clumps, and therefore several are borderline Jeans unstable with 60% having already formed stars. It remains unclear as to whether the OB association has directly triggered star formation in the Dust Arc; however, the stark contrast in environmental conditions along the length of the Arc is likely influencing the ongoing star formation.

W40-N is a fragmented cloud thought to be formed from the result of the large-scale merger of two filaments (Mallick et al., 2013). It has a comparable mass and number of dense cores (nine, four of which are protostellar) to the Dust Arc. Despite having a number BRC associated with its cores, W40-N is not experiencing the same level of heating as the Dust Arc. It is likely that much of the star formation in this cloud has evolved without significant influence from OS1a; however, given the continued expansion of the H II region, this situation will likely change in the future. The cloud has a total mass of 73±5 $M_\odot$. Allowing for a SFE of 40% (Könyves et al., 2015), this cloud could go on to form up to one OB star, though given fragmented nature and subsequent evolution of OS1a, this scenario is unlikely.

W40-S resembles a star-forming filament that has undergone unaided collapse and fragmentation into a row of cores, similar to the Chamaeleon region (Boulanger et al., 1998; Young et al., 2005; Belloche et al., 2011). There are four major cores, all of which are starless. The mean mass of the clouds is 6±1 $M_\odot$, impling that they will each go on to form a single star between 1

and 2 $M_\odot$. These cores may come to resemble some of the higher density isolated cores in the region, for example W40-SMM 10, 16, 28 and 29 which appear as bright, highly condensed objects containing a single protostar.

7.5 Conclusions and summary

I observed the W40 complex as part of the James Clerk Maxwell Telescope (JCMT) Gould Belt Survey (GBS) of nearby star-forming regions with SCUBA-2 at 450 and 850 μm. The ^{12}CO 3–2 line at 345.796 GHz was observed separately using HARP. The HARP data were used to subtract CO contributions to the SCUBA-2 850 μm map. In addition, archival radio data from Condon & Kaplan (1998b) and Rodríguez et al. (2010) were examined to assess the largI e- and small-scale free-free flux contributions to both SCUBA-2 bands from the high-mass stars in the W40 complex OB association.

I produce maps of dust temperature and column density and estimate the Jeans stability, M_{850}/M_J, of submillimeter clumps. In conjunction with a new composite YSO candidate catalogue, I probe whether dust heating is caused by internal or external sources and what implications this heating has for star formation in the region. Throughout this paper I refer to the Dust Arc, W40-N, W40-S and isolated clumps as various morphological features of the W40 complex. A schematic layout of these features is presented in Figure 7.10. My key results on the W40 complex are summarised as follows:

1. 82 clumps were detected by FELLWALKER in the 850 μm data and 21 of these have at least one protostar embedded within them. Clump temperatures range from 10 to 36 K. The mean temperatures of clumps in the Dust Arc, W40-N and W40-S are 26±4, 21±4 and 17±3 K.

2. The mean temperature of the isolated clumps is 15±2 K defined as being located in a region where the *Herschel* 70 μm flux, produced by the nebulosity SH2-64 surrounding the O9.5 star OS1aS, is less than 1000 MJy/Sr. This result is consistent with temperatures observed in the Serpens MWC 297 region and other Gould Belt regions (Sadavoy et al. 2010 and Chun-Yuan Chen et al. 2016). Globally, I find the population of clumps within the nebulosity Sh2-64 are more stable, as a function of peak column density, than that outside.

3. I find that clump temperature correlates with proximity to OS1a and the H II region. I conclude that external radiative heating from the OB association is raising the temperature of the clumps. There is no evidence that embedded protostars are internally heating the filaments, though external influences may be masking such heating.

4. The eastern Dust Arc has exceptionally high temperatures (mean 35±5 K), Jeans masses (mean 17 $M_\odot$), and Jeans stable clouds (mean M/M_J = 0.43). Partial radiative heating of the Dust Arc (internally or externally) has likely influenced the evolution of star formation in the filament, favouring it in the cooler west, and potentially suppressing it in the warmer east.

The W40 complex represents a high-mass star-forming region with a significant cluster of evolved PMS-stars and filaments forming new protostars from dense, starless cores. The region is complex and requires careful study to appreciate which radiative sources, from external and internal, are heating clumps of gas and dust. The region is dominated by an OB association that is powering an H II region. In the near future I can expect this H II region to expand and envelop many surrounding filaments. Within a few Myrs, I expect OS1a to go supernova. This event will likely have a cataclysmic impact on star formation within the region. Any filament mass that has not been converted into stars, or eroded by the H II region, may be destroyed at this point, bringing an end to star formation in the W40 complex in its current form.

Table 7.3: A sample of submillimeter clumps and their respective SCUBA-2 and *Herschel* fluxes.

Index[a]	IAU object name[a]	70 μm intensity[b] (MJy/Sr)	450 μm flux[c] (Jy)	850 μm flux[c] (Jy)	21 cm intensity[d] (Jy/pix)	Clump area (Pixels)
W40-SMM1	JCMTLSG J1831210-0206203	8304	93.50	10.44	0.124	759
W40-SMM2	JCMTLSG J1831102-0204413	3834	56.38	6.77	0.006	422
W40-SMM3	JCMTLSG J1831104-0203503	3622	71.64	9.26	0.005	807
W40-SMM4	JCMTLSG J1831096-0206263	1982	26.72	3.06	0.011	189
W40-SMM5	JCMTLSG J1831212-0206563	5007	41.98	4.73	0.091	350
W40-SMM6	JCMTLSG J1831106-0205413	2322	54.28	6.54	0.008	438
W40-SMM7	JCMTLSG J1831168-0207053	4854	62.94	6.87	0.013	514
W40-SMM8	JCMTLSG J1831468-0204263	2185	46.21	5.96	0.003	405
W40-SMM9	JCMTLSG J1831388-0203353	3533	32.30	3.77	0.015	313

[a]Position of the highest value pixel in each clump (at 850 μm).
[b]Mean *Herschel* 70 μm intensity.
[c]Integrated SCUBA-2 fluxes over the clump properties. The uncertainty at 450 μm is 0.017 Jy/pix and at 850 μm is 0.0025 Jy/pix. There is an additional systematic error in calibration of 10.6 % and 3.4 % at 450 μm and 850 μm, respectively.
[d]Mean VLA 21 cm intensity at 15″ pixels.

Table 7.4: The properties of a sample of submillimeter clumps in the W40 complex.

Index	S_{850}[a] (Jy)	Mass[b] ($M_\odot$)	Temp[c]. (K)	Column density[d] (H_2 cm^{-2})	YSO density[e] (YSOcs pc^2)	Protostars[e] (per clump)	M_J[f] ($M_\odot$)	M/M_J	Distance[g] (pc)
W40-SMM1	10.44	12.5±2.6	33.6±5.7	75±16 $\times10^{21}$	147	4	20.6±3.5	0.6±0.2	0.3
W40-SMM2	6.77	9.65±1.66	28.1±3.7	69±12 $\times10^{21}$	17	0	12.9±1.7	0.8±0.2	0.6
W40-SMM3	9.26	16.63±3.32	23.0±3.2	83±17 $\times10^{21}$	22	1	14.6±2.0	1.1±0.3	0.7
W40-SMM4	3.06	4.01±0.67	30.2±3.9	62±10 $\times10^{21}$	26	1	9.2±1.2	0.4±0.1	0.7
W40-SMM5	4.73	5.55±1.15	33.1±5.5	57±12 $\times10^{21}$	86	1	13.8±2.3	0.4±0.1	0.3
W40-SMM6	6.54	9.92±1.66	27.8±3.7	73±12 $\times10^{21}$	21	1	12.9±1.7	0.8±0.2	0.6
W40-SMM7	6.87	7.3±1.48	35.8±6.0	44±8.8 $\times10^{21}$	47	0	18.1±3.0	0.4±0.1	0.5
W40-SMM8	5.96	10.82±1.72	23.8±2.8	60±10 $\times10^{21}$	25	1	10.6±1.3	1.0±0.2	0.7
W40-SMM9	3.77	5.97±1.24	26.3±4.2	48±10 $\times10^{21}$	56	0	10.4±1.6	0.6±0.2	0.5

[a]Integrated SCUBA-2 850 μm fluxes of the clumps. The 850 μm uncertainty is 0.0025 Jy. There is an additional systematic error in calibration of 3.4 %.
[b]As calculated with equation 6.1. These results do not include the systematic error in distance (10 %) or opacity (100 %).
[c]Mean temperature as calculated from the temperature maps. Where no temperature data is available an arbitrary value of 15±2 K is assigned that is consistent with previous authors (Friesen et al. 2009, Kirk et al.,2006).
[d]Peak column density of the clamp. These results do not include the systematic error in distance (10 %) or opacity (100 %).
[e]Calculated from composite YSO catalogue outlined in Chapter 2, Section 5.2.
[f]As calculated with Equation 1.4. These results have a systematic uncertainty due to distance of 10 %.
[g]Projected distance between clump and OS1a, the primary ionising star in the W40 complex OB association.

Table 7.5: Submillimeter clumps and their respective SCUBA-2 and *Herschel* fluxes, part 52 Notation given in Table 7.3.

Index[a]	IAU object name[a]	70 μm intensity[b] (MJy/Sr)	450 μm flux[c] (Jy)	850 μm flux[c] (Jy)	21 cm intensity[d] (Jy/pix)	Clump area (Pixels)
W40-SMM10	JCMTLSG J1831038-0209502	8089	24.49	3.57	0.004	389
W40-SMM11	JCMTLSG J1831104 -0206442	8808	43.46	4.71	0.011	422
W40-SMM12	JCMTLSG J1831432-0204443	4633	24.85	3.29	0.010	264
W40-SMM13	JCMTLSG J1831480-0201413	5147	52.29	6.36	0.006	602
W40-SMM14	JCMTLSG J1831142-0207233	10960	36.24	3.96	0.010	289
W40-SMM15	JCMTLSG J1831392-0216563	2600	13.75	2.05	0.001	273
W40-SMM16	JCMTLSG J1832286-0152203	2567	14.29	2.6	0.003	355
W40-SMM17	JCMTLSG J1831482-0204023	5521	47.22	5.78	0.006	634
W40-SMM18	JCMTLSG J1832050-0221113	9001	7.77	1.23	0.005	179
W40-SMM19	JCMTLSG J1831240-0205293	15325	2.33	0.43	0.035	49
W40-SMM20	JCMTLSG J1831356-0203533	7182	12.02	1.42	0.052	165
W40-SMM21	JCMTLSG J1831466-0202173	4626	57.65	6.82	0.004	760
W40-SMM22	JCMTLSG J1832160-0234443	3491	6.22	1.05	0.000	169
W40-SMM23	JCMTLSG J1831334-0204143	5294	10.51	1.21	0.022	160
W40-SMM24	JCMTLSG J1831374-0215263	726	22.34	2.93	0.002	477
W40-SMM25	JCMTLSG J1831488-0200443	4300	10.4	1.28	0.007	166

Table 7.6: The properties of submillimeter clumps in the W40 complex, part 2. Notation given in Table 7.4.

Index	S_{850}[a] (Jy)	Mass[b] ($M_\odot$)	Temp[c]. (K)	Column density[d] (H_2 cm^{-2})	YSO density[e] (YSOcs pc^2)	Protostars[e] (per clump)	M_J[f] ($M_\odot$)	M/M_J	Distance[g] (pc)
W40-SMM10	0.027	10.52±1.78	16.5±1.6	80.2±13.6	36	2	7.3±0.7	1.5±0.3	1.1
W40-SMM11	0.028	5.19±1.13	33.8±5.8	38.2±8.3	26	0	15.5±2.7	0.3±0.1	0.68
W40-SMM12	0.027	7.41±1.25	20.8±2.5	74.2±12.5	41	0	7.5±0.9	1.0±0.2	0.5
W40-SMM13	0.027	9.56±2.12	26.3±4.3	45.3±10.0	30	1	14.4±2.4	0.7±0.2	0.9
W40-SMM14	0.025	3.99±0.81	36.2±6.1	32.2±6.5	24	0	13.7±2.3	0.3±0.1	0.5
W40-SMM15	0.023	6.55±1.27	15.9±1.7	79.5±15.4	23	0	5.9±0.6	1.1±0.2	1.7
W40-SMM16	0.02	12.24±1.96	12.5±0.9	119.5±19.1	8	0	5.3±0.4	2.3±0.4	2.9
W40-SMM17	0.02	9.07±2.16	25.5±4.5	36.5±8.7	11	0	14.3±2.5	0.6±0.2	0.7
W40-SMM18	0.018	4.4±0.81	14.4±1.3	60.8±11.2	5	0	4.3±0.4	1.0±0.2	2.7
W40-SMM19	0.018	2.28±0.48	14.2±2	135.7±28.6	216	1	2.2±0.3	1.0±0.3	0.1
W40-SMM20	0.017	2.31±0.53	24.9±4.2	33.0±7.6	61	0	7.1±1.2	0.3±0.1	0.3
W40-SMM21	0.019	9.48±2.41	27.8±5.3	31.2±7.9	27	1	17.1±3.3	0.6±0.2	0.8
W40-SMM22	0.015	4.08±0.78	13.7±1.3	53.2±10.1	0	0	4.0±0.4	1.0±0.2	4.6
W40-SMM23	0.015	1.91±0.48	25.0±4.4	24.8±6.2	74	0	7.0±1.2	0.3±0.1	0.3
W40-SMM24	0.014	6.47±1.66	19.8±3.2	37.8±9.7	31	2	9.6±1.6	0.7±0.2	1.5
W40-SMM25	0.014	2.24±0.56	23.1±4	27.8±6.9	26	0	6.6±1.1	0.3±0.1	1.0

Table 7.7: Submillimeter clumps and their respective SCUBA-2 and *Herschel* fluxes, part 3. Notation given in Table 7.3.

Index[a]	IAU object name[a]	70 μm intensity[b] (MJy/Sr)	450 μm flux[c] (Jy)	850 μm flux[c] (Jy)	21 cm intensity[d] (Jy/pix)	Clump area (Pixels)
W40-SMM26	JCMTLSG J1831544-0218472	3363	5.81	0.76	0.003	108
W40-SMM27	JCMTLSG J1831536-0219142	2481	22.69	3.02	0.004	505
W40-SMM28	JCMTLSG J1831524-0229382	347	1.96	0.34	0.000	62
W40-SMM29	JCMTLSG J1832134-0157292	2398	1.7	0.27	0.007	40
W40-SMM30	JCMTLSG J1832146-0157292	2788	4.51	0.65	0.006	127
W40-SMM31	JCMTLSG J1831112-0202413	12844	18.51	2.35	0.006	409
W40-SMM32	JCMTLSG J1831462-0205473	2428	6.07	0.74	0.003	127
W40-SMM33	JCMTLSG J1830496-0156023	1585	5.44	0.85	0.005	173
W40-SMM34	JCMTLSG J1831520-0201293	556	4.77	0.67	0.009	105
W40-SMM35	JCMTLSG J1831576-0150053	18	3.86	0.86	0.003	182
W40-SMM36	JCMTLSG J1831058-0203353	1570	10.43	1.63	0.005	253
W40-SMM37	JCMTLSG J1831598-0200113	174	3.61	0.6	0.000	117
W40-SMM38	JCMTLSG J1832476-0151562	58	1.4	0.27	0.001	60
W40-SMM39	JCMTLSG J1831450-0203113	3455	4.71	0.54	0.003	75
W40-SMM40	JCMTLSG J1831524-0157323	205	3.18	0.43	0.004	93
W40-SMM41	JCMTLSG J1831414-0217173	188	2.87	0.41	0.001	86

Table 7.8: The properties of submillimeter clumps in the W40 complex, part 3. Notation given in Table 7.4.

Index	S_{850}[a] (Jy)	Mass[b] ($M_\odot$)	Temp[c]. (K)	Column density[d] (H_2 cm^{-2})	YSO density[e] (YSOcs pc^2)	Protostars[e] (per clump)	M_J[f] ($M_\odot$)	M/M_J	Distance[g] (pc)
W40-SMM26	0.013	1.7±0.39	19.6±2.9	35.2±8.1	9	0	4.5±0.7	0.4±0.1	2.2
W40-SMM27	0.012	6.67±1.76	19.7±3.3	31.5±8.3	8	0	9.9±1.7	0.7±0.2	2.2
W40-SMM28	0.011	1.83±0.33	11.6±0.9	60.6±11.1	0	0	2.0±0.2	0.9±0.2	3.6
W40-SMM29	0.011	1.19±0.22	12.8±1.1	50.5±9.2	9	1	1.8±0.2	0.7±0.1	2.0
W40-SMM30	0.01	2.14±0.49	15.1±1.8	34.8±7.92	7	0	3.8±0.4	0.6±0.1	2.1
W40-SMM31	0.011	4.24±1.28	22.5±4.6	22.2±6.7	19	1	10.1±2.1	0.4±0.2	0.7
W40-SMM32	0.01	1.55±0.45	20.4±3.9	22.1±6.3	24	1	5.1±1	0.3±0.1	0.7
W40-SMM33	0.009	2.97±0.66	14.6±1.6	38.0±8.4	28	2	4.3±0.5	0.7±0.2	1.9
W40-SMM34	0.01	1.7±0.42	18.3±2.9	32.8±8.1	29	1	4.2±0.7	0.4±0.1	1.0
W40-SMM35	0.008	5.57±1.28	10.3±1	51.4±11.8	8	0	3.1±0.3	1.8±0.4	2.5
W40-SMM36	0.01	4.88±1.04	16.0±2	31.9±6.8	20	0	5.7±0.7	0.9±0.2	0.8
W40-SMM37	0.008	2.58±0.54	12.9±1.3	31.9±6.6	27	1	3.1±0.3	0.8±0.2	1.4
W40-SMM38	0.007	1.5±0.36	11.2±1.2	424.0±10.3	4	0	1.9±0.2	0.8±0.2	3.5
W40-SMM39	0.01	0.67±0.21	29.5±7.1	13.4±4.2	31	0	5.7±1.4	0.1±0	0.7
W40-SMM40	0.007	1.09±0.34	18.0±3.5	21.6±6.8	18	0	3.9±0.7	0.3±0.1	1.4
W40-SMM41	0.007	1.22±0.34	16.1±2.6	22.4±6.3	24	0	3.3±0.5	0.4±0.1	1.8

Table 7.9: Submillimeter clumps and their respective SCUBA-2 and *Herschel* fluxes, part 4. Notation given in Table 7.3.

Index[a]	IAU object name[a]	70 μm intensity[b] (MJy/Sr)	450 μm flux[c] (Jy)	850 μm flux[c] (Jy)	21 cm intensity[d] (Jy/pix)	Clump area (Pixels)
W40-SMM42	JCMTLSG J1831510-0157563	274	4.01	0.55	0.005	127
W40-SMM43	JCMTLSG J1832236-0153352	59	0.88	0.14	0.002	32
W40-SMM44	JCMTLSG J1832038-0201443	253	4.34	0.6	0.004	135
W40-SMM45	JCMTLSG J1831574-0200293	1532	1.75	0.29	0.002	60
W40-SMM46	JCMTLSG J1831242-0157503	1518	3.23	0.44	0.003	108
W40-SMM47	JCMTLSG J1831344-0215323	1394	1.75	0.25	0.002	57
W40-SMM48	JCMTLSG J1831462-0200143	1894	4.92	0.58	0.008	117
W40-SMM49	JCMTLSG J1831240-0156233	823	2.15	0.3	0.003	84
W40-SMM50	JCMTLSG J1830506-0145263	14	0.41	0.1	0.007	26
W40-SMM51	JCMTLSG J1831294-0215143	346	1.66	0.2	0.002	49
W40-SMM52	JCMTLSG J1831206-0200203	585	0.91	0.11	0.002	30
W40-SMM53	JCMTLSG J1831534-0201113	151	0.77	0.11	0.005	21
W40-SMM54	JCMTLSG J1831232-0208443	2259	1.1	0.2	0.002	46
W40-SMM55	JCMTLSG J1831284-0213263	734	1.49	0.23	0.002	64
W40-SMM56	JCMTLSG J1831282-0215593	314	0.73	0.1	0.002	29
W40-SMM57	JCMTLSG J1831486-0155383	135	0.24	0.03	0.010	10

Table 7.10: The properties of submillimeter clumps in the W40 complex, part 4. Notation given in Table 7.4.

Index	S_{850}[a] (Jy)	Mass[b] ($M_\odot$)	Temp[c]. (K)	Column density[d] (H_2 cm^{-2})	YSO density[e] (YSOcs pc^2)	Protostars[e] (per clump)	M_J[f] ($M_\odot$)	M/M_J	Distance[g] (pc)
W40-SMM42	0.007	1.4±0.45	17.7±3.4	20.1±6.4	21	1	4.4±0.8	0.3±0.1	1.3
W40-SMM43	0.007	0.8±0.2	11.1±1.2	38.5±9.4	6	0	1.4±0.2	0.6±0.2	2.6
W40-SMM44	0.007	1.88±0.53	15.5±2.4	24.8±7.0	7	0	4.0±0.6	0.5±0.2	1.4
W40-SMM45	0.007	1.27±0.29	12.7±1.4	31.4±7.1	34	1	2.2±0.2	0.6±0.1	1.3
W40-SMM46	0.007	1.15±0.38	17.5±3.4	21.0±6.9	1	0	4.0±0.8	0.3±0.1	1.1
W40-SMM47	0.007	0.74±0.24	16.3±3.1	28.3±9.1	31	0	2.7±0.5	0.3±0.1	1.5
W40-SMM48	0.007	1.09±0.38	21.9±5.1	17.8±6.2	21	1	5.3±1.2	0.2±0.1	1.0
W40-SMM49	0.006	0.61±0.3	20.3±6.5	9.5±4.7	3	0	4.1±1.3	0.1±0.1	1.3
W40-SMM50	0.005	0.32±0.08	15.0±2	14.7±3.9	0	0	1.7±0.2	0.2±0.1	3.2
W40-SMM51	0.006	0.55±0.2	16.9±3.6	17.2±6.1	17	0	2.6±0.6	0.2±0.1	1.4
W40-SMM52	0.005	0.33±0.11	16.3±3.1	17.0±5.7	17	0	2.0±0.4	0.2±0.1	0.8
W40-SMM53	0.007	0.28±0.09	17.1±3.2	16.6±5.1	31	0	1.7±0.3	0.2±0.1	1.1
W40-SMM54	0.006	0.65±0.16	15.0±2	15.6±3.9	36	0	2.3±0.3	0.3±0.1	0.5
W40-SMM55	0.005	0.9±0.28	13.7±2.2	18.2±5.6	13	0	2.4±0.4	0.4±0.1	1.2
W40-SMM56	0.005	0.34±0.09	15.0±2	13.8±3.6	16	0	1.8±0.2	0.2±0.1	1.5
W40-SMM57	0.005	0.1±0.03	15.0±2	12.8±3.6	4	0	1.1±0.1	0.1±0	1.6

Table 7.11: Submillimeter clumps and their respective SCUBA-2 and *Herschel* fluxes, part 5. Notation given in Table 7.3.

Index[a]	IAU object name[a]	70 μm intensity[b] (MJy/Sr)	450 μm flux[c] (Jy)	850 μm flux[c] (Jy)	21 cm intensity[d] (Jy/pix)	Clump area (Pixels)
W40-SMM58	JCMTLSG J1832232-0155022	8	0.65	0.1	0.002	29
W40-SMM59	JCMTLSG J18314560221023	260	0.98	0.13	0.0008	37
W40-SMM60	JCMTLSG J1832126-0159353	25	0.26	0.04	0	12
W40-SMM61	JCMTLSG J18305367-0154263	24	0.15	0.05	0.005	13
W40-SMM62	JCMTLSG J1831560-0203083	909	0.94	0.12	0.003	26
W40-SMM63	JCMTLSG J1831164-0201563	3098	0.89	0.1	0.002	26
W40-SMM64	JCMTLSG J1832036-0201083	54	0.73	0.1	0.004	26
W40-SMM65	JCMTLSG J1831322 -0209053	1166	0.41	0.1	0.004	30
W40-SMM66	JCMTLSG J1831184-0215023	305	0.47	0.06	0.000	17
W40-SMM67	JCMTLSG J1831382-0213053	1107	1.2	0.15	0.002	42
W40-SMM68	JCMTLSG J1832214-0155563	8	0.16	0.02	0.000	7
W40-SMM69	JCMTLSG J1832022-0202053	77	0.23	0.04	0.000	10
W40-SMM70	JCMTLSG J1831484-0208383	458	0.8	0.1	0.006	33
W40-SMM71	JCMTLSG J1831514-0218113	321	0.65	0.07	0.000	20
W40-SMM72	JCMTLSG J1831306-0216263	267	0.37	0.05	0.000	13

Table 7.12: The properties of submillimeter clumps in the W40 complex, part 5. Notation given in Table 7.4.

Index	S_{850}[a] (Jy)	Mass[b] ($M_\odot$)	Temp[c]. (K)	Column density[d] (H_2 cm^{-2})	YSO density[e] (YSOcs pc^2)	Protostars[e] (per clump)	M_J[f] ($M_\odot$)	M/M_J	Distance[g] (pc)
W40-SMM58	0.005	0.32±0.09	15.0±2	12.8±3.4	4	0	1.8±0.2	0.2±0.1	2.5
W40-SMM59	0.005	0.35±0.14	16.9±3.9	15.0±5.9	13	0	2.3±0.5	0.2±0.1	2.4
W40-SMM60	0.005	0.13±0.04	15.0±2	12.6±3.4	1	0	1.2±0.2	0.1±0	1.8
W40-SMM61	0.004	0.16±0.04	15.0±2	12.3±3.2	6	0	1.2±0.2	0.1±0	2.0
W40-SMM62	0.006	0.27±0.1	19.1±4.3	16.3±5.7	4	0	2.2±0.5	0.1±0.1	1.1
W40-SMM63	0.005	0.28±0.11	17.0±3.9	12.8±4.4	20	0	1.9±0.4	0.1±0.1	0.6
W40-SMM64	0.005	0.25±0.1	17.3±4	10.3±4.0	10	0	2.0±0.4	0.1±0.1	1.4
W40-SMM65	0.004	0.32±0.09	15.0±2	11.8±3.2	27	0	1.8±0.2	0.2±0.1	0.6
W40-SMM66	0.004	0.19±0.05	15.0±2	11.4±3.1	12	0	1.4±0.2	0.1±0	1.4
W40-SMM67	0.004	0.41±0.16	16.4±3.7	12.0±4.7	18	0	2.4±0.5	0.2±0.1	1.2
W40-SMM68	0.004	0.07±0.02	15.0±2	11.0±3.0	1	0	0.9±0.1	0.1±0	2.4
W40-SMM69	0.005	0.12±0.03	15.0±2	12.4±3.3	8	0	1.1±0.1	0.1±0	1.3
W40-SMM70	0.004	0.4±0.14	13.6±2.5	12.7±4.6	22	0	1.7±0.3	0.2±0.1	0.9
W40-SMM71	0.004	0.15±0.07	19.9±5.9	7.7±3.5	11	0	2.0±0.6	0.1±0	2.1
W40-SMM72	0.004	0.15±0.06	15.0±3.1	11.6±4.3	19	0	1.2±0.3	0.1±0.1	1.6

Table 7.13: Submillimeter clumps and their respective SCUBA-2 and *Herschel* fluxes, part 4. Notation given in Table 7.3.

Index[a]	IAU object name[a]	70 μm intensity[b] (MJy/Sr)	450 μm flux[c] (Jy)	850 μm flux[c] (Jy)	21 cm intensity[d] (Jy/pix)	Clump area (Pixels)
W40-SMM73	JCMTLSG J1832214-0156323	10	0.31	0.05	0	15
W40-SMM74	JCMTLSG J1831574-0156383	85	0.25	0.03	0.003	11
W40-SMM75	JCMTLSG J1830534-0155353	60	0.39	0.07	0.004	24
W40-SMM76	JCMTLSG J1831560-0157413	215	0.21	0.03	0	9
W40-SMM77	JCMTLSG J1831206-0211263	2951	0.45	0.05	0.002	17
W40-SMM78	JCMTLSG J1830472-0156533	126	0.17	0.03	0.005	8
W40-SMM79	JCMTLSG J1832258-0154023	9	0.14	0.03	0	8
W40-SMM80	JCMTLSG J1831262-0205473	5666	0.17	0.02	0	6
W40-SMM81	JCMTLSG J1830598-0159593	1520	0.22	0.03	0.004	10
W40-SMM82	JCMTLSG J1832146-0234112	10	0.09	0.02	0	7

Table 7.14: The properties of submillimeter clumps in the W40 complex, part 4. Notation given in Table 7.4.

Index	S_{850}[a] (Jy)	Mass[b] ($M_\odot$)	Temp[c]. (K)	Column density[d] (H_2 cm^{-2})	YSO density[e] (YSOcs pc^2)	Protostars[e] (per clump)	M_J[f] ($M_\odot$)	M/M_J	Distance[g] (pc)
W40-SMM73	0.004	0.15±0.04	15.0±2	10.7±2.9	1	0	1.3±0.2	0.1±0	2.3
W40-SMM74	0.004	0.11±0.03	15.0±2	10.8±3.1	5	0	1.1±0.1	0.1±0	1.6
W40-SMM75	0.004	0.22±0.06	15.0±2	10.4±3.0	12	0	1.6±0.2	0.1±0	1.9
W40-SMM76	0.004	0.09±0.03	15.0±2	11.0±3.0	16	0	1.0±0.1	0.1±0	1.5
W40-SMM77	0.004	0.17±0.05	15.0±2	9.8±2.7	23	0	1.4±0.2	0.1±0	0.9
W40-SMM78	0.003	0.08±0.02	15.0±2	9.5±2.7	29	2	0.9±0.1	0.1±0	1.9
W40-SMM79	0.004	0.08±0.02	15.0±2	10.0±2.7	8	0	0.9±0.1	0.1±0	2.6
W40-SMM80	0.004	0.08±0.02	15.0±2	12.3±3.1	224	0	0.8±0.1	0.1±0	0.1
W40-SMM81	0.003	0.09±0.03	15.0±2	9.3±2.6	9	0	1.1±0.1	0.1±0	1.3
W40-SMM82	0.003	0.07±0.02	15.0±2	9.2±2.6	0	0	0.9±0.1	0.1±0	4.5

8

Radiative heating in the JCMT GBS

8.1 Temperature maps of the JCMT GBS

In this chapter I apply the Kernel-convolution method for producing temperature maps from SCUBA-2 data, developed in Chapter 5, to the majority of JCMT GBS regions. I apply a consistent clump finding method across all the regions to produce a single clump catalogue that includes real dust temperatures. I use this clump catalogue, alongside various YSOc (primarily Dunham et al. 2015 c2d+GBS) and OB star catalogues, to assess the global evidence for external and internal heating of pre/protostellar clumps and ask 'what are the dominant mechanisms by which radiative feedback influences star formation?'. Many of the methods, analysis and discussion presented here build on previous work presented in Chapters 6 and 7.

Temperature maps for the JCMT GBS regions were created using an automated version of the Kernel-convolution method (discussed in Chapter 5 Section 4). A constant β of 1.8 was used in the temperature equation, following the logic outlined in Chapter 5. In a divergence from previous methods, a cut level of 3σ at 450 and 850 μm was used across all regions. Using this level provides greater coverage across all regions than a 5σ cut, but can compromise on the uncertainty towards the edges. However, the secondary cut level of 34.1% on the temperature maps, based on the propagated uncertainty throughout the region, is sufficient to remove those data points that have exceptionally high uncertainty. As a result I can maximise the coverage across all regions whilst ensuring a high degree of confidence in the temperatures calculated.

In addition to maps for temperature, maps of column density are also calculated using the 850 μm flux and dust of temperature, where available, and a constant value of 20 K where a derived temperature is not. The value 20 K is chosen to be representative of lower density material on the outer edges of clumps which has been shown to increase in temperature, relative to the

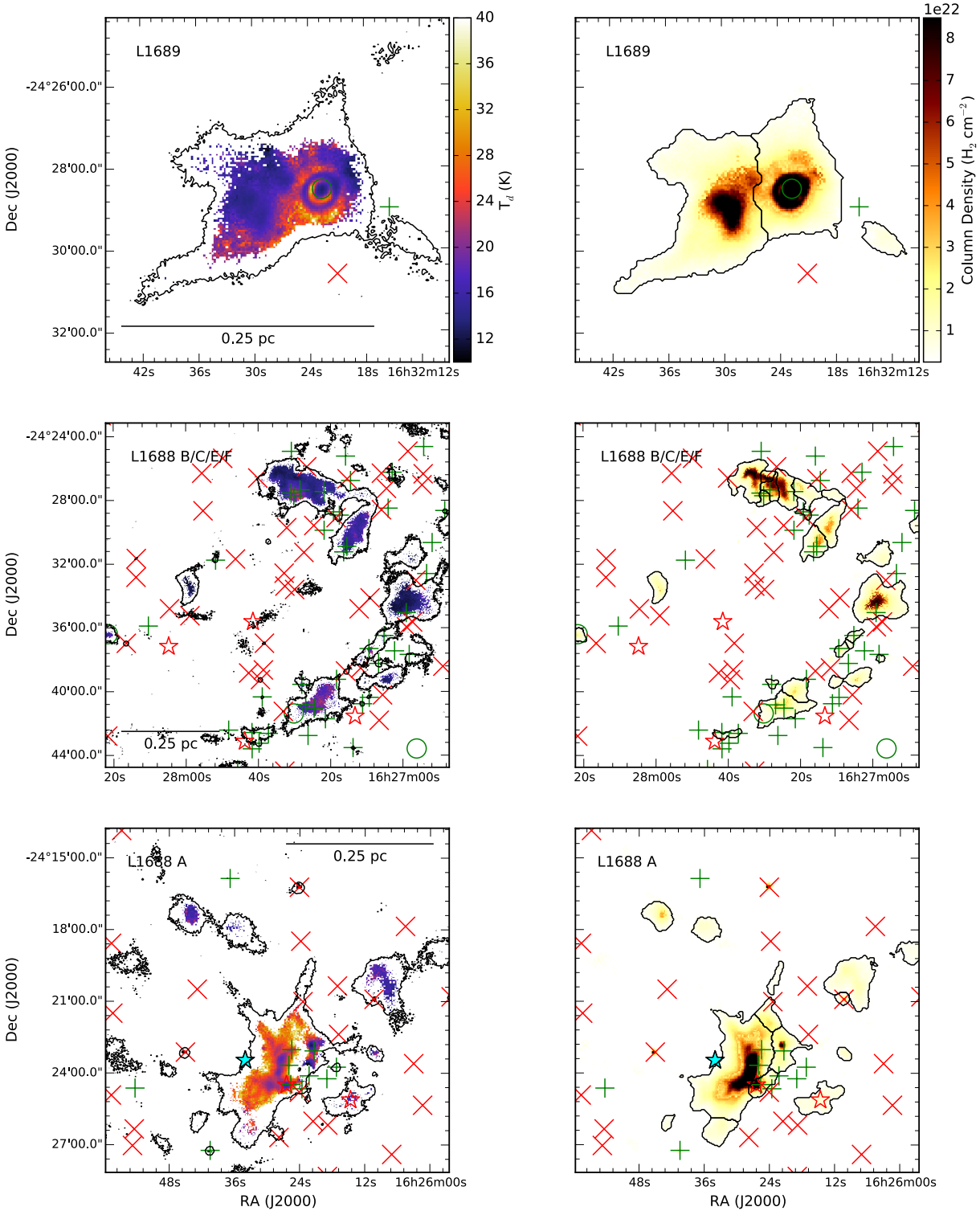

Figure 8.1: SCUBA-2 dust temperature (left) and column density (right) maps for the Ophiuchus L1688 and L1689 regions. YSOcs from the Dunham et al. (2015) c2d+GBS catalogue are marked (green circle = Class 0, green plus = Class I, red cross = Class II, red star = Class III). OB stars are marked as black stars. Black contours mark the 850 μm 5σ level on the temperature maps and the FELLWALKER clumps on the column density maps (see Section 8.4 for more details). The cyan star marks the major OB star in the region, S1 (B4Ve).

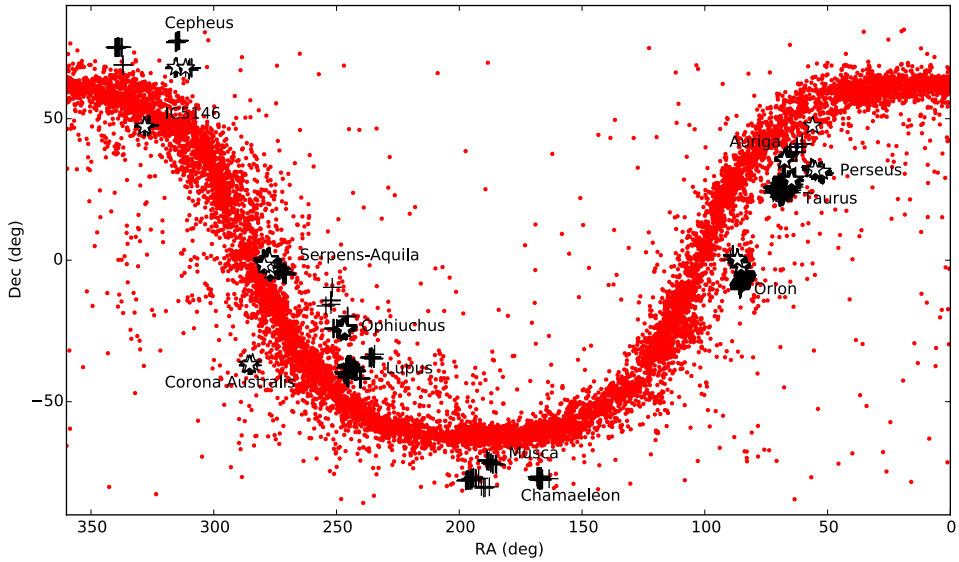

Figure 8.2: The Reed et al. (2003) Catalogue of Galactic OB Stars (red markers) overlaid with the Dunham et al. (2015) c2d+GBS YSOc catalogue (black crosses) for the various JCMT GBS regions. White stars mark the OB stars specifically located within the JCMT GBS regions (either from the Reed et al. 2003 catalogue or additional sources, outlined in Table 8.4). Note that the Orion A complex is a well known location of massive star formation and features many OB stars. However, as the Orion A region from further analysis (see text for details) these OB stars are not included in my sub-catalogue.

interior (taken as 15 K), due to heating from the ISRF (Evans et al. 2001 and Shirley et al. 2002b). 20 K is also used for models of Bonnor-Ebert (BE) spheres carried out by Motte et al. (1998) and Johnstone et al. (2000). Dust opacity at 850 μm is kept at a constant value across all regions, in line with a constant β. The specific distances to each region are given in Tables 2.13 and 2.14. The Ophiuchus region is shown in Figure 8.1 as an example of both dust temperature and column density.

8.2 Catalogues

As outlined in Chapter 2 Section 4, Dunham et al. (2015) combine the regions covered by the SGBS and the c2d (Evans et al. 2003, Evans et al. 2009) catalogues to produce a consistent YSOc catalogue for the bulk of the JCMT GBS regions. I go further and combine the Dunham et al. (2015) catalogue with the Megeath et al. (2012) catalogue (that covers the Orion A and B regions) and the Rebull et al. (2010) catalogue (that covers the Taurus regions) to extend the coverage. This combined Dunham et al. (2015) c2d+GBS catalogue has near complete coverage and is used to analyse star formation across the survey. Note that the Serpens East and Pipe regions are not included in the Dunham et al. (2015) c2d+GBS catalogue and are therefore not analysed any further.

8.2.1 OB Stars

In Chapters 6 and 7 I find significant evidence that OB star populations can heat their local environments. I therefore look to survey the OB star population of the JCMT GBS regions. As OB stars represent some of the brightest objects in the Galaxy, they are often some of the most well studied and surveyed. de Zeeuw et al. (1999a) present a robust survey of OB stars associated with, amongst others, the Perseus, Cepheus and Lupus regions, and Hernández et al. (2004) survey Herbig stars associated with Orion and Perseus regions.

These examples are region specific surveys so instead I turn to the Reed (2003) Catalogue of Galactic OB Stars which covers the entire Galactic plane, as shown in Figure 8.2. The Reed (2003) catalogue does not distinguish distance and therefore careful selection of any OB stars that are associated with a JCMT GBS region is required to discern the local members from those projected along the line-of-sight. Each Reed (2003) candidate was examined in the SIMBAD database (Wenger et al., 2000) with the aim to compare its proper motions with any OB members confirmed in the literature (see those references listed in Tables 2.13 and 2.14).

Through these methods I compiled a new catalogue of OB (and A) stars associated with the JCMT GBS regions and this is presented in Appendix Table 8.4. It was found that, whilst the Reed (2003) Catalogue of Galactic OB Stars provided an excellent starting point, it was incomplete. Through the literature and the SIMBAD database I was able to identify and verify (through proper motions) any missing O and B Class candidates in the regions.

Some regions, for example Aquila W40 complex, contain multiple OB stars. In these regions I identify a major OB star and these are highlighted in Appendix Table 8.4. The selection criteria is primarily based on spectral class, favouring the most massive stars; however, it is also important to take into account proximity to any clumps. For example, HD147889 is the most massive star in the Ophiuchus region with a B2III classification. However, Figure 8.1 illustrates how the B4Ve star S1 appears to be blistering from the L1688 A cloud. Pattle et al. (2015) suggest that S1 is the primary source of heating for L1688 A, due to its close proximity, whereas HD147889 is the primary source of heating for the rest of L1688. Perseus West is another similar case with the young embedded SVS3 B5 star heating local material in NGC 1333 and the more massive (O9.5V), but more distant, HD 278942 producing the G159.6-18.5 H II region and heating other parts of the Perseus cloud (Bally et al., 2008). HD 278942 is the most massive member of the Perseus OB2 OB association. This association is itself thought to have been influenced, or even triggered by the 'fossil' Cas-Tau OB association (distance approximately 180 pc) where an ancient supernova has produced a 100 pc wide shell (Blaauw, 1991; Bally, 2001; Lodieu et al., 2005).

Those regions not listed in Appendix Table 8.4 do not contain local OB stars and are vital for use as a control sample to probe the impact of low-to-intermediate mass star populations on clump heating. Investigations of heating from cluster members in the Serpens MWC 297 region (Chapter 6) and the W40 complex (Chapter 7) are inconclusive due to the dominance of the OB stars there. Throughout much of this chapter I investigate the impact that more massive stars have by making the comparison between regions with OB stars and those without. I compare the temperatures of pixels in each subset in Figure 8.3 (left) and find that whilst the most common temperature is similar in both distributions (approximately 15 K), those pixels in regions with OB

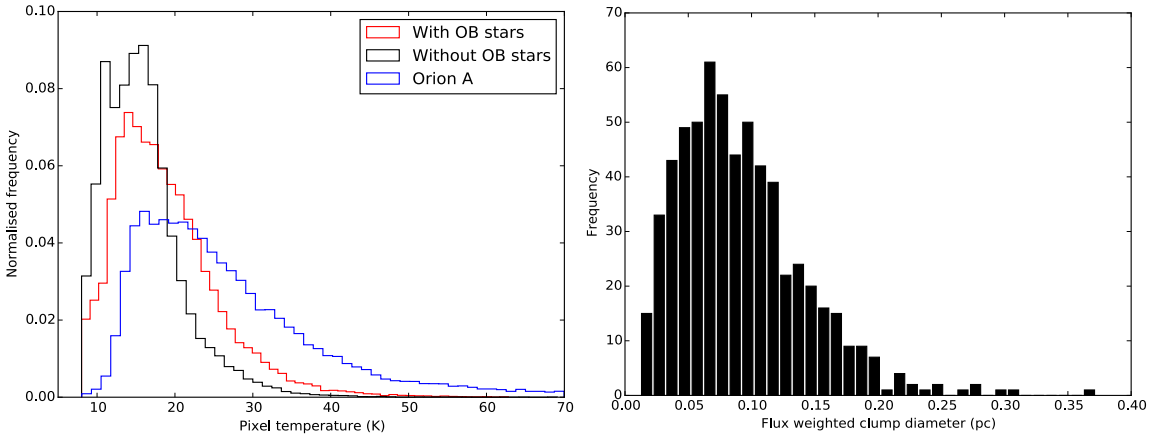

Figure 8.3: Left) the normalised distribution of temperature pixels in JCMT GBS regions that contain OB stars (red) compared to those regions that do not contain OB stars (black). The Orion A region is included separately (blue) to demonstrate its exceptionally high temperatures which extended to values greater than 70 K. Regions with and without OB stars are defined in Table 8.2. Right) the distribution of flux weighted FELLWALKER clump sizes detected in SCUBA-2 850 μm observations of 26 sub-regions of the JCMT GBS.

stars are systematically shifted to higher temperatures (median temperature 17.7 K) than regions without OB stars (median temperature 15.2 K). Note that pixels at temperatures of 8 K or less have been cut from these plots as the majority represent noise artefacts associated with the maps edges, or disc sources where an over-estimate in the value of β is leading to unphysically lower temperatures.

Orion A includes some of the most active areas of star formation in the JCMT GBS regions (Bally 2008, Salji et al. 2015 Kirk et al. 2015). Figure 8.3 (left) demonstrates how temperatures are significantly warmer in Orion A than all other regions. The region is home to large clusters of stars, including many OB stars, which have been proposed to be causing this heating (Salji et al., 2015). Many of these dust temperatures far exceed 50 K and therefore the dust emission at SCUBA-2 bands will lie on the Rayleigh-Jeans tail, and as a result these values will be unreliable. Salji et al. (2015) cap temperatures at 50 K in order to calculate column density; however, as I am explicitly looking to investigate heating this approach is not suitable. As a result Orion A is excluded from further analysis in this Chapter.

8.3 Sample regions

Temperature maps were produced for all the regions listed in Tables 2.13 and 2.14, with the exception of Ophiuchus North where insufficient 450 μm data exist. I present temperature and column density maps for a selection of regions with exceptional heating or other notable features.

8.3.1 ρ Ophiuchus complex

I present the L1688 A/B/C/E/F and L1689 clouds in the ρ Ophiuchus complex in Figure 8.1. The regions are summarised in Table 2.13. The Oph L1688 clouds are a well known area of clustered star formation that are summarised by Wilking et al. (2008). The region contains two notable OB stars. HD147889 (Houk & Smith-Moore, 1988) is an evolved B2III star that, despite being isolated from the main filamentary structure, is believed to be a significant source of heating throughout the complex and is responsible for driving a photo-dissociative region that has been observed on the western limb of the L1688 A (Pattle et al., 2015). S1 (IRAS 16235-2416, Cutri et al. 2003) is a B4Ve Class star that is much younger and is believed to have formed very recently from L1688 A cloud, from which it is currently blistering. Pattle et al. (2015) find that both these stars are having a significant impact on the stability of the L1688 A cloud. Whereas many of the other clouds contain protostars, L1688 A only has one identified protostar. I identify that S1 is the major source of feedback in L1688 A, on account of its proximity, and HD147889 is the major source for the remaining clumps in L1688. The Ophiuchus region also lies in close (11 ± 3 pc) proximity to the Scorpius-Centaurus OB association which also provides significant feedback (Mamajek, 2008). The Oph L1689 cloud is a much lower mass region and does not contain an OB star.

Oph L1689 contains a prominent Class 0 protostar (IRAS 16293-2422B) and this object has the highest column density in Ophiuchus peaking at 1.8×10^{24} H_2 cm^{-2}. FELLWALKER extracts a neighbouring clump that is currently starless and has temperatures less than 15 K. Interpretation of the temperature of IRAS 16293-2422B is limited due to a ringing artefact. However, there is some suggestion of temperatures in excess of 25 K implying there may be some significant heating occurring.

The Oph L1688 B, C, E and F clouds have temperatures less than 20 K and are populated with a number of Class 0/I objects. However, the Oph L1688 A cloud is significantly warmer with a mean temperature of 26 K. As discussed, this heating can be traced to S1 which is believed to have formed from the cloud. Higher temperatures would raise the Jeans mass of the cloud and make gravitational collapse less likely, which may be in part responsible for the lower number of protostars within the cloud relative to its peers.

8.3.2 Orion B 2023 and 2024

Orion B is part of the larger Orion complex, an approximately 100 pc long filament of active star formation (Bally, 2008; Maddalena et al., 1986). A FELLWALKER clump analysis has recently been carried out by Kirk et al. (2016)a and Kirk et al. (2016)b who find a significant number of dense cores that appear highly clustered. Temperature and column density maps of the NGC 2023 and 2024 clusters are presented in Figure 8.4. YSOcs plotted from the Dunham et al. (2015) c2d+GBS catalogue confirm that NGC 2024 has formed a considerable stellar cluster whereas NGC 2023 is much less active in star formation. NGC 2024 has also formed at least two OB stars, most notably the O8 star BCB89-IRS-2b (Cutri et al., 2003).

The column density map of NGC 2024 (Figure 8.4) demonstrates how BCB89-IRS-2b is deeply embedded towards the eastern edge of the cloud, and how it lies in close proximity to a

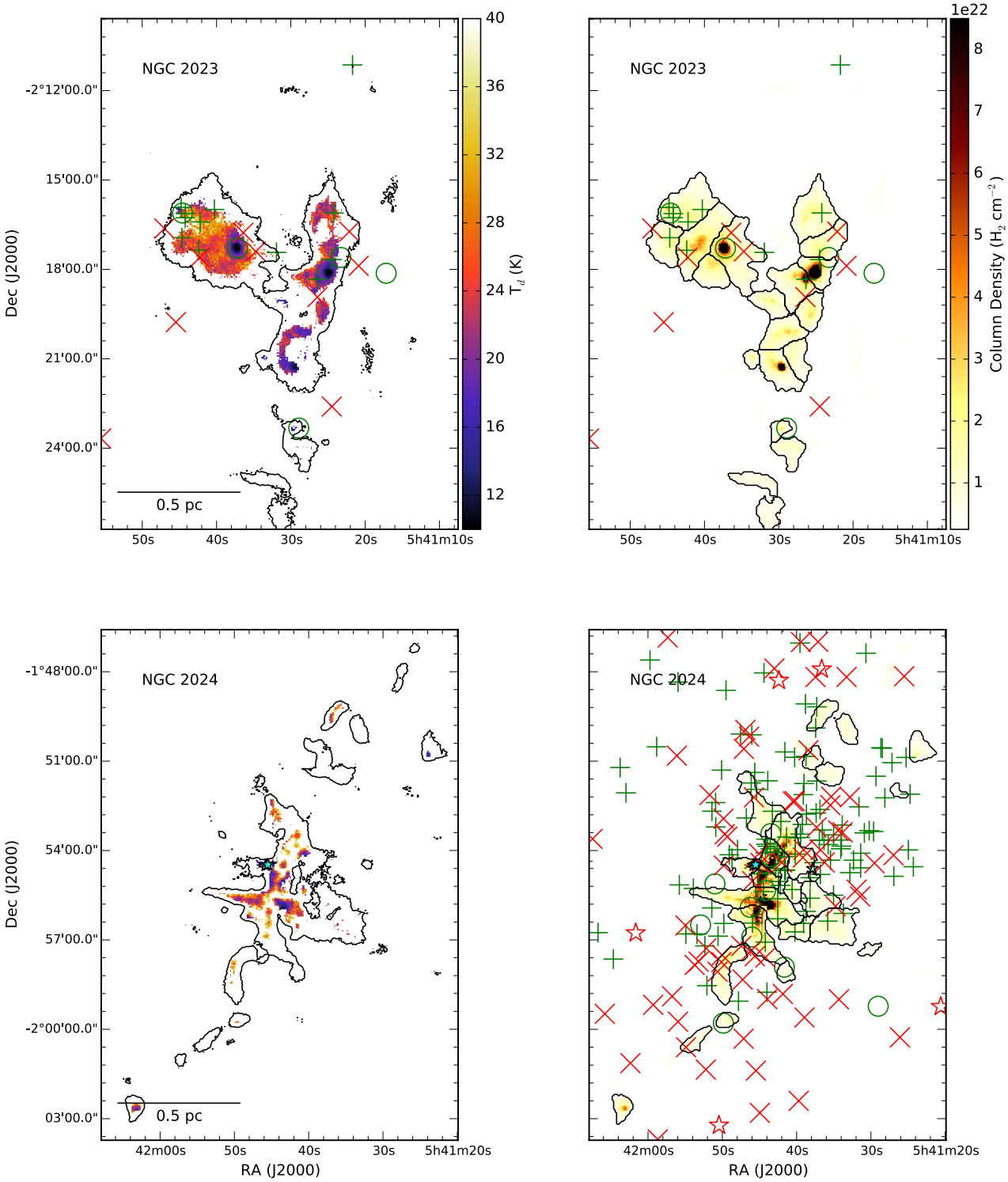

Figure 8.4: SCUBA-2 dust temperature (left) and column density (right) maps for the OrionB 2023/24 region. YSOcs from the Dunham et al. (2015) c2d+GBS catalogue, OB stars and the FELLWALKER clumps based on the 850 μm 5σ contours are marked (see Figure 8.1 for marker designation). The cyan star marks the major OB star in the region, BCB89-IRS-2b (O8).

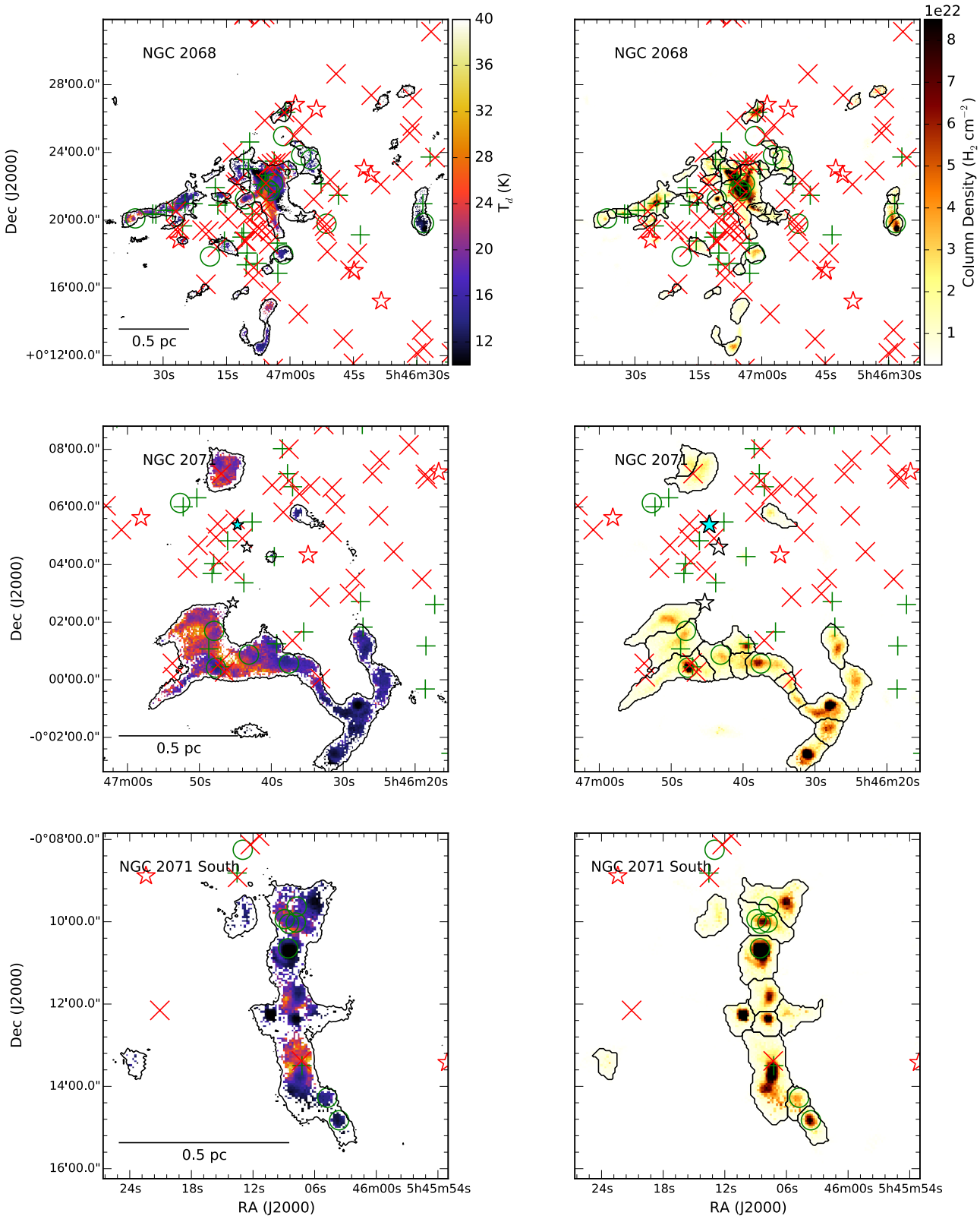

Figure 8.5: SCUBA-2 dust temperature (left) and column density (right) maps for the OrionB 2068/71 region. YSOcs from the Dunham et al. (2015) c2d+GBS catalogue, OB stars and the FELLWALKER clumps based on the 850 μm 5σ contours are marked (see Figure 8.1 for marker designation). The cyan star marks the major OB star in the region, HD 38563 (B2III).

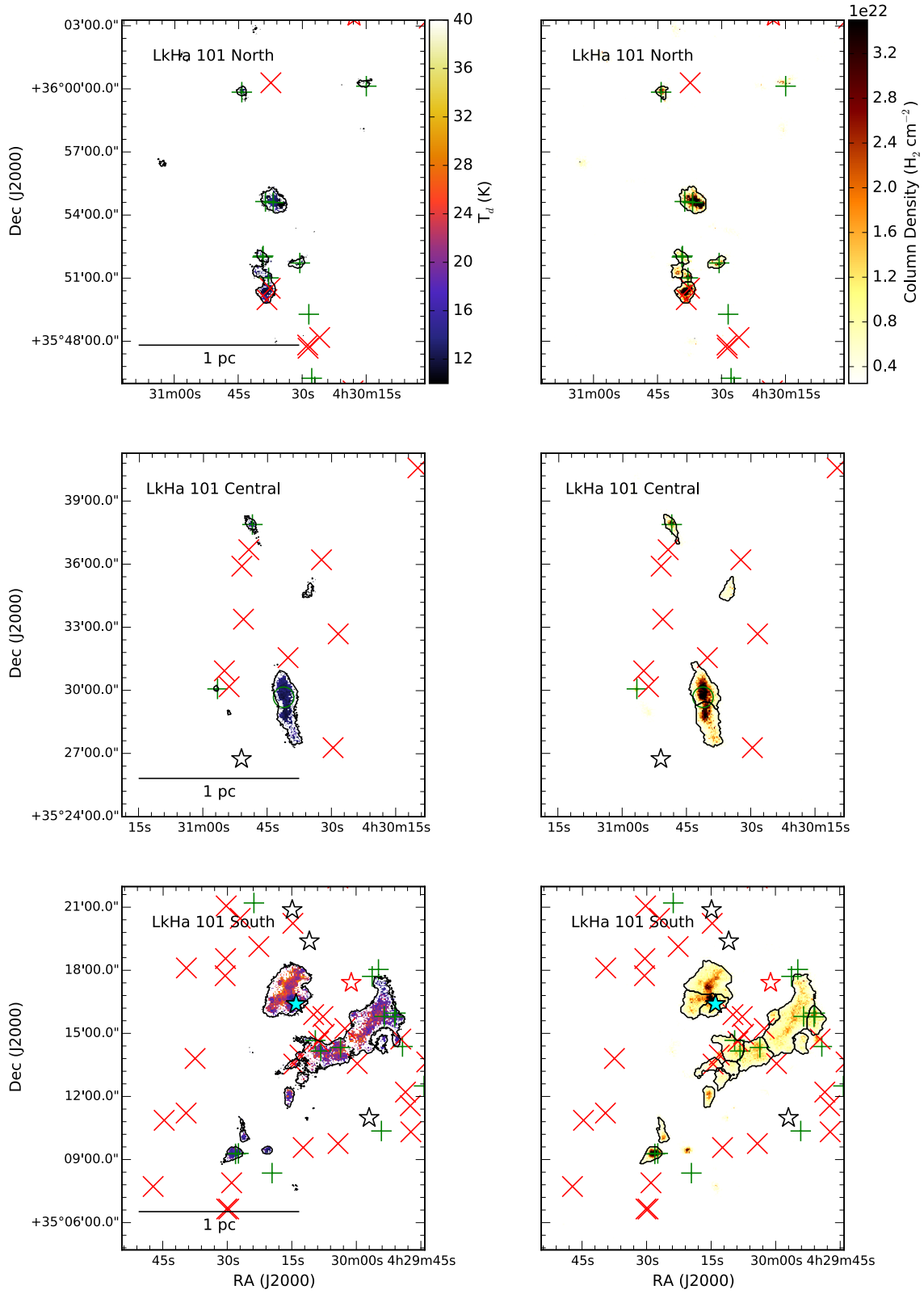

Figure 8.6: SCUBA-2 dust temperature (left) and column density (right) maps for the Auriga LkHα101 region. YSOcs from the Dunham et al. (2015) c2d+GBS catalogue, OB stars and the FELLWALKER clumps based on the 850 μm 5σ contours are marked (see Figure 8.1 for marker designation). The cyan star marks the major OB star in the region, LkHα101 (B0V).

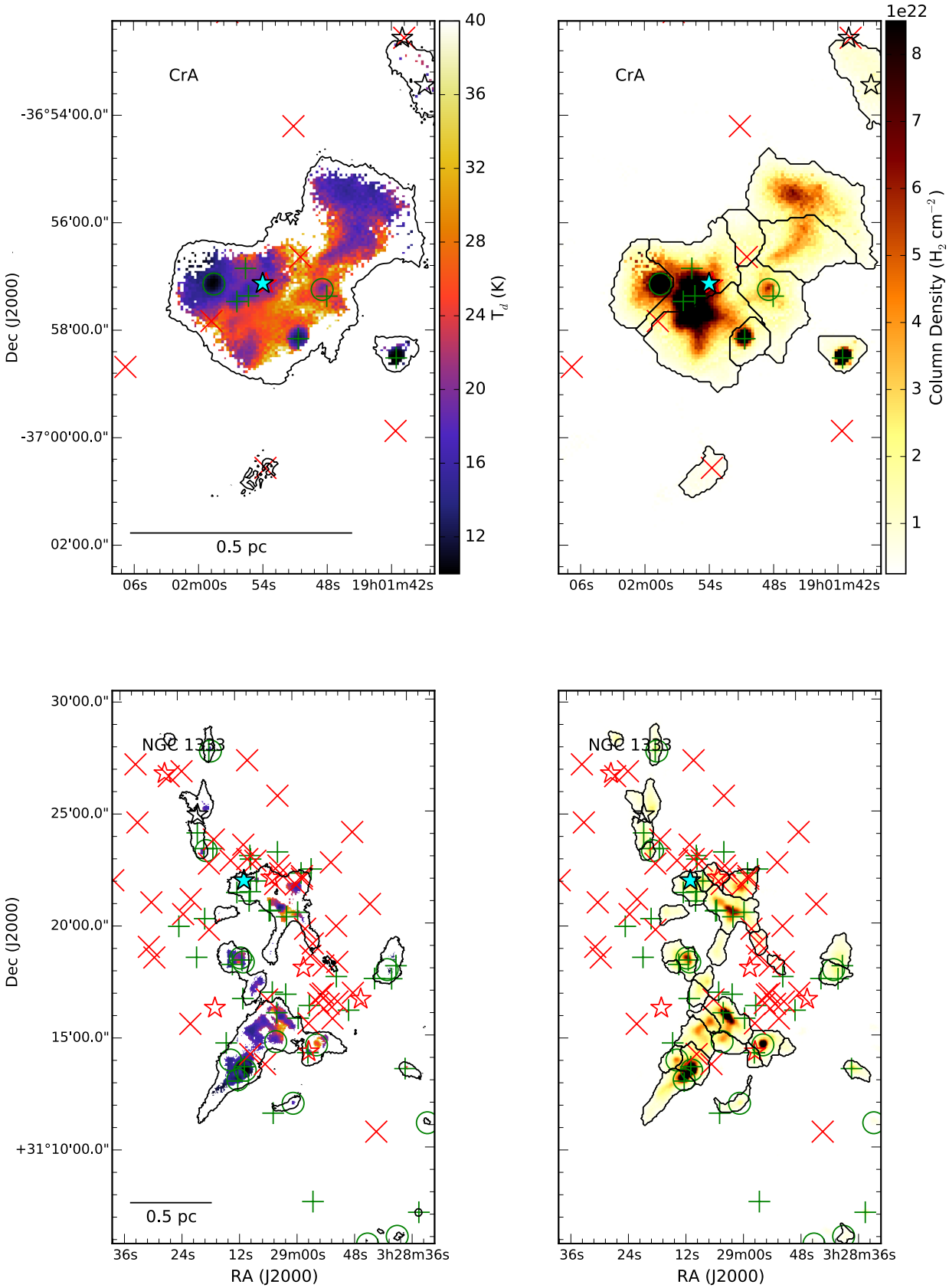

Figure 8.7: SCUBA-2 dust temperature (left) and column density (right) maps for the Corona Australis R CrA core (upper) and Perseus NGC 1333 (lower) region. YSOcs from the Dunham et al. (2015) c2d+GBS catalogue, OB stars and the FELLWALKER clumps based on the 850 μm 5σ contours are marked (see Figure 8.1 for marker designation). The cyan star marks the major OB star in the region, RCrA (A5eII, Corona Australis) and SVS3 (B5, Perseus NGC 1333).

number of dense cores that are forming stars. I note that this region has not been assessed for free-free contamination (see Chapter 4) and that an O8 star would be sufficiently massive for emission to remain partially optically thick up to submillimeter wavelengths, and therefore contaminate the SCUBA-2 bands. The impact of BCB89-IRS-2b on the dust temperatures is striking. NGC 2024 has some of the highest temperatures in the whole of the JCMT GBS and this is likely a direct result of proximity to an embedded O8 star (see section 8.5.1 for further discussion). Many of the higher temperatures may be unreliable as they are pushing towards values where both SCUBA-2 bands would lie on the Rayleigh-Jeans tail. The Dunham et al. (2015) c2d+GBS catalogue classify many Class I objects that are not associated with SCUBA-2 emission. IR contamination from a bright nebulosity (forming around BCB89-IRS-2b) has been known to contaminate YSO fluxes and therefore it is likely that many of the YSO classifications are unreliable in NGC 2024.

NGC 2023 is much less active, containing three to four dense cores and no OB stars. However, significant heating is also observed in the easter part of the cloud. This heating appears to be associated with a cluster of eight Class 0/I objects suggesting that these low-to-intermediate mass YSOcs could be heating the dust there. Alternatively, the OB stars in NGC 2024, located close to the south, could be providing this heating.

8.3.3 Orion B 2068 and 2071

NGC 2068 and 2071 are another two sites of high mass star formation in the Orion complex (Bally, 2008; Kirk et al., 2016). Both are associated with substantial stellar clusters and multiple OB (or A) stars. The filamentary structure in NGC 2068 is highly fragmented and a significant proportion of the mass in this region has gone into forming a substantial cluster of PMS-stars, including HD 290860 (A5 Class, Nesterov et al. 1995). There are a few areas of heating, but mostly temperatures are within the range observed across in JCMT GBS regions which do not contain OB stars.

NGC 2071 appears more evolved than NGC 2068. It has formed four OB stars including the binary HD 38563 (B2II + B2III, Strom et al. 1974) which is the major OB star in this region. There is evidence of a large stellar cluster associated with HD 38563, but its dispersed nature indicates that it is older than NGC 2068. However, star formation is ongoing with a low mass filament present to south of the OB association which contains four Class 0 protostars. As with NGC 2023, there is evidence of raised temperatures in excess of 25 K in region (Figure 8.5), though it is more likely that these are caused by the external influence of HD 38563 rather than the embedded star formation.

NGC 2071 south is markedly different from the previously described regions as there is no evidence of a PMS-star cluster. Dust emission resembles a single uninterrupted filament with at least nine dense cores, six of these contain Class 0/I protostars. This evidence implies that the filament is very young. Temperatures associated with the Class 0 objects drop below 10 K in some cases. However, temperatures associated with an embedded Class I source are much higher, approaching 25 K. Again, it is debatable whether this is a result of embedded stars or exposure to HD 38563.

8.3.4 Auriga LkHα 101

The Auriga-California Molecular Cloud is similar in mass and morphology to the Orion A cloud but does not have the same levels of star formation with the majority of complex relatively quiescent (Lada et al. 2009 and Broekhoven-Fiene et al. 2014). Very few parts of the cloud exist at sufficiently high densities for SCUBA-2 to be sensitive to and as a result there is comparatively less data to analyse in this region. The majority of the high column density material is found at the southern end of the filament where it has formed the B0V star LkHα 101 and an associated stellar cluster NGC 1529 (Gutermuth et al., 2009). LkHα 101 has been observed to be embedded within a larger cloud and to be a prominent free-free emitter that contaminates SCUBA-2 bands (Sandell et al., 2011).

The northern part of Auriga LkHα 101 is populated with a number of isolated cores, the majority of which are cold (less than 15 K) and contain Class 0/I protostars (Figure 8.6). The southern part of the cloud is dominated by LkHα 101 and NGC 1529 but also features two substantial filamentary structures. LkHα 101 is embedded in the northern clump along with two starless cores. The southern filament is associated with a number of Class I objects but contains no dense cores, suggesting that those YSOcs may be PMS-stars contaminated by the nebulosity of LkHα 101. Both filaments show signs of raised temperatures but the heating is not as extensive as that observed in Orion B 2024. Broekhoven-Fiene et al. (2014) conclude that Auriga is very early in its evolution, perhaps suggesting that LkHα 101 has not had sufficient time to heat its surroundings further.

8.3.5 Corona Australis

Corona Australis is a low-to-intermediate mass star forming region made up of five cores (Neuhäuser & Forbrich, 2008), the most substantial of which (R CrA core) is presented in Figure 8.7 (upper panel). R CrA core is named after the brightest star (A5eII Class) in the region. It is also associated with the Coronet proto-cluster (Peterson et al., 2011) of A and late B class stars and the NGC 6729 reflection nebula (Knacke et al., 1973). Outflows have been observed by Strom et al. (1974) inferring star formation is active and ongoing.

R CrA core has a complex column density morphology with at least four dense cores embedded in the east of the cloud (Figure 8.7 upper panel), each associated with a Class 0/I YSOc. The A5eII star R CrA appears to be deeply embedded here but it lacks an associated dense core and, given its advanced evolutionary stage, it may be more reasonable to assume that it is in the foreground of the cloud. By contrast, the western part of the cloud is more extended, lower density and almost completely starless. There is also considerable temperature variation across the cloud. The Class 0/I protostars have some of the coldest temperatures, as low as 10 K in some places. However, temperatures in the extended cloud are significantly warmer, exceeding 35 K in some places. Given the relatively low mass of R CrA and its updated position, it is a mater of debate whether this heating is being driven by external or internal forces. CrA effectively demonstrates that substantial temperature gradients can exist over lengths scales comparable to a typical core (0.05 pc).

Table 8.1: FELLWALKER parameter settings

Parameter	Setting
FlatSlope	1σ
MinPix	4
MaxJump	1
MinDip	3σ
MinHeight	5σ
Noise	5σ
FWHMbeam	4.87

8.3.6 Perseus NGC 1333

Perseus is a diverse, extensive region of which NGC 1333 is just part. NGC1333 is a young cluster with a reflection nebula being produced from a number of bright, young B stars, the chief of which is SVS3, a B5 Class star (Walawender et al., 2008). As discussed in Chapter 5, Section 6, dust temperature maps of NGC 1333 have been made by Hatchell et al. (2013) and Chun-Yuan Chen et al. (2016), both of whom find evidence of heating that they attribute to SVS3. Knee & Sandell (2000) also provide evidence for molecular outflows in NGC 1333, inferring active star formation.

NGC 1333 is a highly fragmented region mapped in Figure 8.7 (lower panel) that is similar in morphology to Auriga LkHα 101 (Figure 8.6). Both are consistent with a scenario whereby a first generation of star formation clears out the bulk of the cloud and leaves a stellar cluster and a small number of OB stars alongside a number of dense cores. Many of the dense cores in NGC 1333 are populated with Class 0/I protostars and these objects are likely driving the molecular outflows identified by Snell & Edwards (1981); Knee & Sandell (2000). The region has a diverse range of temperatures, though broadly speaking they are warmer (between 15 and 20 K) than average. Unlike Hatchell et al. (2013) and Chun-Yuan Chen et al. (2016), SVS3 and its companion BD+30549 (B8) are not associated with hot spots, though the severity of uncertainty clipping used has limited coverage in these areas. As discussed in Chapter 5, evidence from Chun-Yuan Chen et al. (2016) suggest that use of a constant β may explain these discrepancies.

8.4 The SCUBA-2 clump catalogue

I use the Starlink FELLWALKER algorithm (Berry, 2015) to identify clumps in the SCUBA-2 850 μm regions listed in Tables 2.13 and 2.14 (excluding Orion A, Ophiuchus North and Pipe). Details of FELLWALKER follow Chapter 7 and the parameters used to refine clump selection are given in Table 8.1. Clumps are based on a 850 μm signal-to-noise threshold of five. Note that the *FWHMbeam* parameter is set to 4.87 pixels, equivalent to one beam width of the JCMT at 850 μm (14.6″). Use of an accurate beam size allows for full beam deconvolution of FELLWALKER clumps to produce a flux weighted radius. This adaptation allows for more accurate clump sizes to be calculated whilst omitting clumps that are smaller than the beam. Very often these sources correspond to either Class II disc sources (for which our estimation of β is incorrect) or low luminosity noise artefacts. Omitting these objects further strengthens the catalogue.

Where FELLWALKER has been used in previous Chapters, often the SCUBA-2 850 μm maps

Table 8.2: JCMT GBS regions included in the FELLWALKER SCUBA-2 850 μm clump catalogue. Note that RA and Dec give the location of the brightest clump in each region.

Region	RA (J2000)	Dec (J2000)	Total 850 μm clumps	Total temperature clumps	Major OB stars
Auriga LkHα101	04:30:10.42	+35:13:26.9	28	28	1
Auriga Main	04:10:08.39	+40:02:24.5	14	14	0
Auriga Central	04:10:41.40	+38:07:53.3	4	1	0
Cepheus L1228	20:57:13.11	+77:35:43.8	2	2	0
Cepheus L1251	22:38:48.61	+75:11:31.2	8	8	0
Cepheus South	20:39:05.72	+68:02:17.8	12	6	1
Corona Australis	19:01:56.27	-36:57:29.5	15	14	1
IC5146	21:47:22.84	+47:32:12.0	32	26	1
Lupus	15:43:02.22	-34:09:09.2	7	2	0
Ophiuchus L1688	16:26:27.70	-24:24:00.2	44	19	2
Ophiuchus L1689	16:32:22.97	-24:28:36.5	20	5	1
Orion B 2023	05:41:43.11	-01:54:24.3	71	51	1
Orion B 2068	05:47:04.10	+00:21:40.5	83	83	1
Perseus IC348	03:43:56.95	+32:00:50.9	22	19	2
Perseus NGC1333	03:29:10.65	+31:13:33.9	35	27	2
Perseus West	03:25:36.43	+30:45:16.3	26	15	0
Serpens East	18:37:51.40	-01:45:48.9	36	33	0
Serpens Main	18:29:49.90	+01:15:18.9	17	17	0
Serpens North	18:38:59.10	+00:33:05.6	12	12	0
Serpens NH_3	18:29:06.50	+00:30:40.0	15	15	0
Serpens MWC 297	18:28:08.99	-03:48:10.3	9	9	1
Serpens South	18:30:04.14	-02:03:05.1	41	34	0
Taurus L1495	04:19:58.66	+27:09:59.2	10	2	1
Taurus South	04:29:23.89	+24:32:57.9	5	3	0
Taurus TMC	04:39:53.97	+26:03:09.2	2	2	0
W40 complex	18:31:20.99	-02:06:20.3	49	42	1

have undergone a degree of spatial filtering prior to clump extraction to emphasise the small-scale structure. It was found that using a SNR map of the same region was more effective at highlighting this small-scale structure, whilst also ensuring that noisy artefacts were not accidentally included in the resulting list of clumps.

Following the adaptations described above, I run the FELLWALKER algorithm, with the consistent set of parameters given in Table 8.1, over the set of JCMT GBS regions summarised in Table 8.2, and produce the JCMT GBS Clump Catalogue (JGCC). In total, 619 clumps are detected across a total of 26 distinct sub-regions. As discussed above; Orion A, Ophiuchus North and Pipe are not included in the JGCC. In addition to unreliable temperatures, I find that the morphology of the Orion A filament is more substantial than all the other regions, and as a result this set of FELLWALKER parameters cannot reliably disassemble the region for the purpose of this analysis.

Note that a number of JCMT GBS mosaics contain multiple regions that appear to be isolated from each other. In these cases I have spilt these regions into separate maps and run independent clump extraction on each. The flux weighted clump sizes range between 0.01 and 0.37 pc and

Table 8.3: Global statistics on JGCC members

	Mean	Min	Max
Mass ($M_\odot$)	4.3±1.2	0.02	83
Temperature (K)	16.0±2.6	7.1	41.9
Column density (H_2 cm^{-2})	$75\pm19\times10^{21}$	8	2162
Volume density (cm^{-3})	2.9×10^5	0.2×10^5	6.6×10^6
Jeans mass ($M_\odot$)	4.6±0.7	0.5	30.7

are illustrated in Figure 8.3 (right). The median clump size extracted with this set of parameters is 0.08 pc, larger than a typical protostellar core (0.05 pc, Rygl et al. 2013), confirming that the FELLWALKER clumps represent more extended, filamentary structures and are not directly comparable with algorithms designed or parameterised to extract YSOcs (for example, *getsources*, as used by Maury et al. 2011 and Könyves et al. 2015).

In addition to clump size and position, the JGCC also includes; total 850 μm flux, mass, temperature, column density, Jeans mass and Jeans stability (M_{850}/M_J) and protostellar population (following Chapter 7). Uncertainties are also calculated where appropriate. The YSO surface density is also calculated by convolving YSO point sources over a spatial scale of approximately 0.7 pc. In addition to these various properties, the plane of the sky distance (in pc) to the nearest major OB star in a region is also calculated. An example of the JGCC is presented in Table 8.5 (the full Table is represent in Appendix Table A.1). The methods and challenges associated with calculating individual properties have been discussed in detail in Chapters 6 and 7.

A selection of statistics for the global clump population are presented in Table 8.3. I believe that this is first time that such an extensive catalogue of clumps has been produced covering such a diverse range of star forming regions. Observations of smaller regions, like those presented in Chapters 6 and 7, have put the typical isolated clump temperature at 15 K, consistent with the value assumed by Kirk et al. (2006). The JGCC results are a slightly higher value of 16.0±2.6 K, but consistent within the uncertainty. Of the total sample, 24% have a M_{850}/M_J greater than one and only 8% of all clumps could considered truly unstable ($M_{850}/M_J \geq 2$) when the impact of non-spherical geometry, is considered. 46% of all clumps contain at least one Class 0/I protostar. This fraction rises to 58% when considering just the unstable clumps. However, only 6% of starless clouds are unstable inferring that the bulk of clumps in the Gould Belt that are sufficiently massive/cool have already proceeded to form stars that the remaining starless clumps will remain relatively quiescent unless they cool further or accrete further mass. However, I note that there may also be a selection bias with the SCUBA-2 data reduction pipeline removing more of the larger scale, lower density clumps that are most likely to be starless.

8.5 Sources of heating in the JCMT GBS regions

Throughout Chapters 6 and 7 I have investigated heating in the Serpens MWC 297 region and Aquila W40 complex. In this Chapter I look to extend those investigations to cover the majority of the JCMT GBS of star forming regions. The Serpens MWC 297 region and Aquila W40 complex

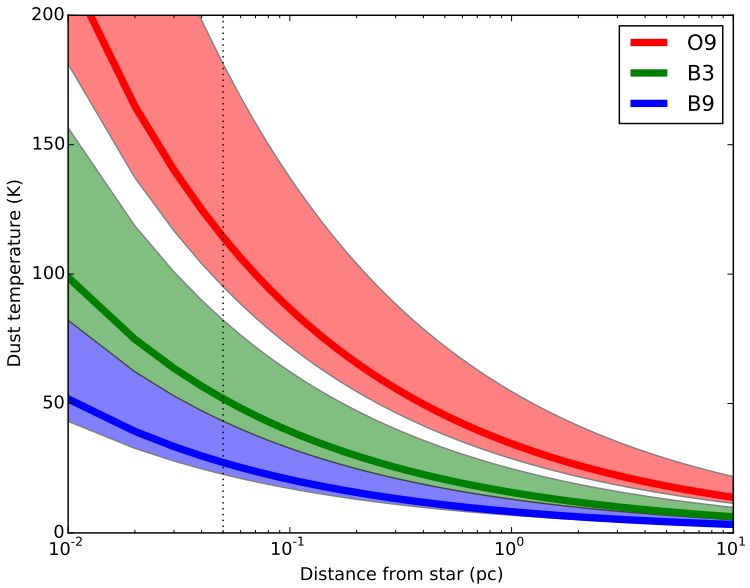

Figure 8.8: Dust temperature, as a function of distance, when irradiated by an O9 (red), B3 (green) and B9 (blue) star. Bold lines represent the typical dust grain size of 0.1 μm (Stahler & Palla, 2004). The filled spaced marks the maximum and minimum range of grain size (0.005 to 0.25 μm following Mathis et al. 1977). The typical core size of 0.05 pc is marked as the black dotted line.

both provided very specific scenarios, often with multiple competing influences. By examining and comparing regions with and without evidence of heating, I build a more general and robust picture of the influence of internal and external radiative feedback on the star formation process.

8.5.1 External influences: OB stars

OB stars are amongst the most potent sources of external radiative feedback available in star forming regions. Near IR observations by *Herschel* observe how OB stars heat lower density dust and lead to the formation of a mid IR bright nebulosity. A number of JCMT GBS regions include this phenomenon, notably Serpens MWC 297 and the Aquila W40 complex that were featured in Chapters 6 and 7.

The stellar energy density of a star with a given luminosity can be modelled as a function of clump-star distance using a Habing field (G_o, Equation 1.15), allowing for the dust temperature, T_d, to be modelled as

$$T_d = 33.5 \left(\frac{1\,\mu\mathrm{m}}{a} \right)^{0.2} \left(\frac{G_o}{10^4} \right)^{0.2} \mathrm{(K)}, \tag{8.1}$$

for an assumed grain size, a, and $\beta = 1$ (Tielens, 2005). Stahler & Palla (2004) define a typical grain size of 0.1 μm and this value is used to calculate the dust temperatures of the ISM irradiated by a range of massive stars, from O9 to B9, and the results are presented in Figure 8.8. As discussed in Chapter 5, Section 6, dust grain size has been observed to vary with the local environment of the ISM and a range of 0.005 to 0.25 μm is commonly used in modelling (Mathis et al.,

1977).

At clump-star distances greater than 1 pc, the heating provided by class B stars is comparable to typical clump temperatures (15 K) and therefore these objects are unlikely to have a significant impact on the ISM. By contrast the more massive stars can heat the dust up to temperatures in excess of 30 K. At clump-star distances less than 1 pc, the O stars and early B stars become increasingly more effective at heating their environment, with late B stars only significantly impacting the dust within their local envelope. The dust temperatures reached by heating from the most massive stars at distances less than 1 pc are in excess of 50 K. These temperatures are beyond the ability of the SCUBA-2 flux ratio method to measure reliably and therefore any temperatures measured within 0.05 pc of a B3 star and 0.38 pc of an 09 star should be treated with scepticism.

Chapters 6 and 7 find evidence that the clump temperatures are negatively correlated with distance to a local OB star (Figure 7.7 left). Chapter 7 find evidence that the O9.5V star OS1aS is effective at raising clump temperatures out to a clump-star distance of 1.2 pc. Beyond this the clump temperature approaches a mean value of 15±2 K, implying that the OB star is no longer having a significant influence.

Extending this method to all regions in the JCMT GBS allows for a more robust analysis of the impact of OB stars on clump temperature. As discussed in Chapter 4, the ionising potential of an OB star is a logarithmic dependance on mass with those classed B4 or earlier capable of producing an H II region. I therefore separate those 12 regions (Table 8.4) with OB (and A) stars into three subsets: O Class, Early B Class (B0-B4) and late B Class (B5 or lower), based on the classification of the major OB star in the region.

The distributions of clump temperatures in these subsets are presented in Figure 8.9 (upper). The temperature distribution of clumps with early and late B type stars has a KS-probability of 97% similarity and both peak at 15 K, suggesting that the bulk of clumps in these regions are not being heated beyond the typical clump temperature of 15 K. However, clumps in regions with O type stars are systematically shifted to warmer temperatures, peaking at 18 K and extending as far as 40 K. The KS-test shows only a 67% similarity between B and O star regions.

The temperatures of clumps in each subset are plotted against the clump-star distance to the major OB star in each region in Figure 8.9 (lower). As expected, the clumps in regions with O stars (OrionB 2023 and Aquila W40 complex) appear systematically warmer (consistent with the Figure 8.9 upper). All subsets show the anti-correlation identified in Chapter 7. Not all clumps in the subset will be heated by OB stars. By-eye the O stars are influential to a range of approximately 3 pc, and I use this value as an upper limit for clumps included in an uncertainty weighted linear regression fit for each of the three subsets, from which a 'heating range' is defined as the distance from the major OB star at which the clump temperature drops to 15 K. The heating ranges of the three classes are found to be; 0.13±0.15 pc, 0.29±0.11 pc and 3.6±0.2 pc for late B, early B and O type stars, respectively. The substantial uncertainties on the B star values reflects that, by trimming the sample at 3 pc, unheated clumps will likely be included in the linear fit and as a result these values are likely under-estimates.

The heating range of B type stars, in particular late B types, is less than a factor of three larger than the typical size of a core, suggesting that any radiative feedback will be limited to

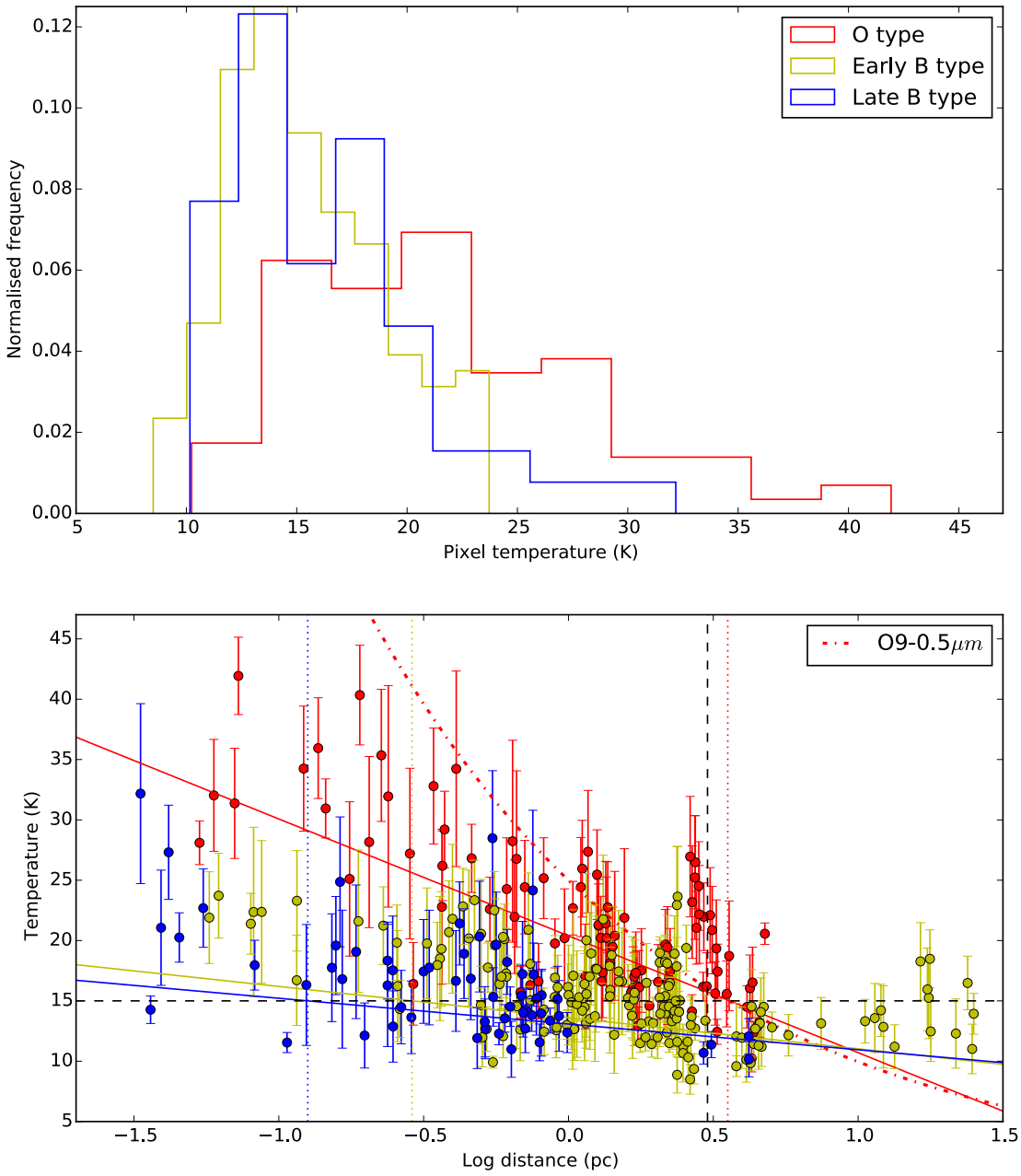

Figure 8.9: Upper) temperature distribution, as a function of clump-star distance, for clumps in regions with major; O type stars (red), early B type stars (B0 to B4, yellow) and late B type stars (B5 to B9, blue). See text for details. Lower) Clump temperature plotted against plane of the sky distance from the major OB star in the region. Solid lines of the corresponding colour show uncertainty weighted linear regression fits. Dashed lines show typical clump temperature of 15 K and the cut point of 3 pc from which the fit was calculated. The red dash-dotted line shows the Tielens (2005) models (Equation 8.1, Figure 8.8) for a O9 Class star and optimal grain size (0.5 μm).

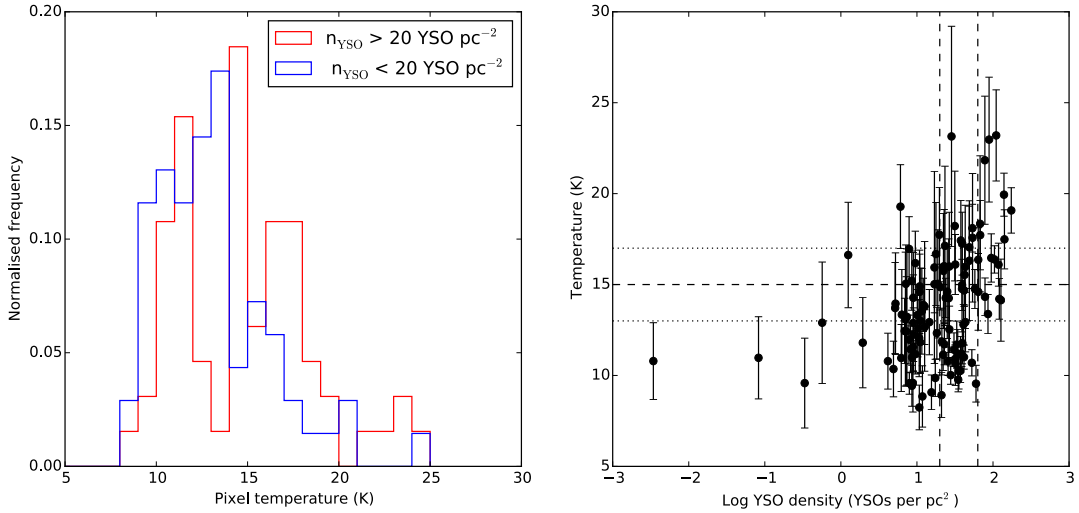

Figure 8.10: Left) temperature distribution for clumps in regions without OB stars. Red represents clumps in clustered environments (where the YSO density exceeds 20 YSOs per pc^2). Blue represents clumps in unclustered environments (less than 20 YSOs per pc^2). Right) clump temperature plotted against YSO density. The black dashed line indicates the partition between clustered and unclustered environments (20 YSOs per pc^2, Chapter 7) and the typical clump temperature of 15±2 K (bounds marked as dotted lines).

only the ISM in their immediate environment. This range is consistent with the location of heated clumps observed in Serpens MWC 297 (Chapter 6) and Ophiuchus (Figure 8.1), for example.

By contrast, the impact of O stars on their environment is much more pronounced. The heating range of 3.6±0.2 pc is sufficiently large as to encompass a substantial part of many star forming complexes which has far reaching consequence for the star formation in these region. The range of heating for O stars has greater precision than the equivalent value for B stars as it covers objects that are relatively close in Class (O9.5 to O8). In contrast the range of heating for B stars covers B0 class through to A0 Class, covering almost three orders of magnitude in stellar luminosity. The Tielens (2005) model (Equation 8.1) of an O9 star is plotted in Figure 8.9 (lower) to illustrate the comparable results.

Throughout this analysis I have made the assumption that the major OB star dominates over all other members where clusters exist. This is true where one member dominates over another, for example in the W40 complex, but where OB stars are of comparable masses this assumption could lead to a systematic underestimation of the cluster luminosity. However, unless the members are clustered on a length scale less than the heating range then they can be considered independent of each other. For every OB star formed, a significant cluster of low-to-intermediate mass stars will also be formed in line with the core mass function of the region (André et al., 2010). In the following section I look to assess whether low-to-intermediate mass star clusters can provide evidence of clump heating, and how this compares to heating from OB stars.

8.5.2 External influences: YSO clusters

The results from the OB star analysis assumed that the major OB star in a region dominates the heating over all other members. This is accurate when compared to isolated high-mass stars. Models of the initial mass function (IMF) by Kroupa & Weidner (2003) and Chabrier (2005), as well as observations of the core mass functions derived from Gould belt regions by André et al. (2010) all describe how large stellar clusters form in parallel with high mass stars. For example, the W40 complex contains both OB stars and a PMS-stellar cluster that is detected in the X-ray by Kuhn et al. (2010). Taking the mean mass of a cluster member to be $1\,M_{\odot}$, the total mass of low mass objects in the W40 complex is comparable to that of the high mass objects, inferring that there are the resources available to provide a comparable level of radiative feedback. Where stellar clusters are observed within the heating range length-scale then they may provide additional radiative feedback. By targeting regions with highly clustered YSOcs, but with no OB stars, I aim to investigate whether there is any evidence of heating.

From the Aquila W40 complex composite YSOc catalogue (outlined in Chapter 2 and used in Chapter 7), I estimate that there are approximately 36 YSOcs within the cluster associated with the OB association. By assuming each of these YSOs to be solar in nature, I can estimate the total luminosity from the low-to-intermediate star cluster to be $36\,L_{\odot}$, a value that is equivalent to a single A2V star. This rough estimate would suggest that the dust heating from the low-to-intermediate star cluster would be dominated by the OB stars in the region (OS1aS alone has a stellar luminosity of over $57{,}600\,L_{\odot}$).

I extract a subset of clumps from the JGCC that are members of regions without OB stars. Based on the stellar cluster in the Aquila W40 complex presented in Chapter 7, I define a mean YSO density of 20 YSOs per pc^2 as the partition between an unclustered and clustered environment. The two samples are presented in Figure 8.10 (left) and they are found to be highly similar with a KS-probability of 67.5%.

Temperature is plotted against YSO density for all clumps in regions without OB stars in Figure 8.10 (right). The majority of clumps fall within the typical clump bounds of 15±2K̇ and provide limited information regarding heating. I note that this temperature is a lower limit for the majority of clumps with a YSO density greater than 60 YSOs per pc^2. Likewise, 15 K is an upper limit for the majority of clumps with a YSO density lower than 20 YSOs per pc^2. An uncertainty weighted linear regression analysis shows a positive correlation that is consistent with these findings; however, considerable scatter on the results limits a more detailed analysis.

Examining the subset of clumps with a YSO density greater than 60 YSOs per pc^2 in Figure 8.11 (left), I find this sample has a mean temperature of 17.4±1.9 K, representing a significant increase in temperature away from the typical clump temperature. This result is replicated in the KS-probability which, at 8.2%, further outlines the dis-similarity between the two regimes. These findings provide tentative evidence that clumps in the most clustered environments (greater than 60 YSOs per pc^2) provide a limited degree of heating to their immediate environments. However, the four warmest clumps in the sample are all associated with Serpens Main, a tightly clustered region with vigorous outflow activity (Davis et al. 1999 and Eiroa et al. 2005) which has been linked to raised dust temperatures in the cloud (Eiroa et al., 2008). After excluding the Serpens

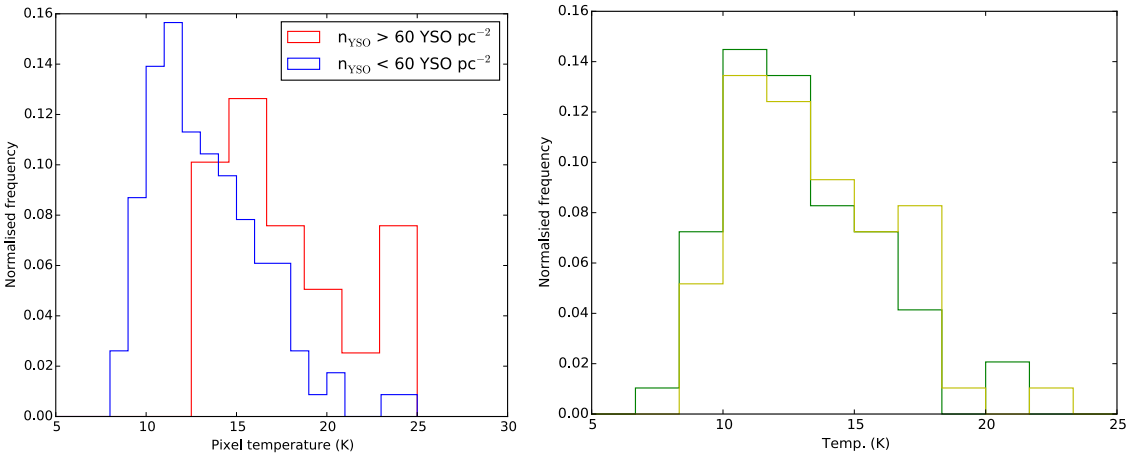

Figure 8.11: Left) revised temperature distribution for clumps in regions without OB stars. Red represents clumps in highly clustered environments (where the YSO density exceeds 60 YSOs per pc^2). Blue represents clumps in unclustered environments (less than 60 YSOs per pc^2). Right) the temperature distribution of clumps in regions without OB stars. Yellow marks clumps that are proto-stellar, green marks clumps that are pre-stellar. Both sets have clumps with a YSO density greater than 60 YSOs per pc^2 removed.

Main clumps I find little evidence of significant heating associated with low-to-intermediate mass YSOc clusters, a result that is consistent with the total power output of the cluster relative to that of the OB association in the Aquila W40 complex. This chapter does not assess the relationship between protostellar outflows and clump temperature, and therefore I cannot verify outflow heating (or rule out cluster heating) though I can verify that any heating is dominated by that from OB stars.

8.5.3 Internal influences: protostars

So far I have assessed the impact of external stars on clump temperature. However, during the Class 0/I stages the protostars are deeply embedded and should provide a degree of radiative feedback into their immediate environment. In Chapter 4 I discussed the evidence for massive embedded stars producing ultra-compact H II (UCH II) regions through the heating and ionisation of their local envelope. However, where the star is sufficiently powerful that the free-free emission produced by the UCH II region is optically thick at submillimeter wavelengths, this emission will contaminate SCUBA-2 bands and can lead to dust temperatures appearing much cooler than they should. This effect has been analysed in detail in MWC 297 (B1.5Ve) and has also been observed in other embedded high mass stars that are associated with uncharacteristically cold spots, for example, LkHα101 (B0V, Sandell et al. 2011) and BCB89-IRS-2b (O8V, Cutri et al. 2003). As each candidate free-free contaminant has not been individually investigated and subtracted, I cannot reliable investigate the local heating produced by the OB stars in the JGCC.

Shirley et al. (2002b) and Young et al. (2003) model low-to-intermediate mass Class 0 and Class I sources, respectively, observed with SCUBA. They define a dusty core, of a given opacity, with a power law density distribution heated internally by a blackbody with an effective temperature of 6000 K, and externally by an ISRF (Evans et al. 2001). Temperature and flux are modelled

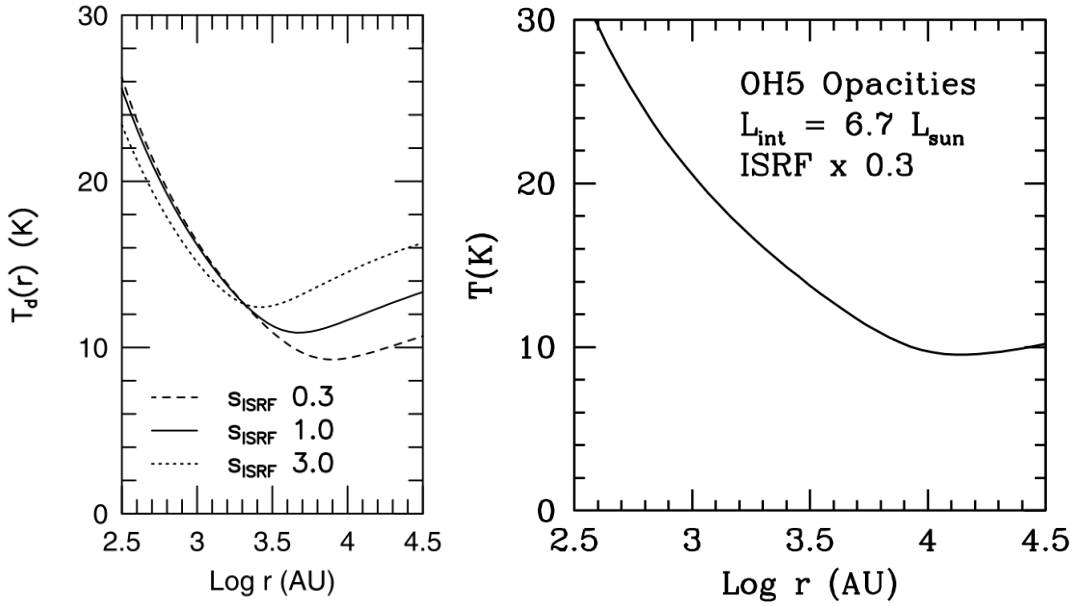

Figure 8.12: Model temperature profiles in protostars produced using a one-dimensional radiative transfer code. Left) taken from Shirley et al. 2002, Figure 4. A model of the Class 0 protostar B335 demonstrating the impact of various strength ISRFs on the temperature profile. Right) taken from Young et al. 2003, Figure 7. A model of the Class I protostar CB 230.

through a one-dimensional radiative transfer code and fit to the observed SED. Examples of the temperature profiles for each class of protostar are given in Figure 8.12. In both examples, temperature reaches a minimum (of around 10 K) at the typical core size of 0.05 pc before increasing towards the centre of the object. At the resolution limit of the JCMT (which varies given the distance of the source) temperatures increase by a factor of two, which is within the capabilities of the SCUBA-2 flux ratio methods to observe.

As discussed in Chapter 5, Section 6, Hatchell et al. (2013) and Chun-Yuan Chen et al. (2016) have observed local dust heating in Perseus NGC 1333 that has been attributed to embedded protostars. However, these results are not readily replicated by the Kernel-convolution method for reasons discussed in the previous section (Figure 8.7). I use the JGCC to investigate if these results are unique to the NGC 1333 or if they are repeated globally.

As discussed in the previous sections, there is evidence that OB stars and sufficiently dense stellar clusters can heat clumps. I therefore produce a subset of clumps from the JGCC based on regions without OB stars and N_{YSO} less than 60 YSOs pc^{-2}. I further divide this subset into pre-stellar (starless) and proto-stellar (contains at least one Class 0/I protostar) clumps based on YSOc occupancy and compare their distributions in Figure 8.11 (right). I find the two subsets have a high probability of being drawn from the same sample with a KS-similarity of 97%. Likewise the mean temperatures of the distribution are consistent at 12.9±2.4 K (pre-stellar) and 13.6±1.7 K (proto-stellar). It is interesting to note that with the heated clumps, the clump temperature is now less than the typical value of 15 K (though the results are consistent within the uncertainties)

The results presented in Figure 8.11 (right) imply that there is no evidence that low-to-

intermediate protostars heat their immediate environment and produce a hot spot. This result is in contrast to the earlier work of Hatchell et al. (2013) and Chun-Yuan Chen et al. (2016) in Perseus NGC 1333 but consistent with the core temperatures calculated by Könyves et al. (2015) in the Aquila region. It is important to note that these results are region specific, and that those results presented in Figure 8.11 (right) are the first to incorporate protostellar heating across the JCMT GBS and remove bias for heating by external influences.

In order to further investigate the perceived lack of heated dust observed in my SCUBA-2 temperature maps of protostars I turn to theoretical simulations of YSOs, like those modelled by Shirley et al. (2002b), Young et al. (2003) and Robitaille et al. (2006). Robitaille & Whitney (2014) builds on much of this work to produce an SED from a model YSO, built from 14 free parameters. The SED is dominated by emission from three distinct components within the YSO; the envelope, disc and star.

As discussed throughout this thesis, the earliest stages of star formation are dominated by a cool (less than 15 K) envelope component. As demonstrated in Figure 8.12, more evolved YSOs are more effective at heating, and therefore the envelope will develop a temperature gradient with time that follows Equation 8.1.

The accretion disc also forms in close proximity to the protostar also develops a temperature gradient typically modelled as between 20 and 50 K. The envelope in PMS-stars is largely dispersed and Buckle et al. (2015) is able observe PMS-star discs and calculate a median mass of $1.6{\times}10^{-3}\,\mathrm{M}_{\odot}$. Comparing this value to the JGCC mean clump mass of $4.3\,\mathrm{M}_{\odot}$ gives an observed disc/envelope fraction of the order 10^{-4} (0.04%) which is not sufficiently massive to have a significant impact on the temperature observed by SCUBA-2.

Assessing the impact of heating of the envelope by an internal source has been modelled using one and two dimensional radiative transfer simulations by Shirley et al. (2002b), Young et al. (2003) and Robitaille et al. (2006) who produce SEDs for comparison with observations. A similar analysis is required to robustly analyse whether and when protostellar heating can impact on the temperatures calculated with the SCUBA-2 flux ratio and this goes beyond the scope of this thesis.

8.6 How does heating influence star formation?

In the previous sections I have outlined the evidence for clump heating across the JCMT GBS and that these processes are dominated by external mechanisms over internal. Whilst I find tentative evidence that especially dense low-to-intermediate mass star clusters may provide some external heating, this mechanism is significantly weaker than the radiative feedback from individual massive stars, in particular O Class stars. I now discuss whether this heating is having a significant impact on the star formation, and what this can tell us about how different regions evolve.

Throughout this section I compare those clumps where there is direct evidence for heating from OB stars to the rest of the sample. I therefore create two new subsets. The first takes all 'heated' clumps that are in regions with major OB stars and lie within the upper bound of the respective heating ranges, i.e, within 0.28, 0.40 and 3.8 pc of late B, early B and O type stars, re-

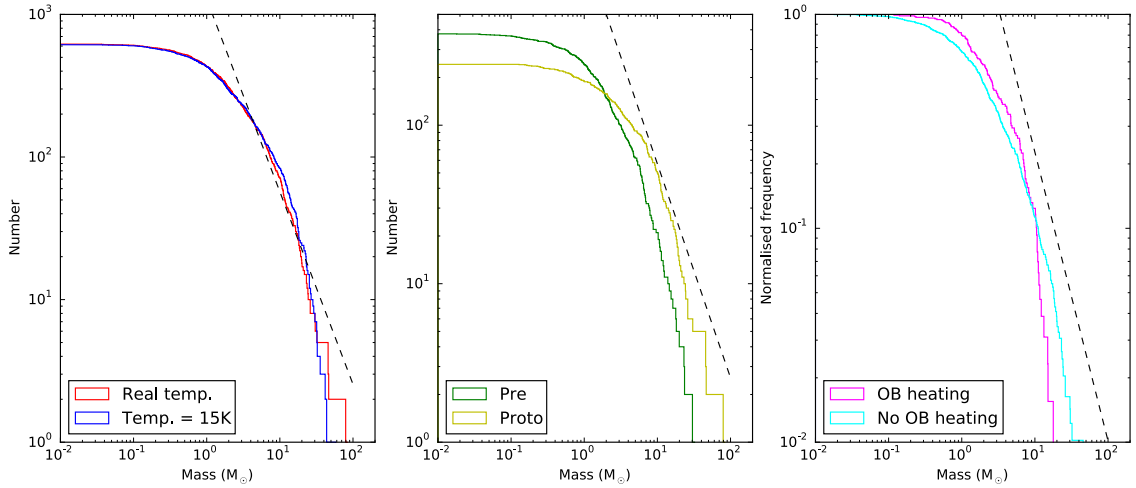

Figure 8.13: Cumulative mass functions (CMF) of JGCC clumps. Left) shows all clumps, calculated with a unique temperature (red), compared to all clumps, calculated with a single constant temperature of 15 K (blue). Center) shows all pre-stellar clumps (green) compared to proto-stellar clumps (yellow). Right) shows the normalised CMF of clumps with OB heating (magenta) compared to those without (cyan). The dashed line indicates the Salpeter mass function of $N \propto M^{-1.35}$.

spectively (thus producing a conservative sample of heated clumps). The remaining objects make up a list of 'isolated' clumps. There are a total of 129 heated clumps (21% of all clumps) and they have a mean temperature of 21.3±3.8 K. This value is significantly larger than the isolated clumps which have a mean temperature of 14.6±2.4 K, a value that is consistent with the temperature of the isolated clumps in Chapter 7.

In early catalogues clump temperature has often been taken as a constant value across a region, in line with existing YSO models (Motte et al., 1998; Johnstone et al., 2000; Kirk et al., 2006). More recently, authors such as André et al. (2010), Salji et al. (2015) and Pattle et al. (2015) have been calculating temperature-corrected masses. Kirk et al. (2016) use a constant value of 20 K for the Orion B complexes; however, Figures 8.4 and 8.5 demonstrate that this assumption is wholly inaccurate for this region given the heating caused by BCB89-IRS-2b. However, in regions without OB star heating I find that the mean temperature of the isolated clumps is 15±2 K, a value that is consistent with cores in the Perseus region modelled as Bonnor-Ebert spheres by Kirk et al. (2006) and those calculated from kinetic gas temperatures in Ophiuchus by Friesen et al. (2009). Figure 8.13 (left) demonstrates the cumulative mass function (CMF) of the clumps with real temperatures, compared to those using a constant value of 15 K, following Kirk et al. (2006). Both distributions are very similar, with a fixed temperature slightly over-estimating the mass above 6.25 $M_\odot$ and slightly under-estimating above 32.5 $M_\odot$. Both distributions most resemble a Salpeter mass function between 4 and 24 $M_\odot$.

In a similar fashion I compare the CMF of pre-stellar and proto-stellar clumps in Figure 8.13 (center). These distributions demonstrate that protostellar clumps are consistently more massive but pre-stellar clumps are more numerous. The mass of clumps that have and have not been heated by OB stars are compared in Figure 8.13 (right). It is notable that there are more low mass clumps

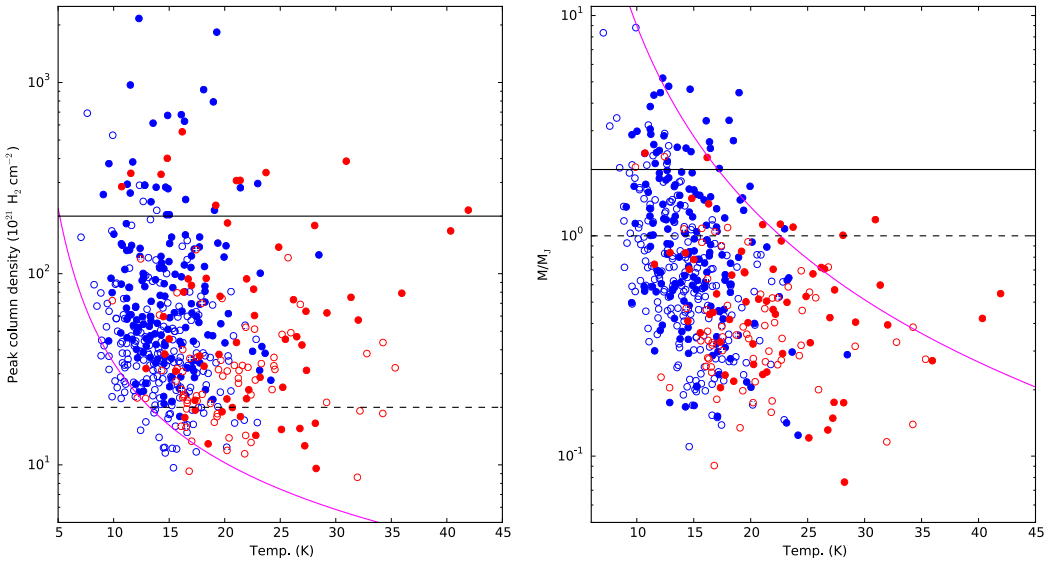

Figure 8.14: Left) peak clump column density and right) Jeans stability as a function of temperature. In both plots blue markers represent clumps from regions without OB star heating and red represents clumps from regions with OB star heating. Filled markers are proto-stellar clumps, hollow markers are pre-stellar clumps. Dashed lines mark lower thresholds of peak column density (left) and YSO occupancy (right), solid lines show respective upper thresholds. On both plots the magenta line illustrates the inherent anti-correlation that exists between the two properties for a source of constant flux, distance and mass.

in regions with OB stars. This mass range (less than 10 $M_\odot$) encompasses all clumps that will go on to form low-mass solar type stars inferring these regions will form larger clusters. However, this observation can be explained by a selection bias. Given that OB stars only form in high mass star forming regions, they are therefore likely to be associated with more substantial clusters. Furthermore, the potential heating from any OB stars can result in low mass clumps becoming sufficiently bright that they can be detected by SCUBA-2, where previously they would not have been. I also note there is a greater quantity of high mass clumps in regions without OB stars. As discussed in Chapter 1, the IMF describes how GMCs that form OB stars are, by definition, more massive than those that do not. In order to explain this observed discrepancy, I consider that the regions with OB stars are more evolved than those without, with a substantial amount of their dust having been used up in star formation and insufficient remaining for further massive star formation.

The ratio of Jeans and SCUBA-2 850 μm masses, M_{850}/M_J, has been used to infer the gravitational stability of clumps in Chapters 6 and 7. Clumps can be considered unstable when $M_{850}/M_J \geq 1$, though in reality the limits of the models discussed in Chapter 1 Section 1 mean that ≥ 2 is a more confident threshold for instability. Chapter 6 showed that direct heating of a clump by the B1.5Ve star MWC 297 is raising its temperature and as a result the clump has become more stable, and is less likely to form stars. Likewise, Chapter 7 found that clumps within the nebulosity Sh2-64 (in the Aquila W40 complex) have systematically lower values of M_{850}/M_J as a result of heating by the O9.5V star OS1aS.

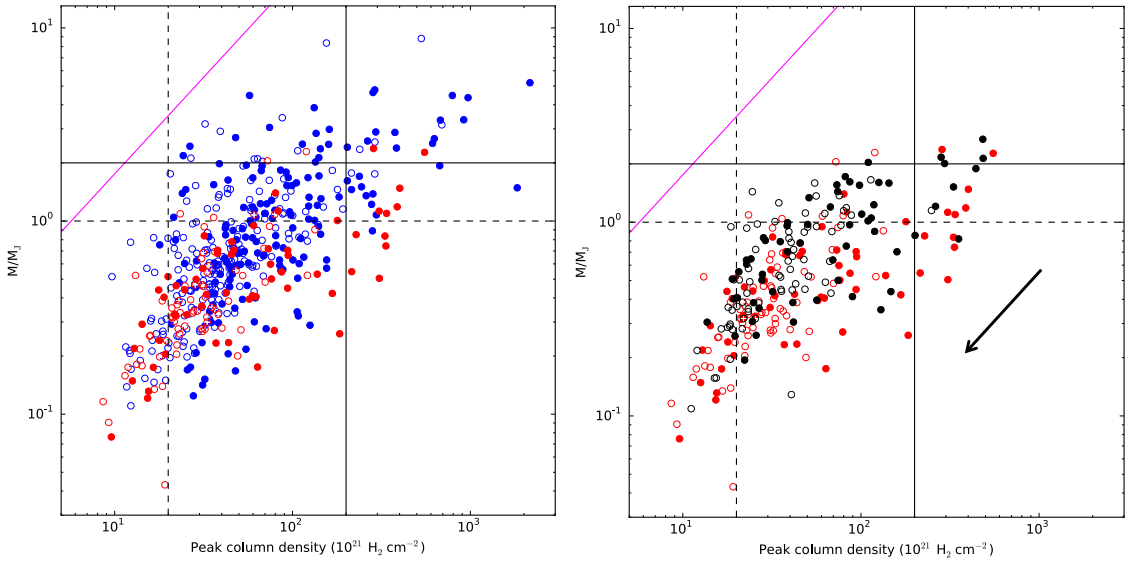

Figure 8.15: Left) clump stability-column density relation. Right) show how the column density and stability of heated clumps would look if they were unheated and had a temperature of 15 K (black). All markers and lines follow those outlined in the Figure 8.14.

The relationship between M_{850}/M_J and clump temperature is illustrated in Figure 8.14 (right). Note that these properties have an inherent anti-correlation. I find that the heated clumps largely display this correlation, but isolated clumps do not. The vast majority of tentatively unstable clumps (M_{850}/M_J greater than 1) are cool and proto-stellar. All of the confidently unstable clumps (M_{850}/M_J greater than 2) have temperatures lower than 20 K and the majority of these are isolated from OB stars. By contrast, the majority of clumps with temperatures greater than 20 K are associated with heated regions and are stable. However, many of these same clumps are also protostellar. Among the stable clumps, the two populations are fairly evenly balanced between pre- and proto-stellar.

The peak clump column density-temperature relationship (Figure 8.14 left) does not naturally follow the anti-correlation between those two properties. This can likely be explained as I am extracting a single, peak value for column density, as opposed to a mean value across the clump, as is followed for temperature. Unlike M_{850}/M_J, peak column density does not appear to be linked to heating by OB stars. Many of the more substantial clumps, like those presented in the Dust Arc of the Aquila W40 complex (Chapter 7) have been observed to have high average temperatures, but in reality their morphology includes heated edges and a cold central core where the column density is highest and a star is forming.

The Gould Belt-wide sample of proto-stellar clumps presented in Figures 8.14 (right) and 8.15 (left) provide evidence for peak column density thresholds of star formation. Pre-stellar clumps are most populous at low column densities and proto-stellar are most populous at high column densities. I mark a lower threshold for star formation of approximately $2{\times}10^{22}$ H_2 cm^{-2}. Whilst the regular, isolated proto-stellar clumps mostly lie above this, a number of heated proto-stellar clumps lie below it. I note that all of these members are also exceptionally stable, suggesting

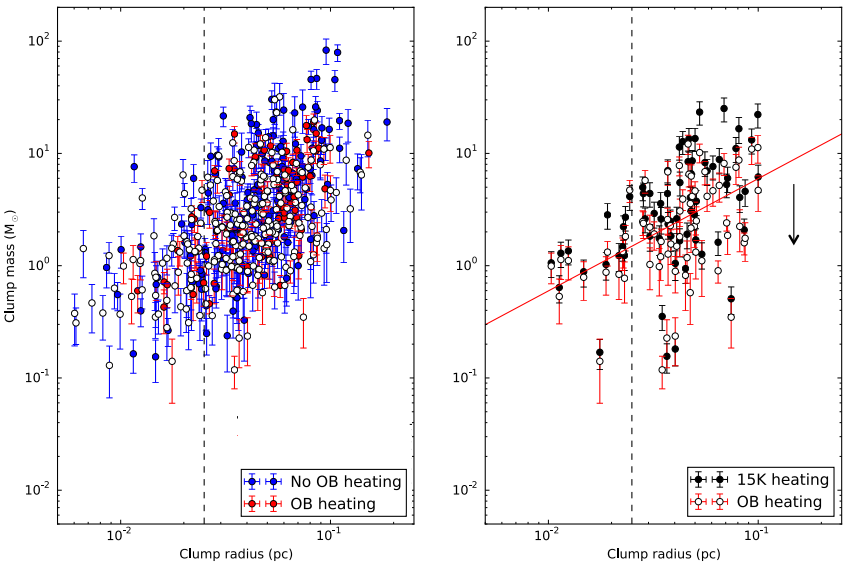

Figure 8.16: Clump mass-size relations for all clumps in the JGCC (left). Red markers indicate OB heated clumps, blue indicates non-OB heated clumps. Filled clumps are proto-stellar and hollow clumps are pre-stellar. Right) only the pre-stellar, OB star heated clumps with masses based on their unique, calculated temperature (hollow) and modelled with a temperature of 15 K (filled). The solid lines show a the mass-radius relationship for critical isothermal Bonnor-Ebert spheres with the mean clump temperature of 22 K. The regime above this line can be considered unstable. The typical core size of 0.05 pc is also marked.

that in the past they were sufficiently cool as to initiate star formation, but then subsequent irradiation by an OB star has raised the raised the temperature of the extended envelope and increased stability. Conversely, the majority of clumps above $2{\times}10^{23}$ H_2 cm^{-2} are protostellar. A minority are not but they are some of the most gravitationally unstable objects in the whole of the sample. These objects likely contain very low luminosity objects and are prime targets to investigate Class 0 objects that were not included in the Dunham et al. (2015) c2d+GBS catalogue.

As discussed in the previous section, YSO occupancy has no notable effect on clump temperatures. This is further demonstrated in a clump mass-size diagram, Figure 8.16 (left), where I compare proto- and pre-stellar clumps from OB and non-OB heated regions. As discussed in Figure 8.3 (right) the bulk of clumps are larger than a typical core size of 0.05 pc. Those proto-stellar clumps with lesser diameters may be candidate Class I/II disc objects that resemble a point source. Proto-stellar clumps without heating dominate masses greater than 20 $M_\odot$. However, at lower masses there is no obvious trend between heated and isolated regions.

I recalculate the masses of the pre-stellar, a.k.a starless, clumps in OB heated regions, using a constant temperature of 15 K that is consistent with an isolated clump, and find that higher temperatures are consistently reducing the mass (Figures 8.15 right and 8.16 right). Likewise I calculate the Jeans mass and Bonnor-Ebert (BE) mass (M_{BE}) of the starless clouds with a fixed temperature of 15 K using (Sadavoy et al., 2010),

$$M_J = 1.9\left(\frac{\bar{T}_d}{10\,K}\right)\left(\frac{R_c}{0.07\,pc}\right) M_\odot, \tag{8.2}$$

and (Pattle et al., submitted)

$$M_{\rm BE} \approx 2.4 \frac{k_B \bar{T}_{\rm d}}{\mu m_p G} R_{\rm BE}, \tag{8.3}$$

respectively. In both scenarios the clumps are considered isothermal where $\bar{T}_{\rm d}$ is the mean dust temperature across the clump, and $R_{\rm c}$ and $R_{\rm BE}$ are the cloud radius, taken as the FELLWALKER clump size (all other constants have their usual meaning). The conditions for BE stability ($M_{850}/M_{\rm BE}$) are the same as Jeans stability (as outlined above). I also note that a significant number of clumps throughout the JCMT GBS remain starless even though they have masses that exceed both the Jeans and BE critical mass.

The JGCC provides substantial evidence of how OB stars can raise the temperatures of clumps and both Equations 8.2 and 8.3 are a function of temperature. Figures 8.14 (right), 8.15 (right) and 8.16 (right) describe how, as a direct result of external heating by previous generations of OB stars, the Jeans and BE stability of clumps increase. I find that up to 10% starless clumps move from a regime of instability to a regime of stability, and star formation is less likely as a result.

Alternatively, Figure 8.16 (right) describes how heating of clumps would allow them reach greater masses before exceeding the BE critical mass and undergoing collapse to form stars. However, I find that clumps in excess of $20\,M_\odot$ only exist in regions without OB star heating (Figure 8.16 left). One possible explanation for this discrepancy might be that FELLWALKER has been ineffective at isolating single cores within filaments in a minority of regions, and that the most massive isolated clumps possibly contain multiple cores. Whether such a clump would or is undergoing fragmentation to form many, lower mass stars, or fragmentation is being suppressed favouring more massive star formation, requires a future study of the morphology and stellar populations of heated star forming regions in the JCMT GBS.

The trend of OB star heating increase clump stability is repeated in the proto-stellar clumps; however, by definition star formation has already occurred within these objects. One likely explanation would be that this star formation has occurred on a similar timescale as that of the OB stars, so that any heating took place primarily in the exterior layers of the envelope, and only after the initial collapse had started. Whether this heating influences the existing star formation by possibly suppressing fragmentation, for example, requires radiative transfer modelling and goes beyond the scope of this thesis.

8.7 Summary and conclusions

In this chapter I have automated the Kernel-convolution SCUBA-2 flux ratio method to the extent that it can produce dust temperature maps for all JCMT GBS regions. From this unprecedented collection of temperature maps of star forming regions I examine prominent regions of heating and assess the statistical evidence for its influence on star formation.

I produce a single consistent catalogue of clumps (identified using the clump finding algorithm FELLWALKER), incorporating real temperatures from 26 distinct sub-regions (of 10 star forming GMCs). YSOcs populations, taken from the Dunham et al. (2015) c2d+GBS catalogue, are

incorporated to determine whether clumps are pre- or proto-stellar. I also produce a secondary catalogue of OB stars that are located in some, but not all, of the regions, and calculate the plane of the sky clump-star distance. This catalogue is one of the largest of its type to date and it offers an unparalleled opportunity to examine star formation and heating on a statistical scale.

The conclusions of this chapter can be summarised as follows:

- 11 JCMT GBS sub-regions contain OB stars, the most massive being an O8 star in Orion B 2024. Note the Orion A region is not included in this sample or latter analysis as the heating is too extreme to be reliably interpreted by the SCUBA-2 flux ratio method. Regions with an OB star have higher temperatures than those without OB stars, supporting the findings for the Serpens MWC 297 region and the Aquila W40 complex, as discussed in Chapters 6 and 7.

- A total of 619 clumps feature in the JCMT GBS Clump Catalogue (JGCC) based on the SCUBA-2 850 μm band emission. 21% of these do not have sufficiently bright SCUBA-2 450 μm emission for a dust temperature to be calculated and are therefore are attributed a temperature of 15±2 K, the typical clump temperature calculated for isolated clumps in Chapters 6 and 7, those calculated from kinetic gas temperatures in Ophiuchus by Friesen et al. (2009), and assumed for Bonnor-Ebert models by Kirk et al. (2006). 46% of clumps are proto-stellar but only 8% are gravitationally unstable with $M_{850}/M_J \geq 2$.

- An anti-correlation is observed between clump temperature and plane of the sky distance to the nearest major OB star that is in line with the Tielens (2005) model of stellar dust heating via radiative transfer. I define a 'heating range', a distance from an OB star at which there is no longer evidence for heating above that of a typical isolated clump (15 K) using a weighted linear regression fit. This heating range is length-scale of significant heating that varies depending on stellar class. I determine the following ranges; 0.13±0.15 pc, 0.29±0.11 pc and 3.6±0.2 pc for late B, early B and O type stars, respectively. There is insufficient evidence to argue that low-to-intermediate YSOc clusters and embedded protostars provided significant levels of heating.

- I find that clumps heated by OB stars (within the upper bounds to the heating range of each respective Class group) are significantly warmer than those isolated from heating (21.3±3.8 K to 14.6±2.4 K, respectively). I find that external heating makes a significant impact on clump mass and both Bonnor-Ebert and Jeans stability. By comparing the stability of clumps with a fixed temperature of 15 K to those based on their calculated real temperatures, I demonstrate that radiative feedback from massive stars is preventing currently starless clouds from collapsing, and potentially suppressing fragmentation of existing Class 0/I objects. The net result of OB star heating can be to displace up to 10% of clumps out of a regime that favours star formation.

Table 8.4: OB stars associated with star formation in the JCMT GBS star forming regions (excluding Orion A). Stars highlighted with a $*$ are consider the 'major' OB star within the region.

Name	Region	RA (J2000)	Dec (J2000)	Class	Reference
LkHα101*	Auriga	04:30:14.0	+35:16:23.9	B0V	Cutri et al. (2003)
LDN1482A	Auriga	04:29:28.6	+35:13:18.8	B9	Cutri et al. (2003)
LDN1482F	Auriga	04:29:52.5	+35:22:23.9	B7	Cutri et al. (2003)
LDN1482B	Auriga	04:29:57.0	+35:10:59.1	B7	Cutri et al. (2003)
LDN1482E	Auriga	04:30:10.9	+35:19:23.1	B4/2	Cutri et al. (2003)
LDN1482H	Auriga	04:30:51.0	+35:26:44.9	B8	Cutri et al. (2003)
043014.90+352052.5	Auriga	04:30:14.9	+35:20:52.5	B9	Wolk et al. (2010)
OS1aS*	Aquila	18:31:19.8	-02:06:43.2	O9.5V	Smith et al. (1985)
OS2b	Aquila	18:31:22.6	-02:05:31.5	B4V	Smith et al. (1985)
OS3	Aquila	18:31:24.0	-02:04:10.7	B3V	Smith et al. (1985)
IRS 5	Aquila	18:31:14.8	-02:03:49.7	B1V	Shuping et al. (2012)
IRAS18265-0205	Aquila	18:29:11.9	-02:03:50.0	-	Beichman et al. (1988)
IRAS18352-0148	Aquila	18:37:50.5	-01:45:39.4	-	Beichman et al. (1988)
HD200775*	Cepheus	21:01:37.0	+68:09:47.9	B2Ve	Guetter (1968)
PVCep	Cepheus	20:45:53.9	+67:57:38.7	A5	Cutri et al. (2003)
RCrA*	CrA	19:01:54.0	-36:57:07.9	A5eII	Gray et al. (2006)
TYCrA	CrA	19:01:41.0	-36:52:33.9	B9e	Vieira et al. (2003)
V686CrA	CrA	18:56:40.0	-36:20:35.9	B8IV	Houk (1982)
HD176269	CrA	19:01:03.3	-37:03:39.3	B9v	Torres et al. (2006)
HD176270	CrA	19:01:04.3	-37:03:41.7	B9v	Torres et al. (2006)
HD 177076	CrA	19:04:44.4	-36:50:41.0	A0V	Torres et al. (2006)
HD 176386	CrA	19:01:38.9	-36:53:26.6	B9V	Torres et al. (2006)
BD+463474*	IC5146	21:53:29.0	+47:16:00.1	B0V	Høg et al. (2000)
BD+463471	IC5146	21:52:34.0	+47:13:44.1	A0.5III	Gray & Corbally (1998)
HD147889*	Ophiuchus	16:25:24.3	-24:27:56.0	B2III	Houk & Smith-Moore (1988)
S1*	Ophiuchus	16:26:34.0	-24:23:27.9	B4Ve	Cieza et al. (2007)
BCB89-IRS-2b*	Orion B 2023	05:41:45.5	-01:54:28.7	O8	Cutri et al. (2003)
BCB89-IRS-2	Orion B 2023	05:41:45.8	-01:54:29.8	Be	Choi 2015
NGC-2024-1	Orion B 2023	05:41:37.8	-01:54:36.5	B0.5V	Cutri et al. (2003)
*Zet-Ori-A	Orion B 2023	05:40:45.5	-01:56:33.3	09.7I	Skiff (2014)
*Zet-Ori-B	Orion B 2023	05:40:45.5	-01:56:33.3	B0III	Skiff (2014)
HD 38563 *	Orion B 2068	05:46:44.7	+00:05:22.8	B2II + B2III	Strom et al. (1974)
HD 290862	Orion B 2068	05:46:43.4	+00:04:36.1	B3/5	Strom et al. (1974)
SSC75 M 78 11	Orion B 2068	05:46:45.3	+00:02:40.2	A0II	Strom et al. (1974)
HD 290860	Orion B 2068	05:46:57.4	+00:20:10.2	A5	Nesterov et al. (1995)
SVS3*	Perseus	03:29:10.4	+31:21:59.0	B5	Straižys et al. (2002)
BD+30549	Perseus	03:29:12.0	+31:24:56.9	B8	van Leeuwen (2007)
HD23478	Perseus	03:46:40.9	+32:17:25.0	B3IV	Herbst (2008)
HD281159*	Perseus	03:44:34.0	+32:09:46.1	B5V	Herbst (2008)
IC34812	Perseus	03:44:35.3	+32:10:04.9	A2	de Zeeuw et al. (1999a)
HD278942	Perseus	03:39:55.7	+31:55:33.2	O9.5V	Andersson et al. (2000)
MWC297*	Serpens	18:27:39.5	-03:49:52.2	B1.5Ve	Drew et al. (1997)
VVSer	Serpens	18:28:47.9	+00:08:39.8	A5	Tisserand et al. (2013)
V892Tau*	Taurus	04:18:41.0	+28:19:14.9	A0Ve	Skiff (2014)

Table 8.5: A sample of the JCMT GBS Clump Catalogue (JGCC). The full table can be found in Appendix Table A.1.

JGCC ID	Object name (J2000)	S_{850} (Jy)	Mass ($M_\odot$)	Temp. (K)	N_{H_2} ($\times^{21}$ cm^{-2})	D (pc)	Proto stars	n_{YSO} (pc^{-2})	M_J ($M_\odot$)	M_{850}/M_J	d_{OB} (pc)
Auriga LKHa101-SMM1	JGCC J043014.59+351623.9	2.3	9.3±2.9	14.8±2.4	401±123	0.09	1	25	6.3±1.0	1.5±0.5	0.02
Auriga Main-SMM1	JGCC J041008.39+400224.5	1.3	2.2±0.7	20.8±3.6	47±15	0.06	0	0	6.7±1.1	0.3±0.1	-
Auriga CN-SMM1	JGCC J041041.40+380753.3	2.1	5.2±1.3	16.2±1.8	139±34	0.05	0	8	5.5±0.6	1.0±0.3	-
Cepheus L1228-SMM1	JGCC J205713.11+773543.8	3.7	3.3±0.8	11.1±0.9	183±43	0.12	3	6	2.5±0.2	1.3±0.3	-
Cepheus L1251-SMM1	JGCC J223848.61+751131.2	6.6	7.2±1.8	16.1±1.7	96±24	0.16	4	20	6.4±0.7	1.1±0.3	-
Cepheus South-SMM1	JGCC J203905.72+680217.8	2.9	4.0±1.3	13.3±1.8	192±64	0.08	0	0	3.5±0.5	1.2±0.4	10.57
CrA-SMM1	JGCC J190156.27-365729.5	17.1	2.7±0.4	19.2±1.2	228±35	0.14	3	10	3.1±0.2	0.9±0.1	0.02
IC5146-SMM1	JGCC J214722.84+473212.0	9.7	83.1±21.3	18.5±2.4	48±12	0.19	3	50	30.7±4.0	2.7±0.8	17.7
Lupus-SMM1	JGCC J154302.22-340909.2	3.9	0.8±0.2	17.0±1.8	108±26	0.1	1	1	2.6±0.3	0.3±0.1	-
OphSco L1688-SMM1	JGCC J162627.70-242400.2	78.5	10.1±2.6	23.7±3.5	338±88	0.3	2	12	9.2±1.4	1.1±0.3	0.06
OphSco L1689-SMM1	JGCC J163222.97-242836.5	46.5	8.6±2.8	19.3±2.3	1834±591	0.18	1	1	5.8±0.7	1.5±0.5	-
OrionB N2023-SMM1	JGCC J054143.11-015424.3	11.2	7.3±1.0	41.9±3.2	215±31	0.07	9	225	13.4±1.0	0.5±0.1	0.07
OrionB N2068-SMM1	JGCC J054705.00+002145.1	46.1	79.3±13.4	19.0±1.1	792±134	0.22	6	66	17.8±1.0	4.5±0.8	2.07
Perseus IC348-SMM1	JGCC J034356.95+320050.9	7	7.2±1.5	13.4±1.0	238±49	0.12	2	25	4.2±0.3	1.7±0.4	0.86
Perseus NGC1333-SMM1	JGCC J032910.65+311333.9	17.7	20.0±4.6	12.3±0.9	2162±500	0.11	2	28	3.8±0.3	5.2±1.3	0.58
Perseus West-SMM1	JGCC J032536.43+304516.3	11.8	9.1±2.1	14.9±1.3	673±158	0.12	2	7	4.7±0.4	1.9±0.5	-
Serpens Main-SMM1	JGCC J182949.90+011518.9	24	46.5±9.3	18.1±1.3	918±183	0.17	3	53	13.9±1.0	3.3±0.7	-
Serpens N-SMM1	JGCC J183859.10+003305.6	2.1	2.3±0.5	12.7±1.0	100±21	0.08	1	7	2.5±0.2	0.9±0.2	-
Serpens NH3-SMM1	JGCC J182906.50+003040.0	13.2	26.0±6.2	17.2±1.7	135±32	0.17	3	36	12.8±1.3	2.0±0.5	-
Serpens MWC297-SMM1	JGCC J182808.99-034810.3	10.5	19.8±3.6	9.9±0.5	530±97	0.17	0	28	2.3±0.1	8.8±1.7	0.55
Serp South-SMM1	JGCC J183004.14-020305.1	23.2	17.4±2.7	16.4±0.8	627±97	0.16	8	100	6.5±0.3	2.7±0.4	-
Taurus L1495-SMM1	JGCC J041958.66+270959.2	1.8	0.9±0.2	11.4±1.1	85±21	0.08	1	3	1.4±0.1	0.6±0.2	3.11
Taurus south-SMM1	JGCC J042923.89+243257.9	0.6	0.3±0.1	11.6±1.4	61±17	0.03	1	2	0.9±0.1	0.3±0.1	-
Taurus tmc-SMM1	JGCC J043953.97+260309.2	5.4	1.6±0.4	15.2±1.6	155±35	0.13	2	9	2.8±0.3	0.6±0.1	-
W40-SMM1	JGCC J183120.99-020620.3	10.9	13.2±3.1	31.4±4.6	75±18	0.15	1	133	22.2±3.2	0.6±0.2	0.07

S_{850} - SCUBA-2 850 μm integrated flux across the clump, n_{H_2} - column density, D - flux weighted clump diameter, n_{YSO} - surface density of YSOs per pc^2, M_J - Jeans mass, M_{850}/M_J - Jeans stability, d_{OB} - distance, across the plane of the sky, between the clump and the nearest major OB star.

9 Conclusions

9.1 Further work

Throughout this thesis I have developed methods for decontaminating and reducing SCUBA-2 data and embarked on a local and a global analysis of heating and star formation throughout the James Clerk Maxwell Telescope (JCMT) Gould Belt survey (GBS)[1] of star forming regions. Along that path a number of interesting science questions have been raised that I have addressed in the relevant Chapters. Regrettably, and inevitably, I have not had the time or resources to investigate each line of enquiry to its fullest extent. In this final section I seek to summarise some of the unfinished work from this thesis and discuss various future directions.

9.1.1 Further methods and data

I have been using Submillimetre Common-User Bolometer Array 2 (SCUBA-2, Holland et al. 2013) data produced by the JCMT GBS. In parallel, the SCUBA-2 data reduction (DR) team have been developing and improving the DR pipeline (including feedback from my own research). I have outlined how internal release (IR) 1 data products were used in the analysis of the Serpens MWC 297 region (Chapter 6) and IR2 data products were used in analysis of the Aquila W40 complex (Chapter 7) and the JCMT GBS Clump Catalogue (Chapter 8). In late 2015/early 2016 IR3 data products have become available. These data represent a significant step forward in reduction techniques, with solutions to the excessive large-scale structure in the data array and data reduction artefacts contributing to the variance array incorporated by the DR team into the process. Reproducing all of the results and analysis here with the IR3 data, when it becomes available, would be preferable, and practical given the automation incorporated into the temperature map and clump

[1] Presented in full in Chapter 2

finding methods used in Chapter 8.

In Chapter 3 I focused on analysis of ^{12}CO 3-2 line data. This line traces lower density gas and is effective at tracing outflows. Further analysis of my ^{12}CO 3-2 line data could involve calculating the momentum, momentum flux and kinetic energy following the methods Duarte-Cabral et al. (2013), allowing further analysis of the contribution of the outflows to turbulence in the Aquila W40 complex. In addition to the integrated intensity map of ^{12}CO 3-2 line data presented in Figure 3.6, I could also explore production of first and second moment maps of velocity and velocity dispersion to better highlight the kinetic motion of the gas.

^{12}CO 3-2 is a poor tracer of higher density material and is ineffective at tracing cloud structure, as is observed in the extinction at 7 km s^{-1} in the Aquila W40 region in FIgure 3.12. Shimoikura et al. (2015) make use of the HCO^+ 4-3 line to observe gas populations at higher densities to compensate for this extinction. These lower abundance lines provide more information about the velocity structure of the denser parts of the cloud, allowing for a virial analysis of core stability to be completed. Given my successful proposal to observe the ^{12}CO 3-2 line in the Aquila W40 complex, the science case for continued observation of this region, in lower abundance lines such as C^{18}O 1-0, is strong. Extending this coverage to include W40-S and Serpens South could also further advise on whether these regions are physically associated with the OB association or not by comparing the systemic velocity of the various clouds.

Likewise, further radio observations of compact free-free sources in the Aquila W40 complex can better constrain the free-free spectral index. However, the variability observed by Rodríguez et al. (2010) and Ortiz-León et al. (2015) raise concerns over the reliability of $\alpha_{\rm ff}$ calculated over a small number of observations. Whilst raw data in the Very Large Array (VLA) archive is available for reduction, with the aim to expand the set of observations of OS2a, it is unlikely that $\alpha_{\rm ff}$ for this object will be determined as robustly as MWC 297, where Alonso-Albi et al. (2009) collate 37 separate photometric measurements in order to measure $\alpha_{\rm ff}$.

I have developed and compared two forms of the decontaminated SCUBA-2 450 μm/850 μm flux ratio method, from which dust temperatures can be calculated. There are a small number of unresolved problems with these methods that require further work to solve, the most significant of which is the use of a kernel based on the two-component beam of Dempsey et al. (2013) rather than a kernel built from updated JCMT beam maps. The deficiencies between the model and real JCMT beam are a likely candidate for the ringing artefact seen around bright sources that is discussed in Chapter 5, Section 5. Correcting this depends on the development of reliable beam maps from observations, or advanced beam models. However, an alternative explanation might be that the artefact is the result of a pointing discrepancy across the 12 scans in each flux ratio mosaic. Examining prominent examples of ringing, for example Ophiuchus L1689 (Figure 8.1), with individual scans could help clarify the cause of the artefact.

I have also compared the SCUBA-2 ratio method to alternative flux ratios in Chapter 5. Whilst longer wavelengths may offer greater coverage, the location of the Rayleigh-Jeans tail reduces the upper limit on temperatures that can be reliably observed. For the 450 μm/850 μm flux ratio this value is approximately 50 K. I find that by adopting a 450 μm/1.2 mm ratio it is possible to reliably calculate dust temperatures up to 100 K and with an improved resolution of

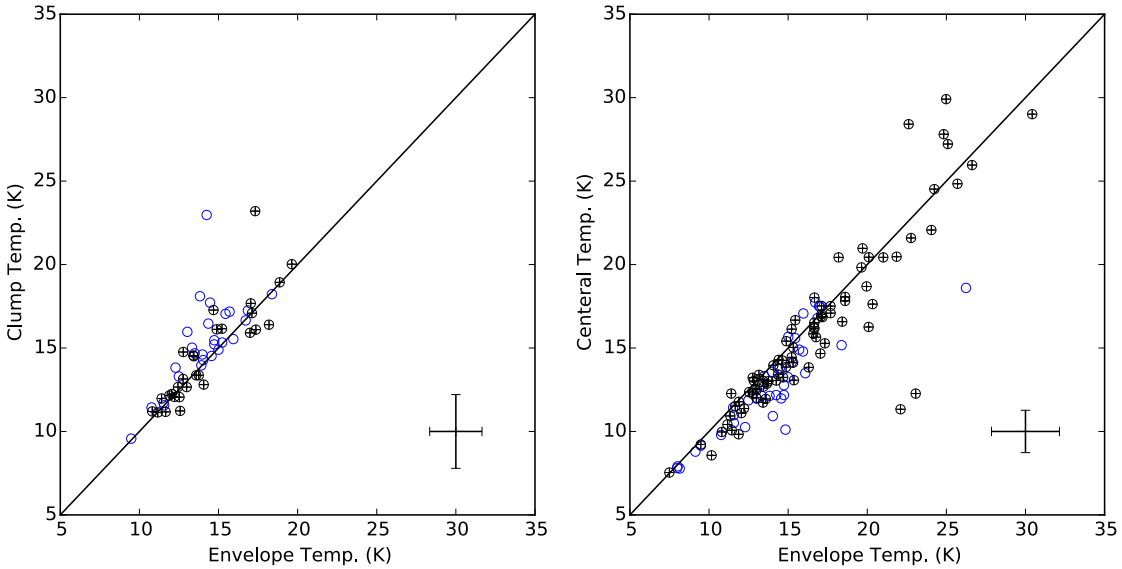

Figure 9.1: The gaussian weighted temperature of Class 0/I protostars from the Dunham et al. (2015) c2d+GBS catalogue compared to their corresponding clump temperatures (left) and central temperatures (right). In both plots the mean error is presented separately. Blue markers represent Class 0 objects and black (with crosses) represent Class I objects (as classified by bolometric temperature, Chapter 1).

13″, at the expense of coverage.

The ratio method itself is limited in its assumption of constant β. As discussed, work by Chun-Yuan Chen et al. (2016) outline how full SED fitting can be used to constrain both dust temperature and opacity. However, even including the SCUBA-2 850 μm data alongside *Herschel* PACS observations does not completely remove this degeneracy. Future work could combine both SCUBA-2 bands, and longer wavelengths, with *Herschel* observations to better constrain these results. I note this is a non-trivial task and could likely be the subject of a whole thesis in its own right.

9.1.2 Further analysis

The bulk of the analysis of star formation in this thesis revolves around SCUBA-2 850 μm clumps extracted by the clump finding algorithm FELLWALKER. FELLWALKER is parameterised to extract extended clumps. These objects are irregular in shape and size and manifest themselves often as filament segments that encompass a core and any extended structure with a signal to noise ratio (SNR) greater than five. Other local property studies of clumps in star forming regions have used alternative algorithms such as CUTEX (Pattle et al., 2015), *getsources* (Maury et al. 2011 and Könyves et al. 2015) and GAUSSCLUMPS (Zhang et al., 2015) that have often been parameterised to extract centrally condensed cores. My temperature maps show that it is common for regions of greatest heating to be found in the extended, low column density parts of filaments that are often omitted by these methods. Having identified a set of clumps with significant heating, one future path might be to re-run the clump finding process with an algorithm optimised for extracting a set

of cores as opposed to clumps. This sample could then be directly compared to any existing core catalogues, for example Maury et al. (2011) and Könyves et al. (2015).

An alternative to using a clump finding algorithm is to extract the temperatures of a core based on the known locations of Class 0/I protostars, taken from the Dunham et al. (2015) c2d+GBS catalogue. I run a pilot study, calculating temperatures by defining a normalised Gaussian with a FWHM equivalent to the typical core size of 0.05 pc (Rygl et al., 2013), and calculating the weighted temperature, T', using,

$$T' = \frac{\sum_i^N G_i T_i}{\sum_i^N G_i}, \tag{9.1}$$

where i is the pixel index, T_i is the pixel temperature and G_i is the value of the Gaussian at the pixel offset from centre. In this way I extract a provisional catalogue of weighted mean temperatures associated with the embedded protostars, and avoid distorting the mean value where the clump size considerably exceeds that of the core. An example of the provisional results of the Dunham et al. (2015) c2d+GBS protostar temperature (DPT) catalogue are presented in Appendix Tables A.2. I conduct a crude match between the DPT catalogue and JCMT GBS Clump Catalogue (JGCC, see Chapter 8) within a 15″ aperture, and compare temperatures in Figure 9.1 (left). A number of protostars have temperatures that are systematically lower than their corresponding clump temperatures, though the majority of clumps and protostars show a 1:1 correlation within the uncertainties. Note that only protostars associated with 'isolated' clumps are included in this analysis.

Furthermore, using this method I can extract the temperature at the location each protostar directly from the corresponding temperature map to further investigate the evidence for internal protostellar heating. I compare the Gaussian weighted protostellar temperature to the central temperature in Figure 9.1 (right). Here there is a systematic trend of central temperatures that are cooler than their protostellar envelope, inconsistent with the models of Shirley et al. (2002b) and Young et al. (2003), and the hot spots observed by Hatchell et al. (2013) and Chun-Yuan Chen et al. (2016), but consistent with the conclusions of Chapter 8. However, the majority of temperatures show a 1:1 correlation within the uncertainties, limiting further analysis. I also note that whilst Class I objects have a large temperature range, Class 0 temperatures are limited to less than 18 K, perhaps inferring that some heating from the more evolved Class I objects is influencing the dust temperatures.

Much of the analysis of protostellar temperature presented here is in its earliest stage. Further work is required to improve the robustness of the method and to investigate protostellar mass, Jeans mass and column density. I have defined a protostellar core as 0.05 pc but it would also be of interest to investigate how temperature varies as a function of radius and compare the results to the models published by Shirley et al. (2002b) and Young et al. (2003), and presented in Figure 8.12.

In Chapter 8 I find strong evidence for a negative correlation between clump temperature and the plane of the sky distance to the major OB star in the region. In Figure 8.8 I present the stellar dust heating model (Equation 1.16) overlaid on the observed clump temperatures. The natural progression of this work is to proceed to a more robust model. In Figure 9.2 I present

the O star heated clumps in log-log space and compare the weighted linear regression fit to the Tielens (2005) model fit, using a number of parameters. These results suggest that the largest dust grains sizes provide the best fits (given the well constrained stellar classification of O9). However, the presence of UV radiation that forms the H II region around O stars is believed to prevent grain growth, making these model results unlikely. Furthermore, the power law gradient of the model is fundamentally dissimilar from the observed set of clumps and the linear fit. As this is a fixed parameter, it is apparent that the Tielens (2005) models are overly simplistic and do not adequately explain the observed physics. One possible explanation could require the inclusion of an additional background Habing field from the ISRF into Equation 1.15. Furthermore, Equations 1.13 and 1.14 demonstrate how Tielens (2005) model the dust as either graphite or silicate and can achieve a reduced gradient of 0.06.

A final note on further work must go to the JGCC. As discussed, this catalogue represents an assessment of clump populations in the Gould Belt, allowing for a truly global statistical investigation into the relative morphologies and structures of nearby star forming regions. Furthermore, by incorporating real temperatures into the catalogue, I demonstrate the diverse range of clump heating that is observed throughout the JCMT GBS regions, and allow for a more realistic assessment of clump masses, column densities and Jeans stability. However, the survey is not entirely complete with the Orion A region unaccounted for. Salji et al. (2015) produce temperature maps of the Orion A filament but caps the temperatures of a large proportion of the pixels at 50 K as their values exceed the Rayleigh-Jeans limit ($h\nu/k_BT \ll 1$) as a result of proposed heating by a population of young OB stars forming in the massive filament. This approach is not suitable for the analysis of heating that I carry out. It may be necessary to conduct a flux ratio calculation with shorter wavelengths, or move to full SED fitting to fully understand the heating in this region.

9.2 Summary of methods

This thesis is primarily focused on pursuing the aims and goals of the JCMT GBS; to observe dense star-forming regions in the Gould Belt and discern the connection between the protostars and the molecular cloud from which they form (Ward-Thompson et al., 2007). I make use of the SCUBA-2 instrument to observe the thermal dust continuum at the 450 and 850 μm bands where cold starless clouds and earliest phases of star formation are brightest. SCUBA-2 observations and data reduction were completed by various members of the JCMT GBS and SCUBA-2 data reduction teams. My work focuses on refinement of data reduction techniques with the following methods; pre-production data selection, data array noise calculation and post-production large-scale structure filtering.

I complement SCUBA-2 observations with ^{12}CO 3-2 line emission observed with the Heterodyne Array Receiver Programme for B-band (HARP, Buckle et al. 2009) instrument. Chapter 3 outlines how I was the PI of a HARP proposal to observe ^{12}CO 3–2 line emission for the purposes of decontamination of the SCUBA-2 850 μm band in the Aquila W40 complex. Following the methods of Drabek et al. (2012), I find contamination between 3 and 10% in the majority of the filaments. In a minority of areas contamination reaches up to 20%. Using the spectra published by

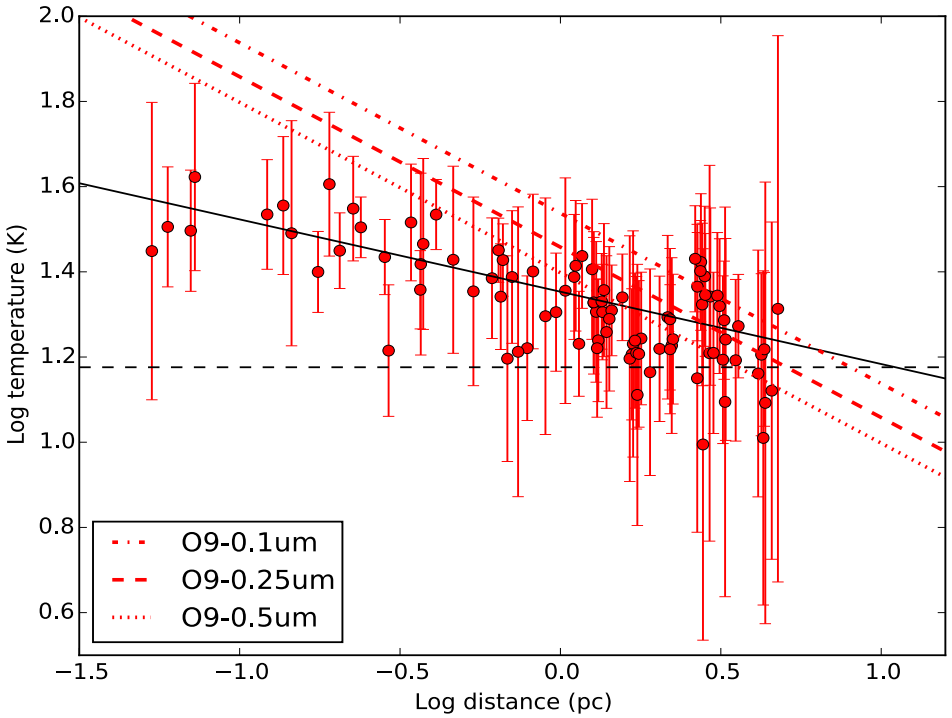

Figure 9.2: Clump temperature plotted against plane of the sky distance from the major O stars. The solid line shows the uncertainty weighted linear regression fit. The dashed, dotted and dot-dashed lines show the Tielens (2005) models (Equation 1.16) for the specified grain size.

Canto et al. (1984), I also estimate ^{12}CO 3–2 contamination of 13 % of peak flux at the location of MWC 297 (in the Serpens MWC 297 region).

I also use ^{12}CO 3-2 line emission to observe where embedded Class 0/I protostars are producing molecular outflows. I observe six confirmed and six candidate outflows across the Aquila W40 complex confirming the presence of active star formation. I note that extinction around 7 km s^{-1} limits full analysis of this region. The most prominent outflow observed is the 0.8 M$_\odot$ Class 0 protostar MM5 in the western Dust Arc, as identified by Maury et al. (2011), with a maximum line-wing offset of 7.5 km s^{-1}. Line wing offsets have been observed in excess of 30 km s^{-1} in the Serpens Main region, inferring that outflow activity is relatively weak in the Aquila W40 complex.

Sandell et al. (2011) highlight a number of higher mass Herbig stars where free-free emission is observed directly as a contaminating point source in SCUBA data. I assess the physical characteristics of individual radio sources in the Serpens MWC 297 region and the Aquila W40 complex, given published VLA radio observations (either point-like or extended). I develop a method where by the free-free emission is extrapolated up to and subtracted from SCUBA-2 bands, for a given value of $\alpha_{\rm ff}$.

The B1.5Ve star MWC 297 was found to contribute approximately 73±5% and 82±4% of the 450 and 850 μm integrated flux respectively. Residual dust at 850 μm represents a 3σ detection and therefore any disc around the star lies below the mass sensitivity of SCUBA-2. The Herbig AeBe star OS2a (in the Aquila W40 complex) was found to contribute approximately 9%

and 12% of the 450 and 850 μm integrated flux respectively. This is based on a optimistic assumption of $\alpha_{\rm ff}$ = 1.0, consistent with a jet UCH II region, and optically thick emission at SCUBA-2 wavelengths. Unlike in MWC297, free-free decontamination has a very limited impact on the flux and temperature of OS2a, leaving a point-like core with a minimum temperature of 9 K and peak column density of $1.4{\times}10^3$ H_2 cm^{-3}. It is difficult to reconcile the presence of a hot UCH II region from an evolved Herbig AeBe star, with an embedded, extremely cold and massive envelope, which is typically associated with less evolved protostars. Further work is required to fully characterise this object.

The extended free-free emission produced by the H II region in the Aquila W40 complex (powered by the 09.5 star OS1aS) was also examined and found to contribute to approximately 0.5% and 5% of the 450 and 850 μm peak flux respectively, given a typically flat spectrum ($\alpha_{\rm ff}$ = -0.1).

The SCUBA-2 flux ratio method is limited by use of a constant dust opacity spectral index (β = 1.8) and the coverage of the 450 μm data and is only applicable for temperatures less than 50 K as a result of the Rayleigh-Jeans limit. Despite this, the flux ratio method remains a highly effective method for studying the heating of pre- and proto-stellar clumps in a range of star forming environments, from quiescent regions to those with OB stars, stellar clusters and H II regions.

I develop two separate versions of the flux ratio method (Reid & Wilson, 2005) that, amongst other things, implement a two component JCMT beam model that is based on the observations of Dempsey et al. (2013). These methods are as follows:

- **The two-component beam method**, as used in Chapter 6. I employ a two-component beam (2CB) cross-convolution that uses both JCMT main beam and secondary beam models of Dempsey et al. (2013) to achieve a common resolution of 19.9″.

- **The Kernel-convolution method**, as used in Chapters 7 and 8. I employ a Model-Kernel, developed by Pattle (priv. comm.), that is based on the 2CB model of Dempsey et al. (2013), and implemented using the method of Aniano et al. (2011). The Kernel-convolution method convolves only the 450 μm map and can achieve an improved resolution of 14.9″.

Both the 2CB and Kernel-convolution methods produce consistent flux ratios with a Pearson-correlation coefficent of 96%. The Kernel-convolution method can achieve the highest resolution, at a cost of propagating uncertainties that are twice as large as the 2CB method.

I produce maps of temperature and column density for 26 subregions of 10 star forming clouds within the JCMT GBS. I publish local property studies of the Serpens MWC 297 region (Chapter 6, Rumble et al. 2015) and the Aquila W40 complex (Chapter 7, Rumble et al. 2016), carrying out ^{12}CO 3-2 and free-free decontamination where available. The remaining regions form part of a global statistical analysis of the JCMT GBS (Chapter 8, Rumble et al. in prep.). In each analysis I use the FELLWALKER clump finding algorithm to produce a catalogue of clumps based on the SCUBA-2 850 μm data. FELLWALKER is parameterised to extract extended clumps associated with single dense cores. A mean temperature and peak column density was subsequently calculated for each clump, along with a number of other properties including mass, Jeans mass, size,

etc. Clump catalogues are also compared to archival populations of YSOcs to determine where star formation is occurring.

9.3 Conclusions

I have discussed how methods for ^{12}CO 3-2 line and free-free continuum decontamination have been developed for SCUBA-2 data. Removing the ^{12}CO 3–2 contamination from the Aquila W40 complex significantly increases the dust temperatures calculated per pixel, on average, by 3.3 K where contamination is less that 10%, and by 16.4 K where contamination is greater than 10%. Removal of free-free contamination from the SCUBA-2 observations of MWC 297 saw the complete removal of a cold (less than 10 K) spot associated with the B1.5Ve star. However, a similar assessment of the Herbig AeBe star OS2a had a very limited effect on the dust temperature. Whilst I find that MWC 297 and OS2a have similar free-free luminosities The total 850 μm luminosity of OS2a is over 150 times as bright as MWC 297, indicating that the former has a far greater proportion of mass in its envelope/disc, indicative of its young evolutionary status.

In Chapter 6 I present published results on a local property study of heating and star formation in the Serpens MWC 297 region. 22 clumps are detected with FELLWALKER. I construct SEDs of the YSOcs and identify one Class 0/I, two Class I and three Class II sources using $T_{\rm bol}$ and $L_{\rm smm}/L_{\rm bol}$. In addition, I identify two Class 0 and one Class I objects that are not included in SGBS. I find evidence that the B1.5Ve star MWC 297 is raising temperatures of a neighbouring clump to 46±2 K to the extent that it is now gravitationally stable ($M_{850}/M_J \leq 1$). The clump appears centrally condensed inferring that collapse had previously begun prior to exposure by MWC 297, and that radiative feedback from the star may now be suppressing further collapse, to the extent that it is currently starless. Across the region I find that pre-stellar clumps are consistently warmer than proto-stellar clumps with mean temperatures of 32±4 K compared to 15±2 K. I note that pre-stellar clumps heated by MWC 297 are included in this calculation and therefore these does not necessarily reflect the typical clump temperature.

In Chapter 7 I conduct a further local property study of the Aquila W40 complex that detects 82 clumps with FELLWALKER and 21 of these have at least one protostar embedded within them, inferring that the region is actively forming stars. I find maximum clump temperatures of 36 K and clump temperature is negatively correlated with the proximity to the primary ionising source in the region, OS1aS, up until a plane of the sky distance of 1.2 pc, inferring that external radiative heating from the O9.5 star is heating the clumps. 'Isolated' clumps at greater distances have a mean temperature of 15±2 K, consistent with the proto-stellar clumps in Serpens MWC 297. As in Serpens MWC 297, heating of clumps is observed to be raising the Jeans mass and decreasing M/M_J, making clumps within the nebulosity less likely to collapse and form stars than those outside of it.

My results provide evidence for a temperature gradient along the length of the Dust Arc, suggesting that the eastern Dust Arc is located towards the interior of the H II region and the western end towards the exterior. A number of Class 0/I protostars are found embedded along the length of the filament in addition to evidence of related outflows in ^{12}CO 3-2 line emission,

inferring that star formation is ongoing. However, heating by OS1aS is raising the stability of clumps here and making further star formation/or fragmentation less likely.

I automate much of the previously discussed methodology and produce a consistent set of temperature maps and clumps for the 26 subregions in the JCMT GBS with the aim of conducting a global statistical analysis of clump heating and its impact on star formation. I find evidence that massive OB stars heat clumps, and this heating is consistent with models of radiative heating of dust (Tielens, 2005). I define a heating range as the distance from an OB star at which the clump temperature drops to 15 K. I find that OB star heating is anti-correlated with distance, with O stars providing the most prominent heating with a range of 3.6±0.2 pc. Heated clumps have a mean temperature of 21±4 K with a maximum clump temperature of 42 K observed. By modelling these clumps with a constant temperature of 15 K I provide evidence that heating from OB stars is having a significant impact on clump mass and both Bonnor-Ebert and Jeans stability, pushing 10% of clumps below the stability threshold of $M_{850}/M_J = 1$, and into a regime that is less favourable for star formation.

By contrast, 'isolated' clumps that lie outside of the sphere of influence of OB stars consistently have temperatures of 15±2 K. This value has been replicated in each of the three analyses I have conducted and is consistent with cores in the Perseus region modelled as Bonnor-Ebert spheres by Kirk et al. (2006) and the kinetic gas temperatures in Ophiuchus by Friesen et al. (2009). I find that the 'isolated' clump temperature is largely invariant with occupancy of a low-to-medium mass (less than 10 $M_\odot$) Class 0/I protostar. This finding is in contrast to the hot spots observed by Hatchell et al. (2013) and Chun-Yuan Chen et al. (2016) in NGC 1333, and radiative transfer models of Class 0/I protostars of Shirley et al. (2002b) and Young et al. (2003). A possible explanation for this discrepancy is likely the use of a constant dust opacity spectral index.

Bibliography

2016

Adams F. C., Lada C. J., Shu F. H., 1987, ApJ, 312, 788

Agladze N. I., Sievers A. J., Jones S. A., Burlitch J. M., Beckwith S. V. W., 1996, ApJ, 462, 1026

Allen L. E., Calvet N., D'Alessio P., Merin B., Hartmann L., Megeath S. T., Gutermuth R. A., Muzerolle J., Pipher J. L., Myers P. C., Fazio G. G., 2004, ApJS, 154, 363

Alonso-Albi T., Fuente A., Bachiller R., Neri R., Planesas P., Testi L., Berné O., Joblin C., 2009, A&A, 497, 117

Altenhoff W. J., Downes D., Goad L., Maxwell A., Rinehart R., 1970, A&AS, 1, 319

Alves F. O., Franco G. A. P., 2007, A&A, 470, 597

AMI Consortium 2012, MNRAS, 423, 1089

Andersson B.-G., Wannier P. G., Moriarty-Schieven G. H., Bakker E. J., 2000, AJ, 119, 1325

André P., Di Francesco J., Ward-Thompson D., Inutsuka S.-I., Pudritz R. E., Pineda J. E., 2014, Protostars and Planets VI, pp 27–51

André P., Men'shchikov A., Bontemps S., Könyves V., Motte F., Schneider N., Didelon P., Minier V., Saraceno P., Ward-Thompson D., 2010, A&A, 518, L102

André P., Motte F., 2000, in Favata F., Kaas A., Wilson A., eds, Star Formation from the Small to the Large Scale Vol. 445 of ESA Special Publication, FIRST and the Earliest Stages of Star Formation. p. 219

André P., Ward-Thompson D., Barsony M., 1993, ApJ, 406, 122

Andre P., Ward-Thompson D., Barsony M., 2000, Protostars and Planets IV, p. 59

Aniano G., Draine B. T., Gordon K. D., Sandstrom K., 2011, PASP, 123, 1218

Arce H. G., Goodman A. A., 1999, ApJ, 517, 264

Arce H. G., Shepherd D., Gueth F., Lee C.-F., Bachiller R., Rosen A., Beuther H., 2007, Protostars and Planets V, pp 245–260

Arzoumanian D., André P., Didelon P., Könyves V., Schneider N., Men'shchikov A., 2011, A&A, 529, L6

Bally J., 2001, in Woodward C. E., Bicay M. D., Shull J. M., eds, Tetons 4: Galactic Structure, Stars and the Interstellar Medium Vol. 231 of Astronomical Society of the Pacific Conference Series, The Formation, Evolution, and Destruction of Molecular Clouds. p. 204

Bally J., 2008, Overview of the Orion Complex. Astronomical society of the pacific, p. 459

Bally J., Reipurth B., Davis C. J., 2007, Protostars and Planets V, pp 215–230

Bally J., Walawender J., Johnstone D., Kirk H., Goodman A., 2008, The Perseus Cloud. Astronomical society of the pacific, p. 308

Bastien P., Jenness T., Molnar J., 2005, in Adamson A., Aspin C., Davis C., Fujiyoshi T., eds, Astronomical Polarimetry: Current Status and Future Directions Vol. 343 of Astronomical Society of the Pacific Conference Series, A Polarimeter for SCUBA-2. p. 69

Bate M. R., 2009, MNRAS, 392, 1363

Bate M. R., 2012, MNRAS, 419, 3115

Bate M. R., Bonnell I. A., 2005, MNRAS, 356, 1201

Bate M. R., Tricco T. S., Price D. J., 2014, MNRAS, 437, 77

Beckwith S. V. W., Sargent A. I., 1991, ApJ, 381, 250

Beckwith S. V. W., Sargent A. I., Chini R. S., Guesten R., 1990, AJ, 99, 924

Beichman C. A., Neugebauer G., Habing H. J., Clegg P. E., Chester T. J., eds, 1988, Infrared astronomical satellite (IRAS) catalogs and atlases. Volume 1: Explanatory supplement Vol. 1

Belloche A., Parise B., Schuller F., André P., Bontemps S., Menten K. M., 2011, A&A, 535, A2

Belloche A., Parise B., van der Tak F. F. S., Schilke P., Leurini S., Güsten R., Nyman L.-Å., 2006, A&A, 454, L51

Benson P. J., Myers P. C., 1989, ApJS, 71, 89

Bergner Y. K., Kozlov V. P., Krivtsov A. A., Miroshnichenko A. S., Yudin R. V., Yutanov N. Y., Dzhakusheva K. G., Kuratov K. S., Mukanov B. D., 1988, Astrofizika, 28, 529

Berrilli F., Corciulo G., Ingrosso G., Lorenzetti D., Nisini B., Strafella F., 1992, ApJ, 398, 254

Berry D. S., 2015, Astronomy and Computing, 10, 22

Berry D. S., Reinhold K., Jenness T., Economou F., 2007, in Shaw R. A., Hill F., Bell D. J., eds, Astronomical Data Analysis Software and Systems XVI Vol. 376 of Astronomical Society of the Pacific Conference Series, CUPID: A Clump Identification and Analysis Package. p. 425

Berry D. S., Reinhold K., Jenness T., Economou F., , 2013, CUPID: Clump Identification and Analysis Package

Bertoldi F., 1989, ApJ, 346, 735

Bertoldi F., Carilli C. L., Menten K. M., Owen F., Dey A., Gueth F., Graham J. R., Kreysa E., Ledlow M., Liu M. C., Motte F., Reichertz L., Schilke P., Zylka R., 2000, A&A, 360, 92

Bertoldi F., McKee C. F., 1992, ApJ, 395, 140

Beuther H., Shepherd D., 2005, in Kumar M. S. N., Tafalla M., Caselli P., eds, Cores to Clusters: Star Formation with Next Generation Telescopes Vol. 324, Precursors of UCHII Regions and the Evolution of Massive Outflows. pp 105–119

Bieging J. H., Peters W. L., 2011, ApJS, 196, 18

Blaauw A., 1991, in Lada C. J., Kylafis N. D., eds, NATO Advanced Science Institutes (ASI) Series C Vol. 342 of NATO Advanced Science Institutes (ASI) Series C, OB Associations and the Fossil Record of Star Formation. p. 125

Blitz L., Shu F. H., 1980, ApJ, 238, 148

Bohlin R. C., Savage B. D., Drake J. F., 1978, ApJ, 224, 132

Bonnell I. A., Vine S. G., Bate M. R., 2004, MNRAS, 349, 735

Bonnor W. B., 1956, MNRAS, 116, 351

Bontemps S., André P., Könyves V., Men'shchikov A., Schneider N., Maury A., Peretto N., Arzoumanian D., Attard M., Motte F., Minier V., 2010, A&A, 518, L85

Bontemps S., Andre P., Terebey S., Cabrit S., 1996, A&A, 311, 858

Boulanger F., Bronfman L., Dame T. M., Thaddeus P., 1998, A&A, 332, 273

Broekhoven-Fiene H., Matthews B. C., Harvey P. M., Gutermuth R. A., Huard T. L., Tothill N. F. H., Nutter D., Bourke T. L., DiFrancesco J., Jørgensen J. K., 2014, ApJ, 786, 37

Brunt C. M., 2010, A&A, 513, A67

Buckle J. V., Drabek-Maunder E., Greaves J., Richer J. S., Matthews B. C., Johnstone D., Kirk H., 2015, MNRAS, 449, 2472

Buckle J. V., Hills R. E., Smith H., Dent W. R. F., Bell G., Curtis E. I., Dace R., Gibson H., Graves S. F., Leech J., Richer J. S., Williamson R., Withington S., Yassin G., 2009, MNRAS, 399, 1026

Buckle J. V., Richer J. S., Davis C. J., 2012, MNRAS, 423, 1127

Calvet N., Gullbring E., 1998, ApJ, 509, 802

Cambrésy L., 1999, A&A, 345, 965

Canto J., Rodriguez L. F., Calvet N., Levreault R. M., 1984, ApJ, 282, 631

Casali M. M., Eiroa C., Duncan W. D., 1993, A&A, 275, 195

Cesaroni R., Galli D., Lodato G., Walmsley C. M., Zhang Q., 2007, Protostars and Planets V, pp 197–212

Chabrier G., 2005, in Corbelli E., Palla F., Zinnecker H., eds, The Initial Mass Function 50 Years Later Vol. 327 of Astrophysics and Space Science Library, The Initial Mass Function: from Salpeter 1955 to 2005. p. 41

Chandler C. J., Gear W. K., Sandell G., Hayashi S., Duncan W. D., Griffin M. J., Hazella S., 1990, MNRAS, 243, 330

Chapin E. L., Berry D. S., Gibb A. G., Jenness T., Scott D., Tilanus R. P. J., Economou F., Holland W. S., 2013, MNRAS, 430, 2545

Chavarria-K. C., de Lara E., Finkenzeller U., Mendoza E. E., Ocegueda J., 1988, A&A, 197, 151

Chen H., Myers P. C., Ladd E. F., Wood D. O. S., 1995, ApJ, 445, 377

Chun-Yuan Chen M., Di Francesco J., Johnstone D., Sadavoy S., Hatchell J., Mottram J. C., Kirk H., 2016, ArXiv:1605.06136

Churchwell E., 1993, in Cassinelli J. P., Churchwell E. B., eds, Massive Stars: Their Lives in the Interstellar Medium Vol. 35 of Astronomical Society of the Pacific Conference Series, Observations of Newly Formed Massive Stars. pp 35–44

Cieza L., Padgett D. L., Stapelfeldt K. R., Augereau J.-C., Harvey P., Evans II N. J., Merín B., 2007, ApJ, 667, 308

Clark F. O., 1991, ApJS, 75, 611

Clube S. V. M., 1967, Monthly Notes of the Astronomical Society of South Africa, 26, 118

Cohen M., Kuhi L. V., 1979, ApJS, 41, 743

Comerón F., 1992, PhD thesis, Departament d'Astronomia i Meteorologia, Universitat de Barcelona, Av. Diagonal, 647, E-08028, Spain

Commerçon B., Hennebelle P., Henning T., 2011, ApJL, 742, L9

Condon J. J., Kaplan D. L., 1998a, ApJS, 117, 361

Condon J. J., Kaplan D. L., 1998b, VizieR Online Data Catalog, 211, 70361

Condon J. J., Ransom S. M., , 2016

Connelley M. S., Greene T. P., 2010, AJ, 140, 1214

Crutcher R., 2001, in Wootten A., ed., Science with the Atacama Large Millimeter Array Vol. 235 of Astronomical Society of the Pacific Conference Series, Magnetic Fields in Star Formation Regions. p. 1

Crutcher R., 2005, in Chyzy K. T., Otmianowska-Mazur K., Soida M., Dettmar R.-J., eds, The Magnetized Plasma in Galaxy Evolution Magnetic Fields and Star Formation. pp 103–110

Currie M. J., Berry D. S., 2015, KAPPA — Kernel Application Package (2.3) User's Guide

Curtis E. I., Richer J. S., 2010, MNRAS, 401, 455

Curtis E. I., Richer J. S., Buckle J. V., 2010, MNRAS, 401, 455

Curtis E. I., Richer J. S., Swift J. J., Williams J. P., 2010, MNRAS, 408, 1516

Cutri R. M., Skrutskie M. F., van Dyk S., Beichman C. A., Carpenter J. M., Chester T., Cambresy L., Evans T., Fowler J., Gizis J., Howard E., Huchra J., 2003, VizieR Online Data Catalog, 2246, 0

Dale J. E., Ercolano B., Bonnell I. A., 2012, MNRAS, 424, 377

Dallacasa D., 2016, Thermal Bremsstrahlung

Dame T. M., Hartmann D., Thaddeus P., 2001, ApJ, 547, 792

Dame T. M., Thaddeus P., 1985, ApJ, 297, 751

Dame T. M., Ungerechts H., Cohen R. S., de Geus E. J., Grenier I. A., May J., Murphy D. C., Nyman L.-A., Thaddeus P., 1987, ApJ, 322, 706

Damiani F., Micela G., Sciortino S., 2006, A&A, 447, 1041

Davis C. J., Dent W. R. F., Matthews H. E., Coulson I. M., McCaughrean M. J., 2000, MNRAS, 318, 952

Davis C. J., Matthews H. E., Ray T. P., Dent W. R. F., Richer J. S., 1999, MNRAS, 309, 141

de Zeeuw P. T., Hoogerwerf R., de Bruijne J. H. J., Brown A. G. A., Blaauw A., 1999a, AJ, 117, 354

de Zeeuw P. T., Hoogerwerf R., de Bruijne J. H. J., Brown A. G. A., Blaauw A., 1999b, AJ, 117, 354

Deharveng L., Zavagno A., Anderson L. D., Motte F., Abergel A., André P., Bontemps S., Leleu G., Roussel H., Russeil D., 2012, A&A, 546, A74

Dempsey J. T., Friberg P., Jenness T., Tilanus R. P. J., Thomas H. S., Holland W. S., Bintley D., Berry D. S., Chapin E. L., Chrysostomou A., Davis G. R., Gibb A. G., Parsons H., Robson E. I., 2013, MNRAS, 430, 2534

Dempsey J. T., Holland W. S., Chrysostomou A., Berry D. S., Bintley D., Chapin E. L., Craig S. C., Coulson I. M., Davis G. R., Friberg P., Jenness T., Gibb A. G., Parsons H. A. L., Scott D., Thomas H. S., Tilanus R. P. J., Robson I., Walther C. A., 2012, in Millimeter, Submillimeter, and Far-Infrared Detectors and Instrumentation for Astronomy VI Vol. 8452, A new era of wide-field submillimetre imaging: on-sky performance of SCUBA-2. p. 845202

Di Francesco J., Evans II N. J., Caselli P., Myers P. C., Shirley Y., Aikawa Y., Tafalla M., 2007, Protostars and Planets V, pp 17–32

Di Francesco J., Evans II N. J., Harvey P. M., Mundy L. G., Butner H. M., 1994, ApJ, 432, 710

Di Francesco J., Evans II N. J., Harvey P. M., Mundy L. G., Butner H. M., 1998, ApJ, 509, 324

Djupvik A. A., André P., Bontemps S., Motte F., Olofsson G., Gålfalk M., Florén H.-G., 2006, A&A, 458, 789

Dobashi K., Uehara H., Kandori R., Sakurai T., Kaiden M., Umemoto T., Sato F., 2005, PASJ. , 57, 1

Dobbs C. L., Bonnell I. A., Clark P. C., 2005, MNRAS, 360, 2

Drabek E., Hatchell J., Friberg P., Richer J., Graves S., Buckle J. V., Nutter D., Johnstone D., Di Francesco J., 2012, MNRAS, 426, 23

Draine B. T., Lee H. M., 1984, ApJ, 285, 89

Drew J. E., Busfield G., Hoare M. G., Murdoch K. A., Nixon C. A., Oudmaijer R. D., 1997, MNRAS, 286, 538

Duarte-Cabral A., Bontemps S., Motte F., Hennemann M., Schneider N., André P., 2013, A&A, 558, A125

Duarte-Cabral A., Dobbs C. L., Peretto N., Fuller G. A., 2011, A&A, 528, A50

Duarte-Cabral A., Fuller G. A., Peretto N., Hatchell J., Ladd E. F., Buckle J., Richer J., Graves S. F., 2010, A&A, 519, A27

Dunham M. M., Allen L. E., Evans II N. J., Broekhoven-Fiene H., Cieza L. A., Di Francesco J., Gutermuth R. A., Harvey P. M., Hatchell J., Heiderman A., Huard T. L., Johnstone D., Kirk J. M., Matthews B. C., Miller J. F., Peterson D. E., Young K. E., 2015, ApJS, 220, 11

Dunham M. M., Crapsi A., Evans II N. J., Bourke T. L., Huard T. L., Myers P. C., Kauffmann J., 2008, ApJS, 179, 249

Dyson J.E. Williams D., 1997, The Physics of the Interstellar Medium. Vol. 2, CRC Press

Dzib S., Loinard L., Mioduszewski A. J., Boden A. F., Rodríguez L. F., Torres R. M., 2010, ApJ, 718, 610

Dzib S., Loinard L., Mioduszewski A. J., Boden A. F., Rodríguez L. F., Torres R. M., 2011, in Revista Mexicana de Astronomia y Astrofisica Conference Series Vol. 40 of Revista Mexicana de Astronomia y Astrofisica Conference Series, VLBA astrometry of the AeBe star EC 95 in Serpens. pp 231–232

Ebert R., 1955, Zeitschrift fuer Astrophysik, 37, 217

Eiroa C., Casali M. M., 1992, A&A, 262, 468

Eiroa C., Casali M. M., Miranda L. F., Ortiz E., 1994, A&A, 290, 599

Eiroa C., Djupvik A. A., Casali M. M., 2008, in Reipurth B., ed., , Handbook of Star Forming Regions, Volume II. Monograph, p. 693

Eiroa C., Torrelles J. M., Curiel S., Djupvik A. A., 2005, AJ, 130, 643

Enoch M. L., Evans II N. J., Sargent A. I., Glenn J., 2009, ApJ, 692, 973

Enoch M. L., Young K. E., Glenn J., Evans II N. J., Golwala S., Sargent A. I., Harvey P., Aguirre J., Goldin A., Haig D., Huard T. L., Lange A., Laurent G., Maloney P., Mauskopf P., Rossinot P., Sayers J., 2006, ApJ, 638, 293

Erickson E. F., Knacke R. F., Tokunaga A. T., Haas M. R., 1981, ApJ, 245, 148

Evans II N. J., Allen L. E., Blake G. A., Boogert A. C. A., Bourke T., Harvey P. M., Kessler J. E., Koerner D. W., Lee C. W., Mundy L. G., Myers P. C., Padgett D. L., Pontoppidan K., Sargent A. I., Stapelfeldt K. R., van Dishoeck E. F., Young C. H., Young K. E., 2003, PASP, 115, 965

Evans II N. J., Rawlings J. M. C., Shirley Y. L., Mundy L. G., 2001, ApJ, 557, 193

Evans N. J. II., Dunham M. M., Jørgensen J. K., Enoch M. L., Merín B., van Dishoeck E. F., Alcalá J. M., Myers P. C., Stapelfeldt K. R., 2009, ApJS, 181, 321

Evans N. J. II., Harvey P. M., Dunham M., Huard T., Mundy L., Lai S.-p., Chapman N., Brooke T., Enoch M., Stapelfeldt K., 2007, Technical report, Final Delivery of Data from the c2d Legacy Project: IRAC and MIPS. Spitzer Science Center, Pasadena, CA

Fazio G. G., Hora J. L., Allen L. E., Ashby M. L. N., Barmby P., Deutsch L. K., Huang J.-S., Kleiner S., 2004, ApJS, 154, 10

Fich M., Dahl G. P., Treffers R. R., 1990, AJ, 99, 622

Flaherty K. M., Pipher J. L., Megeath S. T., Winston E. M., Gutermuth R. A., Muzerolle J., Allen L. E., Fazio G. G., 2007, ApJ, 663, 1069

Font A. S., Mitchell G. F., Sandell G., 2001, ApJ, 555, 950

Forbrich J., Öberg K., Lada C. J., Lombardi M., Hacar A., Alves J., Rathborne J. M., 2014, A&A, 568, A27

Foster J. B., Rosolowsky E. W., Kauffmann J., Pineda J. E., Borkin M. A., Caselli P., Myers P. C., Goodman A. A., 2009, ApJ, 696, 298

Franco G. A. P., 2002, MNRAS, 331, 474

Friesen R. K., Di Francesco J., Shirley Y. L., Myers P. C., 2009, ApJ, 697, 1457

Fuente A., Rodríguez-Franco A., Testi L., Natta A., Bachiller R., Neri R., 2003, ApJL, 598, L39

Goldreich P., Kwan J., 1974, ApJ, 189, 441

Goldsmith P. F., 2001, ApJ, 557, 736

Gordon K. D., Galliano F., Hony S., 2010, A&A, 518, L89

Gordon M. A., 1995, A&A, 301, 853

Gould B., 1874, Proc. of the American Association for Advanced Sciences, 115

Graves S. F., Richer J. S., Buckle J. V., Duarte-Cabral A., Fuller G. A., Hogerheijde M. R., Owen J. E., Brunt C., 2010, MNRAS, 409, 1412

Gray R. O., Corbally C. J., 1998, AJ, 116, 2530

Gray R. O., Corbally C. J., Garrison R. F., McFadden M. T., Bubar E. J., McGahee C. E., O'Donoghue A. A., Knox E. R., 2006, AJ, 132, 161

Greene T. P., Wilking B. A., Andre P., Young E. T., Lada C. J., 1994, ApJ, 434, 614

Greenstein J. L., 1973, ApJL, 184, L23

Grenier I. A., 2004, ArXiv:astro-ph/0409096

Griffin M. J., Abergel A., Abreu A., Ade P. A. R., André P., Augueres J.-L., Babbedge T., 2010, A&A, 518, L3

Guetter H. H., 1968, PASP, 80, 197

Gutermuth R. A., Bourke T. L., Allen L. E., Myers P. C., Megeath S. T., Matthews B. C., Jørgensen J. K., Di Francesco J., Ward-Thompson D., Huard T. L., Brooke T. Y., Dunham M. M., Cieza L. A., Harvey P. M., Chapman N. L., 2008, ApJL, 673, L151

Gutermuth R. A., Megeath S. T., Myers P. C., Allen L. E., Pipher J. L., Fazio G. G., 2009, ApJS, 184, 18

Gutermuth R. A., Megeath S. T., Pipher J. L., Allen L. E., Myers P. C., 2004, in American Astronomical Society Meeting Abstracts Vol. 36 of Bulletin of the American Astronomical Society, A Survey of Protostars and Disks in the Embedded Clusters GGD 12-15 and IRAS 20050+2720: New Results from Spitzer. p. 1533

Gutermuth R. A., Myers P. C., Megeath S. T., Allen L. E., Pipher J. L., Muzerolle J., Porras A., Winston E., Fazio G., 2008, ApJ, 674, 336

Habart E., Testi L., Natta A., Vanzi L., 2003, A&A, 400, 575

Habing H. J., Israel F. P., 1979, ARAA, 17, 345

Harvey P., Dunham M. M., 2009, ApJ, 695, 1495

Harvey P., Merín B., Huard T. L., Rebull L. M., Chapman N., Evans II N. J., Myers P. C., 2007, ApJ, 663, 1149

Harvey P. M., Chapman N., Lai S.-P., Evans II N. J., Allen L. E., Jørgensen J. K., 2006, ApJ, 644, 307

Harvey P. M., Huard T. L., Jørgensen J. K., Gutermuth R. A., Mamajek E. E., Bourke T. L., Merín B., Cieza L., Brooke T., Chapman N., Alcalá J. M., Allen L. E., Evans II N. J., Di Francesco J., Kirk J. M., 2008, ApJ, 680, 495

Harvey P. M., Thronson Jr. H. A., Gatley I., 1979, ApJ, 231, 115

Hatchell 2010, JCMT Gould Belt Survey

Hatchell J., Dunham M. M., 2009, A&A, 502, 139

Hatchell J., Fuller G. A., Richer J. S., 2007, A&A, 472, 187

Hatchell J., Fuller G. A., Richer J. S., Harries T. J., Ladd E. F., 2007, A&A, 468, 1009

Hatchell J., Hogerheijde M., Di Francesco J., Ward-Thompson D., the JCMT GBS membership 2011, JCMT GBS

Hatchell J., Richer J. S., Fuller G. A., Qualtrough C. J., Ladd E. F., Chandler C. J., 2005, A&A, 440, 151

Hatchell J., Terebey S., Huard T., Mamajek E. E., Allen L., Bourke T. L., Dunham M. M., Gutermuth R., Harvey P. M., Jørgensen J. K., Merín B., Noriega-Crespo A., Peterson D. E., 2012, ApJ, 754, 104

Hatchell J., Wilson T., Drabek E., Curtis E., Richer J., Nutter D., Di Francesco J., Ward-Thompson D., JCMT GBS Consortium 2013, MNRAS, 429, L10

Heiderman A., Evans II N. J., 2015, ApJ, 806, 231

Hennebelle P., Chabrier G., 2011, ApJL, 743, L29

Henning T., Sablotny R. M., 1995, Advances in Space Research, 16, 17

Herbig G. H., 1960, ApJS, 4, 337

Herbig G. H., 1974, PASP, 86, 604

Herbig G. H., Andrews S. M., Dahm S. E., 2004, AJ, 128, 1233

Herbst W., 2008, Star Formation in IC 348. Astronomical society of the pacific, p. 372

Hernández J., Calvet N., Briceño C., Hartmann L., Berlind P., 2004, AJ, 127, 1682

Herschel J., 1847, Results of Astronomical Observations nade during the years 1834,5,6,7,8, at the Cape of Good Hope. London, Smith, Elder and co.

Heyer M. H., Terebey S., 1998, ApJ, 502, 265

Hildebrand R. H., 1983, QJRAS, 24, 267

Hillenbrand L. A., Strom S. E., Vrba F. J., Keene J., 1992, ApJ, 397, 613

Hirota T., Bushimata T., Choi Y. K., Honma M., Imai H., 2007, in Chapman J. M., Baan W. A., eds, IAU Symposium Vol. 242 of IAU Symposium, Astrometry of H_2O maser sources in nearby molecular clouds with VERA. pp 158–159

Ho P. T. P., Moran J. M., Lo K. Y., 2004, ApJL, 616, L1

Høg E., Fabricius C., Makarov V. V., Urban S., Corbin T., Wycoff G., Bastian U., Schwekendiek P., Wicenec A., 2000, A&A, 355, L27

Holland W., MacIntosh M., Fairley A., Kelly D., Montgomery D., Gostick D., Atad-Ettedgui E., Ellis M., Robson I., Hollister M., Woodcraft A., 2006, in Society of Photo-Optical Instrumentation Engineers (SPIE) Conference Series Vol. 6275 of Society of Photo-Optical Instrumentation Engineers (SPIE) Conference Series, SCUBA-2: a 10,000-pixel submillimeter camera for the James Clerk Maxwell Telescope

Holland W. S., Bintley D., Chapin E. L., Chrysostomou A., Davis G. R., Dempsey J. T., Duncan W. D., Fich M., Friberg P., Halpern M., Irwin K. D., Jenness T., Kelly B. D., MacIntosh M. J., Robson E. I., 2013, MNRAS, 430, 2513

Hollenbach D. J., Yorke H. W., Johnstone D., 2000, Protostars and Planets IV, p. 401

Houk N., 1982, Michigan Catalogue of Two-dimensional Spectral Types for the HD stars. Volume 3. Declinations -40 to -26. University of Michigan

Houk N., Smith-Moore M., 1988, Michigan Catalogue of Two-dimensional Spectral Types for the HD Stars. Volume 4, Declinations -26.0 to -12.0.. University of Michigan

Houlahan P., Scalo J., 1992, ApJ, 393, 172

Hovey G. J., Burgess T. A., Casorso R. V., Dent W. R., Dewdney P. E., Force B., Lightfoot J. F., Willis A. G., Yeung K. K., 2000, in Butcher H. R., ed., Radio Telescopes Vol. 4015, New spectral line multibeam correlator system for the James Clerk Maxwell Telescope. pp 114–125

Huang Y.-H., Hirano N., 2013, ApJ, 766, 131

Huttemeister S., Wilson T. L., Henkel C., Mauersberger R., 1993, A&A, 276, 445

Jeans J. H., 1902, Royal Society of London Philosophical Transactions Series A, 199, 1

Jenness T., Chapin E. L., Berry D. S., Gibb A. G., Tilanus R. P. J., Balfour J., Tilanus V., Currie M. J., , 2013, SMURF: SubMillimeter User Reduction Facility

Jenness T., Currie M. J., Tilanus R. P. J., Cavanagh B., Berry D. S., Leech J., Rizzi L., 2015, MNRAS, 453, 73

Jijina J., Adams F. C., 1996, ApJ, 462, 874

Johnstone D., Wilson C. D., Moriarty-Schieven G., Joncas G., Smith G., Gregersen E., Fich M., 2000, ApJ, 545, 327

Juvela M., Demyk K., Doi Y., Hughes A., Lefèvre C., Marshall D. J., Meny C., Montillaud J., Pagani L., Paradis D., Ristorcelli I., Malinen J., Montier L. A., Paladini R., Pelkonen V.-M., Rivera-Ingraham A., 2015, A&A, 584, A94

Kaas A. A., Olofsson G., bontemps S., André P., Nordh L., Huldtgren M., Prusti T., Persi P., Delgado A. J., Motte F., Abergel A., 2004, A&A, 421, 623

Kackley R., Scott D., Chapin E., Friberg P., 2010, in Society of Photo-Optical Instrumentation Engineers (SPIE) Conference Series Vol. 7740 of Society of Photo-Optical Instrumentation Engineers (SPIE) Conference Series, JCMT Telescope Control System upgrades for SCUBA-2. p. 1

Kahn F. D., 1974, in Pinkau K., ed., NATO Advanced Science Institutes (ASI) Series C Vol. 6 of NATO Advanced Science Institutes (ASI) Series C, Star Formation and Star Destruction. p. 235

Kauffmann J., Bertoldi F., Bourke T. L., Evans II N. J., Lee C. W., 2008, A&A, 487, 993

Kauffmann J., Pillai T., Shetty R., Myers P. C., Goodman A. A., 2010a, ApJ, 712, 1137

Kauffmann J., Pillai T., Shetty R., Myers P. C., Goodman A. A., 2010b, ApJ, 716, 433

Kirk H., Di Francesco J., Johnstone D., Duarte-Cabral A., Sadavoy S., 2016, ApJ, 817, 167

Kirk H., Di Francesco J., Johnstone D., Duarte-Cabral A., Sadavoy S., Hatchell J., Mottram J. C., Buckle J., Berry D. S., Broekhoven-Fiene H., Currie M. J., 2015, ArXiv e-prints

Kirk H., Johnstone D., Di Francesco J., 2006, ApJ, 646, 1009

Kirk H., Johnstone D., Di Francesco J., Lane J., Buckle J., Berry D. S., Broekhoven-Fiene H., Currie M. J., Fich M., Hatchell J., Jenness T., The JCMT Gould Belt Survey team 2016, ApJ, 821, 98

Kirk J. M., Ward-Thompson D., Di Francesco J., Bourke T. L., Evans N. J., Merín B., Allen L. E., Cieza L. A., Dunham M. M., Harvey P., Huard T., Jørgensen J. K., Miller J. F., Noriega-Crespo A., Peterson D., Ray T. P., Rebull L. M., 2009, ApJS, 185, 198

Knacke R. F., Strom K. M., Strom S. E., Young E., Kunkel W., 1973, ApJ, 179, 847

Knee L. B. G., Sandell G., 2000, A&A, 361, 671

Koenig X. P., Allen L. E., Gutermuth R. A., Hora J. L., Brunt C. M., Muzerolle J., 2008, ApJ, 688, 1142

Könyves V., André P., Men'shchikov A., Palmeirim P., Arzoumanian D., Schneider N., Roy A., Didelon P., Maury A., Shimajiri Y., Di Francesco J., Bontemps S., Peretto N., 2015, A&A, 584, A91

Könyves V., André P., Men'shchikov A., Schneider N., Arzoumanian D., Bontemps S., Attard M., Motte F., Didelon P., 2010, A&A, 518, L106

Kraemer K. E., Jackson J. M., Kassis M., Deutsch L. K., Hora J. L., Simon R., Hoffmann W. F., Fazio G. G., Dayal A., Bania T. M., Clemens D. P., Heyer M. H., 2003, ApJ, 588, 918

Kroupa P., 2001, MNRAS, 322, 231

Kroupa P., Weidner C., 2003, ApJ, 598, 1076

Krumholz M. R., 2006a, ArXiv:astro-ph/0607429

Krumholz M. R., 2006b, ApJL, 641, L45

Krumholz M. R., 2015, Notes on star formation, The Open Astronomy Bookshelf

Krumholz M. R., Klein R. I., McKee C. F., 2007, ApJ, 656, 959

Krumholz M. R., McKee C. F., Klein R. I., 2005, Nature, 438, 332

Kuhn M. A., Getman K. V., Feigelson E. D., 2015, ApJ, 802, 60

Kuhn M. A., Getman K. V., Feigelson E. D., Reipurth B., Rodney S. A., Garmire G. P., 2010, ApJ, 725, 2485

Kuiper T. B. H., Knapp G. R., Rodriguez Kuiper E. N., 1976, A&A, 48, 475

Kurtz S., 2005, in Cesaroni R., Felli M., Churchwell E., Walmsley M., eds, Massive Star Birth: A Crossroads of Astrophysics Vol. 227 of IAU Symposium, Hypercompact HII regions. pp 111–119

Kurtz S., Churchwell E., Wood D. O. S., 1994, ApJS, 91, 659

Kutner M. L., Ulich B. L., 1981, ApJ, 250, 341

Lada C. J., Lada E. A., 2003, ARAA, 41, 57

Lada C. J., Lombardi M., Alves J. F., 2009, ApJ, 703, 52

Lada C. J., Wilking B. A., 1984, ApJ, 287, 610

Ladd E. F., Myers P. C., Goodman A. A., 1994, ApJ, 433, 117

Larmor . J., 1897, Philosophical Magazine Series 5, 44, 503

Larson R. B., 1969, MNRAS, 145, 271

Larson R. B., 1981, MNRAS, 194, 809

Larson R. B., Starrfield S., 1971, A&A, 13, 190

Lee C. W., Kim M.-R., Kim G., Saito M., Myers P. C., Kurono Y., 2013, ApJ, 777, 50

Lefloch B., Lazareff B., 1994, A&A, 289, 559

Levshakov S. A., Henkel C., Reimers D., Wang M., 2014, A&A, 567, A78

Lindblad P. O., 1967, Bull. Astr. Inst. Netherlands, 19, 34

Lodieu N., McCaughrean M. J., Barrado Y Navascués D., Bouvier J., Stauffer J. R., 2005, A&A, 436, 853

Longmore S. N., Pillai T., Keto E., Zhang Q., Qiu K., 2011, ApJ, 726, 97

Lu X., Zhang Q., Liu H. B., Wang J., Gu Q., 2014, ApJ, 790, 84

Maddalena R. J., Morris M., Moscowitz J., Thaddeus P., 1986, ApJ, 303, 375

Mairs S., Johnstone D., Kirk H., Graves S., Buckle J., JCMT Gould Belt survey Team 2015, MNRAS, 454, 2557

Mairs S., Johnstone D., Offner S. S. R., Schnee S., 2014, ApJ, 783, 60

Malbet F., Benisty M., de Wit W.-J., Kraus S., Meilland A., Millour F., Tatulli E., Berger J.-P., Chesneau O., Hofmann K.-H., Isella A., Natta A., Petrov R. G., Preibisch T., Stee P., Testi L., Weigelt G., Antonelli P., Beckmann U., 2007, A&A, 464, 43

Mallick K. K., Kumar M. S. N., Ojha D. K., Bachiller R., Samal M. R., Pirogov L., 2013, ApJ, 779, 113

Mamajek E. E., 2008, Astronomische Nachrichten, 329, 10

Mannings V., 1994, MNRAS, 271, 587

Manoj P., Ho P. T. P., Ohashi N., Zhang Q., Hasegawa T., Chen H.-R., Bhatt H. C., Ashok N. M., 2007, ApJL, 667, L187

Masunaga H., Inutsuka S.-i., 2000, ApJ, 531, 350

Masunaga H., Miyama S. M., Inutsuka S.-i., 1998, ApJ, 495, 346

Mathis J. S., Mezger P. G., Panagia N., 1983, A&A, 128, 212

Mathis J. S., Rumpl W., Nordsieck K. H., 1977, ApJ, 217, 425

Mattsson L., 2010, A&A, 515, A68

Matzner C. D., 2002, ApJ, 566, 302

Matzner C. D., Levin Y., 2005, ApJ, 628, 817

Maury A. J., André P., Men'shchikov A., Könyves V., Bontemps S., 2011, A&A, 535, A77

McKee C. F., Ostriker E. C., 2007, ARAA, 45, 565

McKee C. F., Tan J. C., 2003, ApJ, 585, 850

McMullin J. P., Mundy L. G., Blake G. A., Wilking B. A., Mangum J. G., Latter W. B., 2000, ApJ, 536, 845

Megeath S. T., Allen L. E., Gutermuth R. A., Pipher J. L., Myers P. C., Calvet N., Hartmann L., Muzerolle J., Fazio G. G., 2004, ApJS, 154, 367

Megeath S. T., Gutermuth R., Muzerolle J., Kryukova E., Flaherty K., Hora J. L., Allen L. E., Hartmann L., Myers P. C., Pipher J. L., Stauffer J., Young E. T., Fazio G. G., 2012, AJ, 144, 192

Men'shchikov A., André P., Didelon P., Könyves V., Schneider N., Motte F., Bontemps S., Arzoumanian D., Attard M., Abergel A., Baluteau J.-P., Bernard J.-P., Cambrésy L., 2010, A&A, 518, L103

Mezger P. G., Henderson A. P., 1967, ApJ, 147, 471

Mitchell G. F., Johnstone D., Moriarty-Schieven G., Fich M., Tothill N. F. H., 2001, ApJ, 556, 215

Molinari S., Brand J., Cesaroni R., Palla F., Palumbo G. G. C., 1998, A&A, 336, 339

Molinari S., Schisano E., Faustini F., Pestalozzi M., di Giorgio A. M., Liu S., 2011, A&A, 530, A133

Mora A., Merín B., Solano E., Montesinos B., de Winter D., Eiroa C., 2001, A&A, 378, 116

Motte F., Andre P., Neri R., 1998, A&A, 336, 150

Murray N., 2011, ApJ, 729, 133

Myers A. T., McKee C. F., Cunningham A. J., Klein R. I., Krumholz M. R., 2013, ApJ, 766, 97

Myers P. C., Adams F. C., Chen H., Schaff E., 1998, ApJ, 492, 703

Myers P. C., Benson P. J., 1983, ApJ, 266, 309

Myers P. C., Ladd E. F., 1993, ApJL, 413, L47

Natta A., Grinin V., Mannings V., 2000, Protostars and Planets IV, pp 559–588

Natta A., Prusti T., Neri R., Wooden D., Grinin V. P., Mannings V., 2001, A&A, 371, 186

Nesterov V. V., Kuzmin A. V., Ashimbaeva N. T., Volchkov A. A., Röser S., Bastian U., 1995, A&AS, 110

Neuhäuser R., Forbrich J., 2008, The Corona Australis Star Forming Region. Astronomical society of the pacific, p. 735

Nutter D., Ward-Thompson D., 2007, MNRAS, 374, 1413

Offner S. S. R., Klein R. I., McKee C. F., Krumholz M. R., 2009, ApJ, 703, 131

Olnon F. M., 1975, A&A, 39, 217

Ortiz-León G. N., Loinard L., Mioduszewski A. J., Dzib S. A., Rodríguez L. F., 2015, ApJ, 805, 9

Ossenkopf V., 1993, A&A, 280, 617

Ossenkopf V., Henning T., 1994, A&A, 291, 943

Oster L., 1961, ApJ, 134, 1010

Padoan P., Nordlund Å., 2002, ApJ, 576, 870

Palla F., Stahler S. W., 1993, ApJ, 418, 414

Panagia N., Felli M., 1975, A&A, 39, 1

Pattle K., Ward-Thompson D., Kirk J. M., White G. J., Drabek-Maunder E., 2015, MNRAS, 450, 1094

Peretto N., Gaudel M., Louvet F., Fuller G. A., Traficante A., Duarte-Cabral A., 2016, in EAS Publications Series Vol. 75 of EAS Publications Series, Star formation in infrared dark clouds: Self-gravity and dynamics. pp 167–170

Persi P., Palagi F., Felli M., 1994, A&A, 291, 577

Peterson D. E., Caratti o Garatti A., Bourke T. L., Forbrich J., Gutermuth R. A., Jørgensen J. K., Allen L. E., Patten B. M., Dunham M. M., Harvey P. M., Merín B., Chapman N. L., Cieza L. A., Huard T. L., Knez C., Prager B., Evans N. J., 2011, ApJS, 194, 43

Pezzuto S., Elia D., Schisano E., Strafella F., Di Francesco J., Sadavoy S., 2012, A&A, 547, A54

Pirogov L., Ojha D. K., Thomasson M., Wu Y.-F., Zinchenko I., 2013, MNRAS, 436, 3186

Poglitsch A., Waelkens C., Geis N., Feuchtgruber H., Vandenbussche B., Rodriguez L., Krause O., Renotte E., van Hoof C., Saraceno P., Cepa J., Kerschbaum F., 2010, A&A, 518, L2

Pollack J. B., Hollenbach D., Beckwith S., Simonelli D. P., Roush T., Fong W., 1994, ApJ, 421, 615

Pontoppidan K. M., Dullemond C. P., Blake G. A., Evans II N. J., Geers V. C., Harvey P. M., Spiesman W., 2007, ApJ, 656, 991

Pöppel W. G. L., 2001, in Montmerle T., André P., eds, From Darkness to Light: Origin and Evolution of Young Stellar Clusters Vol. 243 of Astronomical Society of the Pacific Conference Series, The Gould Belt System. p. 667

Predehl P., Schmitt J. H. M. M., 1995, A&A, 293

Preibisch T., 2003, A&A, 410, 951

Racine R., 1968, AJ, 73, 233

Radhakrishnan V., Goss W. M., Murray J. D., Brooks J. W., 1972, ApJS, 24, 49

Rathborne J. M., Jackson J. M., Zhang Q., Simon R., 2008, ApJ, 689, 1141

Rebull L. M., Padgett D. L., McCabe C., Hillenbrand L. A., Stapelfeldt K. R., Noriega-Crespo A., Carey S. J., Brooke T., Huard T., Terebey S., 2010, ApJS, 186, 259

Rebull L. M., Padgett D. L., McCabe C.-E., Hillenbrand L. A., Stapelfeldt K. R., Noriega-Crespo A., Carey S. J., Brooke T., Huard T., Terebey S., Audard M., Monin J.-L., Fukagawa M., Güdel M., Knapp G. R., Menard F., 2010, ApJS, 186, 259

Reed B. C., 2003, AJ, 125, 2531

Reid M. A., Wilson C. D., 2005, ApJ, 625, 891

Rey-Raposo R., Dobbs C., Duarte-Cabral A., 2015, MNRAS, 446, L46

Reynolds S. P., 1986, ApJ, 304, 713

Rieke G. H., Young E. T., Engelbracht C. W., Kelly D. M., Low F. J., Haller E. E., Beeman J. W., 2004, ApJS, 154, 25

Robitaille T. P., Whitney B. A., 2014, in Stamatellos D., Goodwin S., Ward-Thompson D., eds, Advances in Solid State Physics Vol. 36 of Advances in Solid State Physics, A New Set of Model Spectral Energy Distributions for Young Stellar Objects. Springer International Publishing, New York City, p. 157

Robitaille T. P., Whitney B. A., Indebetouw R., Wood K., 2007, ApJS, 169, 328

Robitaille T. P., Whitney B. A., Indebetouw R., Wood K., Denzmore P., 2006, ApJS, 167, 256

Robson I., Holland W., 2007, in Baker A. J., Glenn J., Harris A. I., Mangum J. G., Yun M. S., eds, From Z-Machines to ALMA: (Sub)Millimeter Spectroscopy of Galaxies Vol. 375 of Astronomical Society of the Pacific Conference Series, SCUBA-2: The Submillimeter Mapping Machine. p. 275

Rodney S. A., Reipurth B., 2008, The W40 Cloud Complex. Astronomical society of the pacific, p. 683

Rodríguez L. F., Gómez Y., Tafoya D., 2007, ApJ, 663, 1083

Rodríguez L. F., Rodney S. A., Reipurth B., 2010, AJ, 140, 968

Rodríguez L. F., Zapata L. A., Dzib S. A., Ortiz-León G. N., Loinard L., Macías E., Anglada G., 2014, ApJL, 793, L21

Röser S., Schilbach E., Schwan H., Kharchenko N. V., Piskunov A. E., Scholz R.-D., 2008, A&A, 488, 401

Rosolowsky E., Leroy A., 2006, PASP, 118, 590

Rosolowsky E. W., Pineda J. E., Foster J. B., Borkin M. A., Kauffmann J., Caselli P., Myers P. C., Goodman A. A., 2008, ApJS, 175, 509

Rosolowsky E. W., Pineda J. E., Kauffmann J., Goodman A. A., 2008, ApJ, 679, 1338

Rumble D., Hatchell J., Gutermuth R. A., Kirk H., Buckle J., Beaulieu S. F., Berry D. S., Broekhoven-Fiene H., 2015, MNRAS, 448, 1551

Rumble D., Hatchell J., Pattle K., Kirk H., Buckle J., Berry D. S., 2016, MNRAS, 460, 4150

Rybicki G., Lightman A., 1979, Radiative processes in astrophysics.. New York, Wiley-Interscience

Rygl K. L. J., Benedettini M., Schisano E., Elia D., Molinari S., Pezzuto S., André P., Bernard J. P., White G. J., Polychroni D., Bontemps S., Cox N. L. J., Di Francesco J., 2013, A&A, 549, L1

Sadavoy S. I., Di Francesco J., André P., Pezzuto S., Bernard J.-P., Maury A., Men'shchikov A., Motte F., 2014, ApJL, 787, L18

Sadavoy S. I., Di Francesco J., Bontemps S., Megeath S. T., Rebull L. M., Allgaier E., Carey S., Gutermuth R., Hora J., Huard T., McCabe C.-E., Muzerolle J., Noriega-Crespo A., Padgett D., Terebey S., 2010, ApJ, 710, 1247

Sadavoy S. I., Di Francesco J., Johnstone D., Currie M. J., Drabek E., Hatchell J., Nutter D., André P., Arzoumanian D., Benedettini M., 2013, ApJ, 767, 126

Saigo K., Tomisaka K., 2011, ApJ, 728, 78

Salji C., 2014, in Protostars and Planets VI Posters Filament identification and characterisation in Gould Belt Clouds. p. 19

Salji C. J., Richer J. S., Buckle J. V., Francesco J. D., Hatchell J., Hogerheijde M., Johnstone D., Kirk H., Ward-Thompson D., JCMT GBS Consortium 2015, MNRAS, 449, 1782

Salpeter E. E., 1955, ApJ, 121, 161

Sandell G., Goss W. M., Wright M., Corder S., 2009, ApJL, 699, L31

Sandell G., Weintraub D. A., Hamidouche M., 2011, ApJ, 727, 26

Sanders D. B., Mirabel I. F., 1985, ApJL, 298, L31

Scalo J. M., 1986, Fund. Cosmic Physics, 11, 1

Schnee S. L., Ridge N. A., Goodman A. A., Li J. G., 2005, ApJ, 634, 442

Schneider N., Csengeri T., Bontemps S., Motte F., Simon R., Hennebelle P., Federrath C., Klessen R., 2010, A&A, 520, A49

Schneider N., Stutzki J., Winnewisser G., Block D., 1998, A&A, 335, 1049

Schwartz P. R., 1982, ApJ, 252, 589

Sharpless S., 1959, ApJS, 4, 257

Shetty R., Kauffmann J., Schnee S., Goodman A. A., 2009, ApJ, 696, 676

Shetty R., Kauffmann J., Schnee S., Goodman A. A., Ercolano B., 2009, ApJ, 696, 2234

Shetty R., Roman-Duval J., Hony S., Cormier D., Klessen R. S., Konstandin L. K., Loredo T., Pellegrini E. W., Ruppert D., 2015, ArXiv e-prints:1509.00639

Shimajiri Y., Kitamura Y., Nakamura F., Momose M., Saito M., Tsukagoshi T., Hiramatsu M., Shimoikura T., Dobashi K., Hara C., Kawabe R., 2015, ApJS, 217, 7

Shimoikura T., Dobashi K., Nakamura F., Hara C., Tanaka T., Shimajiri Y., Sugitani K., Kawabe R., 2015, ApJ, 806, 201

Shirley Y. L., Evans N. J., Rawlings J. M. C., 2002a, ApJ, 575, 337

Shirley Y. L., Evans N. J., Rawlings J. M. C., 2002b, ApJ, 575, 337

Shirley Y. L., Evans N. J., Rawlings J. M. C., Gregersen E. M., 2000a, ApJS, 131, 249

Shirley Y. L., Evans N. J., Rawlings J. M. C., Gregersen E. M., 2000b, ApJS, 131, 249

Shirley Y. L., Mueller K. E., Young C. H., Evans N. J., 2003, in De Buizer J. M., van der Bliek N. S., eds, Galactic Star Formation Across the Stellar Mass Spectrum Vol. 287 of Astronomical Society of the Pacific Conference Series, Submillimeter Dust Continuum Studies of Low and High Mass Star Formation. pp 298–304

Shklovskii I. S., 1967, Astronomicheskii Zhurnal, 44, 930

Shu F. H., 1977, ApJ, 214, 488

Shu F. H., Adams F. C., Lizano S., 1987, ARAA, 25, 23

Shuping R. Y., Vacca W. D., Kassis M., Yu K. C., 2012, AJ, 144, 116

Skiff B. A., 2014, VizieR Online Data Catalog, 1

Skinner S. L., Brown A., Stewart R. T., 1993, ApJS, 87, 217

Skrutskie M. F., Cutri R. M., Stiening R., Weinberg M. D., Schneider S., Carpenter J. M., 2006, AJ, 131, 1163

Smith J., Bentley A., Castelaz M., Gehrz R. D., Grasdalen G. L., Hackwell J. A., 1985, ApJ, 291, 571

Snell R. L., Edwards S., 1981, ApJ, 251, 103

Spezzi L., Vernazza P., Merín B., Allen L. E., Evans II N. J., Jørgensen J. K., Bourke T. L., Cieza L. A., Dunham M. M., Harvey P. M., Huard T. L., Peterson D., Tothill N. F. H., The Gould's Belt Team 2011, ApJ, 730, 65

Stahler S., Palla F., 2004, The Formation of Stars. Wiley-VCH

Stahler S. W., Palla F., 1993, in American Astronomical Society Meeting Abstracts #182 Vol. 25 of Bulletin of the American Astronomical Society, The Pre-Main Sequence Evolution of Intermediate-Mass Stars. p. 915

Stahler S. W., Palla F., Ho P. T. P., 2000, Protostars and Planets IV, pp 327–352

Stamatellos D., Whitworth A. P., Bisbas T., Goodwin S., 2007, A&A, 475, 37

Stark A. A., Blitz L., 1978, ApJL, 225, L15

Stern D., Eisenhardt P., Gorjian V., Kochanek C. S., Caldwell N., Eisenstein D., Brodwin M., Brown M. J. I., Cool R., Dey A., Green P., Jannuzi B. T., Murray S. S., Pahre M. A., Willner S. P., 2005, ApJ, 631, 163

Straižys V., Corbally C. J., Kazlauskas A., Černis K., 2002, Baltic Astronomy, 11, 261

Straižys V., Černis K., Bartašiūtė S., 2003, A&A, 405, 585

Strom S. E., Grasdalen G. L., Strom K. M., 1974, ApJ, 191, 111

Stutz A., Launhardt R., Linz H., Krause O., Henning T., Kainulainen J., Nielbock M., Steinacker J., André P., 2010, A&A, 518, L87

Stutzki J., , 2014, GAUSSCLUMPS: Gaussian-shaped clumping from a spectral map, Astrophysics Source Code Library

Stutzki J., Bensch F., Heithausen A., Ossenkopf V., Zielinsky M., 1998, A&A, 336, 697

Stutzki J., Guesten R., 1990, ApJ, 356, 513

Szymczak M., Hrynek G., Kus A. J., 2000, A&AS, 143, 269

Tafoya D., Gómez Y., Rodríguez L. F., 2004, ApJ, 610, 827

Tanaka T., Nakamura F., Awazu Y., Shimajiri Y., Sugitani K., Onishi T., Kawabe R., Yoshida H., Higuchi A. E., 2013, ApJ, 778, 34

Tassis K., Mouschovias T. C., 2004, ApJ, 616, 283

Terebey S., Shu F. H., Cassen P., 1984, ApJ, 286, 529

Testi L., Birnstiel T., Ricci L., Andrews S., Blum J., Carpenter J., Dominik C., Isella A., Natta A., Williams J. P., Wilner D. J., 2014, Protostars and Planets VI, pp 339–361

Thomas H. S., Currie M. J., 2014, The SCUBA-2 Data Reduction Cookbook. Starlink Project

Thompson M. A., White G. J., Morgan L. K., Miao J., Fridlund C. V. M., Huldtgren-White M., 2004, A&A, 414, 1017

Tielens A. G. G. M., 2005, The Physics and Chemistry of the Interstellar Medium. Vol. 1, Cambridge University Press

Tielens A. G. G. M., Hollenbach D., 1985, ApJ, 291, 722

Tisserand P., Clayton G. C., Welch D. L., Pilecki B., Wyrzykowski L., Kilkenny D., 2013, A&A, 551, A77

Torres C. A. O., Quast G. R., da Silva L., de La Reza R., Melo C. H. F., Sterzik M., 2006, A&A, 460, 695

Ubach C., Maddison S. T., Wright C. M., Wilner D. J., Lommen D. J. P., Koribalski B., 2012, MNRAS, 425, 3137

Urquhart J. S., Morgan L. K., Figura C. C., Moore T. J. T., Lumsden S. L., Hoare M. G., Oudmaijer R. D., Mottram J. C., Davies B., Dunham M. K., 2011, MNRAS, 418, 1689

Urquhart J. S., Morgan L. K., Thompson M. A., 2009, A&A, 497, 789

Vallee J. P., 1987, A&A, 178, 237

Vallee J. P., MacLeod J. M., 1991, A&A, 250, 143

Vallée J. P., MacLeod J. M., 1992, in American Astronomical Society Meeting Abstracts #179 Vol. 24 of Bulletin of the American Astronomical Society, The W40 Complex at Millimeter Wavelengths. p. 688

van der Wiel M. H. D., Naylor D. A., Kamp I., Ménard F., Thi W.-F., Woitke P., Olofsson G., Pontoppidan K. M., Di Francesco J., Glauser A. M., Greaves J. S., Ivison R. J., 2014, MNRAS, 444, 3911

van Leeuwen F., 2007, A&A, 474, 653

Veneziani M., Elia D., Noriega-Crespo A., Paladini R., Carey S., Faimali A., Molinari S., Pestalozzi M., Piacentini F., Schisano E., 2012, VizieR Online Data Catalog, 354

Vieira S. L. A., Corradi W. J. B., Alencar S. H. P., Mendes L. T. S., Torres C. A. O., Quast G. R., Guimarães M. M., da Silva L., 2003, AJ, 126, 2971

Vink J. S., O'Neill P. M., Els S. G., Drew J. E., 2005, A&A, 438, L21

Walawender J., Bally J., Francesco J. D., Jørgensen J., Getman K. ., 2008, NGC 1333: A Nearby Burst of Star Formation. Astronomical society of the pacific, p. 346

Walsh A. J., Burton M. G., Hyland A. R., Robinson G., 1998, MNRAS, 301, 640

Wang P., Li Z.-Y., Abel T., Nakamura F., 2010, ApJ, 709, 27

Wang Y., Wu Y., Zhang Q., Mao R.-Q., Miller M., 2007, A&A, 461, 197

Ward-Thompson D., Di Francesco J., Hatchell J., Hogerheijde M. R., Nutter D., Bastien P., Basu S., Bonnell I., Bowey J., Brunt C., Buckle J., 2007, PASP, 119, 855

Ward-Thompson D., Pattle K., Kirk J. M., André P., Di Francesco J., 2015, ArXiv e-prints

Ward-Thompson D., Scott P. F., Hills R. E., Andre P., 1994, MNRAS, 268, 276

Watson M., 2010, MSc thesis, University of Hertfordshire.

Wenger M., Ochsenbein F., Egret D., Dubois P., Bonnarel F., Borde S., Genova F., Jasniewicz G., Laloë S., Lesteven S., Monier R., 2000, A&AS, 143, 9

Westerhout G., 1958, A&A, 14, 215

White G. J., Casali M. M., Eiroa C., 1995, A&A, 298, 594

White G. J., Drabek-Maunder E., Rosolowsky E., Ward-Thompson D., Davis C. J., Gregson J., Hatchell J., 2015, MNRAS, 447, 1996

Whitehouse S. C., Bate M. R., 2006, MNRAS, 367, 32

Whitney B. A., Wood K., Bjorkman J. E., Cohen M., 2003, ApJ, 598, 1079

Wilking B. A., Gagné M., Allen L. E., 2008, in Reipurth, B. ed., Handbook of Star Forming Regions, Volume II Star Formation in the ρ Ophiuchi Molecular Cloud. p. 351

Williams J. P., de Geus E. J., Blitz L., 1994, ApJ, 428, 693

Williams J.P. Myers P., 2000, ApJ, 537

Winston E., Megeath S. T., Wolk S. J., Muzerolle J., Gutermuth R., Hora J. L., Allen L. E., Spitzbart B., Myers P., Fazio G. G., 2007, ApJ, 669, 493

Winston E., Megeath S. T., Wolk S. J., Spitzbart B., Gutermuth R., Allen L. E., Hernandez J., Covey K., Muzerolle J., Hora J. L., Myers P. C., Fazio G. G., 2010, AJ, 140, 266

Witt A. N., Cottrell M. J., 1980, ApJ, 235, 899

Wolfire M. G., Cassinelli J. P., 1987, ApJ, 319, 850

Wolk S. J., Winston E., Bourke T. L., Gutermuth R., Megeath S. T., Spitzbart B. D., Osten R., 2010, ApJ, 715, 671

Wood D. O. S., Churchwell E., 1989, ApJS, 69, 831

Wood D. O. S., Myers P. C., Daugherty D. A., 1994, ApJS, 95, 457

Wright A. E., Barlow M. J., 1975, MNRAS, 170, 41

Wu Y., Zhang Q., Yu W., Miller M., Mao R., Sun K., Wang Y., 2006, A&A, 450, 607

Yorke H. W., Sonnhalter C., 2002, ApJ, 569, 846

Young C. H., Shirley Y. L., Evans II N. J., Rawlings J. M. C., 2003, ApJS, 145, 111

Young K. E., Harvey P. M., Brooke T. Y., Chapman N., Kauffmann J., Bertoldi F., Lai S.-P., Alcalá J., Bourke T. L., Spiesman W., Allen L. E., Blake G. A., Evans II N. J., 2005, ApJ, 628, 283

Zacharias M., Zacharias N., 2012, in IAU Joint Discussion Vol. 7 of IAU Joint Discussion, Radio-optical reference frame offsets from CTIO and UCAC4 data. p. 13P

Zacharias N., Finch C. T., Girard T. M., Henden A., Bartlett J. L., Monet D. G., Zacharias M. I., 2013, AJ, 145, 44

Zeilik II M., Lada C. J., 1978, ApJ, 222, 896

Zhang C. Y., Laureijs R. J., Clark F. O., 1988, A&A, 196, 236

Zhang G., Li D., Hyde A. K., Qian L., Lyu H., Wu Z., 2015, Science China Physics, Mechanics, and Astronomy, 58, 5561

Zhu L., Wu Y.-F., Wei Y., 2006, Chinese Journal of Astronomy and Astrophysics, 6, 61

Ziener R., Eislöffel J., 1999, A&A, 347, 565

A

Long tables

A.1 The JCMT GBS Clump Catalogue

Table A.1: The JCMT GBS Clump Catalogue (JGCC). See Table 8.5 for full description.

ID	Coords. (J2000)	S_{850} (Jy)	Mass ($M_\odot$)	Temp. (K)	N_{H_2} ($\times^{21}$ cm^{-2})	D (pc)	Proto stars	n_{YSO} (pc^{-2})	M_J ($M_\odot$)	M_{850}/M_J	d_{OB} (pc)
Auriga LKHa101-SMM1	J043014.59+351623.9	2.3	9.3±2.9	14.8±2.4	401±123	0.09	1	25	6.3±1.0	1.5±0.5	0.02
Auriga LKHa101-SMM2	J043036.79+355438.7	2.7	9.9±2.5	12.8±1.3	86±22	0.09	2	14	5.4±0.5	1.8±0.5	5.04
Auriga LKHa101-SMM3	J043048.03+345841.7	2	9.6±1.8	11.2±0.8	294±55	0.06	2	30	3.3±0.2	2.9±0.6	2.49
Auriga LKHa101-SMM4	J043038.75+355023.7	1.7	6.2±1.5	12.9±1.4	98±24	0.07	0	25	4.3±0.5	1.4±0.4	4.5
Auriga LKHa101-SMM5	J043028.04+350920.9	1.3	3.2±0.8	16.2±1.9	64±16	0.05	2	19	4.6±0.5	0.7±0.2	1
Auriga LKHa101-SMM6	J043015.81+351711.9	6.3	8.7±2.6	23.3±4.2	34±10	0.16	0	11	14.9±2.7	0.6±0.2	0.12
Auriga LKHa101-SMM7	J043015.57+351641.9	3.3	5.2±1.5	21.9±3.8	52±15	0.13	0	10	9.9±1.7	0.5±0.2	0.06
Auriga LKHa101-SMM8	J043041.36+352944.7	3.7	12.2±3.3	13.3±1.5	60±16	0.14	1	9	7.3±0.8	1.7±0.5	1.89
Auriga LKHa101-SMM9	J043015.57+351208.9	0.8	1.4±0.5	19.6±3.9	24±8	0.05	0	5	5.1±1.0	0.3±0.1	0.56
Auriga LKHa101-SMM10	J043040.86+352853.7	3.1	10.6±3.4	13.1±1.9	45±14	0.17	0	4	7.2±1.1	1.5±0.5	1.79
Auriga LKHa101-SMM11	J043048.78+353756.6	0.6	2.1±0.7	13.4±2.1	57±20	0.08	1	12	3.5±0.6	0.6±0.2	2.97
Auriga LKHa101-SMM12	J043003.81+351417.9	3.4	5.5±1.9	20.7±4.3	20±7	0.14	1	35	10.7±2.2	0.5±0.2	0.39
Auriga LKHa101-SMM13	J042955.73+351535.8	8.7	14.5±5.2	20.6±4.5	24±9	0.3	0	24	17.7±3.9	0.8±0.3	0.5
Auriga LKHa101-SMM14	J043038.01+355102.7	0.4	1.5±0.5	13.1±1.9	45±14	0.02	1	29	2.6±0.4	0.6±0.2	4.58
Auriga LKHa101-SMM15	J043009.44+351405.9	2	3.5±1.4	19.8±4.6	19±7	0.13	1	43	8.7±2.0	0.4±0.2	0.32
Auriga LKHa101-SMM16	J042951.32+351553.7	1.3	2.9±1.1	17.3±3.7	29±11	0.09	2	30	6.3±1.4	0.5±0.2	0.61
Auriga LKHa101-SMM17	J043026.09+350959.9	0.5	1.1±0.4	16.9±3.5	25±10	0.06	0	9	4.1±0.9	0.3±0.1	0.9
Auriga LKHa101-SMM18	J043030.61+355141.8	0.5	2.3±0.8	11.2±1.6	46±16	0.04	1	16	2.6±0.4	0.9±0.3	4.64
Auriga LKHa101-SMM19	J043044.48+355953.6	0.4	1.4±0.4	12.2±1.7	36±11	0.02	1	10	2.3±0.3	0.6±0.2	5.75
Auriga LKHa101-SMM20	J043000.62+351550.8	0.5	0.8±0.3	19.3±4.7	18±7	0.04	0	26	4.2±1.0	0.2±0.1	0.36
Auriga LKHa101-SMM21	J043039.75+355205.7	0.4	1.2±0.5	14.5±2.8	23±9	0.04	1	24	3.2±0.6	0.4±0.2	4.72
Auriga LKHa101-SMM22	J043010.42+351326.9	0.7	1.0±0.4	21.8±6.2	11±5	0.07	0	26	6.2±1.8	0.2±0.1	0.4
Auriga LKHa101-SMM23	J043040.48+355114.7	0.5	1.4±0.5	14.1±2.8	27±10	0.04	0	26	3.2±0.6	0.4±0.2	4.62
Auriga LKHa101-SMM24	J043012.63+351256.9	0.6	0.9±0.4	20.2±5.7	12±6	0.06	0	16	5.5±1.5	0.2±0.1	0.45
Auriga LKHa101-SMM25	J042954.02+351441.8	0.7	1.5±0.6	16.4±3.9	16±7	0.07	0	25	4.8±1.1	0.3±0.2	0.58
Auriga LKHa101-SMM26	J043035.24+353453.8	0.5	2.5±1.3	10.7±2.4	22±11	0.07	0	3	3.0±0.7	0.9±0.5	2.49
Auriga LKHa101-SMM27	J043014.10+351338.9	0.6	1.2±0.6	18.5±5.1	13±6	0.1	1	20	5.5±1.5	0.2±0.1	0.36
Auriga LKHa101-SMM28	J043031.83+354511.8	0.2	0.7±0.3	12.1±2.7	40±19	0.03	1	21	1.8±0.4	0.4±0.2	3.8
Auriga Main-SMM1	J041008.39+400224.5	1.3	2.2±0.7	20.8±3.6	47±15	0.06	0	0	6.7±1.1	0.3±0.1	-
Auriga Main-SMM2	J042538.56+370701.4	6.6	18.6±6.0	14.6±2.3	43±14	0.24	2	10	11.4±1.8	1.6±0.6	-
Auriga Main-SMM3	J042138.23+373438.7	2.3	5.3±1.8	16.7±2.8	33±11	0.11	0	15	7.5±1.3	0.7±0.3	-
Auriga Main-SMM4	J041006.76+400241.3	1.8	3.3±1.2	20.4±4.3	35±13	0.12	0	0	8.3±1.8	0.4±0.2	-
Auriga Main-SMM5	J042141.08+373357.5	1.1	3.9±1.2	12.9±1.8	42±13	0.08	1	13	4.2±0.6	0.9±0.3	-
Auriga Main-SMM6	J042508.19+371520.2	0.4	1.2±0.4	13.6±1.9	34±10	0.02	0	0	2.6±0.4	0.5±0.2	-
Auriga Main-SMM7	J041010.97+400129.6	1.4	6.1±2.1	11.2±1.7	43±15	0.1	0	0	4.4±0.7	1.4±0.5	-
Auriga Main-SMM8	J040954.32+400628.2	2.6	8.7±3.5	13.3±2.6	33±13	0.24	0	0	7.5±1.5	1.2±0.5	-
Auriga Main-SMM9	J042504.10+371625.4	0.6	2.6±1.2	11.0±2.3	33±15	0.08	0	0	3.0±0.6	0.9±0.4	-
Auriga Main-SMM10	J042118.17+373351.2	0.6	2.9±1.2	10.6±1.8	29±11	0.07	0	0	3.0±0.5	1.0±0.4	-
Auriga Main-SMM11	J042145.17+373322.7	0.3	1.6±0.6	11.0±1.8	27±10	0.04	0	6	2.3±0.4	0.7±0.3	-
Auriga Main-SMM12	J042515.45+371145.6	0.2	1.4±0.6	9.1±1.7	42±19	0.01	0	0	1.5±0.3	0.9±0.5	-
Auriga Main-SMM13	J041015.31+400243.8	0.5	1.1±0.5	17.2±4.7	16±8	0.07	0	0	4.6±1.3	0.2±0.1	-
Auriga Main-SMM14	J042117.71+373538.8	0.1	0.9±0.5	9.9±2.3	23±12	0.03	0	0	1.5±0.4	0.6±0.3	-
Auriga CN-SMM1	J041041.40+380753.3	2.1	5.2±1.3	16.2±1.8	139±34	0.05	0	8	5.5±0.6	1.0±0.3	-
Auriga CN-SMM2	J041045.73+380438.3	0.6	1.7±0.5	15.0±2.0	18±5	0.08	0	16	4.1±0.5	0.4±0.1	-
Auriga CN-SMM3	J041049.28+380438.3	0.6	1.6±0.5	15.0±2.0	17±5	0.06	0	13	3.8±0.5	0.4±0.1	-
Auriga CN-SMM4	J041032.76+380550.2	0.2	0.6±0.2	15.0±2.0	11±4	0.03	0	3	2.5±0.3	0.2±0.1	-

Table A.1: The JCMT GBS Clump Catalogue (JGCC). See Table 8.5 for full description.

ID	Coords. (J2000)	S_{850} (Jy)	Mass ($M_\odot$)	Temp. (K)	N_{H_2} ($\times^{21}$ cm^{-2})	D (pc)	Proto stars	n_{YSO} (pc^{-2})	M_J ($M_\odot$)	M_{850}/M_J	d_{OB} (pc)
Cepheus L1228-SMM1	J205713.11+773543.8	3.7	3.3±0.8	11.1±0.9	183±43	0.12	3	6	2.5±0.2	1.3±0.3	-
Cepheus L1228-SMM2	J205736.32+774319.9	0.4	0.4±0.2	11.1±2.3	26±12	0.05	0	0	1.1±0.2	0.3±0.2	-
Cepheus L1251-SMM1	J223848.61+751131.2	6.6	7.2±1.8	16.1±1.7	96±24	0.16	4	20	6.4±0.7	1.1±0.3	-
Cepheus L1251-SMM2	J223523.57+751705.8	3.7	3.3±1.0	18.2±3.0	86±26	0.12	1	21	6.0±1.0	0.6±0.2	-
Cepheus L1251-SMM3	J223031.21+751408.1	1	1.4±0.3	13.3±1.4	47±11	0.05	1	6	2.4±0.3	0.6±0.2	-
Cepheus L1251-SMM4	J223104.42+751335.7	1.8	2.9±0.9	12.4±1.8	49±16	0.18	0	4	3.5±0.5	0.8±0.3	-
Cepheus L1251-SMM5	J223937.22+751214.9	2	7.9±3.0	8.2±1.2	88±34	0.11	0	10	2.3±0.3	3.4±1.4	-
Cepheus L1251-SMM6	J222944.49+751323.5	1	1.8±0.7	12.1±2.1	33±12	0.08	0	6	2.6±0.5	0.7±0.3	-
Cepheus L1251-SMM7	J223932.35+751054.1	0.6	2.1±1.0	8.8±1.7	79±37	0.06	0	11	1.5±0.3	1.4±0.7	-
Cepheus L1251-SMM8	J223733.48+751135.0	0.2	0.6±0.4	9.6±2.5	37±22	0.04	0	2	1.1±0.3	0.6±0.4	-
Cepheus South-SMM1	J203905.72+680217.8	2.9	4.0±1.3	13.3±1.8	192±64	0.08	0	0	3.5±0.5	1.2±0.4	10.57
Cepheus South-SMM2	J204553.49+675738.3	1.3	1.8±0.7	13.1±2.1	121±43	0.04	0	3	2.3±0.4	0.8±0.3	7.45
Cepheus South-SMM3	J210141.61+681200.3	2.4	1.5±0.6	21.6±5.9	33±14	0.08	0	18	5.0±1.4	0.3±0.2	0.19
Cepheus South-SMM4	J210020.75+681320.2	1.9	2.2±1.0	14.6±3.5	89±39	0.07	2	12	3.1±0.7	0.7±0.4	0.66
Cepheus South-SMM5	J210129.23+681027.3	2.2	1.3±0.6	22.4±7.0	23±11	0.07	0	16	4.9±1.5	0.3±0.1	0.08
Cepheus South-SMM6	J203546.30+675304.8	1.3	1.9±1.0	12.8±3.4	47±24	0.07	0	0	2.7±0.7	0.7±0.4	12.23
Cepheus South-SMM7	J210131.38+681115.3	3.2	3.5±0.9	15.0±2.0	40±10	0.12	1	18	4.0±0.5	0.9±0.3	0.13
Cepheus South-SMM8	J210017.01+681247.1	1.7	1.8±0.5	15.0±2.0	28±8	0.1	0	10	3.5±0.5	0.5±0.2	0.67
Cepheus South-SMM9	J210221.43+675417.9	0.4	0.4±0.1	15.0±2.0	18±6	0.04	1	9	2.0±0.3	0.2±0.1	1.34
Cepheus South-SMM10	J210226.75+675417.8	0.5	0.5±0.2	15.0±2.0	15±5	0.04	0	9	2.1±0.3	0.2±0.1	1.36
Cepheus South-SMM11	J210216.54+680918.0	0.8	0.8±0.3	15.0±2.0	17±5	0.08	0	8	2.6±0.3	0.3±0.1	0.31
Cepheus South-SMM12	J203556.86+675408.3	0.4	0.4±0.1	15.0±2.0	12±4	0.07	0	0	2.1±0.3	0.2±0.1	12.13
CrA-SMM1	J190156.27-365729.5	17.1	2.7±0.4	19.2±1.2	228±35	0.14	3	10	3.1±0.2	0.9±0.1	0.02
CrA-SMM2	J190155.27-365744.5	23.9	2.4±0.4	25.7±1.8	121±19	0.14	0	10	4.6±0.3	0.5±0.1	0.02
CrA-SMM3	J191020.25-370826.1	3.3	2.9±0.5	7.6±0.2	691±116	0.07	0	0	0.9±0.0	3.1±0.5	3.84
CrA-SMM4	J190158.78-365708.5	6.1	1.6±0.3	14.3±1.1	331±61	0.1	1	10	1.9±0.2	0.8±0.2	0.04
CrA-SMM5	J190141.76-365832.6	1.9	0.7±0.2	11.5±0.8	335±72	0.03	1	10	1.0±0.1	0.7±0.2	0.11
CrA-SMM6	J190150.77-365808.5	2.8	0.5±0.1	20.3±2.0	184±34	0.05	1	11	1.8±0.2	0.3±0.1	0.05
CrA-SMM7	J190148.51-365714.6	7.1	0.7±0.1	27.3±3.9	64±14	0.12	2	11	3.8±0.5	0.2±0.0	0.04
CrA-SMM8	J190258.78-370736.8	2.2	0.5±0.1	14.5±1.6	106±26	0.07	2	3	1.5±0.2	0.3±0.1	0.63
CrA-SMM9	J190146.51-365532.6	9.4	1.6±0.4	18.0±2.1	70±15	0.17	0	10	3.3±0.4	0.5±0.1	0.08
CrA-SMM10	J190147.26-365635.6	7.3	0.9±0.2	22.7±3.2	51±11	0.13	0	10	3.3±0.5	0.3±0.1	0.05
CrA-SMM11	J190150.51-365635.5	1.6	0.1±0.0	32.2±7.5	19±6	0.07	0	10	2.7±0.6	0.0±0.0	0.03
CrA-SMM12	J190138.25-365323.6	2.3	0.3±0.2	19.1±5.5	17±8	0.15	0	6	2.6±0.8	0.1±0.1	0.18
CrA-SMM13	J190218.34-370132.1	0.8	0.2±0.1	12.9±3.0	22±10	0.08	0	4	1.2±0.3	0.2±0.1	0.25
CrA-SMM14	J190134.50-365338.6	0.7	0.2±0.1	12.1±2.7	22±10	0.07	0	6	1.0±0.2	0.2±0.1	0.2
CrA-SMM15	J190153.28-370035.5	0.5	0.1±0.0	15.0±2.0	12±4	0.08	0	8	1.1±0.2	0.1±0.0	0.13
IC5146-SMM1	J214722.84+473212.0	9.7	83.1±21.3	18.5±2.4	48±12	0.19	3	50	30.7±4.0	2.7±0.8	17.7
IC5146-SMM2	J214508.22+473306.3	0.7	7.6±2.1	16.5±2.2	52±14	0.02	1	35	8.4±1.1	0.9±0.3	23.88
IC5146-SMM3	J214452.16+474031.8	1.5	20.8±5.6	13.9±1.7	55±15	0.08	2	67	10.7±1.3	1.9±0.6	25.07
IC5146-SMM4	J214759.11+473625.1	0.7	6.0±1.9	18.3±3.2	25±8	0.04	1	35	9.9±1.7	0.6±0.2	16.42
IC5146-SMM5	J215336.70+471903.2	0.9	9.4±3.0	16.1±2.7	42±13	0.05	1	53	9.9±1.6	1.0±0.3	0.92
IC5146-SMM6	J215337.58+471948.2	1.6	18.1±5.3	15.2±2.3	36±11	0.09	1	35	11.7±1.8	1.5±0.5	1.12
IC5146-SMM7	J214924.26+472851.1	1	12.4±3.8	14.2±2.2	39±12	0.07	0	0	9.1±1.4	1.4±0.5	11.99
IC5146-SMM8	J215333.17+471415.2	1.2	18.4±5.8	12.7±1.8	39±12	0.08	1	92	9.3±1.4	2.0±0.7	0.52
IC5146-SMM9	J214724.75+473103.4	0.5	6.1±2.5	15.3±3.4	21±9	0.05	0	4	7.9±1.7	0.8±0.4	17.54

Table A.1: The JCMT GBS Clump Catalogue (JGCC). See Table 8.5 for full description.

ID	Coords. (J2000)	S_{850} (Jy)	Mass ($M_\odot$)	Temp. (K)	N_{H_2} ($\times^{21}$ cm^{-2})	D (pc)	Proto stars	n_{YSO} (pc^{-2})	M_J ($M_\odot$)	M_{850}/M_J	d_{OB} (pc)
IC5146-SMM10	J214730.26+473201.5	0.6	6.6±2.6	15.9±3.4	18±7	0.06	1	57	8.7±1.9	0.8±0.3	17.35
IC5146-SMM11	J215312.55+471457.0	1.9	31.9±10.0	12.4±1.9	39±12	0.11	0	12	10.9±1.7	2.9±1.0	0.82
IC5146-SMM12	J214722.66+473342.0	0.6	9.5±4.1	12.5±2.5	25±11	0.06	0	2	7.5±1.5	1.3±0.6	17.81
IC5146-SMM13	J215350.85+471345.2	1.4	11.8±4.4	18.9±4.3	22±8	0.09	1	27	14.8±3.3	0.8±0.3	1.2
IC5146-SMM14	J215354.67+471321.2	1	8.6±3.0	18.8±4.0	22±8	0.07	0	5	11.9±2.5	0.7±0.3	1.41
IC5146-SMM15	J214934.15+472713.4	1.2	16.2±6.7	13.6±2.9	29±12	0.13	0	0	10.6±2.2	1.5±0.7	11.42
IC5146-SMM16	J215355.85+471354.2	1.2	10.7±4.3	17.9±4.3	20±8	0.09	0	20	13.1±3.2	0.8±0.4	1.39
IC5146-SMM17	J214856.30+473025.9	0.3	6.4±2.4	11.2±1.8	38±14	0.04	0	0	4.8±0.8	1.3±0.5	13.36
IC5146-SMM18	J214706.43+473305.6	0.9	10.5±3.3	15.0±2.0	14±4	0.1	1	20	11.8±1.6	0.9±0.3	18.5
IC5146-SMM19	J215334.63+472057.2	2.1	23.0±9.0	15.9±3.5	25±10	0.14	1	22	15.8±3.5	1.5±0.7	1.39
IC5146-SMM20	J215314.60+471621.0	1.5	23.4±9.6	12.6±2.6	27±11	0.11	0	0	11.0±2.3	2.1±1.0	0.68
IC5146-SMM21	J214558.75+473601.7	0.6	10.3±4.9	12.3±2.9	24±11	0.08	1	26	7.4±1.7	1.4±0.7	21.76
IC5146-SMM22	J215331.38+472203.2	1	11.7±4.9	15.2±3.5	21±9	0.09	1	24	11.2±2.6	1.0±0.5	1.68
IC5146-SMM23	J214458.18+474003.5	1.5	30.1±12.1	11.0±2.1	32±13	0.11	0	7	9.5±1.8	3.2±1.4	24.76
IC5146-SMM24	J215306.95+471520.9	1.5	24.3±9.9	12.7±2.6	24±10	0.12	1	17	11.2±2.3	2.2±1.0	1.05
IC5146-SMM25	J215335.52+471727.2	1.5	25.9±10.9	12.0±2.4	26±11	0.15	1	28	10.6±2.2	2.4±1.1	0.5
IC5146-SMM26	J214706.21+473935.5	0.6	7.3±2.4	15.0±2.0	12±4	0.1	1	23	10.3±1.4	0.7±0.3	19.03
IC5146-SMM27	J214852.05+473134.3	0.3	3.4±1.0	15.0±2.0	12±3	0.04	0	0	6.4±0.9	0.5±0.2	13.65
IC5146-SMM28	J214535.38+473540.7	0.3	3.2±1.0	15.0±2.0	12±4	0.03	0	6	6.3±0.8	0.5±0.2	22.79
IC5146-SMM29	J215317.81+471939.0	0.5	6.6±3.7	14.5±4.4	12±7	0.07	0	0	8.5±2.6	0.8±0.5	1.14
IC5146-SMM30	J214650.85+473426.1	0.2	1.9±0.7	15.0±2.0	8±3	0.02	0	0	5.5±0.7	0.3±0.1	19.29
IC5146-SMM31	J214531.14+473615.6	0.2	1.9±0.6	15.0±2.0	11±3	0.04	1	30	5.1±0.7	0.4±0.1	23.02
IC5146-SMM32	J215350.55+471233.2	0.3	3.8±2.1	15.4±4.7	10±5	0.06	0	13	7.3±2.2	0.5±0.3	1.39
Lupus-SMM1	J154302.22-340909.2	3.9	0.8±0.2	17.0±1.8	108±26	0.1	1	1	2.6±0.3	0.3±0.1	-
Lupus-SMM2	J154459.64-341707.7	4.4	1.4±0.8	13.1±3.7	38±20	0.19	0	3	2.5±0.7	0.6±0.3	-
Lupus-SMM3	J154513.44-341706.7	0.7	0.2±0.0	15.0±2.0	20±5	0.05	0	3	1.2±0.2	0.1±0.0	-
Lupus-SMM4	J154516.58-341703.5	0.6	0.2±0.0	15.0±2.0	16±5	0.06	0	3	1.2±0.2	0.1±0.0	-
Lupus-SMM5	J154254.00-340803.3	3.6	0.9±0.3	15.0±2.0	14±4	0.23	0	1	3.3±0.4	0.3±0.1	-
Lupus-SMM6	J154529.38-342335.4	0.1	0.0±0.0	15.0±2.0	14±4	0.11	0	2	0.7±0.1	0.1±0.0	-
Lupus-SMM7	J154525.99-342341.7	0.2	0.0±0.0	15.0±2.0	12±4	0.03	0	2	0.7±0.1	0.1±0.0	-
OphSco L1688-SMM1	J162627.70-242400.2	78.5	10.1±2.6	23.7±3.5	338±88	0.3	2	12	9.2±1.4	1.1±0.3	0.06
OphSco L1688-SMM2	J162626.60-242430.2	8.3	1.3±0.3	21.4±2.5	308±69	0.07	1	14	2.5±0.3	0.5±0.1	0.08
OphSco L1688-SMM3	J162727.67-242712.4	8.1	1.8±0.6	16.4±3.1	80±25	0.12	1	12	2.2±0.4	0.8±0.3	1.14
OphSco L1688-SMM4	J162621.78-242251.2	5.7	1.2±0.5	16.7±3.7	94±35	0.14	1	13	2.7±0.6	0.4±0.2	0.12
OphSco L1688-SMM5	J162728.98-242639.4	3.1	1.0±0.3	13.1±2.1	96±28	0.07	0	11	1.2±0.2	0.8±0.3	1.15
OphSco L1688-SMM6	J162725.47-242657.4	10	2.8±0.9	14.2±2.6	77±26	0.17	1	13	2.7±0.5	1.0±0.4	1.12
OphSco L1688-SMM7	J162732.94-242627.3	14.7	4.5±1.6	13.5±2.5	91±32	0.21	0	10	3.4±0.6	1.3±0.5	1.19
OphSco L1688-SMM8	J162729.65-242742.4	2.5	0.4±0.2	20.0±5.5	43±18	0.07	2	12	1.9±0.5	0.2±0.1	1.15
OphSco L1688-SMM9	J162658.88-243415.5	21.2	7.3±2.6	12.6±2.3	92±32	0.27	1	10	4.1±0.7	1.8±0.7	0.91
OphSco L1688-SMM10	J162726.83-244051.4	10.6	2.1±1.0	17.7±5.3	56±27	0.23	2	13	4.4±1.3	0.5±0.3	1.24
OphSco L1688-SMM11	J162712.73-242951.5	7.7	1.8±0.8	15.5±4.1	50±23	0.17	0	13	3.1±0.8	0.6±0.3	1
OphSco L1688-SMM12	J162623.98-242200.2	3	0.8±0.2	15.0±2.0	43±12	0.16	0	10	2.1±0.3	0.4±0.1	0.11
OphSco L1688-SMM13	J162714.93-243036.5	6.7	1.7±0.8	14.9±3.9	51±24	0.16	2	9	2.9±0.8	0.6±0.3	1.02
OphSco L1688-SMM14	J162643.75-241730.4	2.6	0.6±0.3	16.2±4.6	40±19	0.09	0	13	2.1±0.6	0.3±0.2	0.26
OphSco L1688-SMM15	J162721.55-244000.4	4.9	1.0±0.5	17.0±5.3	36±18	0.14	1	4	2.9±0.9	0.3±0.2	1.18
OphSco L1688-SMM16	J162720.42-242709.4	4.2	1.1±0.6	14.7±4.4	37±19	0.16	0	13	2.5±0.7	0.4±0.3	1.07

Table A.1: The JCMT GBS Clump Catalogue (JGCC). See Table 8.5 for full description.

ID	Coords. (J2000)	S_{850} (Jy)	Mass ($M_\odot$)	Temp. (K)	N_{H_2} ($\times^{21}$ cm^{-2})	D (pc)	Proto stars	n_{YSO} (pc^{-2})	M_J ($M_\odot$)	M_{850}/M_J	d_{OB} (pc)
OphSco L1688-SMM17	J162709.44-243721.5	1.2	0.2±0.1	17.1±5.5	32±17	0.06	1	14	1.6±0.5	0.2±0.1	1.04
OphSco L1688-SMM18	J162758.69-243338.9	3.6	1.3±0.7	12.2±3.2	50±25	0.13	0	5	1.9±0.5	0.7±0.4	1.44
OphSco L1688-SMM19	J162608.18-242023.9	3.5	0.9±0.2	15.0±2.0	27±7	0.15	0	13	2.5±0.3	0.4±0.1	0.27
OphSco L1688-SMM20	J162610.16-241944.9	3.1	0.8±0.2	15.0±2.0	27±7	0.15	0	12	2.3±0.3	0.3±0.1	0.54
OphSco L1688-SMM21	J162705.04-243915.5	2.9	1.0±0.5	12.8±3.5	45±23	0.12	0	7	1.8±0.5	0.5±0.3	1.03
OphSco L1688-SMM22	J162821.37-243626.2	1.3	0.3±0.2	15.3±5.0	29±16	0.08	1	3	1.6±0.5	0.2±0.1	1.66
OphSco L1688-SMM23	J162728.15-243933.4	0.7	0.2±0.0	15.0±2.0	30±8	0.05	1	13	1.1±0.1	0.2±0.0	1.23
OphSco L1688-SMM24	J162632.75-242612.3	2.2	0.5±0.1	15.0±2.0	24±7	0.12	0	11	2.0±0.3	0.3±0.1	0.11
OphSco L1688-SMM25	J162705.04-243630.5	0.9	0.2±0.1	15.0±2.0	25±7	0.07	1	12	1.4±0.2	0.2±0.1	0.99
OphSco L1688-SMM26	J162610.36-242311.9	0.6	0.1±0.0	15.0±2.0	21±6	0.05	0	1	1.1±0.1	0.1±0.0	0.22
OphSco L1688-SMM27	J162858.53-242051.8	3.2	0.8±0.2	15.0±2.0	25±7	0.12	0	11	2.3±0.3	0.3±0.1	1.99
OphSco L1688-SMM28	J162657.56-243139.5	3.3	0.8±0.2	15.0±2.0	22±6	0.18	0	11	2.7±0.4	0.3±0.1	0.87
OphSco L1688-SMM29	J162828.66-241917.0	1.3	0.3±0.1	15.0±2.0	21±6	0.08	0	1	1.6±0.2	0.2±0.1	1.73
OphSco L1688-SMM30	J162614.96-242506.0	2.2	0.5±0.2	15.0±2.0	19±5	0.14	0	13	2.2±0.3	0.3±0.1	0.19
OphSco L1688-SMM31	J162635.85-241751.4	1.6	0.4±0.1	15.0±2.0	19±5	0.1	0	14	1.8±0.2	0.2±0.1	0.23
OphSco L1688-SMM32	J162717.78-242854.5	0.5	0.1±0.0	15.0±2.0	17±5	0.07	2	5	1.1±0.1	0.1±0.0	1.04
OphSco L1688-SMM33	J162711.86-243803.5	0.4	0.1±0.0	15.0±2.0	19±5	0.03	0	13	1.0±0.1	0.1±0.0	1.07
OphSco L1688-SMM34	J162710.98-243933.5	0.9	0.2±0.1	15.0±2.0	18±5	0.07	0	12	1.4±0.2	0.2±0.1	1.09
OphSco L1688-SMM35	J162710.31-242742.5	1.4	0.4±0.1	15.0±2.0	16±4	0.13	0	9	1.8±0.2	0.2±0.1	0.98
OphSco L1688-SMM37	J162830.19-241853.0	1.6	0.4±0.1	15.0±2.0	17±5	0.12	0	13	1.8±0.2	0.2±0.1	1.75
OphSco L1688-SMM36	J162612.11-242448.0	0.4	0.1±0.0	15.0±2.0	16±4	0.03	0	10	0.9±0.1	0.1±0.0	0.21
OphSco L1688-SMM38	J162647.02-242918.4	1.8	0.4±0.1	15.0±2.0	16±4	0.12	0	11	2.1±0.3	0.2±0.1	0.76
OphSco L1688-SMM39	J162642.85-242615.4	0.2	0.1±0.0	15.0±2.0	14±4	0.03	0	4	0.8±0.1	0.1±0.0	0.14
OphSco L1688-SMM40	J162738.73-244245.2	1	0.3±0.1	15.0±2.0	15±4	0.12	1	11	1.6±0.2	0.2±0.1	1.37
OphSco L1688-SMM41	J162557.22-241850.6	0.8	0.2±0.1	15.0±2.0	12±4	0.09	0	5	1.6±0.2	0.1±0.0	0.39
OphSco L1688-SMM42	J162614.32-242245.0	0.1	0.0±0.0	15.0±2.0	11±4	0.02	0	27	0.7±0.1	0.1±0.0	0.18
OphSco L1688-SMM43	J162705.04-243257.5	0.3	0.1±0.0	15.0±2.0	12±4	0.04	0	2	0.9±0.1	0.1±0.0	0.95
OphSco L1688-SMM44	J162658.44-243757.5	0.2	0.1±0.0	15.0±2.0	11±3	0.02	0	16	0.8±0.1	0.1±0.0	0.96
OphSco L1689-SMM1	J163222.97-242836.5	46.5	8.6±2.8	19.3±2.3	1834±591	0.18	1	1	5.8±0.7	1.5±0.5	-
OphSco L1689-SMM2	J163229.14-242908.7	31.4	6.8±2.3	16.6±2.9	149±51	0.28	0	1	5.8±1.0	1.2±0.5	-
OphSco L1689-SMM3	J163135.85-240130.6	2.5	1.6±0.5	9.1±1.0	259±85	0.1	1	4	1.2±0.1	1.4±0.5	-
OphSco L1689-SMM4	J163138.94-244956.7	17.4	3.2±1.6	18.2±5.6	37±19	0.25	0	1	5.4±1.7	0.6±0.3	-
OphSco L1689-SMM5	J163157.08-245718.5	4.9	1.5±0.8	13.2±3.7	42±23	0.19	0	5	2.5±0.7	0.6±0.4	-
OphSco L1689-SMM6	J163153.50-245601.0	2.2	0.6±0.2	15.0±2.0	30±9	0.1	1	5	1.9±0.2	0.3±0.1	-
OphSco L1689-SMM7	J163152.18-245616.1	0.7	0.2±0.0	15.0±2.0	27±8	0.03	1	5	1.0±0.1	0.2±0.1	-
OphSco L1689-SMM8	J163447.40-243758.0	3.1	0.8±0.2	15.0±2.0	22±7	0.13	0	0	2.5±0.3	0.3±0.1	-
OphSco L1689-SMM9	J163229.67-235551.1	1.5	0.4±0.1	15.0±2.0	20±7	0.09	0	0	1.7±0.2	0.2±0.1	-
OphSco L1689-SMM10	J163143.26-240026.8	1.4	0.4±0.1	15.0±2.0	20±7	0.1	0	3	1.7±0.2	0.2±0.1	-
OphSco L1689-SMM11	J163244.20-235310.2	2.9	0.7±0.2	15.0±2.0	19±6	0.15	0	0	2.5±0.3	0.3±0.1	-
OphSco L1689-SMM12	J163249.41-235224.5	0.9	0.2±0.1	15.0±2.0	17±5	0.08	0	0	1.4±0.2	0.2±0.1	-
OphSco L1689-SMM13	J163200.33-245551.1	0.7	0.2±0.1	15.0±2.0	19±6	0.08	0	5	1.2±0.2	0.1±0.1	-
OphSco L1689-SMM14	J163212.69-242943.8	0.7	0.2±0.1	15.0±2.0	15±5	0.08	0	1	1.3±0.2	0.1±0.0	-
OphSco L1689-SMM15	J163143.67-235953.7	0.9	0.2±0.1	15.0±2.0	15±5	0.15	0	2	1.6±0.2	0.1±0.1	-
OphSco L1689-SMM16	J163146.91-245058.8	1.2	0.3±0.1	15.0±2.0	16±5	0.1	0	2	1.6±0.2	0.2±0.1	-
OphSco L1689-SMM17	J163133.07-240318.8	1.1	0.3±0.1	15.0±2.0	14±5	0.11	1	4	1.7±0.2	0.2±0.1	-
OphSco L1689-SMM18	J163146.23-245619.8	0.6	0.2±0.1	15.0±2.0	14±5	0.09	0	5	1.3±0.2	0.1±0.0	-

Table A.1: The JCMT GBS Clump Catalogue (JGCC). See Table 8.5 for full description.

ID	Coords. (J2000)	S_{850} (Jy)	Mass ($M_\odot$)	Temp. (K)	N_{H_2} ($\times^{21}$ cm^{-2})	D (pc)	Proto stars	n_{YSO} (pc^{-2})	M_J ($M_\odot$)	M_{850}/M_J	d_{OB} (pc)
OphSco L1689-SMM19	J163202.85-244723.9	0.5	0.1±0.1	15.0±2.0	11±4	0.1	0	1	1.3±0.2	0.1±0.0	-
OphSco L1689-SMM20	J163206.57-244644.4	0.1	0.0±0.0	15.0±2.0	9±4	0.04	0	0	0.5±0.1	0.0±0.0	-
OrionB N2023-SMM1	J054143.11-015424.3	11.2	7.3±1.0	41.9±3.2	215±31	0.07	9	225	13.4±1.0	0.5±0.1	0.07
OrionB N2023-SMM2	J054144.51-015539.3	19.2	19.1±3.3	30.9±2.4	388±67	0.17	5	133	16.1±1.3	1.2±0.2	0.15
OrionB N2023-SMM3	J054145.32-015603.3	13.3	8.3±1.5	40.3±4.1	167±31	0.13	4	113	19.7±2.0	0.4±0.1	0.19
OrionB N2023-SMM4	J054144.31-015448.3	6.2	7.0±0.8	28.1±1.8	179±20	0.06	3	194	6.9±0.4	1.0±0.1	0.05
OrionB N2023-SMM5	J054125.11-021806.3	6.3	14.9±2.5	16.2±1.2	552±94	0.07	1	32	6.6±0.5	2.3±0.4	2.92
OrionB N2023-SMM6	J054141.71-015351.3	6.6	4.7±1.0	35.9±4.2	79±17	0.13	6	225	17.2±2.0	0.3±0.1	0.14
OrionB N2023-SMM7	J054137.32-021718.3	9.5	15.1±3.6	21.1±3.0	307±74	0.17	2	30	13.4±1.9	1.1±0.3	2.77
OrionB N2023-SMM8	J054126.51-021818.3	5.6	7.2±1.6	22.0±2.8	94±21	0.12	1	24	10.2±1.3	0.7±0.2	2.93
OrionB N2023-SMM9	J054227.71-012000.6	1.3	4.3±0.9	12.4±0.9	123±25	0.06	1	6	3.6±0.3	1.2±0.3	4.35
OrionB N2023-SMM10	J054202.73-020745.3	1.4	2.6±0.6	17.0±2.0	87±21	0.04	1	6	4.8±0.6	0.5±0.1	1.68
OrionB N2023-SMM11	J054129.71-022118.3	3.7	6.9±1.6	17.4±2.3	134±32	0.11	0	4	7.6±1.0	0.9±0.2	3.27
OrionB N2023-SMM12	J054140.72-021709.3	10.7	10.5±2.4	26.5±3.9	47±11	0.17	1	43	14.8±2.2	0.7±0.2	2.74
OrionB N2023-SMM13	J054203.13-020236.3	1.3	1.3±0.3	26.0±4.0	49±12	0.04	0	5	6.6±1.0	0.2±0.1	1.12
OrionB N2023-SMM14	J054145.72-015430.3	1.6	7.3±1.6	10.7±0.9	285±62	0.07	1	161	3.1±0.3	2.4±0.6	0.01
OrionB N2023-SMM15	J054138.72-021745.3	3.8	4.1±1.0	24.5±3.7	32±7	0.1	0	28	9.0±1.4	0.5±0.1	2.82
OrionB N2023-SMM16	J054149.72-015742.3	2.7	1.9±0.6	34.2±8.1	19±6	0.14	0	94	13.4±3.2	0.1±0.1	0.41
OrionB N2023-SMM17	J054141.92-021615.3	6.4	6.3±1.7	27.0±5.0	42±12	0.16	6	41	14.8±2.7	0.4±0.1	2.63
OrionB N2023-SMM18	J054113.10-014745.3	2	2.6±0.7	21.2±3.4	27±7	0.07	0	13	6.6±1.1	0.4±0.1	1.27
OrionB N2023-SMM19	J054126.70-014451.4	1.2	1.6±0.5	20.2±3.4	31±9	0.07	0	16	5.9±1.0	0.3±0.1	1.29
OrionB N2023-SMM20	J054125.91-021933.3	2.4	3.1±0.8	22.1±3.9	32±9	0.08	0	16	7.6±1.4	0.4±0.1	3.08
OrionB N2023-SMM21	J054144.31-015248.3	2.3	2.1±0.8	28.2±7.1	17±6	0.15	2	145	11.9±3.0	0.2±0.1	0.21
OrionB N2023-SMM22	J054144.12-021706.3	3.3	3.4±1.0	25.2±5.1	25±8	0.11	1	44	10.5±2.1	0.3±0.1	2.73
OrionB N2023-SMM23	J054128.71-022006.3	3.4	4.7±1.3	20.9±3.6	33±9	0.12	0	6	8.6±1.5	0.5±0.2	3.13
OrionB N2023-SMM24	J054125.51-021603.3	5.3	6.2±1.9	23.2±4.7	29±9	0.15	1	18	12.3±2.5	0.5±0.2	2.67
OrionB N2023-SMM25	J054058.69-020842.3	5.9	10.9±3.0	16.9±2.6	36±10	0.19	0	1	10.5±1.6	1.0±0.3	2.22
OrionB N2023-SMM26	J054107.09-022721.3	2.2	5.3±1.3	14.5±1.7	53±13	0.11	0	7	5.7±0.7	0.9±0.3	4.13
OrionB N2023-SMM27	J054111.70-014812.3	1	1.3±0.4	21.3±3.8	31±9	0.05	0	8	4.9±0.9	0.3±0.1	1.27
OrionB N2023-SMM28	J054125.11-021721.3	3.3	4.1±1.2	22.2±4.1	25±7	0.13	1	30	9.3±1.7	0.4±0.1	2.83
OrionB N2023-SMM29	J054230.91-012048.6	1.2	5.3±1.5	10.2±1.1	58±16	0.09	0	4	3.3±0.4	1.6±0.5	4.29
OrionB N2023-SMM30	J054136.71-014927.3	1	1.0±0.4	26.8±7.3	16±6	0.08	1	45	7.4±2.0	0.1±0.1	0.66
OrionB N2023-SMM31	J054141.51-015636.3	1.3	1.2±0.4	27.2±7.1	13±5	0.09	2	98	8.1±2.1	0.1±0.1	0.28
OrionB N2023-SMM32	J054139.71-013557.4	1.3	2.2±0.8	17.5±3.5	23±8	0.1	0	0	5.8±1.2	0.4±0.2	2.24
OrionB N2023-SMM33	J054140.71-015518.3	0.7	0.7±0.3	25.1±6.4	15±6	0.05	1	183	5.8±1.5	0.1±0.1	0.18
OrionB N2023-SMM34	J054136.31-013745.4	0.5	0.9±0.3	16.6±3.1	20±7	0.08	0	5	3.7±0.7	0.2±0.1	2.04
OrionB N2023-SMM35	J054123.90-015048.3	0.8	1.6±0.5	16.6±3.1	22±7	0.08	0	27	4.8±0.9	0.3±0.1	0.79
OrionB N2023-SMM36	J054053.68-022703.3	1.6	3.3±1.0	16.0±2.8	29±9	0.09	2	12	5.3±0.9	0.6±0.2	4.23
OrionB N2023-SMM37	J054149.32-015942.3	0.5	0.4±0.2	28.2±8.4	10±4	0.03	1	48	5.6±1.7	0.1±0.0	0.64
OrionB N2023-SMM38	J054122.50-014254.4	0.8	1.0±0.4	21.9±5.7	14±6	0.06	0	17	5.8±1.5	0.2±0.1	1.56
OrionB N2023-SMM39	J054129.71-022321.3	0.6	1.2±0.4	15.6±2.7	31±10	0.05	1	8	3.3±0.6	0.4±0.1	3.52
OrionB N2023-SMM40	J054136.31-015627.3	2.6	3.1±1.3	22.8±6.4	14±6	0.14	2	69	10.7±3.0	0.3±0.1	0.37
OrionB N2023-SMM41	J054130.91-021903.3	1.8	3.6±1.1	16.2±2.8	31±9	0.09	0	13	5.6±1.0	0.6±0.2	3
OrionB N2023-SMM42	J054054.28-022754.3	2.5	4.8±1.5	16.5±2.9	32±10	0.13	0	6	6.8±1.2	0.7±0.3	4.32
OrionB N2023-SMM43	J054138.51-013621.4	0.5	0.9±0.3	16.5±3.5	16±6	0.04	0	1	3.4±0.7	0.3±0.1	2.2
OrionB N2023-SMM44	J054058.49-020727.3	0.9	1.9±0.5	15.0±2.0	21±6	0.07	0	1	4.0±0.5	0.5±0.1	2.11
OrionB N2023-SMM45	J054128.11-022057.3	1.7	2.5±0.8	19.3±4.0	19±6	0.1	0	4	6.5±1.4	0.4±0.2	3.24

Table A.1: The JCMT GBS Clump Catalogue (JGCC). See Table 8.5 for full description.

ID	Coords. (J2000)	S_{850} (Jy)	Mass ($M_\odot$)	Temp. (K)	N_{H_2} ($\times^{21}$ cm^{-2})	D (pc)	Proto stars	n_{YSO} (pc^{-2})	M_J ($M_\odot$)	M_{850}/M_J	d_{OB} (pc)
OrionB N2023-SMM46	J054133.51-022054.3	0.5	1.0±0.3	15.6±2.6	27±8	0.02	0	1	3.0±0.5	0.3±0.1	3.21
OrionB N2023-SMM47	J054135.51-015127.3	0.8	1.8±0.5	15.0±2.0	17±5	0.07	0	91	4.2±0.6	0.4±0.1	0.47
OrionB N2023-SMM48	J054137.71-015554.3	1.4	2.6±1.0	16.4±3.4	18±7	0.11	2	142	6.0±1.2	0.4±0.2	0.29
OrionB N2023-SMM49	J054133.51-015000.3	0.7	1.7±0.5	15.0±2.0	17±5	0.07	0	36	4.0±0.5	0.4±0.1	0.65
OrionB N2023-SMM50	J054124.30-014436.4	0.5	0.8±0.3	20.2±5.1	12±5	0.05	0	16	4.4±1.1	0.2±0.1	1.35
OrionB N2023-SMM51	J054121.50-014200.4	0.4	0.8±0.3	16.1±3.4	16±6	0.03	0	11	3.1±0.7	0.3±0.1	1.67
OrionB N2023-SMM52	J054138.11-015057.3	0.5	1.1±0.3	15.0±2.0	16±4	0.05	1	78	3.4±0.5	0.3±0.1	0.48
OrionB N2023-SMM53	J054129.11-022354.3	1.4	2.2±0.8	18.7±4.6	21±8	0.1	0	6	6.1±1.5	0.4±0.2	3.59
OrionB N2023-SMM54	J054113.90-014700.4	0.3	0.6±0.2	17.3±3.7	19±7	0.02	1	15	2.9±0.6	0.2±0.1	1.31
OrionB N2023-SMM55	J054141.51-015809.3	0.4	0.9±0.2	15.0±2.0	16±4	0.04	1	63	3.0±0.4	0.3±0.1	0.46
OrionB N2023-SMM56	J054111.50-014603.4	0.8	1.2±0.5	20.4±5.3	14±6	0.09	0	11	5.4±1.4	0.2±0.1	1.44
OrionB N2023-SMM57	J054305.31-011839.5	0.5	1.1±0.3	15.0±2.0	14±4	0.1	0	1	3.8±0.5	0.3±0.1	4.95
OrionB N2023-SMM58	J054123.10-014339.4	0.3	0.6±0.2	15.0±2.0	15±4	0.03	0	17	2.6±0.3	0.2±0.1	1.47
OrionB N2023-SMM59	J054233.11-012536.5	0.4	0.8±0.2	15.0±2.0	14±4	0.04	0	0	3.1±0.4	0.3±0.1	3.77
OrionB N2023-SMM60	J054124.31-022857.3	0.3	0.7±0.2	15.0±2.0	16±4	0.04	0	0	2.6±0.4	0.3±0.1	4.21
OrionB N2023-SMM61	J054153.92-020024.3	0.5	1.2±0.3	15.0±2.0	14±4	0.08	0	32	3.6±0.5	0.3±0.1	0.76
OrionB N2023-SMM62	J054135.12-023015.3	0.8	1.8±0.5	15.0±2.0	16±4	0.08	0	0	4.1±0.5	0.4±0.1	4.33
OrionB N2023-SMM63	J054131.71-022615.3	0.9	2.0±0.6	15.0±2.0	15±4	0.09	0	0	4.7±0.6	0.4±0.1	3.86
OrionB N2023-SMM64	J054131.71-022500.3	0.9	2.1±0.6	15.0±2.0	15±4	0.11	0	1	4.5±0.6	0.5±0.1	3.71
OrionB N2023-SMM65	J054121.90-014512.4	0.3	0.7±0.2	15.0±2.0	12±3	0.04	0	18	2.9±0.4	0.2±0.1	1.33
OrionB N2023-SMM66	J054112.50-014400.4	0.2	0.5±0.1	15.0±2.0	13±4	0.03	0	7	2.4±0.3	0.2±0.1	1.61
OrionB N2023-SMM67	J054109.90-015803.3	0.3	0.6±0.2	15.0±2.0	12±3	0.03	0	7	2.7±0.4	0.2±0.1	1.16
OrionB N2023-SMM68	J054130.31-015718.3	0.2	0.4±0.1	15.0±2.0	9±3	0.04	0	17	2.5±0.3	0.2±0.1	0.57
OrionB N2023-SMM69	J054126.10-015209.3	0.1	0.3±0.1	15.0±2.0	9±3	0.04	0	50	2.3±0.3	0.1±0.0	0.65
OrionB N2023-SMM70	J054154.93-020800.3	0.3	0.7±0.2	15.0±2.0	9±3	0.08	0	1	3.3±0.4	0.2±0.1	1.66
OrionB N2023-SMM71	J054204.13-020421.3	0.2	0.4±0.1	15.0±2.0	8±3	0.04	0	3	2.4±0.3	0.2±0.1	1.32
OrionB N2068-SMM1	J054705.00+002145.1	46.1	79.3±13.4	19.0±1.1	792±134	0.22	6	66	17.8±1.0	4.5±0.8	2.07
OrionB N2068-SMM2	J054608.61-001044.6	4.9	21.6±4.3	11.5±0.8	970±193	0.06	1	25	5.0±0.3	4.4±0.9	2.23
OrionB N2068-SMM3	J054725.00+002057.1	7.9	16.4±4.2	16.5±2.0	244±63	0.2	4	40	10.9±1.3	1.5±0.4	2.24
OrionB N2068-SMM4	J054607.41-001335.5	7.4	12.8±2.7	19.4±1.9	145±30	0.12	1	18	9.8±1.0	1.3±0.3	2.55
OrionB N2068-SMM5	J054631.21-000235.7	3.7	11.3±2.2	12.7±0.8	239±46	0.08	0	0	4.8±0.3	2.4±0.5	1.05
OrionB N2068-SMM6	J054628.01-000053.7	4.4	13.8±2.5	12.8±1.0	291±53	0.1	0	4	5.4±0.4	2.6±0.5	0.91
OrionB N2068-SMM7	J054647.60+000027.2	7.1	11.1±2.9	20.1±2.9	140±36	0.22	2	33	11.9±1.7	0.9±0.3	0.6
OrionB N2068-SMM8	J054710.80+002112.1	2	3.6±0.9	18.2±2.1	109±27	0.06	1	74	6.0±0.7	0.6±0.2	2.07
OrionB N2068-SMM9	J054628.40+001927.1	2.4	9.3±1.7	11.5±0.8	264±48	0.06	1	9	3.6±0.2	2.6±0.5	1.77
OrionB N2068-SMM10	J054701.20+002621.1	2.6	9.2±1.9	11.6±0.8	141±29	0.09	1	31	4.3±0.3	2.1±0.5	2.58
OrionB N2068-SMM11	J054608.41-000959.6	2.7	4.7±1.1	18.2±2.2	81±19	0.09	4	35	6.3±0.8	0.8±0.2	2.15
OrionB N2068-SMM12	J054650.00+000203.2	5.7	7.0±1.7	22.8±3.2	45±11	0.14	0	26	11.3±1.6	0.6±0.2	0.43
OrionB N2068-SMM13	J054706.60+002239.1	4.1	14.3±2.6	12.4±1.0	136±25	0.11	2	74	5.0±0.4	2.8±0.6	2.19
OrionB N2068-SMM14	J054610.21-001217.6	1.2	4.4±1.0	11.6±1.1	179±41	0.04	0	11	3.0±0.3	1.5±0.4	2.37
OrionB N2068-SMM15	J054639.60+000112.2	2	3.6±0.8	17.8±2.0	69±16	0.07	1	34	5.4±0.6	0.7±0.2	0.53
OrionB N2068-SMM16	J054638.00+000036.2	3.9	7.4±1.5	17.0±1.8	70±14	0.11	1	27	6.8±0.7	1.1±0.2	0.61
OrionB N2068-SMM17	J054607.81-001153.6	1.8	3.4±0.8	17.9±2.4	76±19	0.06	0	14	5.1±0.7	0.7±0.2	2.36
OrionB N2068-SMM18	J054648.20+000133.2	6.5	7.7±1.8	23.3±3.3	42±10	0.15	2	36	11.9±1.7	0.6±0.2	0.47
OrionB N2068-SMM19	J054807.80+003351.1	0.8	4.0±0.8	9.8±0.6	167±35	0.03	0	8	2.2±0.1	1.8±0.4	4.25
OrionB N2068-SMM20	J054603.81-001450.5	1.1	3.3±0.6	12.7±1.0	98±19	0.05	1	15	3.1±0.2	1.1±0.2	2.74
OrionB N2068-SMM21	J054737.20+002006.1	1.8	2.1±0.6	23.6±4.1	38±11	0.07	1	13	7.2±1.3	0.3±0.1	2.38

Table A.1: The JCMT GBS Clump Catalogue (JGCC). See Table 8.5 for full description.

ID	Coords. (J2000)	S_{850} (Jy)	Mass ($M_\odot$)	Temp. (K)	N_{H_2} ($\times^{21}$ cm^{-2})	D (pc)	Proto stars	n_{YSO} (pc^{-2})	M_J ($M_\odot$)	M_{850}/M_J	d_{OB} (pc)
OrionB N2068-SMM22	J054643.00+000048.2	3.6	4.5±1.1	22.5±3.2	39±9	0.1	1	38	8.6±1.2	0.5±0.1	0.55
OrionB N2068-SMM23	J054608.01-001220.6	1	2.7±0.6	14.1±1.7	109±26	0.04	0	13	3.3±0.4	0.8±0.2	2.41
OrionB N2068-SMM24	J054646.00+000715.2	3.1	4.1±1.1	21.2±3.2	28±8	0.11	0	30	8.9±1.3	0.5±0.1	0.23
OrionB N2068-SMM25	J054606.21-000935.6	2.2	5.9±1.6	14.2±1.9	90±24	0.11	0	31	5.3±0.7	1.1±0.3	2.15
OrionB N2068-SMM26	J054640.80+000033.2	2	3.0±0.6	20.3±2.3	37±7	0.06	0	32	5.3±0.6	0.6±0.1	0.59
OrionB N2068-SMM27	J054732.80+002024.1	1	1.6±0.5	18.9±3.1	47±13	0.04	2	35	4.6±0.8	0.4±0.1	2.32
OrionB N2068-SMM28	J054706.80+001230.2	1.5	3.4±0.9	15.3±2.0	52±13	0.08	0	4	4.7±0.6	0.7±0.2	1.09
OrionB N2068-SMM29	J054627.01+000109.2	2.3	5.3±1.3	15.0±1.8	59±15	0.09	1	16	5.4±0.7	1.0±0.3	0.74
OrionB N2068-SMM30	J054647.20+000724.2	1.3	1.9±0.5	19.8±3.1	29±8	0.06	0	21	5.6±0.9	0.3±0.1	0.26
OrionB N2068-SMM31	J054701.80+001806.1	1.9	4.6±1.2	14.6±1.7	42±11	0.09	1	35	5.4±0.6	0.8±0.2	1.62
OrionB N2068-SMM32	J054702.40+002048.1	2	8.3±1.7	11.4±1.1	107±22	0.09	0	37	3.6±0.3	2.3±0.5	1.94
OrionB N2068-SMM33	J054743.60+003821.1	0.9	3.2±0.8	11.4±1.1	85±20	0.04	0	13	2.8±0.3	1.2±0.3	4.36
OrionB N2068-SMM34	J054745.20+003842.1	0.8	2.6±0.7	12.7±1.6	95±26	0.04	0	11	3.0±0.4	0.9±0.3	4.42
OrionB N2068-SMM35	J054624.41-000002.7	2.7	5.9±1.4	15.3±1.9	45±11	0.11	0	6	6.0±0.7	1.0±0.3	0.9
OrionB N2068-SMM36	J054628.01-000138.7	1.9	5.7±1.1	13.0±1.2	65±13	0.08	0	1	4.0±0.4	1.4±0.3	0.99
OrionB N2068-SMM37	J054629.60+002012.1	2.4	8.3±1.8	12.0±1.1	67±14	0.1	1	11	4.3±0.4	1.9±0.4	1.85
OrionB N2068-SMM38	J054712.80+002221.1	1.1	2.2±0.7	16.2±2.6	44±13	0.07	0	60	4.5±0.7	0.5±0.2	2.22
OrionB N2068-SMM39	J054605.01-001417.5	0.9	2.4±0.5	13.7±1.3	48±10	0.04	1	19	2.9±0.3	0.8±0.2	2.66
OrionB N2068-SMM40	J054716.20+002124.1	1	2.3±0.7	15.4±2.2	34±10	0.07	0	50	4.3±0.6	0.5±0.2	2.16
OrionB N2068-SMM41	J054657.20+002009.1	2.1	23.1±6.5	7.1±0.6	155±44	0.11	0	27	2.8±0.3	8.3±2.5	1.82
OrionB N2068-SMM42	J054633.81-000005.7	0.8	1.4±0.4	18.1±2.9	31±8	0.05	0	16	4.0±0.6	0.4±0.1	0.74
OrionB N2068-SMM43	J054632.41-000041.7	0.6	1.6±0.4	14.3±1.8	44±11	0.04	0	9	2.7±0.3	0.6±0.2	0.82
OrionB N2068-SMM44	J054725.20+003509.1	1.1	5.9±1.4	9.6±0.9	64±15	0.07	0	1	2.8±0.3	2.1±0.5	3.8
OrionB N2068-SMM45	J054726.20+001957.1	0.9	2.4±0.7	14.0±2.0	38±11	0.1	0	51	3.8±0.6	0.6±0.2	2.16
OrionB N2068-SMM46	J054735.40+002021.1	0.5	0.6±0.2	22.9±4.9	17±5	0.03	0	23	4.2±0.9	0.1±0.1	2.37
OrionB N2068-SMM47	J054706.60+002312.1	0.5	1.2±0.3	14.7±2.2	33±10	0.03	0	71	2.8±0.4	0.4±0.1	2.25
OrionB N2068-SMM48	J054712.20+002303.1	1.4	3.6±1.0	14.3±2.1	35±10	0.09	0	45	4.5±0.7	0.8±0.3	2.29
OrionB N2068-SMM49	J054654.80+002254.1	0.7	1.7±0.5	14.5±2.3	31±10	0.07	0	32	3.6±0.6	0.5±0.2	2.14
OrionB N2068-SMM50	J054636.20+000548.2	0.7	1.8±0.6	14.3±2.4	31±10	0.08	0	45	3.9±0.6	0.5±0.2	0.26
OrionB N2068-SMM51	J054655.20+002336.1	2	4.7±1.5	14.5±2.4	34±11	0.12	1	29	5.7±1.0	0.8±0.3	2.22
OrionB N2068-SMM52	J054606.21-001214.6	1	2.3±0.7	15.0±2.4	35±11	0.08	0	11	4.1±0.7	0.6±0.2	2.42
OrionB N2068-SMM53	J054715.60+001842.1	1.4	2.8±1.0	16.5±3.3	23±8	0.1	1	54	5.8±1.1	0.5±0.2	1.86
OrionB N2068-SMM54	J054705.00+001503.1	1.7	2.1±0.8	21.8±5.3	17±7	0.11	0	8	8.2±2.0	0.3±0.1	1.32
OrionB N2068-SMM55	J054657.40+002357.1	0.3	1.0±0.3	13.3±2.3	36±12	0.02	1	37	2.3±0.4	0.4±0.2	2.27
OrionB N2068-SMM56	J054710.80+002330.1	0.8	2.0±0.6	13.8±2.2	43±13	0.06	1	50	3.3±0.5	0.6±0.2	2.33
OrionB N2068-SMM57	J054613.81-000526.7	0.5	1.1±0.4	15.2±2.8	28±10	0.03	0	23	3.0±0.6	0.3±0.1	1.61
OrionB N2068-SMM58	J054659.60+002309.1	0.7	1.2±0.4	18.1±4.0	19±7	0.07	0	50	4.5±1.0	0.3±0.1	2.19
OrionB N2068-SMM59	J054629.20+002109.1	0.5	1.6±0.5	13.2±2.1	38±12	0.04	0	11	2.6±0.4	0.6±0.2	1.96
OrionB N2068-SMM60	J054612.41-000947.6	0.9	2.3±0.8	13.9±2.4	29±10	0.08	0	31	3.8±0.7	0.6±0.2	2.07
OrionB N2068-SMM61	J054632.60+002739.1	0.8	4.5±1.4	9.4±1.2	53±17	0.06	0	8	2.4±0.3	1.9±0.7	2.71
OrionB N2068-SMM62	J054628.40+002142.1	0.4	1.4±0.4	12.0±1.8	44±14	0.04	0	11	2.2±0.3	0.6±0.2	2.03
OrionB N2068-SMM63	J054740.80+004012.1	0.5	1.9±0.7	11.3±2.0	36±13	0.11	0	28	2.6±0.5	0.7±0.3	4.53
OrionB N2068-SMM64	J054758.80+001703.1	0.4	1.2±0.4	13.0±2.4	28±10	0.06	0	0	2.6±0.5	0.5±0.2	2.64
OrionB N2068-SMM65	J054658.40+002430.1	0.4	1.0±0.5	15.0±3.8	18±8	0.05	0	38	3.3±0.8	0.3±0.2	2.35
OrionB N2068-SMM66	J054711.00+001324.2	0.5	0.9±0.4	17.6±4.4	20±8	0.06	0	1	4.2±1.0	0.2±0.1	1.25
OrionB N2068-SMM67	J054759.60+003533.1	0.3	0.8±0.3	14.5±3.0	21±8	0.03	1	15	2.7±0.6	0.3±0.1	4.29
OrionB N2068-SMM68	J054638.00+002706.1	0.6	4.2±1.6	8.5±1.2	68±25	0.06	0	8	2.1±0.3	2.0±0.8	2.63

Table A.1: The JCMT GBS Clump Catalogue (JGCC). See Table 8.5 for full description.

ID	Coords. (J2000)	S_{850} (Jy)	Mass ($M_\odot$)	Temp. (K)	N_{H_2} ($\times^{21}$ cm^{-2})	D (pc)	Proto stars	n_{YSO} (pc^{-2})	M_J ($M_\odot$)	M_{850}/M_J	d_{OB} (pc)
OrionB N2068-SMM69	J054705.00+001700.1	0.4	0.8±0.4	16.6±4.4	16±8	0.04	0	41	3.6±0.9	0.2±0.1	1.53
OrionB N2068-SMM70	J054735.00+003545.1	0.6	1.9±0.8	11.9±2.5	23±10	0.08	0	0	2.9±0.6	0.7±0.3	3.97
OrionB N2068-SMM71	J054709.20+002403.1	0.3	1.8±0.8	8.9±1.5	37±16	0.03	0	45	1.6±0.3	1.2±0.5	2.37
OrionB N2068-SMM72	J054718.40+002242.1	0.6	1.6±0.7	14.2±3.0	22±9	0.11	0	24	3.9±0.8	0.4±0.2	2.33
OrionB N2068-SMM73	J054623.21-001326.6	0.4	1.1±0.4	13.5±3.0	31±13	0.04	0	3	2.7±0.6	0.4±0.2	2.36
OrionB N2068-SMM74	J054712.60+001536.1	0.2	0.4±0.2	16.6±4.0	15±6	0.02	0	11	2.5±0.6	0.2±0.1	1.49
OrionB N2068-SMM75	J054722.40+000657.2	0.5	1.1±0.5	15.6±3.6	16±7	0.06	0	2	3.7±0.8	0.3±0.1	1.15
OrionB N2068-SMM76	J054653.00+002221.1	0.2	0.5±0.3	15.3±4.1	12±6	0.03	0	31	2.6±0.7	0.2±0.1	2.06
OrionB N2068-SMM77	J054710.80+001551.1	0.2	0.4±0.2	17.4±5.0	12±6	0.01	0	18	2.7±0.8	0.1±0.1	1.49
OrionB N2068-SMM78	J054720.20+001606.1	0.2	0.5±0.2	15.1±3.8	19±8	0.01	0	9	2.3±0.6	0.2±0.1	1.68
OrionB N2068-SMM79	J054742.80+003612.1	0.5	2.3±1.0	10.1±1.9	27±12	0.09	0	1	2.4±0.4	1.0±0.4	4.11
OrionB N2068-SMM80	J054651.40+000909.2	0.3	0.6±0.3	14.7±3.2	12±5	0.04	0	5	2.7±0.6	0.2±0.1	0.5
OrionB N2068-SMM81	J054722.80+001539.1	0.3	0.6±0.3	15.7±4.4	12±6	0.04	0	5	3.0±0.8	0.2±0.1	1.69
OrionB N2068-SMM82	J054629.21-001544.5	0.2	1.0±0.4	10.3±1.8	25±10	0.02	0	0	1.7±0.3	0.6±0.3	2.59
OrionB N2068-SMM83	J054717.20+002336.1	0.1	0.4±0.2	14.1±3.8	14±7	0.02	0	19	1.9±0.5	0.2±0.1	2.41
Perseus IC348-SMM1	J034356.95+320050.9	7	7.2±1.5	13.4±1.0	238±49	0.12	2	25	4.2±0.3	1.7±0.4	0.86
Perseus IC348-SMM2	J034357.17+320305.9	5.7	5.7±1.3	13.8±1.4	283±63	0.12	2	29	4.1±0.4	1.4±0.3	0.75
Perseus IC348-SMM3	J034444.12+320136.0	1.3	0.8±0.2	18.2±2.7	71±20	0.05	2	15	3.0±0.4	0.3±0.1	0.61
Perseus IC348-SMM4	J034351.03+320323.8	4.9	3.9±1.1	15.5±2.2	63±17	0.15	1	21	5.0±0.7	0.8±0.2	0.81
Perseus IC348-SMM5	J034401.42+320157.0	2.6	1.8±0.5	17.2±2.6	44±12	0.1	2	33	3.9±0.6	0.5±0.1	0.76
Perseus IC348-SMM6	J034741.67+325144.1	1.3	1.5±0.4	12.1±1.5	50±14	0.09	1	2	2.3±0.3	0.7±0.2	4.19
Perseus IC348-SMM7	J034403.07+320227.0	2.1	1.9±0.5	14.2±1.7	51±12	0.08	0	31	2.8±0.3	0.7±0.2	0.71
Perseus IC348-SMM8	J034739.31+325217.4	1.4	2.4±0.8	10.2±1.5	88±31	0.11	0	2	2.2±0.3	1.1±0.4	4.2
Perseus IC348-SMM9	J034358.35+320405.9	2	1.6±0.5	15.4±2.5	39±12	0.1	0	23	3.4±0.6	0.5±0.2	0.69
Perseus IC348-SMM10	J034406.14+320212.0	2.5	2.3±0.7	14.0±2.0	41±12	0.13	0	30	3.5±0.5	0.7±0.2	0.7
Perseus IC348-SMM11	J034337.82+320308.6	1	1.2±0.3	12.4±1.7	39±11	0.06	0	6	2.1±0.3	0.6±0.2	0.99
Perseus IC348-SMM12	J034436.80+315851.1	0.9	1.2±0.4	11.6±1.5	47±14	0.07	0	12	1.9±0.3	0.6±0.2	0.8
Perseus IC348-SMM13	J034343.96+320256.7	4.1	3.3±1.1	15.2±2.7	29±9	0.16	0	12	4.9±0.9	0.7±0.3	0.92
Perseus IC348-SMM14	J034449.07+320032.9	0.9	1.0±0.3	12.7±2.0	35±12	0.07	0	10	2.1±0.3	0.5±0.2	0.71
Perseus IC348-SMM15	J034358.12+320217.9	0.4	0.3±0.1	15.2±3.0	28±10	0.03	0	33	1.6±0.3	0.2±0.1	0.77
Perseus IC348-SMM16	J034346.80+320150.8	0.7	0.7±0.3	13.7±2.9	19±8	0.09	0	14	2.2±0.5	0.3±0.1	0.93
Perseus IC348-SMM17	J034415.57+320912.1	0.5	0.5±0.2	13.6±3.0	19±8	0.05	0	22	1.8±0.4	0.3±0.1	0.29
Perseus IC348-SMM18	J034436.57+320103.1	0.3	0.4±0.2	11.0±2.3	24±11	0.04	0	23	1.1±0.2	0.4±0.2	0.64
Perseus IC348-SMM19	J034421.48+315921.1	0.6	0.5±0.1	15.0±2.0	13±4	0.1	1	18	2.3±0.3	0.2±0.1	0.78
Perseus IC348-SMM20	J034049.44+314848.9	0.4	0.3±0.1	15.0±2.0	11±3	0.06	0	0	1.9±0.3	0.2±0.1	3.78
Perseus IC348-SMM21	J034423.36+321006.1	0.2	0.1±0.1	16.8±5.7	9±5	0.04	0	38	1.6±0.5	0.1±0.1	0.17
Perseus IC348-SMM22	J034439.40+315909.0	0.1	0.1±0.0	15.0±2.0	10±3	0.04	0	12	1.2±0.2	0.1±0.0	0.78
Perseus NGC1333-SMM1	J032910.65+311333.9	17.7	20.0±4.6	12.3±0.9	2162±500	0.11	2	28	3.8±0.3	5.2±1.3	0.58
Perseus NGC1333-SMM2	J032912.07+311310.1	12.8	11.2±2.5	13.5±1.1	613±139	0.19	2	16	4.4±0.4	2.5±0.6	0.6
Perseus NGC1333-SMM3	J032903.53+311600.1	14.6	6.5±1.9	21.4±3.4	281±84	0.14	2	40	7.3±1.2	0.9±0.3	0.42
Perseus NGC1333-SMM4	J032855.63+311438.1	7	2.1±0.7	28.5±5.6	125±42	0.1	1	32	7.2±1.4	0.3±0.1	0.55
Perseus NGC1333-SMM5	J032911.37+311831.0	6	3.2±1.0	18.3±3.2	95±29	0.12	3	34	4.9±0.8	0.7±0.2	0.24
Perseus NGC1333-SMM6	J032901.69+312029.8	13.3	4.8±1.6	24.9±5.4	138±45	0.19	4	44	9.1±2.0	0.5±0.2	0.16
Perseus NGC1333-SMM7	J032859.77+312135.6	5.5	2.7±0.9	19.6±4.1	76±26	0.12	2	42	5.3±1.1	0.5±0.2	0.16
Perseus NGC1333-SMM8	J032906.58+311539.4	3.6	1.8±0.6	18.9±3.7	69±22	0.09	0	36	3.5±0.7	0.5±0.2	0.44
Perseus NGC1333-SMM9	J032913.67+311358.3	2.6	1.8±0.5	15.3±2.4	85±25	0.08	1	23	2.9±0.5	0.6±0.2	0.55
Perseus NGC1333-SMM10	J032908.94+311515.7	7.1	4.3±1.5	16.8±3.4	80±28	0.14	0	32	4.6±0.9	0.9±0.4	0.46

Table A.1: The JCMT GBS Clump Catalogue (JGCC). See Table 8.5 for full description.

ID	Coords. (J2000)	S_{850} (Jy)	Mass ($M_\odot$)	Temp. (K)	N_{H_2} ($\times^{21}$ cm^{-2})	D (pc)	Proto stars	n_{YSO} (pc^{-2})	M_J ($M_\odot$)	M_{850}/M_J	d_{OB} (pc)
Perseus NGC1333-SMM11	J032904.04+311454.1	3.8	1.8±0.6	20.3±4.6	62±22	0.1	1	35	4.4±1.0	0.4±0.2	0.49
Perseus NGC1333-SMM12	J032857.29+311414.3	1.4	0.7±0.2	19.6±4.4	55±20	0.06	1	30	3.0±0.7	0.2±0.1	0.56
Perseus NGC1333-SMM13	J032907.72+312157.5	1.6	0.7±0.2	21.1±4.8	44±15	0.06	1	49	3.0±0.7	0.2±0.1	0.04
Perseus NGC1333-SMM14	J032837.21+311332.7	1.5	0.5±0.2	24.2±6.6	28±11	0.07	1	6	4.2±1.1	0.1±0.1	0.75
Perseus NGC1333-SMM15	J032910.54+312142.9	4.1	3.0±0.7	15.0±2.0	46±11	0.12	3	46	3.8±0.5	0.8±0.2	0.02
Perseus NGC1333-SMM16	J032907.21+311724.5	1.6	0.9±0.4	17.4±4.3	43±17	0.06	0	38	2.7±0.7	0.3±0.2	0.32
Perseus NGC1333-SMM17	J032900.66+311202.7	1.3	0.8±0.3	17.2±4.4	31±13	0.12	1	16	3.3±0.8	0.2±0.1	0.69
Perseus NGC1333-SMM18	J032918.90+312316.8	1	0.6±0.2	17.7±4.5	37±15	0.04	2	31	2.4±0.6	0.2±0.1	0.15
Perseus NGC1333-SMM19	J032913.49+311810.2	0.9	0.7±0.3	14.5±3.0	60±22	0.03	1	31	1.6±0.3	0.4±0.2	0.26
Perseus NGC1333-SMM20	J032918.36+312510.7	2.4	1.3±0.6	17.5±4.5	37±15	0.1	0	20	3.8±1.0	0.3±0.2	0.25
Perseus NGC1333-SMM21	J032908.62+311709.7	1.8	1.0±0.4	17.8±4.8	34±15	0.08	1	35	3.2±0.9	0.3±0.2	0.33
Perseus NGC1333-SMM22	J032840.51+311757.2	2.3	2.2±0.8	12.7±2.5	54±21	0.1	4	22	2.7±0.5	0.8±0.4	0.52
Perseus NGC1333-SMM23	J032917.31+312746.6	1.5	0.9±0.4	16.7±4.2	32±14	0.09	2	11	3.1±0.8	0.3±0.1	0.41
Perseus NGC1333-SMM24	J032839.55+311821.0	2.5	2.2±0.9	13.3±2.9	46±19	0.11	0	17	3.1±0.7	0.7±0.3	0.51
Perseus NGC1333-SMM25	J032905.83+312215.3	1.8	1.3±0.3	15.0±2.0	30±7	0.09	0	48	2.7±0.4	0.5±0.1	0.07
Perseus NGC1333-SMM26	J032925.50+312817.5	0.6	0.7±0.3	11.9±2.5	43±18	0.04	0	9	1.4±0.3	0.5±0.2	0.48
Perseus NGC1333-SMM27	J032905.05+311842.2	1.8	1.1±0.6	16.3±5.1	23±12	0.11	0	41	3.3±1.0	0.3±0.2	0.24
Perseus NGC1333-SMM28	J032920.04+312358.9	1.7	1.2±0.3	15.0±2.0	27±7	0.09	1	26	3.0±0.4	0.4±0.1	0.2
Perseus NGC1333-SMM29	J032924.35+313323.4	0.8	0.7±0.3	14.0±3.5	36±16	0.05	1	2	1.9±0.5	0.4±0.2	0.81
Perseus NGC1333-SMM30	J032915.50+312031.4	1.3	0.8±0.4	16.3±5.0	23±12	0.09	0	39	3.0±0.9	0.3±0.2	0.12
Perseus NGC1333-SMM31	J032851.20+311425.5	0.6	0.5±0.1	15.0±2.0	19±5	0.05	0	26	1.9±0.3	0.2±0.1	0.59
Perseus NGC1333-SMM32	J032856.59+311917.2	1.1	0.8±0.2	15.0±2.0	20±5	0.08	0	40	2.5±0.3	0.3±0.1	0.27
Perseus NGC1333-SMM33	J032920.69+312529.0	0.8	0.6±0.2	15.0±2.0	16±5	0.08	0	18	2.4±0.3	0.3±0.1	0.28
Perseus NGC1333-SMM34	J032839.45+310557.1	0.4	0.3±0.1	15.0±2.0	13±4	0.06	1	6	1.8±0.2	0.2±0.0	1.19
Perseus NGC1333-SMM35	J032851.97+311801.6	0.5	0.4±0.1	15.0±2.0	14±4	0.08	0	40	2.1±0.3	0.2±0.1	0.38
Perseus West-SMM1	J032536.43+304516.3	11.8	9.1±2.1	14.9±1.3	673±158	0.12	2	7	4.7±0.4	1.9±0.5	-
Perseus West-SMM2	J033317.84+310933.0	8.1	5.9±1.6	14.9±1.8	278±74	0.14	1	8	4.9±0.6	1.2±0.4	-
Perseus West-SMM3	J033321.35+310727.0	6.2	7.1±1.7	11.7±1.1	384±91	0.11	1	11	3.0±0.3	2.4±0.6	-
Perseus West-SMM4	J032538.85+304404.8	5.6	3.1±0.9	17.7±2.6	156±47	0.11	2	7	4.9±0.7	0.6±0.2	-
Perseus West-SMM5	J032535.70+304537.1	9.5	7.9±1.9	13.9±1.5	214±51	0.18	0	7	4.5±0.5	1.8±0.5	-
Perseus West-SMM6	J033217.73+304947.3	3.6	6.1±1.3	9.6±0.6	376±80	0.08	1	2	2.1±0.1	2.9±0.6	-
Perseus West-SMM7	J033321.11+310742.0	5.1	5.3±1.4	12.3±1.4	290±75	0.11	0	11	3.0±0.3	1.8±0.5	-
Perseus West-SMM8	J032522.48+304513.2	4.6	3.4±1.0	15.0±2.1	144±43	0.11	1	3	3.9±0.6	0.9±0.3	-
Perseus West-SMM9	J033316.20+310654.0	8.4	6.4±2.1	14.6±2.6	76±25	0.16	3	12	5.0±0.9	1.3±0.5	-
Perseus West-SMM10	J033120.52+304524.0	1.9	2.2±0.6	11.4±1.3	133±37	0.07	1	4	2.2±0.2	1.0±0.3	-
Perseus West-SMM11	J032739.26+301304.0	1.2	0.4±0.2	23.1±6.1	31±12	0.05	2	9	3.1±0.8	0.1±0.1	-
Perseus West-SMM12	J032525.74+304507.9	3.6	3.2±1.1	13.3±2.5	60±21	0.11	0	5	3.2±0.6	1.0±0.4	-
Perseus West-SMM13	J032742.99+301228.6	1.5	0.9±0.4	17.1±4.4	35±15	0.08	1	9	3.0±0.8	0.3±0.1	-
Perseus West-SMM14	J032548.74+304225.0	4	2.9±0.8	15.0±2.0	33±9	0.16	0	2	4.3±0.6	0.7±0.2	-
Perseus West-SMM15	J033313.64+311954.0	0.9	0.6±0.2	15.0±2.0	23±7	0.06	1	4	2.4±0.3	0.3±0.1	-
Perseus West-SMM16	J032748.56+301208.5	0.7	0.6±0.3	13.8±3.6	34±16	0.05	1	7	1.8±0.5	0.3±0.2	-
Perseus West-SMM17	J032746.48+301208.1	0.9	0.6±0.3	15.9±5.3	22±13	0.07	0	8	2.4±0.8	0.3±0.2	-
Perseus West-SMM18	J032739.54+301210.1	1.1	0.8±0.2	15.0±2.0	23±6	0.07	0	8	2.3±0.3	0.3±0.1	-
Perseus West-SMM19	J033227.44+305905.5	1.4	1.0±0.3	15.0±2.0	14±5	0.15	0	2	3.4±0.5	0.3±0.1	-
Perseus West-SMM20	J032738.51+301400.9	0.5	0.3±0.1	15.0±2.0	20±6	0.03	1	8	1.6±0.2	0.2±0.1	-
Perseus West-SMM21	J033304.76+310500.0	2.6	1.9±0.5	15.0±2.0	18±5	0.2	0	5	4.2±0.6	0.5±0.1	-
Perseus West-SMM22	J033032.88+302624.1	0.4	0.3±0.1	15.0±2.0	17±5	0.03	1	3	1.6±0.2	0.2±0.1	-

Table A.1: The JCMT GBS Clump Catalogue (JGCC). See Table 8.5 for full description.

ID	Coords. (J2000)	S_{850} (Jy)	Mass ($M_\odot$)	Temp. (K)	N_{H_2} ($\times^{21}$ cm^{-2})	D (pc)	Proto stars	n_{YSO} (pc^{-2})	M_J ($M_\odot$)	M_{850}/M_J	d_{OB} (pc)
Perseus West-SMM23	J033258.93+310339.0	0.9	0.6±0.2	15.0±2.0	15±4	0.1	0	2	2.6±0.3	0.2±0.1	-
Perseus West-SMM24	J033243.53+305959.8	0.5	0.3±0.1	15.0±2.0	12±4	0.06	0	3	2.0±0.3	0.2±0.1	-
Perseus West-SMM25	J033229.05+310238.6	0.3	0.2±0.1	15.0±2.0	11±4	0.05	1	5	1.6±0.2	0.1±0.0	-
Perseus West-SMM26	J033305.23+310636.0	0.2	0.2±0.1	15.0±2.0	12±4	0.02	0	8	1.4±0.2	0.1±0.0	-
Serpens E-SMM1	J183751.40-014548.9	9.7	6.8±1.3	16.6±1.4	119±23	0.15	0	0	6.0±0.5	1.1±0.2	0.02
Serpens E-SMM2	J183826.41-010951.9	3.1	3.0±0.6	13.8±1.3	118±26	0.09	0	0	3.5±0.3	0.9±0.2	2.68
Serpens E-SMM3	J183749.00-014451.9	4.1	2.8±0.7	17.0±2.3	57±14	0.13	0	0	4.6±0.6	0.6±0.2	0.06
Serpens E-SMM4	J183754.20-013709.9	5.3	4.5±0.9	14.9±1.4	70±14	0.12	0	0	4.1±0.4	1.1±0.2	0.62
Serpens E-SMM5	J183755.80-013727.9	4.8	3.7±0.8	15.9±1.9	67±15	0.14	0	0	4.6±0.5	0.8±0.2	0.6
Serpens E-SMM6	J183754.40-013939.9	3.8	2.7±0.7	16.6±2.5	60±16	0.16	0	0	4.6±0.7	0.6±0.2	0.44
Serpens E-SMM7	J183753.40-014415.9	2.7	1.7±0.5	17.7±2.6	61±16	0.09	0	0	4.0±0.6	0.4±0.1	0.11
Serpens E-SMM8	J183753.40-014154.9	2.4	1.8±0.4	15.9±1.9	63±14	0.08	0	0	3.1±0.4	0.6±0.1	0.28
Serpens E-SMM9	J183751.00-014203.9	2	1.5±0.3	15.8±1.7	59±12	0.07	0	0	2.6±0.3	0.6±0.1	0.26
Serpens E-SMM10	J183646.59-011039.9	2.6	2.3±0.6	14.4±1.6	66±16	0.1	0	0	3.6±0.4	0.6±0.2	2.8
Serpens E-SMM11	J183751.40-014145.9	4.4	3.4±0.8	15.5±2.0	50±12	0.15	0	0	4.5±0.6	0.8±0.2	0.28
Serpens E-SMM12	J183753.20-013742.9	1.4	1.1±0.2	16.0±1.9	51±11	0.06	0	0	2.4±0.3	0.5±0.1	0.58
Serpens E-SMM13	J183755.00-013842.9	2.2	1.4±0.4	17.5±2.9	38±11	0.1	0	0	3.7±0.6	0.4±0.1	0.51
Serpens E-SMM14	J183755.00-014327.9	1.6	1.0±0.3	18.7±3.0	36±10	0.07	0	0	3.4±0.5	0.3±0.1	0.18
Serpens E-SMM15	J183753.00-014327.9	4.4	2.5±0.6	19.2±2.8	34±9	0.13	0	0	5.2±0.8	0.5±0.1	0.17
Serpens E-SMM16	J183754.80-014242.9	2.2	1.3±0.4	18.1±3.0	39±11	0.1	0	0	4.0±0.7	0.3±0.1	0.23
Serpens E-SMM17	J183638.79-011333.9	1.7	1.1±0.4	17.5±3.2	30±10	0.1	0	0	4.1±0.7	0.3±0.1	2.67
Serpens E-SMM18	J183802.61-014842.9	1.6	1.2±0.4	15.9±3.0	35±12	0.12	0	0	3.4±0.6	0.4±0.1	0.31
Serpens E-SMM19	J183757.60-013912.9	1.7	1.0±0.3	18.5±3.8	30±10	0.09	0	0	3.7±0.8	0.3±0.1	0.49
Serpens E-SMM20	J183747.20-014357.9	1.7	0.9±0.3	19.4±4.0	20±7	0.09	0	0	4.0±0.8	0.2±0.1	0.14
Serpens E-SMM21	J183754.60-015221.9	1.4	1.1±0.4	15.2±3.0	29±10	0.11	0	0	3.2±0.6	0.3±0.1	0.49
Serpens E-SMM22	J183828.81-010827.9	2.4	2.2±0.9	14.1±3.1	35±14	0.14	0	0	3.9±0.9	0.6±0.3	2.79
Serpens E-SMM23	J183757.40-014424.9	0.6	0.4±0.2	16.0±3.5	26±10	0.04	0	0	2.1±0.5	0.2±0.1	0.15
Serpens E-SMM24	J183802.01-015054.9	0.4	0.3±0.1	14.4±2.8	28±10	0.01	0	0	1.5±0.3	0.2±0.1	0.44
Serpens E-SMM25	J183830.41-011109.9	3.2	4.9±2.2	10.6±2.3	43±20	0.15	0	0	3.4±0.7	1.5±0.7	2.61
Serpens E-SMM26	J183831.21-010818.9	0.8	1.1±0.4	11.3±2.1	33±13	0.07	0	0	1.9±0.4	0.6±0.3	2.81
Serpens E-SMM27	J183752.20-014006.9	0.8	0.6±0.2	16.8±3.9	24±9	0.07	0	0	2.5±0.6	0.2±0.1	0.4
Serpens E-SMM28	J183744.40-014403.9	0.5	0.3±0.1	17.1±4.3	19±8	0.04	0	0	2.1±0.5	0.1±0.1	0.16
Serpens E-SMM29	J183751.00-013945.9	0.5	0.4±0.1	15.2±3.4	20±8	0.05	0	0	1.8±0.4	0.2±0.1	0.43
Serpens E-SMM30	J183615.18-011254.8	0.8	0.6±0.3	15.6±3.9	25±11	0.07	0	0	2.5±0.6	0.2±0.1	2.94
Serpens E-SMM31	J183759.81-015100.9	0.3	0.3±0.1	14.9±4.1	17±9	0.03	0	0	1.6±0.5	0.2±0.1	0.42
Serpens E-SMM32	J183801.80-011336.9	0.4	0.3±0.1	15.0±2.0	14±4	0.05	0	0	1.9±0.2	0.2±0.1	2.34
Serpens E-SMM33	J183834.41-011439.9	1	1.2±0.6	11.8±3.1	25±13	0.13	0	0	2.4±0.6	0.5±0.3	2.39
Serpens E-SMM34	J183804.20-010455.0	0.3	0.2±0.1	15.0±2.0	13±4	0.03	0	0	1.5±0.2	0.1±0.0	2.97
Serpens E-SMM35	J183759.40-014145.9	0.2	0.1±0.1	14.6±3.9	12±6	0.02	0	0	1.2±0.3	0.1±0.1	0.33
Serpens E-SMM36	J183800.61-014442.9	0.1	0.1±0.0	15.0±2.0	8±3	0.03	0	0	1.1±0.1	0.1±0.0	0.2
Serpens Main-SMM1	J182949.90+011518.9	24	46.5±9.3	18.1±1.3	918±183	0.17	3	53	13.9±1.0	3.3±0.7	-
Serpens Main-SMM2	J182956.70+011312.9	12	30.3±5.8	16.1±1.2	679±129	0.11	4	105	9.1±0.7	3.3±0.7	-
Serpens Main-SMM3	J182948.10+011642.9	17.2	45.6±8.4	14.7±0.9	283±52	0.16	5	38	9.8±0.6	4.6±0.9	-
Serpens Main-SMM4	J182959.30+011400.9	11.7	16.9±4.5	23.0±3.4	296±80	0.18	5	84	15.7±2.3	1.1±0.3	-
Serpens Main-SMM5	J182951.30+011639.9	5.9	15.2±3.0	14.8±1.1	203±40	0.09	1	51	6.3±0.5	2.4±0.5	-
Serpens Main-SMM6	J183000.50+011257.9	11.1	24.1±5.0	16.5±1.3	160±33	0.17	3	86	9.7±0.8	2.5±0.6	-
Serpens Main-SMM7	J183000.30+011145.9	13.4	45.4±9.6	12.8±1.1	290±61	0.21	2	41	9.5±0.8	4.8±1.1	-
Serpens Main-SMM8	J182958.50+011315.9	6.9	11.0±1.1	19.9±1.2	122±13	0.11	1	122	6.6±0.4	1.7±0.2	-

Table A.1: The JCMT GBS Clump Catalogue (JGCC). See Table 8.5 for full description.

ID	Coords. (J2000)	S_{850} (Jy)	Mass ($M_\odot$)	Temp. (K)	N_{H_2} ($\times^{21}$ cm^{-2})	D (pc)	Proto stars	n_{YSO} (pc^{-2})	M_J ($M_\odot$)	M_{850}/M_J	d_{OB} (pc)
Serpens Main-SMM9	J182957.70+011403.9	3.3	4.5±0.9	23.2±2.5	101±19	0.08	2	102	7.1±0.8	0.6±0.1	-
Serpens Main-SMM10	J182952.10+011551.9	4.2	8.6±2.0	17.7±1.9	138±32	0.1	2	64	7.1±0.8	1.2±0.3	-
Serpens Main-SMM11	J183000.70+011215.9	5.2	14.1±2.4	14.3±1.0	114±20	0.1	1	74	5.6±0.4	2.5±0.5	-
Serpens Main-SMM12	JGCC J182954.50+011400.9	4.3	6.1±1.7	21.8±3.5	54±15	0.12	0	78	9.8±1.6	0.6±0.2	-
Serpens Main-SMM13	J182947.70+011554.9	3	5.8±1.5	17.4±2.2	63±16	0.09	0	37	6.5±0.8	0.9±0.3	-
Serpens Main-SMM14	J183001.90+011512.9	2.4	6.4±2.1	14.8±2.4	100±32	0.12	0	41	6.0±1.0	1.1±0.4	-
Serpens Main-SMM15	J182931.69+011845.9	2.3	8.5±2.3	12.0±1.3	67±18	0.11	1	7	4.7±0.5	1.8±0.5	-
Serpens Main-SMM16	J182959.70+010948.9	3.9	16.4±3.9	11.2±1.1	74±18	0.17	1	10	5.4±0.5	3.1±0.8	-
Serpens Main-SMM17	J182945.10+011703.9	1.1	2.4±0.8	16.0±3.1	37±13	0.07	0	23	4.4±0.9	0.5±0.2	-
Serpens N-SMM1	J183859.10+003305.6	2.1	2.3±0.5	12.7±1.0	100±21	0.08	1	7	2.5±0.2	0.9±0.2	-
Serpens N-SMM2	J183911.30+003250.6	4.7	5.3±1.5	12.6±1.6	60±17	0.19	1	7	4.5±0.6	1.2±0.4	-
Serpens N-SMM3	J183909.70+001353.6	0.5	0.6±0.2	12.2±1.5	52±15	0.02	1	4	1.4±0.2	0.4±0.1	-
Serpens N-SMM4	J183841.10+003120.6	1.3	1.7±0.5	11.8±1.7	53±17	0.09	0	6	2.4±0.3	0.7±0.2	-
Serpens N-SMM5	J183925.90+003320.6	0.8	1.6±0.5	9.4±1.1	70±22	0.07	0	4	1.6±0.2	1.0±0.3	-
Serpens N-SMM6	J183844.50+003220.6	1.2	1.9±0.7	10.4±1.5	50±17	0.1	0	6	2.1±0.3	0.9±0.3	-
Serpens N-SMM7	J183923.10+001926.6	1.1	1.6±0.5	10.8±1.5	44±15	0.09	0	0	2.1±0.3	0.8±0.3	-
Serpens N-SMM8	J183917.50+002214.6	2.2	2.1±0.8	13.9±2.8	32±12	0.19	0	3	3.9±0.8	0.5±0.2	-
Serpens N-SMM9	J183914.10+002405.6	1.2	1.3±0.6	13.0±2.9	27±12	0.17	0	4	2.9±0.6	0.4±0.2	-
Serpens N-SMM10	J183925.90+001823.6	0.4	0.7±0.3	10.8±2.1	34±15	0.12	0	0	1.5±0.3	0.5±0.2	-
Serpens N-SMM11	J183846.30+003347.6	0.5	0.6±0.3	11.8±2.5	27±12	0.08	0	5	1.6±0.3	0.4±0.2	-
Serpens N-SMM12	J183823.50+003256.6	0.3	0.5±0.2	9.6±1.6	32±13	0.03	0	4	1.0±0.2	0.5±0.2	-
Serpens NH3-SMM1	J182906.50+003040.0	13.2	26.0±6.2	17.2±1.7	135±32	0.17	3	36	12.8±1.3	2.0±0.5	-
Serpens NH3-SMM2	J182909.30+003131.0	5.3	13.1±3.3	15.0±1.6	203±52	0.18	2	16	8.1±0.8	1.6±0.4	-
Serpens NH3-SMM3	J182854.30+002925.0	4.8	11.5±2.8	15.5±1.7	99±24	0.12	2	38	7.6±0.8	1.5±0.4	-
Serpens NH3-SMM4	J182855.90+002940.0	4.8	9.5±2.6	17.0±2.3	62±17	0.14	3	44	9.1±1.2	1.0±0.3	-
Serpens NH3-SMM5	J182954.30+003601.0	1.7	3.7±1.4	16.0±3.4	44±17	0.11	3	35	6.3±1.3	0.6±0.3	-
Serpens NH3-SMM6	J182900.70+003016.0	1.6	2.9±1.0	18.3±3.7	26±9	0.1	0	59	6.6±1.3	0.4±0.2	-
Serpens NH3-SMM7	J182902.10+003052.0	1.1	2.2±0.8	17.6±3.5	35±12	0.07	1	50	5.2±1.1	0.4±0.2	-
Serpens NH3-SMM8	J182931.50+002652.1	2.4	10.2±2.8	10.9±1.2	61±17	0.12	0	0	4.9±0.6	2.1±0.6	-
Serpens NH3-SMM9	J182906.70+003149.0	1.6	3.6±1.2	16.0±3.0	34±12	0.1	0	26	6.0±1.1	0.6±0.2	-
Serpens NH3-SMM10	J182851.90+002928.0	1.6	3.6±1.3	15.7±3.2	26±10	0.12	0	21	6.3±1.3	0.6±0.2	-
Serpens NH3-SMM11	J182857.90+003028.0	0.9	1.9±0.7	16.3±3.3	24±9	0.07	0	46	4.5±0.9	0.4±0.2	-
Serpens NH3-SMM12	J182853.50+003034.0	0.6	1.6±0.7	14.2±3.3	21±9	0.06	0	26	3.5±0.8	0.5±0.2	-
Serpens NH3-SMM13	J182917.30+003252.0	0.6	2.0±1.0	12.9±3.3	17±8	0.11	0	1	3.7±1.0	0.5±0.3	-
Serpens NH3-SMM14	J182858.30+004727.9	0.7	3.0±0.8	11.0±1.5	58±17	0.08	0	9	2.5±0.3	1.2±0.4	-
Serpens NH3-SMM15	J182942.30+003631.0	0.6	2.0±1.0	12.4±3.0	15±7	0.08	0	8	3.5±0.8	0.6±0.3	-
Serpens MWC297-SMM1	J182808.99-034810.3	10.5	19.8±3.6	9.9±0.5	530±97	0.17	0	28	2.3±0.1	8.8±1.7	0.55
Serpens MWC297-SMM2	J182754.16-034240.3	6.5	4.8±1.5	17.0±2.7	124±38	0.15	2	24	3.6±0.6	1.3±0.5	0.59
Serpens MWC297-SMM3	J182907.11-034322.2	2.8	2.8±0.8	13.8±1.8	93±27	0.09	2	38	1.9±0.2	1.5±0.5	1.66
Serpens MWC297-SMM4	J182740.53-034934.3	5.6	1.8±0.7	29.2±7.6	21±8	0.17	0	45	5.6±1.4	0.3±0.1	0.03
Serpens MWC297-SMM5	J182758.97-034946.3	7.6	4.7±1.6	18.0±3.5	23±8	0.2	0	42	4.3±0.8	1.1±0.4	0.35
Serpens MWC297-SMM6	J182810.19-034658.3	15.5	19.0±6.1	12.1±1.8	57±18	0.37	2	29	4.3±0.6	4.5±1.6	0.59
Serpens MWC297-SMM7	J182758.57-034104.3	7.7	3.9±1.4	20.9±4.7	17±6	0.2	0	11	4.7±1.1	0.8±0.3	0.73
Serpens MWC297-SMM8	J182739.72-034840.3	5	2.2±0.9	22.4±5.9	13±5	0.16	0	42	4.3±1.1	0.5±0.3	0.09
Serpens MWC297-SMM9	J182847.48-035046.3	6.8	6.4±3.3	13.7±3.7	21±11	0.28	0	2	3.7±1.0	1.8±1.0	1.23
Serp South-SMM1	J183004.14-020305.1	23.2	17.4±2.7	16.4±0.8	627±97	0.16	8	100	6.5±0.3	2.7±0.4	-
Serp South-SMM2	J183002.54-020247.1	19.2	11.1±1.8	19.1±1.2	215±35	0.16	18	159	7.7±0.5	1.5±0.3	-
Serp South-SMM3	J182937.54-015102.1	5.6	4.1±1.0	16.4±1.8	111±26	0.13	6	57	5.1±0.6	0.8±0.2	-

Table A.1: The JCMT GBS Clump Catalogue (JGCC). See Table 8.5 for full description.

ID	Coords. (J2000)	S_{850} (Jy)	Mass ($M_\odot$)	Temp. (K)	N_{H_2} ($\times^{21}$ cm^{-2})	D (pc)	Proto stars	n_{YSO} (pc^{-2})	M_J ($M_\odot$)	M_{850}/M_J	d_{OB} (pc)
Serp South-SMM4	J182908.16-013050.0	3.3	3.1±0.6	14.3±1.1	123±23	0.08	2	21	3.0±0.2	1.0±0.2	-
Serp South-SMM5	J182905.34-014155.9	2.2	1.9±0.4	15.0±1.4	116±26	0.07	2	35	2.9±0.3	0.7±0.2	-
Serp South-SMM6	J183002.54-020108.1	6.1	4.1±0.8	17.5±1.6	60±11	0.13	3	132	4.9±0.5	0.8±0.2	-
Serp South-SMM7	J182903.54-013904.9	2.9	4.4±0.9	10.8±0.8	141±30	0.12	3	23	2.5±0.2	1.7±0.4	-
Serp South-SMM8	J182957.54-015814.1	14	19.6±3.2	11.2±0.7	132±21	0.22	2	39	5.1±0.3	3.9±0.7	-
Serp South-SMM9	J182957.75-015732.1	4.4	7.7±1.2	10.0±0.5	161±25	0.12	1	26	2.6±0.1	3.0±0.5	-
Serp South-SMM10	J182958.34-020117.1	3.6	3.8±0.7	13.4±1.1	72±13	0.11	2	84	3.1±0.3	1.2±0.2	-
Serp South-SMM11	J182959.54-020102.1	1.4	1.3±0.2	14.2±1.1	69±11	0.05	3	114	2.0±0.2	0.7±0.1	-
Serp South-SMM12	J182941.74-015020.1	4.3	6.7±1.2	10.7±0.7	143±25	0.13	2	49	2.8±0.2	2.4±0.4	-
Serp South-SMM13	J183012.15-020656.2	2	2.9±0.4	11.0±0.7	105±16	0.07	2	38	1.9±0.1	1.6±0.3	-
Serp South-SMM14	J183025.95-021044.2	1.5	1.5±0.5	14.1±2.3	107±34	0.09	5	112	2.9±0.5	0.5±0.2	-
Serp South-SMM15	J183028.96-015605.2	1.1	1.4±0.3	11.8±1.1	54±13	0.06	1	36	2.0±0.2	0.7±0.2	-
Serp South-SMM16	J183012.55-020626.2	1.6	2.7±0.4	10.3±0.6	89±14	0.06	0	35	1.6±0.1	1.7±0.3	-
Serp South-SMM17	J183010.75-020605.2	1.5	2.8±0.5	9.8±0.7	95±17	0.06	1	34	1.7±0.1	1.7±0.3	-
Serp South-SMM18	J183028.36-015650.2	2.2	3.1±0.7	11.2±1.0	66±14	0.11	2	33	2.5±0.2	1.2±0.3	-
Serp South-SMM19	J183016.15-020717.2	1.8	2.4±0.5	11.4±0.9	61±12	0.09	1	29	2.1±0.2	1.1±0.2	-
Serp South-SMM20	J183014.55-020744.2	2.4	3.5±0.6	10.9±0.8	74±12	0.09	0	30	2.2±0.2	1.6±0.3	-
Serp South-SMM21	J183017.35-020838.2	4.1	4.7±1.0	12.5±1.3	57±13	0.13	0	28	3.7±0.4	1.3±0.3	-
Serp South-SMM22	J183017.35-021002.2	1	1.1±0.3	12.9±1.6	46±12	0.06	3	42	2.1±0.3	0.5±0.2	-
Serp South-SMM23	J183025.56-015423.2	0.7	0.9±0.2	11.7±1.3	45±12	0.05	1	30	1.6±0.2	0.6±0.2	-
Serp South-SMM24	J182952.94-015808.1	1.7	2.4±0.6	11.2±1.3	58±15	0.13	2	32	2.4±0.3	1.0±0.3	-
Serp South-SMM25	J183018.56-015326.2	1.2	2.1±0.5	9.9±1.0	80±21	0.11	1	17	1.8±0.2	1.1±0.3	-
Serp South-SMM26	J183006.34-020514.1	1.2	2.0±0.5	10.2±1.0	58±13	0.1	0	38	1.8±0.2	1.1±0.3	-
Serp South-SMM27	J182908.31-020525.9	1.5	1.4±0.4	14.6±2.1	37±10	0.09	1	63	2.8±0.4	0.5±0.1	-
Serp South-SMM28	J183004.55-015959.1	0.2	0.4±0.1	9.5±1.0	44±12	0.02	1	61	0.8±0.1	0.5±0.1	-
Serp South-SMM29	J182947.54-015614.1	0.5	0.7±0.2	10.6±1.2	49±13	0.04	2	29	1.2±0.1	0.6±0.2	-
Serp South-SMM30	J182949.74-015820.1	0.3	0.6±0.2	8.9±1.2	45±16	0.02	0	21	0.9±0.1	0.7±0.3	-
Serp South-SMM31	J183018.95-020744.2	0.5	0.6±0.2	11.9±1.8	42±13	0.05	0	22	1.5±0.2	0.4±0.2	-
Serp South-SMM32	J182946.53-020653.1	0.4	0.4±0.1	13.5±2.4	23±8	0.03	0	11	1.5±0.3	0.3±0.1	-
Serp South-SMM33	J182847.74-013813.9	0.3	0.2±0.1	15.0±3.0	26±9	0.05	2	16	1.5±0.3	0.2±0.1	-
Serp South-SMM34	J182941.37-012311.2	9.4	7.7±1.7	15.0±2.0	97±22	0.15	0	0	3.4±0.5	2.3±0.6	-
Serp South-SMM35	J182948.35-014723.1	0.6	0.9±0.3	10.8±1.5	38±12	0.07	0	4	1.5±0.2	0.6±0.2	-
Serp South-SMM36	J182828.07-021437.5	21.8	17.8±4.0	15.0±2.0	133±30	0.19	0	0	4.8±0.6	3.7±1.0	-
Serp South-SMM37	J182748.91-014913.4	18.8	15.4±3.4	15.0±2.0	145±33	0.19	0	1	4.6±0.6	3.3±0.9	-
Serp South-SMM38	J182747.51-014558.4	2.1	1.8±0.4	15.0±2.0	133±30	0.07	0	7	1.4±0.2	1.2±0.3	-
Serp South-SMM39	J182921.17-012241.1	7	5.7±1.3	15.0±2.0	94±21	0.15	0	0	3.0±0.4	1.9±0.5	-
Serp South-SMM40	J182749.32-014516.5	3	2.4±0.5	15.0±2.0	111±25	0.11	0	4	1.9±0.3	1.3±0.3	-
Serp South-SMM41	J182752.30-015401.4	1.1	0.9±0.2	15.0±2.0	72±16	0.06	0	0	1.3±0.2	0.7±0.2	-
Taurus L1495-SMM1	J041958.66+270959.2	1.8	0.9±0.2	11.4±1.1	85±21	0.08	1	3	1.4±0.1	0.6±0.2	3.11
Taurus L1495-SMM2	J041942.52+271332.7	1.1	0.6±0.2	10.7±0.9	88±22	0.06	1	5	1.1±0.1	0.6±0.1	2.93
Taurus L1495-SMM3	J041840.45+282318.0	3.7	1.1±0.3	15.0±2.0	27±7	0.16	0	5	2.9±0.4	0.4±0.1	0.18
Taurus L1495-SMM4	J041750.20+275602.5	0.5	0.1±0.0	15.0±2.0	12±4	0.06	0	0	1.3±0.2	0.1±0.0	1.12
Taurus L1495-SMM5	J041742.39+280829.3	0.5	0.1±0.0	15.0±2.0	13±4	0.05	0	0	1.2±0.2	0.1±0.0	0.73
Taurus L1495-SMM6	J041951.71+271126.4	0.3	0.1±0.0	15.0±2.0	10±3	0.04	0	3	1.1±0.1	0.1±0.0	3.04
Taurus L1495-SMM7	J041743.09+280605.3	0.2	0.1±0.0	15.0±2.0	11±3	0.03	0	0	0.9±0.1	0.1±0.0	0.8
Taurus L1495-SMM8	J041808.49+280517.8	0.4	0.1±0.0	15.0±2.0	10±3	0.06	0	0	1.2±0.2	0.1±0.0	0.68
Taurus L1495-SMM9	J042121.12+265958.2	0.3	0.1±0.0	15.0±2.0	11±3	0.07	0	2	1.1±0.1	0.1±0.0	3.79
Taurus L1495-SMM10	J041735.19+280314.1	0.2	0.0±0.0	15.0±2.0	9±3	0.04	0	0	0.8±0.1	0.1±0.0	0.94

Table A.1: The JCMT GBS Clump Catalogue (JGCC). See Table 8.5 for full description.

ID	Coords. (J2000)	S_{850} (Jy)	Mass ($M_\odot$)	Temp. (K)	N_{H_2} ($\times^{21}$ cm^{-2})	D (pc)	Proto stars	n_{YSO} (pc^{-2})	M_J ($M_\odot$)	M_{850}/M_J	d_{OB} (pc)
Taurus south-SMM1	J042923.89+243257.9	0.6	0.3±0.1	11.6±1.4	61±17	0.03	1	2	0.9±0.1	0.3±0.1	-
Taurus south-SMM2	J043537.37+240919.7	1.9	0.6±0.2	13.7±2.5	25±9	0.11	0	2	2.0±0.4	0.3±0.1	-
Taurus south-SMM3	J043535.13+240817.0	0.4	0.2±0.1	12.9±2.6	27±11	0.03	1	1	0.9±0.2	0.2±0.1	-
Taurus south-SMM4	J042921.91+243315.8	0.8	0.2±0.1	15.0±2.0	18±5	0.09	0	2	1.5±0.2	0.1±0.0	-
Taurus south-SMM5	J043155.60+243300.0	0.7	0.2±0.1	15.0±2.0	18±5	0.05	0	0	1.3±0.2	0.2±0.0	-
Taurus tmc-SMM1	J043953.97+260309.2	5.4	1.6±0.4	15.2±1.6	155±35	0.13	2	9	2.8±0.3	0.6±0.1	-
Taurus tmc-SMM2	J043913.84+255322.6	0.5	0.2±0.1	14.3±2.5	48±16	0.02	0	9	1.0±0.2	0.2±0.1	-
W40-SMM1	J183120.99-020620.3	10.9	13.2±3.1	31.4±4.6	75±18	0.15	1	133	22.2±3.2	0.6±0.2	0.07
W40-SMM2	J183109.98-020441.3	7.2	10.2±1.9	26.8±2.8	69±13	0.11	0	18	14.1±1.5	0.7±0.2	0.46
W40-SMM3	J183109.58-020626.3	3.3	4.3±0.8	29.2±3.2	62±12	0.07	1	27	10.5±1.1	0.4±0.1	0.37
W40-SMM4	J183110.38-020353.3	9.8	17.7±4.0	22.6±2.7	83±19	0.15	1	21	15.7±1.8	1.1±0.3	0.54
W40-SMM5	J183121.19-020656.3	5.3	6.2±1.4	32.0±4.6	57±13	0.11	1	78	15.8±2.3	0.4±0.1	0.06
W40-SMM6	J183110.58-020541.3	6.9	10.4±1.9	26.2±2.9	73±13	0.12	1	22	14.5±1.6	0.7±0.2	0.37
W40-SMM7	J183116.79-020705.3	7.7	8.1±1.8	34.2±5.2	44±10	0.14	0	43	21.2±3.2	0.4±0.1	0.12
W40-SMM8	J183110.38-020644.3	4.2	4.6±1.0	32.8±4.8	38±8	0.1	0	26	14.1±2.1	0.3±0.1	0.34
W40-SMM9	J183146.81-020426.3	6.5	11.6±2.1	22.7±2.2	60±11	0.1	1	27	12.3±1.2	0.9±0.2	1.04
W40-SMM10	J183103.78-020950.3	3.7	10.7±2.3	16.3±1.5	80±17	0.1	2	40	7.7±0.7	1.4±0.3	0.74
W40-SMM11	J183143.21-020444.3	3.5	7.8±1.5	19.8±2.0	74±14	0.08	0	45	8.3±0.9	0.9±0.2	0.9
W40-SMM12	J183138.60-020335.3	4.1	6.5±1.5	25.2±3.4	48±11	0.09	0	54	11.8±1.6	0.6±0.1	0.82
W40-SMM13	J183114.19-020723.3	3.9	3.9±0.8	35.3±5.5	32±7	0.09	0	26	14.2±2.2	0.3±0.1	0.23
W40-SMM14	J183148.01-020144.3	7	10.7±2.6	25.5±3.7	45±11	0.14	1	28	15.9±2.3	0.7±0.2	1.26
W40-SMM15	J183139.20-021656.3	2.2	6.8±1.6	15.7±1.8	79±19	0.07	0	26	6.3±0.7	1.1±0.3	1.64
W40-SMM16	J183148.21-020402.3	6.8	11.3±3.1	24.4±4.1	36±10	0.2	0	11	16.2±2.7	0.7±0.2	1.1
W40-SMM17	J183205.02-022111.2	1.3	4.7±1.0	14.1±1.4	61±14	0.05	0	10	4.4±0.4	1.1±0.3	2.67
W40-SMM18	J183228.63-015220.2	2.6	12.1±2.4	12.4±1.0	120±23	0.09	0	10	5.3±0.4	2.3±0.5	3.26
W40-SMM19	J183146.61-020217.3	8	11.1±3.0	27.4±5.1	31±9	0.18	1	28	19.6±3.6	0.6±0.2	1.17
W40-SMM20	J183135.60-020353.3	1.5	2.5±0.6	24.4±3.9	33±8	0.06	0	61	7.8±1.2	0.3±0.1	0.71
W40-SMM21	J183216.04-023444.1	1.1	4.4±1.0	13.2±1.2	53±11	0.05	2	26	3.8±0.4	1.2±0.3	4.56
W40-SMM22	J183137.40-021526.3	3.2	7.1±2.1	19.5±3.3	38±11	0.13	2	30	10.4±1.8	0.7±0.2	1.42
W40-SMM23	J183133.40-020414.3	1.3	2.2±0.6	24.3±4.2	25±7	0.06	0	77	7.7±1.3	0.3±0.1	0.61
W40-SMM24	J183154.42-021847.3	0.8	1.8±0.5	19.7±2.9	35±9	0.05	0	11	5.1±0.8	0.4±0.1	2.16
W40-SMM25	J183148.81-020044.3	1.3	2.4±0.6	22.8±3.8	28±7	0.06	0	26	7.0±1.2	0.3±0.1	1.37
W40-SMM26	J183153.62-021914.3	3.4	7.5±2.3	19.4±3.4	32±9	0.16	0	10	11.0±1.9	0.7±0.2	2.2
W40-SMM27	J183146.21-020547.3	1	2.1±0.7	20.2±4.1	22±7	0.06	1	26	6.5±1.3	0.3±0.1	0.97
W40-SMM28	J183111.99-020241.3	2.8	5.3±1.8	22.0±4.7	22±7	0.12	1	22	11.4±2.4	0.5±0.2	0.65
W40-SMM29	J183105.78-020335.3	2	6.3±1.6	15.7±2.2	32±8	0.1	0	19	6.7±0.9	0.9±0.3	0.68
W40-SMM30	J183152.01-020132.3	0.8	2.0±0.6	18.1±3.1	33±9	0.06	1	28	4.9±0.8	0.4±0.1	1.39
W40-SMM31	J183113.59-020611.3	1.1	1.2±0.5	31.9±9.2	9±3	0.07	0	33	10.4±3.0	0.1±0.1	0.24
W40-SMM32	J183049.57-015602.3	0.8	3.0±0.8	14.6±2.1	38±11	0.05	1	30	4.2±0.6	0.7±0.2	1.9
W40-SMM33	J183141.41-021717.3	0.5	1.3±0.4	16.2±2.9	22±7	0.05	0	30	3.6±0.7	0.4±0.1	1.73
W40-SMM34	J183159.82-020011.3	0.6	2.7±0.7	12.9±1.6	32±8	0.04	1	25	3.3±0.4	0.8±0.2	1.74
W40-SMM35	J183157.61-015005.3	0.8	5.7±1.3	9.9±0.9	72±17	0.06	0	7	2.8±0.3	2.1±0.5	2.78
W40-SMM36	J183146.21-020014.3	0.8	1.5±0.6	21.4±5.1	18±7	0.08	1	21	6.3±1.5	0.2±0.1	1.35
W40-SMM37	J183203.82-020144.3	0.8	2.3±0.8	16.1±3.0	25±8	0.08	0	9	4.9±0.9	0.5±0.2	1.76
W40-SMM38	J183152.41-015732.3	0.4	1.1±0.4	17.5±3.5	22±7	0.02	0	17	3.7±0.7	0.3±0.1	1.79
W40-SMM39	J183151.01-015756.3	0.5	1.4±0.4	17.3±3.4	22±7	0.04	1	19	4.1±0.8	0.3±0.1	1.71
W40-SMM40	J183124.19-015750.3	0.4	1.1±0.4	16.6±3.3	21±7	0.02	0	6	3.6±0.7	0.3±0.1	1.3
W40-SMM41	J183335.28-020926.0	5.6	18.1±4.1	15.0±2.0	121±27	0.14	0	0	4.9±0.7	3.7±1.0	4.94

Table A.1: The JCMT GBS Clump Catalogue (JGCC). See Table 8.5 for full description.

ID	Coords. (J2000)	S_{850} (Jy)	Mass ($M_\odot$)	Temp. (K)	N_{H_2} ($\times^{21}$ cm^{-2})	D (pc)	Proto stars	n_{YSO} (pc^{-2})	M_J ($M_\odot$)	M_{850}/M_J	d_{OB} (pc)
W40-SMM42	J183138.20-021305.3	0.2	0.5±0.2	17.0±4.3	13±6	0.02	0	20	2.9±0.7	0.2±0.1	1.14
W40-SMM43	J183351.10-021655.9	3.7	12.0±2.7	15.0±2.0	115±26	0.1	0	0	4.0±0.5	3.0±0.8	5.69
W40-SMM44	J183142.20-012938.3	2	6.6±1.5	15.0±2.0	88±20	0.07	0	9	3.2±0.4	2.1±0.5	5.45
W40-SMM45	J183344.29-021304.9	1.8	5.8±1.3	15.0±2.0	97±22	0.05	0	0	2.9±0.4	2.0±0.5	5.33
W40-SMM46	J183313.45-015023.1	1.2	2.4±0.2	20.6±0.9	81±5	0.05	0	0	3.2±0.1	0.7±0.1	4.76
W40-SMM47	J183349.10-021716.9	1	3.2±0.7	15.0±2.0	94±21	0.06	0	0	2.2±0.3	1.4±0.4	5.64
W40-SMM48	J183350.31-022128.9	0.8	2.6±0.6	15.0±2.0	80±18	0.05	0	0	2.1±0.3	1.3±0.3	5.87
W40-SMM49	J183351.91-022201.8	1.2	4.1±0.9	15.0±2.0	87±20	0.06	0	0	2.7±0.4	1.5±0.4	5.96

A.2 The JCMT GBS Protostar Catalogue

Table A.2: The Dunham et al. (2015) c2d+GBS protostar temperature (DPT) catalogue. The Gaussian weighted temperature for a protostar ($T_{envelope}$) compared to the temperature at the location of the protostar ($T_{central}$). Note that Orion and Aquila regions are not included in this prototype catalogue.

Region	RA[a] (J2000)	Dec[a] (J2000)	$T_{envelope}$ (K)	$T_{central}$ (K)	α_E^a	$T_{bol,E}^a$ (K)
Auriga	04:30:56.59	+35:30:02.5	13.0±2.5	12.5±2.3	2.2	81.0
Auriga	04:30:15.31	+36:00:05.8	9.5±1.4	9.2±1.4	1.6	180.0
Auriga	04:30:27.31	+35:09:17.9	14.6±1.3	14.3±1.0	1.6	140.0
Auriga	04:30:36.79	+35:54:32.7	14.1±0.8	14.0±0.6	1.3	120.0
Auriga	04:30:41.11	+35:29:38.7	12.5±0.9	11.9±0.7	1.3	53.0
Auriga	04:30:48.53	+35:37:50.6	13.8±1.9	13.0±1.3	1.3	100.0
Auriga	04:30:28.04	+35:09:14.9	15.2±1.1	16.1±1.1	1.3	230.0
Auriga	04:30:46.32	+34:58:56.7	11.4±1.4	10.1±0.9	1.3	75.0
Auriga	04:30:24.68	+35:45:17.8	13.5±3.0	0.0±0.0	1.2	200.0
Auriga	04:30:38.01	+35:50:59.7	12.8±1.3	13.2±1.2	1.2	220.0
Auriga	04:30:44.23	+35:59:47.6	11.9±1.4	11.8±1.3	0.9	240.0
Auriga	04:30:30.61	+35:51:41.8	10.8±1.1	10.0±0.8	0.8	240.0
Auriga	04:30:03.81	+35:14:20.9	21.0±3.0	20.4±2.6	0.8	140.0
Auriga	04:30:09.69	+35:14:38.9	16.3±4.2	0.0±0.0	0.3	540.0
Auriga	04:29:51.32	+35:15:47.7	16.6±2.7	15.8±2.2	0.5	520.0
Auriga	04:30:08.46	+35:14:08.9	18.6±3.1	17.8±2.6	0.4	180.0
Auriga	04:30:48.52	+34:58:53.6	12.6±1.2	0.0±0.0	-0.7	450.0
Auriga	04:30:38.77	+35:54:35.7	13.6±2.1	0.0±0.0	0.1	690.0
Auriga	04:29:51.07	+35:15:56.7	14.7±2.2	13.2±1.5	-0.3	940.0
Auriga	04:30:31.58	+35:45:11.8	12.5±2.8	12.4±2.6	-0.3	360.0
Auriga	04:30:39.25	+35:51:59.7	13.4±2.0	12.7±1.6	-0.7	1400.0
Auriga	04:29:49.36	+35:14:23.7	13.6±4.5	0.0±0.0	-0.1	860.0
Cepheus	20:57:08.39	+77:36:58.8	12.0±2.9	0.0±0.0	0.3	180.0
Cepheus	20:57:07.46	+77:36:55.8	12.1±2.9	0.0±0.0	0.2	2400.0
Cepheus	20:57:14.04	+77:35:43.8	11.2±0.6	10.4±0.2	-0.0	530.0
Cepheus	22:38:47.04	+75:11:34.3	17.4±0.9	0.0±0.0	1.9	120.0
Cepheus	22:38:43.14	+75:11:37.3	16.7±1.6	16.5±1.4	0.9	78.0
Cepheus	22:38:53.29	+75:11:22.1	13.9±1.2	0.0±0.0	0.5	150.0
Cepheus	22:39:13.73	+75:12:15.6	9.7±2.3	0.0±0.0	1.2	500.0
Cepheus	21:00:21.29	+68:13:17.2	13.4±2.8	11.7±1.6	1.4	100.0
Cepheus	21:00:22.39	+68:12:59.2	15.4±4.0	13.1±3.1	0.5	100.0
CrA	19:01:56.52	-36:57:29.5	20.1±0.8	16.3±0.2	2.6	210.0
CrA	19:01:55.27	-36:57:23.5	20.3±0.7	17.6±0.3	2.5	310.0
CrA	19:02:58.78	-37:07:36.7	14.6±1.6	12.0±0.5	1.5	66.0
CrA	19:01:48.51	-36:57:14.6	26.2±3.3	18.6±0.9	1.2	23.0
CrA	19:01:58.53	-36:57:08.4	14.8±0.8	10.1±0.2	0.7	15.0
CrA	19:01:50.77	-36:58:08.5	23.1±2.5	12.3±0.3	1.0	270.0
CrA	19:01:48.01	-36:57:23.6	26.6±3.5	26.0±2.4	1.0	130.0
CrA	19:01:41.51	-36:58:32.6	11.9±0.9	9.8±0.2	0.3	390.0
CrA	19:01:55.52	-36:56:50.5	19.7±1.7	21.0±1.4	0.5	370.0
CrA	19:03:06.91	-37:12:48.4	10.2±0.8	8.6±0.3	-0.2	610.0
CrA	19:02:56.77	-37:07:18.8	14.3±1.9	0.0±0.0	0.0	300.0
CrA	19:03:01.05	-37:07:54.6	16.0±2.1	0.0±0.0	0.1	740.0
IC5146	21:53:36.70	+47:19:00.2	14.9±1.5	15.4±1.5	1.9	190.0
IC5146	21:53:33.47	+47:14:18.2	12.4±1.3	0.0±0.0	1.1	230.0
IC5146	21:53:49.67	+47:13:51.2	18.9±4.3	0.0±0.0	0.5	540.0
IC5146	21:52:38.08	+47:14:38.1	14.4±2.3	14.3±2.2	0.6	120.0
IC5146	21:53:07.25	+47:14:35.9	11.3±2.1	0.0±0.0	0.5	650.0
IC5146	21:53:34.93	+47:20:42.2	17.0±3.7	0.0±0.0	-0.1	700.0
IC5146	21:53:38.76	+47:19:33.2	16.7±3.7	18.0±4.6	0.0	680.0
OphSco	16:26:59.32	-24:35:06.5	13.0±2.8	0.0±0.0	1.9	120.0
OphSco	16:26:25.72	-24:24:33.2	22.8±3.4	21.6±2.4	1.4	84.0
OphSco	16:27:09.44	-24:37:21.5	17.1±5.5	17.5±5.4	1.1	420.0
OphSco	16:26:21.56	-24:23:06.2	16.9±3.8	0.0±0.0	1.1	250.0

a - Protostar (Class 0/I objects, selected as α_E greater than 0) positions, extinction corrected spectral index (α_E) and extinction corrected bolometeric temperature ($T_{bol,E}$) taken from the Dunham et al. (2015) c2d+GBS catalogue.

Table A.2: The Dunham et al. (2015) c2d+GBS protostar temperature (DPT) catalogue. Full description given in Table A.2

Region	RA[a] (J2000)	Dec[a] (J2000)	$T_{envelope}$ (K)	$T_{central}$ (K)	α_E^a	$T_{bol,E}^a$ (K)
OphSco	16:27:26.83	-24:40:54.4	17.0±4.7	14.7±2.6	1.1	300.0
OphSco	16:27:24.63	-24:41:06.4	18.0±5.6	0.0±0.0	1.2	230.0
OphSco	16:26:25.73	-24:23:03.2	24.1±5.0	22.1±4.6	0.6	200.0
OphSco	16:26:26.17	-24:23:42.2	24.8±3.1	27.8±4.1	-0.1	530.0
OphSco	16:27:16.47	-24:31:18.5	14.2±4.0	0.0±0.0	0.0	670.0
OphSco	16:26:23.75	-24:24:42.2	22.1±5.1	11.3±2.8	0.1	810.0
OphSco	16:27:15.59	-24:30:57.5	14.3±3.6	0.0±0.0	-0.0	680.0
OphSco	16:27:28.55	-24:27:24.4	18.2±3.9	20.4±5.4	-0.1	450.0
OphSco	16:27:21.74	-24:27:30.4	14.7±3.6	0.0±0.0	-0.1	290.0
OphSco	16:27:30.09	-24:27:45.4	19.6±5.4	19.8±5.5	-0.0	620.0
PerseusIC348	03:43:58.11	+32:03:08.9	13.4±0.9	13.0±0.5	1.8	200.0
PerseusIC348	03:43:51.27	+32:03:20.8	14.7±1.3	12.8±0.6	1.4	17.0
PerseusIC348	03:44:02.60	+32:02:03.0	15.7±1.9	14.9±1.4	1.5	45.0
PerseusIC348	03:43:57.17	+32:03:02.9	12.3±0.6	10.3±0.1	1.8	23.0
PerseusIC348	03:44:02.84	+32:02:00.0	15.3±1.8	14.1±1.3	0.9	280.0
PerseusIC348	03:44:43.89	+32:01:36.0	18.4±2.4	15.2±0.7	0.7	41.0
PerseusIC348	03:47:41.67	+32:51:41.1	12.2±1.2	11.4±0.8	1.3	330.0
PerseusIC348	03:43:56.71	+32:00:53.9	13.4±0.6	12.8±0.2	0.6	23.0
PerseusIC348	03:44:43.42	+32:01:30.0	18.6±2.8	18.1±2.0	0.6	500.0
PerseusIC348	03:44:13.22	+32:01:36.1	7.5±0.7	7.5±0.7	0.3	470.0
PerseusIC348	03:47:05.47	+32:43:05.5	9.4±2.5	0.0±0.0	0.5	390.0
PerseusIC348	03:43:59.54	+32:00:36.0	13.1±1.8	0.0±0.0	-0.2	400.0
PerseusIC348	03:43:57.42	+32:00:47.9	13.6±0.8	11.9±0.3	-0.1	420.0
PerseusIC348	03:43:45.37	+32:03:56.7	15.6±3.7	0.0±0.0	0.1	650.0
PerseusWest	03:29:52.08	+31:39:02.2	15.0±2.9	15.7±3.0	3.4	40.0
PerseusWest	03:33:17.84	+31:09:30.0	15.0±1.3	13.3±0.4	2.9	44.0
PerseusWest	03:29:13.67	+31:13:55.3	15.2±2.2	14.2±1.3	2.5	36.0
PerseusWest	03:33:14.34	+31:07:12.0	16.0±3.0	17.1±3.2	2.7	36.0
PerseusWest	03:29:17.31	+31:27:43.6	16.7±4.2	17.7±4.8	1.7	34.0
PerseusWest	03:33:16.44	+31:06:51.0	14.0±2.0	13.6±1.4	1.6	26.0
PerseusWest	03:33:16.67	+31:07:51.0	15.2±3.9	14.4±3.3	1.7	120.0
PerseusWest	03:29:23.65	+31:33:26.3	13.9±3.5	0.0±0.0	1.5	64.0
PerseusWest	03:29:18.43	+31:23:16.8	17.4±4.2	0.0±0.0	1.1	24.0
PerseusWest	03:29:13.26	+31:18:10.2	14.9±3.1	13.9±2.5	1.6	270.0
PerseusWest	03:32:18.20	+30:49:47.3	9.5±0.5	9.2±0.4	0.9	26.0
PerseusWest	03:29:17.78	+31:27:46.7	16.7±4.1	16.2±3.8	0.9	240.0
PerseusWest	03:31:21.22	+30:45:30.1	10.8±1.1	9.8±1.0	1.5	32.0
PerseusWest	03:33:20.41	+31:07:18.0	11.5±1.1	11.4±1.0	0.6	55.0
PerseusWest	03:29:18.90	+31:23:22.8	17.7±4.3	17.1±4.2	-0.7	410.0
SerpensMain	18:29:49.30	+01:16:15.9	16.8±0.8	15.7±0.6	3.5	150.0
SerpensMain	18:29:49.90	+01:15:18.9	13.8±0.1	12.1±0.0	2.5	13.0
SerpensMain	18:29:59.90	+01:13:12.9	17.2±0.7	16.9±0.7	2.2	120.0
SerpensMain	18:29:09.30	+00:31:31.0	13.3±0.4	12.1±0.2	2.1	36.0
SerpensMain	18:28:55.10	+00:29:52.0	17.0±1.2	17.5±1.1	1.6	51.0
SerpensMain	18:28:55.90	+00:29:46.0	15.4±0.9	15.6±0.9	1.6	26.0
SerpensMain	18:29:52.30	+01:15:54.9	14.2±0.6	13.1±0.4	1.7	250.0
SerpensMain	18:28:56.90	+00:30:07.0	17.1±2.8	17.0±2.6	1.6	190.0
SerpensMain	18:29:06.30	+00:30:43.0	16.9±0.4	16.8±0.4	1.3	67.0
SerpensMain	18:29:06.90	+00:30:34.0	17.7±0.5	17.5±0.4	1.4	83.0
SerpensMain	18:30:00.70	+01:13:00.9	14.4±0.4	13.8±0.3	1.5	29.0
SerpensMain	18:29:52.30	+01:15:45.9	14.5±0.5	13.8±0.4	1.3	69.0
SerpensMain	18:29:53.10	+01:14:51.9	25.0±4.5	29.9±6.1	1.2	140.0
SerpensMain	18:28:54.30	+00:29:31.0	15.9±0.8	14.8±0.6	1.1	69.0
SerpensMain	18:29:48.30	+01:16:42.9	13.5±0.2	13.3±0.1	1.1	30.0
SerpensMain	18:29:59.70	+01:11:57.9	12.9±0.5	12.6±0.4	1.5	120.0
SerpensMain	18:29:51.30	+01:16:36.9	12.8±0.3	12.2±0.2	1.1	170.0
SerpensMain	18:29:57.70	+01:13:00.9	17.0±0.6	17.5±0.6	1.1	59.0
SerpensMain	18:29:59.50	+01:14:00.9	14.2±0.4	12.2±0.1	0.9	44.0
SerpensMain	18:29:52.70	+00:36:13.0	16.1±3.7	13.5±2.2	0.5	68.0

Table A.2: The Dunham et al. (2015) c2d+GBS protostar temperature (DPT) catalogue.

Region	RA[a] (J2000)	Dec[a] (J2000)	$T_{envelope}$ (K)	$T_{central}$ (K)	α_E^a	$T_{bol,E}^a$ (K)
SerpensMain	18:29:49.70	+01:17:03.9	12.8±0.4	13.0±0.4	1.0	570.0
SerpensMain	18:29:58.10	+01:12:51.9	20.0±1.5	18.7±1.2	0.3	420.0
SerpensMain	18:29:58.90	+01:14:21.9	21.9±1.4	20.5±1.1	0.5	430.0
SerpensMain	18:29:59.50	+01:10:39.9	11.3±0.7	10.9±0.6	0.2	480.0
SerpensMain	18:30:02.10	+01:13:57.9	24.2±5.4	24.5±5.4	0.4	700.0
SerpensMain	18:29:09.30	+00:31:28.0	13.7±0.4	12.9±0.2	0.1	420.0
SerpensMain	18:29:32.09	+01:18:39.9	11.4±1.0	12.3±1.1	-0.1	710.0
SerpensMain	18:29:49.90	+01:14:54.9	20.1±1.3	20.4±1.2	-0.0	490.0
SerpensMain	18:29:53.30	+00:36:07.0	18.4±4.4	16.6±3.2	-0.3	890.0
SerpensMain	18:29:57.10	+01:14:42.9	30.4±6.3	29.0±5.6	0.3	500.0
SerpensMain	18:29:57.90	+01:13:03.9	17.1±0.6	16.9±0.6	-0.0	760.0
SerpensMain	18:29:57.90	+01:14:06.9	17.3±0.6	15.3±0.4	-0.1	700.0
SerpensMain	18:29:59.30	+01:12:24.9	15.3±0.9	15.0±0.8	0.1	410.0
SerpensMain	18:30:02.70	+01:12:27.9	14.4±0.9	13.4±0.7	0.2	540.0
SerpensMain	18:28:52.90	+00:28:46.0	15.4±2.7	16.7±3.6	-0.1	910.0
SerpensMain	18:29:03.10	+00:30:10.0	20.9±6.7	0.0±0.0	-0.6	780.0
SerpensMain	18:29:16.31	+00:18:22.2	16.3±4.4	13.8±3.2	0.1	620.0
SerpensMain	18:29:47.10	+01:16:24.9	16.6±1.1	16.3±0.9	-0.1	810.0
SerpensMain	18:30:00.30	+01:09:45.9	11.7±0.9	11.5±0.9	-0.4	340.0
SerpensMain	18:29:54.50	+00:36:01.0	13.0±1.3	12.0±0.9	-0.3	59.0
SerpensMain	18:29:55.90	+01:14:27.9	25.7±5.0	24.8±4.3	-0.5	1100.0
SerpensMain	18:30:00.30	+01:14:03.9	25.1±3.5	27.2±4.0	-0.6	1300.0
SerpensMain	18:30:01.10	+01:13:24.9	22.6±3.4	28.4±5.3	-0.2	840.0
SerpensN	18:38:59.10	+00:33:05.6	13.0±0.7	12.0±0.3	2.1	140.0
SerpensN	18:39:01.50	+00:30:11.6	10.2±1.9	0.0±0.0	1.3	130.0
SerpensN	18:39:09.50	+00:13:53.6	12.0±1.3	11.1±0.7	0.1	700.0
SerpensN	18:39:09.70	+00:32:41.6	13.2±1.7	13.4±1.7	0.1	800.0
Taurus	04:18:40.68	+28:19:15.0	8.0±0.5	7.8±0.4	0.0	0.0
Taurus	04:20:25.87	+28:19:24.4	6.8±1.4	0.0±0.0	0.0	0.0
Taurus	04:29:23.89	+24:33:00.9	11.6±1.4	11.0±1.1	1.0	0.0
Taurus	04:30:51.70	+24:41:44.8	8.0±0.8	7.9±0.7	0.0	0.0
Taurus	04:32:15.52	+24:28:58.8	9.1±1.0	8.8±0.8	0.0	0.0
Taurus	04:39:14.06	+25:53:19.6	14.0±2.4	10.9±1.0	1.0	0.0
Taurus	04:39:35.33	+25:41:44.6	11.6±0.8	10.5±0.4	1.0	0.0
Taurus	04:39:54.19	+26:03:09.2	14.7±1.2	12.2±0.4	1.0	0.0
Taurus	04:41:12.54	+25:46:34.3	13.6±2.5	0.0±0.0	1.0	0.0
Taurus	04:39:55.93	+25:45:03.3	8.1±0.5	7.8±0.4	0.0	0.0